Imperial College London

PROPERTIES AND TOUGHENING OF SILICA NANOPARTICLE- AND CARBON NANOTUBE-MODIFIED EPOXY POLYMERS

A thesis submitted for the degree of Doctor of Philosophy of Imperial College London and the Diploma of Imperial College

June 2011

By Tsung-Han Hsieh

Department of Mechanical Engineering

Imperial College London

ABSTRACT

The present work investigates the material properties of a thermosetting epoxy polymer modified with various reinforcements of micron-sized glass beads and rubber particles, and nano-sized silica particles and carbon nanotubes. The Young's modulus of the modified epoxies with rigid additives was significantly increased, especially for the nanocomposites containing high contents of nanosilica or nanotubes.

The fracture testing showed that the combination of the soft rubber particles and carbon nanotubes provided the best way to improve the toughness and fatigue performance, because a synergistic effect on the fracture behaviour was obtained in the hybrid-modified epoxies. Fractography showed various mechanisms caused by the addition of the toughening particles, and the main toughening mechanisms are dependent on the modifiers used. Nanotubes operated the debonding, pull-out and void growth mechanisms improve the toughness and fatigue performance of their composites. The inclusion of the rigid spherical particles into the epoxy increased the toughness and fatigue performance via mechanisms of shear band yield and plastic void growth. Rubber cavitation was considered to be the main toughening mechanism in the rubber-modified materials.

Several dispersion methods were examined for the multi-walled carbon nanotubes, and the best way to get well-dispersed nanotubes without significant damage was identified. The level of the nanotube dispersion was assessed using a greyscale analysis and transmission optical microscopy. Finally, a sonication process using an ultrasonic probe was chosen to prepare the nanotube-modified epoxies.

Modelling work was carried out to predict the toughening contribution from the nanosilica and nanotubes. There was a good agreement between the predictions and the experimental results for the toughness. The modified Halpin-Tsai equation was used to calculate the increased modulus caused by the addition of the nanotubes, and the predicted modulus can fit well with the measured values, even at high nanotube contents which resulted in serious agglomeration.

ACKNOWLEDGMENTS

Foremost, I would like to thanks my supervisors, Dr. A. C. Taylor and Prof. A. J. Kinloch for their help and support throughout this project. Ambrose guided me with patience and cleared up the problems I encountered through the course of this PhD. My thanks also to Tony for all of his assistance and suggestions during this project. I would like to thanks Dr. S Sprenger at Nanoresins and Dr. I. A. Kinloch at the University of Manchester for their support of materials in this project.

I would like to give a special thanks to Dr. K. Masania for his help during the course in this PhD. Kunal has been a fantastic partner in the research and kindly shared his data for me. My thanks also to Dr. K Zuo for all his help in sample preparation and fatigue testing, Dr. M. Ardakani for his help with the microscopy and Dr. R. D. Brooker for the AFM training.

A special thanks to many past and present colleagues in the Mechanics of Materials group, in particular to Dr. Y. Liu, Dr. J. Sohn-Lee, Ms. S. Awang-Ngah, Mr. S. H. Lee and Mr. J. Chen. Without the support of my colleagues, the work in this project would have seemed much harder. I also acknowledge the technical and administrative support at the Department of Mechanical Engineering, in particular, Mr. C. R. Jerrard, Mr. A. Choda, Dr. L. Wanigasooriya and Ms. V. Crawford.

Last but not least, I must thank my family for their support and unconditional love, not just through the past four years of my PhD, but up until now. Thanks also to my brother for being a best friend and supporting me with funding during the course of this PhD.

TABLE CONTENTS

ABSTRACT **2**

ACKNOWLEDGMENTS **3**

TABLE CONTENTS **4**

LIST OF FIGURES **8**

LIST OF TABLES **18**

NOMENCLATURE **20**

CHAPTER 1 INTRODUCTION **26**

1.1 Introduction to the Project 26

1.2 Project Aims and Objectives 28

1.3 Thesis Structure 29

CHAPTER 2 LITERATURE REVIEW **31**

2.1 Introduction 31

2.2 Fracture Mechanics 32

2.2.1 Introduction 32

2.2.2 Quasi-static Fracture 32

2.2.3 Fatigue Fracture 34

2.3 Epoxy Polymers 37

2.4 Rubber Particles Toughening Mechanisms 39

2.4.1 Introduction 39

2.4.2 Rubber Bridging 39

2.4.3 Shear Banding 40

2.4.4 Rubber Cavitation 41

2.5 Rigid Particle Toughening 45

2.5.1 Introduction 45

2.5.2 Crack Pinning and Crack Deflection 45

2.5.3 Debonding and Void Growth 48

2.6 Nanoparticle toughening 49

2.6.1 Introduction 49

2.6.2 Toughening Mechanisms for Nanoparticles 49

2.7 Carbon Nanotube Toughening 52

2.7.1 Introduction 52

2.7.2 Toughening Mechanisms in Carbon nanotubes 54

2.8 Conclusions 59

CHAPTER 3 MATERIALS AND MANUFACTURING **60**

3.1 Introduction 60

3.2 Polymer Matrix 61

3.3 Modifiers 62

3.3.1 Glass Bead Microparticles 62

3.3.2 Silica nanoparticles 64

3.3.3 Rubber Microparticles 66

3.3.4 Multi-walled Carbon Nanotubes 68
3.4 Manufacturing 73
3.4.1 Casting Mould and Temperature Cycle 73
3.4.2 CTBN-modified Polymer 75
3.4.3 Glass Bead Microparticle-modified Polymer 76
3.4.4 Nanosilica-modified polymer 78
3.4.5 Hybrid of CTBN/nanosilica 78
3.4.6 Multi-walled Carbon Nanotube-modified polymer 79
3.4.7 Hybrid of CTBN/MWCNTs or Nanosilica/MWCNTs 79
3.5 Conclusions 81
CHAPTER 4 EXPERIMENTAL METHODS 82
4.1 Introduction 82
4.2 Tensile tests 83
4.3 Single edge notch bend tests 86
4.4 Plane-strain Compression Tests 90
4.5 Fatigue tests 93
4.6 Differential Scanning Calorimetry test 99
4.7 Atomic Force Microscopy 100
4.8 Scanning Electron Microcsopy 101
4.9 Summary 102
CHAPTER 5 MULTI-WALLED CARBON NANOTUBE DISPERSION 103
5.1 Introduction 103
5.2 Dispersion Methods 106
5.3 Hot Stage Investigation 120
5.4 Conclusions 124
CHAPTER 6 SILICA NANOPARTICLE AND GLASS MICROPARTICLE-MODIFIED EPOXY 125
6.1 Introduction 125
6.2 Silica Nanoparticle-modified Epoxy Polymers 127
6.2.1 Morphology of Nanosilica-modified Epoxy Polymers 128
6.2.2 Mechanical and Thermal Properties 133
6.2.3 Fracture Toughness and Fracture Energy 137
6.2.4 Fractography and Toughening Mechanisms 141
6.2.5 Compressive Properties 151
6.3 Glass Bead Microparticle-modified Epoxy Polymers 154
6.3.1 Mechanical and Thermal Properties 157
6.3.2 Fracture Toughness and Fracture Energy 161
6.3.3 Fractography and Toughening Mechanisms 166
6.4 Comparison Between Nanoparticle and Microparticle-modified Epoxy Polymers 179
6.5 Conclusions 181
CHAPTER 7 CARBON NANOTUBE-MODIFIED EPOXY 183
7.1 Introduction 183

7.2 Microstructure 185
7.2.1 Unmodified Epoxy 185
7.2.2 MWCNT-modified Epoxy 185
7.3 Mechanical and Thermal Properties 188
7.4 Toughness 191
7.4.1 Fracture toughness and fracture energy 191
7.4.2 Fractography 195
7.4.3 Toughening Mechanisms 196
7.5 Compressive Properties 202
7.6 Fracture Behaviour under Fatigue Loading Conditions 208
7.6.1 Fracture Mechanics Fatigue Data 208
7.6.2 Fractography 212
7.6.3 Fatigue Toughening Mechanisms 215
7.7 Relationship between Static and Fatigue Results 220
7.8 Nanotube Size Effect on the Toughening Performance and Fatigue Performance 225
7.8.1 Introduction 225
7.8.2 Morphology 225
7.8.3 Mechanical Properties and Fracture Behaviour 229
7.8.4 Fractography and Toughening Mechanisms 230
7.8.5 Fracture Behaviour under Fatigue Loading Conditions 232
7.8.6 Fatigue Toughening Mechanisms 233
7.9 Greyscale Analysis 238
7.9.1 Sample preparation 238
7.9.2 Results 240
7.10 Conclusions 243
CHAPTER 8 HYBRID-MODIFIED EPOXY 245
8.1 Introduction 245
8.2 Microstructure 248
8.2.1 Single-phase Modified Epoxy 248
8.2.2 Hybrid-modified Epoxy 249
8.3 Mechanical and Thermal Properties 253
8.4 Toughness 256
8.4.1 Fracture Toughness and Fracture Energy 256
8.4.2 Fractography 261
8.4.3 Toughening Mechanisms 264
8.5 Fracture Behaviour under Fatigue Loading Conditions 272
8.5.1 Fracture Mechanics Fatigue Data 272
8.5.2 Fractography 275
8.5.3 Fatigue Toughening Mechanisms 281
8.6 TOM Observation of the Nanotube Dispersion in Hybrid Modified Polymers 290
8.7 The Effect of the Addition of Hybrid Nano-reinforcements on the Mechanical Properties of Modified Epoxy Polymers 292
8.7.1 Mechanical and Thermal Properties 293
8.7.2 Toughness 295
8.7.3 Toughening Mechanisms 297

8.7.4 Dispersion 299
8.8 Conclusions 303
CHAPTER 9 ANALYTICAL MODEL OF NANOSILICA- AND NANOTUBE-MODIFIED EPOXY 305
9.1 Introduction 305
9.2 Toughening of Nanosilica-modified Epoxy 306
9.2.1 Introduction 306
9.2.2 Shear Band Yielding due to Nanosilica 307
9.2.3 Plastic Void Growth due to Nanosilica 308
9.2.4 Modelling of the Toughness of Nanosilica-modified Epoxy 309
9.2.5 Modelling of the Toughness of Glass Microparticle-modified Epoxy 314
9.3 Toughness of Nanotube-modified Epoxy 317
9.3.1 Introduction 317
9.3.2 Debonding due to Nanotubes 318
9.3.3 Nanotube Pull-out 320
9.3.4 Plastic Void Growth due to Nanotubes 322
9.3.5 Modelling of the Toughness of MWCNT-modified Epoxy 324
9.3.6 The Nanotube Size Effect on the Toughness 326
9.4 The Young's Modulus of Nanotube-modified Epoxy 330
9.4.1 The Modified Halpin-Tsai Equation 330
9.4.2 Modelling of the Young's Modulus of MWCNT-modified Epoxy 336
9.4.3 The Nanotube Size Effect on the Young's Modulus 338
9.5 Conclusions 341
CHAPTER 10 CONCLUDING REMARKS AND FUTURE WORK 343
10.1 Conclusions 343
10.1.1 Nanosilica-modified Epoxy 344
10.1.2 Glass Bead Microparticle-modified Epoxy 345
10.1.3 Nanotube-modified Epoxy 347
10.1.4 Rubber-modified Epoxy 349
10.1.5 Hybrid-modified Epoxy 350
10.1.6 Analytical Modelling 352
10.2 Recommendations for Future Work 354
REFERENCES 356

LIST OF FIGURES

Figure 2.2.1 Schematic model showing the plastic zone [9]. 34
Figure 2.2.2 Fatigue testing curve, showing (I) threshold (stop propagating) region, (II) crack propagation (linear) region and (III) crack initiation (fast fracture) region, modified from [17].....36
Figure 2.3.1 The epoxide endgroup, R represents the molecular structure of the remaining epoxy polymer [25].....37
Figure 2.3.2 Molecular structure of DGEBA [26]. 38
Figure 2.4.1 Crack profiles in a rubber-modified epoxy material, (a) microscopy images and (b) model of rubber bridging [34]. 40
Figure 2.4.2 Distribution of the von Mises Stress around rubber particles, showing a high stress ligament and shear band between rubber particles[38].....41
Figure 2.4.3 The microstructure of the rubber-toughened epoxy polymer, showing (a) original (undeformed) microstructure before loading and (b) fracture surface after fracture tests [42]. 42
Figure 2.4.4 Schematic diagram of the mechanisms occurring at the crack tip in (a) unmodified epoxy, (b) rubber-modified epoxy before rubber cavitation and (c) after rubber cavitation [43]. 43
Figure 2.4.5 Distribution of the von Mises stress around rubber particles in a unit cell under triaxial loading, showing (a) before cavitation and (b) after cavitation [44].....44
Figure 2.5.1 The crack pinning mechanism, showed by (a) a schematic model and (b) a optical micrograph of the glass particle toughened polymer [53]. 46
Figure 2.5.2 Fracture surfaces of the glass microparticle-modified polymer materials, showing crack pinning and deflection [45, 55]. 47
Figure 2.5.3 The crack deflection mechanism in microparticle-modified polymers [57].....47
Figure 2.5.4 Fracture surface images, showing particle interfacial debonding, and subsequent plastic void growth in the microparticle-modified polymers [58]. ..48
Figure 2.6.1 Schematic showing crack tip in the nanosilica-modified polymer [7]…50
Figure 2.6.2 Plastic void growth mechanism in the nanosilica-modified polymer using (a) FEG-SEM and (b) AFM [5]. 51
Figure 2.7.1 Schematic view of a crack propagating in a composite: (a) through a microfibre (carbon fibre): (b) through a series of nanotubes (CNTs) of total volume equivalent to the volume of the microfibre in (a) [86]. 54
Figure 2.7.2 SEM image of the fracture surface of MWCNT-modified polymer [87]. 55
Figure 2.7.3 The observation of crack-bridging in DWCNT/epoxy composites via SEM [86].....56
Figure 2.7.4 The observation of crack-bridging in MWCNT/PS composites via TEM [88].....56
Figure 2.7.5 schematic models showing (a) CNT pull-out and (b) CNT crack bridging [86].....57
Figure 2.7.6 Schematic model showing the nanotube telescopic pull-out mechanism [85].....58

Figure 3.3.1 TEM image of the epoxy nanocomposite containing 5.0 wt% silica nanoparticles, showing well-dispersed particles [91]. *65*

Figure 3.3.2 The particle number density versus the particle size for the nanosilica particles, determined by small angle neutron scattering (SANS) [91]. *65*

Figure 3.3.3 TEM image of the epoxy nanocomposite containing 5.0 wt% silica nanoparticles, showing nanosilica agglomeration [91]. *66*

Figure 3.3.4. Optical micrographs of a sample of 9.0 wt% CTBN rubber/DGEBA polymer during curing, showing how the morphology of the rubber-modified epoxy varies with respect to temperature and time [23] *67*

Figure 3.3.5 The equipment of the CVD process used for generating the aligned multi-walled carbon nanotubes. *69*

Figure 3.3.6 FEG-SEM image of the aligned multi-walled carbon nanotubes (standard nanotubes). *70*

Figure 3.3.7 FEG-SEM image of the aligned multi-walled carbon nanotubes (low quality nanotubes). *70*

Figure 3.3.8 Raman spectra of the carbon nanotubes synthesized on the SiN_x-coated substrate [92]. *71*

Figure 3.3.9 Raman spectra taken in (a) single-walled carbon nanotubes, and (b) multi-walled carbon nanotubes [94] *72*

Figure 3.4.1 The casting gravity mould. *73*

Figure 3.4.2 Temperature cycle used in the study. *75*

Figure 3.4.3 The airtight mould used for preparing glass bead-modified bulk polymer samples. *77*

Figure 4.2.1 Tensile testing specimen geometry (unit : mm) [95, 96]. *83*

Figure 4.2.2 The test set up used to measure the Young's modulus of the polymer-based composites. *85*

Figure 4.3.1 Schematic of the SENB test [97]. *87*

Figure 4.3.2 Determination of K_Q [97]. *88*

Figure 4.4.1 Geometry for the plane-strain compression specimens and indenters [23, 99]. *90*

Figure 4.4.2 The set square and indentors used in the PSC tests. *91*

Figure 4.5.1 Schematic diagram of the CT specimen, showing the dimensions in mm [100] *94*

Figure 4.5.2 CT specimen and the testing set up for the fatigue tests. *94*

Figure 4.5.3 Schematic diagram of the sinusoidal loading used in the fatigue tests, showing all the displacement-related parameters. *96*

Figure 4.5.4 A typical plot of log(da/dN) versus log(G_{max}) of the unmodified anhydride-cured DGEBA epoxy, showing the linear Paris low region and threshold region. *98*

Figure 4.6.1 The DSC curve plotting the heat flow versus temperature for the unmodified anhydride-cured DGEBA epoxy, showing the glass transition temperature region. *99*

Figure 4.7.1 The atomic force microscope. *100*

Figure 4.8.1 The FEG-SEM used in this study. *101*

Figure 5.1.1 The change of the viscosity versus time for the anhydride-cured DGEBA epoxy polymer as the resin went through the cure cycle [23]. *105*

Figure 5.2.1 FEG-SEM images of the multi-walled carbon nanotubes before being added into the epoxy resin, showing (a) aligned multi-walled carbon nanotube films with thickness around 140 μm, and (b) individual nanotubes with a mean diameter of 120 nm.....107

Figure 5.2.2 Photograph of the ultrasonic bath, used for dispersing the multi-walled carbon nanotubes in the epoxy resin.....108

Figure 5.2.3 Optical microscope images of the uncured nanotube-modified epoxy resins, showing the nanotube dispersion effect caused by different dispersion methods of using the ultrasonic probe for (a)10 minutes, (b)20 minutes, (c)30 minutes, (d) 60 minutes, (e)120 minutes, and (f)using the ultrasonic bath for 40 hours, all the samples at 60 °C. 110

Figure 5.2.4 The specimen of the uncured sample used for the dispersion tests.....111

Figure 5.2.5 FEG-SEM images of the nanotubes after sonication for 30 minutes, showing (a) nanotube length of 120 μm and (b) nanotube diameter of 120 nm. 116

Figure 5.2.6 Photograph showing (a) the experiment for extracting the sonicated nanotubes from the nanotube-modified epoxy resin, (b)-(c) the nanotubes deposited on the surface of a Teflon filter paper. 117

Figure 5.2.7 FEG-SEM of the multi-walled carbon nanotubes after probe sonication for 30 minutes deposited on a standard filter paper.....118

Figure 5.2.8 FEG-SEM images of the nanotubes after probe sonication for 120 minutes, showing (a) nanotube length of 70 μm and (b) nanotube diameter of 120 nm.....119

Figure 5.3.1 Photograph showing the hot stage fitted to the optical microscope. ...120

Figure 5.3.2 The line graph showing the cure schedule in the hot stage investigation, and the imaged points at different temperatures during the cure cycles. 122

Figure 5.3.3 The hot stage images for the sample containing of 0.05 wt% nanotubes dispersed with the epoxy matrix using the ultrasonic probe sonication for 30 minutes. The images were taken at (a) 60 °C, (b) 80 °C, (c)90 °C, (d)100 °C, (e) 120 °C and (f) 150 °C. 123

Figure 6.2.1 Atomic force microscopy image of the cured unmodified polymer.....129

Figure 6.2.2 Field emission gun scanning electron microscopy image of the unmodified polymer (the direction of crack growth is from the right to the left). 129

Figure 6.2.3 Atomic force microscopy image of the nanocomposites, showing the sample of (a)10-F400 and (b)20-F400. 131

Figure 6.2.4 Atomic force microscopy image of the nanocomposites with the treated nanoparticles, showing the sample of (a) 10-F400-S and (b) 10-XP. 132

Figure 6.2.5 Young's modulus of the nanocomposites. 134

Figure 6.2.6 The stress-strain curve for 10 wt% untreated (10-F400) and treated (10-F400-S) nanosilica-modified polymers in plane stress.....135

Figure 6.2.7 Photograph of the thin tensile specimen. 136

Figure 6.2.8 Residual strength as a function of thickness [115]. 136

Figure 6.2.9 The typical load versus displacement curve of the SENB test on the unmodified epoxy polymer. 139

Figure 6.2.10 The fracture toughness of the nanocomposites with various nanosiilca loading and surface treatments.....140

Figure 6.2.11 The fracture energy of the nanocomposites with various nanosilica loading and surface treatments. *140*

Figure 6.2.12 Field emission gun scanning electron microscopy images of the fracture surfaces, showing (a) unmodified polymer and nanocomposites with (b) 10 wt% "F400" nanosilica, (c) 10 wt% "Nanopox XP" nanosilica, (d) 10wt% "F400" nanosilica with the additional silane treatment. *142*

Figure 6.2.13 Field emission gun scanning electron microscopy images of the nanocomposites with 10 wt% of "F400" nanosilica particles, showing plastic void growth as circled. *144*

Figure 6.2.14 Field emission gun scanning electron microscopy images of the nanocomposites with 10 wt% of "Nanopox XP" nanosilica particles, showing plastic void growth as circled. *145*

Figure 6.2.15 Field emission gun scanning electron microscopy images of the nanocomposites with 10 wt% of "F400" nanosilica particles with the additional silane treatment, showing plastic void growth as circled. *146*

Figure 6.2.16 Relative fracture energy versus content of silica nanoparticles, for "F400", "F400-S" and "Nanopox XP" systems, (note this uses $G_{Ic(unmodified)}$ *of "Control-S" for the "F400-S" system).* *149*

Figure 6.2.17 Field emission gun scanning electron microscopy images of "Control-S" sample, showing (a)-(b) river lines, (c) plate-like fractures. *150*

Figure 6.2.18 Compressive stress versus compressive strain for the unmodified polymer and the nanosilica-modified polymers. *152*

Figure 6.3.1 Optical microscopy images of the glass bead microparticles, showing (a) small glass beads with a mean diameter of 3.5 µm. and (b) large glass beads with a mean diameter of 275 µm. *155*

Figure 6.3.2 Young's modulus of the glass bead microparticle-modified epoxy polymers. *158*

Figure 6.3.3 Relative modulus versus content of dispersed spheres with various diameters: (□) d = 5~10 µm, (△) d = 10~20 µm, (╳) d = 30~40 µm and (○) d = 75-90 µm [121]. *159*

Figure 6.3.4 Glass transmission temperature of the glass bead microparticle-modified epoxy polymers. *160*

Figure 6.3.5 The cured plate of the large glass bead/epoxy composite (10-L-Control), showing the glass beads sinking to the bottom of the mould. *162*

Figure 6.3.6 Fracture toughness of the glass bead microparticle-modified epoxy polymers. *164*

Figure 6.3.7 Fracture energy of the glass bead microparticle-modified epoxy polymers. *165*

Figure 6.3.8 FEG-SEM images of the fracture surfaces, (a,b) 10-S-Control, (c,d) 20-S-Control, (e,f) 10-S-Silane and (g,h) 10-S-Frekote. *167*

Figure 6.3.9 The schematic tail structure on the fracture surface of particle-modified composites. *168*

Figure 6.3.10 FEG-SEM images of the microparticle-modified polymers with 10wt% untreated small glass beads (10-S-Control), showing (a) crack deflection (b) tail structure behind the particle and (b, c)debonding and subsequent plastic void growth. *169*

Figure 6.3.11 FEG-SEM images of the microparticle-modified polymers with 10wt% silane treated small glass beads, showing (a) crack deflection (b,c) debonding, and subsequent plastic void growth. 171

Figure 6.3.12 Schematic illustration of the path of a crack around a rigid particle in the composite, showing (a) crack approaching particle, (b) crack tip moving around equator of poorly-bonded particle and (c) crack tip attracted to poles of well-bonded particle [46]…….172

Figure 6.3.13 FEG-SEM images of the microparticle-modified polymers with 10wt% release agent "Frekote" treated small glass beads, showing (a) glass bead agglomeration and (b,c) debonding,and subsequent plastic void growth. 174

Figure 6.3.14 Optical microscopy and FEG-SEM images of the fracture surface of the polymer-based composite reinforced with 10 wt% of untreated large glass beads (10-L-Control), showing (a) glass bead agglomerates via optical microscopy, (b) glass bead agglomerates via FEG-SEM and (c)particle debonding, and subsequent plastic void growth. 176

Figure 6.3.15 Optical microscopy and FEG-SEM images of the fracture surface of the polymer-based composite reinforced with 10 wt% of the silane treated large glass beads (10-L-Silane), showing (a) glass bead agglomerates via optical microscopy, (b) glass bead agglomerates via FEG-SEM and (c) glass bead bonded well with epoxy polymer. 177

Figure 6.3.16 Optical microscopy and FEG-SEM images of the fracture surface of the polymer-based composite reinforced with 10 wt% of the release agent treated large glass beads (10-L-Frekote), showing (a) glass bead agglomerates via optical microscopy, (b) glass bead agglomerates via FEG-SEM and (c) particle debonding, and subsequent plastic void growth.....178

Figure 6.4.1 Normalised fracture energy of the composites with the silica nanoparticles and glass bead microparticles with various surface treatments. 180

Figure 7.2.1 AFM images of the morphology of the MWCNT-modified epoxy polymers with (a) 0.1 wt%, (b) 0.2 wt% and (c) 0.5 wt% of the MWCNTs. 187

Figure 7.3.1 The mechanical and thermal properties of the MWCNT-modified composites. 189

Figure 7.3.2 Glass transition temperature versus nanotube content [128].....190

Figure 7.4.1 The fracture toughness and fracture energy of MWCNT-modified composites. 193

Figure 7.4.2 The comparison between the experimental toughness in this study and the toughness reported in literature (all the matrices are epoxy, and the nanotubes are untreated) [74, 129-132].....194

Figure 7.4.3 Field emission gun scanning electron microscopy (FEG-SEM) images of the fracture surfaces, showing (a) unmodified, (b) 0.1 wt%, (c) 0.2 wt% and (d) 0.5 wt% of MWCNTs.....196

Figure 7.4.4 Field emission gun scanning electron microscopy (FEG-SEM) images captured of 0.5 wt% MWCNTs sample. (a,b) showing the nanotube pull-out, (c,d) showing nanotube bridging.....197

Figure 7.4.5 The schematic model of nanotube pull-out mechanism. (a) nanotube original state, (b) nanotube ruptures, (c) nanotube pull-out (efficient pull-out), and (d) nanotube completely pulled out from the fracture surface.....198

Figure 7.4.6 Field emission gun scanning electron microscopy (FEG-SEM) images captured of 0.5 wt% MWCNTs sample showing the debonding and plastic void growth around the nanotubes. 201

Figure 7.5.1 Compressive stress versus compressive strain for unmodified polymer and MWCNT-modified nanocomposite at 0.5 wt%. 204

Figure 7.5.2 The state of the specimen at different levels of stress during plane strain compression test on unmodified epoxy polymer (the thickness of the specimen is 3 mm). 205

Figure 7.5.3 Samples of the unmodified epoxy polymer and the nanocomposite with 0.5wt% nanotubes for TOM observation. 206

Figure 7.5.4 TOM images from compressed samples of the unmodified polymer and the nanocomposite with 0.5 wt% nanotubes, (the length of the compressed region is 12 mm). 207

Figure 7.6.1 Rate of crack growth versus maximum applied strain energy release rate in the fatigue cycle for the unmodified epoxy and nanocomposites. 209

Figure 7.6.2 The threshold fracture energy and the ratio of G_{th}/G_{Ic} versus the weight percent of the MWCNTs. 211

Figure 7.6.3 Photograph and schematic of the fracture surface of tested compact tension specimen after fatigue failure. 212

Figure 7.6.4 FEG-SEM images of the fatigue fracture surfaces of the nanocomposite containing 0.2 wt% MWCNTs, showing the regions of (a,b) crack initiation, (c,d) propagation, (e,f) threshold. (Crack growth is from the right to the left). 214

Figure 7.6.5 A schematic fatigue crack. 216

Figure 7.6.6 FEG-SEM images showing voids around nanotubes in the threshold region of the fatigue fracture surface of the nanocomposite containing (a) 0.2wt% MWCNTs, (b) 0.5 wt% MWCNTs. 217

Figure 7.6.7 Tensile stress-strain curve for epoxy at different stain rates [140]. 217

Figure 7.6.8 SEM image showing CNT bridging and pullout of the fatigue crack in the modified polymer with 0.2 wt% nanotubes. 219

Figure 7.7.1 The relationship between the maximum fracture energy at the threshold region and the quasi-static fracture energy of the MWCNT-modified nanocomposites. 220

Figure 7.7.2 The relative fracture energy and relative threshold fracture energy versus the weight percent of the MWCNTs. 223

Figure 7.7.3 The schematic illustration of the nanotube pull-out mechanism in different level of applied stress, (a) at a high applied stress, (b) at a low applied stress. 224

Figure 7.8.1 The FEG-SEM images showing the as-received appearance of the low quality multi-walled carbon nanotubes. 226

Figure 7.8.2 AFM images of the morphology of the modified epoxy polymer with the low quality multi-walled carbon nanotubes at 0.2 wt%. 228

Figure 7.8.3 Field emission gun scanning electron microscopy (FEG-SEM) images of 0.2 wt% low quality MWCNTs sample, showing (a) the fracture surface at a low magnification, (b) the dispersion of the nanotubes, (c) the nanotube pull-out, (d) nanotube agglomerate. 232

Figure 7.8.4 Rate of crack growth versus maximum applied strain energy release rate for unmodified epoxy and nanotube-modified epoxy with different types of multi-wall carbon nanotubes. 233

Figure 7.8.5 FEG-SEM images of the fatigue fracture surfaces of the nanocomposite containing 0.2wt% low quality MWCNTs, for the regions of (a,b) crack initiation, (c,d) propagation, (e,f) threshold. (the direction of fatigue crack growth is from right to left). 235

Figure 7.8.6 The FEG-SEM images of the nanotube-modified epoxy polymer by the low quality carbon nanotubes at 0.2 wt% showing the nanotube pull-out and plastic void growth (indicated with arrows). 236

Figure 7.8.7 The FEG-SEM images of the nanotube-modified epoxy polymer with the low quality carbon nanotubes at 0.2 wt%, showing the crack deflection mechanism. 237

Figure 7.9.1 The TOM images and the greyscale histogram (umber of pixels versus grayscale value) of the nanotube-modified epoxy polymer with (a) 0.1wt% MWCNTs, (b) 0.2 wt% MWCNTs, (c) 0.5wt% MWCNTs. 239

Figure 7.9.2 The TOM image and the greyscale histogram of the well-dispersed nanotube sample with 0.001 wt% (with a single and narrow peak, low value of the standard deviation and the mean lies in the centre of range). 240

Figure 7.9.3 The greyscale analysis results showing the mean value of the histogram image versus the nanotube loading. 241

Figure 7.9.4 The TOM images and the greyscale histogram of the nanotube-modified amine-cured epoxy polymer with (a) 0.1wt% MWCNTs, (b) 0.2 wt% MWCNTs (the MWCNTs are from Thomas Swan & Co Ltd.) [108]. 242

Figure 8.2.1 Atomic force microscopy (AFM) image of modified material with 9.0 wt% CTBN rubber particles. 248

Figure 8.2.2 AFM image of the hybrid-modified epoxy polymer (9R-0.2C) containing 9.0 wt% rubber particles and 0.2 wt% carbon nanotubes, showing nanotube agglomerates as circled. 250

Figure 8.2.3 AFM image of the hybrid-modified epoxy polymer (10N-0.2C) containing 10 wt% nanosilica particles and 0.2 wt% carbon nanotubes, showing nanotube agglomerates as circled. 250

Figure 8.2.4 AFM image of the hybrid-modified epoxy polymer (9R-10N) containing 10 wt% nanosilica particles and 9 wt% rubber particles in different scanning size (a) 10 μm square and (b) 5 μm square, showing nanosilica agglomerates as circled. 251

Figure 8.3.1 The Young's modulus of the hybrid-modified epoxy polymers. 255

Figure 8.4.1 The fracture toughness and fracture energy of hybrid-modified epoxy polymers. 257

Figure 8.4.2 The schematic illustration showing the synergistic effect of the hybrid-toughener of nanotubes and rubber particles on the fracture energy. 259

Figure 8.4.3 The schematic illustration showing no synergistic effect caused by the addition of the nano-reinforcements (nanosilica and nanotubes) on the fracture energy. 260

Figure 8.4.4 FEG-SEM images of the fracture surfaces of (a) unmodified polymer and single-phase modified epoxy polymers with (b)10 wt% nanosilica, (c) 9.0 wt% rubber particles, and (d) 0.2 wt% multi-walled carbon nanotubes. 262

Figure 8.4.5 FEG-SEM images of the fracture surfaces for the foumulations with various hybrid reinforcements, (a) 9R-0.2C, (b) 10N-0.2C, (c) 9R-10N. 263

Figure 8.4.6 Field emission gun scanning electron microscopy (FEG-SEM) images of 9 wt% CTBN rubber particles (9R) sample showing rubber particle cavitation. 265

Figure 8.4.7 Field emission gun scanning electron microscopy (FEG-SEM) images captured of 9 wt% CTBN and 0.2 wt% carbon nanotubes (9R-0.2C) hybrid-modified epoxy polymer sample, showing (a) rubber cavitation and nanotube pull-out, (b) showing void growth associated with the nanotubes, (c-d) showing the nanotubes punctured into the rubber particles and void associated with rubber particle, (e-f) showing voids growth in nanotube-rich areas. 266

Figure 8.4.8 The viscosity versus of weight loading of CTBN rubber particles [147]. 268

Figure 8.4.9 FEG-SEM images of the 10N-0.2C hybrid-modified epoxy polymer sample, showing (a) nanotube pull-out, (b) plastic void growth associated with nanotube debonding, (c) void growth caused by the nanotube debonding, as indicated by arrows, and nanosilica debonding as circled.....269

Figure 8.4.10 FEG-SEM image of the fracture surface for the 10N-9R hybrid-modified epoxy polymer sample, showing rubber cavitation and void growth caused by the nanosilica as circled.....270

Figure 8.5.1 Rate of crack growth versus maximum applied strain energy release rate in the fatigue cycle for unmodified epoxy and modified epoxy with single-phase and hybrid reinforcements. 273

Figure 8.5.2 FEG-SEM images of the fatigue fracture surfaces of the modified polymer containing 10 wt% nanosilica particles (10N), for the regions of (a,b) crack initiation, (c,d) propagation, (e,f) threshold. (Crack growth is from right to left). 276

Figure 8.5.3 FEG-SEM images of the fatigue fracture surfaces of the modified polymer containing 9 wt% CTBN rubber particles (9R), for the regions of (a,b) crack initiation, (c,d) propagation, (e,f) threshold. (Crack growth is from right to left). 277

Figure 8.5.4 FEG-SEM images of the fatigue fracture surfaces of the hybrid-modified polymer containing 9 wt% CTBN rubber particles and 0.2 wt% MWCNTs (9R-0.2C), for the regions of (a,b) crack initiation, (c,d) propagation, (e,f) threshold. (Crack growth is from right to left).....278

Figure 8.5.5 FEG-SEM images of the fatigue fracture surfaces of the hybrid-modified polymer containing 9 wt% CTBN rubber particles and 10 wt% nanosilica particles (9R-10N), for the regions of (a,b) crack initiation, (c,d) propagation, (e,f) threshold. The nanosilica agglomerates are indicated (Crack growth is from right to left).....279

Figure 8.5.6 FEG-SEM images of the fatigue fracture surfaces of the hybrid-modified polymer containing 10 wt% nanosilica particles and 0.2 wt% MWCNTs (10N-0.2C), for the regions of (a,b) crack initiation, (c,d) propagation, (e,f) threshold. (Crack growth is from right to left).....280

Figure 8.5.7 FEG-SEM image of the fracture surface at the threshold region of the rubber-modified polymer (9R), showing the ridges starting at rubber particles, as indicated (crack growth is from right to left). 281

Figure 8.5.8 FEG-SEM image of the fracture surface at the threshold region of the (9R) rubber-modified polymer showing rubber-particle cavitation and subsequent void growth.....282

Figure 8.5.6 A high magnification FEG-SEM image of the fracture surface at threshold region of the nanosilica/epoxy material (10N), showing plastic void growth as circled.....283

Figure 8.5.7 FEG-SEM image of the fracture surface at the threshold region for the nanotube-modified polymer at 0.2 wt% (0.2C), showing nanotube pull-out and plastic void growth as indicated. 284

Figure 8.5.8 FEG-SEM image of the fracture surface at the threshold region of the hybrid-modified polymer containing 9 wt% rubber particles and 10 wt% silica nanoparticles (9R-10N), showing rubber cavitation and subsequent void growth, and nanosilca plastic void growth as circled.....285

Figure 8.5.9 FEG-SEM images of the fracture surface at the threshold region for the 9R-0.2C hybrid-modified polymer, showing nanotube pull-out and plastic void growth, and rubber cavitation. 287

Figure 8.5.10 FEG-SEM images of fracture surface at the threshold of the nano-hybrid modified polymer containing 10 wt% nanosilica and 0.2 wt% nanotubes (10N-0.2C), showing nanotube pull-out, nanotube plastic void growth and nanosilica plastic void growth as circled. 288

Figure 8.6.1 TOM images and the greyscale histogram of the hybrid modified epoxy polymers with nanotubes, (a) 9R-0.2C sample, (b) 10N-0.2C sample.....291

Figure 8.7.1 Young's modulus of the R1D1 nanocomposites. 294

Figure 8.7.2 Fracture energy of the R1D1 nanocomposites containing nanosilica and MWCNTs. 296

Figure 8.7.3 FEG-SEM image of the fracture surface of R1D1 nanocomposite showing nanotube pull-out as indicated (6.0 wt% silica and 0.18% nanotubes). 298

Figure 8.7.4 FEG-SEM image of the fracture surface of R1D1 nanocomposite showing void growth around the nanotube as indicated (6.0 wt% silica and 0.18% nanotubes).....298

Figure 8.7.5 FEG-SEM image of the fracture surface of R1D1 nanocomposite showing void growth associated with nanosilica debonding as circled (6.0 wt% silica and 0.18% nanotubes). 299

Figure 8.7.6 AFM images of the nanocompiste containing 6.0 wt% nanosilica and 0.18 wt% MWCNTs using R1D1 nano-reinforcement. 300

Figure 8.7.7 TOM images of R1D1 nanocomposites with various concentrations of nanosilica particles and multi-walled carbon nanotubes. 301

Figure 8.7.8 TOM images and greyscale histograms of the R1D1 nanocomposites of 6.0 wt% nanosilica system with various nanotube loadings at (a) 0.024 wt%, (b) 0.06 wt%, (c) 0.12 wt% and (d) 0.18 wt%. 302

Figure 9.2.1 The experimental results of the fracture energy and the predicted values of the fracture energy in the F400 system (the individual contributions are shown inset).....311

Figure 9.2.2 The experimental results of the fracture energy and the predicted values of the fracture energy of the F400-S and Nanopox XP nanocomposites (the individual contributions are shown inset).....313

Figure 9.2.3 The experimental results of the fracture energy fitted by the predicted values of the fracture energy of the small glass bead-modified epoxies.....316

Figure 9.3.1 The illustration of the plastic void growth mechanism. 323

Figure 9.3.2 The experimental results of the fracture energy fitted by the predicted values of the fracture energy (the individual contributions are shown inset). .326

Figure 9.3.3 the effect of nanotube length on the fracture energy (nanotube diameter = 120 nm).....327

Figure 9.3.4 The effect of the nanotube diameter on the fracture energy (nanotube lenght = 120 μm). 328

Figure 9.3.5 The effect of the nanotube diameter on the fracture energy (various nanotubes with the same aspect ratio = 1000). 329

Figure 9.4.1 Experimental Young's modulus of the MWCNT-modified epoxy polymer fitted by Halpin-Tsai equation with the orientation factor by various Young's modulus of the multi-walled carbon nanotubes (the best fit is E_f =1100 GPa). 333

Figure 9.4.2 The effect of the agglomeration-related constant a on the Young's modulus of the MWCNT-modified epoxy polymer (the best fit is a_C=9.15). 334

Figure 9.4.3 The effect of the agglomeration-related constant b_C on the Young's modulus of the MWCNT-modified epoxy polymer (the best fit is b_C=0.12). 335

Figure 9.4.4 The experimental results of the Young's modulus fitted by the modified Halpin-Tsai equation with the orientation factor, α, and the (agglomeration-related) exponential shape factor, ξ.....337

Figure 9.4.5 The effect of the nanotube length on the stiffness of nanotube-modified polymers (a fixed nanotube diameter = 120 nm).....339

Figure 9.4.6 The effect of the nanotube diameter on the stiffness of nanotube-modified polymers (a fixed nanotube length = 120 μm). 340

LIST OF TABLES

Table 2.7.1 Summary of characteristics of carbon nanotubes [71].....53
Table 3.3.1 The typical openings in laboratory sieve series [90].....63
Table 5.2.1 Summary of ultrasonic bath and ultrasonic probe [109]. 112
Table 5.2.2 Summary of the dispersion testing results. 113
Table 6.2.1 Formulations of nanocomposites with silica nanoparticles. 128
Table 6.2.2 The mechanical and thermal properties of the nanosilica-modified nanocomposites......133
Table 6.2.3 The fracture toughness and fracture energy of the nanosilica-modified polymer composites......139
Table 6.2.4 Summary of the results from the photographic analysis of the fracture surfaces of the nanocomposites, showing the amount of the void growth and the diameter of the voids......147
Table 6.2.5 The plane strain compression testing results of compressive Young's modulus, E_c, compressive true yield strength, σ_{yc}, compressive yield strain, ε_{yc}, and compressive failure strain, γ_{fc}, of the nanocomposites reinforced with the silica nanoparticles......152
Table 6.3.1 Surface treatments used in glass bead microparticle-modified epoxy polymers and their effects on particle/epoxy adhesion......156
Table 6.3.2 Formulations of glass bead microparticle-modified epoxy polymers with various surface treatments......156
Table 6.3.3 The mechanical and thermal properties of the glass bead microparticle-modified epoxy polymers......158
Table 6.3.4 The fracture toughness and fracture energy of the glass bead microparticle-modified epoxy polymers.....162
Table 7.3.1 The mechanical and thermal properties of the MWCNT-modified composites......188
Table 7.4.1 The fracture toughness and fracture energy of the MWCNT-modified composites......191
Table 7.4.2 The summary of the toughening mechanisms of the MWCNTs-modified epoxy polymers......200
Table 7.5.1 The plane strain compression testing results of compressive Young's modulus, E_c, compressive true yield stress, σ_{yc},, compressive yield strain, ε_{yc}, and compressive failure strain, γ_{fc}, of the nanocomposites. 203
Table 7.6.1 Summary of the fatigue testing results of fatigue threshold and Paris-law gradient of the MWCNT-modified polymers......208
Table 7.6.2 The summary of the toughening mechanisms of the MWCTs-modified epoxy polymers with 0.2 wt% nanotubes. 218
Table 7.8.1 The dimensions and morphology of standard nanotubes and low quality nanotubes, and the characteristics of their nanocomposites. 227
Table 7.9.1 The summary of the greyscale analysis.....241
Table 8.1.1 The formulations of the hybrid-modified epoxy polymers. 246
Table 8.2.1 Summary of the morphology of the hybrid-modified epoxy polymers. ..252

Table 8.3.1 The mechanical and thermal properties of hybrid-modified epoxy polymers. 254
Table 8.4.1 The fracture toughness and fracture energy of hybrid-modified epoxy polymers. 256
Table 8.4.2 Summary of the toughening mechanisms caused by the hybrid reinforcements. 271
Table 8.5.1 Summary of the fatigue testing results of the maximum applied strain energy release rate in the threshold region and Paris-law gradient of the hybrid-modified epoxy polymers. 274
Table 8.5.2 Summary of the fatigue toughening mechanisms caused by the hybrid reinforcements. 289
Table 8.7.1 The formulations of the hybrid-modified epoxy composites with R1D1 nano-hybrid reinforcements. 292
Table 8.7.2 The mechanical and thermal properties of the nanocomposites with R1D1 nano-reinforments. 294
Table 8.7.3 Fracture toughness and fracture energy of R1D1 nanocomposites. 295
Table 9.2.1 The parameters used in the modelling for predicting the fracture energy of the nanosilica-modified polymers. 310
Table 9.2.2 The measured and predicted values of the fracture energy in the F400 system. 310
Table 9.2.3 The measured and predicted values of the fracture energy in the F400-S system. 312
Table 9.2.4 The measured and predicted values of the fracture energy in the Nanopox XP system. 312
Table 9.2.5 The measured and predicted values of the fracture energy in the S-Control system (containing untreated small glass beads). 314
Table 9.2.6 The measured and predicted values of the fracture energy in the S-Silane system (containing silane-treated small glass beads). 314
Table 9.2.7 The measured and predicted values of the fracture energy in the S-Frekote system (containing Frekote-treated small glass beads). 315
Table 9.3.1 The weight percent of the multi-walled carbon nanotubes corresponding to the volume fraction of nanotubes. 319
Table 9.3.2 The parameters used in the modelling studies for predicting the fracture energy of the MWCNT-modified epoxy polymers. 324
Table 9.3.3 The predicted and measured values of the fracture energy of the MWCNT-modified epoxy polymers. 325
Table 9.4.1 The parameters used in the modified Halpin-Tsai equation for fitting the Young's modulus of the nanotube-modified epoxy polymer. 335
Table 9.4.2 The predicted and measured values of the Young's modulus of the MWCNT-modified epoxy polymer. 337

NOMENCLATURE

Abbreviations

AFM	Atomic force microscopy
AEW	Anhydride equivalent weight
ASTM	American society for testing and materials
CFRP	Carbon-fibre reinforced polymer
CNT	Carbon nanotube
CT	Compact tension
CTBN	Carboxyl-terminated butadiene-acrylonitrile
CTOD	Crack tip opening displacement
CVD	Chemical vapour deposition
DGEBA	Diglycidyl ether of bisphenol A
DSC	Differential scanning calorimetry
EEW	Epoxide equivalent weight
FCP	Fatigue crack propagation
FEG-SEM	Field emission gun scanning electron microscopy
FRP	Fibre reinforced polymer
GFRP	Glass-fibre reinforced polymer
ISO	International organization for standardization
LEFM	Linear elastic fracture mechanics
MWCNT	Multi-walled carbon nanotube
PSC	Plane strain compression
RIFT	Resin infusion under flexible tooling
SANS	Small angle neutron scattering
SCCM	Standard cubic centimetre per minute
SD	Standard deviation
SEM	Scanning electron microscopy
SENB	Single-edge notched bend
SSA	Specific surface area
SWCNT	Single-walled carbon nanotube

TEM	Transmission electron microscopy
TOM	Transmission optical microscopy
vol. %	Volume fraction
wt. %	Weight fraction
xC	Carbon nanotube content (by wt.)
y-F400	Nanosilica (F400) content (by wt.)
y-F400-S	Nanosilica (F400 plus silane) content (by wt.)
y-XP	Nanosilica (Nnaopox XP) content (by wt.)
y-L-Control	Large glass bead (untreated) content (by wt.)
y-L-Frekote	Large glass bead (Frekote-treated) content (by wt.)
y-L-Silane	Large glass bead (silane-treated) content (by wt.)
y-S-Control	Small glass bead (untreated) content (by wt.)
y-S-Frekote	Small glass bead (Frekote-treated) content (by wt.)
y-S-Silane	Small glass bead (silane-treated) content (by wt.)
yN-xC	Nanosilica content and carbon nanotube content (by wt.)
zR	CTBN content (by wt.)
zR-xC	CTBN content and carbon nanotube content (by wt.)
zR-yN	CTBN content and nanosilica content (by wt.)

English Alphabet

a	Crack length
a_C	Agglomeration-related constant
A	Material constant
b_C	Agglomeration-related constant
B	Thickness
B_c	Compressed thickness
C	Specimen compliance
da	Change in crack length
dN	Change in number of load cycles
da/dN	Crack growth rate per cycle
D	Diameter
D_f	Diameter of fibre or nanotube
e	Extension
E	Young's modulus
E_c	Compressive Young's modulus
E_f	Young's modulus of nanotube
$f(x)$	SENB shape factor as a function of x
$f'(x)$	CT shape factor as a function of x
$F'(r_y)$	Modified function with respect to r_p and r_y
G_{Ic}	Fracture energy or critical strain energy release rate
G_{if}	Interfacial fracture energy
G_{max}	Maximum fracture energy
G_{min}	Minimum fracture energy
G_{th}	Maximum fracture energy at threshold
K_{Ic}	Fracture toughness or critical stress intensity factor
K_Q	Trial value of K_{Ic}
K_{max}	Maximum fracture toughness
K_{min}	Minimum fracture toughness
K_{sp}	Stress concentration factor for a rigid particle
K_v	Stress concentrations factor for a void
l_c	Critical length of fibre

l_d	Length of debonded fibre
l_e	Efficient pull-out length
l_f	Length of fibre
L	Length
L_g	Gauge length
L_s	Length of span
m	Paris law constant
N	Number of cycles
N_f	Number of fibres
P	Tensile load
P_c	Critical load
P_Q	5% offset of P_{max}
P_{max}	Maximum load
r_f	Radius of fibre or nanotube
r_p	Radius of particles
r_{pz}	Radius of the plastic zone
r_{pzu}	Radius of the plastic zone for the unmodified
r_y	Radius of the plastic ahead of the crack-tip
R_δ	Displacement rate
T_g	Glass transmission temperature
v_f	Volume fraction
v_{fp}	Volume fraction of particles showed voids
v_{fv}	Volume fraction of voids
w_f	Weight fraction
W	Width

Greek Alphabet

α	Orientation factor
γ_f	Failure stain
γ_{fc}	Compressive failure strain
δ	Displacement
δ_{ampl}	Displacement amplitude
δ_{CTOD}	Crack tip opening displacement
δ_{Ic}	Displacement required to grow the crack in on cycle
δ_{max}	Maximum displacement
δ_{mean}	Mean displacement
δ_{min}	Minimum displacement
ε	Strain
ε_c	Compressive strain
ε_{yc}	Compressive yield strain
ΔG_{db}	Toughening increment from debonding
ΔG_p	Toughening increment from pull-out
ΔG_s	Toughening increment from shear band yielding
ΔG_{vc}	Toughening increment from plastic void growth (nanotube)
ΔG_{vp}	Toughening increment from plastic void growth (nanoparticle)
ΔG	Fracture energy range
ΔK	Fracture toughness range
ξ	Shape factor
η	Material constant as a function of ξ, E_f and E_m
μ_m	Material constant for pressure dependency
ν	Poisson's ratio
σ	Stress
σ_c	Compressive stress
σ_{cnt}	Failure stress of carbon nanotube
σ_{cri}	Critical stress
σ_E	Engineering stress
σ_y	Yield stress
σ_{yc}	Compressive yield stress

σ_{ycu}	Compressive yield stress of unmodified polymer
σ_{yt}	Tensile yield stress
σ_{ytu}	Tensile yield stress of unmodified polymer
ρ_f	Density of reinforcement
ρ_m	Density of matrix
τ_i	Interfacial shear stress
ψ	Toughening increment
Ø	Diameter

CHAPTER 1

INTRODUCTION

1.1 Introduction to the Project

Epoxy polymers have now been extensively used as adhesives and as the matrix for the fibre-reinforced polymer (FRP) composites due to various advantages they possess, such as good thermal stability and high Young's modulus. As adhesives, epoxy polymers possess many advantages, e.g. a high resistance to chemical attack, improved stress distribution across bonded joints, relatively high modulus and flexibility in component design [1]. Furthermore, adhesives are applied inside the joint, they provide an invisible well-sealed bond with the assembly, and can easily join irregularly shaped surfaces. Also, adhesives can bond dissimilar and heat sensitive materials. All of these are advantages over the conventional methods of joining used in industry, such as welding and bolting. As a polymer matrix for the FRP composites, epoxy resins have a low viscosity which is good for resin infusion. However, epoxy polymers are inherently brittle with a poor resistance to crack propagation due to their highly cross-linked nature when they are cured. Therefore, modification to improve the toughness of the epoxy polymers is required [2-4].

Several studies have reported that the inclusion of toughening particles can efficiently enhance the toughness of the epoxy polymers. The modification of using rubber microparticles has been found to toughen epoxy polymers, but at the cost of a decrease in the modulus [5]. The combination of micron-sized glass particles with epoxy resins can increase the toughness of the epoxy polymers, but the addition of these rigid particles resulted in an increase in the viscosity of the final mixture, which limited the use of the epoxy resins to be the matrix in the infusion process for manufacturing the FRP composites [5]. The inclusion of nano-scale reinforcements, such as silica nanoparticles or carbon nanotubes, has recently shown much promise by improving the toughness without any undesirable decrease in the other material properties [5-12].

For this study, rubber microparticles, glass bead microparticles, silica nanoparticles and multi-walled carbon nanotubes were used to modify epoxy polymers.

1.2 Project Aims and Objectives

The primary objective of this study was to investigate the fracture behaviour of the modified epoxy polymers under quasi-static and fatigue loading conditions. The toughenners used in this study have a wide range of dimensions from nano- to micro-sized. In the modified epoxy polymers with micro-sized reinforcements, rubber and glass bead microparticles were used as the toughenners. In the nanocomposites, the additives used in this study include silica nanoparticles and multi-walled carbon nanotubes. Fracture toughness, fracture energy and fatigue performance of these modified polymers were measured, and the toughening mechanisms caused by the addition of these particles were identified.

In the modified polymer materials with the rigid spherical particles, the dimensions of the toughenners fall in a range from nano-sized of about 20 nm in diameter to micro-sized of about 275 μm. The particle size effect on the toughness was investigated. Furthermore, surface treatments were also introduced to these modified polymers to give different levels of particle/epoxy adhesion, and then the effect of the adhesion on the fracture behaviour of the polymer-based composites was studied.

In addition to using silica nanoparticles as the nano-reinforcement, multi-walled carbon nanotubes synthesised by the chemical vapour deposition technique were used to manufacture the nanocomposites. In order to achieve the best dispersion of the nanotubes in the polymer matrix, various dispersion methods were investigated, and finally the appropriate process for the nanotube-modified polymer sample preparation was found to get the best dispersion of the nanotubes. Nanotubes with different qualities were created by changing the substrates in the chemical vapour deposition process, consequently different dimensions and degrees of alignment of the nanotubes can be obtained. The effect of using the different qualities of the nanotubes on the toughness and fatigue performance of the nanocomposites was investigated. An analytical model based on the toughening mechanisms was built to predict the increased toughness caused by the addition of the nanotubes, and then compared with the experimental results.

1.3 Thesis Structure

This thesis is divided up according to the particles used to prepare the various modified polymer-based composites. Each modified polymer composite was characterised by the morphology, mechanical and thermal properties, toughness and fatigue performance. Various microscopy techniques were used to inspect the fracture surfaces of the modified polymer samples, and the toughening mechanisms caused the addition of reinforcements were identified. Each Chapter in this thesis can be summarised as follows:

Chapter 2 presents a literature survey regarding the previous studies on the toughening modifications for epoxy polymer-based composites. Toughening mechanisms in these modified polymers were also reviewed.

Chapter 3 provides a detailed description of the formulations used in this study. The sample preparation is discussed, including dispersion processes, surface treatments and curing schedules. The chemical vapour deposition process used to create the aligned multi-walled carbon nanotubes is also presented.

Chapter 4 describes the experimental methods used to investigate the material properties. Various microscopy observations used to examine the particle dispersion, morphology and to inspect the fractured samples are also described.

Chapter 5 presents the various dispersion methods used in the nanocomposites modified with the multi-walled carbon nanotubes, and the best way to prepare the nanotube/epoxy materials is identified. In this Chapter, greyscale analysis is introduced to rank the nanotube dispersion from the optical microscopy images, and compared to the morphology of the nanotubes in the cured bulk samples observed by atomic force microscopy.

Chapter 6 describes the study on the polymers modified with rigid particles, silica nanoparticles and glass bead microparticles. The effect of the particle size and the adhesion between the particles and epoxy matrix on the toughness and fatigue

performance is investigated. Various treatments (silane coupling agent, release agent and untreated) have been used to give different levels of adhesion in the glass bead/epoxy materials.

Chapter 7 presents the material properties of the multi-walled carbon nanotube-modified polymer with various weight loadings of nanotubes. At the end of this Chapter, low quality nanotubes with a relatively short length are used to form the nanocomposites, and their fracture toughness and fatigue performance are determined, and then compared with the standard nanotube-modified polymer. The nanotube size effect on the dispersion, modulus, toughness and fatigue performance is investigated and summarised.

Chapter 8 reports on the hybrid-modified polymers with the combination of the toughening fillers of rubber microparticles, silica nanoparticles and multi-walled carbon nanotubes. A synergy effect caused by the addition of the hybrid materials is found in these materials. A comparison of the toughening combination in the hybrid-modified polymers and the single-phase modified polymers is made.

Chapter 9 presents analytical models based on the toughening mechanisms in the nanocomposites discussed in Chapter 6 and Chapter 7. The aim of this Chapter is to predict the increases in the modulus and toughness caused by the addition of the silica nanoparticles and multi-walled carbon nanotubes

Lastly, Chapter 10 presents the conclusions of the project, followed with some recommendations for future work which emerged during the course of this project.

CHAPTER 2

LITERATURE REVIEW

2.1 Introduction

The work discussed in this thesis focuses on the structure and properties of polymer-based composites modified using reinforcements with a wide range of dimensions from the nano- to micro-scale. The additives used include (i) nano-sized reinforcements: multi-walled carbon nanotubes and silica nanoparticles, and (ii) micro-sized particles: rubber microparticles and glass bead microparticles. This Chapter provides an overview of the published literature related to the central themes of this study.

A brief introduction to the principles of fracture mechanics in polymer engineering will be presented, as this thesis is concerned with the fracture behaviour of polymer-based composites. Epoxy polymers are then introduced. The toughening of these polymers with various reinforcements such as rubber microparticles, glass bead microparticles, silica nanoparticles and carbon nanotubes will be discussed in terms of the fracture properties and failure mechanisms.

2.2 Fracture Mechanics

2.2.1 Introduction

Fracture mechanics studies crack propagation in materials, and analyzes the applied stress on a crack to understand the material's resistance to fracture. This analysis is conducted under linear elastic fracture mechanics (LEFM) conditions, in which the analysed material obeys Hooke's Law. An elastic solution is used to calculate the amount of energy required for fracture.

2.2.2 Quasi-static Fracture

This section introduces the elementary fracture mechanics under a quasi-static loading. The derivation of fracture toughness (K_{Ic}) and fracture energy (G_{Ic}), and the specific parameters commonly used to analyze the fracture mechanics have been covered extensively in various elementary text books, e.g. [1].

The critical strain energy release rate, G_{Ic}, is defined as the energy required for crack growth, and can be derived as [13]:

$$G_{Ic} = \frac{P_c}{2B} \cdot \frac{\partial C}{\partial a} \tag{2.1}$$

where P_c is the critical load at the onset of the crack propagation, B is the thickness of the specimen and C is the specimen compliance (the ratio between the displacement and load). C is measured with respect to the crack length, a.

Irwin [14] found the other important parameter of the critical stress intensity factor, K_{Ic}, which is derived from the stress near the crack tip. K_{Ic} can be written as:

$$K_{\mathrm{Ic}} = Y\sigma_{\mathrm{cri}}\sqrt{a} \tag{2.2}$$

where Y is the geometry factor, a is the crack length and σ_{cri} is the critical stress which will make the crack propagate.

As the material contains a crack, a plastic zone will form in front of the crack tip, with radius, r_{y}, which can be derived as:

$$r_{\mathrm{y}} = \frac{1}{2\pi}\left(\frac{K_{\mathrm{Ic}}}{\sigma_{\mathrm{y}}}\right)^2 \qquad \text{for plane stress conditions} \tag{2.3}$$

$$r_{\mathrm{y}} = \frac{1}{6\pi}\left(\frac{K_{\mathrm{Ic}}}{\sigma_{\mathrm{y}}}\right)^2 \qquad \text{for plane strain conditions} \tag{2.4}$$

where σ_{y} is the yield stress. Plane strain and plane stress conditions are defined by the thickness of test specimens. The minimum thickness required to satisfy the plane strain conditions can be seen below [15], and a smaller thickness implies plane stress conditions:

$$B \geq 2.5\left(\frac{K_{\mathrm{Ic}}}{\sigma_{\mathrm{y}}}\right)^2 \tag{2.5}$$

where B is the specimen thickness and σ_{y} is the yield stress. It should be noted that the fracture tests in this study were performed under plane strain conditions. Figure 2.2.1 shows schematically the location of the plastic zone ahead of the crack tip [9].

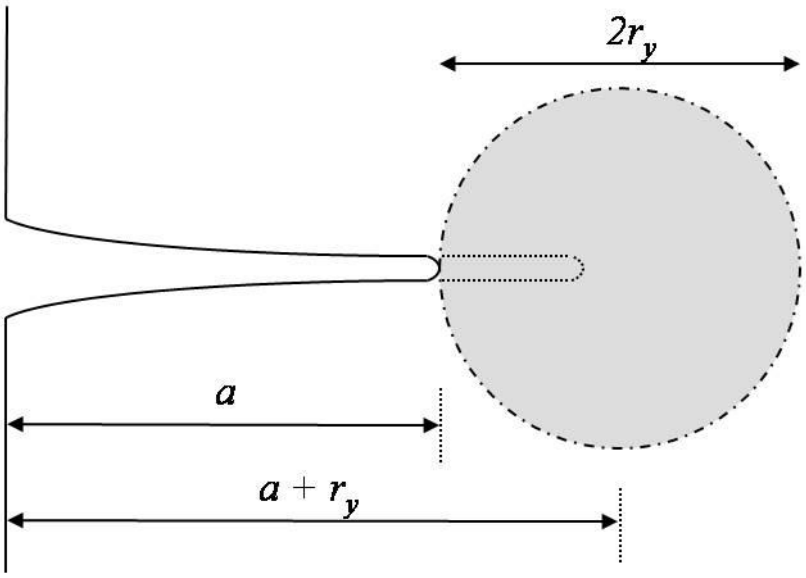


Figure 2.2.1 Schematic model showing the plastic zone [9].

The relationship between the value of G_{Ic} and K_{Ic} for the plane strain condition can be described as:

$$G_{Ic} = \frac{(1-\nu^2)K_{Ic}^2}{E} \tag{2.6}$$

where E is the Young's modulus and ν is the Poisson's ratio of the material.

2.2.3 Fatigue Fracture

The derivations and analyzed parameters above are for quasi-static fracture mechanics. As a significant proportion of the investigation in this study concentrated on the fatigue behaviour, the fracture mechanics caused by cyclic loadings need to be considered. Paris [16] investigated fatigue failure using LEFM conditions, and described the

relationship between the applied stress intensity factor and the fatigue crack growth rate, *da*/*dN*, as:

$$\frac{da}{dN} = A \cdot \Delta K^m \tag{2.7}$$

where *a* is the crack length, *N* is the number of cycles, *A* and *m* are material constants. The stress intensity factor range, ΔK, can be calculated by:

$$\Delta K = (K_{max} - K_{min}) \tag{2.8}$$

where K_{max} and K_{min} are the maximum and minimum stress intensity factors of the cyclic loading. The values of ΔK, K_{max} and K_{min} can be changed to energy forms, ΔG, G_{max} and G_{min} using Equation 2.6, (G_{max} was used in this study).

Figure 2.2.2 shows a typical fatigue testing curve of log crack growth rate versus log G_{max}, which consists of three regions: (I) threshold region, (II) crack propagation (linear) region, and (III) crack initiation (fast crack) region. As the fatigue crack propagation rate is decreased to the point where G_{max} approaches G_{th} (or $(G_{max})_{th}$) at the threshold region (I), the crack stops propagating. The gradient of the fatigue testing curve in the crack propagation (linear) region (II) is identified by the constant, *m*, in Equation (2.7). This value can also characterise the fatigue resistance: the higher the value of the Paris Law *m* parameter, the lower the resistance to the crack propagation during the cyclic loading. The initial value of G_{max} in the crack initiation (fast crack) region (III) reaches to the maximum in the fatigue testing curve, and would approach the quasi-static fracture parameter of G_{Ic} in Equation (2.1).

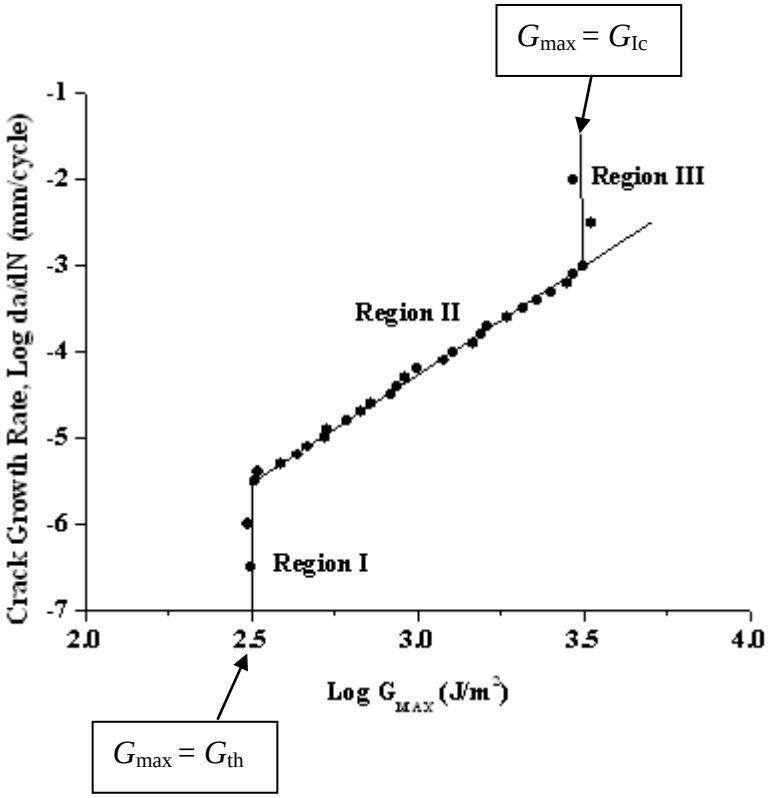


Figure 2.2.2 Fatigue testing curve, showing (I) threshold (stop propagating) region, (II) crack propagation (linear) region and (III) crack initiation (fast fracture) region, modified from [17].

2.3 Epoxy Polymers

Polymers have been extensively used in engineering applications, and can be subdivided into two categories, thermoset and thermoplastic [18]. The polymer used in this study is a thermosetting polymer. Thermosetting polymers are rigid and highly cross-linked materials containing an infinite three-dimensional network of polymer chains. The epoxy polymers, which are grouped under the thermosets, are extensively used as adhesives [19], clearcoats and polymeric matrices in fibre-reinforced composites [20] or nanocomposites [21]. Epoxies exhibit excellent mechanical properties, such as good resistance to temperature and low creep, because they are amorphous and highly cross-linked when cured [18, 22]. However, their high cross-link density results in a low resistance to crack propagation, indicating that they are relatively brittle. This leads to a serious limitation of their applications. Therefore, modification to improve the toughness and fatigue performance of the epoxy polymers is required.

Epoxy resins contain epoxide endgroups, which allow the resin to be reacted with other polymers and consequently a highly cross-linked polymer is formed. Figure 2.3.1 shows the molecular arrangement of the endgroup. The process to form the cross-links is performed with the aid of a curing agent, such as an amine [23] or an anhydride [9, 24]. As can be seen in Figure 2.3.1, at least two polymer chains per group are present for cross-linking, once the epoxide ring is broken.

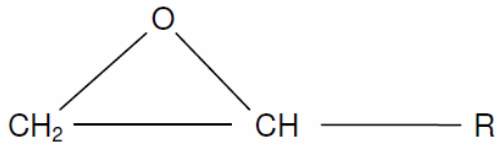


Figure 2.3.1 The epoxide endgroup, R represents the molecular structure of the remaining epoxy polymer [25].

Epoxy consists of the resin and curing agent (hardener). The resin part used in this study is a diglycidyl ether of bisphenol A (DGEBA) epoxy, and its molecular structure is shown in Figure 2.3.2. The DGEBA epoxy resin is made from epichlorohydrin and the disodium salt of bisphenol-A, and its properties depend on the value of *n* in the chemical formula. *n* is the number of repeating units associated with the degree of polymerisation, which typically is in a range from 0 to 25.

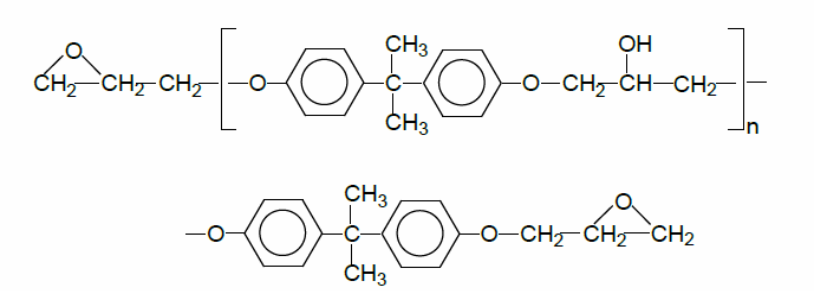


Figure 2.3.2 Molecular structure of DGEBA [26].

The curing agent (or hardener) is used to promote these epoxides to cross-link the polymer. Typically the curing agent has active hydrogen attached to nitrogen, oxygen, or sulphur [22]. The various curing agents directly affect the cross-link density, glass transition temperature and modulus of the polymer. The curing agent used in this study is an anhydride, which gives lower exotherms on the cure in comparison with the epoxy polymer cured by an amine curing agent [27].

Various modifications have been used to enhance the mechanical and thermal properties, such stiffness, toughness, fatigue performance and thermal resistance of expoxies. A large proportion of the investigation in this thesis is focused on the toughness of modified epoxy polymers because epoxies are brittle. The following sections focus on the effect of the toughening performance of the polymer-based composites caused by various reinforcements (rubbery and rigid microparticles, silica nanoparticles and carbon nanotubes), and the toughening mechanisms induced by the inclusion of these additives are described.

2.4 Rubber Particles Toughening Mechanisms

2.4.1 Introduction

In the toughened epoxy materials, the most frequently used toughening modification is to blend rubber particles with epoxy matrices [28]. The most commonly added type of rubber particles is carboxyl-terminated butadiene-acrylonitrile (CTBN) liquid rubber particles, this is the same type of rubber additive used in this study. The modification using the CTBN rubber particles was first applied to toughen epoxy polymers [29]. This method of using the CTBN rubber particles is easy for composites preparation, and the rubber particles are formed as a well-dispersed phase in the cured samples. Kinloch et al. [6, 30] investigated the toughness performance of the CTBN/DGEBA epoxy material, and showed that the inclusion of the rubber particles significantly increased the toughness. The toughening mechanisms from the rubber particles will be summarised.

2.4.2 Rubber Bridging

The toughening mechanisms which can contribute to the increase in the toughness of rubber-modified composites were investigated in several studies [6, 30-37]. Kunz-Douglas [31] examined a propagating crack in the rubber-toughened epoxy composites, and found the rubber particles were stretched and attached between the two crack surfaces. They suggested that this rubber crack bridging mechanism can absorb energy, consequently the resistance to the crack propagation was improved. Figure 2.4.1 shows the microscopy image and the model of the rubber bridging.

However, Kinloch et al. [32, 33] found that the rubber bridging cannot significantly contribute to the increased toughness. They used the finite element method to calculate the increased toughness, and showed that this mechanism was responsible for only around 10% of the overall fracture energy.

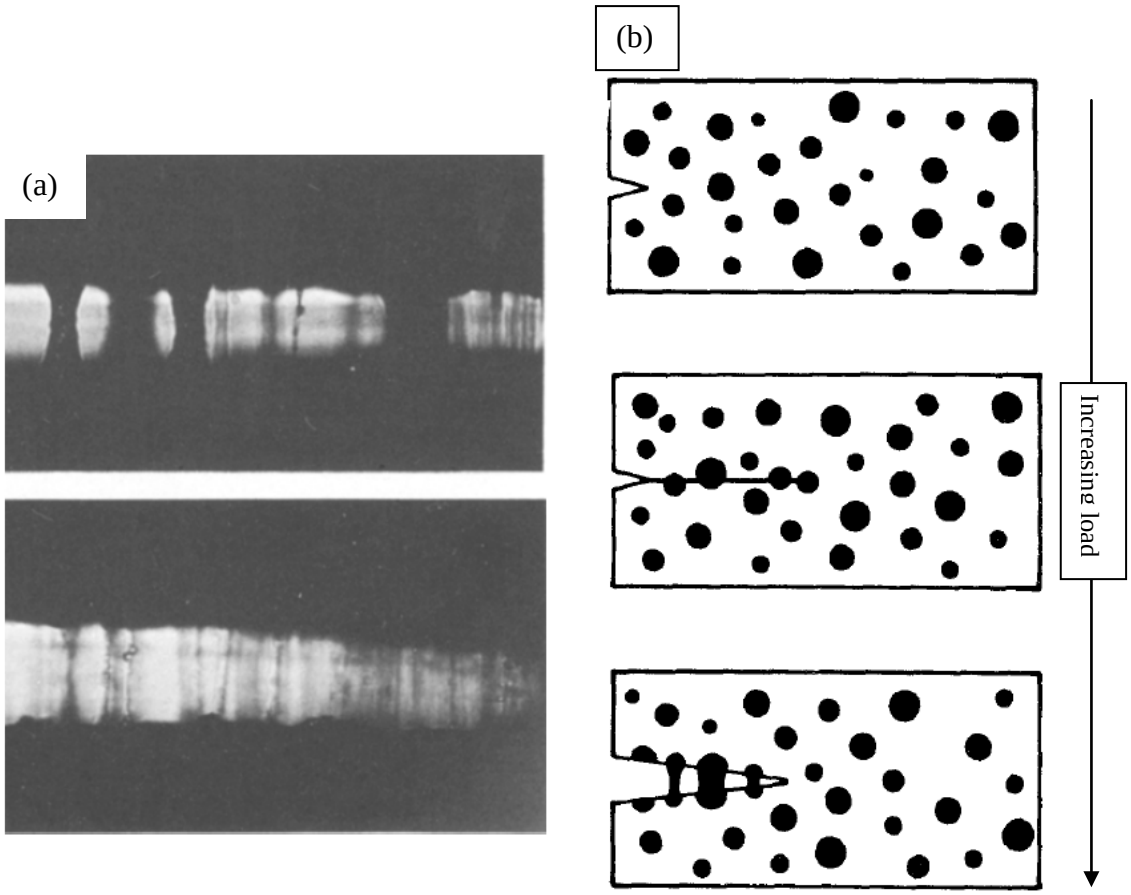


Figure 2.4.1 Crack profiles in a rubber-modified epoxy material, (a) microscopy images and (b) model of rubber bridging [34].

2.4.3 Shear Banding

The growth of localized plastic shear-bands formed between the rubber particles has been found in rubber-modified polymers [34-37]. Figure 2.4.2 shows the stress distribution between the rubber particles using a 2-D finite element analysis method [38]. A high stress ligament between the rubber particles was found in the mixture. This is a shear band. Shear bands occur by mutual deformation of materials by a shear force, in which a massive degree of plastic deformation takes place. The added rubber microparticles were considered as the stress concentrations which promote localised yielding between the particles, and subsequent plastic deformation. This plastic

deformation absorbs the energy and is associated with a large amount of deformation in the polymer matrix. All of these result in the measured increases in the toughness.

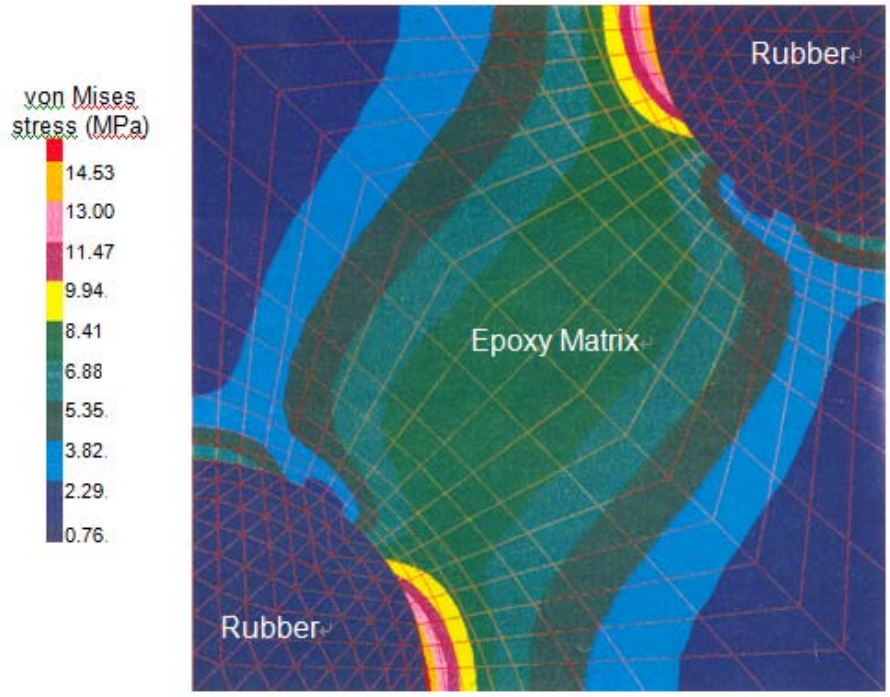


Figure 2.4.2 Distribution of the von Mises Stress around rubber particles, showing a high stress ligament and shear band between rubber particles[38].

2.4.4 Rubber Cavitation

In addition to the toughening mechanisms mentioned above, rubber cavitation has been considered as an important contribution to improve the toughness of the modified polymer with rubber particles [39-44]. Huang and Kinloch [39] investigated the toughening mechanism by inspecting the fracture surfaces of rubber-modified epoxy materials, and clearly found internal cavitation of rubber particles. This rubber cavitation is created either before or after shear banding. The occurrence of rubber cavitation results in a significant increase in the energy dissipation. As the rubber particles start to cavitate, a huge amount of the strain energy can be absorbed by the

rubber cavitation and deformation in the polymer matrix, followed by the plastic void growth. The occurrence of void growth includes the generation of a new surface, which can absorb the surface energy, and plastic deformation in the matrix. Figure 2.4.3 shows images of rubber particles in the cured polymer sample before loading and on the fracture surface. It can be seen that the diameters of the rubber particles on the fracture surface are much larger than the original rubber particles, indicating the rubber particles are cavitated. Besides, plastic void growth was found on the fracture surfaces.

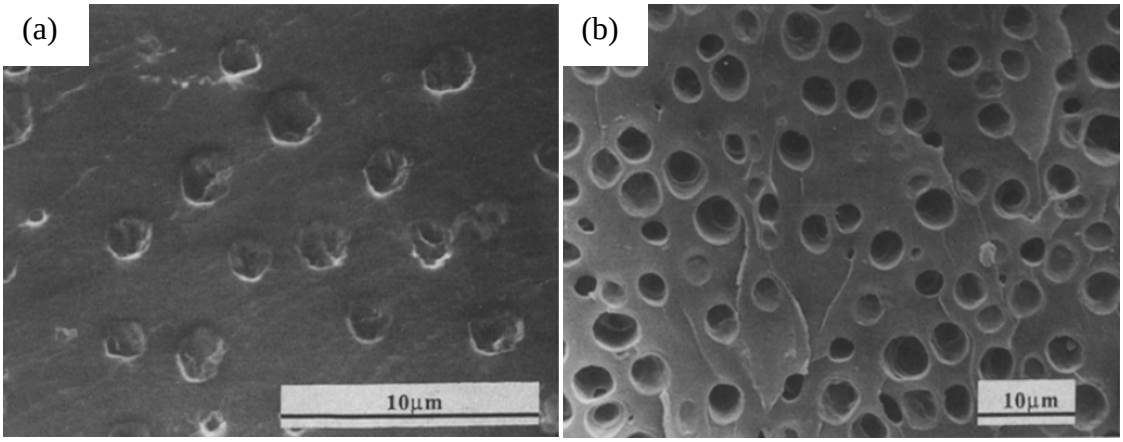


Figure 2.4.3 The microstructure of the rubber-toughened epoxy polymer, showing (a) original (undeformed) microstructure before loading and (b) fracture surface after fracture tests [42].

Yee et al. investigated the microstructure of the rubber-modified polymer during fracture [43], and they found that the occurrence of the rubber cavitation relieved the stresses at the crack tip, consequently delaying further crack propagation by inducing plastic deformation in the vicinity of the crack tip, see Figure 2.4.4.

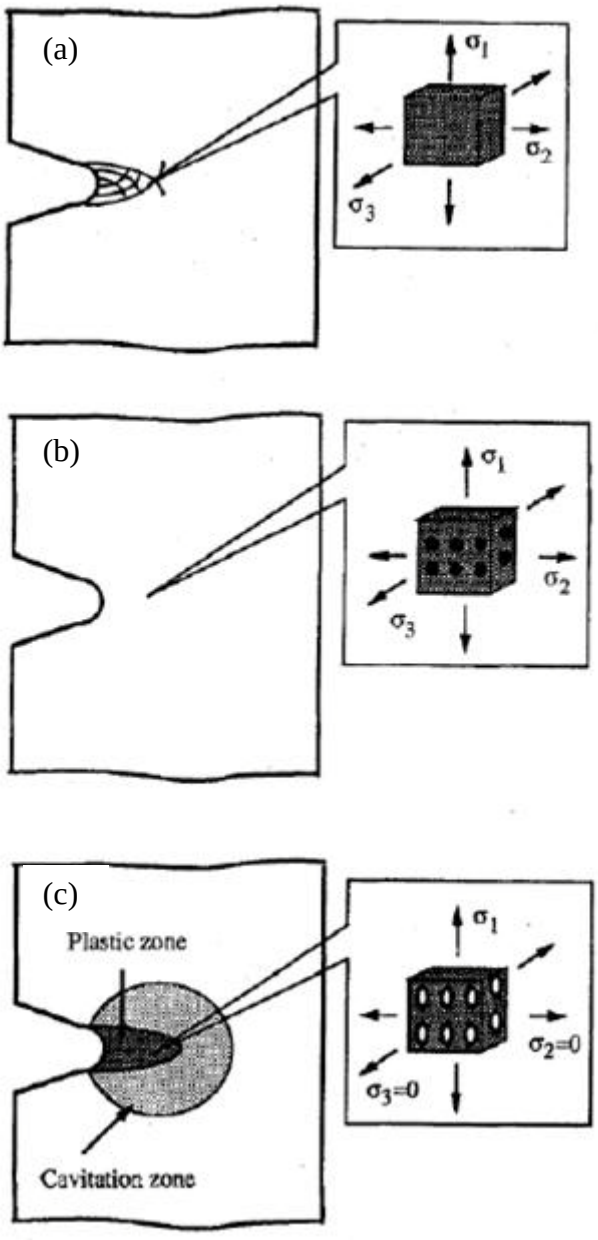


Figure 2.4.4 Schematic diagram of the mechanisms occurring at the crack tip in (a) unmodified epoxy, (b) rubber-modified epoxy before rubber cavitation and (c) after rubber cavitation [43].

Wang et al. [44] developed a 3-D finite element model, see Figure 2.4.5, to investigate the rubber-modified material, and compared with the experimental results. They found that the rubber cavitation results in both plastic void growth inside the particles and increased growth of shear bands.

(a) (b)

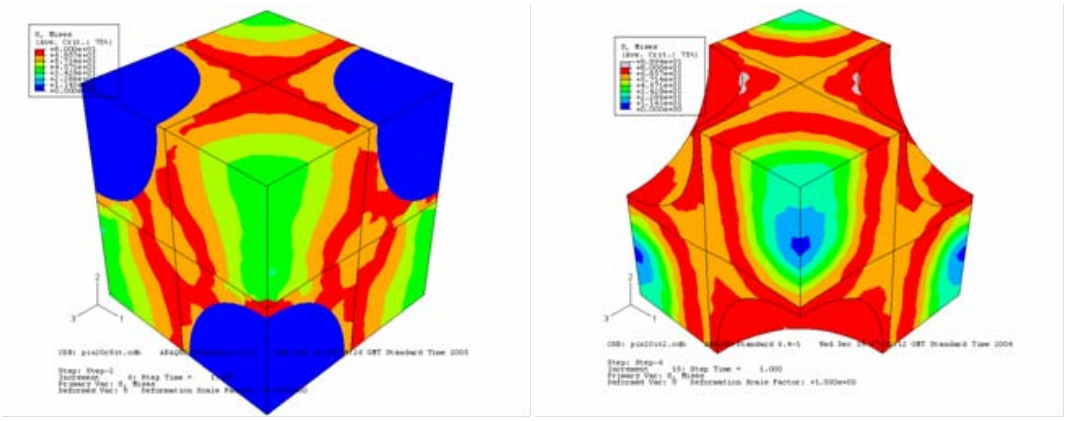


Figure 2.4.5 Distribution of the von Mises stress around rubber particles in a unit cell under triaxial loading, showing (a) before cavitation and (b) after cavitation [44].

2.5 Rigid Particle Toughening

2.5.1 Introduction

The addition of a rubber phase to polymer-based materials leads to an increase in the toughness but at the cost of a decrease in the stiffness of the polymer because rubber is soft [5]. For this reason, rigid particles are increasingly used to toughen epoxy polymers instead of rubber particles because the combination of rigid particles with polymers leads to an increase in the toughness without any compromise of the material properties [45, 46]. In addition, the viscosity of the rigid particle-modified mixtures can be relatively low, compared to rubber/epoxy mixtures. Suitable surface treatments are needed which can increase the adhesion between the particles and polymer matrix, and result in a positive influence on the toughening potential and the dispersibility of tougheners [46-48]. Surfactants are extensively utilized to prevent the agglomeration of fillers and reduce the increase in viscosity caused by adding rigid particles. Although the rigid particles used in this technology are of various types, glass and silica particles are the most widely used [45-49].

The toughening mechanisms which can be responsible for the increase in the toughness of rigid particle-toughened polymer composites have been well reported in the literature, and will be described in following sections.

2.5.2 Crack Pinning and Crack Deflection

In the rigid particle-modified materials, once the propagating crack comes across the rigid particles, the crack front becomes pinned and tends to bow out between the added particles [50-53], see Figure 2.5.1.

Observing the fracture surface of the glass bead-modified polymers, see Figure 2.5.2, shows several tails formed behind the rigid particles, which mean that the crack

deflection mechanism occurs in the material. The crack path is bowed, which absorbs energy, before breaking away from the particles, see Figure 2.5.1 (a). The process of the crack pinning and deflection creates new surfaces, and consequently improves the energy dissipation [45, 54, 55].

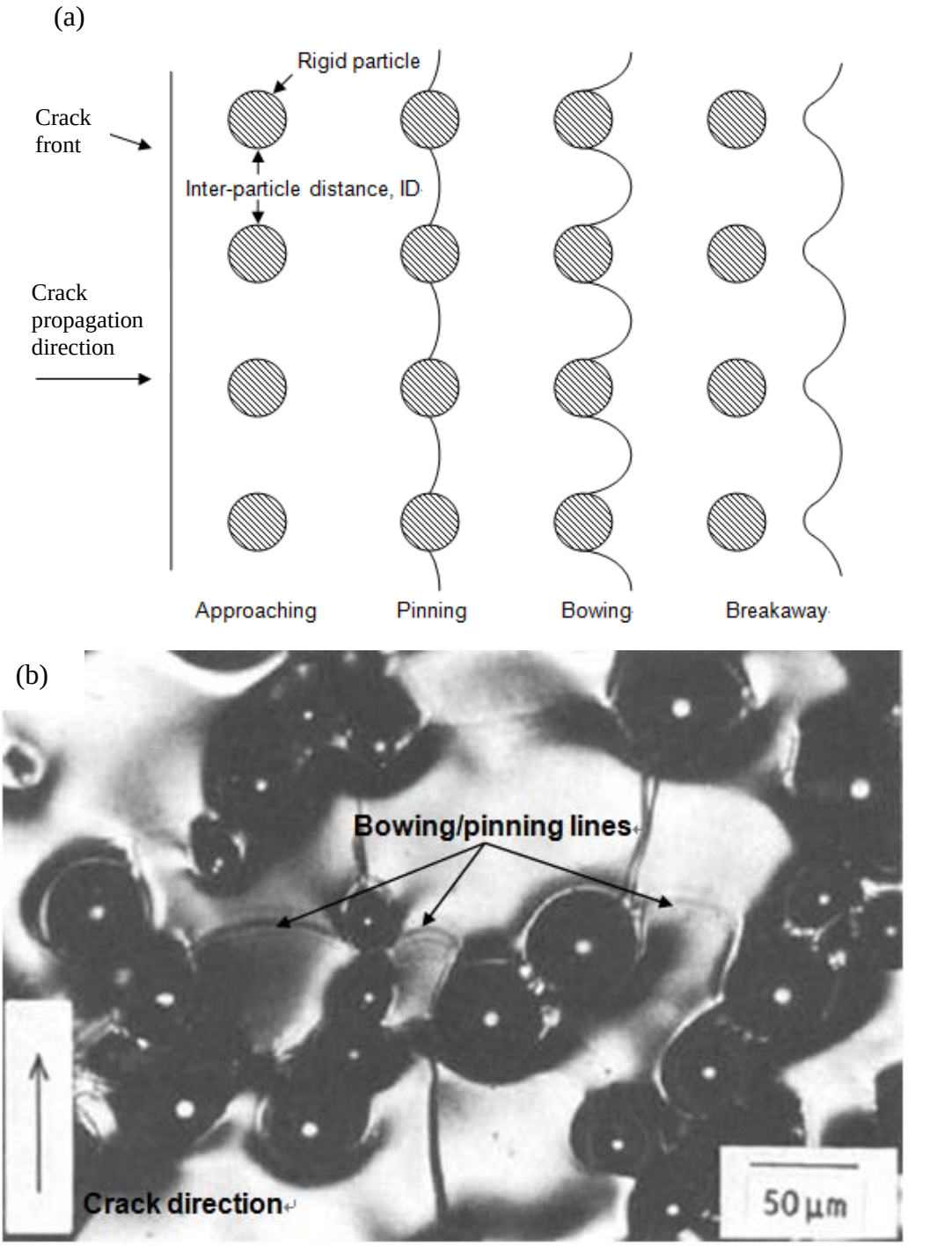


Figure 2.5.1 The crack pinning mechanism, showed by (a) a schematic model and (b) a optical micrograph of the glass particle toughened polymer [53].

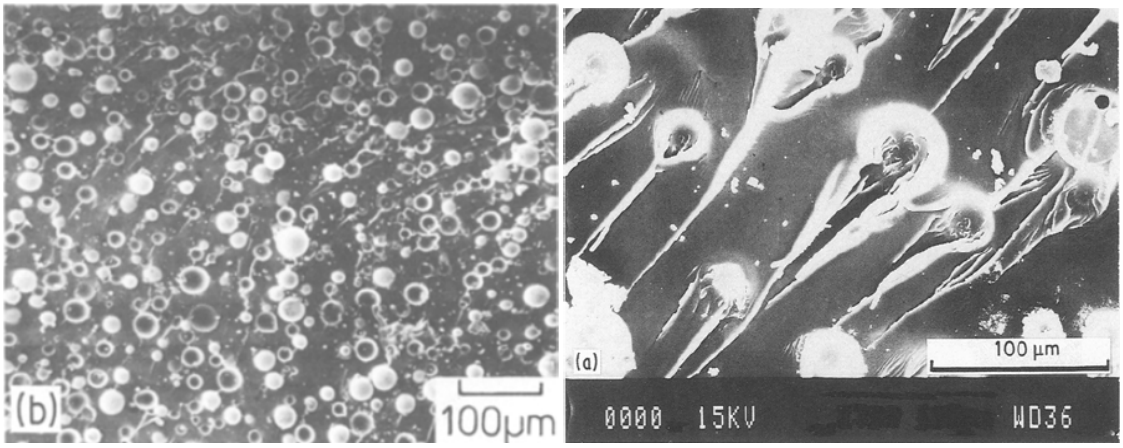


Figure 2.5.2 Fracture surfaces of the glass microparticle-modified polymer materials, showing crack pinning and deflection [45, 55].

Figure 2.5.3 shows the crack deflection of a glass bead-modified polymer using optical microscopy (OM), and clearly shows that the direction of the crack is changed. When the crack tip meets the rigid microparticles, the crack path moves around the equator of the particles in case of poorly-bonded particles. In contrast, the crack propagates through the matrix near the pole of the particles if the added particles are well bonded with the polymer matrix [46, 56]. If crack deflection occurs, the crack is no longer in pure mode I loading, and so more energy is required for crack propagation. Toughening contributions can be provided by energy dissipation caused by interfacial debonding between the particles and matrix, and creating micro-cracks.

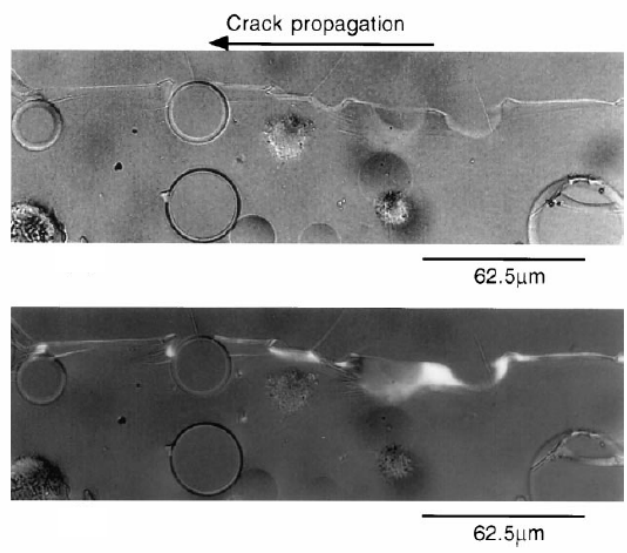


Figure 2.5.3 The crack deflection mechanism in microparticle-modified polymers [57].

2.5.3 Debonding and Void Growth

The toughening contribution caused by the addition of rigid particles has frequently been shown to be due to debonding of the particles followed by plastic void growth [57-59]. In case of the poorly-bonded particle/polymer materials, particles are debonded from the polymeric matrix, followed by plastic void growth due to the plastic deformation in the matrix, see Figure 2.5.4. The plastic deformation in the matrix to form the void growth is associated with energy dissipation, which results in an increase in the toughness. Although the debonding process absorbs little energy compared to the plastic deformation of the matrix, the occurrence of debonding is essential because this allows the matrix to deform plastically via a void growth mechanism.

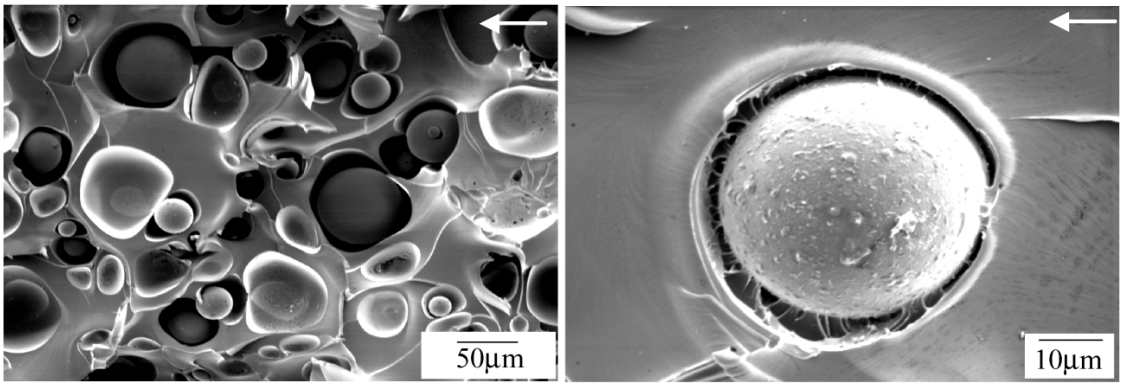


Figure 2.5.4 Fracture surface images, showing particle interfacial debonding, and subsequent plastic void growth in the microparticle-modified polymers [58].

2.6 Nanoparticle toughening

2.6.1 Introduction

Most recently, there has appeared a novel approach to toughen polymers using nano-sized particles, such as nanosilica. As the modified particles are in the range of the nano-scale, they are good for some low-cost processes (e.g. infusion processes) to manufacture fibre-composite materials, and the nanoparticles can be embedded into the interspace of the reinforcing fibres. All of these promote the use of nanoparticles instead of micron-sized rigid particles. Evidence from studies indicates that the addition of nanosilica particles to pristine or rubber-toughened epoxy resins results in an increase in the toughness even at a low concentration of such fillers [60-63]. Discussion of the effect of filler size on toughness shows that smaller fillers are more efficient in toughening polymers, which supports the feasibility of toughening thermosetting polymers through the addition of nanoparticles [64]. In the following sections, the toughening mechanisms caused by the micro- and nano-particles are presented.

2.6.2 Toughening Mechanisms for Nanoparticles

The toughening mechanisms strongly depend on the size of the reinforcements, even if they have the same shape (both microparticles and nanoparticles are spherical). Johnsen et al. [7] investigated the toughness mechanisms in nanosilica-modified polymers. They found that the well-known mechanisms of crack pinning and crack deflection in microparticle-modified polymers could be discounted because the toughening particles are many orders of the magnitude smaller than the crack opening displacement, see Figure 2.6.1. Indeed, crack pinning only occurs if the particles are larger than the plastic zone size [65], thus nanosilica-modified polymer does not cause the crack pinning mechanism.

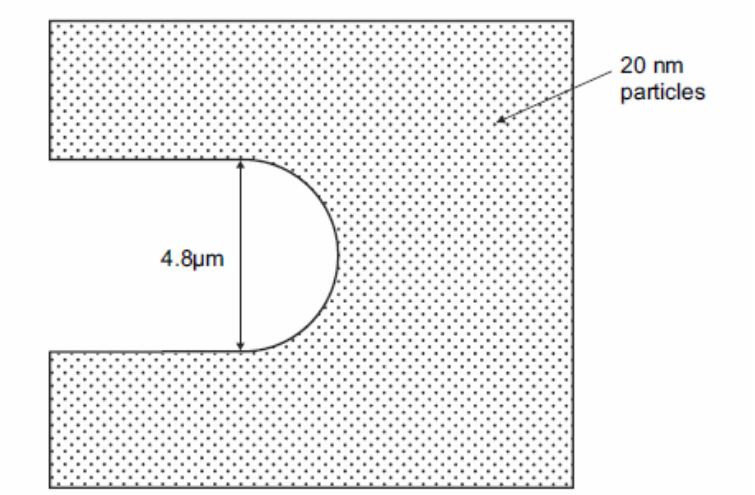


Figure 2.6.1 Schematic showing crack tip in the nanosilica-modified polymer [7].

Particle debonding, followed by plastic void growth, has been demonstrated in microparticle-modified polymers [54]. Johnsen et al. [7] clearly found the plastic void growth toughening mechanism in the modified polymer with the silica nanoparticles, see Figure 2.6.2. The occurrence of the plastic void growth includes the particle debonding and plastic deformation in the polymer matrix. All of these are generally considered to increase the energy dissipation, and increase the toughness of the nanocomposites. Previous work [5] focused on the toughened polymer demonstrated that the plastic void growth is a main toughening mechanism in the nanocomposite using numerical analysis, and the simulation of nanoparticle-toughened materials shows that the plastic void growth results in an increase in the toughness, and a good agreement with experimental results can be obtained.

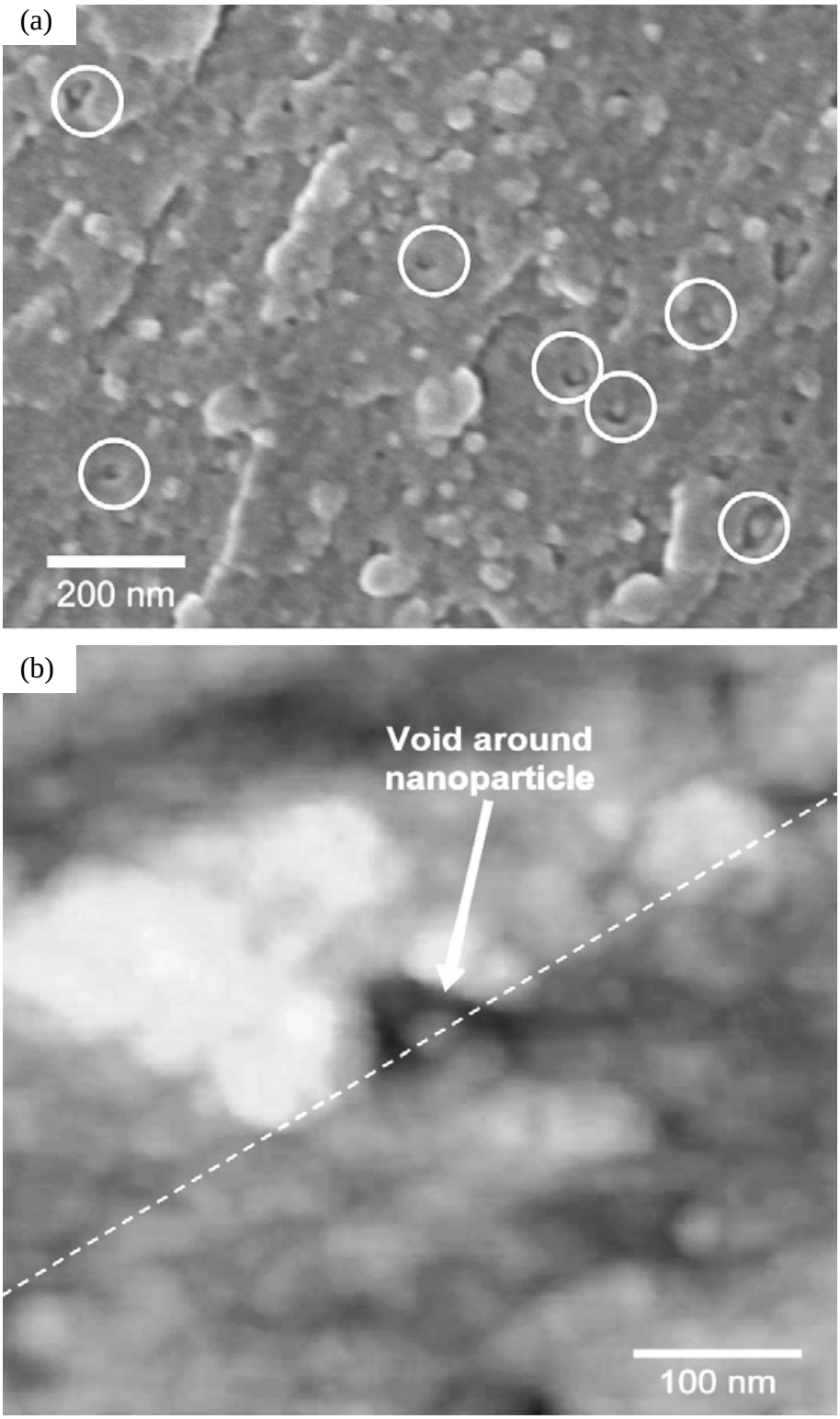


Figure 2.6.2 Plastic void growth mechanism in the nanosilica-modified polymer using (a) FEG-SEM and (b) AFM [5].

2.7 Carbon Nanotube Toughening

2.7.1 Introduction

Recently, the evolution of nanocomposites reinforced with carbon nanotubes (CNTs) has been intensively investigated since the first successful synthesis in 1991 by Iijima [66]. Carbon nanotubes possess exceptional properties compared to conventional fillers. Several studies have been made to probe into the material properties of carbon nanotubes [67-71], and they found that carbon nanotubes have excellent mechanical and thermal properties.

Carbon nanotubes come in two main types, (i) single-walled carbon nanotubes (SWCNTs) which have only one layer of graphene forming the wall, (ii) multi-walled carbon nanotubes (MWCNTs) which consist several rolled layers of graphene, each layer is stacked concentrically. Table 2.7.1 shows the characteristics of carbon nanotubes. Analogous to particle-form fillers (e.g. silica nanoparticles), carbon nanotubes have a high surface area which is capable of transferring the stress in polymer-based composites. Thus, CNTs are considered a strong potential candidate for toughening brittle thermosetting matrices. Both the experimental and theoretical results in the literature show that the addition of carbon nanotubes leads to an improvement in the mechanical properties, such as modulus [72, 73], toughness [74-77] and fatigue performance [78-80].

Table 2.7.1 Summary of characteristics of carbon nanotubes [71].

Elastic modulus	SWCNT MWCNT	~ 1.0 ~ 0.3 – 1.0	TPa TPa
Strength	SWCNT MWCNT	50-500 10-60	GPa GPa
Specific gravity	SWCNT MWCNT	0.5 1.8	g/cm^3 g/cm^3
Specific surface area		10-20	m^2/g
Resistivity		5-50	μΩ cm
Thermal conductivity	Theoretical	3000	$W\ m^{-1}\ K^{-1}$
Thermal expansion	Theoretical	Negligible	
Thermal stability	In air In vacuum	>700 2800	°C °C

In order to achieve an efficient exploitation of the addition of CNTs to toughen polymer-based composites, functionalisation has been widely used to modify the surface of the CNTs via various surface treatments, because using such treatments lead to an enhancement of the interfacial bonding properties between CNTs and matrices. The investigation related to these treatments indicates that not only good interfacial properties of CNTs/epoxy composites can be obtained by the surface modification [81], but also a good dispersibility of CNTs because this surface modification alters the surface characteristic to reduce the tendency to agglomeration. Several recent studies laying stress on the dispersibility of CNTs embedded into polymers showed that functionalisation, such as acid treatments and surfactants, is an appropriate method to avoid the aggregation of CNTs [82, 83].

In the following section, the mechanisms which can contribute to the toughness of modified polymers with carbon nanotubes will be described.

2.7.2 Toughening Mechanisms in Carbon nanotubes

According to previous studies related to fibre-reinforced polymer (FRP) composites [84], the fibre pull-out mechanism is considered to be the main source of energy dissipation and toughness in FRP composite materials. CNTs can be compared to nano-scale carbon fibres, hence the pull-out mechanism may also occur in CNT-toughened polymers [85, 86]. As can be seen in Figure 2.7.1 (schematic view of a crack propagating in composites with the same volume fraction of fibres and nanotubes), the amount of the pull-out mechanism in the nanotube-modified sample is much higher than in the fibre-reinforced sample. This indicates that the modification of using nanotubes to improve the toughness of the composites can be much more efficient than using conventional fibres.

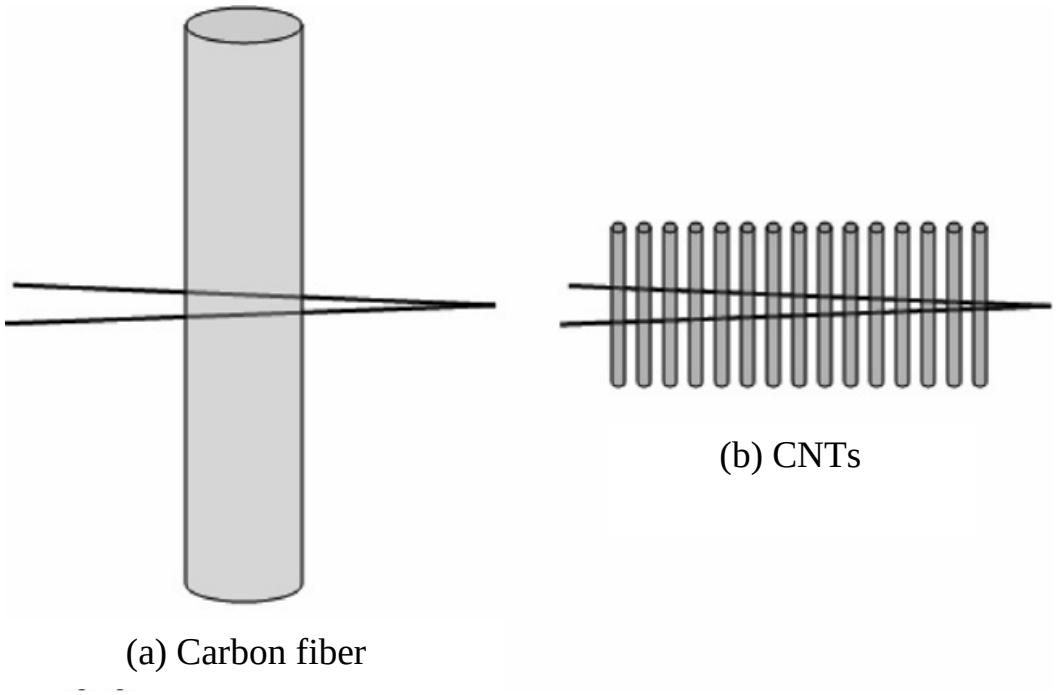


Figure 2.7.1 Schematic view of a crack propagating in a composite: (a) through a microfibre (carbon fibre): (b) through a series of nanotubes (CNTs) of total volume equivalent to the volume of the microfibre in (a) [86].

Figure 2.7.2 shows a SEM image of the fracture surface of a CNT-modified polymer material, where clear evidence of several pulled out nanotubes and voids can be found. The effectiveness of the pull-out mechanism in impeding crack propagation starts with debonding between the nanotubes and matrix, followed by interfacial friction before the nanotubes are completely pulled out from the matrix. The increased toughness in nanotube-modified polymers can be attributed to the interfacial friction in the nanotube pull-out process. The reason why the pull-out length is slightly shorter than the original length is that the nanotubes may be ruptured during pull-out.

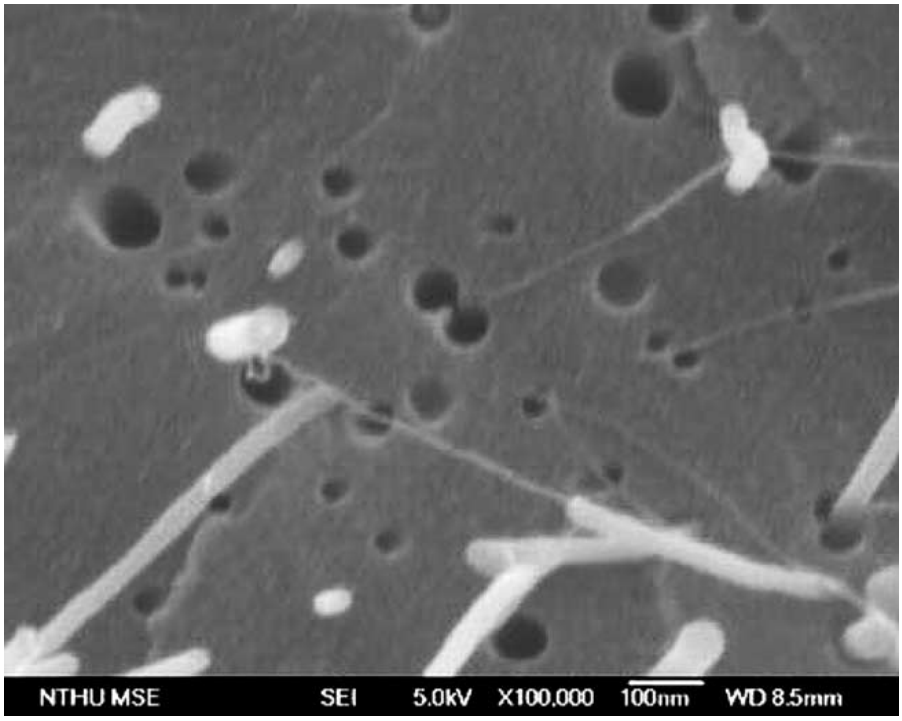


Figure 2.7.2 SEM image of the fracture surface of MWCNT-modified polymer [87].

The research on fracture toughness showed that the presence of CNTs leads to a significant enhancement in the toughness and the micro-mechanism, called crack-bridging, can be detected [86, 88]. This mechanism of bridging behaviour reflects the significant extensibility of the nanotubes, and can be observed through exploring the detail of a crack, see Figure 2.7.3 and Figure 2.7.4. The observation showed that there are several CNTs spanning the crack even if the width of the crack is 1~10μm, without nanotube rupture. This mechanism can resist the advancing crack and lead to an improvement in fracture toughness because of the debonding behaviour between bridged CNTs and matrices and the strain energy from bridged nanotube extension.

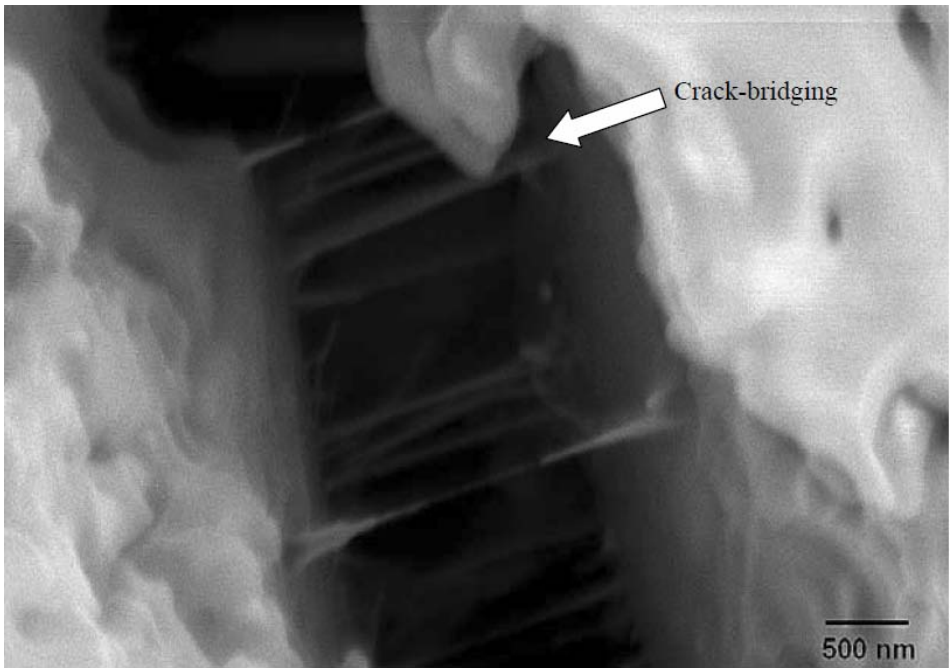


Figure 2.7.3 The observation of crack-bridging in DWCNT/epoxy composites via SEM [86].

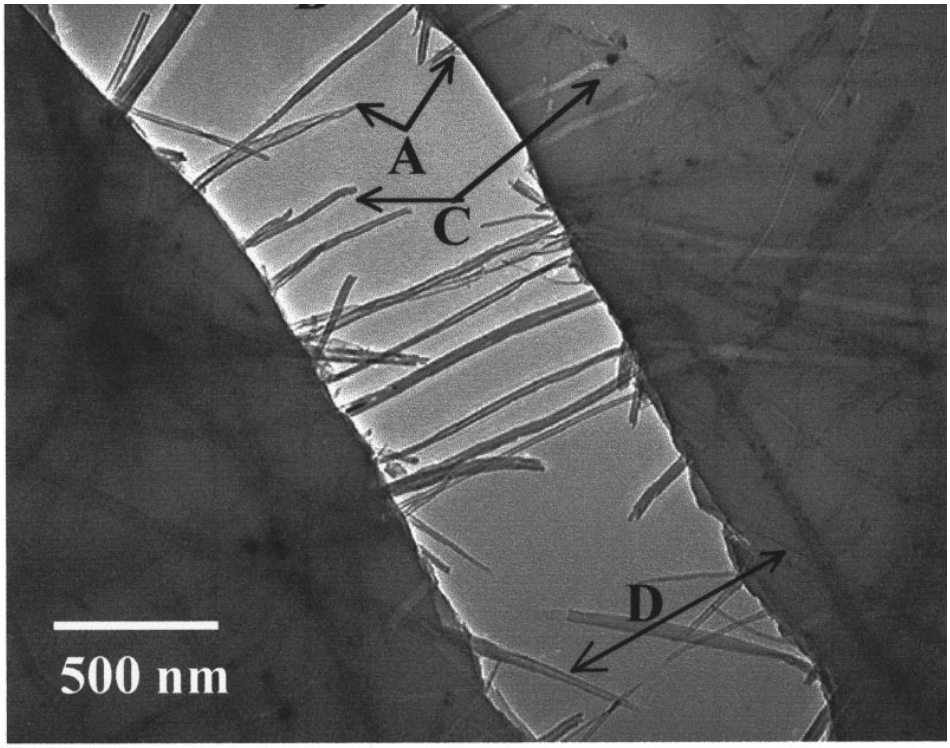


Figure 2.7.4 The observation of crack-bridging in MWCNT/PS composites via TEM [88].

Figure 2.7.5 shows schematic models of the pull-out mechanism caused by the debonding between CNT and matrix, and the crack bridging associated with partial debonding in the middle region of CNT and local bonding at both ends of the CNT. Blanco et al. [89] investigated both toughening mechanisms using an analytical model, and they reported that the contribution of the pull-out mechanism is more significant than the crack bridging.

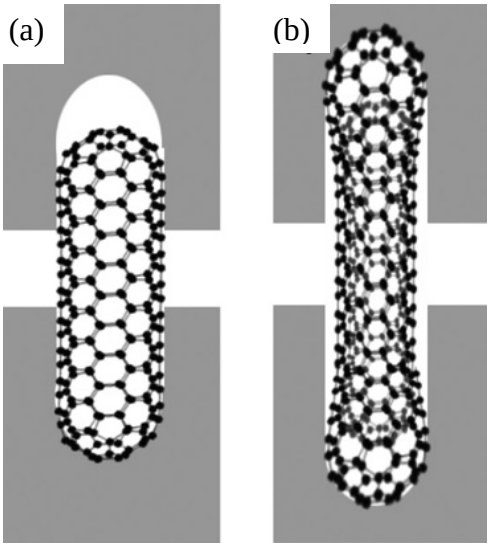


Figure 2.7.5 schematic models showing (a) CNT pull-out and (b) CNT crack bridging [86].

It is worth mentioning that telescopic nanotube pull-out can be discovered if the CNTs used in this technology are multi-walled, see Figure 2.7.6. In this mechanism, the outer-layer of the MWCNT is ruptured and becomes two parts which adhere to the matrix on the surfaces of a crack, and the middle of this telescopic microstructure consists of inner-layer CNTs connecting with ruptured outer-layer CNTs [74, 85]. However, this specific mechanism in MWNT/epoxy composites, the telescopic bridging, has a lesser effect on the toughness due to the weakness of the interfacial property between the inner and outer layers. Therefore, the toughness of SWCNT-toughened polymers is higher than MWCNT-toughened materials.

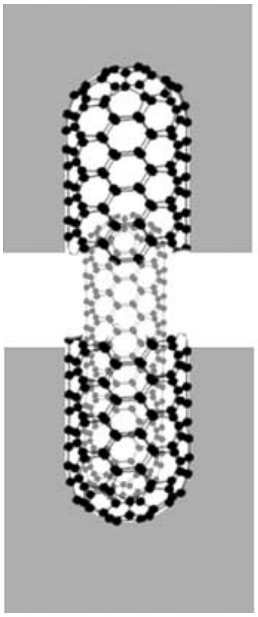


Figure 2.7.6 Schematic model showing the nanotube telescopic pull-out mechanism [85].

2.8 Conclusions

The present Chapter reviewed previous investigations on the characteristics of modified polymer composites with various reinforcements. The basic principles of fracture mechanics and introduction to polymers were described. The toughening mechanisms caused by the addition of rubber microparticles, rigid microparticles, silica nanoparticles and carbon nanotubes were also summarised. The inclusion of these reinforcements with the polymer matrix governs the toughening performance of their composites, and the toughening mechanisms depend on the type of the additives.

CHAPTER 3

MATERIALS AND MANUFACTURING

3.1 Introduction

This Chapter describes in detail the formulations used in this study. The process used to prepare the testing specimens is also stated; this includes the manufacturing techniques that were employed to produce the unmodified and modified bulk polymer samples with various reinforcements. The reinforcements used to improve the mechanical properties of the polymer-based composites can be separated into four types, viz (i) glass bead microparticles, (ii) silica nanoparticles, (iii) multi-walled carbon nanotubes, and (iv) carboxyl terminated butadiene acrylonitrile (CTBN) rubber microparticles.

3.2 Polymer Matrix

As a polymer matrix, LY-556, a diglycidyl ether of bisphenol-A (DGEBA) epoxy resin produced by Huntsman (Basel, Switzerland) was used in this study. This has an epoxide equivalent weight (EEW) of 185 g/eq. A low viscosity accelerated methylhexahydrophthalic acid anhydride curing agent with an anhydride equivalent weight (AEW) of 170 g/eq, Albidur HE 600, from Nanoresins (Geesthacht, Germany) was used as a hardener. The mixing ratio of LY-556 (DGEBA epoxy) and HE 600 (curing agent) is 1:0.914 by weight.

Formulations with various modifiers were prepared, along with the unmodified polymer (control). The concentration of the modifier was calculated by percentage weight (wt%) of the total mixture:

$$wt\% = \frac{wt_{modifier}}{wt_{modifier} + wt_{epoxy} + wt_{hardener}} \times 100\% \quad (3.1)$$

3.3 Modifiers

3.3.1 Glass Bead Microparticles

The glass beads, produced by MO-SCI (Rolla, USA), used to form the glass bead microparticle/epoxy composites have different particle sizes. The large glass bead microparticles have a size of -50+60 mesh, and the small microparticles are -400 mesh. Mesh scale is often used to determine the particle size, and the number of the mesh is identified as the size of openings of the sieve. Table 3.3.1 shows the typical openings in laboratory sieve series. As can be seen the mesh scale with a large number refers to a small opening size. The use of "+" and "—" are used to state the particle size within a range. A "+" indicates that the particles are bigger than the opening size of the sieve, while a "—" indicates that the particles are smaller than the opening size. According to the mesh scale, the large glass beads labelled as -50+60, indicating that their diameter falls in the range from mesh 60 to mesh 50. Using the conversion table below (see Table 3.3.1), the diameter of these large microparticles are between 250 μm to 297 μm. For the small glass beads, the particle size is smaller than 37 μm. A microscope was used to measure the diameter of the glass beads, and then compared with the mesh scale. The measured diameter was 275 ±15 μm for the large glass beads, and the diameter of the small glass beads is in a range between 1 μm to 5 μm. All of these measured results were in a good agreement with their mesh scales. Note that the diameter of the particles chosen would need to take into account when using glass beads to be the reinforcements in an adhesive. The large glass beads with a diameter of 275 μm are not suitable to be the reinforcement for adhesive applications because the diameter may be larger than the thickness of bond line.

In the glass bead/epoxy composites, the effect of the adhesion between the microparticles and epoxy matrix on the toughness was investigated. Therefore, these glass bead microparticles were surface treated before blending with the epoxy matrix. The detail of surface treatments will be described in Section 3.4.3, which explains the sample preparation.

Table 3.3.1 The typical openings in laboratory sieve series [90].

Mesh scale (number)	Opening size (mm)	Opening size (in)
No. 4	4.76	0.187
No. 5	4.00	0.157
No. 6	3.36	0.132
No. 7	2.83	0.111
No. 8	2.38	0.0937
No.10	2.00	0.0787
No. 12	1.68	0.0661
No. 14	1.41	0.0555
No. 16	1.19	0.0469
No. 18	1.00	0.0394
No. 20	0.841	0.0331
No. 25	0.707	0.0278
No. 30	0.595	0.0234
No. 35	0.500	0.0197
No. 40	0.420	0.0165
No. 45	0.354	0.0139
No. 50	***0.297***	***0.0117***
No. 60	***0.250***	***0.0098***
No. 70	0.210	0.0083
No. 80	0.177	0.0070
No.100	0.149	0.0059
No. 120	0.125	0.0049
No. 140	0.105	0.0041
No. 170	0.088	0.0035
No. 200	0.074	0.0029
No. 230	0.063	0.0025
No. 270	0.053	0.0021
No. 325	0.044	0.0017
No. 400	***0.037***	***0.0015***

3.3.2 Silica nanoparticles

The silica nanoparticles used in this study have a narrow particle-size distribution and their mean diameter is around 20 nm. Figure 3.3.1 and Figure 3.3.2 show a transmission electron micrograph of the nanosilica and the particle number density versus the particle size, respectively. As can be seen in the TEM image, these nanoparticles are well-dispersed in the cured polymer sample. In Figure 3.3.2, the diameter of the silica nanoparticles is in a range of 5-35 nm, and a mean value of 20 nm was calculated.

Nanopox F400 from Nanoresins (Geesthacht, Germany), composed of 40 wt% of the silica nanoparticles well-dispersed in a DGEBA epoxy resin, was used as the nano-reinforcement. In order to prevent nanosilica agglomeration (see Figure 3.3.3) in the resin, a standard treatment is used by Nanoresins in the nanosilica-modified epoxy resins. Note that the standard treatment may impede the generation of chemical bonds by additional surface treatment, as the nanoparticles have been covered with a thin layer of the standard treatment. However, it is not known whether the standard treatment coats the nanoparticles completely, or whether there are still sites available for bonding with any additional surface treatment.

In addition to the standard treatment used to improve the dispersion of silica nanoparticles in the resin, surface modifications are used to improve the adhesion between the modifier and matrix. In this study, an additional surface treatment was used to modify the standard silica nanoparticles (i.e. Nanopox F400). The additional surface treatment used is a silane coupling agent, which was introduced into the nanocomposites during the sample preparation, and will be described in Section 3.4.4.

Nanopox XP, produced by Nanoresins (Geesthacht, Germany), consists of 40% of surface treated silica nanoparticles well-dispersed in a DGEBA epoxy resin. This was used as the other nano-reinforcement, in which this surface treatment was introduced by the manufacturer to improve the nanoparticle/epoxy adhesion. The sample preparation for the nanosilica-modified epoxy polymer with Nanopox F400 and Nanopox XP will be described in Section 3.4.4.

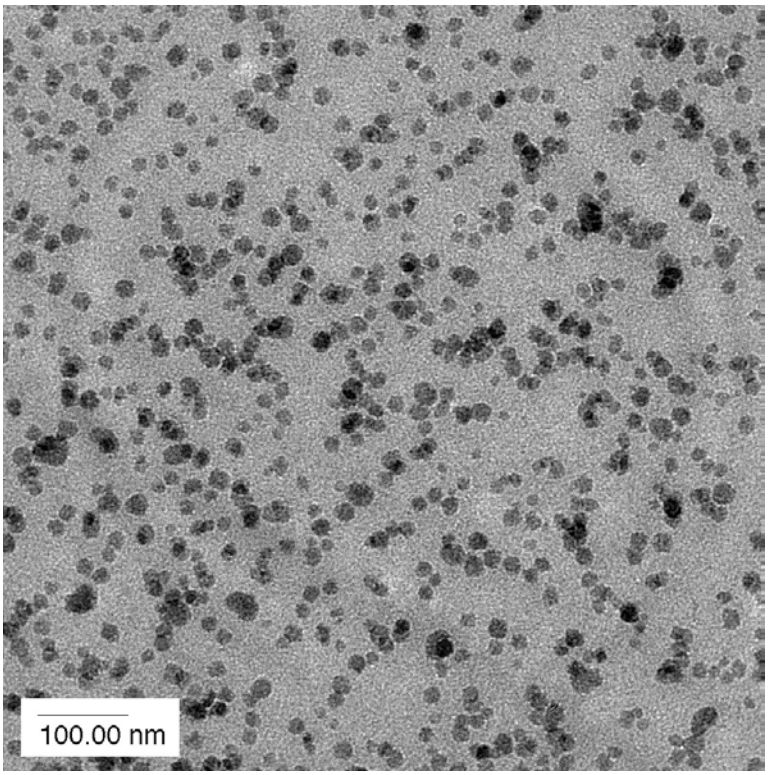


Figure 3.3.1 TEM image of the epoxy nanocomposite containing 5.0 wt% silica nanoparticles, showing well-dispersed particles [91].

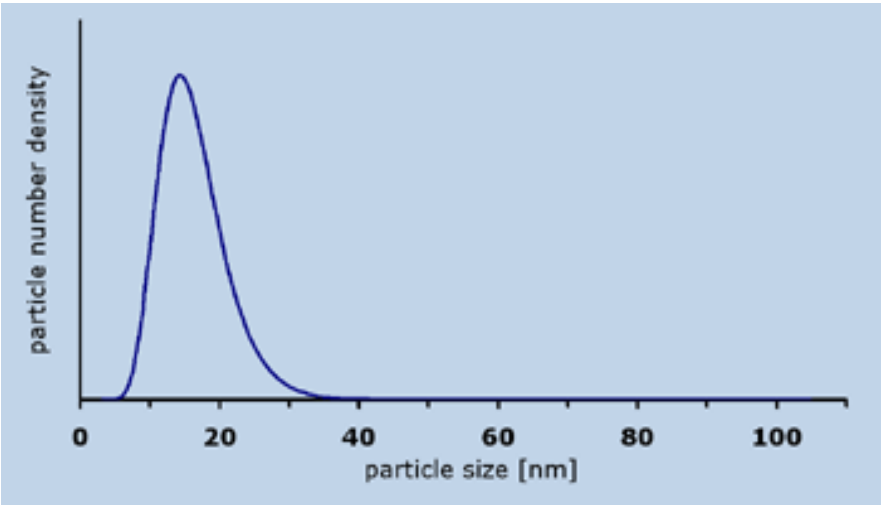


Figure 3.3.2 The particle number density versus the particle size for the nanosilica particles, determined by small angle neutron scattering (SANS) [91].

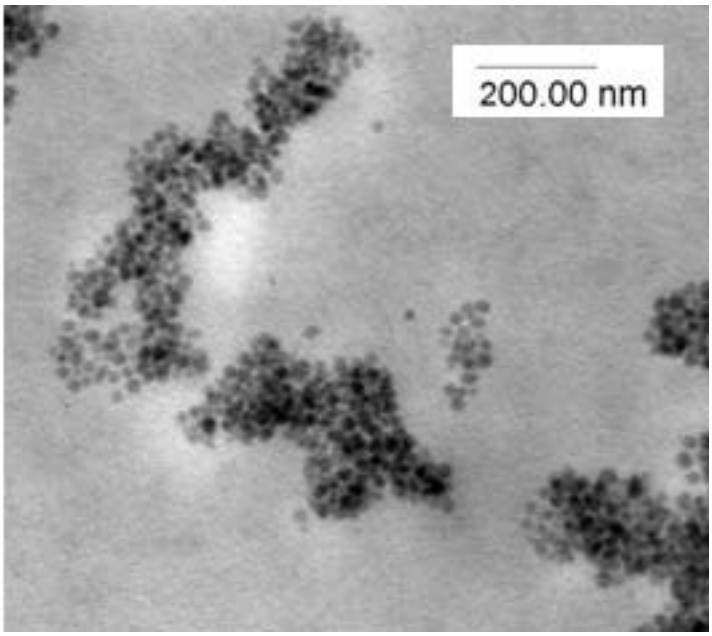


Figure 3.3.3 TEM image of the epoxy nanocomposite containing 5.0 wt% silica nanoparticles, showing nanosilica agglomeration [91].

3.3.3 Rubber Microparticles

The reactive liquid rubber used in this study was a carboxyl-terminated butadiene-acrylonitrile (CTBN) adduct. The rubber-modified DGEBA resin called Albipox 1000 (EEW = 330 g/eq) from Nanoresins, Germany, consists of an adduct of 40 wt% of CTBN rubber in a DGEBA epoxy resin. The CTBN phase-separates via a nucleation and growth process during the curing process to form the spherical CTBN rubber microparticles.

Figure 3.3.4 shows the particulate phase of CTBN rubber particles formed during the curing schedule. Nucleation is visible at 50 minutes into the cure cycle. After 70 minutes and at 150 ºC, the CTBN-epoxy mixture was at the state of vitrification, and hence no further phase separation can occur [23].

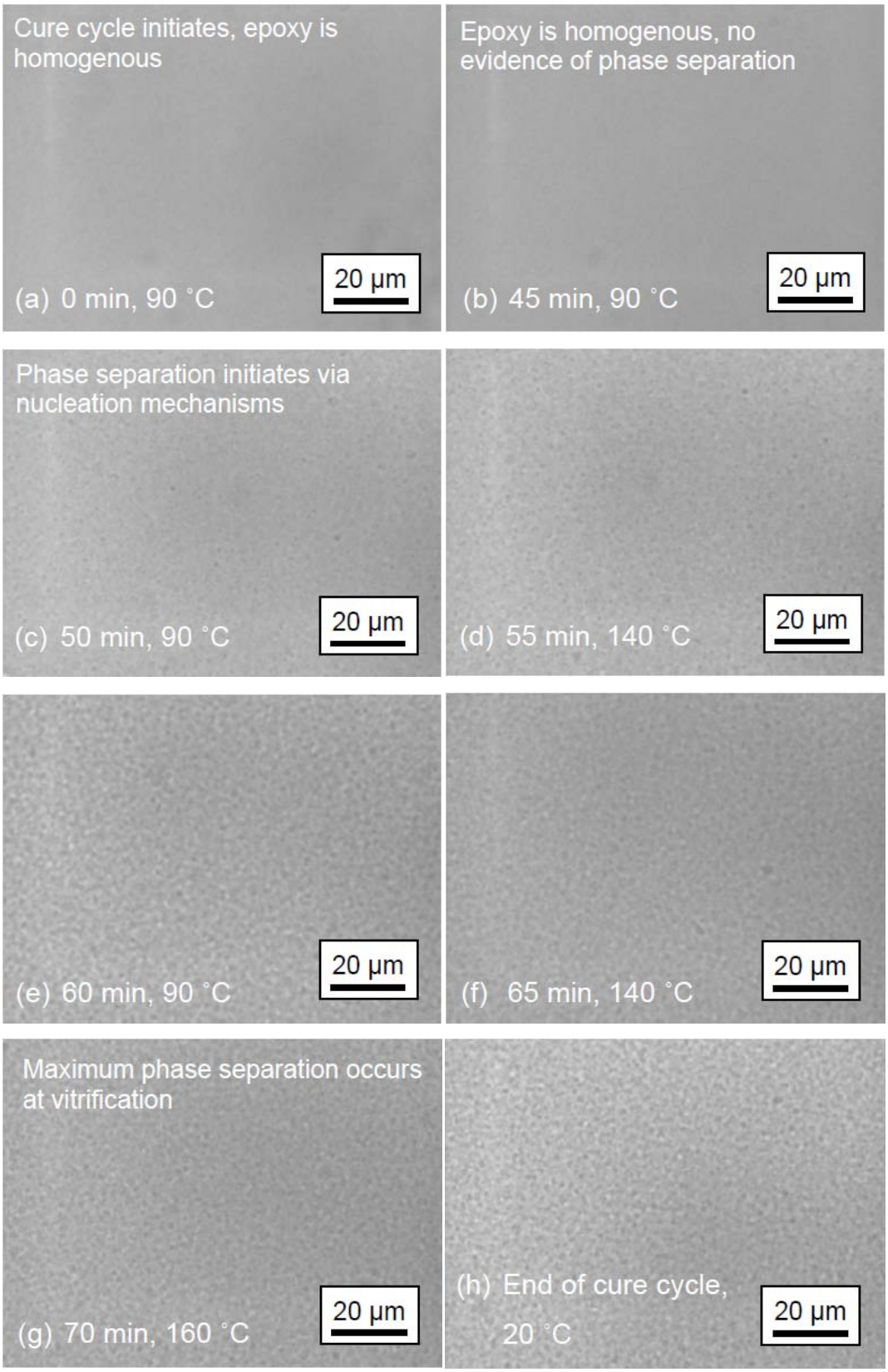


Figure 3.3.4. Optical micrographs of a sample of 9.0 wt% CTBN rubber/DGEBA polymer during curing, showing how the morphology of the rubber-modified epoxy varies with respect to temperature and time [23].

3.3.4 Multi-walled Carbon Nanotubes

The aligned multi-walled carbon nanotubes (MWCNTs) used to manufacture the nanotube-modified nanocomposites, discussed in Chapter 7, were produced using a chemical vapour deposition (CVD) process by the nanomaterials group at the University of Manchester. Figure 3.3.5 shows the apparatus for the CVD process. A liquid solution of ferrocene in toluene (8.76 wt%) was injected at a rate of 0.4 ml/min into a carrier gas preheated at 200 °C. The carrier gas used in the CVD process is argon and hydrogen ($Ar:H_2$ = 2500:250 SCCM; SCCM is standard cubic centimetre per minute), at slightly above atmospheric pressure. The aligned MWCNTs formed at 760 °C, and they were deposited on the silica substrates with a size of 20 mm × 30 mm inside a tubular furnace. The as-produced carbon nanotubes are relatively straight and unentangled, with an average length of 140 μm and an average diameter of 120 nm, see Figure 3.3.6. After cooling, the nanotube films were scraped off the silica substrates using a scalpel, and then were blended with the DGEBA epoxy resin to form the MWCNT-modified polymers. For a detailed description of the CVD process and operating parameters see Garcia-Cespedes et al. [92] and Singh et al. [93].

In this study, two different types of MWCNTs were used. The standard nanotubes, see Figure 3.3.6, have a relatively long length (140 μm), compared with the low quality nanotubes with an average length of 32 μm, see Figure 3.3.7. Both these types of multi-walled carbon nanotubes were synthesised by the CVD process, but the low quality nanotubes were deposited on TiN-coated Cu substrates. Both of these types of nanotubes were used to form the MWCNT-modified polymers, as will be discussed in Chapter 7.

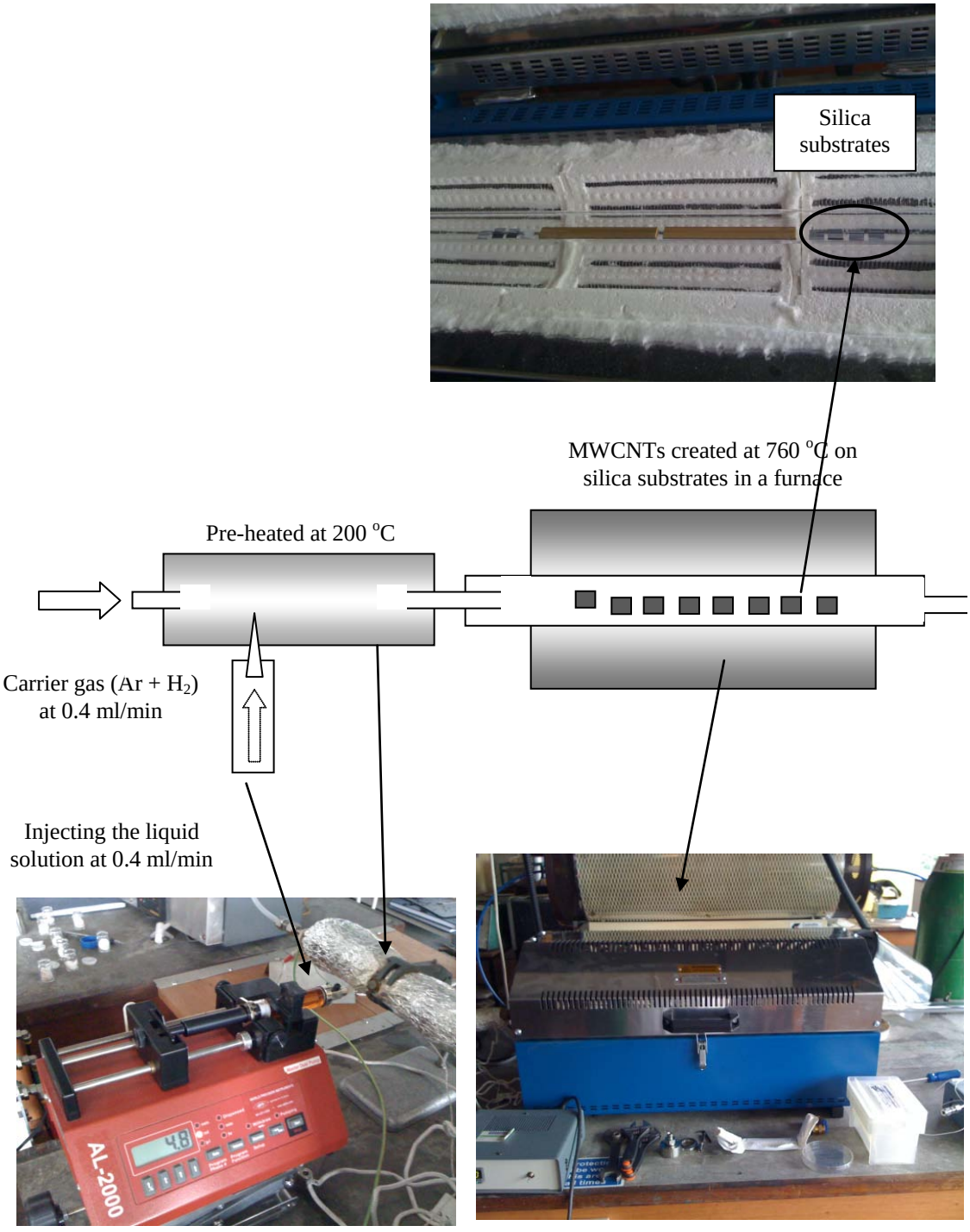


Figure 3.3.5 The equipment of the CVD process used for generating the aligned multi-walled carbon nanotubes.

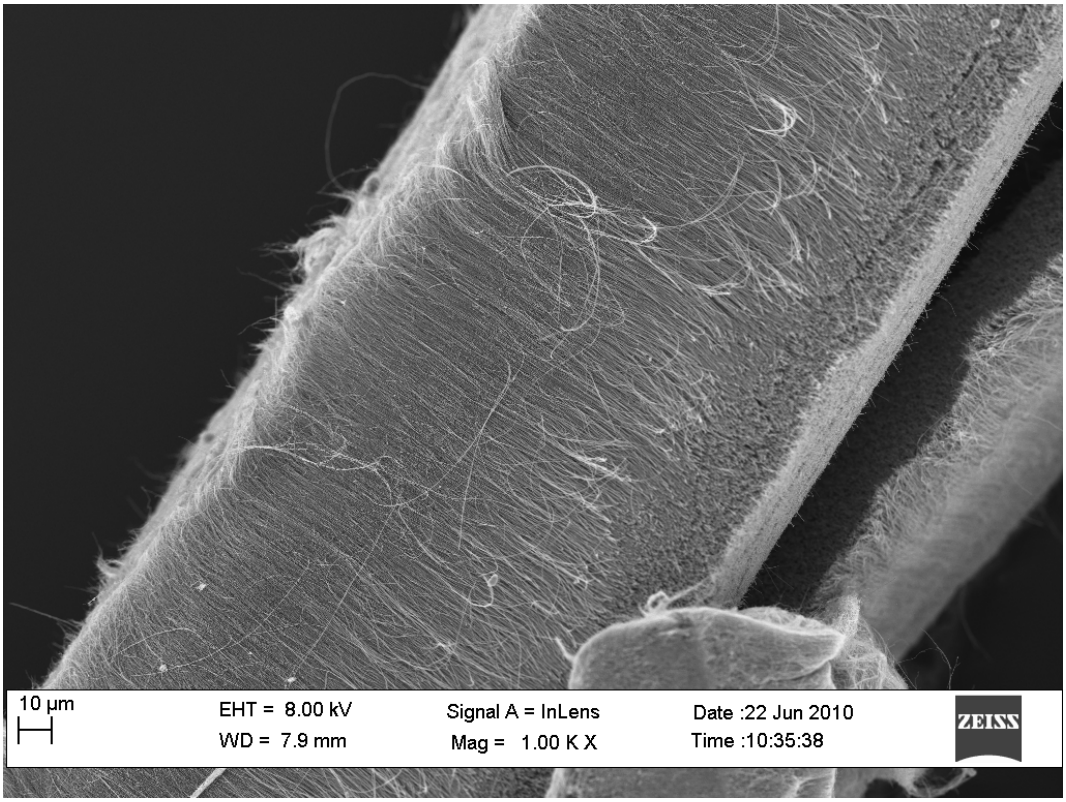


Figure 3.3.6 FEG-SEM image of the aligned multi-walled carbon nanotubes (standard nanotubes).

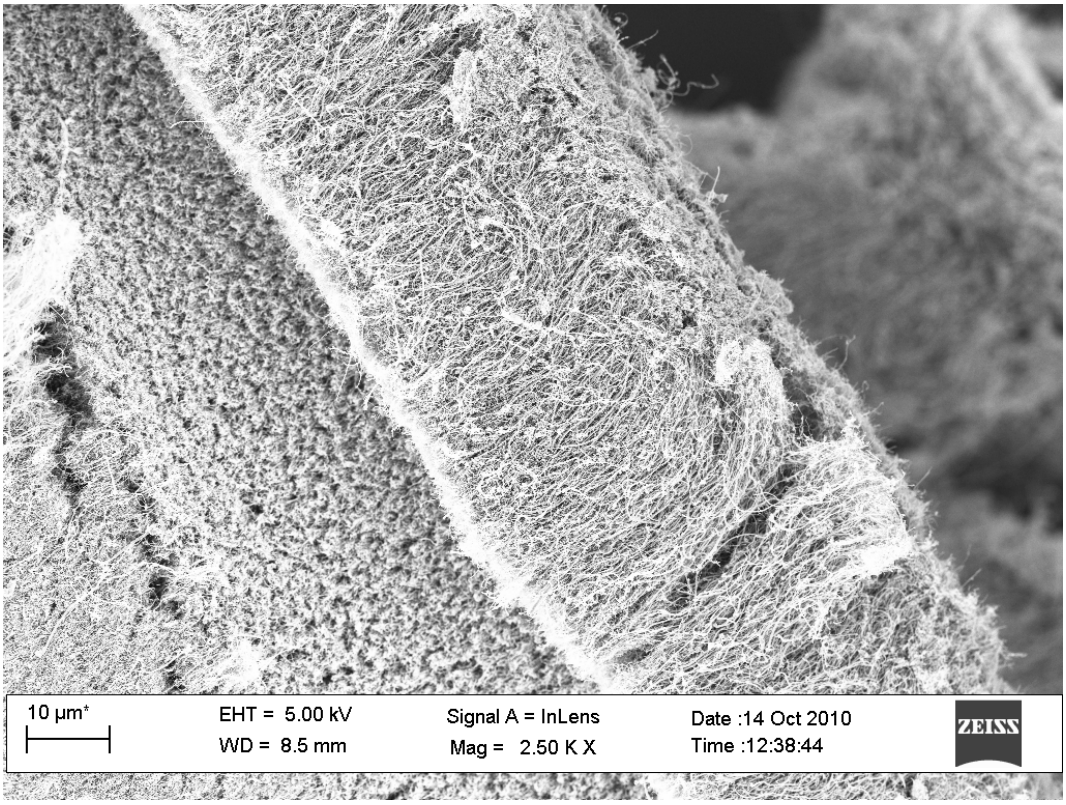


Figure 3.3.7 FEG-SEM image of the aligned multi-walled carbon nanotubes (low quality nanotubes).

A Raman microscope with a laser light wavelength of 488 nm was used to characterize the CVD grown carbon nanotubes [92]. Figure 3.3.8 shows the Raman spectra taken from the nanotubes deposited on SiN_x-coated Cu substrates by Dr. I. A. Kinloch (University of Manchester). The results showed that these carbon nanotubes have an intensity ratio between bands D and G of around 0.4, and no radial breathing modes (RBM) were observed in the low frequency region. All of these demonstrated that the nanotubes synthesised by the CVD process are multi-walled carbon nanotubes. Figure 3.3.9 shows the typical Raman spectra for single-walled and multi-walled carbon nanotubes. For single-walled carbon nanotubes, the intensity of the band D is much smaller than the band G, and RBM exists in the low frequency region [94].

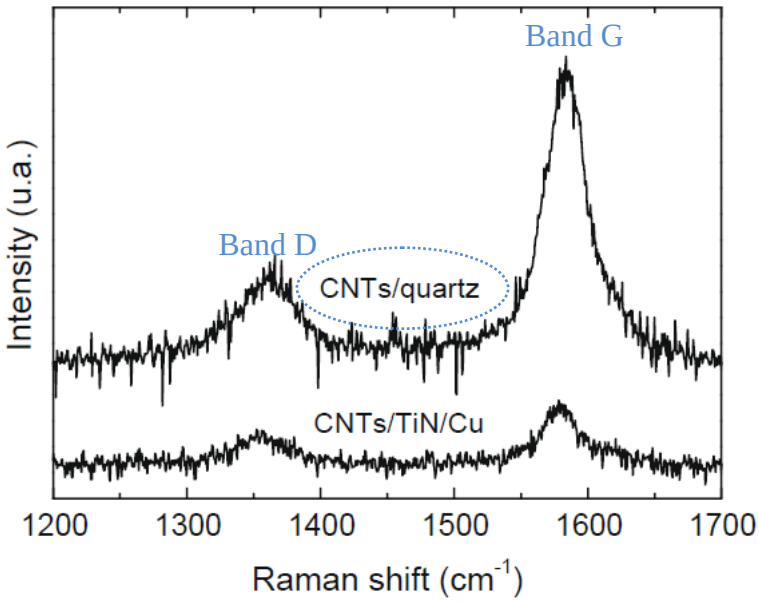


Figure 3.3.8 Raman spectra of the carbon nanotubes synthesized on the SiN_x-coated substrate [92].

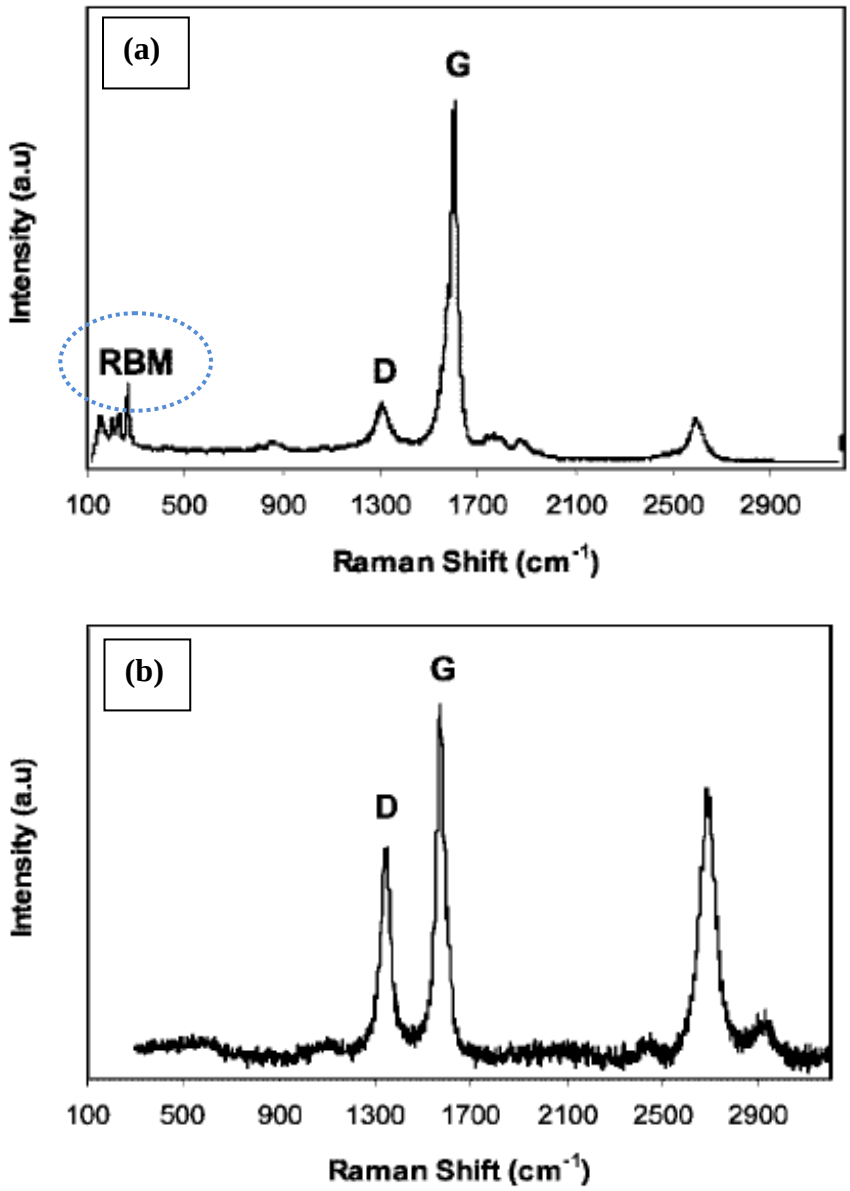


Figure 3.3.9 Raman spectra taken in (a) single-walled carbon nanotubes, and (b) multi-walled carbon nanotubes [94].

3.4 Manufacturing

3.4.1 Casting Mould and Temperature Cycle

In this Section, the procedure for preparing the polymer-based samples is described. Gravity moulds, see Figure 3.4.1, were used to prepare bulk samples via a casting process. Casting using the gravity mould can obtain void-free epoxy plates with uniform thickness. G-clamps and silicone rubber gaskets with a diameter of 3 mm were used to keep the mould closed and sealed. In this study, a 2-mm-thick, 3-mm-thick and a 6-mm-thick mould were used to make polymer plates as required to fit in with the testing standards.



Figure 3.4.1 The casting gravity mould.

As all the polymer matrices used to form the modified-polymer composites with various modifiers use the same anhydride-cured (HE 600) DGEBA epoxy (LY-556), the temperature cycle used to cure the samples after the modified-mixture was poured into the casting mould is the same. The cure cycle used for all the formulations is shown in Figure 3.4.2. As suggested by the manufacturers, the cycle consists of an initiation at 60 °C for casting, i.e. pouring the mixture into the mould. Then the temperature was increased to 100 °C at 10 °C/min, and held at 100 °C for 2 hours to cure the samples. Post-cure was required at the end of the sample preparation; the temperature and duration for the post-cure is 150 °C (ramp at 10 °C/min from 100 °C to 150 °C) and 10 hours, respectively. Finally, the cured polymer was cooled in the oven, and the bulk sample was then removed from the mould once the temperature reached room temperature.

Note that the sample preparation for the modified-epoxy resins was slightly different due the various modifiers used in this study, and will be described in following Sections. A radial flow impeller with 10 blades was fitted on a mechanical stirrer (RZR 2102 control from Heidolph), and was used to disperse the additives and mix the curing agent with the modified-epoxy resin.

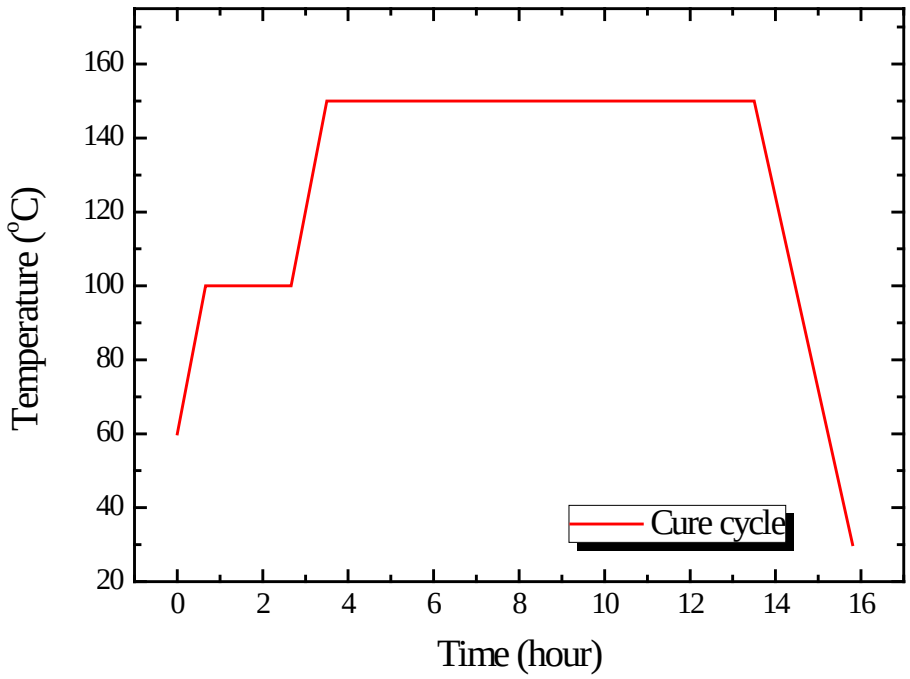


Figure 3.4.2 Temperature cycle used in the study.

3.4.2 CTBN-modified Polymer

In the sample preparation for the modified polymers with the CTBN rubber particles, the epoxy resin (LY-556) was first mixed completely with the CTBN-containing epoxy resin (Albipox 1000) using a mechanical stirrer for 10 minutes at 500 rpm, and then mixed with the hardener (HE-600) using a mechanical stirrer for 20 minutes at 500 rpm. Both of these stirring processes were conducted at room temperature. The final mixture was degassed at 60 °C for 30 minutes using a vacuum oven, before pouring the mixture into the casting mould.

The CTBN rubber was blended with the silica nanoparticles or multi-walled carbon nanotubes to form the hybrid materials (CTBN/silica and CTBN/MWCNTs), and will be described in Section 3.4.5 and Section 3.4.7.

3.4.3 Glass Bead Microparticle-modified Polymer

In the glass bead/epoxy materials, various surface treatments were used to change the level of the adhesion between the glass beads and the matrix. In order to improve the particle/epoxy adhesion, a liquid silane, A187 from Witco (Silquest A187 silane, γ-glycidoxypropyltrimethoxy-silane) was used to prepare a silane solution. The silane solution consists of 1 wt% of A187 blended with a 90:10 mixture by weight of ethanol:deionised water. The pH value of the mixture was controlled at around five by the addition of acetic acid. This silane solution was then stirred for 60 minutes before use.

In contrast to the silane treatment (to improve the adhesion), the adhesion between the glass beads microparticles and the epoxy mixture was reduced using a release agent, Frekote 770-NC from Henkel. A sample containing untreated glass beads was made as the control formulation.

In the modified treatment systems, the glass beads were mixed with 10 wt% (10wt% of the total weight of final mixture, i.e. modifier/epoxy/hardener/treatment) of the silane solution to improve the adhesion or the release agent (Frekote) to reduce the adhesion. The glass beads were left in the solution (silane solution and Frekote) for 30 minutes at room temperature, and then heated using an oven at 150 °C for around 2 hours to dry. Hence the silane solution and Frekote release agent were fully coated on the surfaces of these glass beads microparticles. To remove the agglomerates, the treated particles were sieved using the sieve with opening size of 300 μm for the large glass beads, and 50 μm for the small glass beads.

After surface treatment, the treated particles were mixed with the epoxy resin (LY-556) and hardener (HE 600) using a mechanical stirrer (500 rpm) for 30 minutes at room temperature, and then degassed at 60 °C for 30 minutes in a vacuum oven. The glass bead-modified mixture was then poured into the casting mould. Due to their size and mass, the glass beads have a tendency to sediment. Therefore, after casting, the mould was turned over every 5 minutes during the cure cycle, until vitrification was reached. Note that an airtight mould, see Figure 3.4.3, was used to prepare the glass

bead/epoxy bulk samples. G-clamps and a silicone sealant, BOND-FLEX from Bostik, were used to keep the mould sealed.



Figure 3.4.3 The airtight mould used for preparing glass bead-modified bulk polymer samples.

3.4.4 Nanosilica-modified polymer

Two different nanosilica-modified epoxy resins, (Nanopox F400 and Nanopox XP) were used in this study. The sample preparation of the nanocomposites is similar to the CTBN-modified polymers.

For preparing the nanosilica/epoxy nanocomposites, the nanosilica-modified resin was mixed with the DGEBA (LY-556) and hardener (HE 600) completely using a mechanical stirrer (500 rpm) for 30 minutes at room temperature, followed by a degassing process at 60 °C for 30 minutes in a vacuum oven before casting.

In the nanosilica-modified polymers, silane treatment was introduced to improve the adhesion between the silica nanoparticles (Nanopox F400) and the epoxy matrix. For the nanocomposite containing the silane-treated nanosilica, a liquid silane, A187 from Witco (Silquest A187 silane, γ-glycidoxypropyltrimethoxy-silane) was directly added into the nanosilca-modified epoxy resin (Nanopox F400), and then mixed completely using a mechanical stirrer (500 rpm) for 30 minutes at room temperature. The concentration of A187 used in the surface treatment was 10 wt%. After that, the silane treated Nanopox F400 mixture was blended with the DGEBA and hardener using a mechanical stirrer (500 rpm) for 30 minutes at room temperature, and then degassed at 60 °C for 30 minutes in a vacuum oven. Finally, the mixture was poured into the casting mould, and then run the curing cycle. An additional control formulation of the epoxy modified with 5 wt% of A187 was prepared to investigate effect of the silane treatment on the mechanical properties of the epoxy.

3.4.5 Hybrid of CTBN/nanosilica

If the CTBN rubber was required to blend with the nanosilica to form the hybrid materials (CTBN/nanosilica/epoxy), the CTBN containing epoxy resin (Albipox 1000) was mixed with the nanosilica mixture (Nanopox F400) and DGEBA epoxy resin (LY-556) for 10 minutes using a mechanical stirrer (500 rpm) at room temperature. Then the

hardener was added into the mixture and stirred completely for 20 minutes at room temperature using a mechanical stirrer, at 500 rpm. The final mixture was degassed at 60 °C for 30 minutes using a vacuum oven before casting.

3.4.6 Multi-walled Carbon Nanotube-modified polymer

The dispersion of the CNTs is an important factor for the modified polymer with carbon nanotubes. Various dispersion methods to achieve well-dispersed carbon nanotubes were investigated, see Chapter 5. For preparing the MWCNTs/epoxy nanocomposites, the calculated weight of the multi-walled carbon nanotubes, synthesised by the CVD process, was blended with the DGEBA epoxy resin, and mixed manually using a spatula for around 5 minutes. After that, the mixture containing the epoxy and MWCNTs was sonicated using an ultrasonic probe (CPX 750 from Cole-Parmer) for 30 minutes. The amplitude of the sonicator was set at 30, which is about 20 kHz. The sonication generated heat, consequently the temperature of the mixture increased. Therefore, a thermocouple was used to measure the temperature of the mixture. The sonicator was stopped if the temperature reached 80 °C. In this case, the sonicator was re-started when the temperature cooled down to 60 °C (after around 10 minutes). After the sonication process, the mixture was blended with the hardener (HE 600), and mixed completely using a mechanical stirrer (300 rpm) for 30 minutes at 60 °C, followed by a degassing process at 60 °C for 30 minutes in a vacuum oven. The mixture was finally poured into the casting mould and run through the curing schedule.

3.4.7 Hybrid of CTBN/MWCNTs or Nanosilica/MWCNTs

For preparing the hybrid-toughened polymer with CTBN/MWCNTs and Nanosilica/MWCNTs, the multi-walled carbon nanotubes were blended with the DGEBA epoxy resin, and mixed manually using a spatula for around 5 minutes. Then,

the MWCNTs/epoxy mixture was blended with the CTBN containing epoxy resin (Albipox 1000) or nanosilica-modified resin (Nanopox F400), and mixed using a mechanical stirrer (300 rpm) for 20 minutes at 60 °C, followed by a sonication process. The sonication process is similar to that used for preparing the MWCNTs/epoxy sample in Section 3.4.6, but a longer duration of 40 minutes was used in these hybrid-modified polymers. This is because the hybrid-modified mixture has a relatively high viscosity, compared with the modified epoxy resin with the MWCNTs alone. If the temperature of the mixture reached 80 °C during the sonication, the ultrasonic probe was stopped until the mixture cooled to 60 °C (taking around 15 minutes). Before casting, the mixture was degassed at 60 °C for around 20 minutes in a vacuum oven.

3.5 Conclusions

This Chapter presented the materials including the epoxy polymer and the modifiers used in this study. The sample preparation was also described in detail for each formulation.

As the polymer mixture used to form the polymer-based composites with various reinforcements is the same, the curing schedule used to cure the unmodified or modified polymers is the same. However, the mixing processes and dispersion methods in the sample preparation are slightly different, and depend on the added modifiers. All the bulk polymer samples were formed using a gravity casting process, except for the glass bead/epoxy composites. As serious sedimentation of the glass beads occurred during the curing cycle, a sealed mould, which was turned over during the curing process, was used to manufacture the glass bead microparticle-modified polymer.

CHAPTER 4

EXPERIMENTAL METHODS

4.1 Introduction

This Chapter describes the various experimental methods that were conducted to investigate the microstructure and the material properties of the polymer-based composites in this study.

4.2 Tensile tests

The Young's modulus, *E*, of the cured epoxy-based composites with various additives, was measured using an Instron 5584 or 4466 universal testing machine operated by Bluehill software. According to the ASTM D 638 [95] and BS ISO 527-1 [96] testing standards, the tensile testing specimens, as shown in Figure 4.2.1, were prepared by machining from a 2-mm-thick plate for all formulations. The specimens were cut from the polymer plates using a cutting machine (Accutom-5 from Struers) with a silicon carbide wheel. They have a gauge length of 20 mm with loading end-tabs bonded on at both ends; the loading end-tabs were made from glass fibre-reinforced polymer (GFRP) and mounted on both ends of the specimens using an epoxy structural adhesive, E32 from Permabond (Eastleigh, UK), which was cured at room temperature. Before bonding the end-tabs, the surfaces of the specimens were polished using a grinding machine (Labopol-25 from Struers) to remove defects caused by the cutting process. This is to improve the quality of the surfaces of the testing specimens, and the roughness of the surfaces reached 0.3 μm. The reason why the tensile testing specimen with load end-tabs was substituted for dumbbell-shaped specimens is that the shape of the tensile specimen with end-tabs is rectangular, on which is much easier to do the polishing process for all the surfaces using a grinding machine than for the dumbbell-shaped specimens.

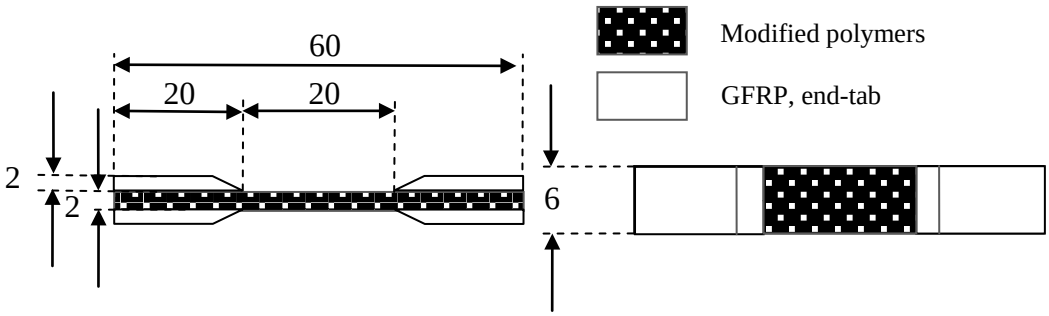


Figure 4.2.1 Tensile testing specimen geometry (unit : mm) [95, 96].

During the tensile testing, the specimen was tested in uniaxial loading with a displacement rate of 1 mm/min at room temperature of around 25 °C, and the load versus displacement data was recorded via a load cell and an extensometer. The extensometer used knife edges, and was attached on the gauge length region of the testing specimens to measure accurate strains. Figure 4.2.2 shows the set up in the tensile tests. At least five replicate tests for each formulation were used in the study. The Young's Modulus, *E*, was the slope of the linear portion of the stress-strain curve, the value of which is calculated by linear fitting the initial one fifth of the experimental data. The equations used to determine the Young's Modulus are as follows:

$$\sigma = \frac{P}{A} \tag{4.1}$$

$$\varepsilon = \frac{e}{L_g} \tag{4.2}$$

$$E = \frac{\sigma}{\varepsilon} \tag{4.3}$$

where σ is the stress, P is the tensile load, A is the cross sectional area of the sample in the gauge region, ε is the strain, e is the extension of the gauge length, L_g is the gauge length and E is the Young's Modulus.

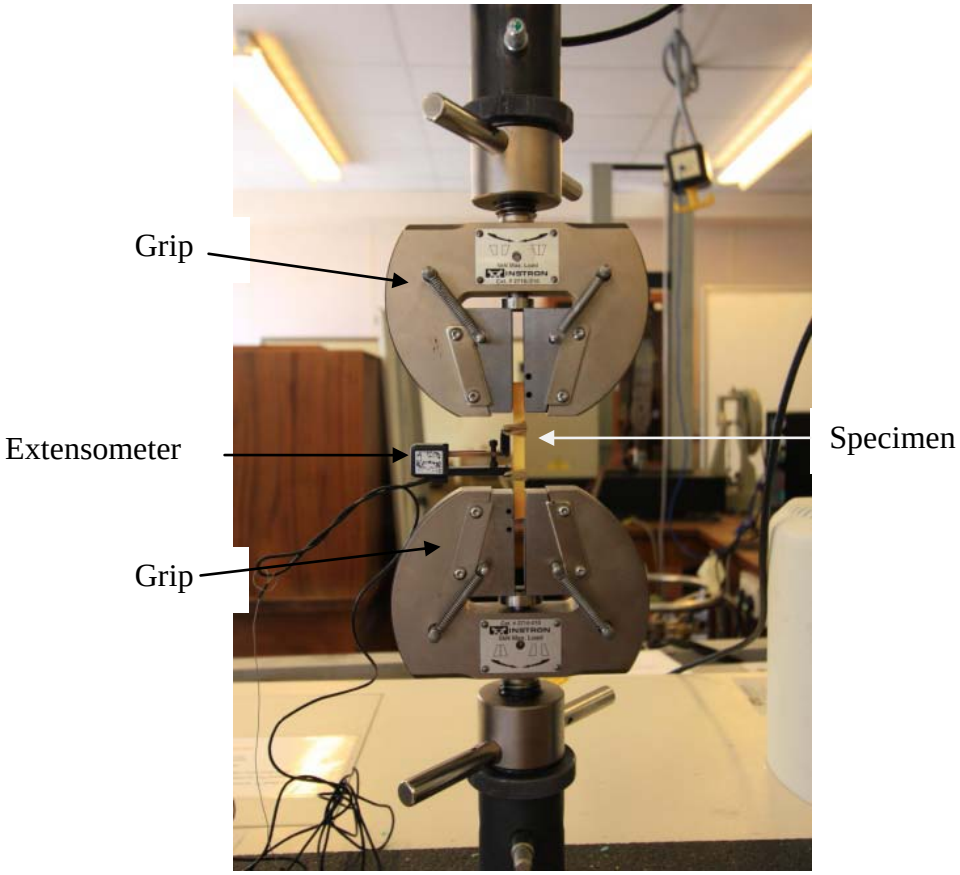
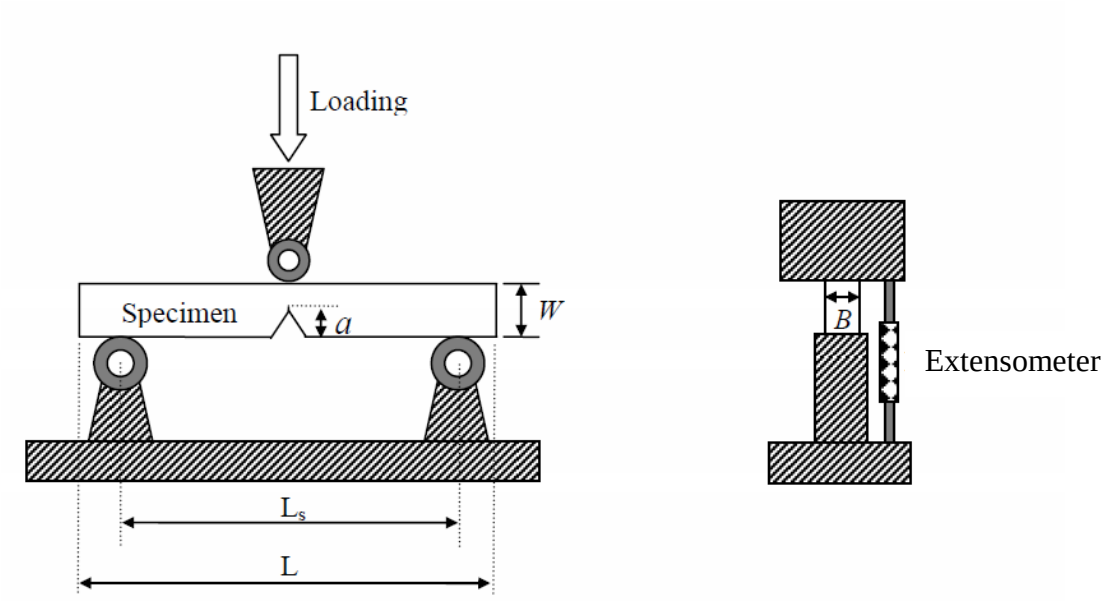


Figure 4.2.2 The test set up used to measure the Young's modulus of the polymer-based composites.

4.3 Single edge notch bend tests

In order to characterise the fracture toughness, single edge notch bend tests (SENB) have been widely used and implemented in accordance with ASTM D 5045 [97] and BS 7448-4 [98]. The specimen preparation and testing procedure of the SENB are as follows. With a rectangular cross section and made from various formulations, each SENB testing specimen was prepared from a 6-mm-thick plate using a cutting machine, Accutom-5 from Struers, and a sharp notch was made using a milling machine. Then the specimens were tapped at the notch root using liquid-nitrogen cooled razor blades to obtain sharp cracks; the crack length should be between 0.45~0.55 of the width of the specimen [97]. After the preparation of the SENB specimens, the width and thickness of the specimens were measured; the crack length was measured after testing. All of these measurements should be accurate within 0.5%, and were taken at not less than three positions. Figure 4.3.1 shows the dimensions of the SENB specimen and the set up of the SENB tests.



where

W = 12.0mm

B = 6.0mm

a = 6.0mm

L = 60.0 mm

L_S = 4W = 48.0mm

Figure 4.3.1 Schematic of the SENB test [97].

During testing, the specimens were subjected to compressive load at the centre of the specimen in line with the notch, and supported on the two supporting rollers with a span of L_S, and with a diameter of 12 mm. An extensometer was used to measure the change of the interval between the loading-point and the support rollers during the testing. The cracked specimen used in the SENB test was assumed to have elastic behaviour, so certain restrictions on the linearity of the load-displacement trace were imposed. For this reason, the condition for the measurement of the fracture toughness of epoxy-based materials is 1 mm/min for the displacement rate. For each formulation, at least six replicate specimens were tested and the average was used to obtain the critical stress-intensity, K_{Ic}, The thickness of the specimen was sufficient to satisfy plane strain conditions.

The critical stress-intensity factor, K_{Ic}, was calculated from:

$$K_Q = (P_{max} BW^{1/2}) f(x) \tag{4.4}$$

where K_Q is the conditional result and P_{max} is the maximum load in the SENB test, or:

$$K_Q = (P_Q BW^{1/2}) f(x) \tag{4.5}$$

where P_Q can be calculated from the load-displacement cure, as shown in Figure 4.3.2.

If P_{max} falls within $\overline{AB}$ and $\overline{AB'}$, see Figure 4.2.2, then P_{max} is used to calculated K_Q. If P_{max} falls outside $\overline{AB}$ and $\overline{AB'}$, P_Q is used to calculate K_Q [97].

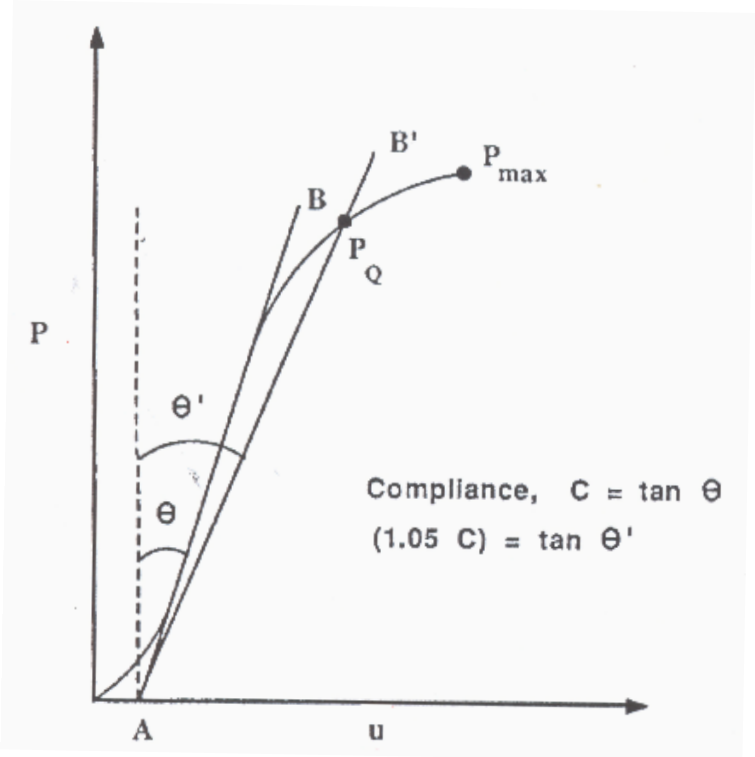


Figure 4.3.2 Determination of K_Q [97].

The value of *f(x)* can be calculated from:

$$f(x) = 6x^{1/2}\,\frac{[1.99 - x(1-x)(2.15 - 3.93x - 2.7x^2)]}{(1+2x)(1-x)^{3/2}} \tag{4.6}$$

and where $0<x<1$, $x=a/W$

If Equation 4.7 is true, then $K_Q = K_{Ic}$. Otherwise, the test is not a valid K_{Ic} test.

$$2.5\left(\frac{K_Q}{\sigma_y}\right)^{1/2} < a, B \text{ and } (W\text{-}a) \tag{4.7}$$

where σ_y is the yield stress, a is the crack length, B is the width of the specimen and W is the height of the specimen.

4.4 Plane-strain Compression Tests

Plane-strain compression (PSC) tests were performed on the modified polymers to investigate the material properties with large deformation. This test was described by Williams and Ford [99]. The PSC testing specimen, as shown in Figure 4.4.1, has dimensions of 3 mm × 40 mm x 40 mm, and was loaded with a compressive loading between two parallel, 12 mm wide indenters.

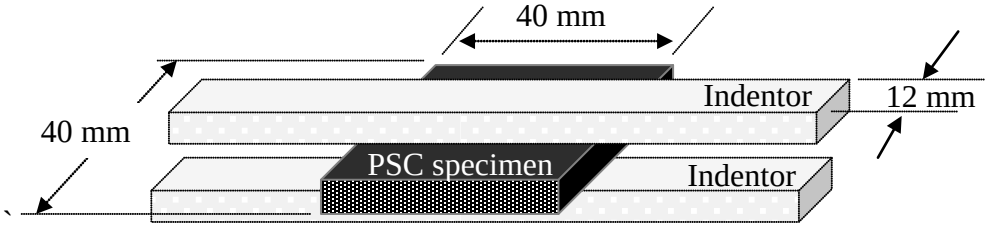


Figure 4.4.1 Geometry for the plane-strain compression specimens and indenters [23, 99].

Figure 4.4.2 shows the apparatus for the PSC tests, a set square was used to ensure the compressive indenters were aligned, perpendicular to the specimen edge. During the testing, a constant displacement rate of 0.1 mm/min was used to approximately match the strain rate from the tensile tests.

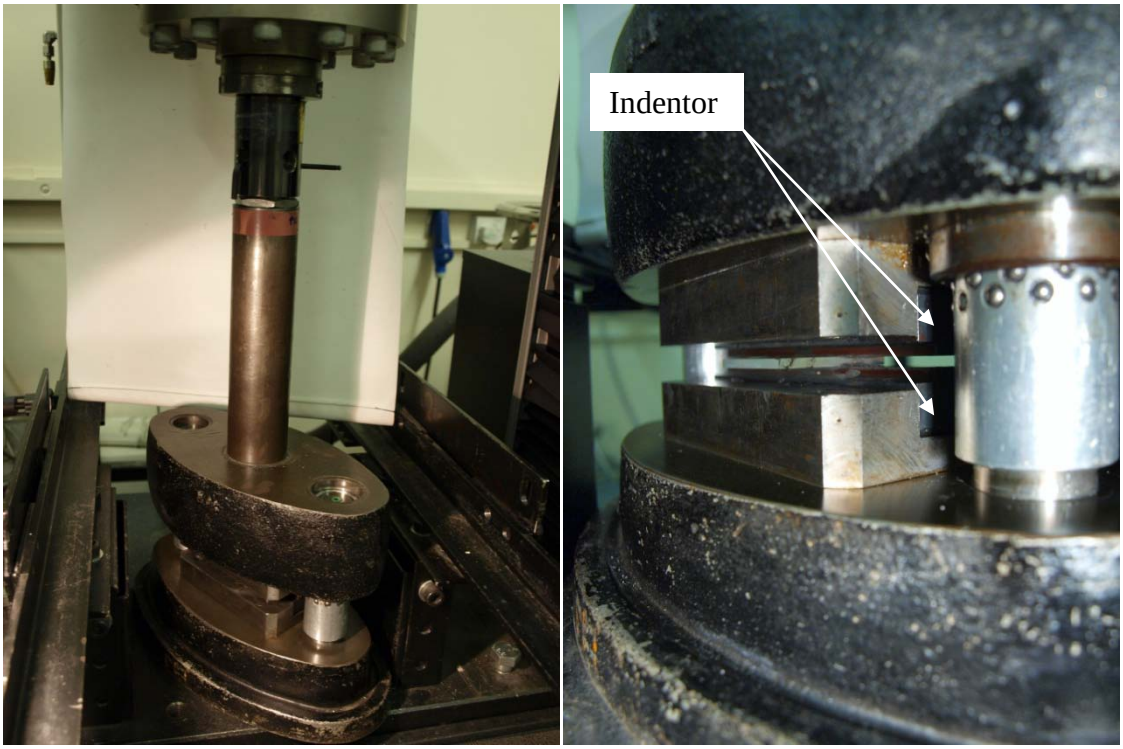


Figure 4.4.2 The set square and indentors used in the PSC tests.

Three replicate tests were conducted for each formulation, and the value of compressive moduls, E_c, compressive yield stress, σ_{yc} and fracture strain, γ_f , was determined. The testing results were corrected for the compliance of the machine, because the maximum compressive load applied in this test reached 240 kN. This led to elastic deformation in the testing rig. The PSC specimens were ground to 4000 grit in order to improve the surface quality because this test method is highly sensitive to friction. Lubrication grease, BR2-Plus from Dow Corning, was used to lubricate the contact surface between the specimen and indentors, in order to reduce the friction effect during the testing. The true compressive stress, σ_c, was calculated from:

$$\sigma_c = \left(\frac{\sqrt{3}}{2}\right)\sigma_E \tag{4.8}$$

where σ_E is the engineering stress.

The true compressive strain, ε_c, was calculated as:

$$\varepsilon_c = \left(\frac{2}{\sqrt{3}}\right)\ln\left(\frac{B_c}{B}\right) \tag{4.9}$$

where B_c is the compressed thickness of the specimen during the testing and B is the initial thickness of the specimen [23, 99].

The compressive modulus was taken from the linear portion of the stress-strain curve in the nominal range of strain between 0-0.02 [23]. The compressive yield stress, σ_{yc}, was the value of the stress which is the first point on the stress-stain curve with zero gradient. Note that the capacity of the load cell in this test was 250 kN, which allows the testing sample to fully fracture and the failure strain can be obtained.

4.5 Fatigue tests

Fatigue tests were performed on compact tension (CT) specimens to measure the fatigue performance of the modified epoxy polymers. Compact tension specimens can be easily and securely mounted on the fatigue testing machine during cyclic loading. This is the reason why the CT specimen was used rather than the single-edge notched specimens. The shape of CT specimen has a long length for crack propagation, which is better for crack growth than SENB specimens, and also provides the space for using commercial crack propagation gauges (Krak gauge, Rumul, Switzerland) to measure the crack length during the fatigue testing.

The CT specimens, as shown in Figure 4.5.1, used in the fatigue testing were made by machining from a 6mm-thick polymer plate, in which all the dimensions are according to the ASTM E647 [100] and ISO 15850 [101]. The fatigue Krak gauge was stuck on the side of the specimen using standard M-bond adhesive resin and curing agent from Vishay (cured at room temperature for 10 hours). Before testing, the specimens were pre-cracked to get a sharp crack at the root of the machined notch by tapping a razor blade as mentioned in Section 4.3 (how to prepare the SENB testing specimen). Two replicate fatigue tests were carried out for each formulation. During the fatigue crack propagation (FCP) test, the incremental crack length, *da*, was measured from the Krak gauge. The crack growth rate is expressed as *da*/*dN* (mm/cycle); *dN* is the number of cycles corresponding to the crack extension.

Servo-hydraulic fatigue testing machines (Instron Model 8872), were used to load the CT specimens in cyclic fatigue. Towards the end of the testing (near the threshold region), the value of the load is small, at around 5 to 8 N, therefore a highly accurate load cell is required. The accuracy of the load cell used for fatigue tests was ± 0.001 N, and its full-scale load is ± 1 kN. The sensor for measuring the displacement has a range of ± 50 mm and an accuracy of ± 0.01 mm. The illustration of the fatigue test is shown in Figure 4.5.2.

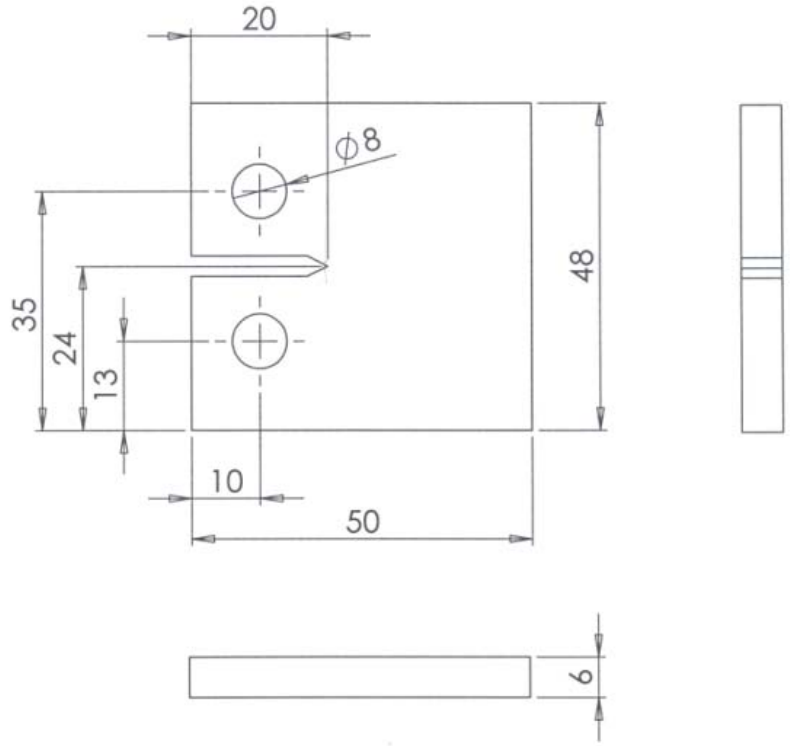


Figure 4.5.1 Schematic diagram of the CT specimen, showing the dimensions in mm [100].

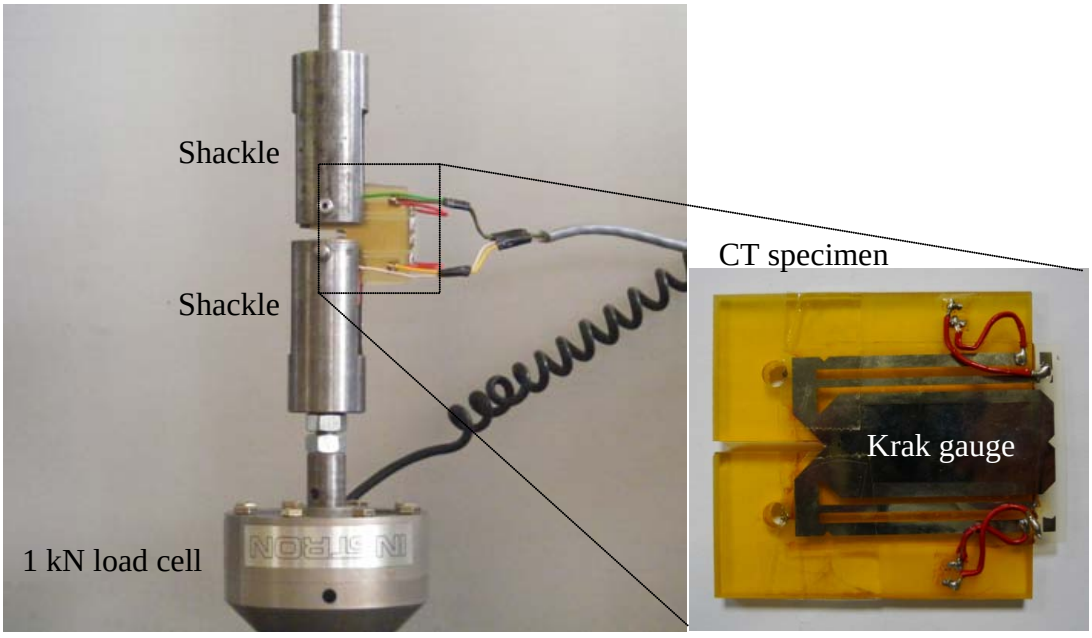


Figure 4.5.2 CT specimen and the testing set up for the fatigue tests.

During the fatigue testing, the CT specimens were gripped on the machine and were subjected to sinusoidal loading, see Figure 4.5.3, with a displacement ratio, $\delta_{min}/\delta_{max}$ of 0.5, at 5 Hz [100, 101]. The maximum displacement, δ_{max}, used was the displacement value when loading the CT specimen to the 2/3 of quasi-static P_Q. P_Q is the load when using the CT specimens for measuring the fracture toughness, or the load which makes the CT specimen fracture at one cycle [97]. The maximum displacement, δ_{max}, the displacement amplitude, δ_{ampl}, the minimum displacement, δ_{min}, and the mean displacement, δ_{mean}, were calculated using the following relationships:

$$\delta_{max} = \frac{2}{3}\delta_{Ic} \tag{4.10}$$

$$R_{\delta} = \frac{\delta_{min}}{\delta_{max}} \tag{4.11}$$

$$\delta_{ampl} = \frac{\delta_{max} - \delta_{min}}{2} \tag{4.12}$$

$$\delta_{mean} = \frac{\delta_{max} + \delta_{min}}{2} \tag{4.13}$$

where δ_{Ic} is the displacement value requires to grow the crack in one cycle, R_{δ} is the displacement ratio. The value of displacement ratio, R_{δ}, of 0.5 was used in this study, and this value is suitable for the CT specimens and ensures the specimen remained in tension throughout the fatigue testing.

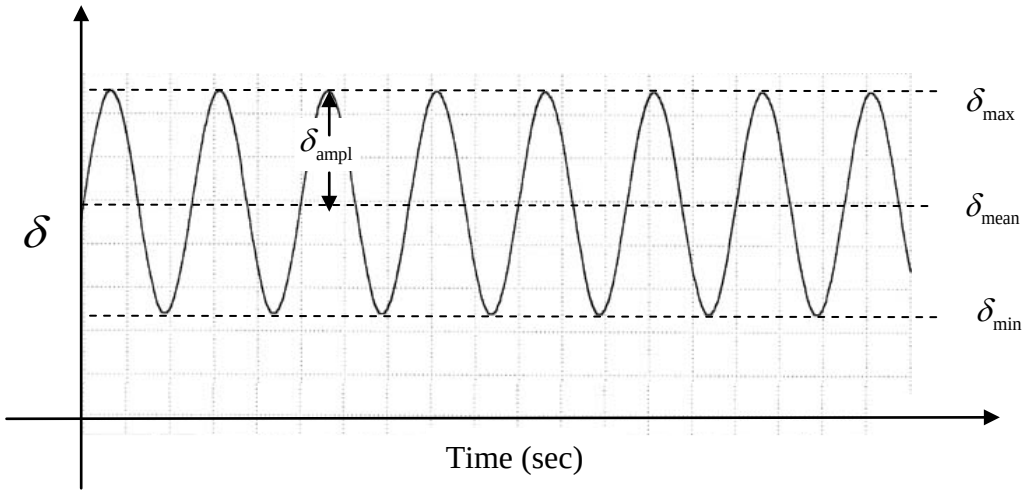


Figure 4.5.3 Schematic diagram of the sinusoidal loading used in the fatigue tests, showing all the displacement-related parameters.

Before the test, the gauge was connected to the controlling computer via a Fractomat control box (Rumul). Software, Chart 4 (supplied by AD Instruments, New Zealand), was installed on the computer to record the cycles, tension load, actuator position and crack length measured from the Krak gauge. Each fatigue test was run until the fatigue threshold could be clearly identified, which was after approximately 5 million cycles. The data recorded from the software during the tests were then used to determine the fatigue performance using the following equations:

$$K_{\max} = f'(x)\frac{P_{\max}}{BW^{1/2}} \tag{4.14}$$

$$K_{\min} = f'(x)\frac{P_{\min}}{BW^{1/2}} \tag{4.15}$$

$$G_{\max} = f'(x)\frac{(1-\nu_2)K_{\max}}{E} \tag{4.16}$$

$$G_{\min} = f'(x)\frac{(1-\nu^2)K_{\min}}{E} \tag{4.17}$$

$$\Delta K = K_{\max} - K_{\min} \tag{4.18}$$

$$\Delta G = G_{\max} - G_{\min} \tag{4.19}$$

where *f'(x)* is calculated from:

$$f'(x) = \frac{2+x}{(1-x)^{3/2}}(0.886 + 4.64x - 13.32x^2 + 14.72x^3 - 5.6x^4) \tag{4.20}$$

and where $0<x<1$, $x=a/W$

Two methods were used to calculate the crack growth rate per cycle, *da*/*dN*; the secant and incremental polynomial methods. The testing standard of ISO 15850 [101] provided the secant method. This method was used to calculate the slope of the straight line connecting two adjacent data points (*i* and *i+1*) on the *a* against *N* curve, as shown in Equation 4.20:

$$\frac{da}{dN} = \frac{(a_{i+1} - a_i)}{(N_{i+1} - N_i)} \tag{4.21}$$

The testing standard of ASTM E647 [100] recommended to use the other method, the incremental polynomial method, to calculate the crack growth rate per cycle, *da*/*dN*. This method involves fitting a second-order polynomial to sets of (2*n*+1) successive data points (*n* can be 1, 2, 3 or 4). In this study, the incremental polynomial method was used, as this can produce less scatter in the data [102], and the value of *n* was taken to be 3.

The fatigue testing results can be presented by plotting the logarithms of ΔG, $G_{\max}$, ΔK or $K_{\max}$ versus the logarithm of *da*/*dN*, see Figure 4.5.4. In this study, $G_{\max}$ was used as the primary parameter for characterising the fatigue performance of the modified polymers in this study. Linear regression was conducted to analyze the data in

the threshold and linear regions. The fatigue curves were plotted by splitting the data in the two regions which were clearly distinguishable, viz (i) a linear Paris Law region, and (ii) a vertical threshold region. The value of G_{max} in the threshold region is defined as the fatigue threshold, G_{th}, which was used to characterise the fatigue property of the materials. The higher the fatigue threshold, the more fatigue resistant the material is considered to be.

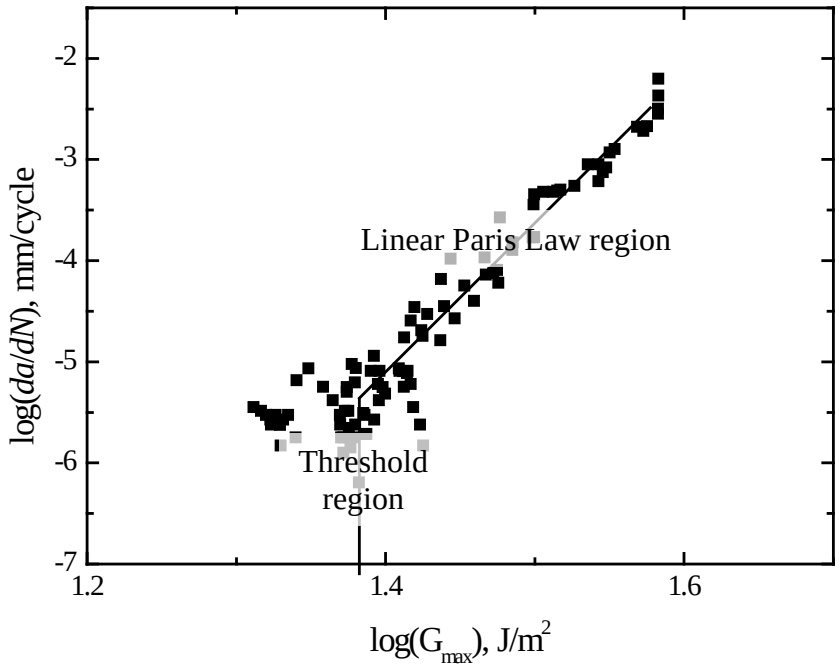


Figure 4.5.4 A typical plot of log(da/dN) versus log(G_{max}) of the unmodified anhydride-cured DGEBA epoxy, showing the linear Paris low region and threshold region.

4.6 Differential Scanning Calorimetry test

Differential scanning calorimetry (DSC) tests were performed on the cured bulk samples to measure the glass transition temperature, T_g, of the modified polymers, and also ensure that the cure cycle used in sample preparation had fully cured all the formulations. DSC is a thermal analytical technique, which investigates the amount of heat required to increase the temperature of the test materials [103].

The DSC test was conducted using a 'TA Instruments Q2000' to monitor the specific energy required to increase the temperature of a sample with a mass of around 10 mg (according to the ISO standard 11357-2 [104]) for all formulations, at a rate 10 °C/min for heating and cooling. Figure 4.6.1 shows a typical DSC curve, plotting the heat flow versus temperature. Each sample was heated twice from 30 °C to 180 °C, in which two repeated values of T_g were obtained. The value of T_g was taken as the mid-point of the inflexion curve in the second heating cycle, and two replicate tests were required for each formulation.

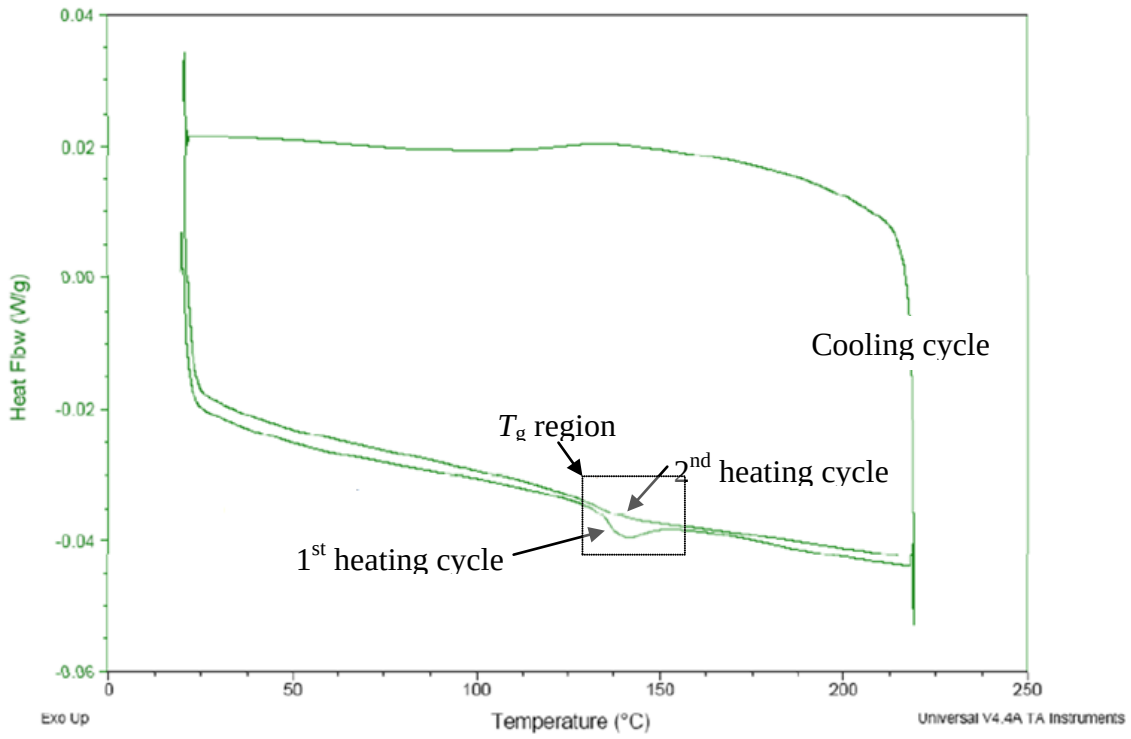


Figure 4.6.1 The DSC curve plotting the heat flow versus temperature for the unmodified anhydride-cured DGEBA epoxy, showing the glass transition temperature region.

4.7 Atomic Force Microscopy

An atomic force microscope (AFM) was used to observe morphology of the modified-epoxy materials. The AFM used in this study was a MultiMode scanning probe microscope (Figure 4.7.1) from Veeco (California, USA), and equipped with a 'J' scanner and a 'NanoScope IV' controller. In this observation, the height and phase image of the object surface can be recorded via a tip scanning across the surface in tapping mode. The level of the object surface used in the AFM should be very smooth. Thus, a 'PowerTome XL' ultramicrotome from RMC products (Arizona, USA) was used to cut a surface for investigation. A silicon probe with a 5 nm-diameter tip was used in the AFM observation, and both height and phase images were captured at 512 ×512 pixel resolution at a scanning rate of 1 Hz.



Figure 4.7.1 The atomic force microscope.

4.8 Scanning Electron Microcsopy

The fracture surfaces of the samples after the SENB and fatigue tests were inspected using scanning election microscopy (SEM). The specimens used in SEM with a height of around 1 mm were cut from the tested specimen using a diamond cutting machine, and were then mounted onto SEM sample substrates using carbon conductive adhesive tabs. The very short samples prepared for the SEM can make them less likely to charge upon imaging.

As the additive reinforcements in this study were almost all in the nano-scale, a scanning electron microscope with a field emission gun (FEG-SEM), a Carl Zeiss Leo 1525 (see Figure 4.8.1), was used in this study. The typical accelerating voltage was set at 5 kV, and the working distance was around 6 mm. Before doing the FEG-SEM, a thin layer of chromium was coated on the fracture surface to improve the conductivity of the sample. A sputter coater, Emitech K575X Peltier, equipped with a chromium target was set at 75 mA for 30 seconds to do the coating process. After the chrome coating, conductive silver paint was used to make a line of electrical conductivity from the surface to the sample stub.



Figure 4.8.1 The FEG-SEM used in this study.

4.9 Summary

This Chapter presented the experimental procedures which were employed to characterise the unmodified and modified epoxy polymers. In the following Chapters, the experimental results for each formulation with various modifiers will be discussed.

CHAPTER 5

MULTI-WALLED CARBON NANOTUBE DISPERSION

5.1 Introduction

Carbon nanotubes, as synthesised, often exist as entangled agglomerates. They also have an undesirable tendency to agglomeration when they are dispersed in polymeric resins to form nanocomposites due to their high aspect ratio [74]. All of these characteristics result in a serious limitation in their applications. In order to fully transfer the outstanding material properties of carbon nanotubes to engineering applications, appropriate dispersion processes are required. In this Chapter, the effect of various dispersion methods on the nanotube dispersion is discussed, and the best way for nanocomposite sample preparation to achieve well-dispersed nanotubes in the epoxy polymer resin is investigated.

Previous studies working on nanotube dispersion showed that entangled and agglomerated carbon nanotubes could be efficiently broken up using sonication technology, and the dispersion of the nanotubes was improved with increasing the duration of the sonication, but at the cost of nanotube damage, i.e. shortening the length and shelling the outer-layer of multi-walled nanotubes [105-107]. However, these investigations did not clearly discuss the degree of nanotube damage caused by the dispersion methods by measuring the nanotube dimensions after nanotubes were blended and sonicated with polymer resins. In this Chapter, the multi-walled carbon nanotubes were extracted from the nanotube-modified polymer resins after sonication, and then the dimensions of the nanotubes were measured. A comparison of the original nanotubes to the sonicated nanotubes was made to examine whether the multi-walled carbon nanotubes were damaged by the dispersion method used for dispersing the nanotubes and preparing the nanotube-modified epoxy polymer.

As the nanotube-modified polymer resin was run through the cure cycle from an uncured mixture to become a fully cured bulk nanocomposite, obvious movement of the nanotubes in the resin was found. Closer examination showed that the dispersion of the cured nanotube/epoxy sample was changed, and slightly downgraded, compared with the uncured samples [108]. This indicates that the nanotubes agglomerated during the cure cycle, and the change of nanotube dispersion is directly associated with the viscosity of the polymer matrix during curing. Masania [23] measured how the viscosity of the anhydride-cured DGEBA epoxy varied during the cure schedule, as shown in Figure 5.1.1, and reported that the nano-size particles may agglomerate when the mixture has a low viscosity. In order to realize the variation in nanotube dispersion during the curing process, an optical microscope equipped with a hot stage, which can run a temperature programme of the cure cycle, was used to investigate when the nanotube agglomerates formed at different temperatures.

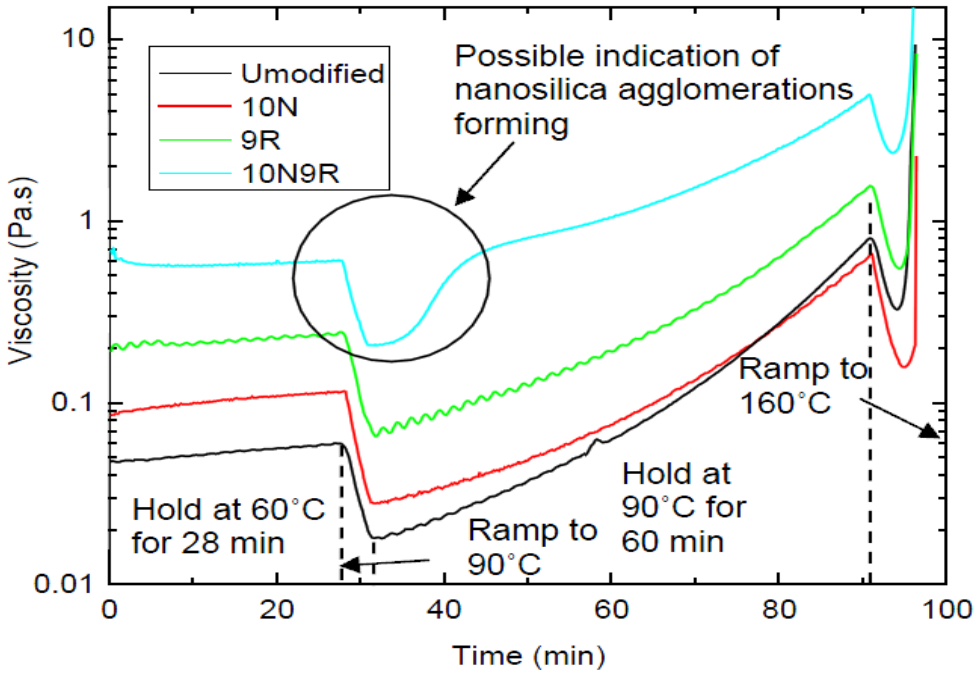


Figure 5.1.1 The change of the viscosity versus time for the anhydride-cured DGEBA epoxy polymer as the resin went through the cure cycle [23].

5.2 Dispersion Methods

Before investigating of the mechanical properties of the multi-walled carbon nanotube-modified epoxy polymers, it is necessary to carry out dispersion tests to find an appropriate dispersion method which can attain the best dispersion without damaging the nanotubes in the epoxy resin. Figure 5.2.1 shows the FEG-SEM images of the multi-walled carbon nanotubes (raw appearance of the standard MWCNTs) before they were mixed with the epoxy resin. These aligned multi-walled carbon nanotubes were removed from the silica substrates after the CVD process. They have an average length of 140 ±8 μm, and a mean diameter of 120 ±21 nm. These measured original dimensions were used as a reference, and then compared with the sonicated nanotubes to evaluate whether the chosen dispersion method damaged the multi-walled carbon nanotubes.

For preparing the nanotube-modified epoxy mixture, a measured amount of the multi-walled carbon nanotubes were mixed into the epoxy resin. In order to save the usage of the multi-walled carbon nanotubes in the dispersion tests, a low concentration of 0.05 wt% of the carbon nanotubes was used in this Chapter. Note that the total amount of the mixture (around 60 ml) used in the dispersion tests was the same as the amount of the epoxy resin used for the sample preparation, as the amount of the resin directly affects the nanotube dispersion under a same dispersion method (a large amount of the resin leads to difficulties in nanotube dispersion). The mixture containing the multi-walled carbon nanotubes was manually mixed using a spatula, and then sonicated.

The sonication process in this Chapter used two different types of sonicators; an ultrasonic bath (MX86 from Grant Instruments, Cambridge), and an ultrasonic probe with a 10 mm-diameter tip. These two sonicators provide different levels of intensity of ultrasound into the nanotube-modified epoxy mixture [109]. After the sonication process, the mixture was blended with the anhydride curing agent, HE 600 from Nanoresins, and mixed using a mechanical stirrer for 30 minutes, followed by a degassing process. All the steps used for preparing the nanotube-modified epoxy resin were described in detail in Chapter 4.

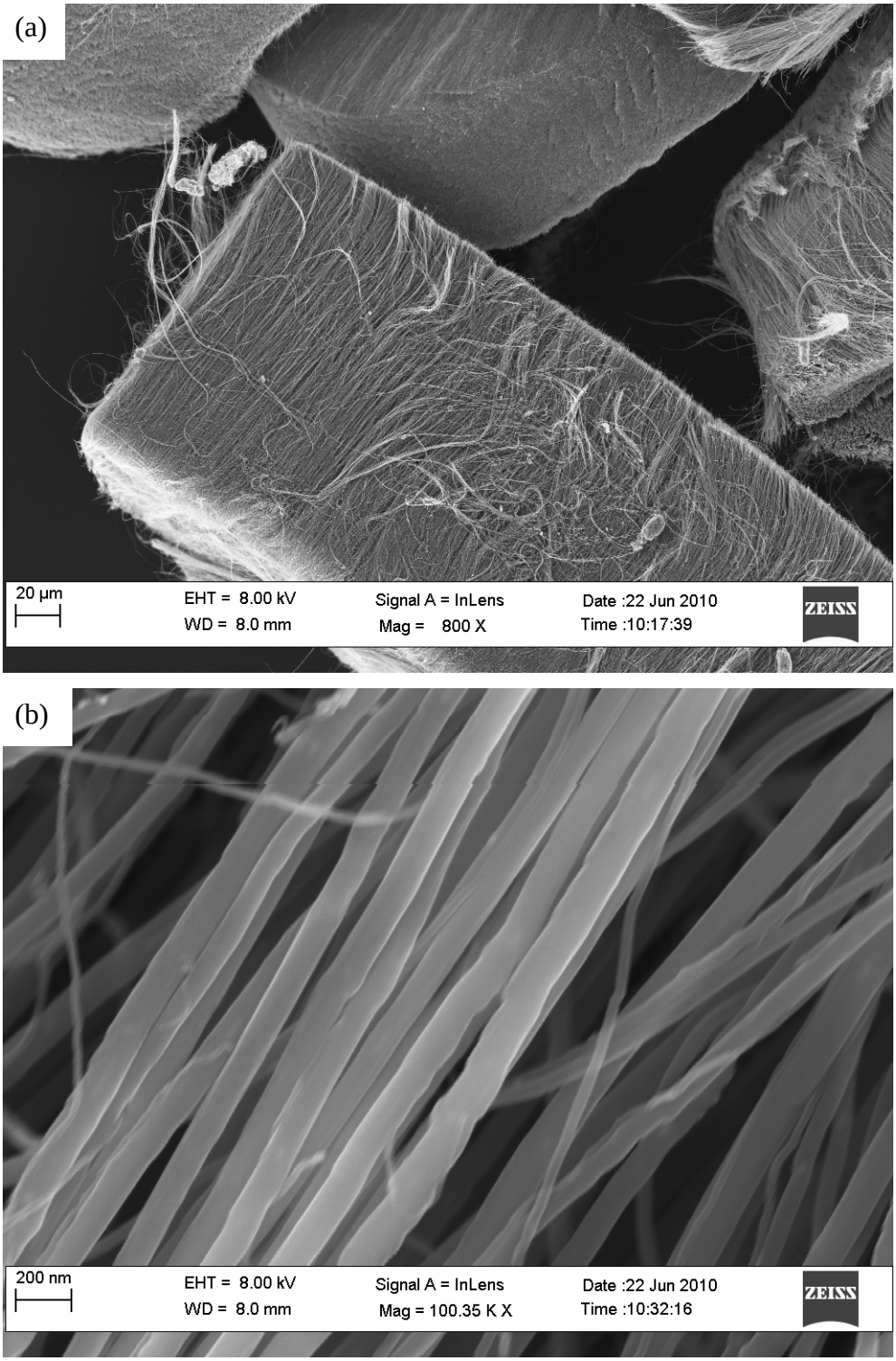


Figure 5.2.1 FEG-SEM images of the multi-walled carbon nanotubes before being added into the epoxy resin, showing (a) aligned multi-walled carbon nanotube films with thickness around 140 µm, and (b) individual nanotubes with a mean diameter of 120 nm.

The effect due to the use of the different sonicators on the nanotube dispersion was investigated using optical microscopy of the uncured nanotube-modified epoxy resins. In the first type of sonication, an ultrasonic bath was used to sonicate and disperse the multi-walled carbon nanotube within the epoxy resin. In this sonication process, water was used to be the medium to transfer the ultrasound to the nanotube-modified resin, which was in a Pyrex beaker, as shown in Figure 5.2.2. A 40-hour-duration was required using the ultrasonic bath to attain well-dispersed nanotubes [108]. Turning to the second dispersion method, the nanotubes in the epoxy resin were sonicated by an ultrasonic probe. Sonication times of 10, 20, 30, 60 and 120 minutes were used with the ultrasonic probe. Note that the use of both sonicators generated heat, consequently increasing the temperature of the mixture, especially for the use of the ultrasonic probe due to the relatively high intensity generated [109]. This may promote the mixture to cure. Therefore a thermometer was used to record the temperature of the mixture during the sonication process, and the sonicator was stopped if the temperature reached 80 °C, as described in Chapter 4, and mixture was allowed to cool.



Figure 5.2.2 Photograph of the ultrasonic bath, used for dispersing the multi-walled carbon nanotubes in the epoxy resin.

Figure 5.2.3 shows the optical microscope images of the nanotube-modified epoxy mixture after sonication using the ultrasonic probe for various durations (Figure 5.2.3 (a)-(e)), and using the ultrasonic bath for 40 hours (Figure 5.2.3 (f)). After the sonication processes, the temperature of the CNT-modified epoxy resin was measured to be around 60 °C. The samples shown in Figure 5.2.3 are uncured modified epoxy with 0.05 wt% multi-walled carbon nanotubes, and these micrographs were imaged from a 0.3 mm-thick uncured mixture dropped onto a microscope slide, see Figure 5.2.4. The temperature of the uncured nanotube-modified epoxy mixture was maintained at 60 °C using a hot stage to keep the all the mixtures at the same viscosity (the detailed information of the hot stage will be discussed in Section 5.3).

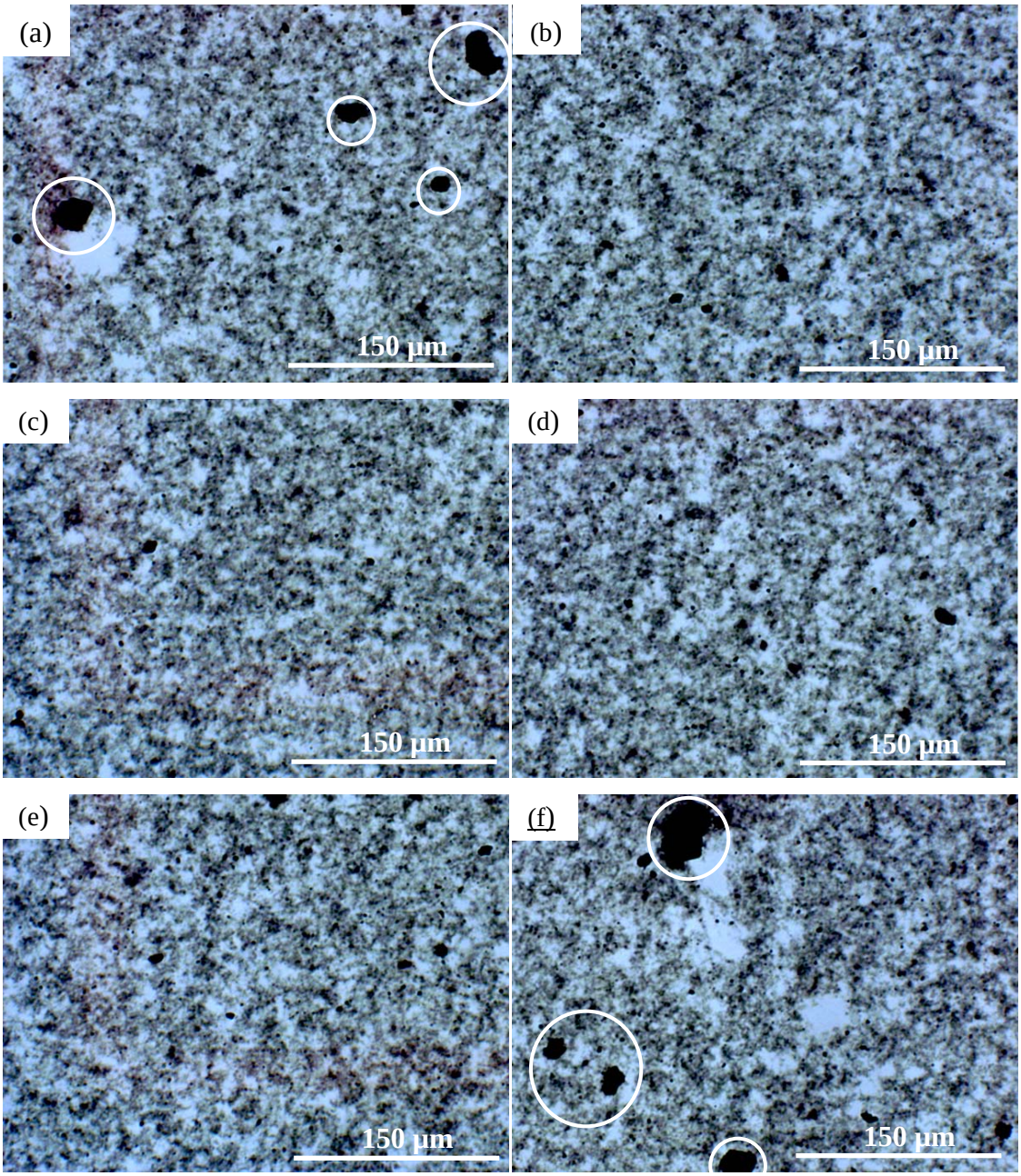


Figure 5.2.3 Optical microscope images of the uncured nanotube-modified epoxy resins, showing the nanotube dispersion effect caused by different dispersion methods of using the ultrasonic probe for (a)10 minutes, (b)20 minutes, (c)30 minutes, (d) 60 minutes, (e)120 minutes, and (f)using the ultrasonic bath for 40 hours, all the samples at 60 °C.

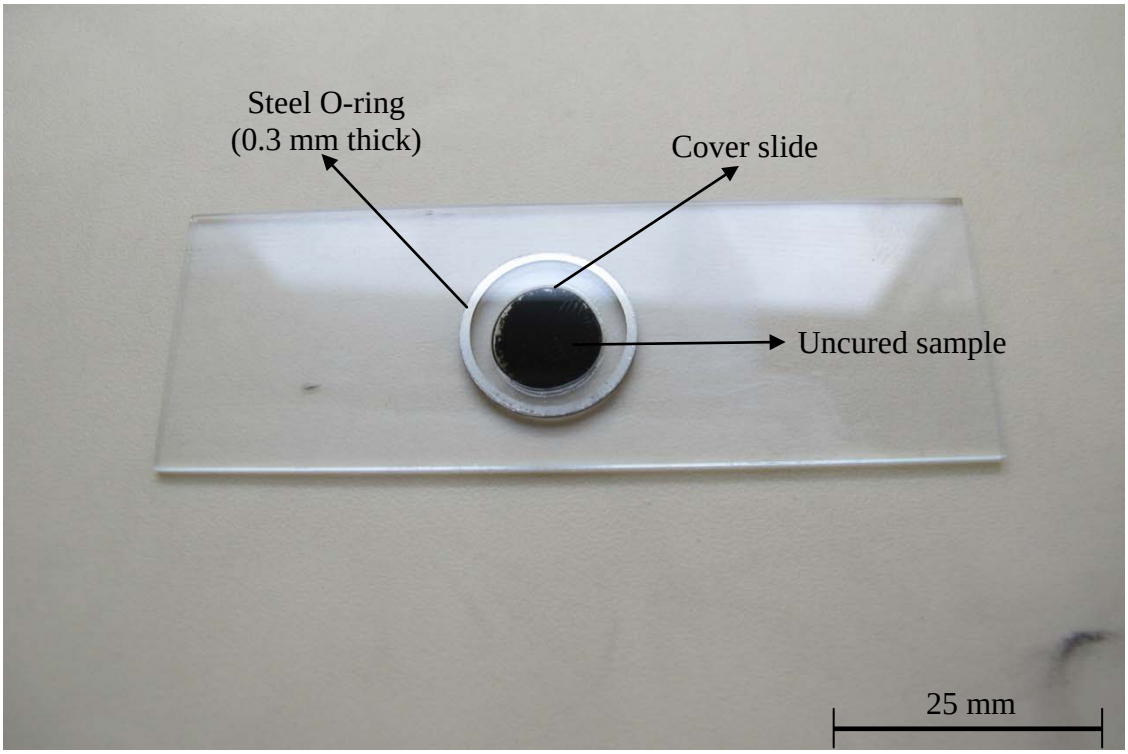


Figure 5.2.4 The specimen of the uncured sample used for the dispersion tests.

From Figure 5.2.3, it is clearly demonstrated that the longer the duration of the sonication using the ultrasonic probe, the better the nanotube dispersion is. For example, Figure 5.2.3 (a) shows the sample after 10 minutes, which had serious nanotube agglomerations; the MWCNTs sonicated for 20 minutes revealed a relatively good dispersion in the uncured epoxy resin, see Figure 5.2.3 (b). However, no significant improvement in the nanotube dispersion is seen if the multi-walled carbon nanotubes were sonicated for more than 20 minutes, see Figure 5.2.2 (b)-(e). In order to save time for the sample preparation and prevent the nanotube damage caused by the sonication [105], a 30-min-duration of the ultrasonic probe was chosen for this dispersion method in the sample preparation, as described in Chapter 4.

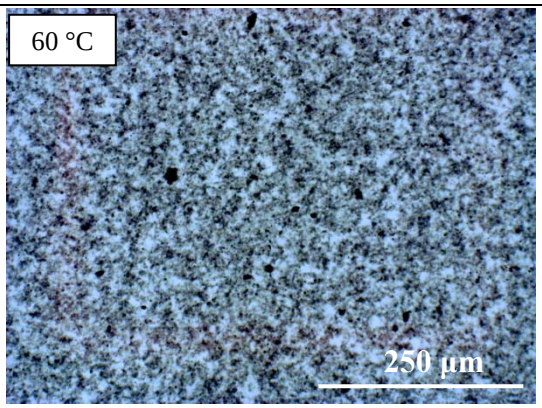
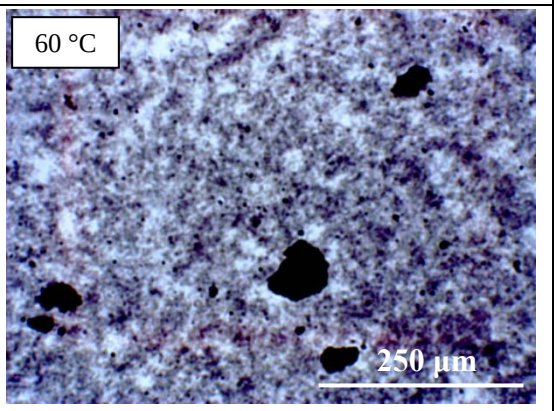
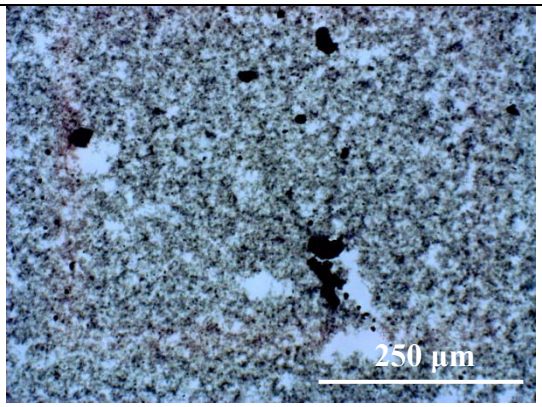
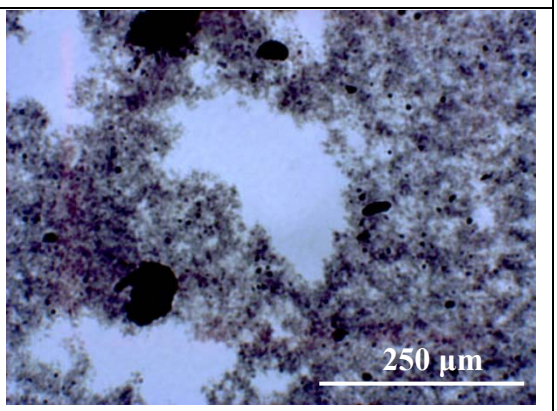
The method using the ultrasonic bath results in the nanotubes not being well dispersed, as can be seen in Figure 5.2.3 (f), even after 40 hours. Several large nanotube agglomerates were found on the optical microscope image of the uncured sample. The investigation of the effect of using the ultrasonic probe and the ultrasonic bath on the

nanotube dispersion clearly demonstrates that the ultrasonic probe sonication is a more effective method for improving nanotube dispersion even with a short-time sonication, compared with the ultrasonic bath. This is because the ultrasonic probe system can provide a much higher intensity of ultrasound into the mixture than the ultrasonic bath (up to 100 times higher) [109]. Table 5.2.1 shows the summary of the advantages and disadvantages of ultrasonic bath and ultrasonic probe. The effect of the various dispersion methods on the nanotube dispersion is summarised in Table 5.2.2, showing the uncured and cured samples containing 0.05 wt% multi-walled carbon nanotubes dispersed using the ultrasonic bath for 40 hours or the ultrasonic probe for 30 minutes.

Table 5.2.1 Summary of ultrasonic bath and ultrasonic probe [109].

	Bath	Probe
Intensity (W/cm^2)	1–5	100
Distance dependant	Yes	No
Variable intensity	No	Yes
Direct application	No	Yes
Cost	Low	High
Sample Throughput	High	Low

Table 5.2.2 Summary of the dispersion testing results.

Ultrasonic Probe (30 minutes)	Ultrasonic Bath (40 hours)
	
 Uncured mixture	 Uncured mixture
 Cured sample	 Cured sample
High level of nanotube dispersion	**Low level of nanotube dispersion**

Previous studies [105-107] focusing on the nanotube dispersion reported that long-time sonication may result in nanotube damage, i.e. shortening of the nanotube length. Therefore, the dimensions of the multi-walled carbon nanotubes after the ultrasonic probe sonication were measured using field emission gun scanning electron microscopy. Figure 5.2.5 shows the FEG-SEM images of the MWCNTs after the sonication for 30 minutes (which is the dispersion method used in this research to prepare the nanocomposites). The sample used to measure the nanotube dimensions (length and diameter) was prepared from the uncured nanotube-modified epoxy resin. The equipment used to extract the dispersed multi-walled carbon nanotubes from the epoxy mixture after sonication, and the extracted nanotubes coated on the surface of a filter paper, are shown in Figure 5.2.6. The final mixture containing the dispersed MWCNTs and epoxy resin was diluted using acetone, and then poured into a funnel. A Teflon filter paper with a pore size of 0.45 μm, TF-450 from GELMAN, was placed on the bottom of the funnel, and a vacuum pump was used to force the dispersed nanotubes in the mixture to deposit on the filter paper, as shown in Figure 5.2.6 (b)-(c), and the residual solution composed of the epoxy resin and acetone was placed in a beaker. The reason why the Teflon filter paper was used instead of standard filter paper is that the Teflon filter paper has a smooth surface. This provides a clearly different appearance to the multi-walled carbon nanotubes. Figure 5.2.7 shows the FEG-SEM images of the standard filter paper coated with the sonicated nanotubes, and it is not possible to clearly find the nanotubes, compared with the use of the Teflon filter paper (Figure 5.2.5).

The measurements from the FEG-SEM image in Figure 5.2.5 showed that the measured length and diameter of the nanotubes were 120 ±19μm and 120 ±22 nm, respectively. This indicates that the use of the ultrasonic probe sonication for 30 minutes slightly shortened the multi-walled carbon nanotubes, but not significantly (the original length of the nanotubes was measured to be 140 μm). The sonication process did not change the transverse dimension of the nanotubes; the diameter of the nanotubes before and after the sonication was 120 nm. The results from this measurement were used for analytical modelling, as discussed in Chapter 9.

Figure 5.2.8 is the FEG-SEM image showing the long-time probe sonication (120 minutes) nanotubes, and serious damage of the nanotubes was found. These

nanotubes have a relatively short average length of 70 μm, with a wide range from 35 μm to 90 μm (original nanotube length =140 μm). This clearly demonstrated that long-time sonication caused nanotube damage. No difference in the diameter of the nanotubes after long-time sonication was recorded.

From these dispersion testing results, the best dispersion method was found to be the use of the ultrasonic probe sonication for 30 minutes to attain the best nanotube dispersion in the sample preparation. In Table 5.2.2, it is worth mentioning that a relatively low level of the nanotube dispersion was found in the cured samples, compared with the uncured samples, using both dispersion methods. This phenomenon will be discussed using the hot stage investigation in the following Section.

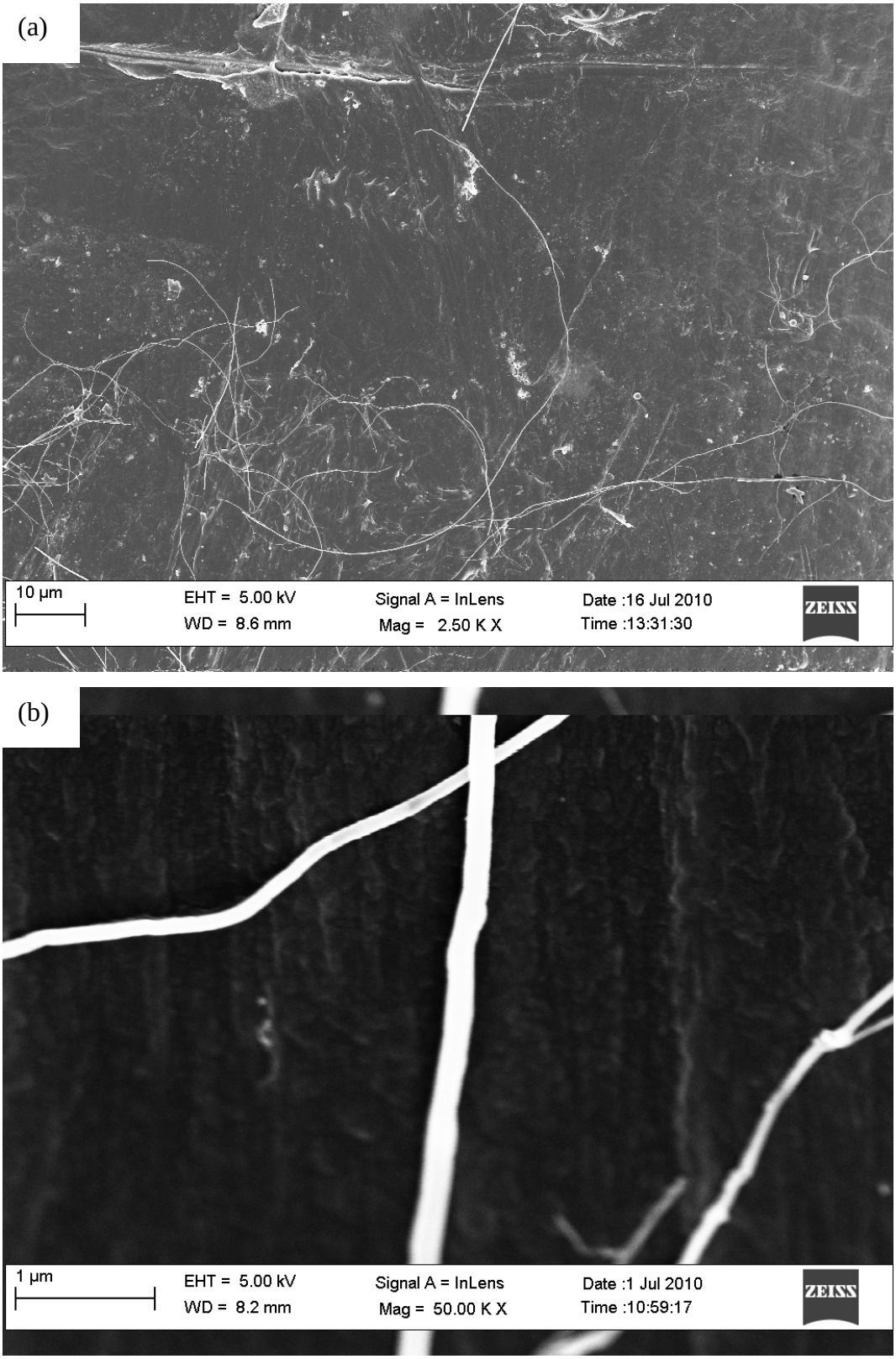


Figure 5.2.5 FEG-SEM images of the nanotubes after sonication for 30 minutes, showing (a) nanotube length of 120 µm and (b) nanotube diameter of 120 nm.

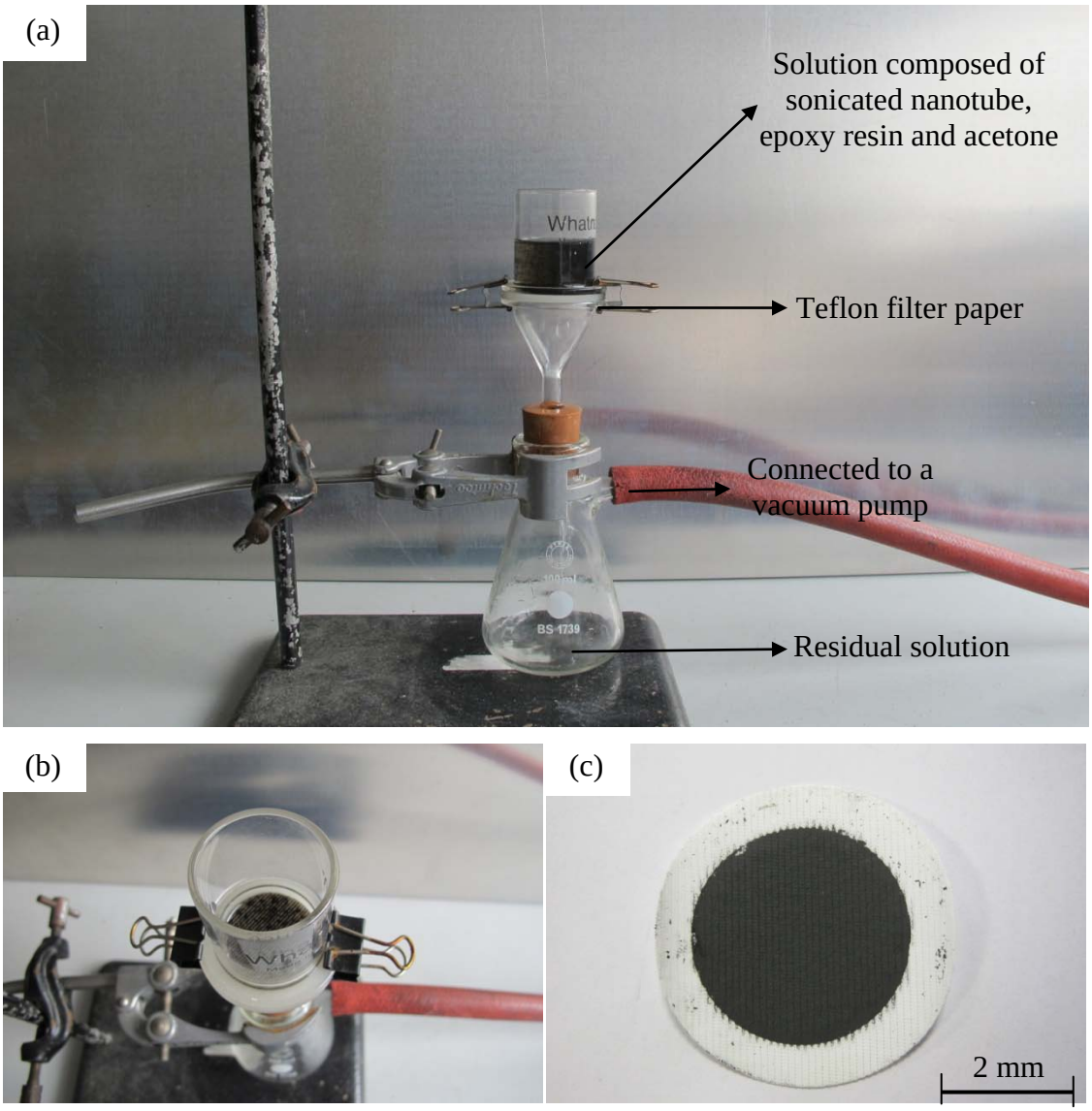


Figure 5.2.6 Photograph showing (a) the experiment for extracting the sonicated nanotubes from the nanotube-modified epoxy resin, (b)-(c) the nanotubes deposited on the surface of a Teflon filter paper.

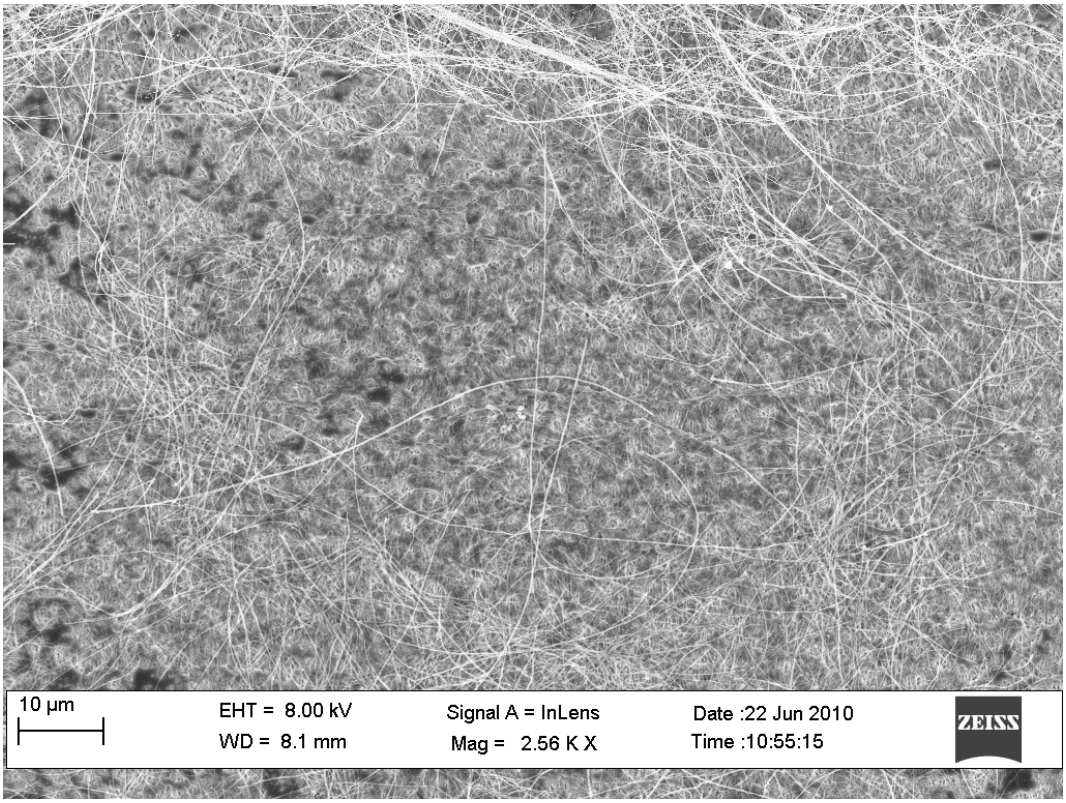


Figure 5.2.7 FEG-SEM of the multi-walled carbon nanotubes after probe sonication for 30 minutes deposited on a standard filter paper.

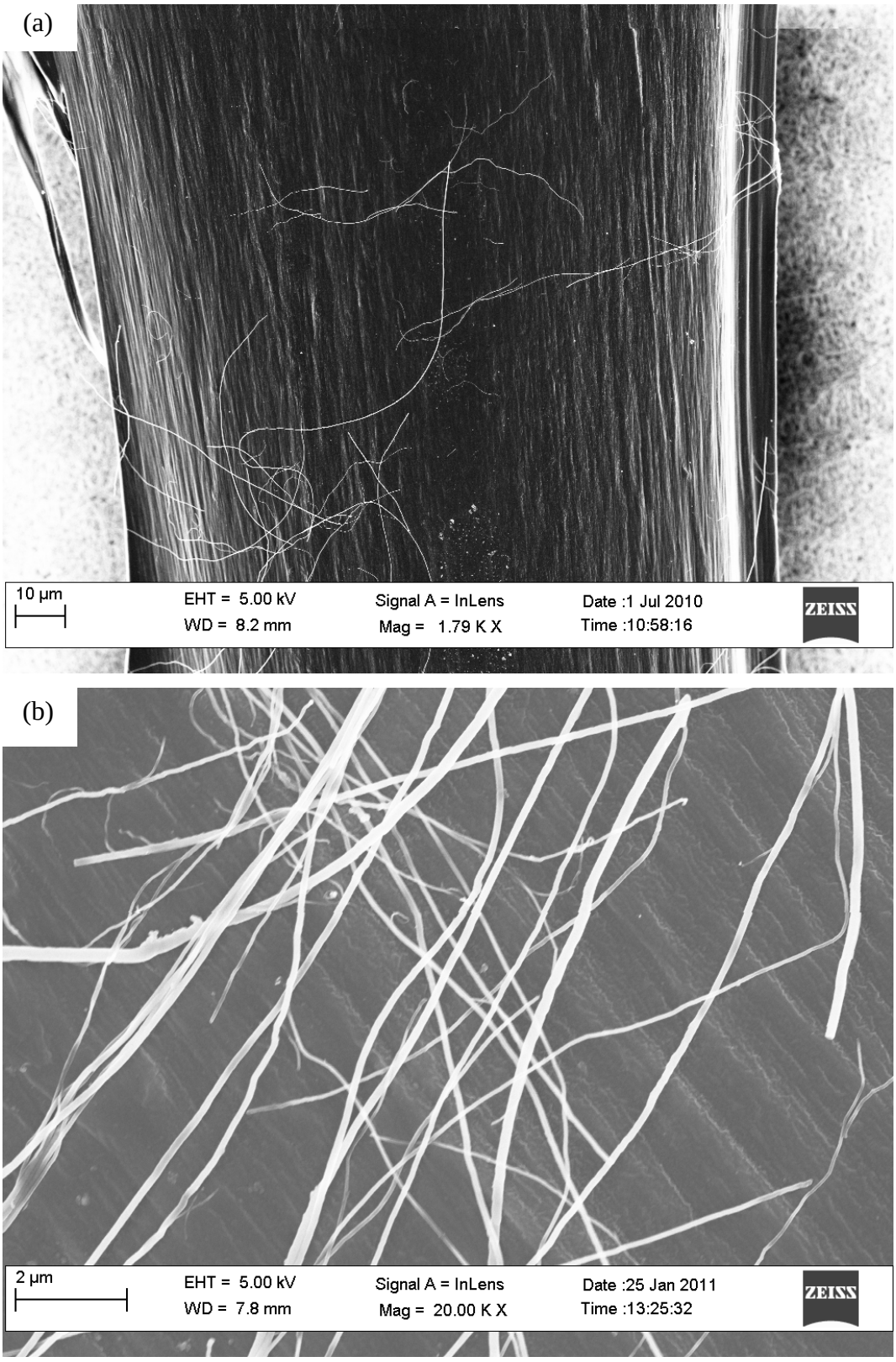


Figure 5.2.8 FEG-SEM images of the nanotubes after probe sonication for 120 minutes, showing (a) nanotube length of 70 µm and (b) nanotube diameter of 120 nm.

5.3 Hot Stage Investigation

As shown in Table 5.2.1, the dispersion of the multi-walled carbon nanotubes changed between the uncured samples containing the MWCNTs/epoxy resin after the sonication process, and the fully cured samples. This variation of the nanotube dispersion during the cure cycle has been demonstrated by Brooker [108]. In order to examine the MWCNTs dispersion during the cure cycle, hot stage investigation, as shown Figure 5.3.1, was performed on the uncured nanotube-modified epoxy polymer samples, and run the curing schedule as described in Chapter 4. A hot stage, THMS600 from Linkam, was fitted onto an optical microscope, and a drop of the uncured mixture after the mixing process (i.e. after the addition of the nanotubes to the epoxy polymer, ultrasonic probe sonication for 30 minutes, addition of the curing agent and degassing) was placed in the hot stage, where a steel o-ring, 0.3-mm-thick (see Figure 5.2.4), was used to keep all the uncured samples used in the hot stage investigation the same thickness. Then, the hot stage was programmed using a computer to run the cure cycles, and a camera was used to record the changes of the nanotube dispersion until the sample was fully cured.

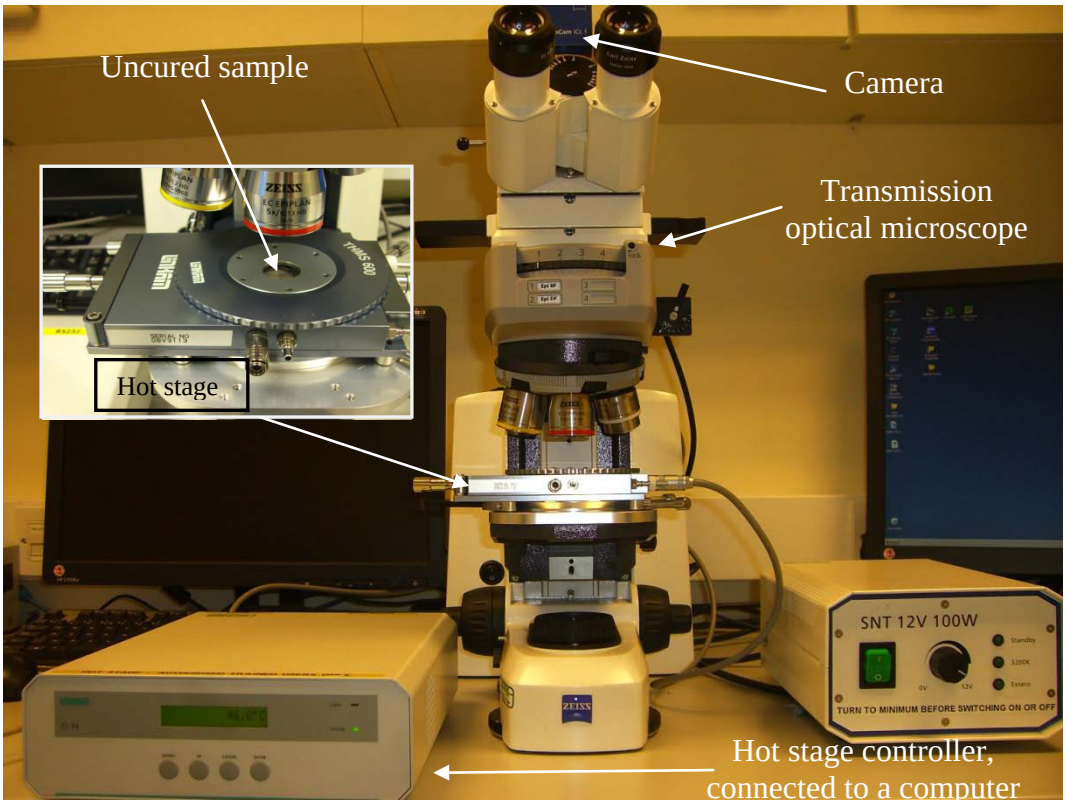


Figure 5.3.1 Photograph showing the hot stage fitted to the optical microscope.

The cure schedule used in the hot stage investigation was the same as that used in the sample preparation discussed in Chapter 4. The hot stage heated the nanotube-modified epoxy resin from 60 °C to 100 °C at 10 °C/min. It was then held at 100 °C for 120 minutes to cure the samples. This was followed by a post-cure process of increasing the temperature to 150 °C at 10 °C/min and holding at 150 °C for 10 hours. The optical microscopy images taken during the cure cycle at different temperatures (see Figure 5.3.2) of the sample containing 0.05 wt% nanotubes dispersed by the chosen method from Section 5.2 are shown in Figure 5.3.3.

The first four images in Figure 5.3.3 were taken during the ramp in temperature up to 100 °C. As the temperature of the nanotube-modified epoxy resin was increased from 60 °C to 100 °C, there was a significant movement of the nanotubes, and the size of the nanotube agglomerates became larger as the temperature was increased. This is because the viscosity of the mixture was reduced as the hot stage heated the mixture. Consequently, the mobility of the epoxy resin was increased, which allowed the dispersed nanotubes to move. After the sample was gelled at the curing step of 100 °C, there was no further agglomeration found during the dwell at 100 °C and the subsequent increase in the temperature to 150 °C for the post-cure. As can be seen in Figure 5.3.3 (e)-(f), both of these images are almost identical. The mobility of the multi-walled carbon nanotubes in the epoxy resin and the change of nanotube dispersion levels are known to be associated with the viscosity of the resin [108].

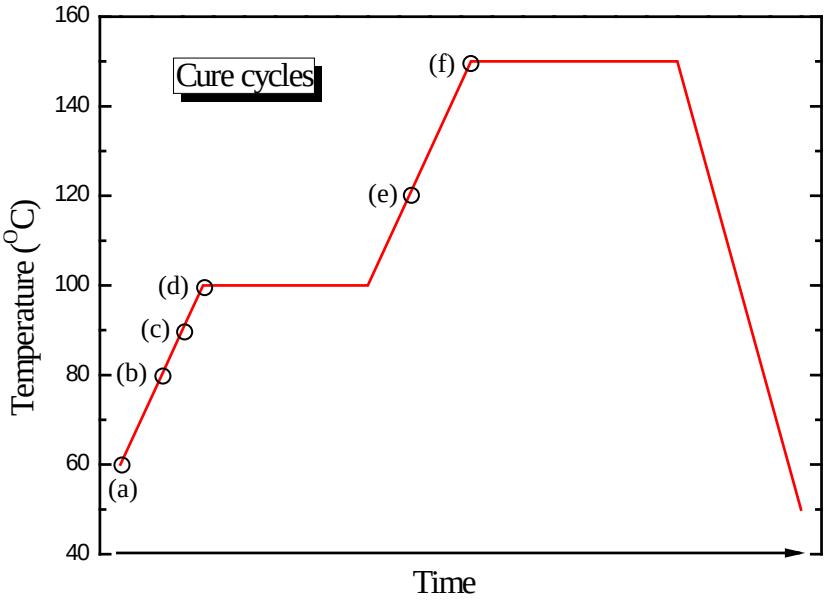


Figure 5.3.2 The line graph showing the cure schedule in the hot stage investigation, and the imaged points at different temperatures during the cure cycles.

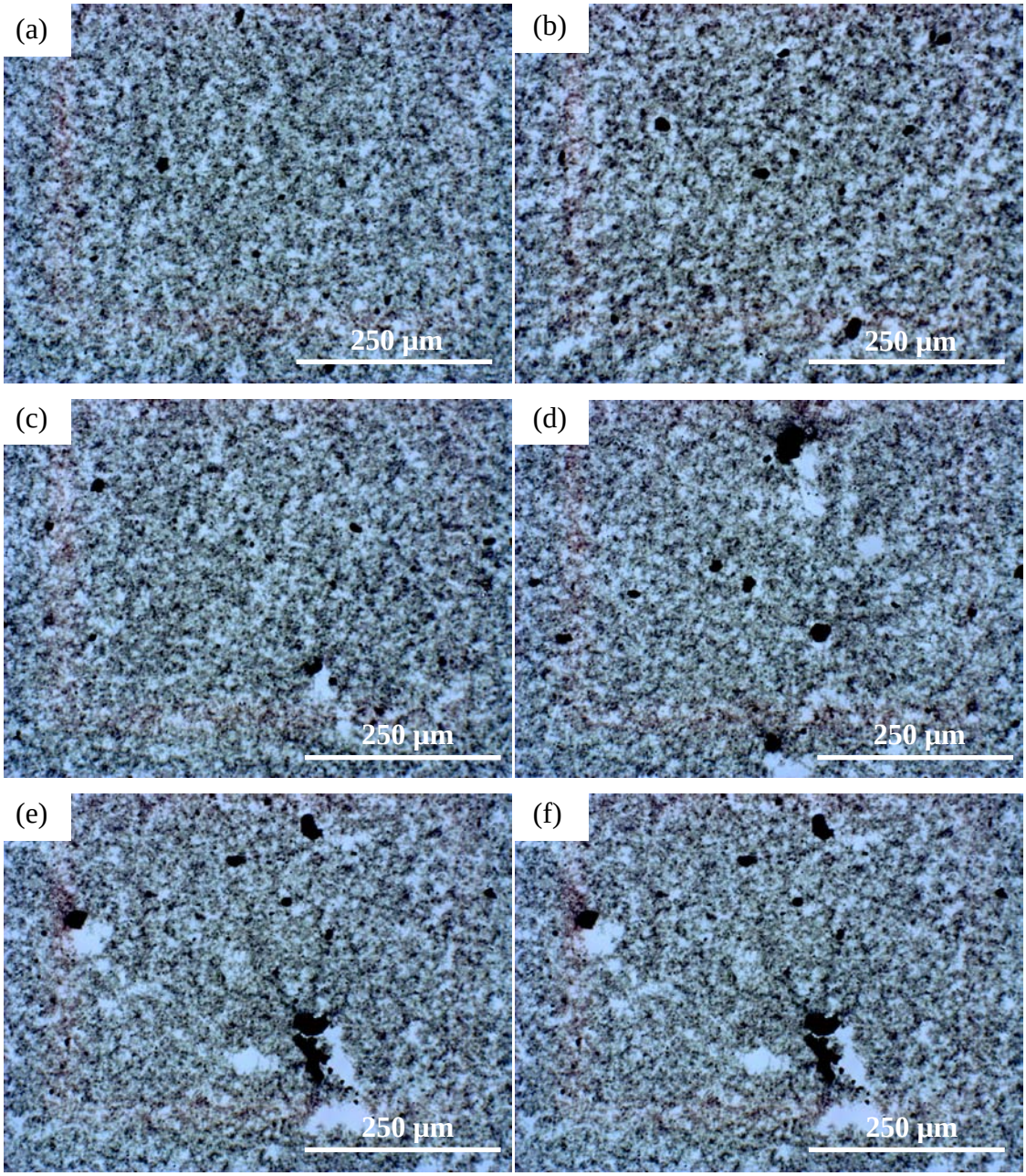


Figure 5.3.3 The hot stage images for the sample containing of 0.05 wt% nanotubes dispersed with the epoxy matrix using the ultrasonic probe sonication for 30 minutes. The images were taken at (a) 60 °C, (b) 80 °C, (c)90 °C, (d)100 °C, (e) 120 °C and (f) 150 °C.

5.4 Conclusions

Dispersion is an important factor associated with the material properties of nanocomposites when using nanotubes to be the nano-reinforcement. In order to attain good nanotube dispersion in the epoxy polymer matrix, a series of dispersion tests were carried out. The results show that the MWCNT agglomerates can be efficiently dispersed using the ultrasonic probe, compared with the sonication using the ultrasonic bath. Although the level of the nanotube dispersion improved with increasing the sonication time, long-time sonication resulted in damage of the nanotubes. The measurement of the nanotube dimensions was performed to evaluate the nanotube damage after the ultrasonic probe sonication. The appropriate dispersion method was found to be ultrasonic probe sonication for 30 minutes in the sample preparation to achieve good nanotube dispersion without damage of the multi-walled carbon nanotubes.

Microscopy observation on the uncured and cured samples of the nanotube-modified epoxy polymer showed that the nanotube dispersion changed somewhere as the uncured nanotube-modified epoxy resin was heated from 60 °C to reach the curing temperature of 100 °C. A hot stage fitted on an optical microscope was used to investigate the variation of the nanotube dispersion during the cure cycle. It was clearly found that the sonicated nanotubes agglomerated during the cure schedule from 60 °C to 100 °C. After the sample was fully cured, there was no further nanotube agglomerateion. The nanotube movement and the change of the nanotube dispersion were attributed to the decrease in the viscosity of the mixture with increasing the temperature of the mixture. Low viscosity of the mixture provides a high level of mobility, consequently the multi-walled carbon nanotubes moved and agglomerated.

CHAPTER 6

SILICA NANOPARTICLE AND GLASS MICROPARTICLE-MODIFIED EPOXY

6.1 Introduction

Rigid particles, such as glass beads [45, 46], aluminium particles [110] and silica nanoparticles [74], have been used to modify epoxy polymers because the combination of rigid particles with polymers leads to a significant increase in the mechanical properties of such polymers without any undesirable decrease in the material properties, e.g. the addition of rubber particles leads to an improvement in toughness but the cost of a decrease in stiffness [5, 62]. In this Chapter, silica nanoparticles and glass bead microparticles were used as reinforcements for the epoxy polymer, and the mechanical properties and toughness were measured. The nanosilica particles had an average diameter around 20 nm, and glass bead microparticles with two different diameters of 3.5 μm and 275 μm were used. The effect of the particle size on the toughness was investigated.

The effect of surface treatments on the toughness of the modified epoxy polymer with the nanometre silica particles and micron-sized glass beads was investigated. For the nanosilica-modified system, silane treatment was used to improve the interfacial bonding between the silica nanoparticles and the epoxy matrix. In the glass microparticle-modified polymers, in addition to the silane treatment, the surfaces of the glass beads were coated with a thin layer of a Frekote, which would provide poor adhesion between the glass beads and the polymer. Frekote, from Henkel, is a commercial mould release agent for polymers. The toughening mechanisms induced by the addition of these spherical reinforcements were identified on the fracture surfaces using field emission gun scanning electron microscopy (FEG-SEM).

6.2 Silica Nanoparticle-modified Epoxy Polymers

The formulations studied in this Section are summarised in Table 6.2.1. The polymeric matrix used for these nanocomposites is an anhydride-cured diglycidyl ether of bisphenol-A (DGEBA) epoxy resin. Dispersed nanosilica particles, called Nanopox F400 from Nanoresins, were used with and without additional silane surface treatment (the sample preparation was described in Chapter 4) to prepare the nanosilica-modified polymers. For the additional silane treatment, an adhesion promoter, called A187 (Silquest A187 silane, γ-glycidoxypropyltrimethoxy-silane) from Witco, was used to increase particle/epoxy adhesion. For the surface treatment process, A187 was directly added with Nanopox F400, and then mixed using a mechanical stirrer at 500 rpm for 30 minutes; the sample preparation of the silane-treated silica nanoparticle-modified polymer was described in Section 3.4.4.

A second grade of Nanopox was also used. Nanopox XP from Nanoresins consists of silica nanoparticles, which are the same as the nanosilica in Nanopox F400, premixed with DGEBA epoxy resin. Here the manufacturer used a modified surface treatment to improve the interfacial bonding between the nanosilica particles and epoxy resin, compared with Nanopox F400. (Note that Nanopox F400 has a standard surface modification to improve the dispersion of the nanosilica in the epoxy resin)

Table 6.2.1 Formulations of nanocomposites with silica nanoparticles.

Formulation	Nanopox F400 (wt%)	Nanopox XP (wt%)	Surface treatment (improvement in adhesion)
Control	NA	NA	NA
10-F400	10	NA	NA
20-F400	20	NA	NA
10-F400-S	10	NA	Additional silane treatment
20-F400-S	20	NA	Additional silane treatment
10-XP	NA	10	Modified treatment
20-XP	NA	20	Modified treatment

(NA: not applicble)

6.2.1 Morphology of Nanosilica-modified Epoxy Polymers

The morphology of the nanosilica/epoxy nanocomposites was studied using atomic force microscopy (AFM) to check the dispersion of the nanoparticles in the cured samples. Starting with imaging of the unmodified epoxy polymer samples, labelled here Control, atomic force microscopy was conducted in tapping mode. The microstructure of the control sample revealed relatively featureless images, as shown in Figure 6.2.1. This indicates that it was a homogeneous thermosetting polymer [5].

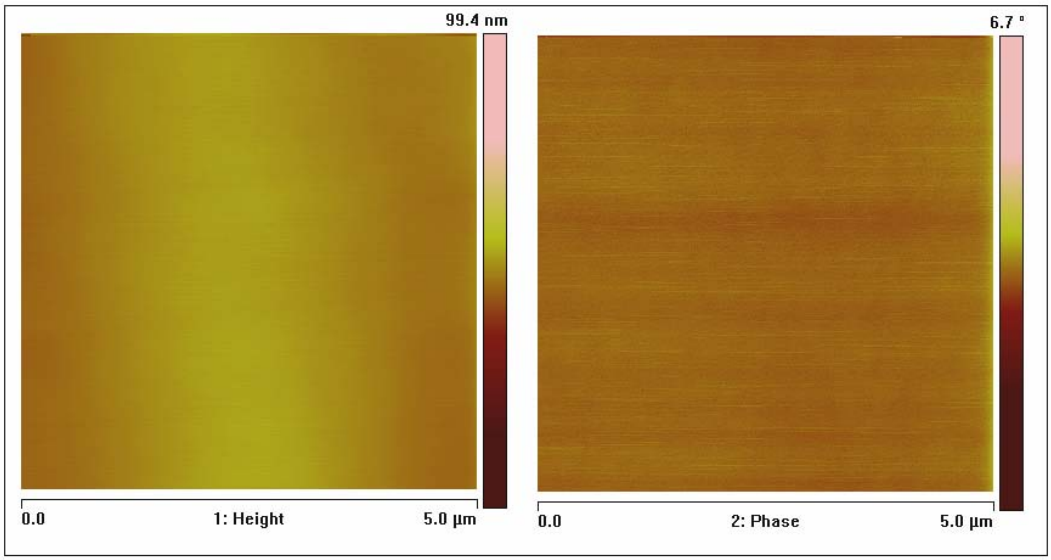


Figure 6.2.1 Atomic force microscopy image of the cured unmodified polymer.

The featureless microstructure of the unmodified polymer was confirmed by field emission gun scanning electron microscopy (FEG-SEM) observation of the fracture surface, as shown in Figure 6.2.2. Only a few striation marks, caused by the existence of inherent flaws causing the crack to grow along different fracture planes, can be seen in this image. This failure surface indicated that the unmodified polymer is a brittle material [111].

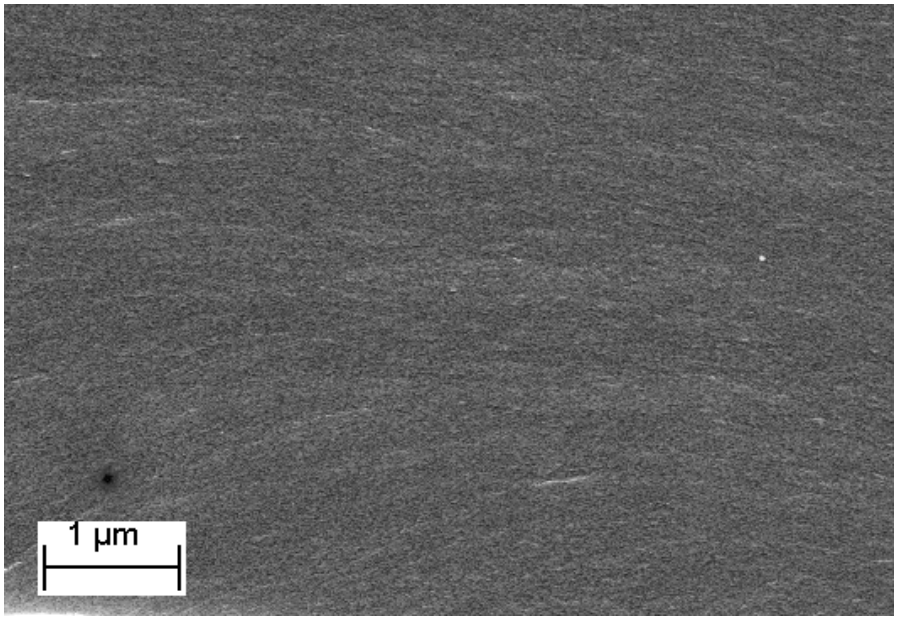
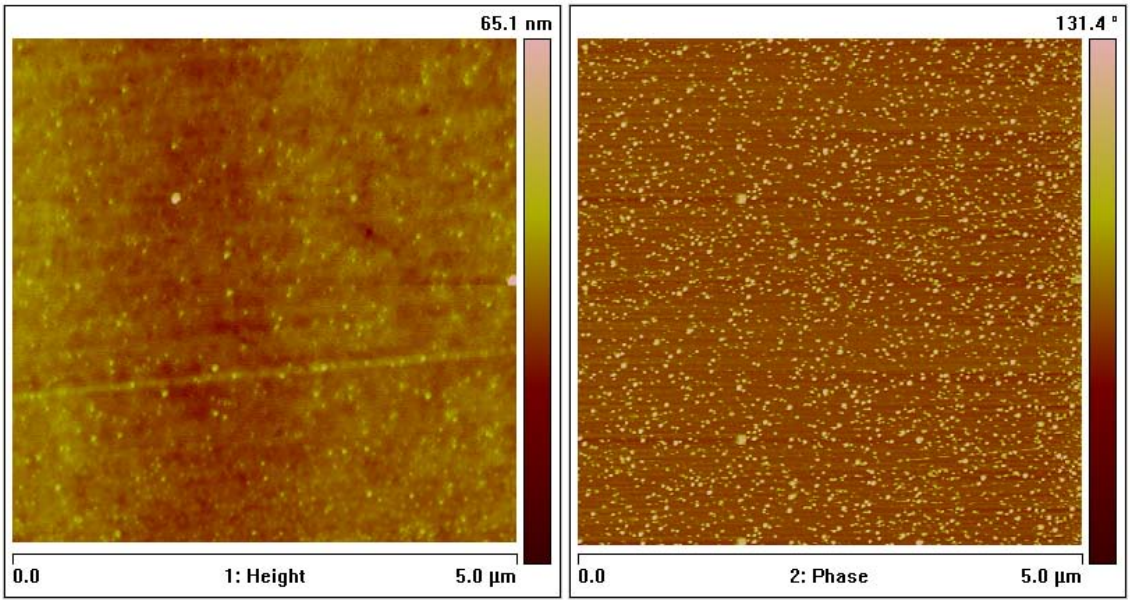
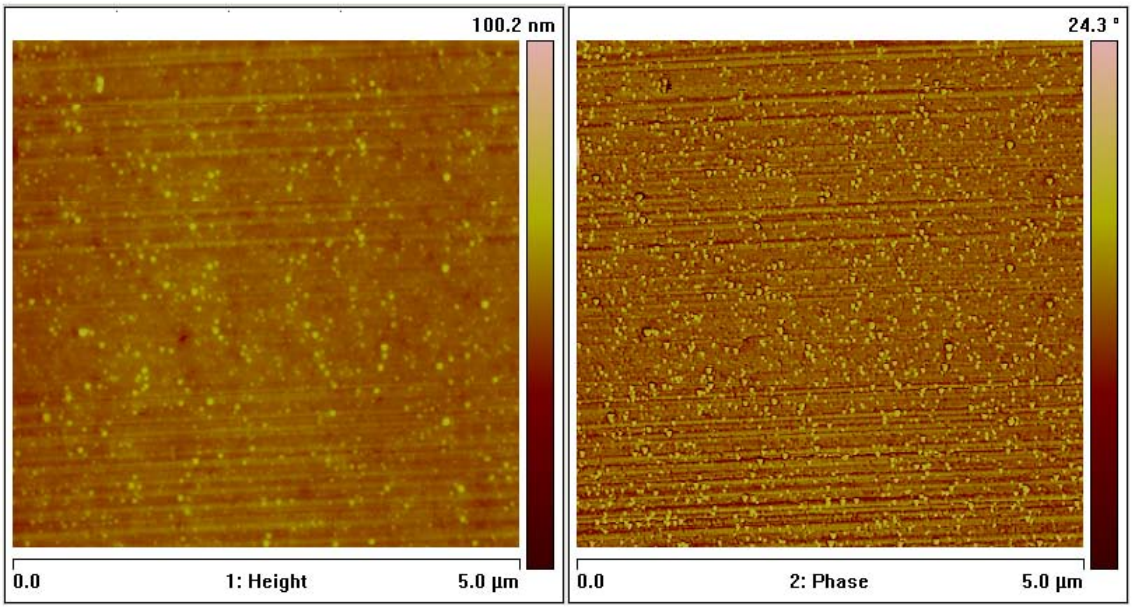


Figure 6.2.2 Field emission gun scanning electron microscopy image of the unmodified polymer (the direction of crack growth is from the right to the left).

Moving on to the AFM images of the nanocomposites reinforced by silica nanoparticles, a good dispersion of the nanoparticles was observed. As can been seen in Figure 6.2.3, dispersed individual silica nanoparticles were readily found from the AFM observation, with an average diameter of 20 nm, as demonstrated in previous work [5]. Even when the concentration of the silica nanoparticles was increased to 20 wt%, the cured nanocomposite with the highest loading of silica nanoparticles still has well-distributed nanoparticles, see Figure 6.2.3 (b). Figure 6.2.4 shows the nanocomposites with the additional silane and the modified treated nanosilica particles. Clear evidence of well-dispersed nanoparticles was observed in these AFM images, indicating that the surface treatment did not degrade the level of the nanosilica dispersion as expected [112]. No clear difference of the nanoparticle size was recorded for all the formulations; the diameter for the nanosilica particles measured from these AFM images was 20 ±2 nm, which has been demonstrated in previous work [5].

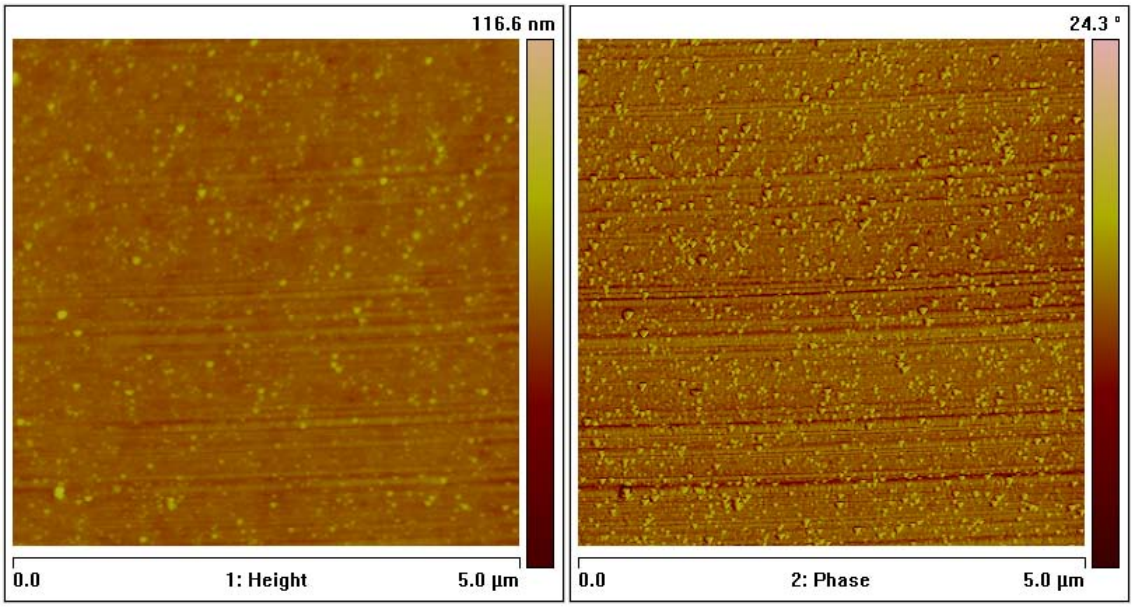


(a)

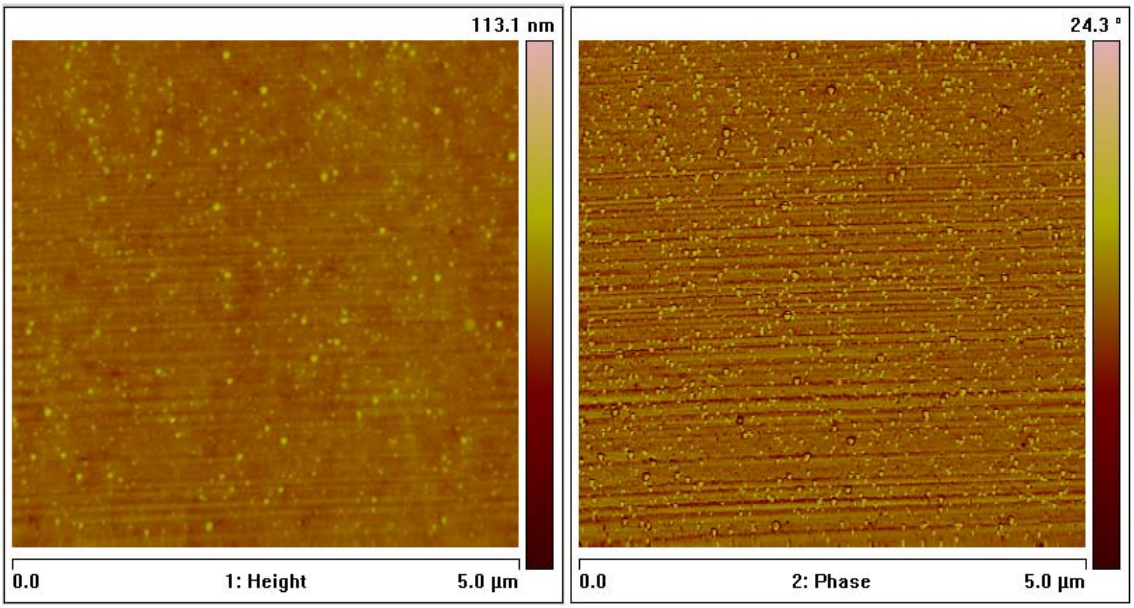


(b)

Figure 6.2.3 Atomic force microscopy image of the nanocomposites, showing the sample of (a)10-F400 and (b)20-F400.



(a)



(b)

Figure 6.2.4 Atomic force microscopy image of the nanocomposites with the treated nanoparticles, showing the sample of (a) 10-F400-S and (b) 10-XP.

6.2.2 Mechanical and Thermal Properties

The Young's modulus of the nanosilica-modified epoxy polymer was measured using tensile tests, and the results are summarised in Table 6.2.2 and Figure 6.2.5. The modulus for the unmodified epoxy was measured to be 2.90 GPa, which is a typical value of the Young's modulus for the anhydride-cured DGEBA epoxy [5]. The presence of the silica nanoparticles in the epoxy polymer resulted in a steady increase in the stiffness. The modulus was measured to be 3.28 GPa for the nanocomposite with 10 wt% silica nanoparticles with the standard treatment (10-F400), and 3.79 GPa with 20 wt% silica nanoparticles (20-F400). Further improvement in the stiffness can be obtained by the introduction of the additional surface treatment to the nanocomposites, but the increases are not significant. The testing results show that a maximum value of 3.85 GPa was measured for the nanocomposite containing 20 wt% nanosilica particles and silane (20-F400-S).

However, the second highest modulus reached was 3.79 GPa for the nanocomposites with 20 wt% nanoparticles in both the F400 and Nanopox XP systems. All of these indicate that any improvement in nanoparticle/epoxy adhesion did not significantly increase the stiffness of the polymer-based nanocomposites, see Figure 6.2.5.

Table 6.2.2 The mechanical and thermal properties of the nanosilica-modified nanocomposites.

Formulation	Nanosilica (wt%)	E (GPa)		T_g (°C)	
		Mean	SD	Mean	SD
Control	0	2.90	0.09	147.8	0.9
10-F400	10	3.28	0.08	148.3	1.4
20-F400	20	3.79	0.05	149.8	2.1
10-F400-S	10	3.31	0.07	145.7	2.4
20-F400-S	20	3.85	0.12	146.2	3.8
10-XP	10	3.25	0.08	144.8	2.9
20-XP	20	3.79	0.08	148.2	3.9

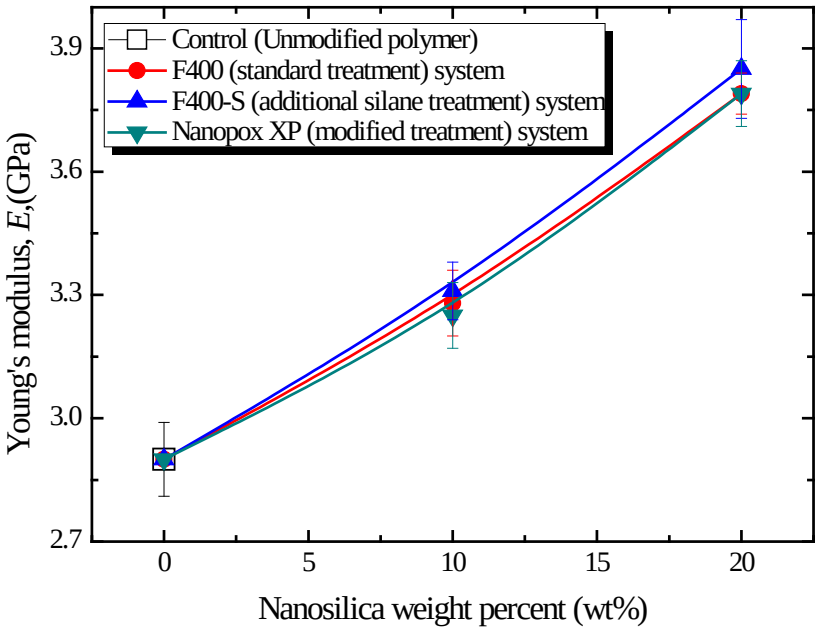


Figure 6.2.5 Young's modulus of the nanocomposites.

The additional surface treatment used in this study is the silane treatment for the F400 system. Silane is widely used as a coupling agent in industrial applications for improving the adhesion between glass reinforcements and polymeric matrixes [48, 113, 114]. It has been reported that the silane can improve the adhesion by creating chemical bonds between the glass or silica additives and polymers [48]. The silica is added to the epoxy resin, and is expected to diffuse to the surface of the nanosilica particles. With good particle/matrix adhesion, the added nanosilica particles can transfer the stress from the polymer matrix as the nanocomposites are subjected to loading, consequently improving the stiffness. However, the testing results showed no obvious increase in the stiffness when the additional silane surface treatment was used in the nanocomposites. The Young's modulus is a well-known material property characterizing the elastic property of the materials. A good interfacial adhesion allows the added particles to be well-bonded with the polymeric matrix even at high stress, where plastic deformation takes place. Figure 6.2.6 shows the stress-strain curve for two types of nanocomposites containing 10 wt% F400 (with standard treated nanosilica) and 10 wt% F400-S (with additional silane). The point where the nanocomposite starts plastic deformation (nonlinearity) shifts to a higher value of stress if the additional silane surface treatment

was used. Besides, the maximum tensile stress was increased for the nanocomposites with the silane surface treatment; the measured yield stress was increased from 60.9 MPa for 10wt% untreated nanosilica to 72.2 MPa for 10wt% nanosilica with the silane additive. Note that the testing data (engineering strain and engineering stress) presented in Figure 6.2.6 was recorded from the uniaxial tensile tests performed on very thin specimens, with a thickness of around 0.5 mm, see Figure 6.2.7, at a low displacement rate of 0.3 mm/min. In order to get plastic deformation in the nanocomposites before fracture, the degree of deformation should be sufficient. Therefore, a thin specimen, in a state of plane stress, was required, and can undergo greater deformation in comparison with a thick specimen when subjected to loading, as shown in Figure 6.2.8.

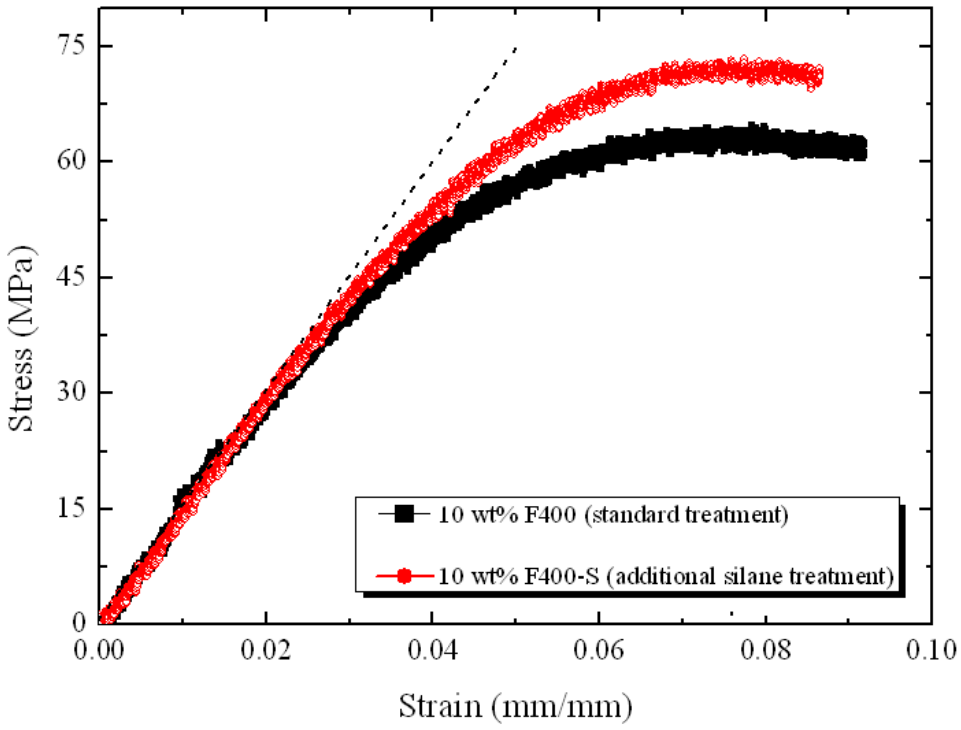


Figure 6.2.6 The stress-strain curve for 10 wt% untreated (10-F400) and treated (10-F400-S) nanosilica-modified polymers in plane stress.

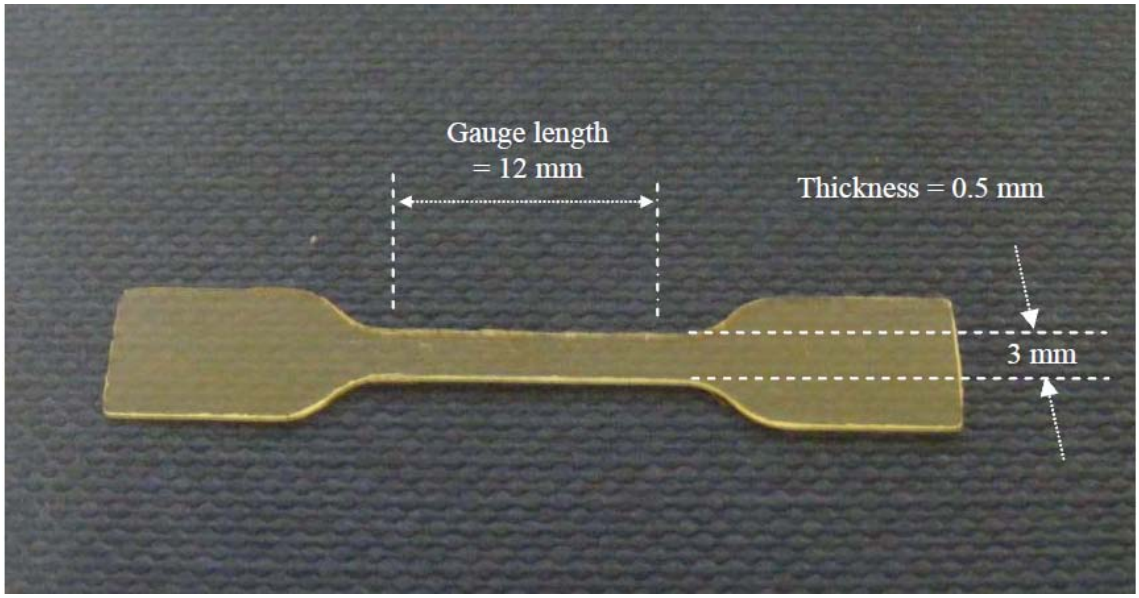


Figure 6.2.7 Photograph of the thin tensile specimen.

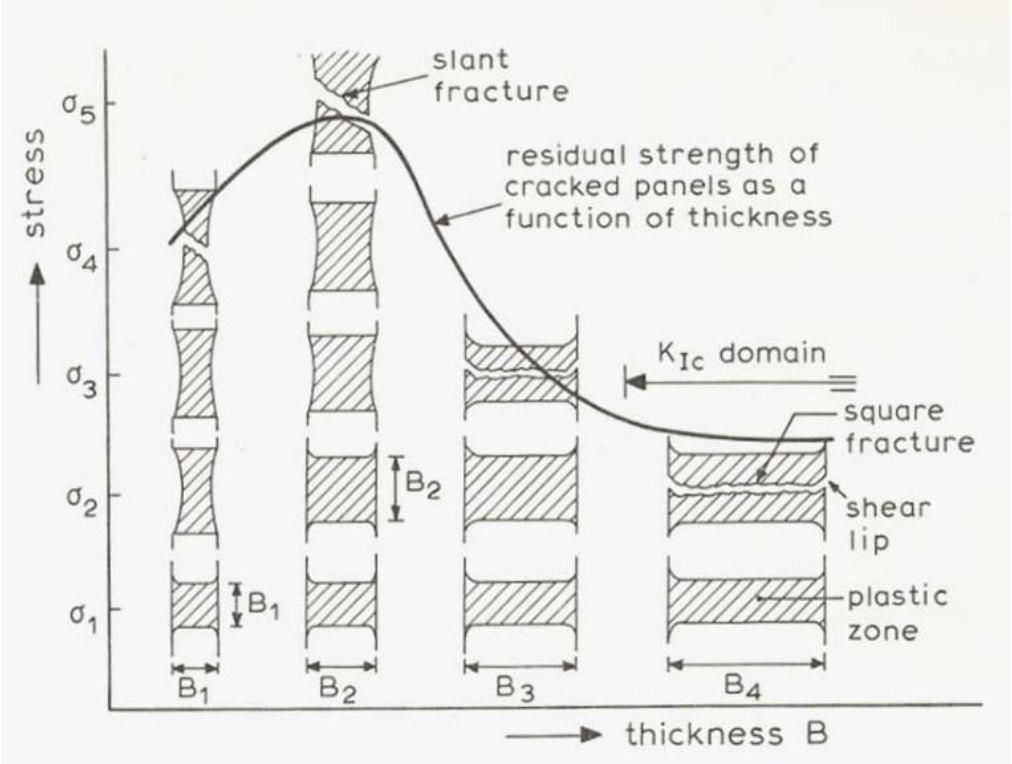


Figure 6.2.8 Residual strength as a function of thickness [115].

Turning to the results (see Table 6.2.2) of the differential scanning calorimetry (DSC) utilized to investigate the effect of the addition of nanosilica and the surface treatment on the glass transmission temperature, T_g. The results show the addition of the silica nanoparticles did not affect the measured value of T_g, all the formulations have an average measured T_g of 147 ±2 °C. The use of the silane surface treatments resulted in a slight decrease in the measured value of T_g, around 2~3 °C for the nanocomposites with the surface treated silica nanoparticles. However, this change in T_g caused by the additional surface treatment still lies within experimental error.

6.2.3 Fracture Toughness and Fracture Energy

Single-edge notched bend (SENB) tests were utilized to investigate the quasi-static fracture behaviour of the nanocomposites reinforced with the silica nanoparticles. The fracture toughness, K_{Ic}, and fracture energy, G_{Ic}, were measured, the values of which were calculated from the load against displacement, as shown in Figure 6.2.9. Six replicate specimens were required for each formulation, and an extensometer was used to accurately measure the displacement. The testing results are summarised in Table 6.2.3.

The fracture toughness, K_{Ic}, was measured to be 0.69 MPa $m^{1/2}$ for the unmodified polymer, which is slightly higher than reported in previous work [5]. This is because a longer post-cure was used in this study, which may change the level of cross-linking in the polymer. From the testing results, it is clearly shown that the addition of the nanosilica particles of F400 (with standard treatment) results in an increase in the toughness. The fracture toughness was increased to 0.92 MPa $m^{1/2}$ for the nanocomposite containing 20wt% nanosilica particles (20-F400), which is around a 33% increment in the fracture toughness in comparison with the unmodified polymer. The increased toughness caused by the addition of these nanosilica particles had been demonstrated by Hsieh et al. [5].

Further increased fracture toughness can be obtained, see Figure 6.2.10, with the additional silane treatment. The maximum measured value of the fracture toughness, K_{Ic}, attained was 0.95 MPa $m^{1/2}$ for the polymer with 20 wt% silane-treated nanoparticles (20-F400-S). This indicates that the surface treatment for improving adhesion led to an increase in the fracture toughness, but not a significant increase when the standard deviations are considered. Both the systems of "F400-S" (F400 with the additional silane treatment) and "Nanopox XP" (with modified treatment by the manufacturer) show the same trend.

Figure 6.2.11 shows the measured value of the fracture energy, G_{Ic}, for the nanocomposites with various nanoparticle loading and surface treatments. The increased fracture energy induced by the addition of nanosilica was clearly demonstrated. For example, the measured value of the fracture energy was increased from 133 J/m^2 for the unmodified polymer to 191 J/m^2 and 220 J/m^2 for the nanocomposites with 10 wt% (10-F400) and 20wt % (20-F400), respectively, of the nanosilica particles with the standard treatment. The fracture energy increased when the surface treatments were introduced to the nanosilica-modified epoxy polymers. A maximum fracture energy of 261 J/m^2 was recorded for the modified polymer with 20 wt% of nanosilica and silane (20-F400-S). The Nanopox XP system also showed relatively high values of the fracture energy, compared with the nanocomposites with F400 nanosilica particles.

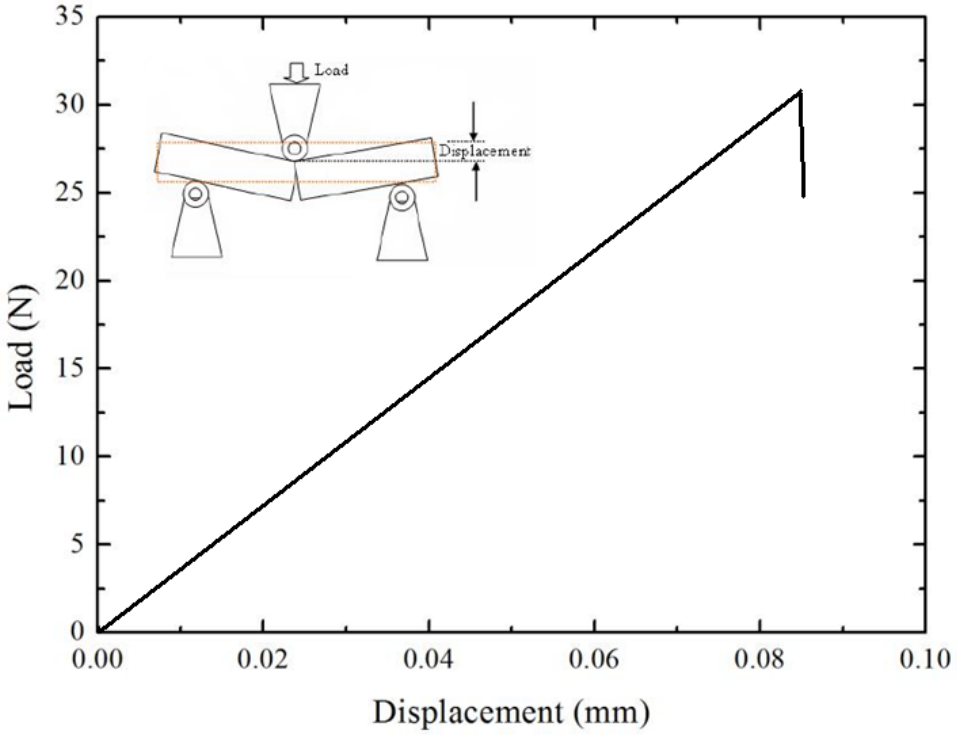


Figure 6.2.9 The typical load versus displacement curve of the SENB test on the unmodified epoxy polymer.

Table 6.2.3 The fracture toughness and fracture energy of the nanosilica-modified polymer composites.

Formulation	Nanosilica (wt%)	K_{Ic} (MPa $m^{1/2}$)		G_{Ic} (J/m^2)	
		Mean	SD	Mean	SD
Control	0	0.69	0.03	133	8
10-F400	10	0.81	0.09	191	21
20-F400	20	0.92	0.06	220	15
10-F400-S	10	0.90	0.08	241	12
20-F400-S	20	0.95	0.05	261	15
10-XP	10	0.87	0.07	249	11
20-XP	20	0.95	0.05	259	20

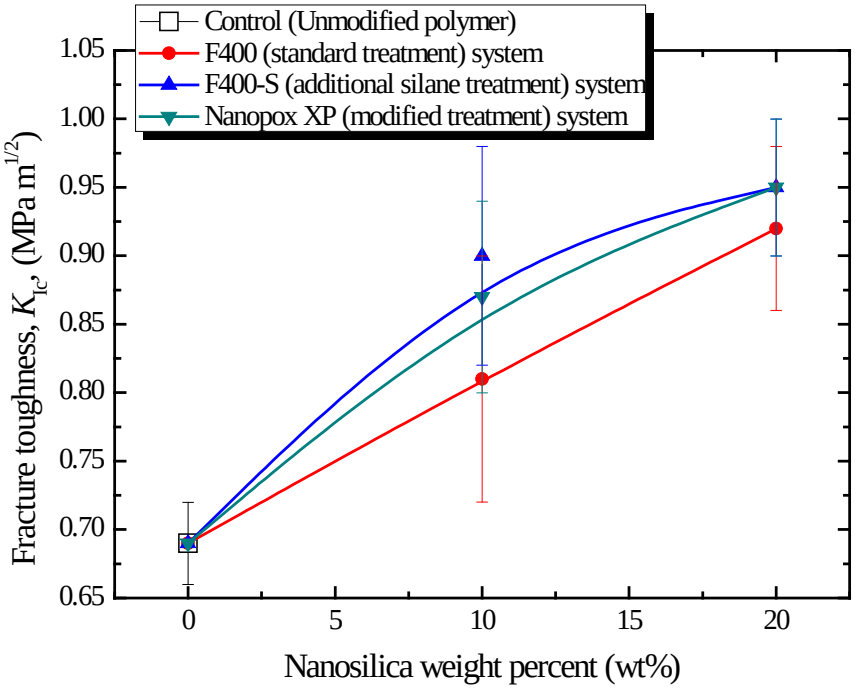


Figure 6.2.10 The fracture toughness of the nanocomposites with various nanosiilca loading and surface treatments.

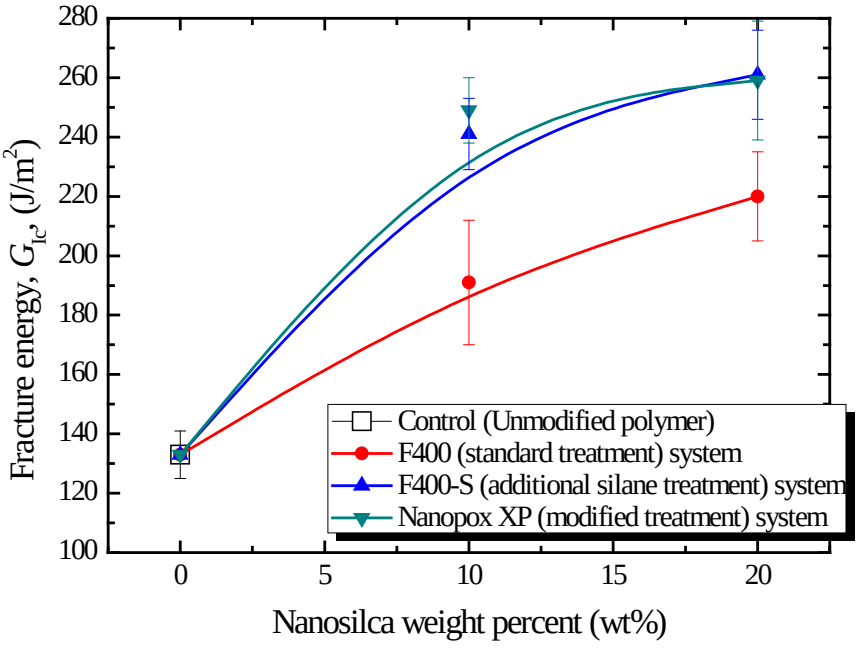


Figure 6.2.11 The fracture energy of the nanocomposites with various nanosilica loading and surface treatments.

6.2.4 Fractography and Toughening Mechanisms

Field emission gun scanning electron microscopy (FEG-SEM) was used to inspect the fracture surfaces of the nanocomposites, from which the toughening mechanisms responsible for the increased toughness caused by the addition of the silica nanoparticles were identified. Figure 6.2.12 shows the fractography of the unmodified polymer and the nanocomposites with 10 wt% silica nanoparticles for each system. A relatively featureless image was observed for the unmodified polymer, this is a typical fracture surface for the anhydride-cured epoxy polymer [5, 23]. In contrast to the unmodified polymer, a large number of river lines were clearly found on the fracture surfaces for the nanosilica-modified polymers. There surfaces were relatively rough, see Figure 6.2.12 (b)-(d), compared with the unmodified polymer, see Figure 6.2.12 (a). This indicates that, during the fracture, more new surfaces were created in the nanocomposites than the unmodified polymer, suggesting an improvement in the toughness

Note that the direction of crack propagation in the all FEG-SEM images of the fracture surfaces is from the right to the left.

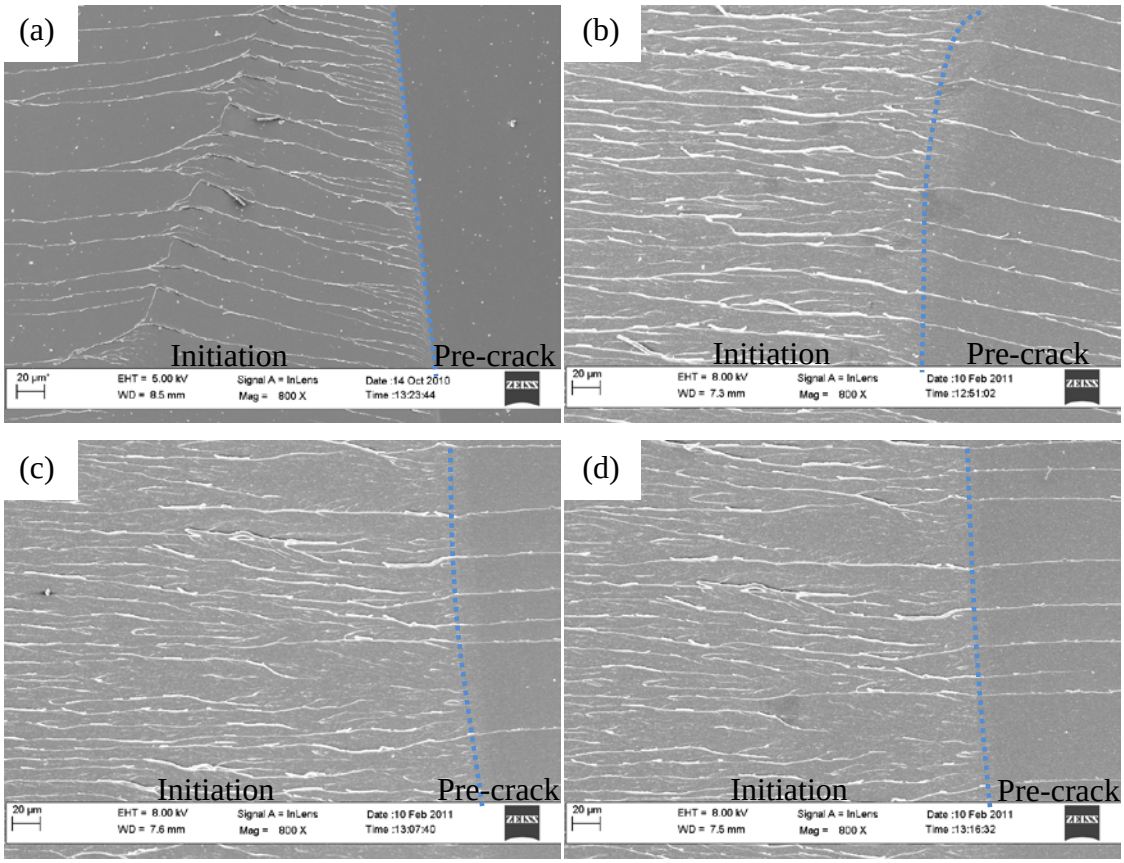


Figure 6.2.12 Field emission gun scanning electron microscopy images of the fracture surfaces, showing (a) unmodified polymer and nanocomposites with (b) 10 wt% "F400" nanosilica, (c) 10 wt% "Nanopox XP" nanosilica, (d) 10wt% "F400" nanosilica with the additional silane treatment.

Figure 6.2.13 ~ Figure 6.2.15 show the fracture surfaces for each system (F400, F400-S and Nanopox XP) at high magnification. Clear evidence of voids due to the nanoparticle debonding and subsequent plastic deformation in the epoxy matrix was found on the fracture surfaces of the "10-F400" and "10-XP" samples, (as shown in Figure 6.2.13 and Figure 6.2.14). However, the sample of "10-F400-S", i.e. the nanocomposite containing 10wt% F400 nanosilica with the additional silane treatment, showed less voids on the fracture surface, as shown in Figure 6.2.15. The images were used to calculate the amount of the silica nanoparticles with void growth (i.e. how many percent of the silica nanoparticles showed void growth around them). The results show that 14 ±2% of nanosilica particles with void growth were present in the sample of "10-F400". No significant difference was recorded from this image analysis as the nanosilica loading was increased (from 10 wt% to 20 wt%), 13 ±4% of nanosilica

particles with void growth was measured in the nanocomposite containing 20wt% nanosilica with the standard treatment (20-F400). The size of these voids is very similar in both nanosilica loadings, and an average diameter of 34 ±3 nm was measured. The amount of the nanosilica void growth and the size of these voids reported in this study are in good agreement with the previous work on the nanosilica/epoxy nanocomposites [5]. For the Nanopox XP sample of "10-XP", 12 ±3% of added nanoparticles with void growth was measured, and the diameter of void growth was measured to be 30 ±5 nm. This is not significantly different from the F400 system. The slightly lower amount of void growth and smaller void diameter present on the fracture surface of Nanopox XP samples may indicate a slightly better nanosilica/epoxy adhesion, compared with the F400 system.

The effect caused by the use of the surface treatment on the particle debonding can be clearly demonstrated in the "F400-S" system, i.e. with the additional silane treatment. As can be seen in Figure 6.2.15, a smaller amount of 5 ±2% of nanoparticles with void growth was measured, and the mean diameter of the voids observed on the fracture surface of the nanocomposite of 10-F400-S was measured to be 25 nm with a standard deviation of 3 nm. This means that the nanosilica particles with the additional surface treatment were well bonded to the epoxy matrix. The results from the photographic analysis are summarised in Table 6.2.4. The effect of the silane surface treatment on the plastic void growth mechanism will be discussed using the plane strain compression tests in the following Section.

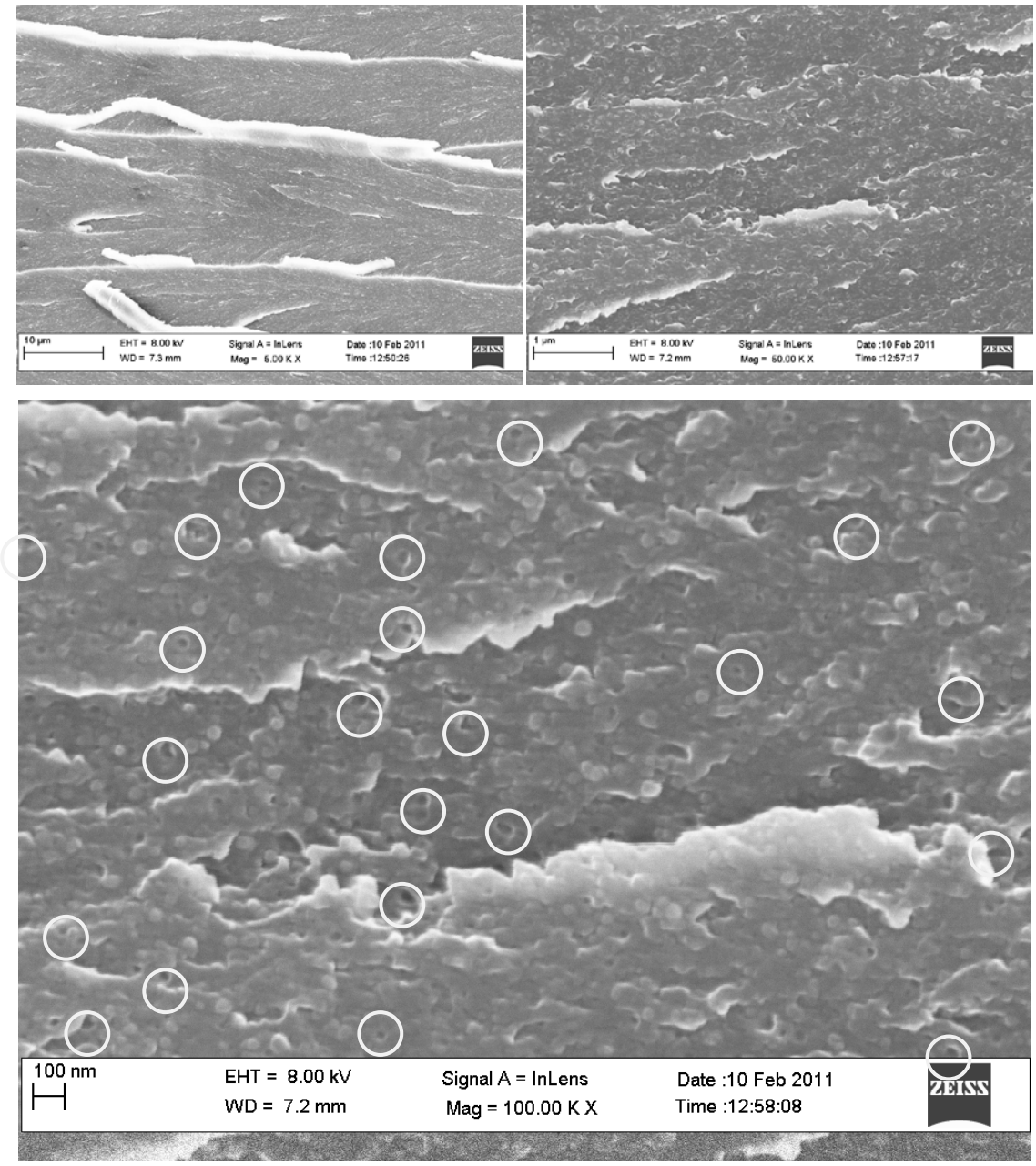


Figure 6.2.13 Field emission gun scanning electron microscopy images of the nanocomposites with 10 wt% of "F400" nanosilica particles, showing plastic void growth as circled.

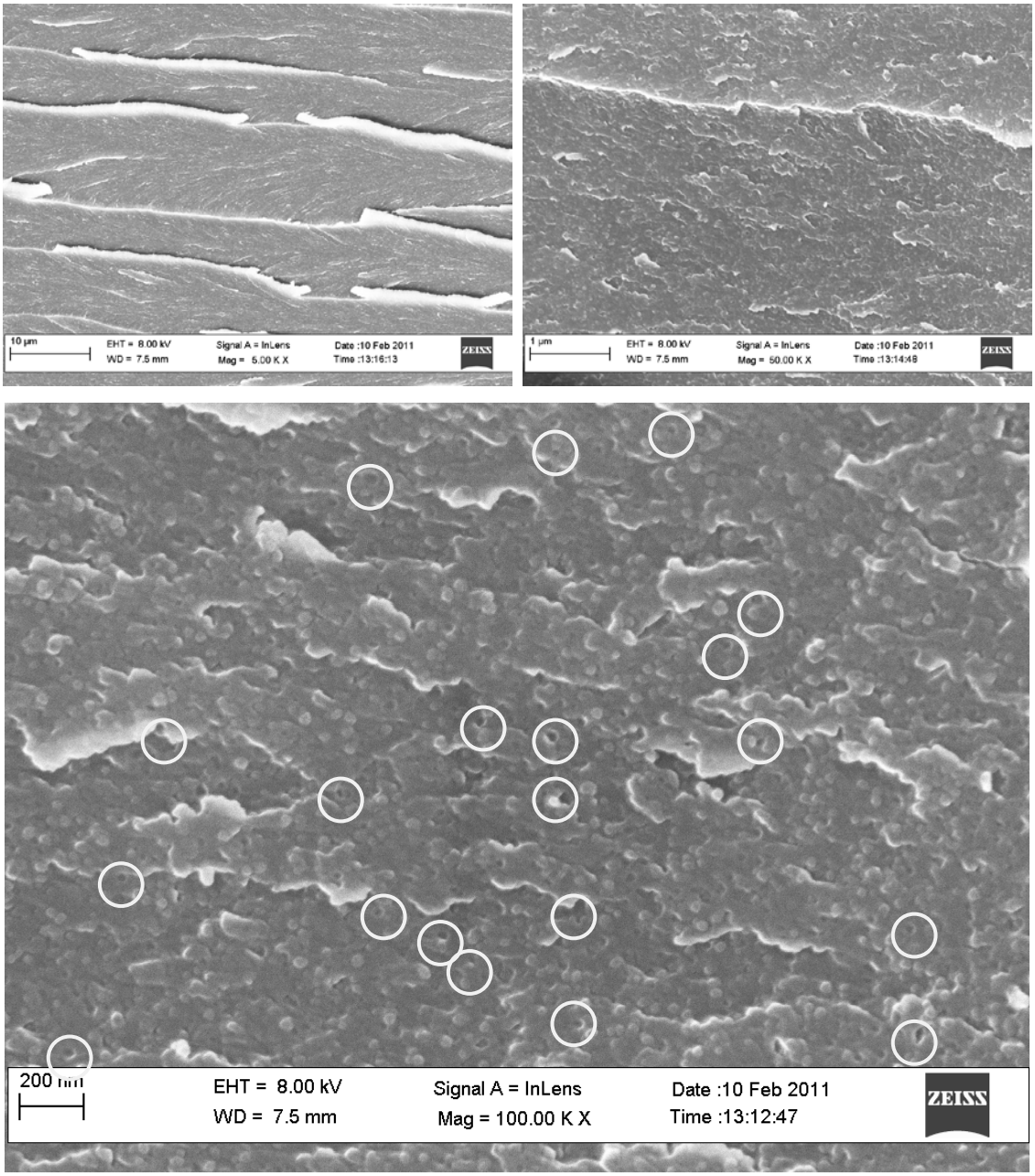


Figure 6.2.14 Field emission gun scanning electron microscopy images of the nanocomposites with 10 wt% of "Nanopox XP" nanosilica particles, showing plastic void growth as circled.

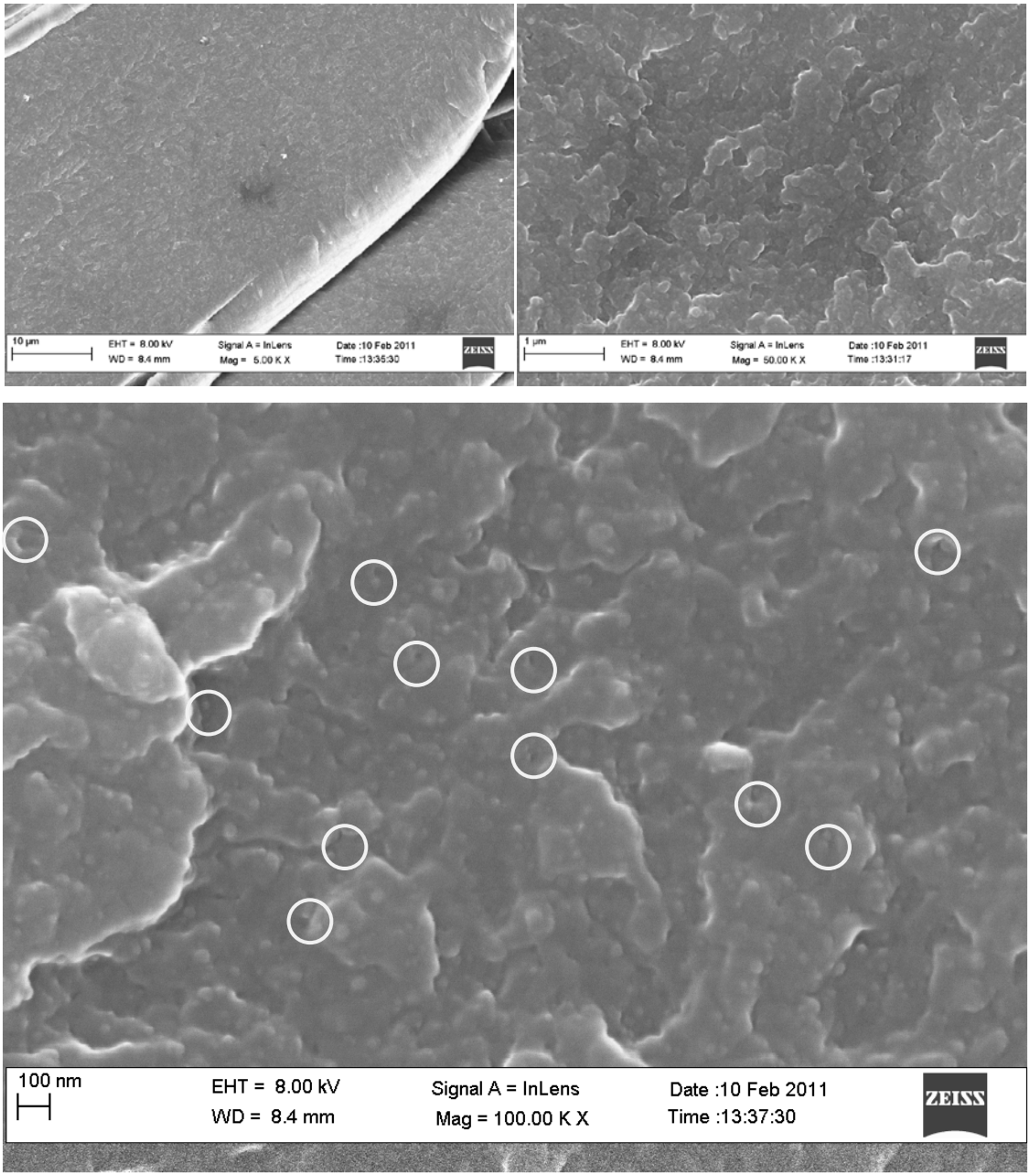


Figure 6.2.15 Field emission gun scanning electron microscopy images of the nanocomposites with 10 wt% of "F400" nanosilica particles with the additional silane treatment, showing plastic void growth as circled.

Table 6.2.4 Summary of the results from the photographic analysis of the fracture surfaces of the nanocomposites, showing the amount of the void growth and the diameter of the voids.

Formulation	Nanosilica (wt%)	Amount of nanosilica with void growth (%)	Diameter of the plastic void (nm)
Control	0	NA	NA
10-F400	10	14 ±2	34 ±4
20-F400	20	13 ±4	34 ±3
10-F400-S	10	5 ±2	25 ±2
20-F400-S	20	5 ±1	25 ±3
10-XP	10	12 ±3	30 ±5
20-XP	20	12 ±2	30 ±2

(NA: not applicable)

The plastic void growth mechanism has been considered as the main toughening contribution caused by the presence of such nanoparticles in polymers [5, 116]. However, the nanocomposite of "20-F400-S", with a smaller amount of plastic void growth mechanism, showed the maximum values of the measured fracture toughness and fracture energy. This may suggest that the addition of the silane may change the properties of the epoxy matrix and not just the nanosilica/epoxy adhesion. Also, the results from plane strain compression tests showed that the sample of "10-F400-S" had the maximum area under the stress-strain curve, as will be discussed in Section 6.2.5. This indicates that the nanocomposite with the additional silane treatment had a relatively higher value of strain energy, consequently the toughness increased.

Figure 6.2.16 shows a normalisation of the increased energy caused by the addition of the silica nanoparticles and surface treatments. The ratio of $G_{Ic(silica-modified)}/G_{Ic(unmodified)}$ is shown in Figure 6.2.16 with various nanosilica loadings for each system. Several studies [46, 117-119] regarding silane treatments clearly demonstrated that the use of the silane treatment as a coupling agent can significantly improve the interfacial adhesion between reinforcements and polymeric matrix, or between substrates and adhesives, but these works did not clearly discuss the effect of the silane treatment on the material properties of polymers without the use of any reinforcements.

Therefore, an additional control formulation (labelled as Control-S) consisting of the anhydride-cured DGEBA epoxy polymer with 10 wt% A187 silane solution was prepared. Values of 0.73 ± 0.02 MPa $m^{1/2}$ and 153 ±14 J/m^2 were measured for the fracture toughness and fracture energy, respectively, of the "Control-S" sample. Both the fracture toughness and fracture energy of this additional control formulation are higher than for the modified polymer (K_{Ic} = 0.69 MPa $m^{1/2}$ and G_{Ic} = 133 J/m^2), indicating that the addition of the silane to the epoxy polymer resulted in a slight increase in the toughness. For the ratio of $G_{Ic(silica\text{-}modified)}/G_{Ic(unmodified)}$ for "F400-S" system , a value of $G_{Ic(unmodified)}$ = 153 J/m^2 was used in Figure 6.2.16. The effectiveness of the addition of the silica nanoparticles on the toughness is clearly shown in Figure 6.2.16 by presenting the relative fracture energy. The greatest effect on the toughness was attained in the system using the "Nanopox XP" silica nanoparticles, which provides nanosilica particles with good interfacial properties between the particles and the epoxy matrix, but not with too strong interfacial adhesion. The introduction of the additional silane surface treatment to "Nanopox F400" nanosilica-modified mixture led to a small improvement in the fracture energy, but not a significant one. This is due to a low level of the plastic void growth mechanism occurring in the system of "F400-S" during the fracture, i.e. the adhesion is too strong for high toughness.

As the nanosilica particles used in this study were pre-mixed with a DGEBA epoxy polymer, the additional silane treatment in the nanosilica-modified polymers was directly added to the "Nanopox F400" nanosilica-modified resin for preparing the "F400-S" nanocomposites rather than using the silane solution on the surfaces of the silica nanoparticles before mixing with the epoxy resin [46]. Therefore, all of the silane coupling agent of the silane (A187) did not form chemical bonds between the silica nanoparticles and epoxy matrix, but some was left in solution in the epoxy matrix, and hence the properties of the matrix were affected. This was also demonstrated in the tensile test, see Figure 6.2.6. The standard method to prepare the silica-treated nanosilica /polymer was reported by Chrusciel et al [120].

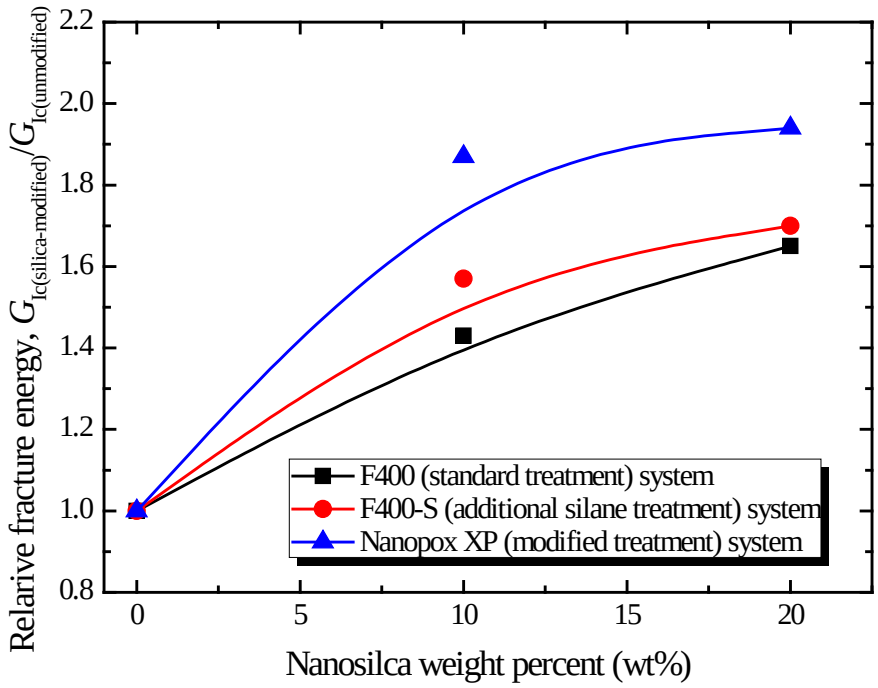


Figure 6.2.16 Relative fracture energy versus content of silica nanoparticles, for "F400", "F400-S" and "Nanopox XP" systems, (note this uses $G_{Ic(unmodified)}$ of "Control-S" for the "F400-S" system).

Figure 6.2.17 shows the fracture surfaces of the "Control-S" material, and the addition of the silane solution to the epoxy polymer caused a different appearance of the fracture surface compared to the unmodified polymer, see Figure 6.2.2 and Figure 6.2.12 (a). More river lines were found on the fracture surfaces, compared with the unmodified polymer. Furthermore, plate-like features were found on the fracture surface from the FEG-SEM observation at high magnification, as shown in Figure 6.2.17 (c). All of these indicate that more new surfaces are created in "Control-S" material during fracture, consequently increasing the toughness.

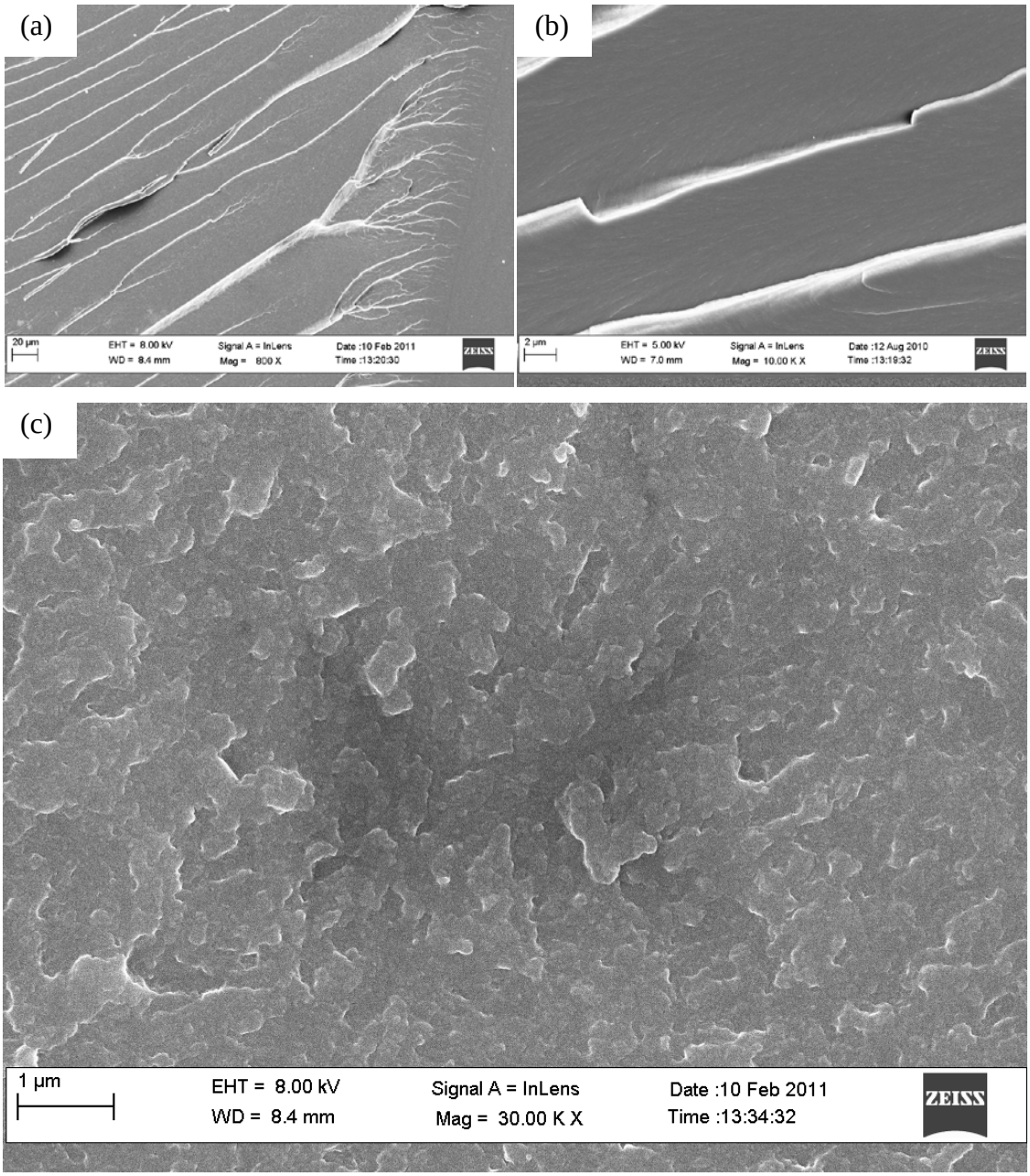


Figure 6.2.17 Field emission gun scanning electron microscopy images of "Control-S" sample, showing (a)-(b) river lines, (c) plate-like fractures.

6.2.5 Compressive Properties

Plane strain compression (PSC) tests were carried out on the unmodified material and the nanocomposites with 10 wt% of silica nanoparticles for each system. In PSC tests, a large degree of deformation of the composites occurs, and the values of compressive Young's modulus, E_c, compressive true yield stress, σ_{yc}, compressive yield strain, ε_{yc}, and compressive failure strain, γ_{fc}, were calculated and are summarised in Table 6.2.5.

The testing results from the plane strain tests show that the compressive Young's modulus, E_c, was increased steadily with the addition of the nanoparticles; the measured value of E_c was 2.60 GPa for the unmodified epoxy, and increased to 2.72 GPa for the nanocomposite with 10 wt% silica nanoparticles (10-F400). Further improvement in the compressive modulus can be attained by the introduction of the additional surface treatments; a peak value of E_c was recorded to be 2.81 GPa for the nanocomposte reinforced using the nanosilica particles with the additional silane treatment (10-F400-S), and 2.77 GPa for the composite with the reinforcement of "Nanopox XP". This indicates that the good nanosilica/epoxy adhesion caused by the use of the surface treatment resulted in an increase in the compressive modulus for the polymer-based nanocomposites. However the increased compressive modulus caused by the additional surface treatment is not significant when the standard deviation was considered. The measured values of E_c for all formulations are in good agreement with the modulus measured from the tensile tests, see Table 6.2.2, and previous studies [5, 23, 116].

The compressive loading was increased to reach the yield point of the nanocomposites. The compressive yield stress, σ_{yc}, was increased by the introduction of the nanosilica with the epoxy matrix, as can be seen in Table 6.2.5 and Figure 6.2.18. For example, the measured value of σ_{yc} was increased from 123 MPa for the unmodified polymer to 135 MPa for the 10-F400 sample. Further increase in σ_{yc} of 146 MPa for the composite containing 10 wt% of F400 nanosilica particles with the additional silane treatment (10-F400-S). This indicates that good adhesion between nanosilica/epoxy resulted in the increase in the yield stress of the epoxies with the silica nanoparticles. Figure 6.2.18 shows the stress-strain curve from the plane strain

compression tests on the nanocomposites, clear evidence of the improvement in the stiffness and the yield stress can be found. However, the length of the strain softening region and the compressive failure strain, γ_{fc}, were slightly reduced for the nanosilica particles with the other surface treatments (F400-S and Nanopox XP).

Table 6.2.5 The plane strain compression testing results of compressive Young's modulus, E_c, compressive true yield strength, σ_{yc}, compressive yield strain, ε_{yc}, and compressive failure strain, γ_{fc}, of the nanocomposites reinforced with the silica nanoparticles.

Formulation	Silica (wt%)	E_c (GPa)		σ_{yc} (MPa)		ε_{yc} (mm/mm)		γ_{fc} (mm/mm)	
		Mean	SD	Mean	SD	Mean	SD	Mean	SD
Control	0.0	2.60	0.08	123	4	0.09	0.01	0.62	0.03
10-F400	10.0	2.72	0.10	135	3	0.08	0.01	0.54	0.04
10-F400-S	10.0	2.81	0.06	146	2	0.08	0.01	0.49	0.03
10-XP	10.0	2.77	0.06	141	3	0.08	0.01	0.52	0.02

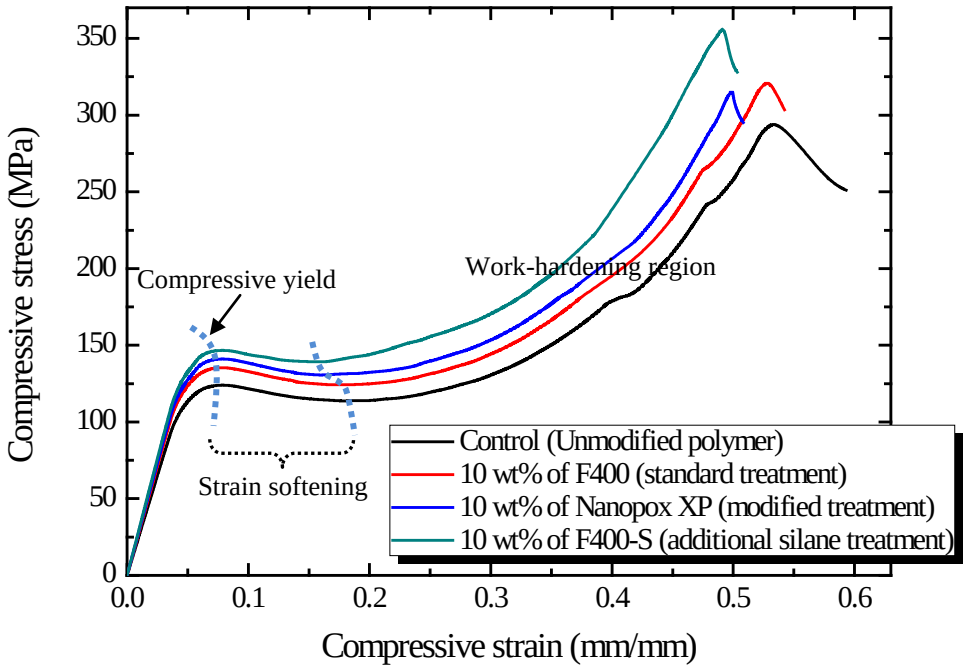


Figure 6.2.18 Compressive stress versus compressive strain for the unmodified polymer and the nanosilica-modified polymers.

The main nanosilica toughening mechanism of plastic void growth would occur in the region between the yield point and the work-hardening phase in the stress-strain curve from plane strain compression tests. In Figure 6.2.18, the region between the yield point and the work-hardening region was reduced for the nanocomposites as the nanosilica particles were treated using the additional surface modifications (F400-S and Nanopox XP). This may result in a lower level of the plastic void grown occurred in such nanocomposites. The results from the FEG-SEM observation of the fracture surfaces showed the same trend, where a relatively small proportion of the nanosilica with void growth was measured for the nanocomposites in the “F400-S” and “Nanopox XP” systems.

More discussions of the plane strain testing on the nanocomposites will be included in Chapter 7.

6.3 Glass Bead Microparticle-modified Epoxy Polymers

This section discusses the toughening performance of glass bead microparticle-modified epoxy polymers, and a comparison between the use of nanoparticles and microparticles to improve the toughness of the epoxy polymer is made. Two different dimensions of glass bead microparticles, see Figure 6.3.1, were used to prepare the composites; one had a mean diameter of 3.5 μm with a wide range between 1 μm to 5 μm (400 mesh), the other had a mean diameter of 275 ±15 μm (+50-60 mesh).

To consider the effect of the glass bead particle/epoxy adhesion on the toughness, various surface treatments were used to modify the surfaces of the microparticles. Table 6.3.1 shows the surface treatments used in the glass bead/epoxy composites, and their effects on the interfacial adhesion. A control (untreated) sample was also made for comparison purposes. Silane treatment is widely used to be a coupling agent to improve the interfacial properties between the reinforcements and the polymeric matrix. In the silane treatment, A187 (Silquest A187 silane, γ-glycidoxypropyltrimethoxy-silane) from Witco was used to prepare the silane solution (see Section 6.4.3), and then used to treat the surfaces of the glass beads before mixing with the epoxy resin [46, 119]. Frekote 770-NC from Henkel, is an industrial release agent commonly used in moulding processes. The introduction of the Frekote surface treatment should result in a reduction in the particle/matrix adhesion. This is contrary to the effect caused by the silane treatment on the particle/epoxy adhesion. All the formulations of the glass bead microparticle-modified polymers with various surface treatments were summarised in Table 6.3.2. The sample preparation for the microparticle-modified polymers was described in Chapter 4.

Note that the AFM observation used to examine the dispersion of the reinforcements did not work for inspecting the morphology of the glass bead-modified epoxy polymers because the maximum scanning size of 20 μm × 20 μm in AFM is smaller than the diameter of the microparticles (1~300 μm). Thus, the morphology and dispersion of the glass beads in the cured epoxy polymer were examined using field emission gun scanning electron microscopy (FEG-SEM), and will be discussed along with the toughening mechanisms, see Section 6.3.3.

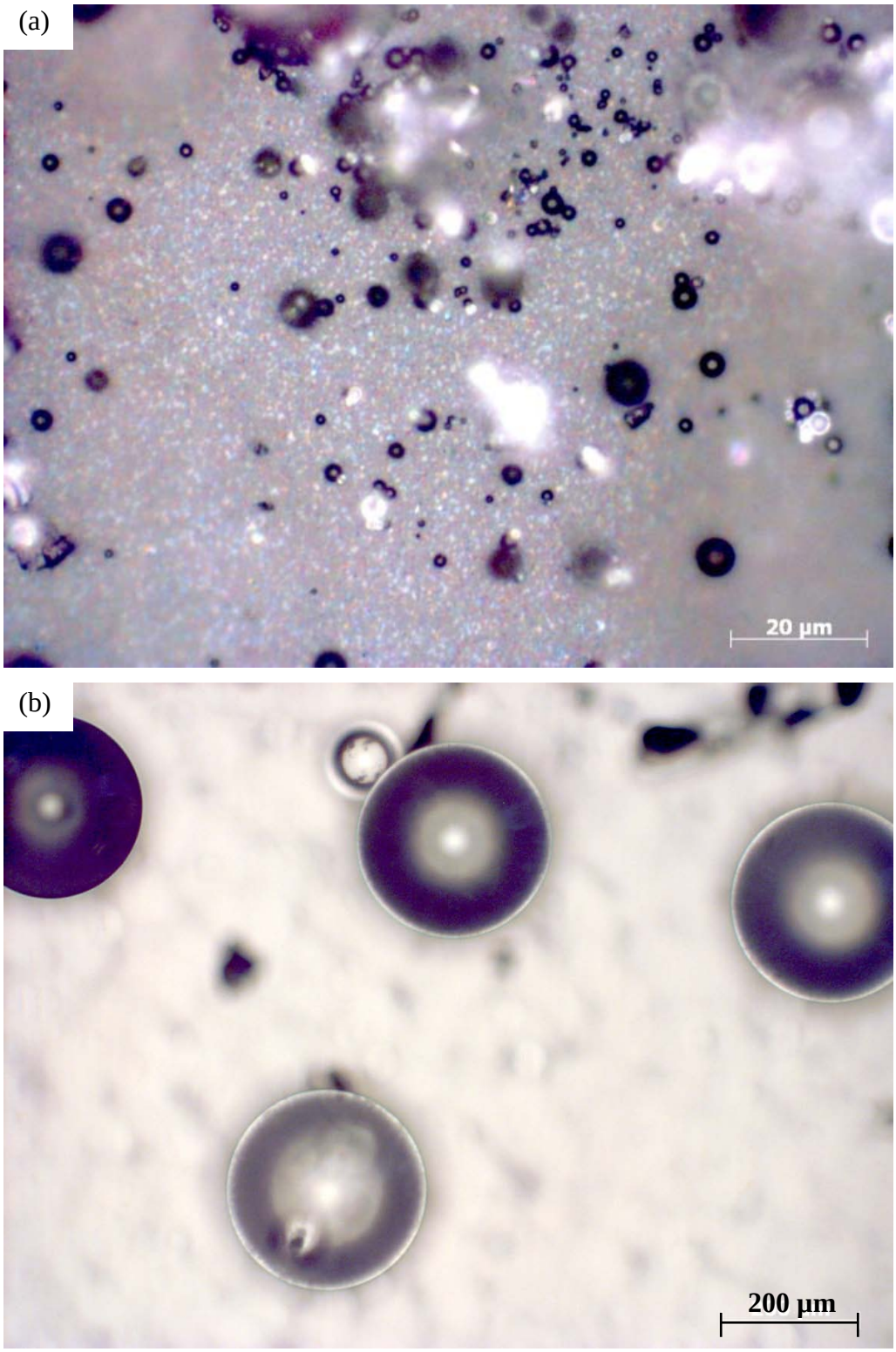


Figure 6.3.1 Optical microscopy images of the glass bead microparticles, showing (a) small glass beads with a mean diameter of 3.5 µm. and (b) large glass beads with a mean diameter of 275 µm.

Table 6.3.1 Surface treatments used in glass bead microparticle-modified epoxy polymers and their effects on particle/epoxy adhesion.

Surface treatment	Effect on particle/epoxy adhesion
Control (untreated)	Control specimen (with untreated glass bead particle)
Frekote	Reduce particle/epoxy adhesion
Silane	Improve particle/epoxy adhesion

Table 6.3.2 Formulations of glass bead microparticle-modified epoxy polymers with various surface treatments.

Formulation	Treatment	Particle wt%	Particle size (μm)
Control (unmodified)	NA	NA	NA
10-S-Control	NA	10	Small (1~5)
10-S-Silane	Silane	10	Small (1~5)
10-S-Frekote	Frekote	10	Small (1~5)
20-S-Control	NA	20	Small (1~5)
20-S-Silane	Silane	20	Small (1~5)
20-S-Frekote	Frekote	20	Small (1~5)
10-L-Control	NA	10	Large (275)
10-L-Silane	Silane	10	Large (275)
10-L-Frekote	Frekote	10	Large (275)
20-L-Control	NA	20	Large (275)

(NA: not applicable)

Note that, there was a challenge for preparing the composites containing the large glass beads because these microparticles sank to the bottom of the mould during the cure schedule. The undesirable agglomeration of the glass beads found, especially for the treated particles, will be discussed in Section 6.3.3. Hence, a maximum glass bead loading of 10 wt% was used in both surface-treated systems (silane and Frekote treatment systems).

6.3.1 Mechanical and Thermal Properties

Tensile tests were carried out on these microparticle-modified epoxy polymers to measure the Young's modulus. Table 6.3.3 and Figure 6.3.2 show the tensile testing results. All the modified epoxy polymers with the addition of the glass bead particles showed an increase in modulus, compared with the unmodified epoxy polymer (Young's modulus = 2.90 GPa). The modulus increased with increasing glass bead loading. However, when the concentration of the glass beads was increased from 10 wt% to 20 wt%, the modulus increased less greatly, as can be clearly seen in Figure 6.3.2. This indicates that the optimum concentration of these microparticles used to improve the modulus of the anhydride-cured DGEBA epoxy polymer falls at around 10 wt%. The reason why the highest loading of glass beads did not efficiently increase the modulus is the agglomeration of the glass beads, see Section 6.3.3.

With the same surface treatment, the use of the small glass bead particles results in a larger increase in the Young's modulus, in comparison with the addition of the large glass beads. For example, in the untreated system, the modulus for the modified polymer with 20 wt% of the small glass beads was increased from 2.90 GPa for the unmodified polymer to 3.20 GPa for the glass bead-modified polymer. However, the addition of 20 wt% of the large glass beads led to a Young's modulus of only 3.12 GPa. Lewis et al [121] investigated the particle size effect on the mechanical properties of the composites with micro-sized particles. They reported that when smaller particles were used, a higher modulus was obtained, see Figure 6.3.3.

Table 6.3.3 The mechanical and thermal properties of the glass bead microparticle-modified epoxy polymers.

Formulation	Treatment	Glass bead (wt%)	E (GPa)		T_g (°C)	
			Mean	SD	Mean	SD
Control	NA	0	2.90	0.09	147.8	0.9
10-S-Control	NA	10	3.18	0.08	148.2	0.8
10-S-Silane	Silane	10	3.75	0.12	146.8	1.2
10-S-Frekote	Frekote	10	3.06	0.05	145.3	2.1
20-S-Control	NA	20	3.20	0.07	148.8	2.4
20-S-Silane	Silane	20	3.81	0.10	147.1	3.0
20-S-Frekote	Frekote	20	3.07	0.05	144.9	2.9
10-L-Control	NA	10	3.13	0.09	147.2	2.5
10-L-Silane	Silane	10	3.31	0.06	146.8	3.2
10-L-Frekote	Frekote	10	2.92	0.09	144.7	2.7
20-L-Control	NA	20	3.12	0.12	148.9	1.8

(NA: not applicable)

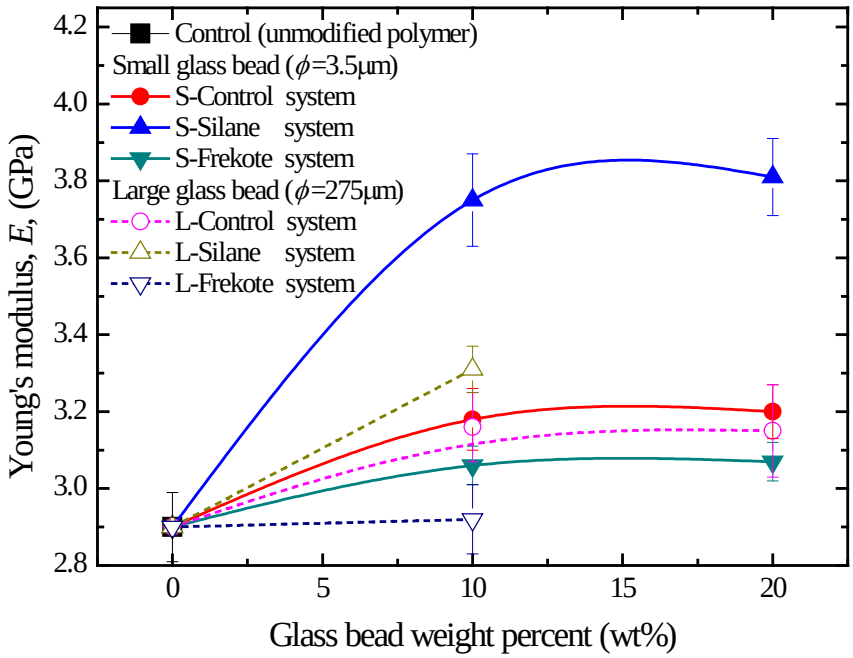


Figure 6.3.2 Young's modulus of the glass bead microparticle-modified epoxy polymers.

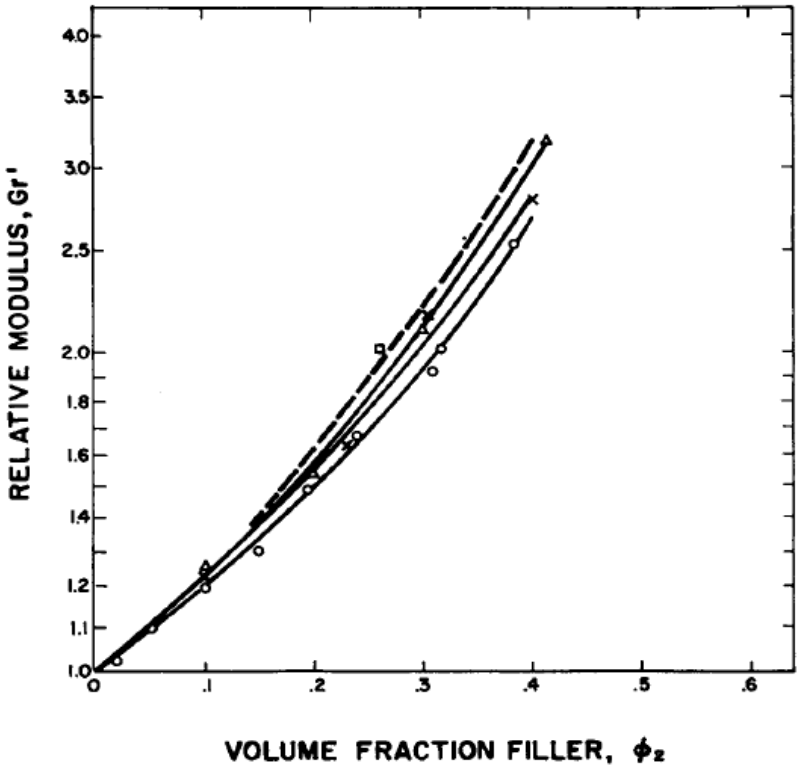


Figure 6.3.3 Relative modulus versus content of dispersed spheres with various diameters: (□) d = 5~10 μm, (△) d = 10~20 μm, (╳) d = 30~40 μm and (○) d = 75-90 μm [121].

Moving on to the effect of the surface treatments on the modulus, two different surface treatments were used to modify the surfaces of these glass beads, consequently different levels of interfacial adhesion between the beads and epoxy matrix were obtained. For the untreated glass bead microparticles, the Young's modulus was measured to be 3.18 GPa for 10 wt% of the small glass bead particles, and 3.13 GPa for the large glass beads at 10 wt%. The addition of the silane treatment, which is commonly used to improve the adhesion, led to a significant increase in the Young's modulus. For example, the samples of "10-S-Silane" and "20-S-Silane" reveal a relatively high modulus of 3.75 GPa and 3.81 GPa, respectively. This is around a 0.6 GPa increment in the measured Young's modulus, compared with the modified polymer with the untreated small glass bead microparticles at corresponding loadings. However, the small microparticles with the surface modification using the release agent (Frekote) provided a low ability to improve the stiffness. For example, the Young's modulus of the composites modified with the Frekote treated small glass bead particles was measured to be 3.06 GPa for 10 wt% (10-S-Frekote), and 3.07 GPa for 20 wt% (20-S-

Frekote). The effect caused by the surface treatments on the modulus can be clearly seen in Figure 6.3.2.

For the large glass bead particles, the introduction of the silane treatment led to a significant improvement in the modulus, but a slight decrease in the Young's modulus was caused by the addition of the Frekote treatment. The variation in the modulus of the composites reinforced with the large glass beads showed the same trend as for the small glass beads.

Turning to the differential scanning calorimetry (DSC) used to measure the glass transmission temperature, T_g. The results show that the addition of the glass bead microparticles did not bring obvious changes in T_g, All the measured values are very similar and have an average value of 147 °C, with a range between 144 °C to 148°C, see Figure 6.3.4. The addition of the Frekote surface treatment resulted in a slight decrease in the measured value of T_g by 2~3 °C. However, even this decrease in T_g is not significant when the experimental variation is considered, see Table 6.3.3.

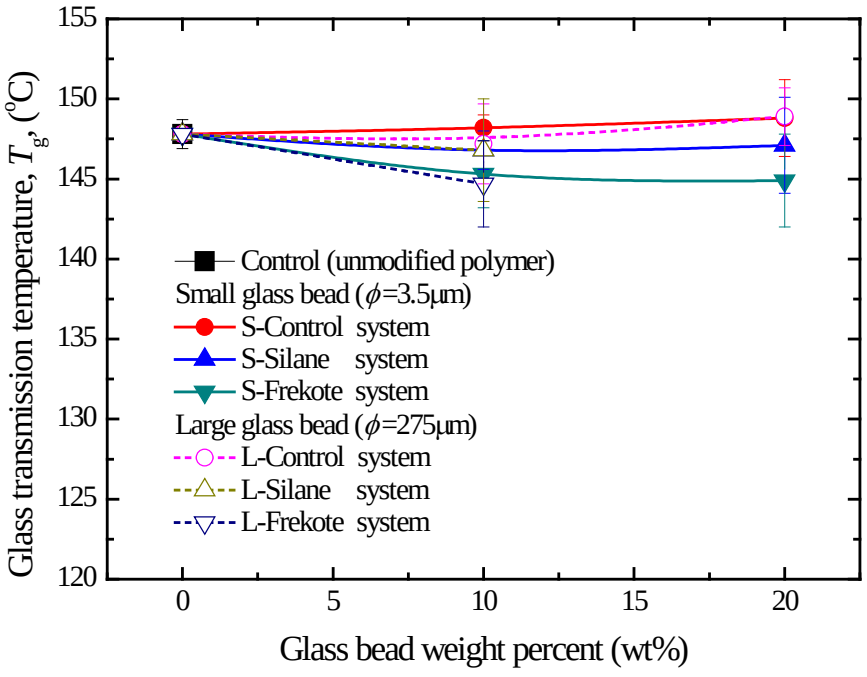


Figure 6.3.4 Glass transmission temperature of the glass bead microparticle-modified epoxy polymers.

6.3.2 Fracture Toughness and Fracture Energy

Table 6.3.4 shows the single-edge notched bend testing results of the microparticle-modified polymers with various particle sizes and surface treatments. The toughness of the epoxy polymer was increased using the small glass beads (1~5 μm in diameter), and the peak value for each system was obtained when the loading was increased to 20 wt%. In contrast, the inclusion of the large glass bead microparticles with an average diameter of 275μm slightly decreased the toughness rather than improving it. This unexpected decrease may suggest that these large microparticles act as stress concentrations rather than efficient toughening. Optical microscopy and FEG-SEM observation clearly showed that the large glass beads had sunk towards the bottom of the mould so serious agglomerations of the large beads formed during the cure cycle, as discussed in the following Section. Even the mould was revolved every 5 minutes during the cure schedule, the large glass bead agglomerates formed on the bottom of the mould due to gravity, see Figure 6.3.5. The undesirable, and rapid sedimentation of the large glass microparticles led to difficulty in the sample preparation. Therefore, the highest weight loading of 20 wt% was not used for the samples containing the large glass bead particles with the surface treatments (“L-Silane “and “L-Frekote” systems).

Table 6.3.4 The fracture toughness and fracture energy of the glass bead microparticle-modified epoxy polymers.

Formulation	Treatment	Glass bead (wt%)	K_{IC} (MPa $m^{1/2}$)		G_{IC} (J/m^2)	
			Mean	SD	Mean	SD
Control	NA	0	0.69	0.03	133	8
10-S-Control	NA	10	0.74	0.05	149	14
10-S-Silane	Silane	10	0.80	0.05	181	11
10-S-Frekote	Frekote	10	0.79	0.03	179	14
20-S-Control	NA	20	0.91	0.05	158	16
20-S-Silane	Silane	20	0.94	0.10	197	13
20-S-Frekote	Frekote	20	0.95	0.07	192	9
10-L-Control	NA	10	0.62	0.04	113	15
10-L-Silane	Silane	10	0.67	0.08	109	10
10-L-Frekote	Frekote	10	0.65	0.07	118	9
20-L-Control	NA	20	0.64	0.04	103	14

(NA = not applicable)

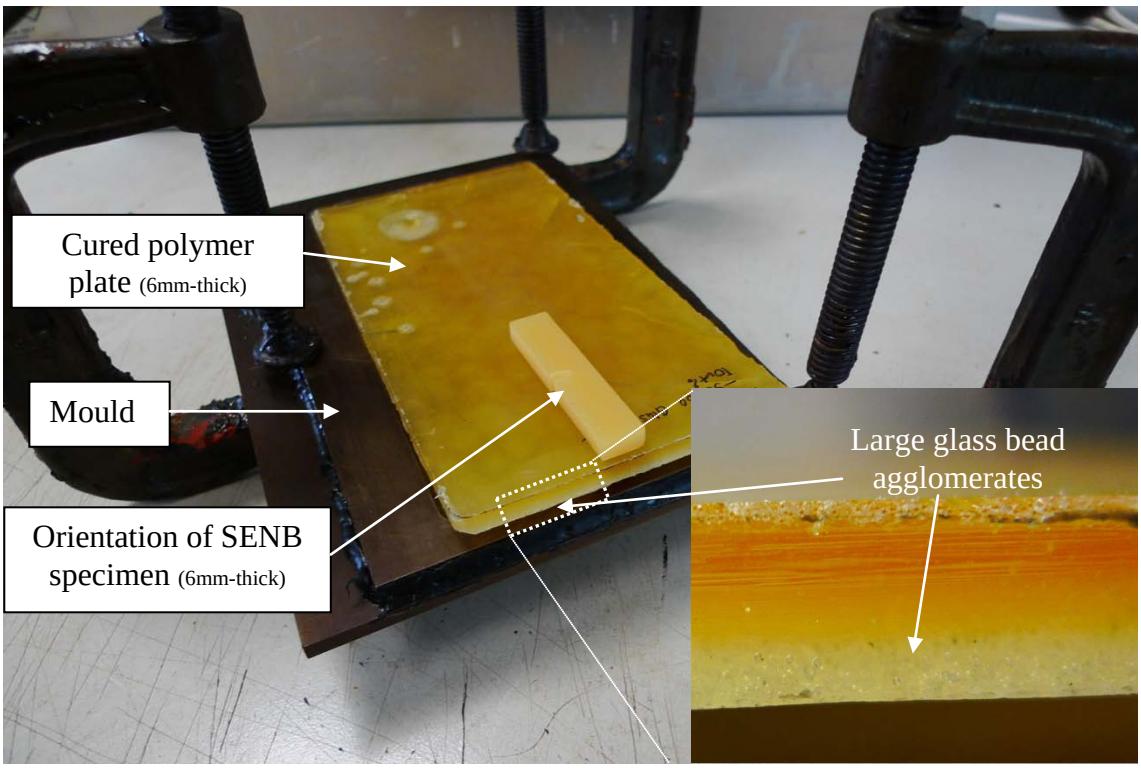


Figure 6.3.5 The cured plate of the large glass bead/epoxy composite (10-L-Control), showing the glass beads sinking to the bottom of the mould.

Figure 6.3.6 shows the measured values of the fracture toughness, K_{Ic}, for the modified polymers containing the glass beads with various diameters (3.5 μm and 275 μm) and surface treatments (silane treatment and Frekote treatment). The inclusion of the small glass bead microparticles with a mean diameter of 3.5 μm increased the fracture toughness of their composites, and the toughness increased steadily with increasing the content of the glass beads. Further increases in the fracture toughness, K_{Ic}, was obtained when the small glass beads were modified using surface treatments (i.e. silane and release agent treatment). As can be seen in Figure 6.3.3, the systems of "S-Silane" and "S-Frekote" shift the fracture toughness to higher values, compared with "S-Control" system. For example, the addition of 20 wt% of untreated small glass beads gave a 32% increment in the fracture toughness, in comparison with the unmodified polymer (0.69 MPa $m^{1/2}$). With the surface treatments of silane and Frekote, the improvement in the fracture toughness was increased further by a 38% increment for both systems, compared with the unmodified polymer. Xu et al [56] used a silane coupling agent to modify the glass particles, and reported that the glass/epoxy composites with good adhesion have a higher value of fracture toughness. This is in good agreement with the experimental results in this study. However, it was expected that the use of the release agent "Frekote" to coat a thin layer on the glass bead surface should reduce the interfacial adhesion of glass bead/epoxy, consequently a lower toughening effect was expected [122]. From the experimental results in this study, both silane and Frekote treatments provided the same effect on the fracture toughness, and similar results were measured for both systems. In following Section, the fracture surfaces of these glass bead/epoxy composites were inspected using FEG-SEM, where the different features on the fracture surfaces caused by the various treatments were found.

Figure 6.3.6 also clearly shows that the addition of the large glass bead microparticles to the epoxy polymer resulted in a decrease in the fracture toughness. The introduction of the surface treatments slightly increased the measured values of the fracture toughness. However, these values are still lower than the unmodified epoxy (0.69 MPa $m^{1/2}$). This is because the large glass beads sank to the bottom of the mould, and large agglomerates formed. This agglomeration was clearly visible to the naked eye. The morphology of the glass bead/epoxy composites will be discussed in the following Section.

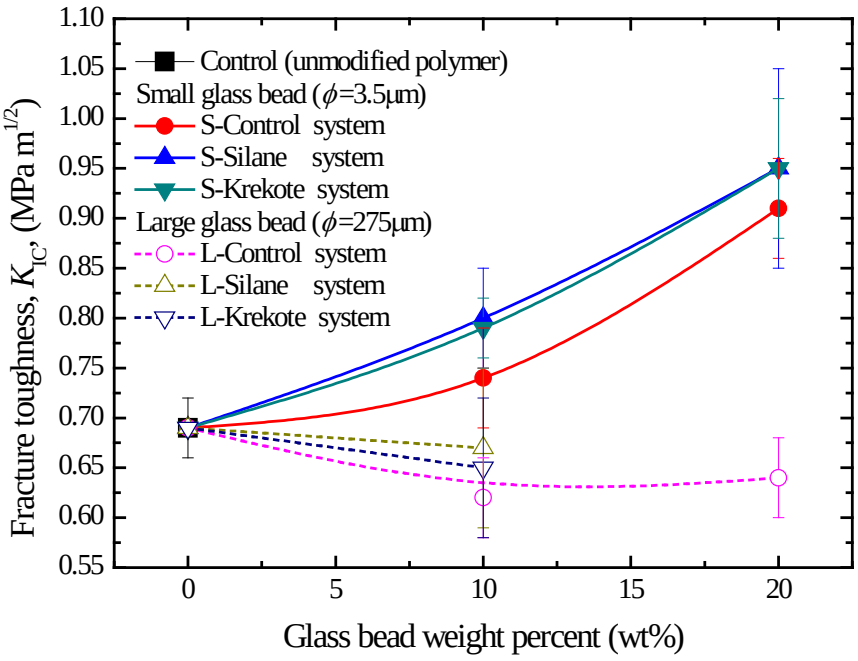


Figure 6.3.6 Fracture toughness of the glass bead microparticle-modified epoxy polymers.

Figure 6.3.7 shows the fracture energy, G_{Ic}, for the all formulations of glass bead microparticle-modified epoxy polymers. The measured values of the fracture energy show the same trend as the fracture toughness; the addition of the small microparticles resulted in an increase in the fracture energy, however the use of the large glass particles led to a decrease. Although the same trend was found in the measured values of the fracture toughness and fracture energy, the improved fracture energy of the small glass bead-modified polymers caused by the introduction of the surface treatments was much more significant than the increased fracture toughness. As mentioned above, around 32% increased fracture toughness was recorded for the microparticle-modified polymer with 20 wt% untreated small glass beads, and further increased by 38% to reach the maximum value of the fracture toughness when treated by the silane coupling agent or Frekote release agent. From the testing results, the fracture energy of the modified polymer with 20 wt% untreated small glass beads was increased by 19%, which is lower than the increment in the fracture toughness. When the surface treatment was used to modify the glass beads, a significant increase in the

fracture energy was found, and a maximum value of 197 J/m^2 was reached for the sample containing 20 wt% small glass beads with the silane treatment. This is around a 48% increment in the fracture energy, compared with the unmodified polymer (133 J/m^2). This indicates that the surface modification associated with the glass bead/epoxy adhesion strongly affects the fracture energy of the composites. Therefore, a wide range of the increment in the fracture energy from 19% to 48% was recorded in the glass bead/epoxy composites with various particle surface modifications.

The addition of the large glass beads resulted in a decrease in the fracture energy of the microparticle-modified polymers, as can be seen in Figure 6.3.7. The decrease in the fracture energy can be attributed to the serious agglomeration of the large glass beads. The dispersion of these glass beads will be discussed using the FEG-SEM observation on the fracture surfaces of the composites.

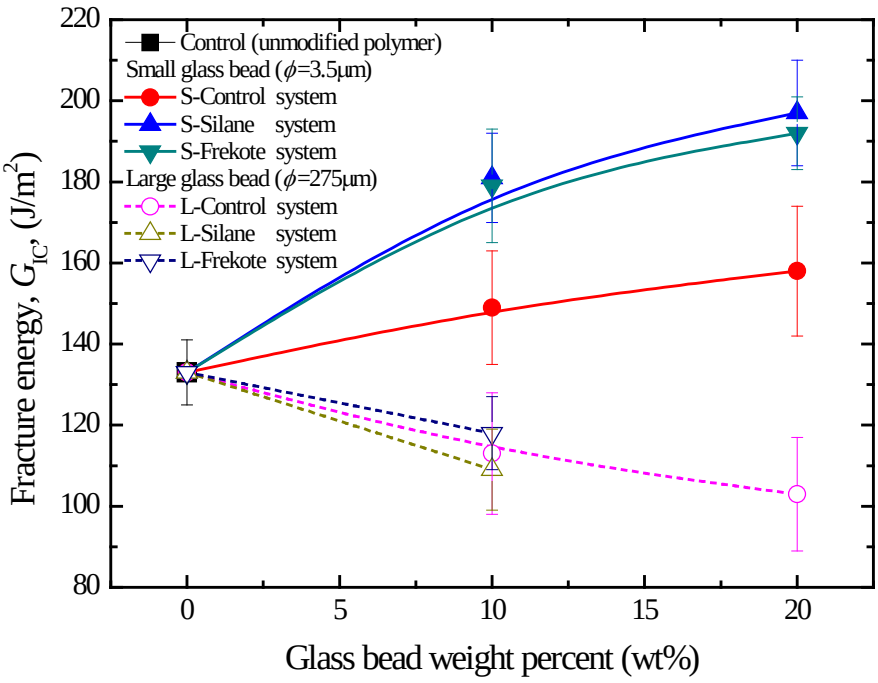


Figure 6.3.7 Fracture energy of the glass bead microparticle-modified epoxy polymers.

6.3.3 Fractography and Toughening Mechanisms

The toughening mechanisms responsible for the increased toughness in the glass bead-modified epoxy polymers, and the dispersion of the glass beads, were investigated using field emission gun scanning electron microscopy (FEG-SEM) of the fracture surfaces after the SENB tests. Figure 6.3.8 shows the fractography of the polymer-based composites reinforced with the small glass beads. River lines were readily found on the fracture surfaces, indicating that these modified polymers are brittle materials [111]. Besides, there are several tails which start behind the glass beads. The occurrence of the tail behind each particle was caused by creating different planes (secondary cracks) on the fracture surfaces, consequently more energy was required and the toughness was improved slightly [57]. Figure 6.3.9 shows schematically the tail structure present on the fracture surface. As can be seen in the lateral view of the fracture surface, the tail structure is formed by creating a new fracture surface (secondary crack), consequently more energy to fracture was required. Also, the crack path is deflected, see Figure 6.3.9 (a), and the direction of the secondary crack may be different from the crack growth, see Figure 6.3.9 (b). Both of these imply the occurrence of crack deflection[57, 123]. Although some studies reported that the occurrence of the tail structure implies the crack pinning mechanism [45], no other pinning feature, i.e. crack bowing between particles [53, 124], was found on the fracture surface using the FEG-SEM at high magnification, as will be discussed later.

In Figure 6.3.8, the dispersion of the glass beads was also evaluated. The sample of “10-S-Silane” shows good dispersion, see Figure 6.3.8 (e, f). In contrast, the polymers with the untreated and Frekote treated small glass beads have several agglomerates, especially for the untreated glass beads. These agglomerates consist of around 5~15 glass beads, and the size of the glass bead agglomerates became larger as the concentration of the glass beads was increased. As can be seen in Figure 6.3.8 (c, d), the sample of “20-S-Control” shows serious agglomeration.

In addition to river line patterns on the fracture surfaces, the toughneing mechanisms and the effect of the glass beads with various surface treatments on the fracture surfaces were identified using the FEG-SEM observation at high magnification.

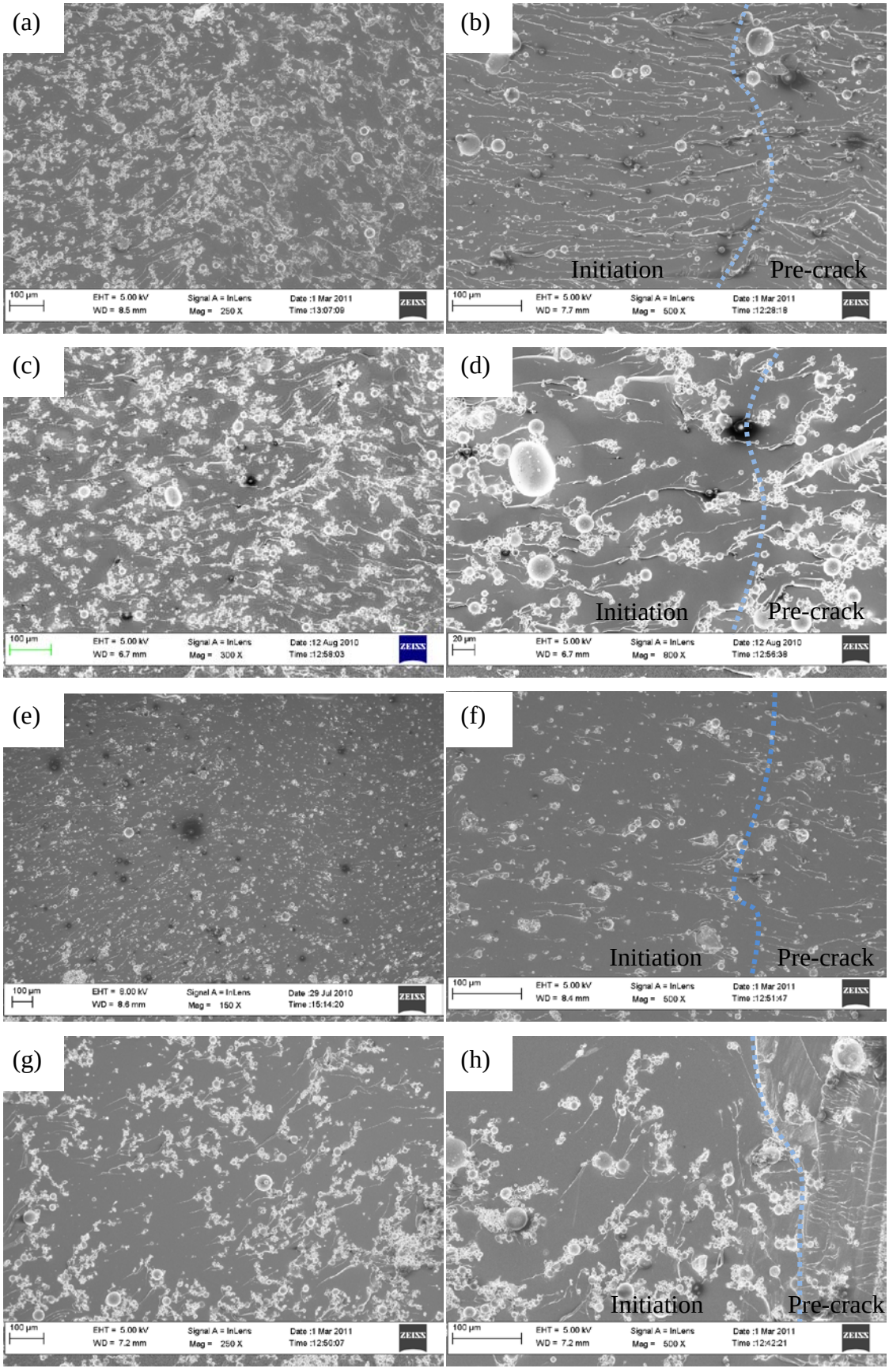
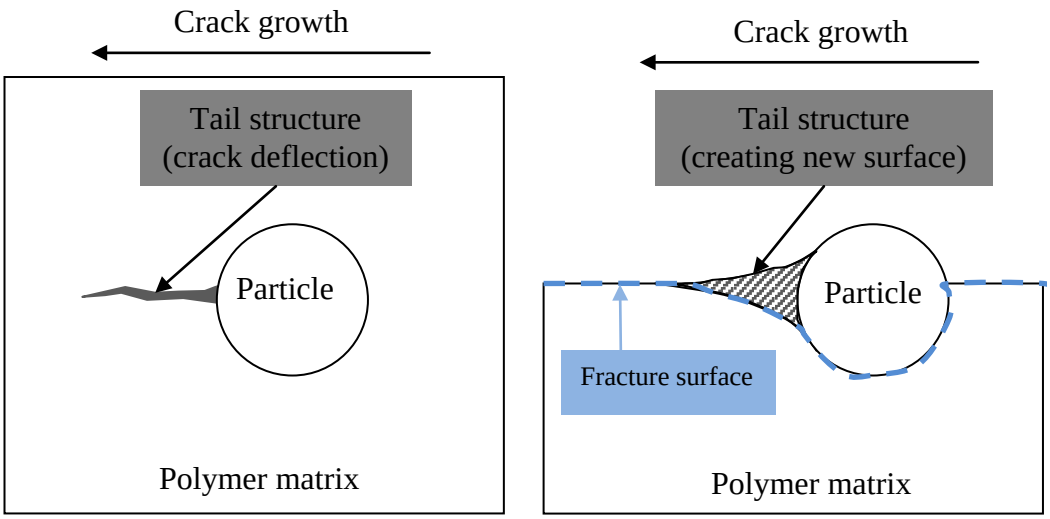


Figure 6.3.8 FEG-SEM images of the fracture surfaces, (a,b) 10-S-Control, (c,d) 20-S-Control, (e,f) 10-S-Silane and (g,h) 10-S-Frekote.



(a) Top view of fracture surface (b) Lateral view of fracture surface

Figure 6.3.9 The schematic tail structure on the fracture surface of particle-modified composites.

Figure 6.3.10 shows the FEG-SEM images of the fracture surfaces of the sample containing 10 wt% untreated small glass beads (10-S-Control). The well-known mechanism in the glass microparticle-modified composites of crack deflection [57, 123] was found on the fracture surface. As the tip of advancing cracks came across the glass beads, the direction of the crack was changed, see Figure 6.3.10 (a). In this case, the path of the crack propagation was through the equator of the glass bead microparticles, due to these being untreated particles with low interfacial bonding between the particles and epoxy matrix. Poor adhesion of glass bead/epoxy can be clearly seen in Figure 6.3.10 (c), the surfaces of the glass beads are clean and relatively smooth, with just a small amount of the epoxy matrix bonded on their surfaces. Clear evidence of interfacial debonding, followed by plastic void growth, was easy to find on the fracture surfaces, see Figure 6.3.10 (b, c). This debonding and plastic deformation in the polymer matrix can efficiently contribute to the increase in the toughness. According to the examination of the fracture surfaces, the main toughening mechanisms in the composite reinforced with untreated small glass beads are considered to be the crack deflection and plastic void growth.

Image analysis was performed to measure the proportion of the glass beads with void growth, and the size of these voids. Around 11% of the added glass microparticles have void growth around them, with an average diameter of 4.1 μm and a standard deviation of 2.8 μm in the "S-Control" composite. The dispersion was examined in these FEG-SEM images, and it seems that good dispersion of the untreated small glass beads was obtained.

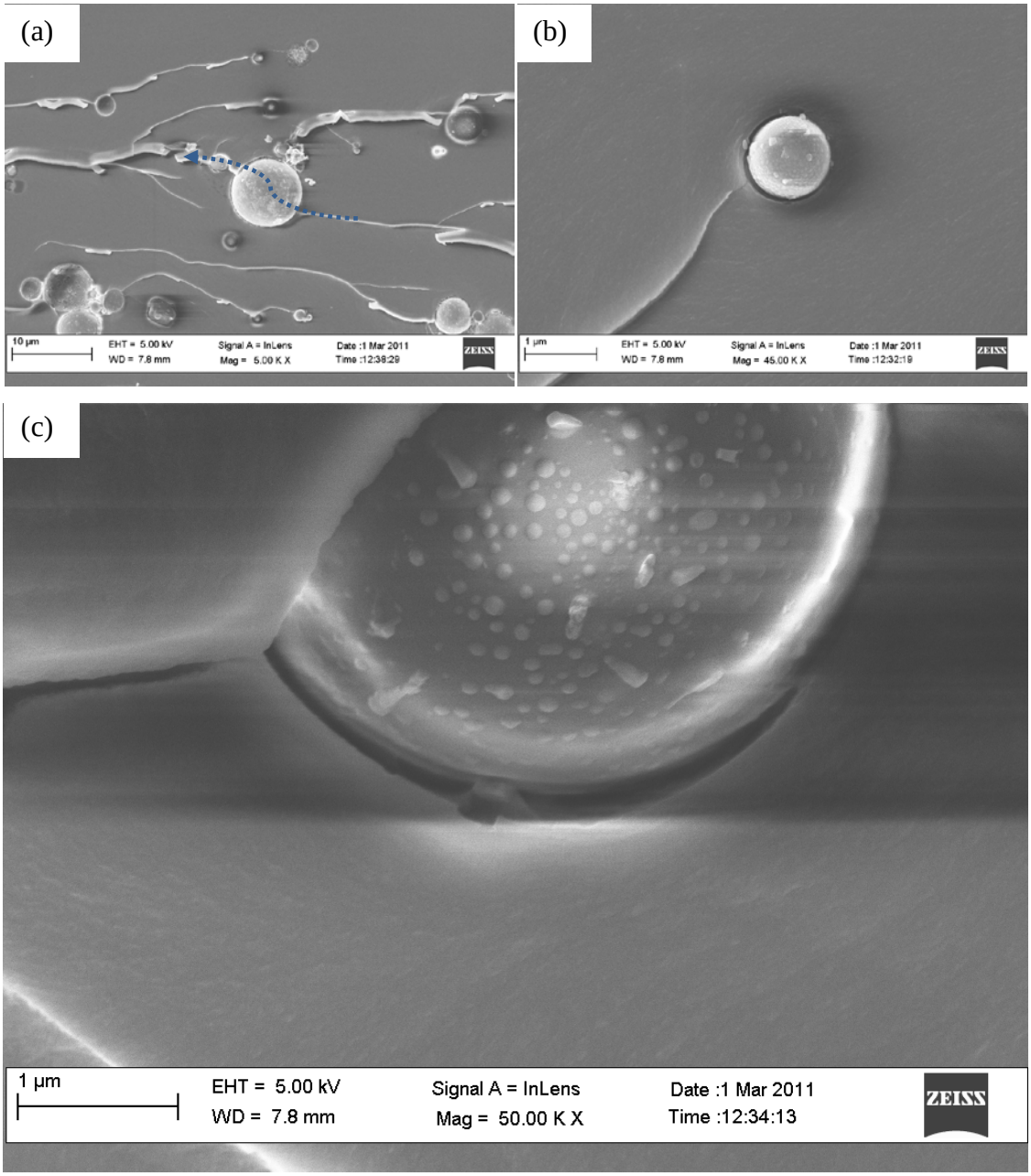


Figure 6.3.10 FEG-SEM images of the microparticle-modified polymers with 10wt% untreated small glass beads (10-S-Control), showing (a) crack deflection (b) tail structure behind the particle and (b, c)debonding and subsequent plastic void growth.

The fracture surfaces of the sample containing the silane treated glass beads at 10 wt% (10-S-Silane) are shown Figure 6.3.11. The silane treatment provided good particle/epoxy adhesion. Tails formed behind the glass particle were clearly found on the fracture surface, see Figure 6.3.11(a). This implies the occurrence of the crack deflection. Different fracture surfaces caused by the untreated and silane treated particles were observed in FEG-SEM images at high magnification, as shown in Figure 6.3.11 (b, c). The use of the silane surface treatment resulted in good adhesion between the glass particles and epoxy matrix. In Figure 6.3.11 (c), the glass particles are not so distinct, compared with the untreated glass bead-modified polymers, see Figure 6.3.10 (a). The hemispheres of the glass microparticles on the fracture surfaces were well-covered with the epoxy matrix. Therefore, the crack propagation was through the matrix above and below the poles of the glass beads. Figure 6.3.12 shows the different paths of crack propagation in rigid particle filled polymers between poorly-bonded and well-bonded particle reinforcements [46].

As good particle/epoxy adhesion was obtained in this case (silane-treated system), a smaller proportion (5%) of particles showed plastic void growth. As can been seen in Figure 6.3.11 (b), there is a relatively low amount of plastic void growth present, compared with the sample with poorly-bonded particles. Partial debonding was found on the fracture surface, see Figure 6.3.11 (c), and the diameter of the voids was measured to be 3.8 μm with a standard deviation of 2.4 μm. This is different from the modified polymer with untreated particles, where the glass beads had full voids around them, as shown in Figure 6.3.10 (c).

The dispersion of the silane treated glass beads in the epoxy polymer was examined using these FEG-SEM images. Well-dispersed glass beads were found on the fracture surfaces. Even when the microparticles are close together in the particle-rich areas, they are still well coated with epoxy matrix.

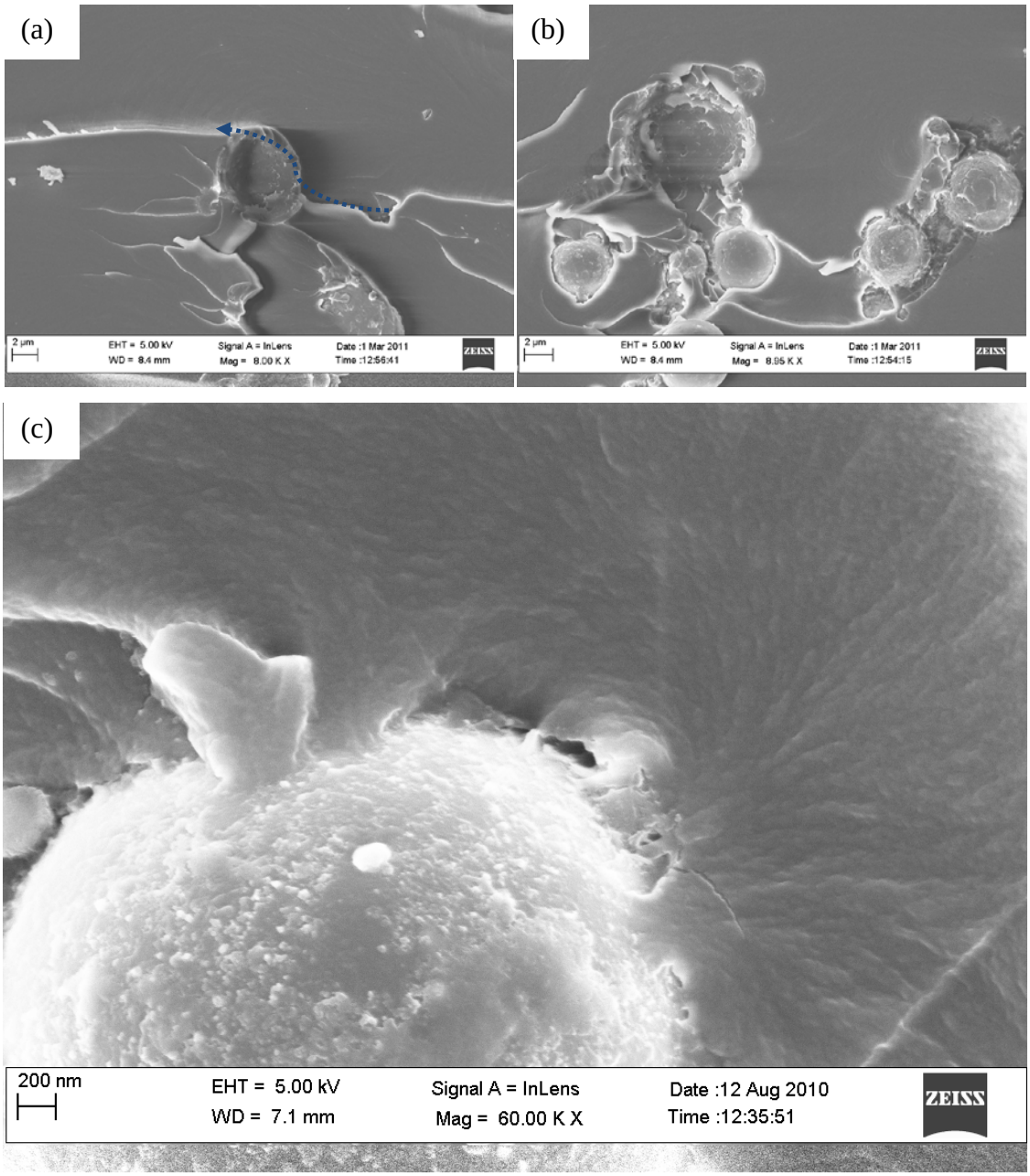


Figure 6.3.11 FEG-SEM images of the microparticle-modified polymers with 10wt% silane treated small glass beads, showing (a) crack deflection (b,c) debonding, and subsequent plastic void growth.

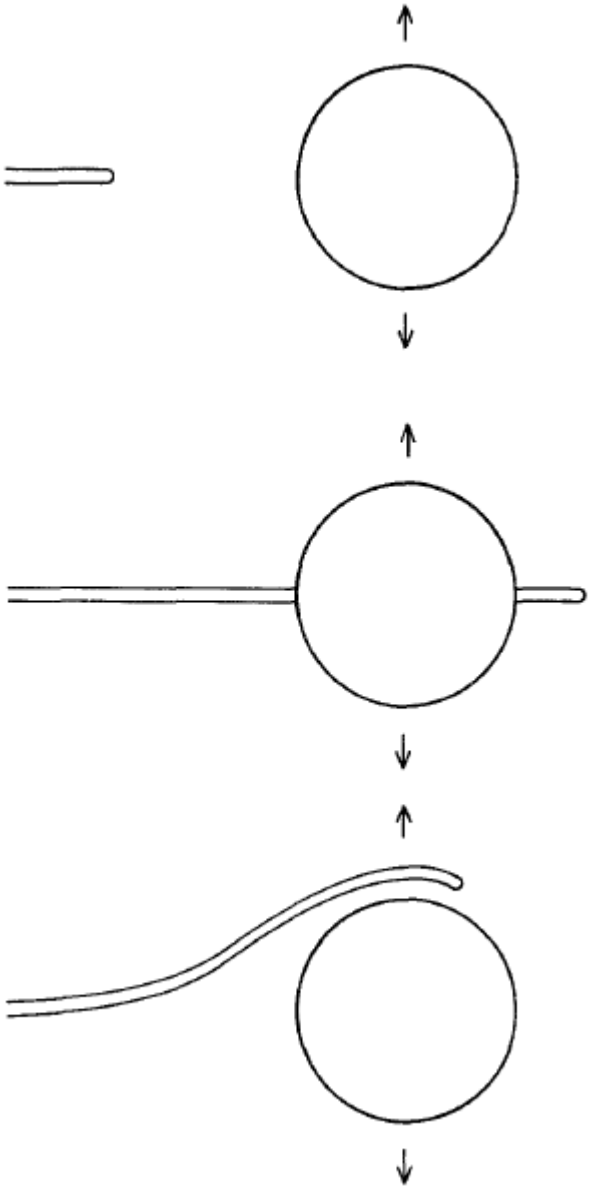


Figure 6.3.12 Schematic illustration of the path of a crack around a rigid particle in the composite, showing (a) crack approaching particle, (b) crack tip moving around equator of poorly-bonded particle and (c) crack tip attracted to poles of well-bonded particle [46].

Figure 6.3.13 shows the fracture surfaces of the modified polymer containing the small glass beads with the release agent (Frekote) surface treatment. Figure 6.3.13 (a) shows serious glass bead agglomerates. Apart from these, the appearance of the fracture surfaces, as shown in Figure 6.3.13 (b), are similar to the fracture surfaces of the untreated glass bead-modified polymer. Both of these systems consist of poorly-bonded particles. The occurrence of the tails behind each glass particle was readily found on the fracture surfaces, indicating the toughening mechanism of crack deflection. The release agent Frekote led to low adhesion between the particle and epoxy matrix, so clean surfaces of the glass beads were observed due to the poorly-bonded particles. Moreover, a relatively high proportion of the glass beads with void growth was found, as shown in Figure 6.3.13 (b), compared with the untreated and silane-treated systems. Image analysis showed that around 20% of the glass particles exhibited void growth, the size of these voids was measured to be 5.2 ±2.8 μm. The results from the image analysis are higher than those in the untreated glass bead/epoxy composites.

From the testing results, both surface treatments resulted in a significant improvement in the toughening performance with the treated small glass bead microparticles. However, the results in this study are different from previous studies [46, 122]. Imanaka et al [122] reported that good adhesion between spherical silica particles and epoxy matrix can slightly increase the fracture toughness, compared with the composites with poor particle/epoxy adhesion. In contrast, Spanoudakis and Young [46] investigated the effect of particle/matrix adhesion on the toughness of glass particle-filled epoxy composites. They reported that the composites with poorly-bonded glass particles had a relatively high value of fracture energy because the particles can promote more plastic void growth, and could consequently improve the toughness even more. The serious agglomeration of the Frekote-treated glass particles formed in this study compromised the toughening contribution of plastic void growth to the composites. This is why the experimental results in this study are different from the previous work [46].

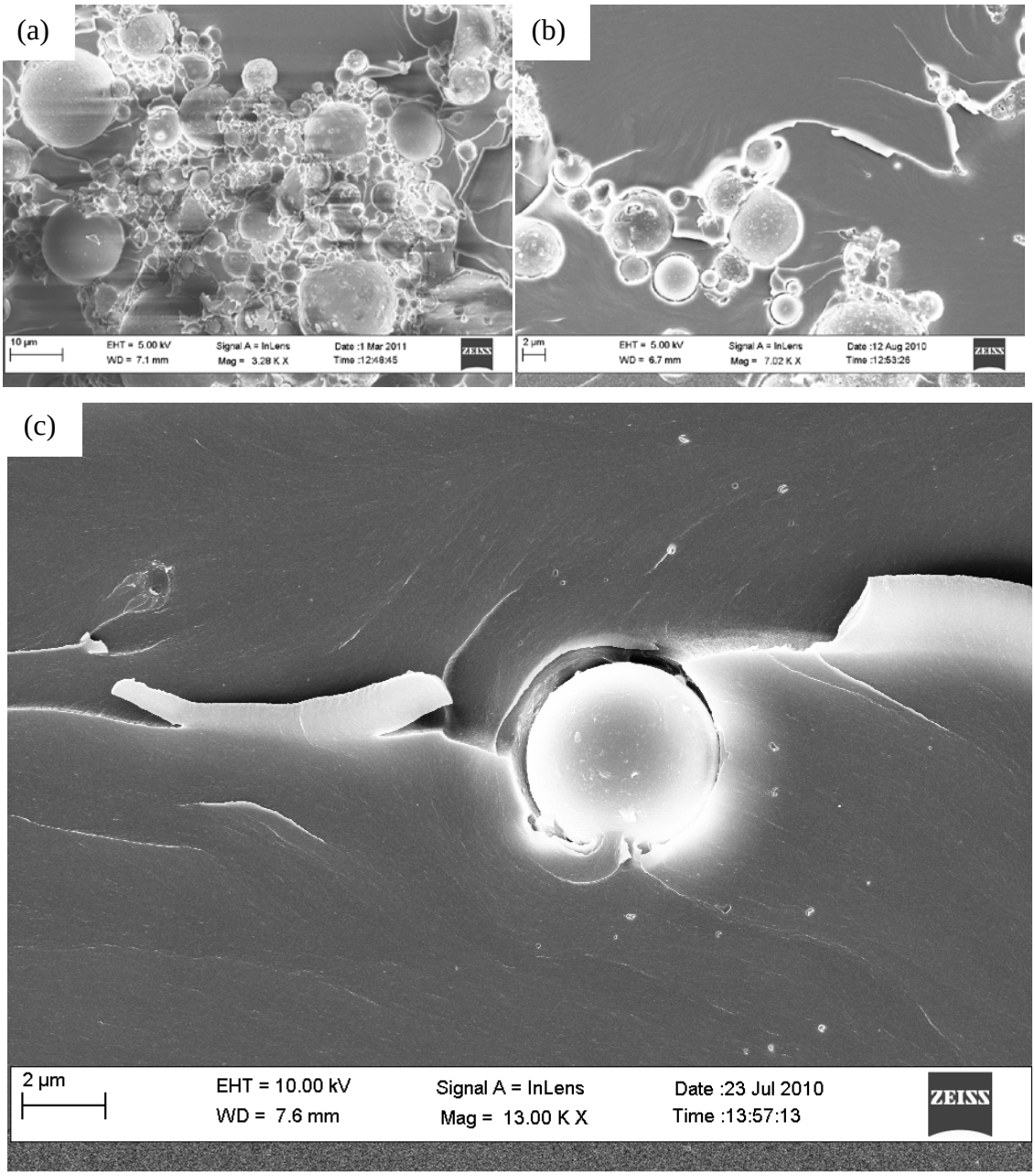


Figure 6.3.13 FEG-SEM images of the microparticle-modified polymers with 10wt% release agent "Frekote" treated small glass beads, showing (a) glass bead agglomeration and (b,c) debonding,and subsequent plastic void growth.

Turning to the microscope observation of fracture surfaces of the composites reinforced with large glass bead particles with a mean diameter of 275 μm, the optical microscopy and FEG-SEM images are shown in Figures 6.3.14 to 6.3.16 for the various surface treatments. The dispersion was examined, and all the samples show serious agglomeration due the added glass particles sinking to the bottom of the casting mould (as shown in Figure 6.3.5) during the cure cycle, see the first two images in Figures 6.3.14 to 6.3.16. This significantly compromised the toughening contribution of the glass beads. Furthermore, the agglomerated glass beads act as stress concentrations, which promote fracture, rather than toughening of the composites. Hence, no improvement in the toughness of the glass bead/epoxy composites was measured. Indeed the fracture energy was reduced, as shown in Figure 6.3.6.

Although a few tails starting at glass particles are observed, a relatively low amount of the crack deflection mechanism was found on the fracture surfaces of these composites, compared with the composites with the small glass beads. Thus, the toughening contribution of crack deflection did not bring an improvement in the toughening performance. The difference in the appearance of the fracture surfaces caused by the various surface treatments was found on the FEG-SEM images at high magnification. Figure 6.3.15 shows the fracture surfaces for the sample containing the silane-treated glass beads, where no clear evidence of the debonding between the glass particles and the polymer matrix was found. The surface of the large glass microparticles was covered well with the epoxy polymer, see Figure 6.3.15 (c). As the glass particles were bonded well with the epoxy polymer, the path of the crack propagation passed through the epoxy matrix above and below the poles of the particles.

In contrast, Figure 6.3.14 and Figure 6.3.16 show the fracture surfaces of the composites with poorly-bonded glass microparticles. Debonding between the particles and the polymeric matrix, followed by void growth, was clearly found on the fracture surfaces, see Figure 6.3.14 (c) and Figure 6.3.16 (c). The size of the voids was measured to be 290 ±8 μm and 295 ±7 μm for the untreated and Frekote treated systems, respectively. No difference in the amount of void growth was observed on the fracture surfaces in these systems, and a measured proportion of 5% of added large glass beads with voids was recorded. However, no glass beads with voids around them were

observed for the composites with the silane-treated large glass beads, see Figure 6.3.15 (c).

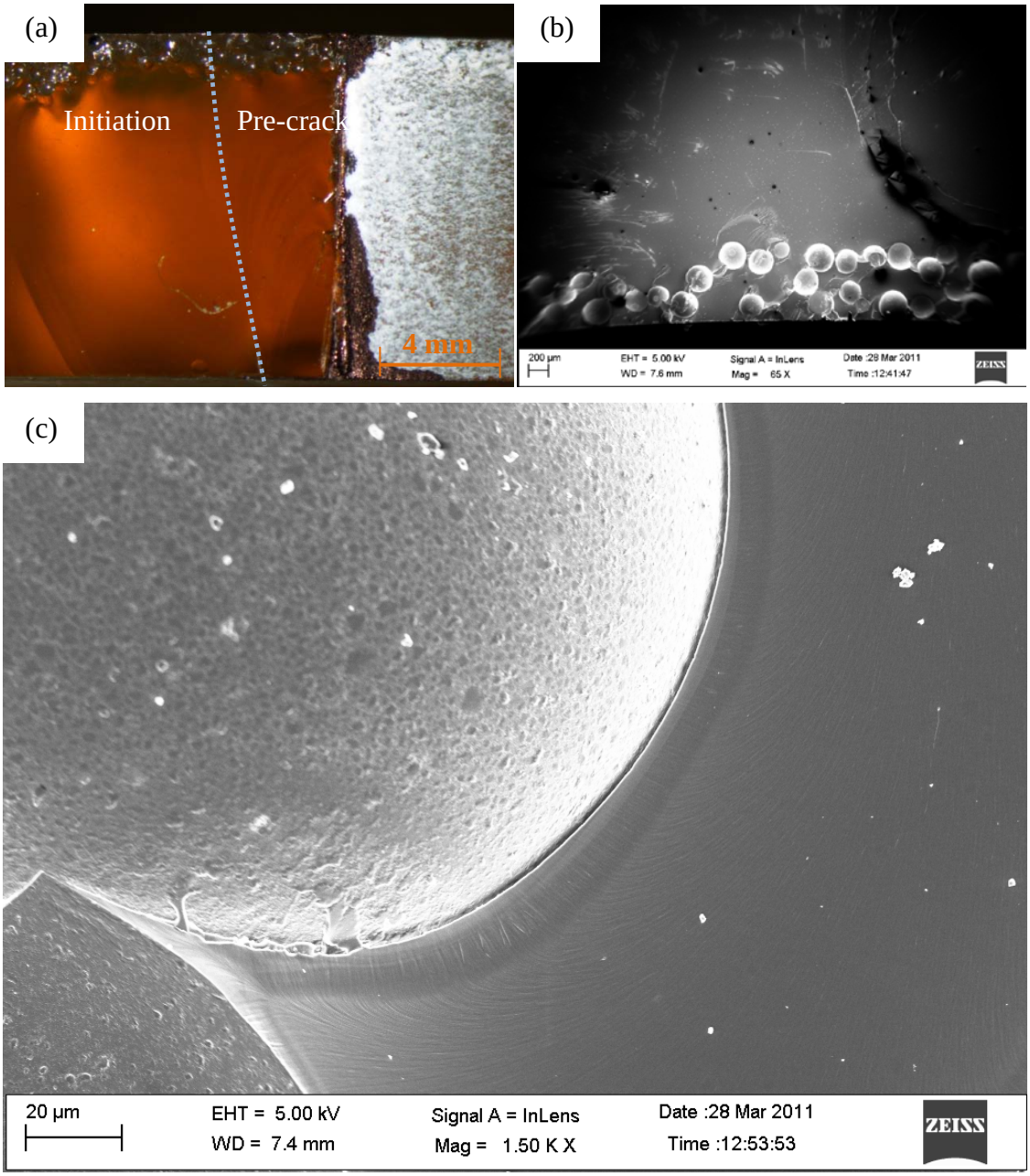


Figure 6.3.14 Optical microscopy and FEG-SEM images of the fracture surface of the polymer-based composite reinforced with 10 wt% of untreated large glass beads (10-L-Control), showing (a) glass bead agglomerates via optical microscopy, (b) glass bead agglomerates via FEG-SEM and (c)particle debonding, and subsequent plastic void growth.

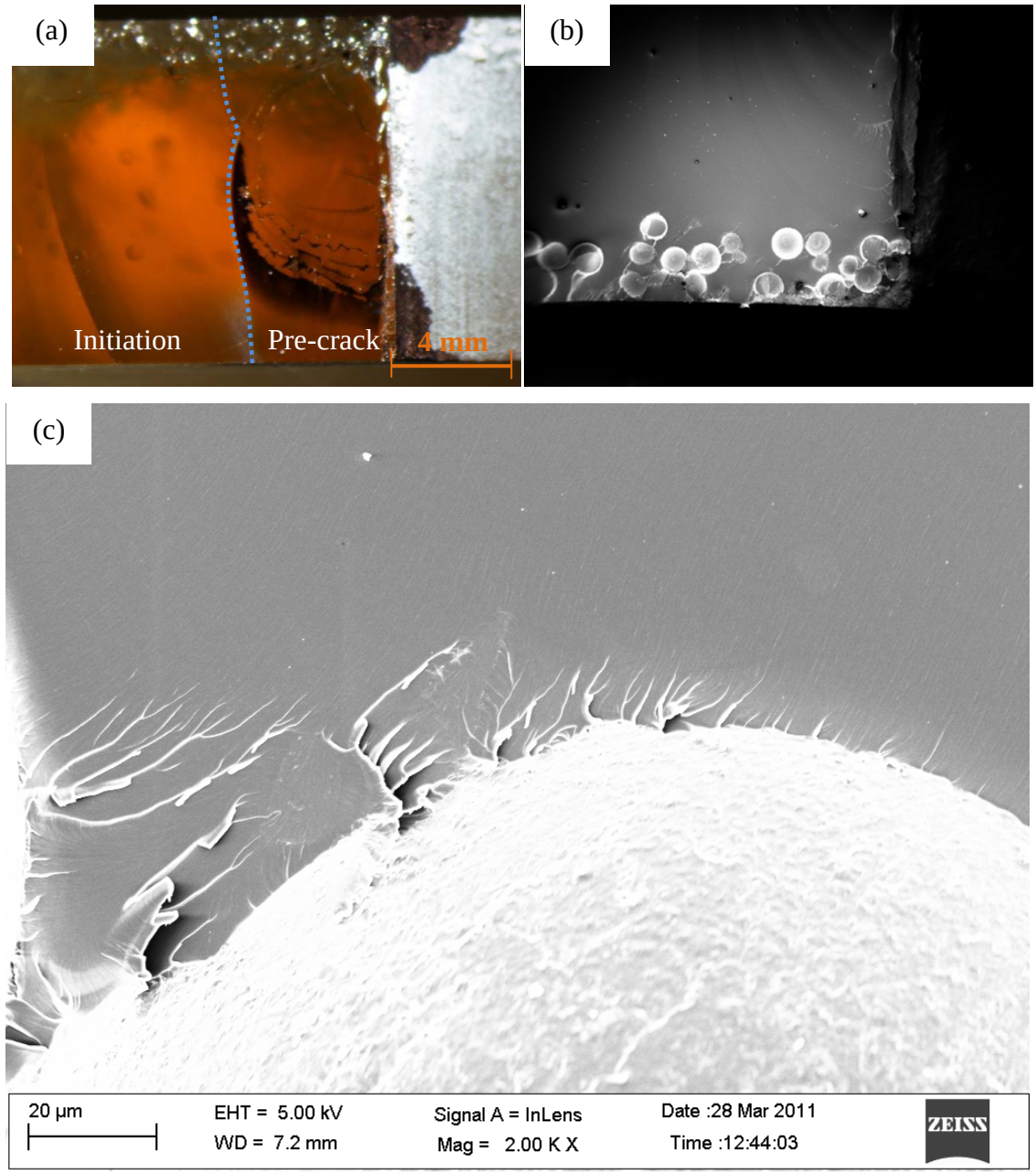


Figure 6.3.15 Optical microscopy and FEG-SEM images of the fracture surface of the polymer-based composite reinforced with 10 wt% of the silane treated large glass beads (10-L-Silane), showing (a) glass bead agglomerates via optical microscopy, (b) glass bead agglomerates via FEG-SEM and (c) glass bead bonded well with epoxy polymer.

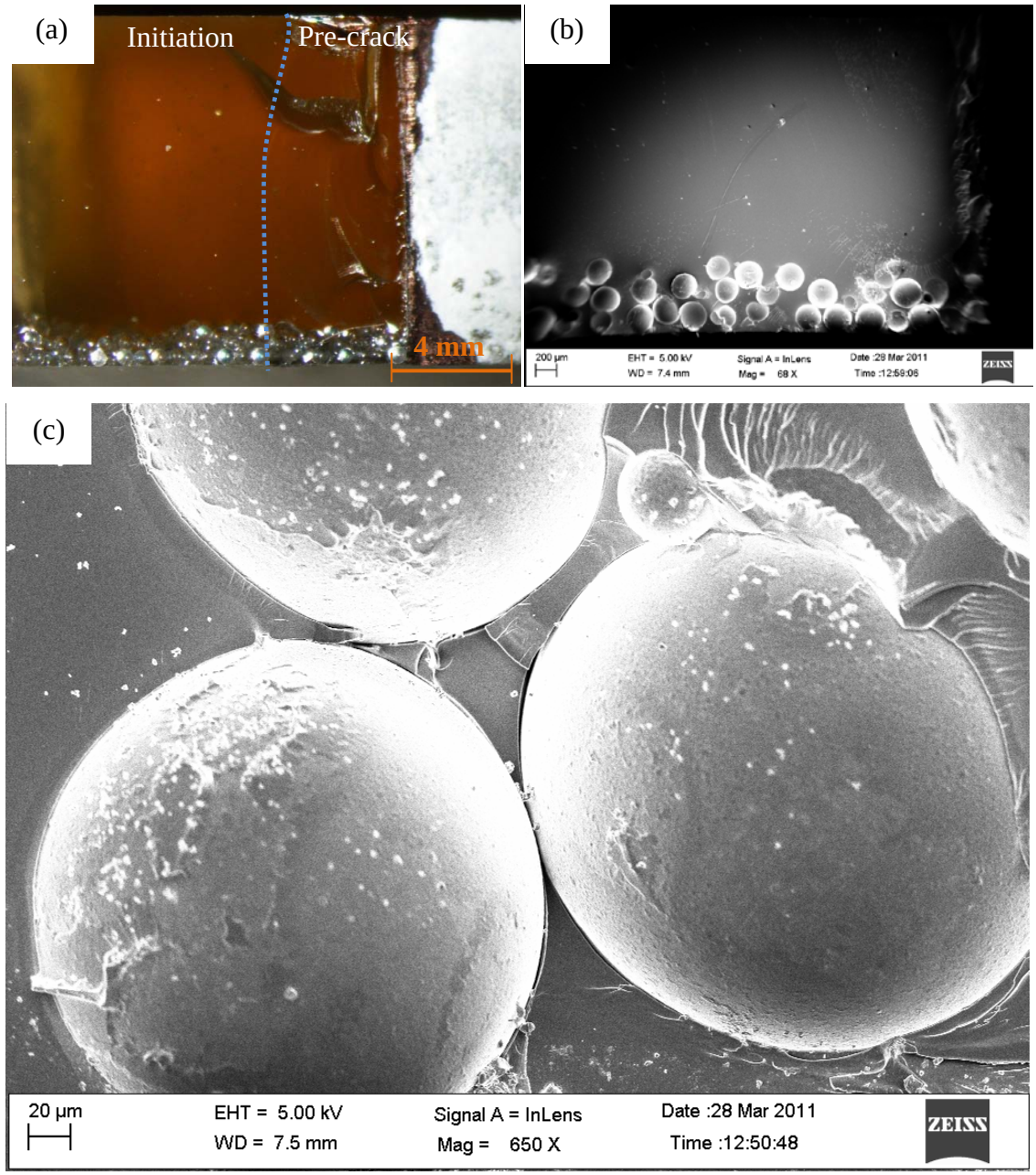


Figure 6.3.16 Optical microscopy and FEG-SEM images of the fracture surface of the polymer-based composite reinforced with 10 wt% of the release agent treated large glass beads (10-L-Frekote), showing (a) glass bead agglomerates via optical microscopy, (b) glass bead agglomerates via FEG-SEM and (c) particle debonding, and subsequent plastic void growth.

6.4 Comparison Between Nanoparticle and Microparticle-modified Epoxy Polymers

The reinforced spherical rigid particles used in this study have various diameters with a range from nanometre to micrometre (20 nm for the silica nanoparticles, and 3.5 μm and 275μm for the glass beads). In this Section, the particle size effect on the toughness of the composites was investigated. As the large glass particles were found to be seriously agglomerated in the cured samples, the investigation of the particle size effect on the toughness included only the composites reinforced with the silica nanoparticles (20 nm in diameter) and the small glass bead microparticles (3.5 μm in diameter). Although several studies [45, 121] focusing the particle size effect on toughness have been made, the varied particle sizes did not cover such a wide range from the micro-scale to nano-scale.

Figure 6.4.1 shows the ratio of $G_{\text{Ic-composite}}/G_{\text{Ic-unmodified}}$ (relative fracture energy) for various loadings of the particle reinforcements. The effectiveness of the nano-sized particles on the fracture energy of the polymer-based composites is much higher than the use of the small glass bead microparticles. Even for the sample containing the standard treated silica nanoparticles, the measured values of the fracture energy are still higher than the composites reinforced with well-bonded microparticles.

The toughening mechanisms in the spherical rigid particle-modified composite depend strongly on the particle size. In the nanosilica/epoxy nanocomposites, the main toughening mechanism was plastic void growth caused by particle debonding from the matrix and subsequent plastic deformation in the epoxy matrix. With increasing the particle size to micro-scale, the major toughening mechanism becomes crack deflection.

According to the experimental results, the nanocomposites have higher toughness than the composites containing the microparticles. This indicates that the contribution of the plastic void growth, the main toughening mechanism in the nanosilica-modified polymer, is much more significant than crack deflection found on the fracture surfaces of the composites reinforced with microparticles. Although plastic void growth was also found on the fracture surfaces of the small glass bead/epoxy

composites, a relatively small proportion of void growth present in the microparticle-reinforced composites was measured. Therefore, the plastic deformation caused by void growth was not sufficient to improve the toughness significantly in glass bead microparticle/epoxy composites.

In Chapter 9, an analytical model is used to predict the fracture energy of the rigid nanoparticle- and microparticle-toughened polymers, and then the predicted results will be compared with the experimental values presented in this Chapter.

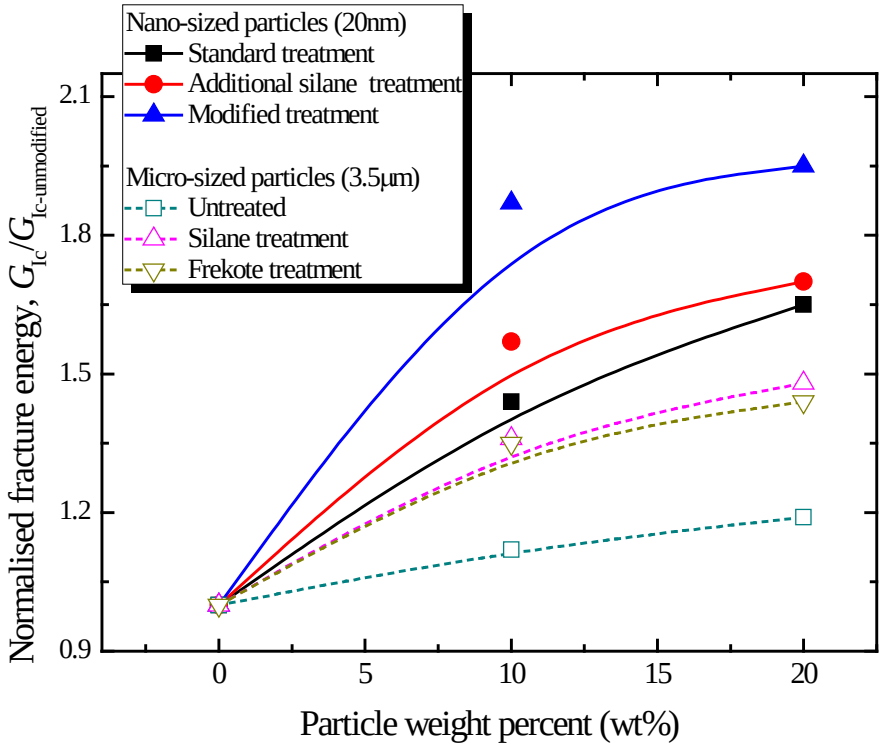


Figure 6.4.1 Normalised fracture energy of the composites with the silica nanoparticles and glass bead microparticles with various surface treatments.

6.5 Conclusions

The silica nanoparticles and glass bead microparticles were used to manufacture composites, and the mechanical properties and fracture behaviour of these modified epoxy polymers were investigated. The addition of these rigid particles results in a steady increase in the modulus, but no significant change in the glass transition temperature. A detailed study was made of the particle size effect on the toughness, where the particle sizes are in a wide range from 20 nm to 275 μm. Evidence from the SENB fracture tests shows that when the smaller particles are used higher values of the fracture energy are measured. The maximum value of the fracture energy was measured to be 220 J/m^2 for the nanocomposite with 20 wt% of the standard treatment silica nanoparticles. Although the inclusion of the glass bead microparticles leads to an improvement in the toughness, the increment in the fracture energy caused by the small glass beads (3.5 μm in diameter) is not as high as the use of the nanosilica. The addition of the largest microparticles (275 μm) did not increase the toughness of the polymer-based composites due to serious agglomeration of these microparticles in cured samples. The particle/matrix adhesion strongly affects the toughness of the rigid particle-modified polymers. The introduction of the surface treatments to the modified polymers significantly improves the toughness. The coupling agent silane treatment and release agent Frekote treatment caused well-bonded particles and poorly-bonded particles with the epoxy matrix. Both of the surface treatments result in a significant increase in the toughening performance.

The difference in the microstructures of the fracture surfaces between the good and poor adhesion was observed using the FEG-SEM. In the nanocomposites, the additional silane treatment was used to improve the nanosilica/epoxy adhesion, and only a small amount of debonding, followed by the plastic void growth was found. The glass bead microparticles present on the fracture surfaces were coated well with the epoxy matrix after the silane treatment. The degree of plastic void growth is relatively low for the silane-treated glass bead/epoxy composites, compared with the composites with untreated or Frekote-treated microparticles.

The main mechanism of toughening is plastic void growth due to the particles debonding and plastic deformation in the epoxy matrix in the nanosilica-modified nanocomposites. With increasing the particle size from nanometre to micrometre, the toughening mechanism changed to crack deflection. The nanocomposites have high values of the fracture energy, compared with the glass bead-modified polymers. Thus, the toughening contribution of the plastic void growth mechanism to the polymer-based composites is much more significant than the crack deflection mechanism in the microparticle-modified polymers.

Plane strain compression tests were performed on the nanosilica-modified polymers, and the results show that the addition of the silica nanoparticles gave an increase in the compressive modulus. When the nanosilica particles were treated to improve the adhesion to the epoxy matrix, the compressive yield stress could reach a relatively high value during the PSC tests, compared with the nanocomposite with the standard treatment.

The silica nanoparticles are well-dispersed in the cured epoxy polymer, even at the highest weight loading of 20 wt%. The small glass beads with a mean diameter of 3.5 μm were also well-dispersed. However, agglomerates consisting of few glass beads were found for the release agent treated glass bead-modified polymer. The addition of the large glass beads with 275 μm in diameter did not improve the toughness of the polymer-based composites due to serious agglomeration.

CHAPTER 7

CARBON NANOTUBE-MODIFIED EPOXY

7.1 Introduction

Carbon nanotubes are well known to have a high potential for use as a nano-reinforcement in polymer-based composites due to their excellent mechanical and thermal properties, and relatively high aspect ratio. Several studies related to carbon nanotubes and their composites have reported that the outstanding properties of the nanotube can completely transfer the stress, and suppress crack propagation, when blending carbon nanotubes with polymers [73, 79]. This Chapter describes the effect of nanotube modification on the mechanical properties of the thermosetting polymer-based nanocomposites. All the formulations discussed in this Chapter contained a diglycdyl ether of bisphenol-A (DGEBA) resin cured by an anhydride curing agent, modified by multi-walled carbon nanotubes (MWCNTs) only. The modulus, toughness and fatigue performance of the MWCNT-modified polymers will be considered. To evaluate the size effect on the mechanical properties of the epoxy nanocomposites, two different types of multi-walled carbon nanotubes were used to form the nanocomposites and then the effect of the nanotube dimensions will be discussed. Both of these nanotube types

were supplied as dry nanotube films synthesised by the chemical vapour deposition (CVD) method. The effect of different nanotube loading on dispersion of the nanotubes was investigated using atomic force microscopy (AFM), field emission gun scanning electron microscopy (FEG-SEM) and transmission optical microscopy (TOM). The testing results showed the effect of the addition of the MWCNTs on the mechanical properties and fatigue performance. Microscopy of the fracture surfaces from the quasi-static and dynamic loading was used to identify the toughening mechanisms in these nanocomposites. In Chapter 9, an analytical model based on toughening mechanisms observed on the fracture surfaces will be built to predict the improved stiffness and toughness from the addition of the multi-walled carbon nanotubes.

(Note that the direction of crack propagation in the microscopic fracture surfaces shown in this Chapter is from the right to the left.)

7.2 Microstructure

7.2.1 Unmodified Epoxy

The morphology of the multi-walled carbon nanotube-modified polymer was studied using atomic force microscopy (AFM) to check the dispersion of the nanotubes in cured samples. The microstructure of the control sample revealed relatively featureless images, as discussed in Chapter 6, indicating that the unmodified epoxy was a homogeneous thermosetting polymer, see Figure 6.2.1.

The featureless microstructure of the unmodified polymer was confirmed by field emission gun scanning electron microscopy (FEG-SEM) observation of the fracture surface, see Figure 6.2.2. Only a few striation marks, caused by the existence of inherent flaws causing the crack to grow along different fracture planes, can be seen in this image. This failure surface indicated that the unmodified polymer is a brittle material [111].

7.2.2 MWCNT-modified Epoxy

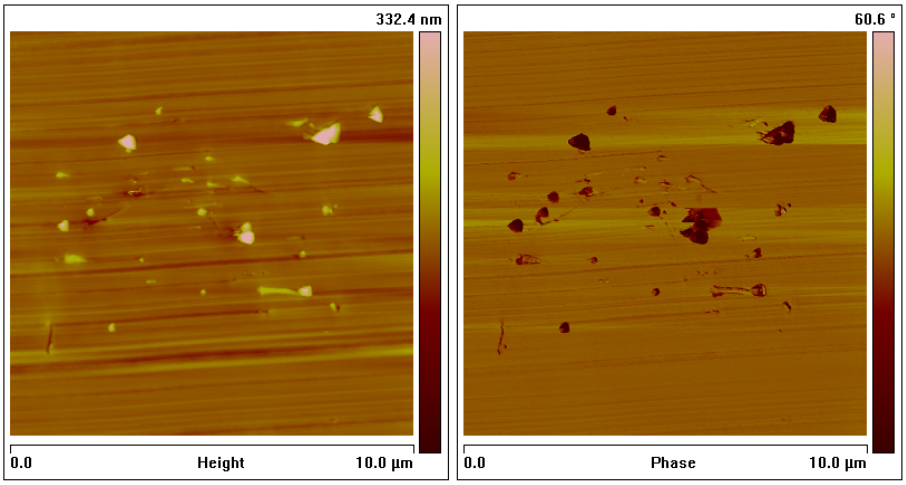
Moving on to the MWCNT-modified epoxy polymer samples, AFM images were captured from cured epoxy polymers with different weight loading of the multi-walled carbon nanotubes, as shown in Figure 7.2.1. In these Figures, the height and the phase (via hardness differences) images are shown on the left-hand and right-hand sides, respectively.

As can be seen in these AFM images, the nanotubes were agglomerated in the bulk samples. Further, as the concentration of the MWCNTs is increased, the size of nanotube agglomerates increases, which indicates that degree of MWCNT dispersion is reduced. The 0.5 wt% MWCNTs/epoxy sample, see Figure 7.2.1 (c), revealed many more agglomerated nanotubes (shown as dark colour in the AFM images) than in the

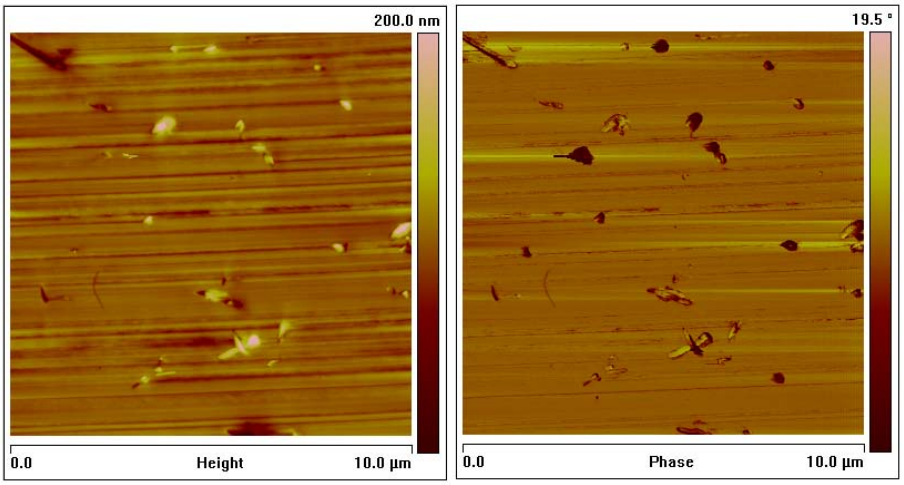
sample containing 0.1 wt%. For example, at the same scanning size of 10 μm square, the samples containing 0.1 wt% and 0.2 wt% exhibited nanotube agglomerates with a size of about 0.2 ~ 0.3 μm square. By contrast, the sample of 0.5 wt% MWCNTs/epoxy revealed relatively crowded nanotube agglomerates with an average size of 0.6 μm square. Due to the small scanning size (maximum scanning size in AFM is 20 μm square), it is difficult to measure the real nanotube agglomeration size. For example in Figure 7.2.1 (a), the nanotube agglomerates appear to be clustered. More information about the size of the agglomerates and of the clusters of agglomerates, if present, may be obtained from the fracture surfaces of the MWCNT-modified epoxy polymers, and will be discussed in more detail in Section 7.4.2.

It should be noted that in the phase images of the AFM study, the relative hardness of the materials is shown. The measured hardness of carbon nanotubes (nanotube hardness = 24 GPa) [125] is much higher than that of cured epoxy resins (epoxy hardness = 0.15 GPa) [126]. However, the relatively soft response of agglomerated MWCNTs, which was apparent, was caused by the AFM probe slipping off the graphitic surface of the nanotubes, rather than reflecting the true hardness of the multi-walled carbon nanotubes. FEG-SEM observation on the fracture surface of tested SENB specimens was also used to examine the nanotube dispersion, and will be discussed in the following Section.

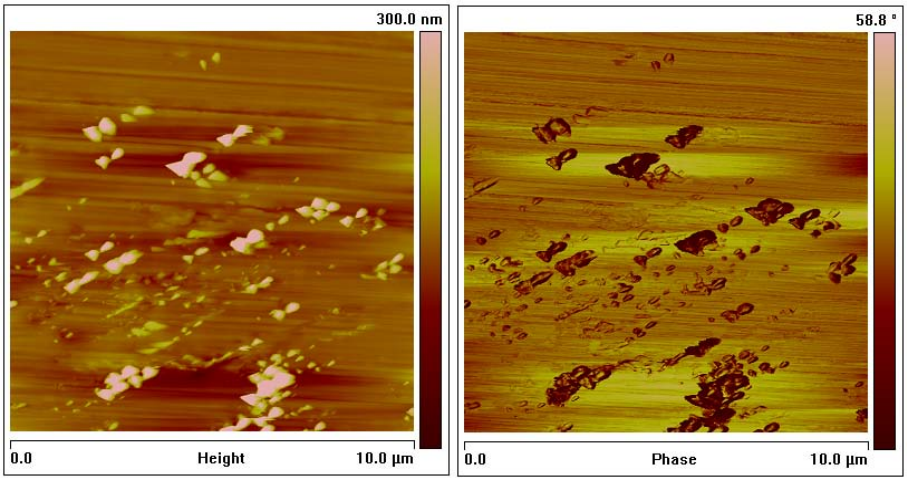
Further investigation into the dispersion in MWCNTs/epoxy composites will be discussed in Section 7.9, where the effect of varying the MWCNT content on the dispersion of the nanotubes was investigated by observing 70-μm-thick slices using a transmission optical microscope (TOM). A greyscale analysis was used to rank the dispersion of the multi-walled carbon nanotubes versus different nanotube concentrations.



(a)



(b)



(c)

Figure 7.2.1 AFM images of the morphology of the MWCNT-modified epoxy polymers with (a) 0.1 wt%, (b) 0.2 wt% and (c) 0.5 wt% of the MWCNTs.

7.3 Mechanical and Thermal Properties

The measured Young's modulus, E, and the glass transition temperature, T_g, of the various formulations (control, 0.1, 0.2, and 0.5 wt% MWCNTs) are summarised in Table 7.3.1. The tensile testing specimens were made from 2-mm-thick plates, with a gauge length of 20 mm and a width of 6 mm. Glass fibre-reinforced polymer composite end-tabs were adhered on the ends of the specimens to allow the specimens to be gripped well (the preparation for the tensile testing specimens was described in Section 4.2). An average Young's modulus of 2.90 GPa was measured for the unmodified epoxy polymer, which is typical for the unmodified anhydride-cured DGEBA polymer [5]. Plotting the Young's modulus versus the weight percent of the carbon nanotubes, as shown in Figure 7.3.1, illustrates more clearly the effect on the stiffness of the polymer-based composite caused by the addition of the multi-walled carbon nanotubes. The modulus increased, as expected [72, 127], as the nanotube loading was increased. A maximum modulus of 3.26 GPa was measured for the highest MWCNT weight fraction of 0.5 wt%. The Young's modulus of carbon nanotubes has a range of 0.2~1.2 TPa [71], which is much higher than the modulus of epoxy polymer. Therefore, an increase in the stiffness of modified polymers by carbon nanotubes is expected. The improved stiffness by the addition of the nanotubes will be checked by the modelling study in Chapter 9.

Table 7.3.1 The mechanical and thermal properties of the MWCNT-modified composites.

Formulation	CNT wt%	E (GPa)		T_g (°C)	
		Mean	SD	Mean	SD
Control	0.0	2.90	0.09	147.8	0.9
0.1C0S0R	0.1	3.01	0.06	147.8	1.4
0.2C0S0R	0.2	3.11	0.05	146.7	1.4
0.5C0S0R	0.5	3.26	0.05	144.7	1.1

Turning to the experimental results of the differential scanning calorimetry (DSC) used for measuring the glass transition temperature, T_g, of the nanocomposites, the results shown in Table 7.3.1 indicate that the glass transition temperature of each formulation is very similar. A T_g of 148 °C was measured for the unmodified epoxy. The addition of nanotubes did not affect the value of T_g, as was observed for the nanosilica modified materials [5]. In the literature, the investigation of the thermo-mechanical properties of nanotube-modified polymers reported that using nanotubes led to an increase in the glass transition temperature. However, the obviously improved T_g was obtained at high nanotube loading, which was more than 0.75 wt%, and with functionalised nanotubes [128]. Gojny et al [128] investigated the functionalisation effect on the thermo-mechanical behaviour of multi-walled carbon nanotube/epoxy composites. They reported that the T_g of the nanotube-modified epoxy polymer was increased from 64 °C for the unmodified epoxy to 80 °C for the nanocomposite containing 0.75 wt% multi-walled nanotubes, and 83 °C for the modified epoxy with 0.75 wt% amino-functionalised nanotubes. However, without the surface treatment, the T_g of the nanocomposites did not change when the nanotube loading was lower than 0.5 wt%, see Figure 7.3.2.

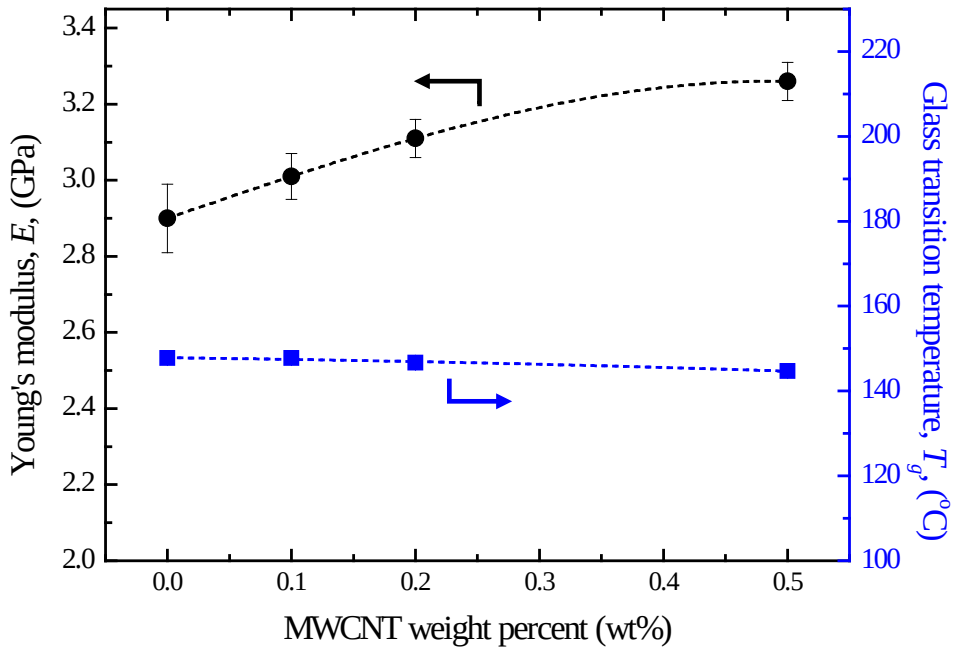


Figure 7.3.1 The mechanical and thermal properties of the MWCNT-modified composites.

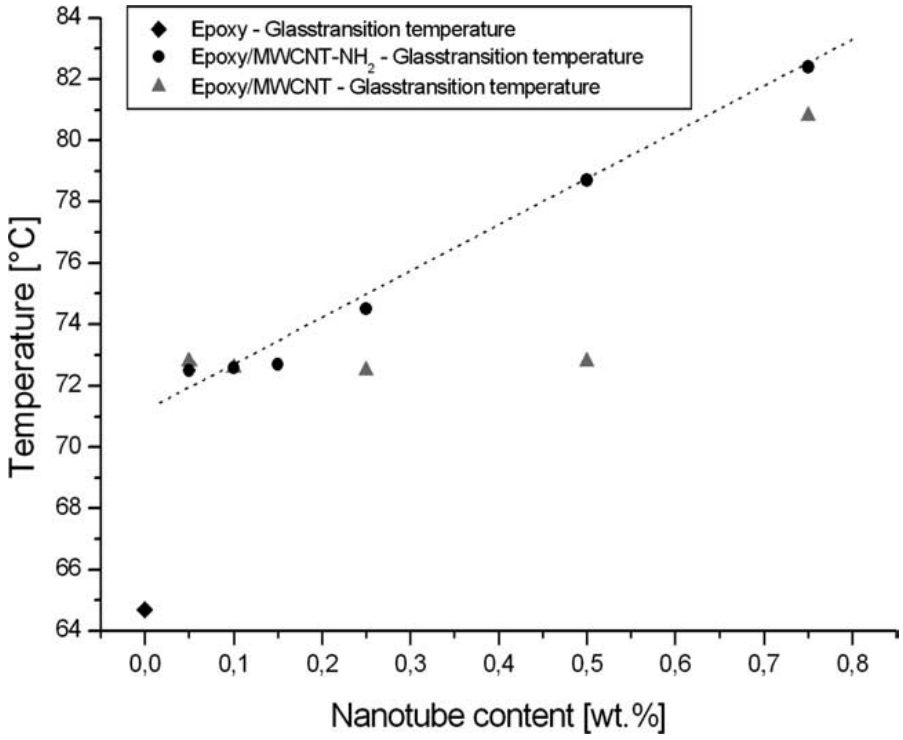


Figure 7.3.2 Glass transition temperature versus nanotube content [128].

7.4 Toughness

7.4.1 Fracture toughness and fracture energy

The experimental determination of the fracture toughness, K_{Ic}, and fracture energy, G_{Ic}, was performed using single-edge notched bend (SENB) tests on specimens with a sharp natural crack. Table 7.4.1 summarises the test data. The fracture toughness and the fracture energy for the unmodified epoxy polymer were determined to be 0.69 MPa $m^{1/2}$ and 133 J/m^2, respectively. All the nanocomposites modified by the addition of the multi-walled carbon nanotubes showed a significant increase in the fracture toughness and the fracture energy, compared with the unmodified polymer.

Table 7.4.1 The fracture toughness and fracture energy of the MWCNT-modified composites.

Formulation	CNT wt%	K_{Ic} (MPa.$m^{1/2}$)		G_{Ic} (J/m^2)	
		Mean	SD	Mean	SD
Control	0.0	0.69	0.03	133	8
0.1C0S0R	0.1	0.85	0.04	162	14
0.2C0S0R	0.2	0.88	0.02	188	7
0.5C0S0R	0.5	0.98	0.05	223	13

Figure 7.4.1 shows the testing results of the toughening performance versus various concentrations of the multi-walled carbon nanotubes. The addition of the multi-walled carbon nanotubes on the toughening performance of the epoxy polymers led to a significant increase in the fracture toughness, K_{Ic}. For example, the measured fracture toughness was increased from 0.69 MPa.$m^{1/2}$ for the neat polymer (without nanotube additives) to a maximum value of 0.98 MPa.$m^{1/2}$ for the nanocomposite containing 0.5 wt% of MWCNTs, this is around a 48% increment compared with the unmodified material. However, at more than 0.2 wt% of nanotubes, the improvement in the toughness was diminished, as the increased toughness did not show a linear trend. This is because nanotubes exhibit an undesirable tendency towards agglomeration. Although sonication was used to achieve a good dispersion of the nanotubes in the uncured resin

(MWCNT/epoxy mixture), the nanotubes agglomerate again during the sample curing process, which has been discussed in Chapter 5. Even at a low nanotube loading of 0.1 wt %, the modification using the nanotubes still revealed a high potential to improve the toughness of polymer-based materials. There was an increase of 23% in the fracture toughness of the nanocomposite with 0.1 wt% carbon nanotubes.

The measured fracture energy, G_{Ic}, of all the formulations was increased significantly and showed the same trend as the measured values of the fracture toughness, as the weight loading of the nanotubes was increased. For the nanocomposite with a nanotube weight loading at 0.5 wt%, a maximum value of 223 J/m^2 was recorded. Comparing the obtained maximum value with the unmodified polymer (133 J/m^2), there was an outstanding increase of 75%, which is higher than the improvement in the fracture toughness (48% increment). This relatively improved value of the fracture energy can be supported by the LEFM method, where the fracture energy is calculated by Equation 2.6 of: $G_{Ic} = (1-\nu^2)K_{Ic}^2/E$, (where the ν is Poisson's ratio, and a value of 0.35 was used). The analysed value of fracture energy is directly proportional to the square of fracture toughness, therefore the value of fracture energy was increased significantly as the fracture toughness was increased if the Young's modulus, E, was a constant or increased somewhat. Although the values of the measured fracture energy shown in this Chapter were calculated by the energy method, these values show good agreement with the values of the fracture energy calculated by LEFM method.

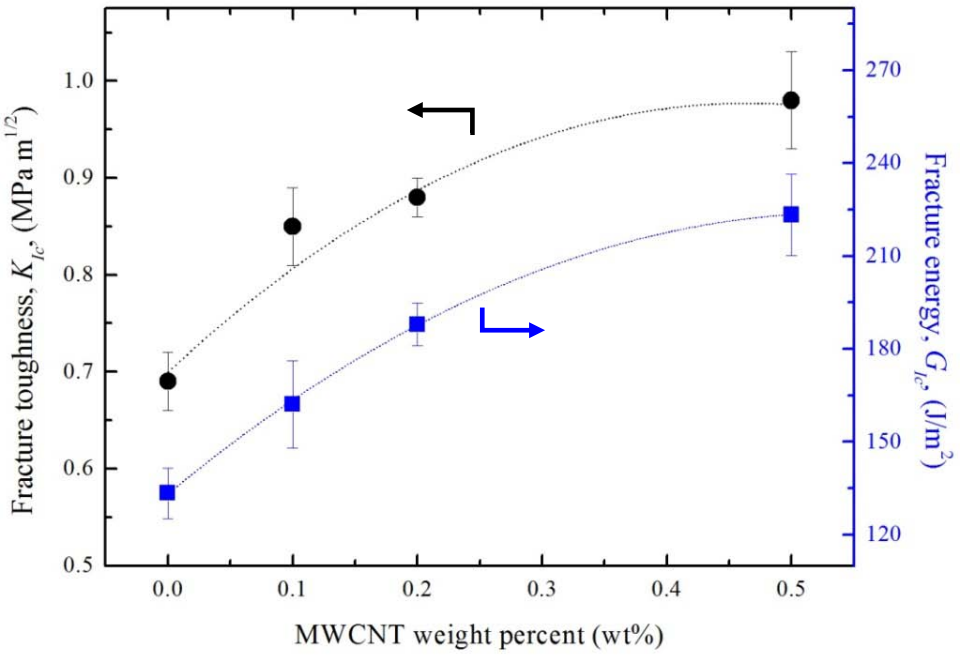


Figure 7.4.1 The fracture toughness and fracture energy of MWCNT-modified composites.

Comparing these experimental results with other studies [74, 129-132] focused on multi-walled carbon nanotube-toughened epoxy polymers, the modification with the multi-walled carbon nanotubes used in this study shows an excellent improvement in the toughness, see Figure 7.4.2. As the rate of the toughness increase is dependent on the matrix used, a normalisation of the toughness for nanotube-modified materials, $K_{Ic(cnt\text{-}modified)}/ K_{Ic(unmodified)}$, was required; the normalised values of the toughness versus the nanotube loadings are shown in Figure 7.4.2. It is clear that at a nanotube loading of 0.5 wt%, the addition of the multi-walled carbon nanotubes (used in this study) resulted in the highest value of the normalised fracture toughness. This may be because the length of the nanotubes used in this study is the longest of 140 μm (the length of CNTs used in the literature [74, 129-132] only up to 40 μm). The effect of the nanotube dimensions on the toughness will be discussed in Section 7.8 and Chapter 9.

The dispersion of nanotubes is one of the most important factor in improving the toughness. In Figure 7.4.2, the experimental results in this study and the literature values [74, 130] showed a significant improvement in toughness due to well-dispersed

nanotubes present. In these studies, a high-intensity ultrasonic process was used to disperse the nanotubes in the polymer resins. However, some values referred to the literature [129] showed a decreased in the toughness of nanotube-modified polymers. This is because the nanotubes had a high aspect ratio (aspect ratio = 5000 [129]), which results in a difficulty in getting good dispersion, i.e. the dispersion of nanotubes is closely linked to the dimensions of nanotubes used, such as length, diameter and aspect ratio (length/diameter). The introduction of silane treatment may improve the dispersion of nanotubes, consequently the enhanced fracture toughness was obtained [129]. Besides, pre-crack in the fracture testing specimens may affect the experimental results. As nanotube-modified polymers are not transparent, it is a challenge to make a sharp pre-crack with a valid crack length. Zhou et al. [130] used cyclic loading with 4~40% of the peak load at 1Hz to make the pre-crack before doing the fracture tests. This would improve the accuracy of the measured fracture toughness. In this study, the surface of the SENB specimens was polished to get glossy surface, so it would be easier to see the crack when making a pre-crack.

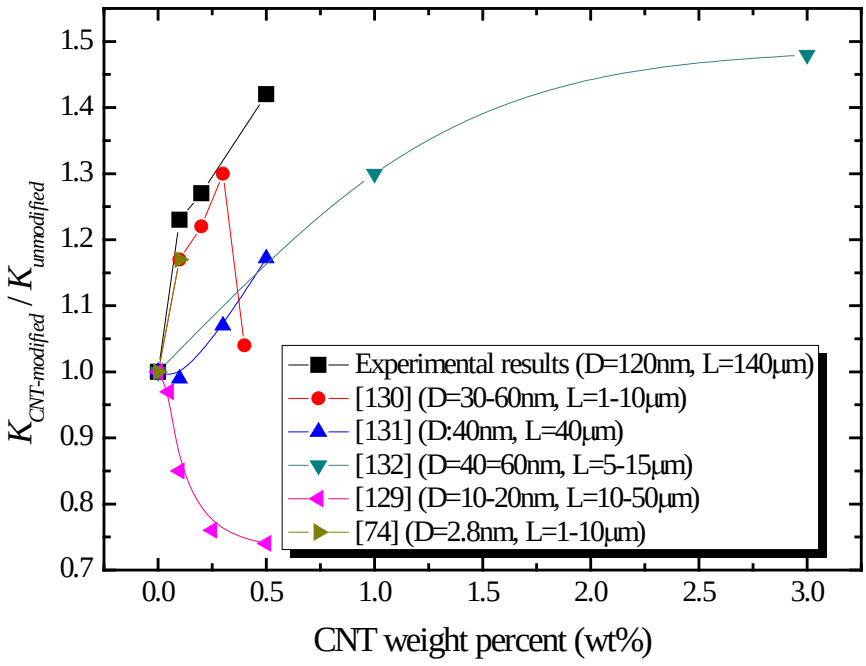


Figure 7.4.2 The comparison between the experimental toughness in this study and the toughness reported in literature (all the matrices are epoxy, and the nanotubes are untreated) [74, 129-132].

7.4.2 Fractography

The improvement in the toughening performance caused by adding the multi-walled carbon nanotubes into the epoxy was supported by the examination of the fracture surfaces of SENB specimens using field emission gun scanning electron microscopy (FEG-SEM). Once again the cracks run from right to left in all the fracture surface images. Figure 7.4.3 shows the FEG-SEM images at low magnification. The fracture surface of the neat polymer, Figure 7.4.3 (a), revealed a relatively smooth surface which is typical of brittle polymer fracture [111], and has been discussed in Chapter 6. In the fractography of the samples containing the multi-walled carbon nanotubes, as shown in Figure 7.4.3 (b-d), these fracture surfaces of the initiation region revealed a relatively rough appearance with numerous river lines; the river lines were caused by the crack propagating along different planes in the fracture surfaces, which is typical behaviour for a brittle thermoset polymer [5]. This also indicates that an increased amount of new surfaces were created during fracture, although the toughening effect due to this is minimal [5]. At these low magnifications, it is not possible to see the individual nanotubes. However, the MWCNT agglomerates interact with the propagating crack, as indicated by the river lines, many of which start at an agglomerate. The toughening mechanisms will be discussed in more detail in Section 7.4.3.

These FEG-SEM images also show the different levels of MWCNT dispersion; the higher weight fractions of nanotubes led to serious agglomerations of nanotubes. The sample containing the highest concentration of 0.5 wt% nanotubes, see Figure 7.4.3 (d), showed numerous MWCNT agglomerates with a size of about 5 ~ 10 μm square, which is much larger that the size of the nanotube agglomerates in the nanocomposites containing 0.1 wt% and 0.2 wt% nanotubes. This confirms that agglomeration was why the rate of increase of the measured toughness was reduced at high nanotube loading. The size of the MWCNT agglomerates in FEG-SEM is larger than observed in AFM, due to the small scanning size in AFM. In common with the AFM observation, the shape of the agglomerates is irregular in the FEG-SEM images.

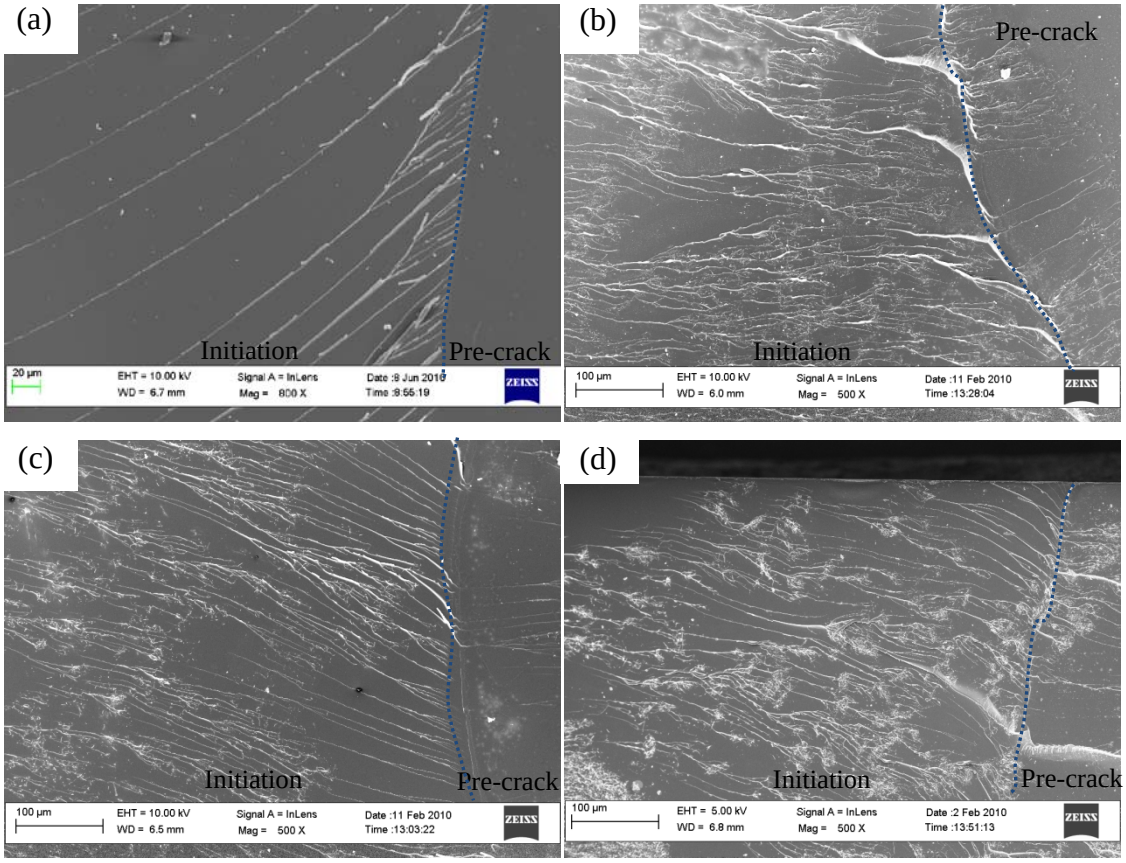


Figure 7.4.3 Field emission gun scanning electron microscopy (FEG-SEM) images of the fracture surfaces, showing (a) unmodified, (b) 0.1 wt%, (c) 0.2 wt% and (d) 0.5 wt% of MWCNTs.

7.4.3 Toughening Mechanisms

The toughening mechanisms which are responsible for the increase in the toughness were identified from high magnification images. The fractography concentrated on the initiation region, which is of great importance as it is within the plastic zone that the toughening mechanisms occurred. As can be seen in Figure 7.4.4, the well-known toughening mechanism of nanotube pull-out and bridging can be clearly observed on the fracture surfaces of the nanocomposites. The pulled-out nanotube length was measured to be up to 10.5 μm, but is typically several microns. The average pulled-out length was 7.82 μm, with a standard deviation of 2.78 μm. This value will be used as the effective nanotube pull-out length in the modelling analysis (will be discussed in

Chapter 9) to predict the increase in the toughness caused by the nanotube pull-out mechanism. For nanotube pull-out and bridging, energy is absorbed by the friction between the nanotubes and the polymeric matrix as the multi-walled carbon nanotubes were pulled out, and consequently the toughness is increased.

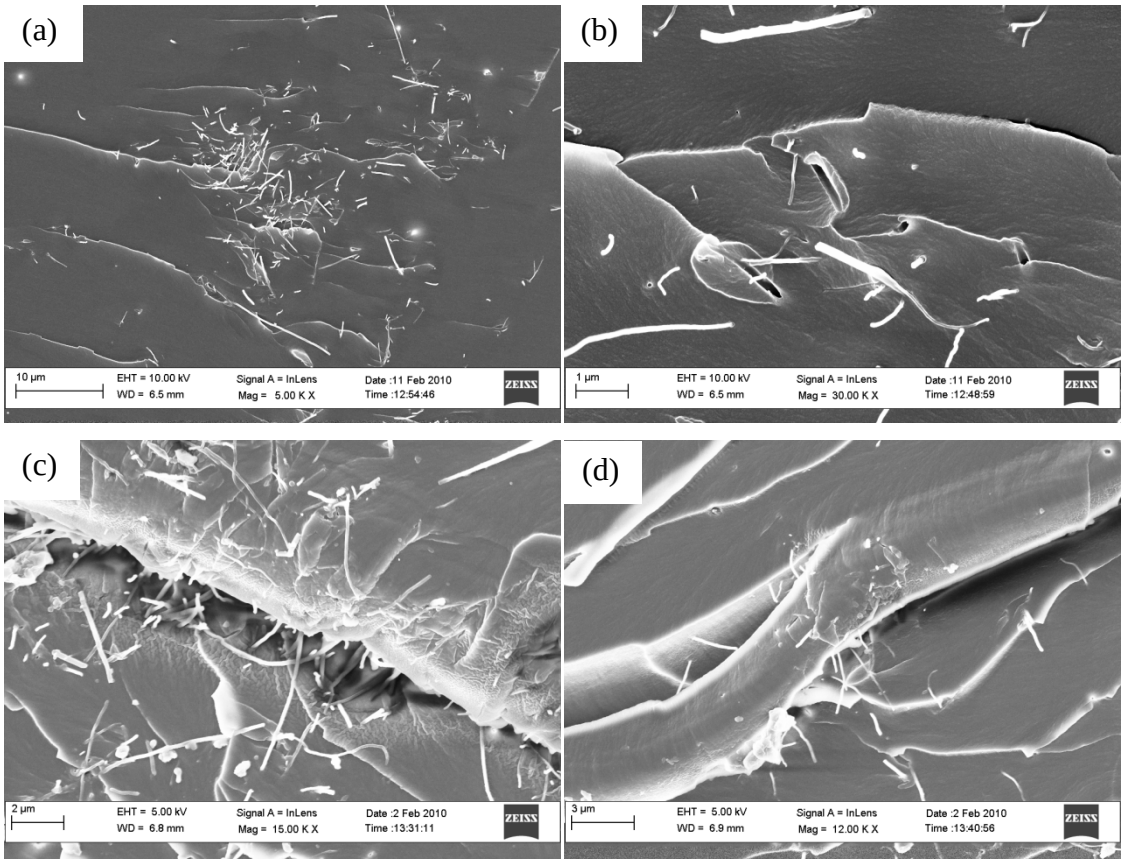


Figure 7.4.4 Field emission gun scanning electron microscopy (FEG-SEM) images captured of 0.5 wt% MWCNTs sample. (a,b) showing the nanotube pull-out, (c,d) showing nanotube bridging.

The average pulled-out nanotube length of 7.82 μm is much shorter than the average nanotube length after the sonication (120 μm), or the thickness of the grown aligned nanotube films (140 μm). If the nanotubes were perfectly straight, this would indicate that the interfacial property between the multi-walled carbon nanotubes and the epoxy matrix is very good, and so can provide a high interfacial shear stress. As the stress increases, the nanotubes will debond and then rupture, followed by the occurrence of nanotube pull-out, as shown schematically in Figure 7.4.5. However, the

agglomerates observed indicate that the nanotubes are not straight in the cured epoxy polymer. Hence, it is to be expected that they will not pull out fully. It is assumed that the nanotubes are under elastic deformation until fracture and no permanent defermation occurs, so the total nanotube length in Figure 7.4.5 (d) is the same as in Figure 7.4.5 (a).

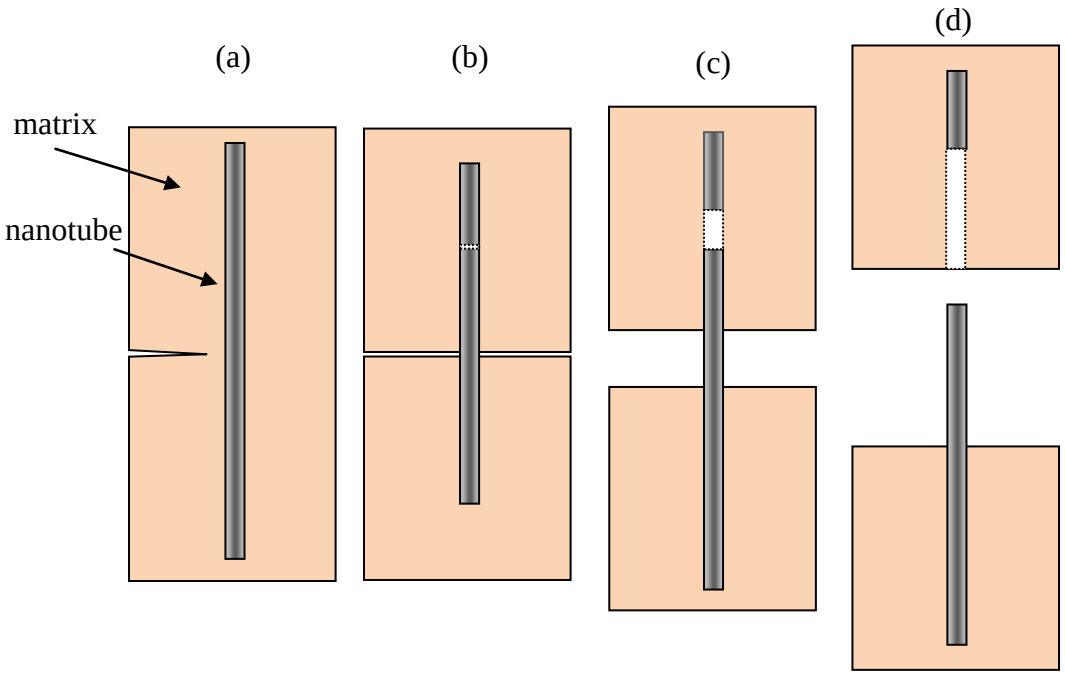


Figure 7.4.5 The schematic model of nanotube pull-out mechanism. (a) nanotube original state, (b) nanotube ruptures, (c) nanotube pull-out (efficient pull-out), and (d) nanotube completely pulled out from the fracture surface.

It is worth mentioning that a clear definition of nanotube bridging mechanism is nanotube elastic deformation during crack growth before nanotube rupture. Hence, the opportune moment of the nanotube bridging mechanism is a transient before nanotube rupture (between Figure 7.4.5 (a) to (b)). Therefore, the nanotube bridging-like features observed on the fracture surface, see Figure 7.4.4 (c,d), result from the efficient nanotube pull-out mechanism, see Figure 7.4.5 (c), rather than the nanotube bridging mechanism. The efficient nanotube pull-out is that pulled out nanotubes have not completely come off the polymeric matrix. The determination of percentage of pulled-out nanotubes using a photographic analysis on the FEG-SEM images showed that all of (100%) the added nanotubes were pulled out in the nanocomposites with 0.1 wt% and 0.2 wt% carbon nanotubes. However, at 0.5 wt%, less nanotubes were pulled out from

the epoxy matrix. This was calculated as 62 ± 5% of the nanotubes on the fracture surface taking part in the pull-out mechanism.

In addition to the toughening mechanism of nanotube pull-out, void growth due to debonding between the MWCNTs and the matrix followed by plastic deformation of the epoxy is clearly observed, as shown in Figure 7.4.6. A photographic analysis was used to calculate the percentage of void growth, and this was measured to be 8 ± 1% of the nanotubes on the fracture surface showed void growth. The diameters of the voids are about 20-30 % larger than the diameter of the nanotubes (120 nm), and the average diameter was measured to be 144 ± 8 nm. This mechanism of plastic void growth has been discussed for the nanocomposite modified by the silica nanoparticles, and was considered to be a major toughening mechanism [5].

All of these toughening mechanisms, as summarised in Table 7.4.2, observed on the fracture surfaces of the MWCNT-modified polymers can efficiently absorb energy, and hence increase the toughness. The modelling analysis composed of these toughening mechanisms will be discussed in Chapter 9, where the relative contributions from each mechanism will be considered.

Table 7.4.2 The summary of the toughening mechanisms of the MWCNTs-modified epoxy polymers.

MWCNT content (wt%)	Toughening mechanism	
0.1	Nanotube pull-out	Pulled-out length: 7.69 μm
		Amount: 100%
	Plastic void growth	Void diameter: 145 nm
		Amount: 8%
0.2	Nanotube pull-out	Pulled-out length: 7.86 μm
		Amount: 100%
	Plastic void growth	Void diameter: 151 nm
		Amount: 8%
0.5	Nanotube pull-out	Pulled-out length: 7.91 μm
		Amount: 62%
	Plastic void growth	Void diameter: 136 nm
		Amount: 8%
Nanotube pull-out	Average pulled-out length: 7.82 μm	
Plastic void growth	Average void diameter: 144 nm	

An additional mechanism of crack deflection was detected in the sample containing 0.5 wt% MWCNTs, which contained large nanotube agglomerates (5 ~ 10 μm square). This indicates that these agglomerated nanotubes can act in a similar way to micrometre-sized reinforcements such as the glass beads which are commonly used as a toughener in polymer-based composite [57]. The occurrence of crack deflection results in new fracture surfaces (sub-cracks). This requires more energy, and consequently contributes to the increase in toughness.

Note that although the multi-walled carbon nanotubes are agglomerated, the wettability of the nanotubes was not affected by increasing the loading of the nanotubes.

Figure 7.4.4 and Figure 7.4.6 show that each nanotube was very well coated with the polymeric matrix even when they were crowded and entangled.

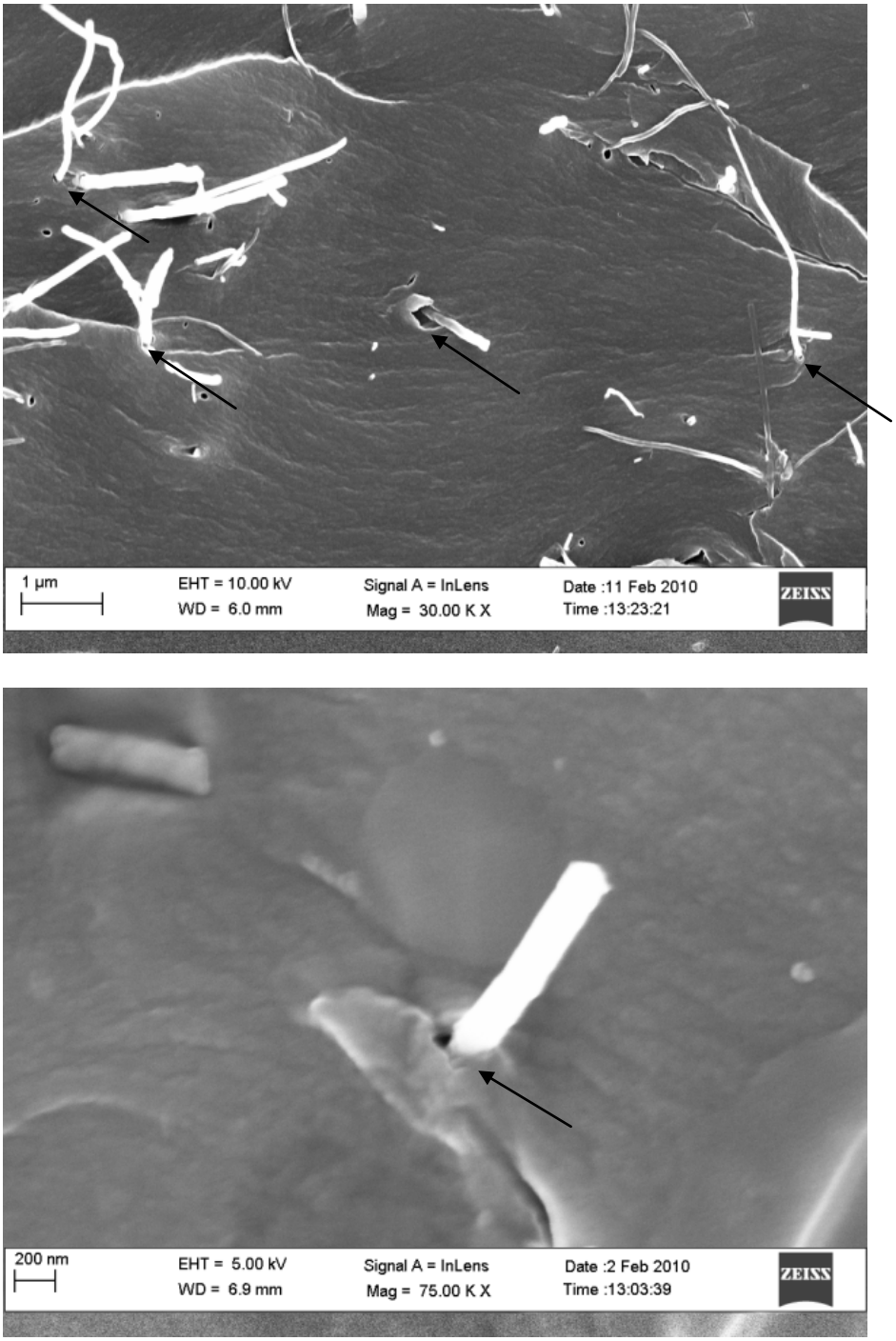


Figure 7.4.6 Field emission gun scanning electron microscopy (FEG-SEM) images captured of 0.5 wt% MWCNTs sample showing the debonding and plastic void growth around the nanotubes.

7.5 Compressive Properties

Plane strain compression tests were carried out on the unmodified material and the nanocomposite with 0.5 wt% multi-walled carbon nanotube loading. The values of the compressive Young's modulus, E_c, compressive true yield stress, σ_{yc}, compressive yield strain, ε_{yc}, and compressive failure strain, γ_{fc}, are summarised in Table 7.5.1.

The measured value of the compressive Young's modulus, E_c, was increased from 2.60 GPa for the unmodified epoxy polymer to 2.79 GPa for the modified epoxy polymer with the addition of the multi-walled carbon nanotubes at 0.5 wt%. This result is in good agreement with the modulus measured from the tensile tests (in tensile testing results, E = 2.90 GPa for the unmodified epoxy, and E = 3.25 GPa for 0.5wt% nanotubes). As the compressive loading was increased to reach the yield point of the materials, both the compressive yield stress and the compressive yield strain were increased slightly by blending the multi-walled nanotubes with the matrix, see Table 7.5.1. The plane strain compression test is mainly aimed at the investigation of the material properties under the condition of plastic deformation. The addition of the multi-walled carbon nanotubes to the epoxy polymer led to an increase in the yield stress (from 123 MPa for the unmodified epoxy to 132 MPa for the 0.5 wt% sample, as shown in Table 7.5.1), as well as the failure strength of the nanocomposites. This is attributed to the added carbon nanotubes possessing a high strength [71]. However, the agglomeration of the carbon nanotubes resulted in a reduction in the failure strain. The nanotube agglomerates or the nanotube-rich areas are analogous to material defects, which cause the premature failure. The compressive failure strain was decreased form 0.62 ±0.03 for the unmodified polymer down to 0.57 ±0.02 for the modified epoxy polymer with 0.5 wt% carbon nanotubes.

Table 7.5.1 The plane strain compression testing results of compressive Young's modulus, E_c, compressive true yield stress, σ_{yc},, compressive yield strain, ε_{yc}, and compressive failure strain, γ_{fc}, of the nanocomposites.

Formulation	CNT wt%	E_c (GPa)		σ_{yc} (MPa)		ε_{yc}		γ_{fc}	
		Mean	SD	Mean	SD	Mean	SD	Mean	SD
Control	0.0	2.60	0.18	123	4	0.09	0.01	0.62	0.03
0.5C0S0R	0.5	2.79	0.15	132	2	0.10	0.02	0.57	0.02

The stress-strain curves from the plane strain compression tests on the unmodified epoxy polymer and the nanocomposite reinforced by 0.5 wt% of MWCNTs are shown in Figure 7.5.1. The curves consist of a linear region at the beginning, and then reach yield. Continuing the compressive loading, the curve of the unmodified polymer sample showed a negative slope, in which inhomogeneous deformation occurred; this is identified as strain softening [133]. The expected shear band yield in polymeric materials may take place during strain softening. This can be demonstrated in Figure 7.5.2. During the plane strain compression testing, a video was set up to record the state of the specimen in different levels of stress, as shown in Figure 7.5.2. The main shear bands caused by the edge effect of the indenter started to occur when the stress reached the yield point, and then many shear bands occurred in the mid-plane of the specimen during the strain softening phase. In contrast to the unmodified polymer with the strain softening phase, the curve of the nanocomposite containing 0.5 wt% carbon nanotubes did not appear to show a strain softening region, see Figure 7.5.1. Both of the samples exhibited a work-hardening region after the strain softening phase until failure.

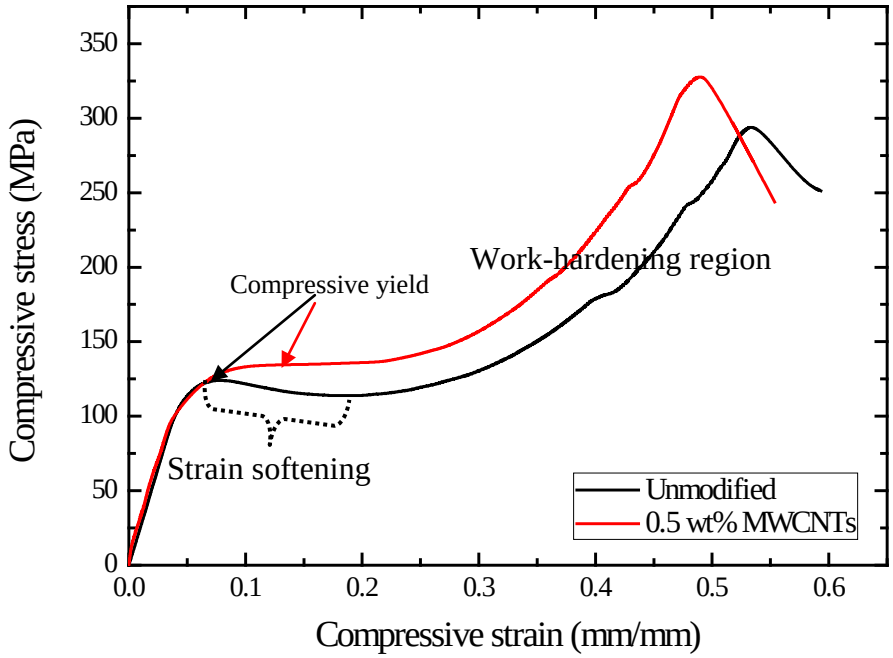


Figure 7.5.1 Compressive stress versus compressive strain for unmodified polymer and MWCNT-modified nanocomposite at 0.5 wt%.

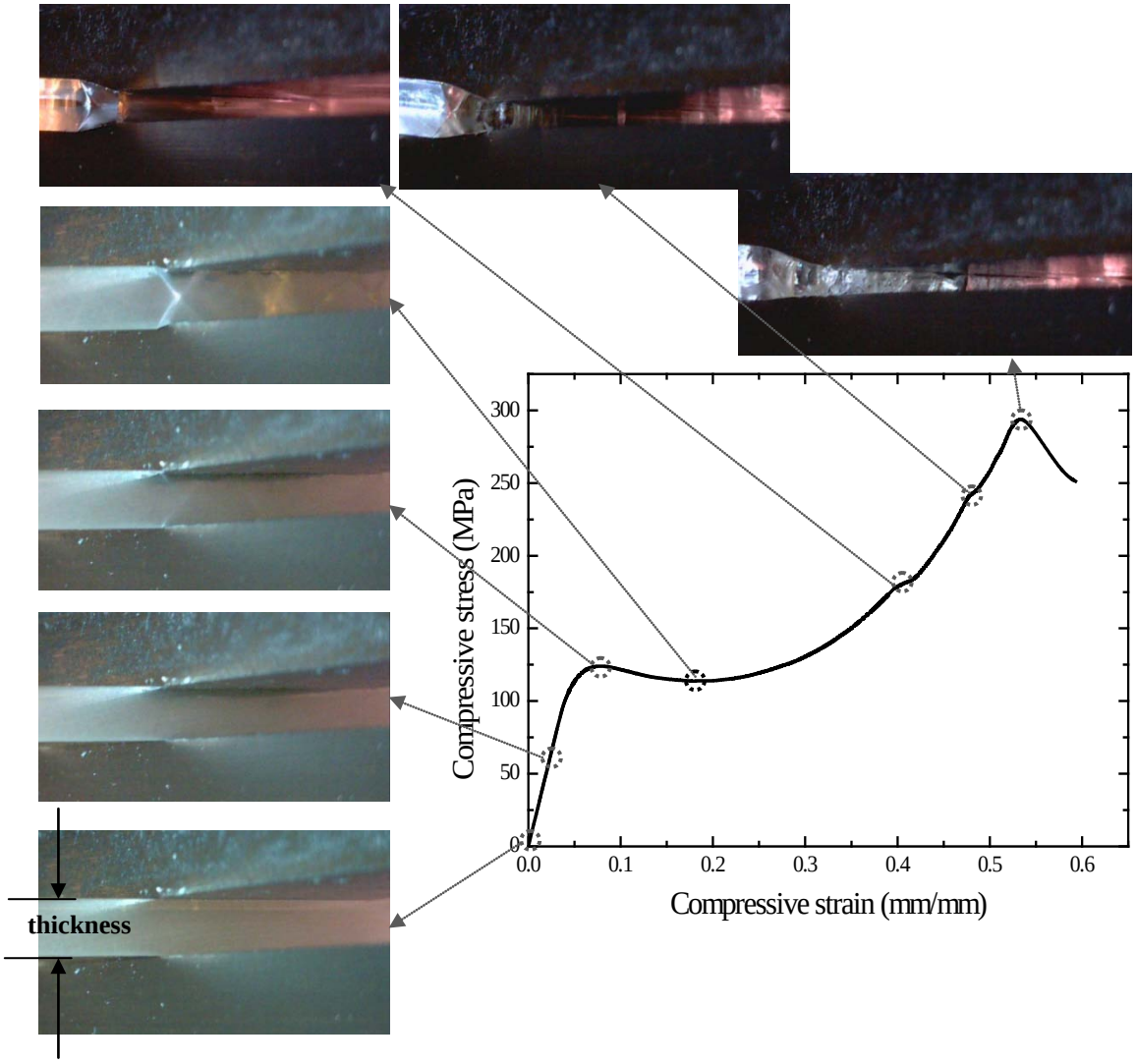


Figure 7.5.2 The state of the specimen at different levels of stress during plane strain compression test on unmodified epoxy polymer (the thickness of the specimen is 3 mm).

Samples of the unmodified epoxy polymer and the nanocomposite with 0.5wt% nanotubes were subjected to a compressive load to the strain softening limit (i.e. the test was stopped as the applied stress increased after the strain softening phase, or as the slope of the stress-strain curve started to be positive). After that, the centre of each tested specimen was sectioned, and then ground down to a 100 μm-thick slice glued to a microscope slide, as shown in Figure 7.5.3. The sectioned slices were examined using transmission cross-polarised light microscopy, as shown in Figure 7.5.4. Evidence of shear band yielding was clearly found in the compressed region of the unmodified

epoxy polymer sample, see Figure 7.5.4 (a). Many shear bands are visible in the deformed region of the compressed specimen. The TOM image of the 0.5 wt% MWCNTs/epoxy shows that shear banding did not readily occur in the compressed region, as can be seen in Figure 7.5.4 (b). In addition to the large shear bands caused by the edge effect, slight shear bands can be observed in the deformed region of the compressed specimen. These were a function of pure shear caused by the reduction of the thickness in the compressed region [134]. Referring to the testing result, no strain softening phase occurred in the compressive stress-strain curve of the MWCNT-modified polymer, thus shear bands are not expected in the tested sample of the nanocomposite.

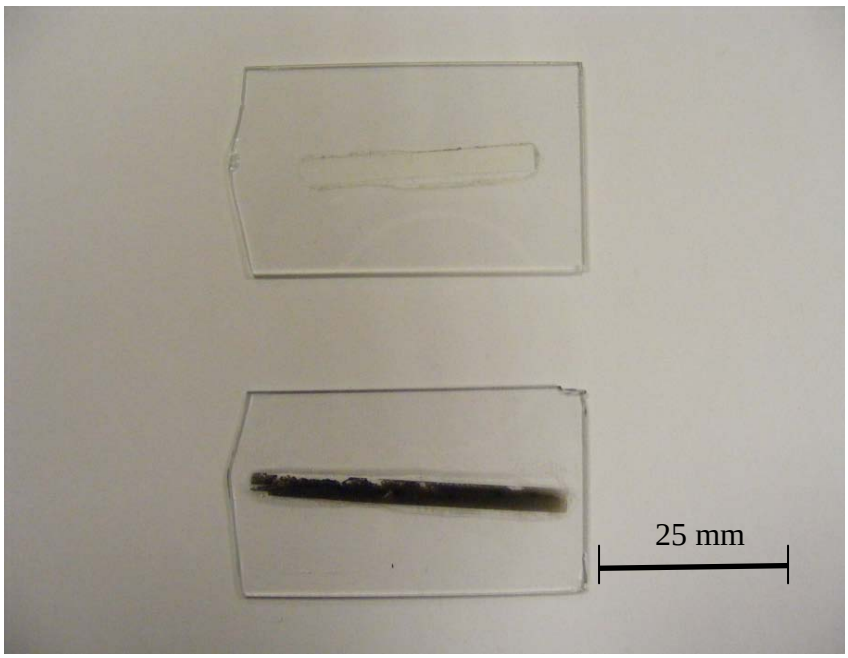
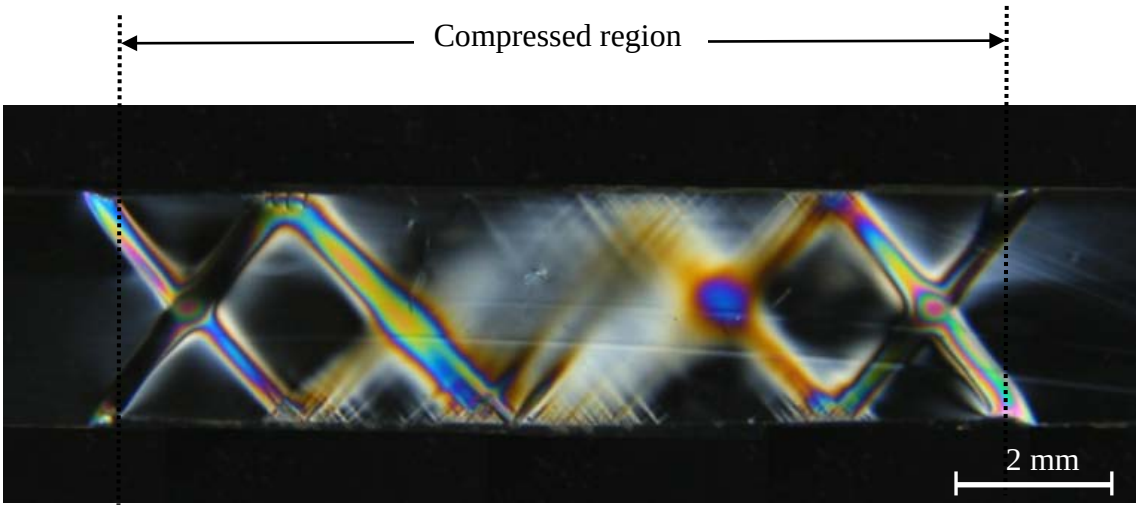
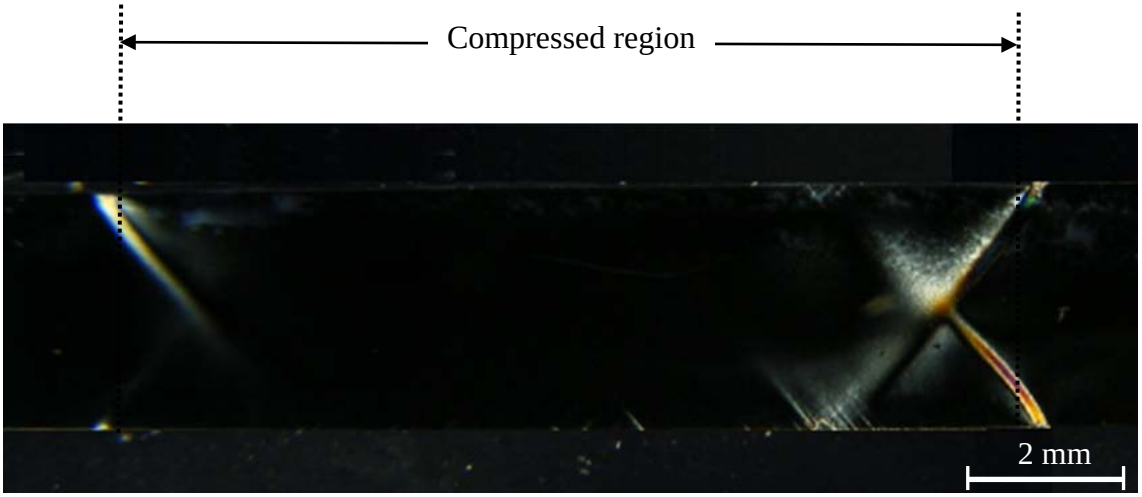


Figure 7.5.3 Samples of the unmodified epoxy polymer and the nanocomposite with 0.5wt% nanotubes for TOM observation.



(a) Unmodified epoxy



(b) 0.5 wt% nanotubes

Figure 7.5.4 TOM images from compressed samples of the unmodified polymer and the nanocomposite with 0.5 wt% nanotubes, (the length of the compressed region is 12 mm).

7.6 Fracture Behaviour under Fatigue Loading Conditions

7.6.1 Fracture Mechanics Fatigue Data

The fatigue performance and fatigue failure behaviour of the multi-walled carbon nanotube-modified polymers under dynamic loading were determined by performing fatigue tests on compact tension (CT) specimens with an initial sharp pre-crack. The fatigue tests were performed using cyclic loading at 5 Hz with a sinusoidal waveform for approximately 5 million cycles. At least two replicate fatigue tests were carried out for each formulation.

The fatigue testing results of crack propagation per cycle (crack propagation rate), da/dN, versus the maximum applied strain energy release rate, G_{max}, are shown in Figure 7.6.1 for the unmodified polymer, and the modified polymers by various weight percent of the multi-walled carbon nanotubes. The data show a linear Paris-law region, and a threshold region where the crack effectively stops growing [16]. Linear regression was used to fit a straight line to the Paris-law region, and the gradient, m, was calculated. It is clear from Figure 7.6.1 that the fatigue performance of the modified polymers revealed a significant increase as the loading of the multi-walled carbon nanotubes was increased. The measured results of the maximum applied strain energy release rate in the threshold region, G_{th}, and the gradient of the linear Paris-law region, m, are summarised in Table 7.6.1.

Table 7.6.1 Summary of the fatigue testing results of fatigue threshold and Paris-law gradient of the MWCNT-modified polymers.

Formulation	CNT wt%	G_{th} (J/m^2)		G_{th}/G_{Ic}	m	
		Mean	SD		Mean	SD
Control	0.0	24	8	0.18	13.2	0.3
0.1C0S0R	0.1	32	4	0.20	14.3	0.2
0.2C0S0R	0.2	53	7	0.28	13.5	0.1
0.5C0S0R	0.5	73	2	0.33	12.7	0.1

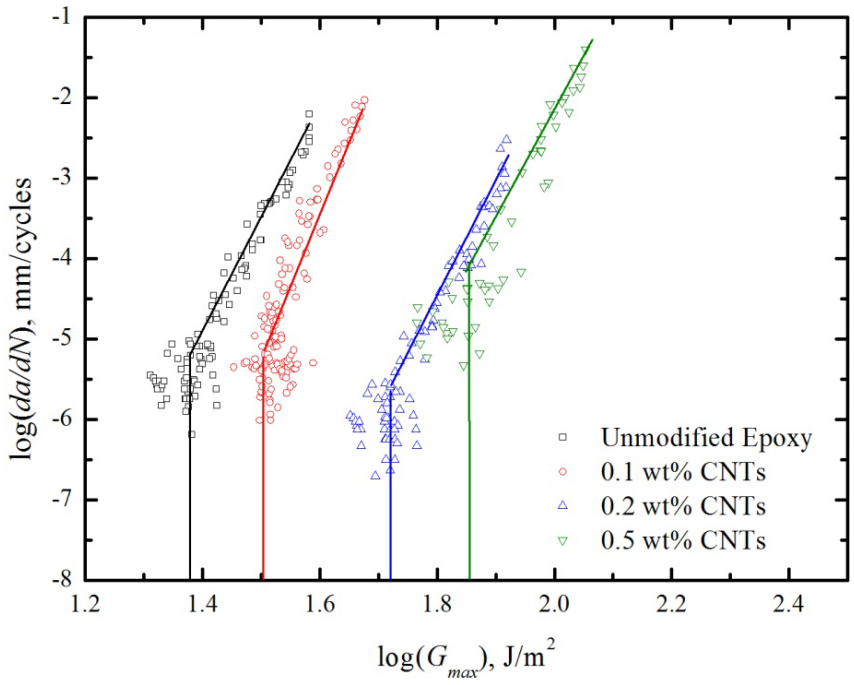


Figure 7.6.1 Rate of crack growth versus maximum applied strain energy release rate in the fatigue cycle for the unmodified epoxy and nanocomposites.

The average value of the maximum applied strain energy release rate in the threshold region, G_{th}, was determined to be 24 J/m^2 for the unmodified epoxy polymer. Comparing this fatigue testing data with the quasi-static fracture testing results of the fracture energy, G_{Ic}, then the value of fatigue threshold, G_{th}, is much lower than G_{Ic} for the unmodified polymer (G_{Ic}=133 J/m^2 for unmodified epoxy). The fatigue testing results, as shown in Table 7.6.1, clearly show that the addition of the multi-walled carbon nanotubes shifts the fatigue testing curve toward higher values of the maximum applied strain energy release rate, indicating the presence of the nanotubes results in the suppression of fatigue crack propagation. This is consistent with the previous studies of fatigue performance of nanotube-modified materials by Koratkar and co-workers [73, 80, 135, 136], however, these authors did not measure the value at threshold, where the crack stops propagating. In this study, the fatigue testing was stopped when the crack reached the threshold region, and the value of G_{th} was calculated. The testing results show that the addition of the multi-walled carbon nanotubes to the polymer-based composite leads to a significant increase in the measured values of G_{th} from 24 J/m^2 for

the unmodified polymer sample to 73 J/m^2 for the modified epoxy polymer containing 0.5 wt% MWCNTs.

Even at a low nanotube loading of 0.2 wt%, an outstanding improvement in the fatigue property of G_{th} to 53 J/m^2 can be attained. This can be clearly seen in Figure 7.6.2 which plots the measured value of G_{th} versus the nanotube content; the measured value of G_{th} for the nanocomposite containing 0.2 wt% nanotubes lies above the trend line. Although the maximum value of G_{th} for the modified epoxy was recorded as 73 J/m^2 for the modified polymer with 0.5 wt% of MWCNTs, the rate of the increased G_{th} slowed down as the nanotube loading is increased above 0.2 wt%. This is because of the agglomeration of the nanotubes at the high concentration of nanotubes. Furthermore, the addition of nanotubes led to an increase in the viscosity of the mixture. The nanocomposite containing 0.2 wt% nanotubes reveals a significant increase in the fatigue property and the viscosity is still fine for casting and engineering applications. The addition of 0.5 wt% nanotubes resulted in a smaller increase in G_{th} than expected, and the viscosity is too high for preparing large samples.

By considering the ratio of G_{th}/G_{Ic}, the effectiveness of using the multi-walled carbon nanotubes to improve the fatigue performance can also be examined, see Figure 7.6.2. The value of G_{th}/G_{Ic} increases with increasing nanotube weight percent. For example, the value of G_{th}/G_{Ic} for the nanotube loading at 0.2 wt% reveals a significant improvement and the value falls above the trend line. Typical values of G_{th}/G_{Ic} for epoxy polymers lie in a range between 0.05 to 0.35 [137-139]. Comparing the fatigue testing results, the measured values of the ratio of G_{th}/G_{Ic} for the MWCNT-modified materials in this study are in a range between 0.2 to 0.33. This means that the modification using the multi-walled carbon nanotubes was a highly effective way to increase the fatigue property of the epoxy polymer. The value of the gradient of the linear Paris-law region, *m*, as shown in Table 7.6.1, for each formulation is around 13, without a clear trend as the content of the multi-walled carbon nanotubes is varied.

A comparison of the fatigue properties of the DGEBA polymer-based composites modified by the multi-walled carbon nanotubes (used in this study) and silica nanoparticles (commonly used as nano-reinforcements for polymer) shows that the multi-wall carbon nanotubes can successfully substitute for the silica nanoparticles

as the toughener for the epoxy polymer. Moreover, a significant improvement in the fatigue performance can be obtained even at low concentrations of the nanotubes. For example, a maximum value of G_{th} was determined to be 64 J/m^2 for the modified epoxy polymer with 20 wt% nanosilica particles [102]. In contrast, a low loading of only 0.5 wt% of the multi-walled carbon nanotubes was needed to reach the maximum value of G_{th}, 73 J/m^2. This indicates that the use of nanotubes to improve the fatigue properties of polymer-based materials is more efficient than the use of silica nanoparticles. This may suggest differences in the toughening mechanisms between the nanosilica/epoxy and nanotube/epoxy materials, as will be discussed in Section 7.6.3.

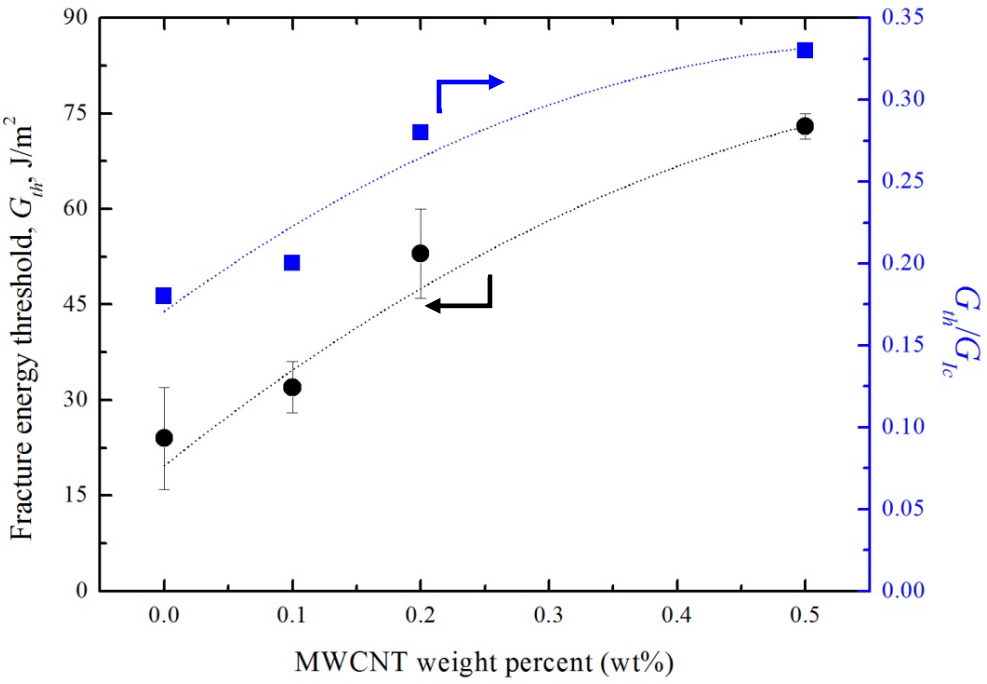


Figure 7.6.2 The threshold fracture energy and the ratio of G_{th}/G_{Ic} versus the weight percent of the MWCNTs.

7.6.2 Fractography

An inspection of the fracture surfaces of the CT specimens after fatigue failure was conducted to study the mechanisms which can contribute to the increase in fatigue performance. The fracture surface caused by fatigue failure was imaged using FEG-SEM along the direction of crack growth, where three different zones are seen: the crack initiation (where G_{max} is large), propagation, and threshold (where $G_{max} = G_{th}$) regions. These regions are schematically shown in Figure 7.6.3. All of these regions of fatigue fracture surfaces were observed in detail, as shown in Figure 7.6.4.

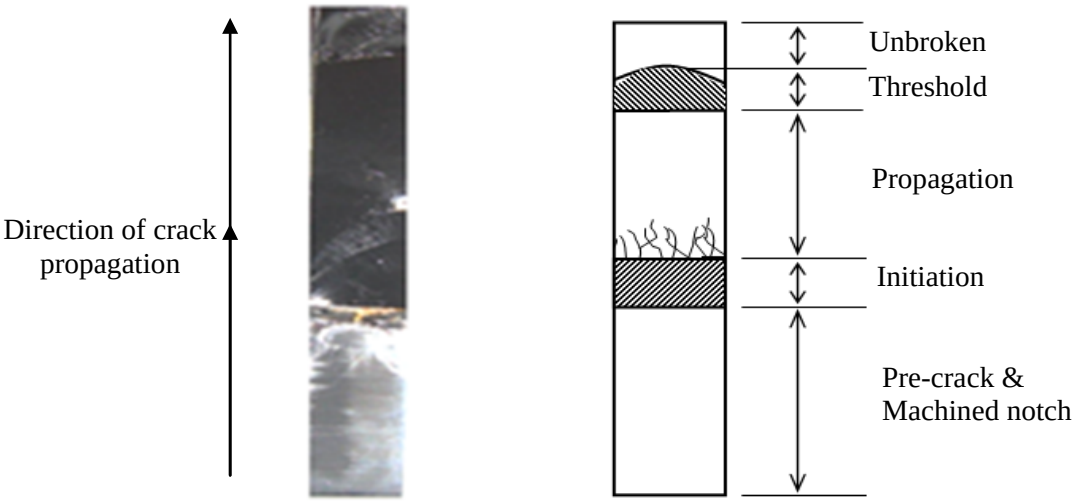


Figure 7.6.3 Photograph and schematic of the fracture surface of tested compact tension specimen after fatigue failure.

The FEG-SEM images show the topography of the different regions of fracture surfaces after fatigue failure, as shown in Figure 7.6.4 (the direction of crack propagation is from the right to the left). The crack initiation region is similar to the fracture surface after the SENB tests, as shown in Figure 7.4.3 (c) for the nanocomposite with the nanotube loading of 0.2 wt%, which showed several river lines. A relatively featureless glassy and smooth surface is seen in both the propagation and threshold regions.

Again, the dispersion of the multi-walled carbon nanotubes was examined from these FEG-SEM images of the fracture surface of the MWCNT-modified epoxy polymer, as shown in Figure 7.6.4. Several nanotube agglomerates were readily found on the fracture surfaces. The relationship between the crack propagation and the agglomeration of nanotubes was also found on the fatigue fracture surfaces. Mostly in the initiation and threshold region, many of the river lines start at nanotube agglomerates or nanotube-rich areas. The toughening mechanisms can also be indentified from these FEG-SEM images, as discussed below.

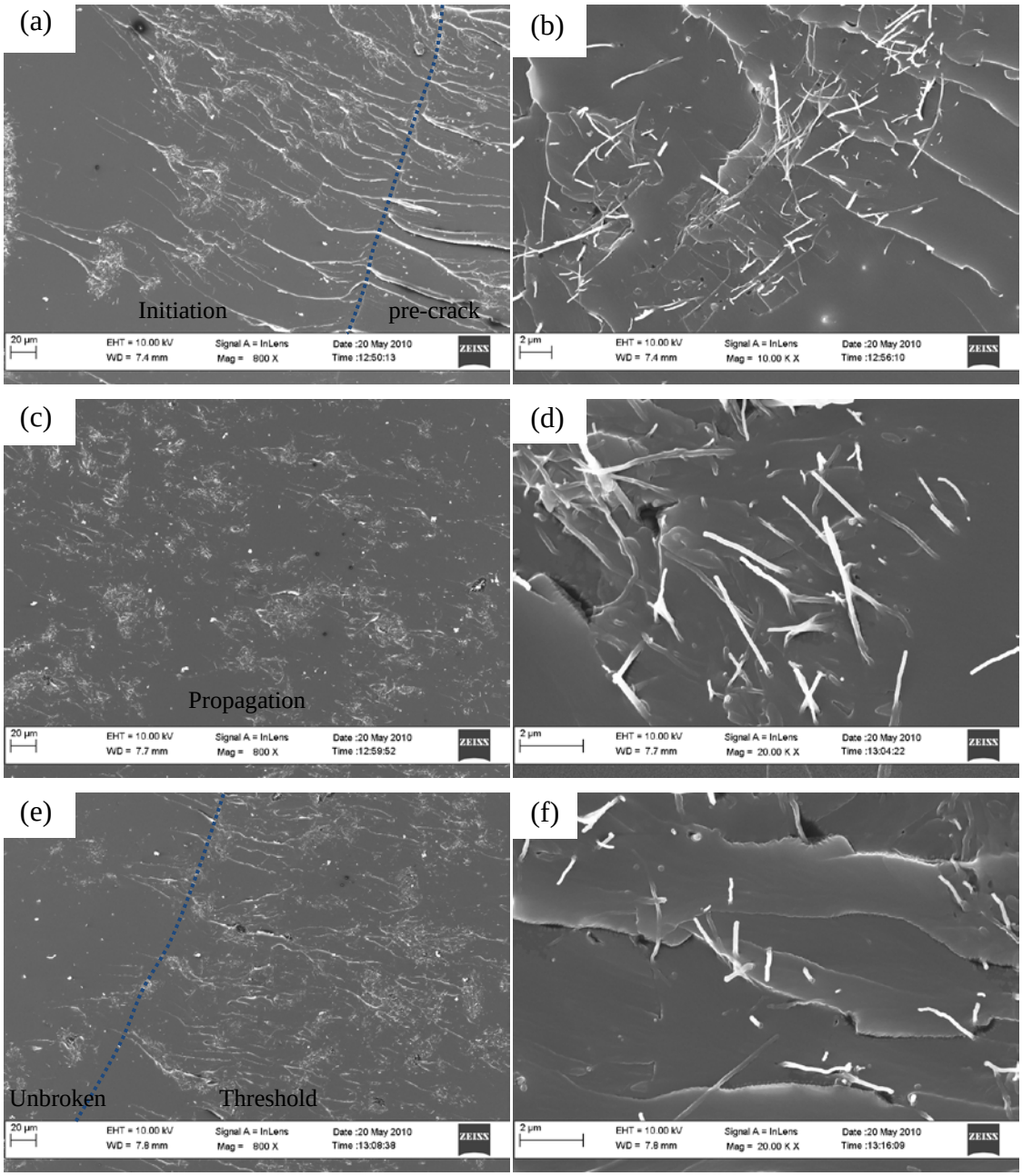


Figure 7.6.4 FEG-SEM images of the fatigue fracture surfaces of the nanocomposite containing 0.2 wt% MWCNTs, showing the regions of (a,b) crack initiation, (c,d) propagation, (e,f) threshold. (Crack growth is from the right to the left).

7.6.3 Fatigue Toughening Mechanisms

From the high magnification FEG-SEM images of the fracture surfaces, as shown in Figure 7.6.4 (b, d, f), clear evidence of the nanotube pull-out mechanism was found on the fracture surfaces of all the fatigue crack growth regions (initiation, propagation and threshold regions). In the crack initiation and crack propagation regions, the nanotube pull-out length was measured to be 7.35 μm with a standard deviation of 2.89 μm, which is very similar to that measured in the quasi-static fracture behaviour (pull-out length = 7.82 μm, discussed in Section 7.4.3). However, a relatively short nanotube pull-out length of 5.98 μm was measured in the threshold region, with a wide range between 3.94 μm to 11.83 μm. This can be explained using a schematic model of crack propagation during fatigue failure, as shown in Figure 7.6.5. The crack opening displacement at the threshold is much smaller than that in the initiation and propagation regions. This results in a relatively short nanotube pull-out length as presented at the threshold. The crack tip opening displacement (CTOD) can be calculated using

$$\delta_{\mathrm{CTOD}} = \frac{G_{\mathrm{Ic}}}{\sigma_{\mathrm{y}}} \tag{7.1}$$

where G_{Ic} is the fracture energy and σ_{y} is the yield stress.

The calculated value of crack tip opening displacement, δ_{CTOD}, shows that the value of CTOD in the threshold region is much smaller than the initiation region. For example, the value of CTOD (using the value of G_{max} from fatigue tests to be G_{Ic} in Equation 7.1) of 0.53 μm and 1.01μm was calculated in the threshold region and initiation region, respectively, for the 0.2 wt% nanotube nanocomposite. The relatively small value of CTOD in the threshold region may lead to a relatively short nanotube pull-out length observed.

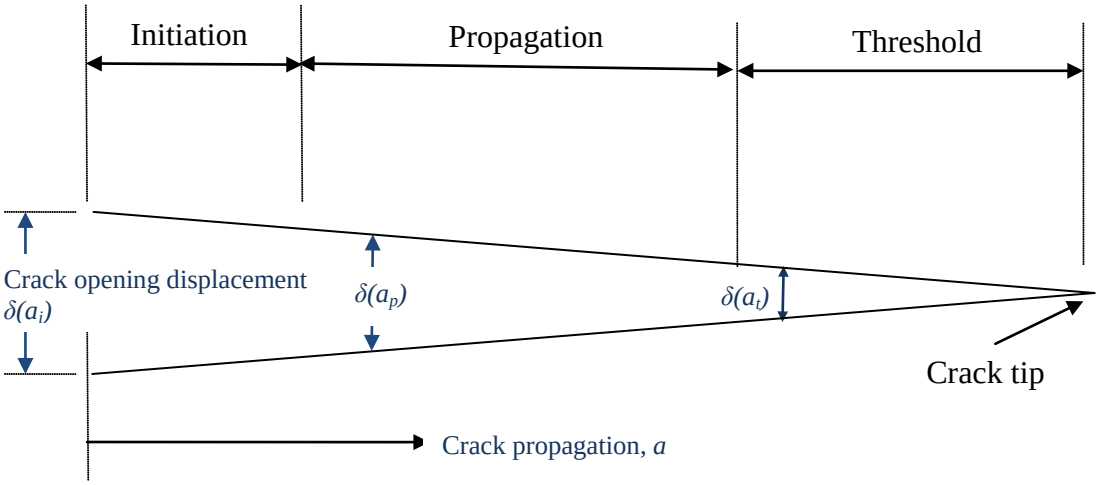


Figure 7.6.5 A schematic fatigue crack.

Following the debonding between the carbon nanotubes and the epoxy matrix, the matrix deformation leads to subsequent plastic void growth, as shown in Figure 7.6.6. The voids in all the fatigue regions had an average diameter of 152 nm, around a quarter bigger than the nanotube diameter of 120 nm. It is worth mentioning that more voids associated with nanotube debonding can be observed in the threshold region than in the initiation and propagation regions. At the threshold region, around 14% of nanotubes were debonded from the matrix and then formed plastic void growth. Only 8% of added nanotubes generated plastic void growth in the initiation and propagation regions. This phenomenon is because of the relatively very slow crack propagation rate at the threshold. The slow crack growth rate at the threshold region allows a high level of plastic deformation in the polymer, compared to the crack propagation with a relatively high crack growth rate at the initiation and propagation regions. It is well known that, under a loading with a high displacement rate, epoxy polymers fracture in a brittle manner, with little plastic deformation. For example, Gilat et al. [140] reported the effect of strain rate on the tensile properties of epoxy polymers, and showed that the ductile response only occurs at a low test rate, because the effect of stress relaxation and plastic deformation in the epoxy resin that can occur in the tensile loading with the relatively long time scale of a low test rate. Furthermore, during the tensile testing, the nonlinearity (plastic deformation) and the maximum stress of the epoxy polymer decrease with decreasing strain rate, as shown in Figure 7.6.7. Therefore, the mechanism of plastic void growth after the occurrence of debonding between the

nanotubes and the matrix is easier to form in the threshold region, where the crack growth rate is relatively slow.

Nanotube pull-out and plastic void growth were recognised to be the main fatigue toughening mechanisms responsible for the increase in the fatigue performance. These fatigue toughening mechanisms are summarised in Table 7.6.2.

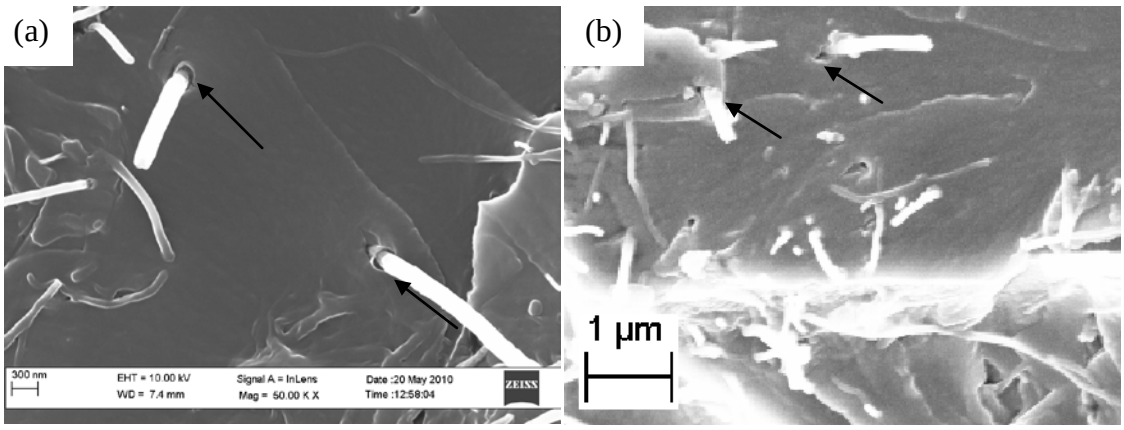


Figure 7.6.6 FEG-SEM images showing voids around nanotubes in the threshold region of the fatigue fracture surface of the nanocomposite containing (a) 0.2wt% MWCNTs, (b) 0.5 wt% MWCNTs.

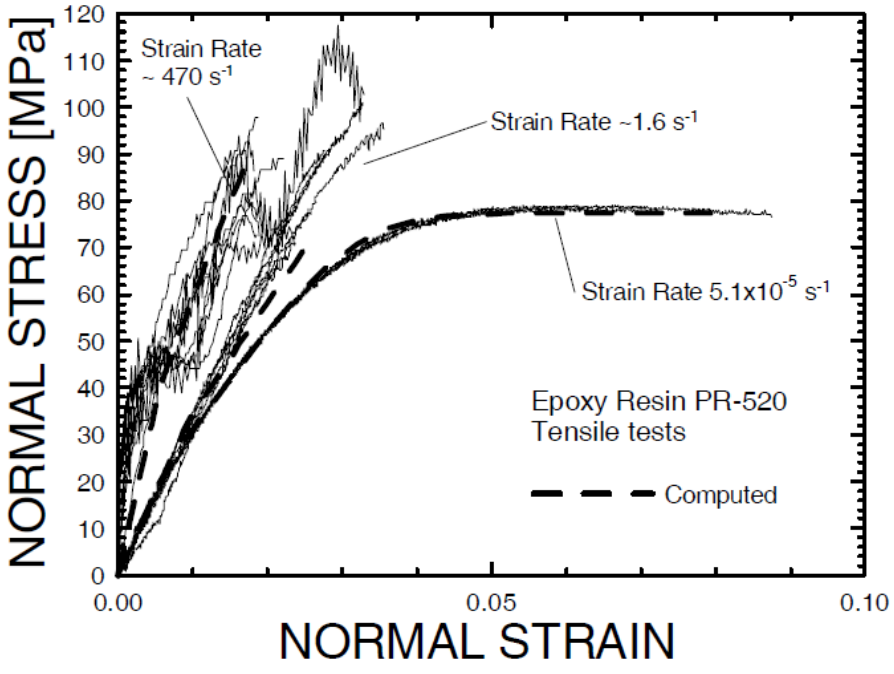


Figure 7.6.7 Tensile stress-strain curve for epoxy at different stain rates [140].

Table 7.6.2 The summary of the toughening mechanisms of the MWCTs-modified epoxy polymers with 0.2 wt% nanotubes.

Fatigue crack growth region	**Toughening mechanism**	
Crack initiation (fast crack)	Nanotube pull-out	Pulled-out length: 7.48 μm
		Amount: 100%
	Plastic void growth	Void diameter: 149 nm
		Amount: 8%
Crack propagation (linear)	Nanotube pull-out	Pulled-out length: 7.22 μm
		Amount: 100%
	Plastic void growth	Void diameter: 151 nm
		Amount: 8%
Threshold (stop propagating)	Nanotube pull-out	Pulled-out length: 5.98 μm
		Amount: 100%
	Plastic void growth	Void diameter: 157 nm
		Amount: 14%

A well-known toughening mechanism, the nanotube bridging mechanism is often referred to the main toughening mechanism in nanotube-modified polymeric materials. Once the nanotubes bridge, the nanotubes are stretched across the crack and extended by crack growth, as both ends of the nanotube are bonded well and inserted into the fracture surfaces. In fact, the bridging-like mechanism observed from the sideview of the tip of the wedged-open fatigue crack using SEM at a low working distance with high current, as shown in Figure 7.6.8, is considered to be the efficient nanotube pull-out mechanism. This apparent bridging is the result of the pulled out nanotube not being completely disengaged from the epoxy matrix yet, as mentioned in Section 7.4.3, due to the small crack opening displacement.

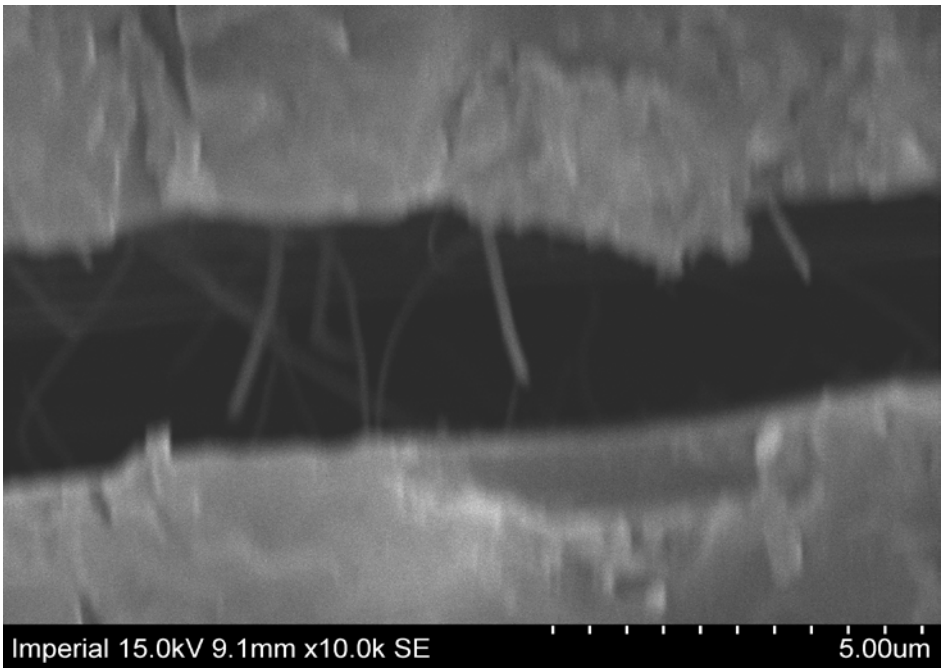


Figure 7.6.8 SEM image showing CNT bridging and pullout of the fatigue crack in the modified polymer with 0.2 wt% nanotubes.

7.7 Relationship between Static and Fatigue Results

Figure 7.7.1 shows the relationship between the maximum strain energy release rate in the threshold region, G_{th}, and the quasi-static fracture energy, G_{Ic}. In this figure, it can be clearly seen that the addition of the multi-walled carbon nanotubes at 0.5 wt% brought a significant increase in the maximum fracture energy at the fatigue threshold region and in the fracture energy. As the MWCNT content is increased from 0.1 wt% to 0.5 wt%, both of the measured values from fracture testing under static and dynamic loading increase. There is an approximately linear relationship between the measured values of G_{th} and G_{Ic}.

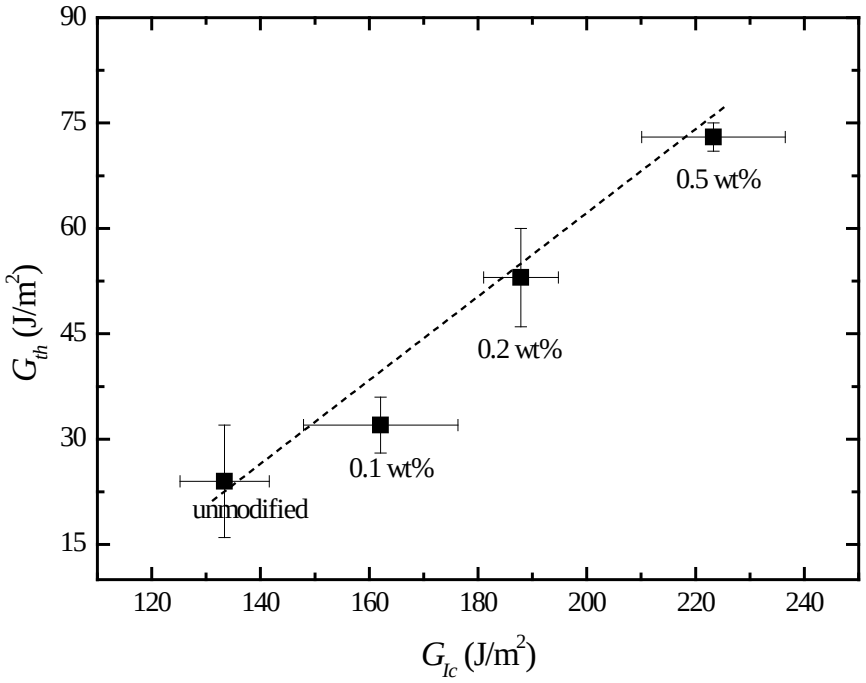


Figure 7.7.1 The relationship between the maximum fracture energy at the threshold region and the quasi-static fracture energy of the MWCNT-modified nanocomposites.

In order to quantify the improvement in the quasi-static fracture behaviour (fracture toughness and fracture energy) and the fatigue performance caused by the inclusion of the multi-walled carbon nanotubes with the thermosetting epoxy polymer, the measured values of G_{Ic} and G_{th} for each formulation were normalised (the measured values of the nanotube-modified polymers divided by the measured value of the

unmodified polymer), as shown in Figure 7.7.2. The normalised values of G_{Ic} and G_{th} reached a maximum for the polymer-based nanocomposites with 0.5 wt% MWCNTs, and both of these improvements were dependent on the weight fraction of the MWCNTs. However, the improvement of the fatigue performance of the nanotube-modified polymer is more substantial than using the carbon nanotubes to improve the static fracture behaviour of the epoxy polymer.

To explain this difference, a model based on the nanotube pull-out mechanism was developed [73, 135], as shown in Figure 7.7.3. The demonstration of the toughening mechanism of nanotube pull-out by scanning electron microscopy observation in sideview along the crack showed that the advancing crack was efficiently arrested before the carbon nanotubes were pulled out completely from the epoxy matrix. As the loading is increased, the crack opening displacement increased. The nanotubes were pulled out from the fracture surface completely when the crack opening displacement was larger than the nanotube pulled-out length, and these nanotubes stopped suppressing crack propagation. According to the schematic model in Figure 7.7.3, the amount of nanotube involved in the pull-out mechanism is strongly dependant on the applied stress as this correlates closely with the crack opening displacement; a low applied stress causes a small crack opening displacement, so a greater number of nanotubes are involved, thus generating a high level of the pull-out mechanism.

The value of fracture energy, G_{Ic}, measured at quasi-static tests is much higher than the measued G_{th} from the fatigue tests. This indicates that the applied stress in the quasi-static tests is higher than the applied stress in fatigue tests. Therefore, the increased fracture energy involved a high applied stress and a low level of nanotube pull-out, and consequently, the effect of the addition of the multi-walled carbon nanotubes on the toughening performance was not so great, compared with the improvement on the fatigue performance caused by the addition of the multi-walled carbon nanotubes to the epoxy polymer.

In Figure 7.7.3, it is clearly illustrated that higher applied stress caused a larger crack opening displacement and hence a shorter zone of efficient nanotube pull-out. This can be checked by considering the crack tip opening displacement (CTOD), the value of CTOD in the quasi-static fracture process was increased from 1.38 μm for the

unmodified epoxy to 2.54 μm for 0.5 wt% nanotube-modified epoxy. These values are much higher than the value of CTOD at the fatigue threshold region (the CTOD at the fatigue threshold is 0.41 μm for the unmodified polymer, and 0.71 μm for the nanotube-modified polymer with 0.5 wt% MWCNTs). From the energy dissipation point of view, cyclic loading applied for fatigue tests can generate more energy dissipation from the interface friction between the nanotubes and the matrix. The outstanding strength of carbon nanotubes allows the efficient pulled out nanotubes to act like a piston, in which a high level of energy is absorbed by the friction, and consequently the fatigue performance will improve.

It is worth mentioning that the FEG-SEM observation on the fracture surfaces of the tested SENB (quasi-static tests) and tested CT (dynamic tests) specimens showed that a relatively higher level of plastic void growth mechanism occurred in the fatigue tests than in the quasi-static tests. Although the measured efficient nanotube pull-out length of 5.98 μm observed on fracture surfaces after fatigue failure is slightly shorter than that observed in the SENB tests, around double the amount of plastic void growth mechanism was attained in the fatigue tests (14%) than that in the SENB tests (8%). This may be why the modification of the multi-walled carbon nanotubes is more effective at improving the fatigue performance than the fracture energy. The effect of the contribution of the pull-out and plastic void growth mechanisms on the toughening mechanism will be investigated via a modelling analysis in Chapter 9.

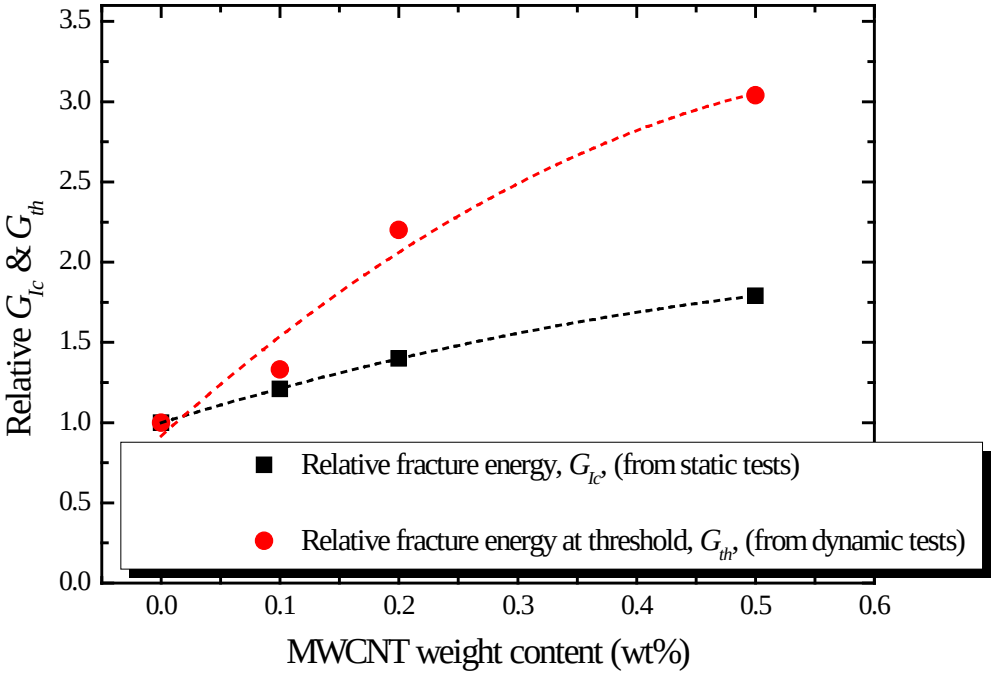
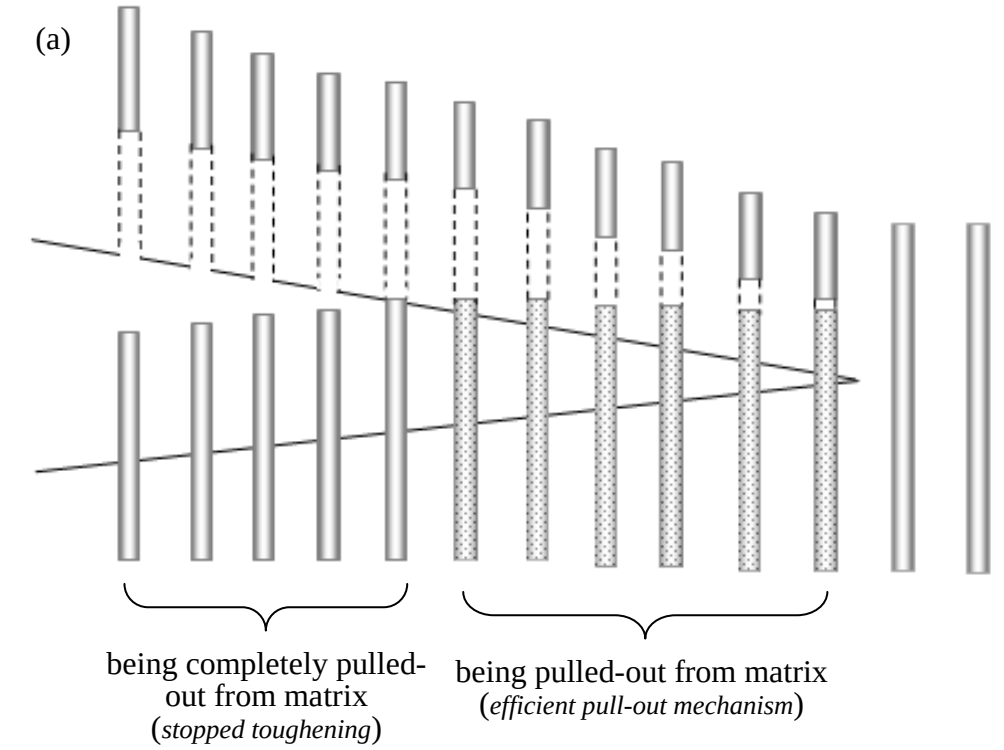


Figure 7.7.2 The relative fracture energy and relative threshold fracture energy versus the weight percent of the MWCNTs.



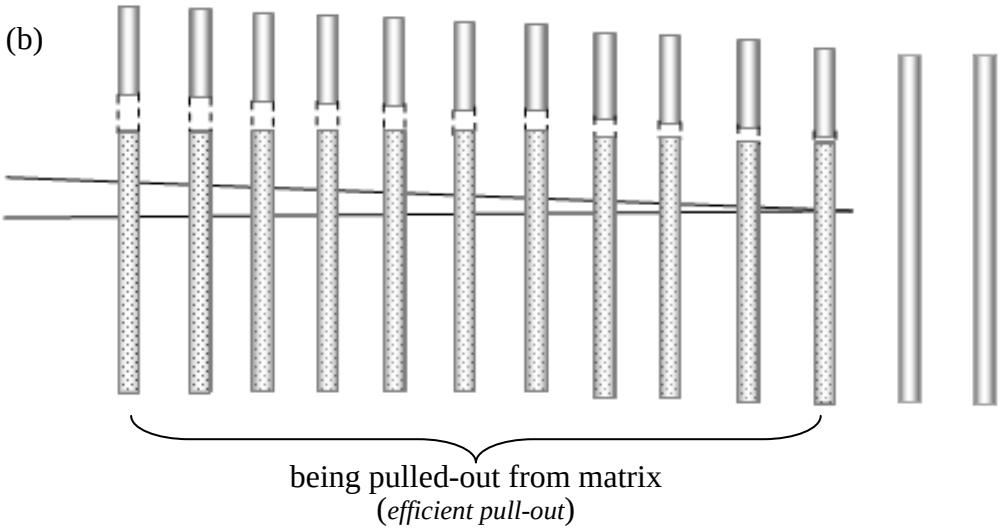


Figure 7.7.3 The schematic illustration of the nanotube pull-out mechanism in different level of applied stress, (a) at a high applied stress, (b) at a low applied stress.

7.8 Nanotube Size Effect on the Toughening Performance and Fatigue Performance

7.8.1 Introduction

According to the experimental results above, the addition of the multi-walled carbon nanotubes led to an improvement in the stiffness and toughness of the polymer-based composites, and could significantly suppress fatigue crack growth. However, the effect of the nanotube dimensions, such as diameter, length and straightness, on the mechanical properties and fatigue performance of the nanocomposites with these nano-sized reinforcements is not clear. In this Section, two different types of nanotubes were used to form nanotube-modified epoxy polymers, which were then characterised. In addition to the above-mentioned standard multi-walled carbon nanotubes with an initial average length and diameter of 140 μm and 120 nm respectively, low quality aligned multi-walled carbon nanotubes synthesised by the chemical vapour deposition (CVD) method were used to form the modified nanocomposites. All the sample preparation and testing conditions for these modified epoxy polymers with different nanotube additives were kept the same, i.e. the only variable was type of multi-walled carbon nanotubes used.

7.8.2 Morphology

Figure 7.8.1 shows the morphology of the low quality MWCNTs before being mixed with the epoxy resin. These had an average length of 32 μm and an average diameter of 180 nm, although a wide range of diameters between 120 nm to 235 nm were measured. In addition, these low quality nanotubes did not grow straight, and were slightly entangled. Here, the concentration of both nanotubes was only 0.2 wt% due to the low mass of the low quality nanotubes obtained. Table 7.8.1 summarises the dimensions of the two types of the nanotubes used.

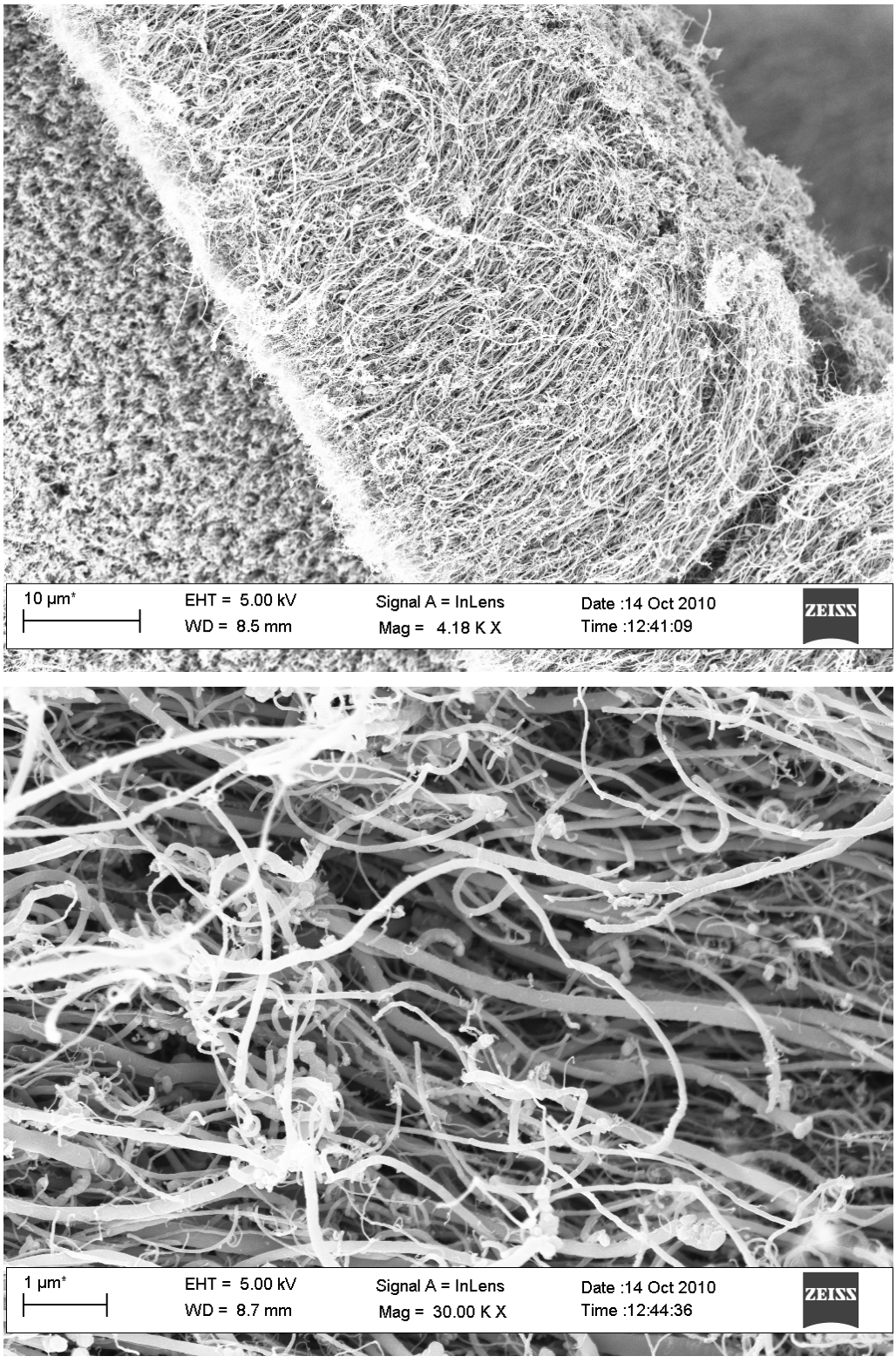
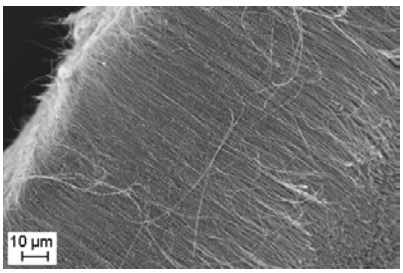
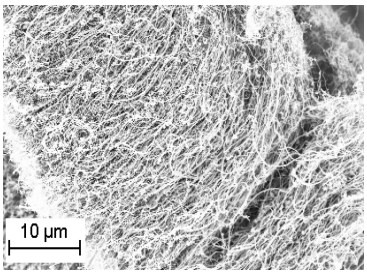
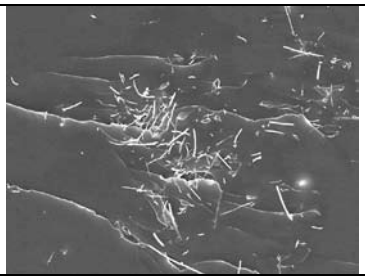
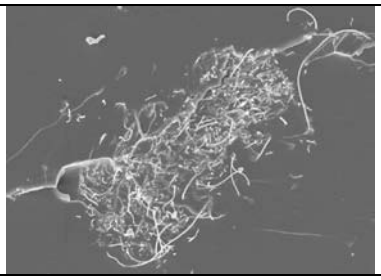


Figure 7.8.1 The FEG-SEM images showing the as-received appearance of the low quality multi-walled carbon nanotubes.

Table 7.8.1 The dimensions and morphology of standard nanotubes and low quality nanotubes, and the characteristics of their nanocomposites.

	Standard MWCNTs	**Low quality** MWCNTs
Nanotubes		
length (μm)	140	32
diameter (nm)	120	180
aspect ratio	1170	180
alignment	aligned well	slightly curled
FEG-SEM image *(before blending with epoxy)*		
Nanocomposites		
Weight percent	0.2 wt%	0.2 wt%
Young's modulus, E (GPa)	3.11	2.94
Fracture toughness, K_{Ic} (MPa $m^{1/2}$)	0.88	0.69
Fracture energy, G_{Ic} (J/m^2)	188	152
FEG-SEM image *(fracture surface)*		
Dispersion	slight agglomeration but nanotubes were wetted well	agglomeration with entangled nanotubes
Toughening mechanism	Pull-out (100%) *Pull-out length: 7.82 μm*	Pull-out (72%) *Pull-out length: 1.78 μm*
	plastic void growth *8% voids*	plastic void growth *3% voids*
Maximum threshold fracture energy, G_{th} (J/m^2)	53	28
Fatigue toughening mechanism	Pull-out (100%) *Pull-out length: 5.98 μm at threshold*	Pull-out (72%) *Pull-out length: 1.35μm at threshold*
	plastic void growth *14% voids at threshold*	plastic void growth *4% voids at threshold*
		Crack deflection by agglomerates

Atomic force microscopy was used to examine the dispersion of the low quality multi-walled carbon nanotubes in the cured bulk samples, as shown in Figure 7.8.2. Table 7.8.2 clearly illustrates the size effect of different nanotubes on the material properties under quasi-static and dynamic loading, as well as the nanotube dispersion in bulk samples. This AFM image clearly shows that the nanotubes were agglomerated, and several nanotube agglomerates were discovered in the modified samples. The size of the low quality nanotube agglomerates was measured to be around 0.4 μm square, which is slightly larger than the agglomerated standard nanotubes. Further investigation into the nanotube dispersion was carried out by the FEG-SEM observation of the fracture surfaces, will be discussed in Section 7.8.4.

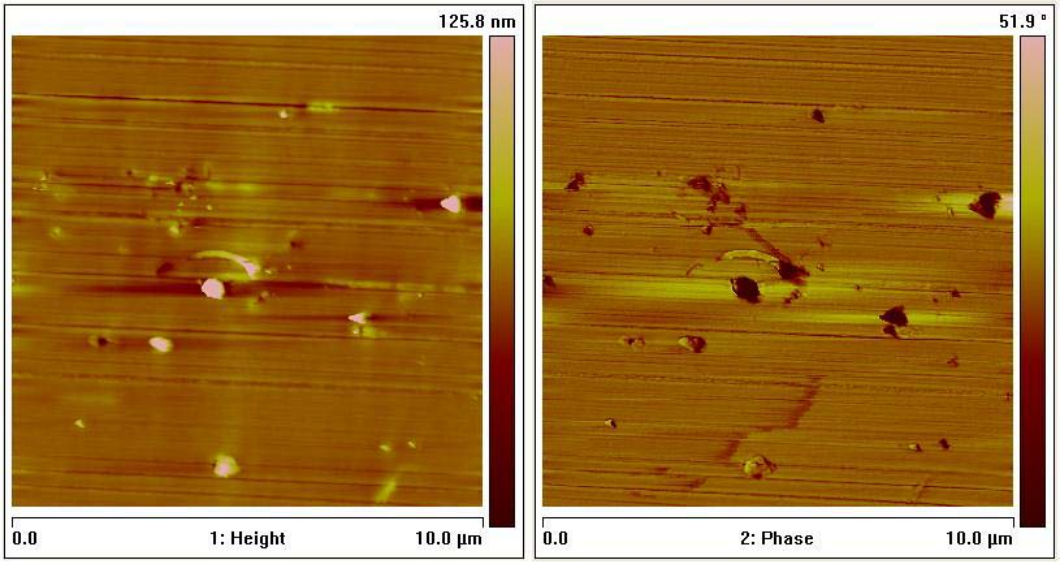


Figure 7.8.2 AFM images of the morphology of the modified epoxy polymer with the low quality multi-walled carbon nanotubes at 0.2 wt%.

7.8.3 Mechanical Properties and Fracture Behaviour

For the tensile testing results, the Young's modulus of the standard MWCNT and low-quality MWCNT-modified epoxy polymer was measured to be 3.11 GPa and 2.94 GPa, respectively. The modified epoxy polymer using the standard nanotubes with long length and small diameter (i.e. a relatively high value of aspect ratio) had a higher modulus. With a long length of 140 μm, the standard multi-walled carbon nanotubes can provide sufficient length to transfer a high level of the load as the modified polymer is subjected to loading, as a result, a higher value of the stiffness was measured. The critical fibre length, l_c, can be calculated from composite theory [18] using

$$l_c = \frac{\sigma_{cnt}}{2\tau_i} d \tag{7.2}$$

where l_c is the critical length, σ_{cnt} is the failure stress of nanotube (36 GPa was used in this study [141]), τ_i is the interfacial shear stress between the nanotubes and matrix (47 MPa was used in this study [142]), and d is the diameter of nanotubes.

The calculated critical fibre length of around 45 μm for the standard nanotubes is much shorter than the standard nanotube length (140 μm). However, the length of low quality nanotubes (with an average length of 32 μm) used is shorter than the critical fibre length of 68 μm, indicating that the low quality nanotubes cannot raise the stiffness and failure stress of the composite. This is the reason why the addition of the standard nanotubes led to the increase in the Young's modulus. Besides, the quality of nanotube dispersion strongly concerns the material properties of nanotube-reinforced polymer composites. The modified epoxy polymer with the low quality nanotubes had a low level of dispersion, hence a reduction in the increased stiffness by the nanotube modification was found in the low quality nanotube-modified materials.

The fracture behaviour of the nanotube-modified polymers was investigated by SENB tests, and is summarised in Table 7.8.1. The addition of the low quality multi-walled carbon nanotubes led to a slight increase in the fracture energy from 133 J/m^2 for the neat epoxy polymer to 152 J/m^2. There was no clear improvement in the fracture toughness, K_{Ic}, as a value of 0.69 MPa m$^{1/2}$ was measured for the low quality nanotube-

modified epoxy, which is the same as the unmodified epoxy polymer. This shows that the addition of the low quality nanotubes with a low aspect ratio of 180 did not improve the toughness of the epoxy polymer. In contrast, the addition of the standard multi-walled carbon nanotubes gave rise to a significant increase in the fracture toughness and the fracture energy of the epoxy. As discussed above, there was around a 40% increase in the fracture energy from blending the standard nanotubes at 0.2 wt% with the epoxy polymer, compared with the unmodified polymer.

The dispersion of the low quality multi-walled carbon nanotubes used in the toughening modification was examined by the FEG-SEM observation of the fracture surfaces, will be discussed in the following Section.

7.8.4 Fractography and Toughening Mechanisms

The FEG-SEM images of the fracture surfaces for the nanocomposite with the low quality multi-walled carbon nanotubes are shown in Figure 7.8.3. Evidence of the nanotube pull-out mechanism was found on the fracture surfaces, as shown in Figure 7.8.3 (c). A mean pull-out length of 1.78 ±0.28 μm was measured. This is much shorter than the pull-out length of the standard nanotubes (7.82 μm). Besides, a relatively small amount of the nanotubes operating the pull-out mechanism in the polymer with 0.2 wt% of the low quality nanotubes, compared with the nanocomposites containing 0.2 wt% standard nanotubes (100% nanotube pull-out). It is believed that the efficient nanotube length is a key factor for the nanotube pull-out mechanism if the nanotubes are well dispersed. Thus, longer nanotubes are much better as the toughener for a polymer-based composite.

Clear evidence of the plastic void growth was found on the fracture surfaces of the nanocomposites with the standard carbon nanotubes, and was considered to be the main toughening mechanism. However, a small amount (3%) of the low quality nanotubes showed with void growth present on the fracture surfaces. This may be why

the addition of the low quality nanotubes did not improve the toughening performance of the epoxy polymer as expected.

The dispersion of the nanotubes was examined from these FEG-SEM images. Many nanotube agglomerates ware readily found on the fracture surfaces of the sample containing the low quality nanotubes, as can be seen in Figure 7.8.3 (a, b). The measured size of the agglomerates is around 20 μm square, which is bigger than that observed in the nanocomposites modified with the standard carbon nanotubes. At a high magnification, see Figure 7.8.3 (d), the low quality nanotubes in the agglomerate are seriously entangled due to their curled appearance, indicating that the entangled nanotubes after CVD process cannot be distributed completely via sonication during the sample preparation. Moreover, the epoxy matrix did not infuse into the nanotube agglomerates well. Figure 7.8.3 (d) shows the absence of polymeric matrix in the nanotube-rich area, where several vacant spaces were found. Hernandex-Perez et al [143] investigated the nanotube size effect on the mechanical properties using nanotubes with various aspect ratios, and reported that the nanotubes with a low aspect ratio were easier to disperse but at the cost of less improvement in the material properties of composites, compared with the nanotubes with a high aspect ratio. However, in this study, the AFM and FEG-SEM observation showed that the use of the low quality nanotubes which have a low aspect ratio resulted in a reduction in the quality of the dispersion. This may be because the low quality nanotubes are curled and entangled initially, which results in difficulty in achieving good dispersion.

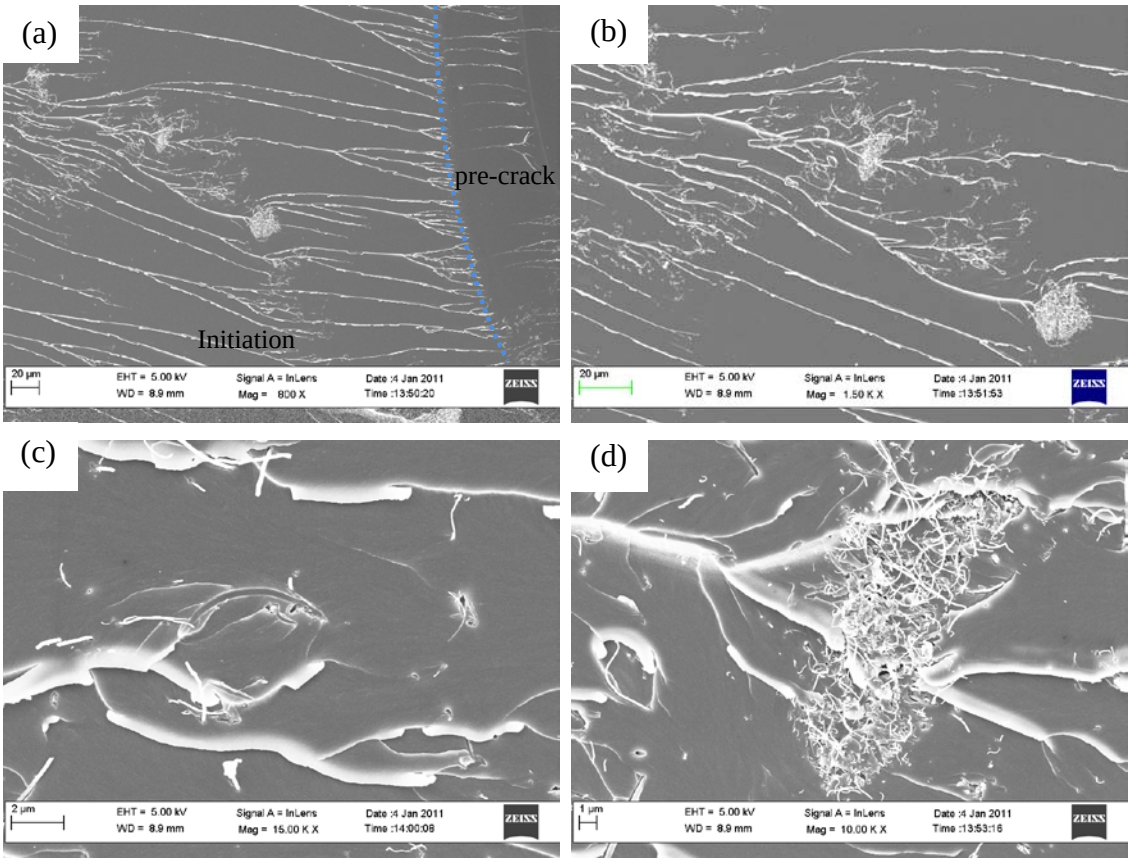


Figure 7.8.3 Field emission gun scanning electron microscopy (FEG-SEM) images of 0.2 wt% low quality MWCNTs sample, showing (a) the fracture surface at a low magnification, (b) the dispersion of the nanotubes, (c) the nanotube pull-out, (d) nanotube agglomerate.

7.8.5 Fracture Behaviour under Fatigue Loading Conditions

Fatigue tests were conducted to investigate the nanotube size effect on the fatigue behaviour of the polymer-based composite. Compact tension specimens used in the fatigue tests were cut from a 6 mm-thick plate, and then were tested under cyclic loading at 5 Hz. The fatigue data were analysed using the method described in Section 4.4.

Figure 7.8.4 presents the fatigue results of the crack growth rate, da/dN, against the maximum applied strain energy release rate, G_{max}. The maximum applied strain

energy release rate in the threshold region, G_{th}, of the low quality nanotube-modified epoxy samples was determined to be of 28 ±4 J/m^2. This is slightly higher than that of the pristine epoxy (24 J/m^2), but when the scatter in the data is considered, there is no significant difference. Indeed, it is far from the improvement on the measured G_{th} caused by the addition of the standard carbon nanotubes. The gradient of the linear Paris-law region for each formulation did not change by the different types of nanotube, all values being around 13.

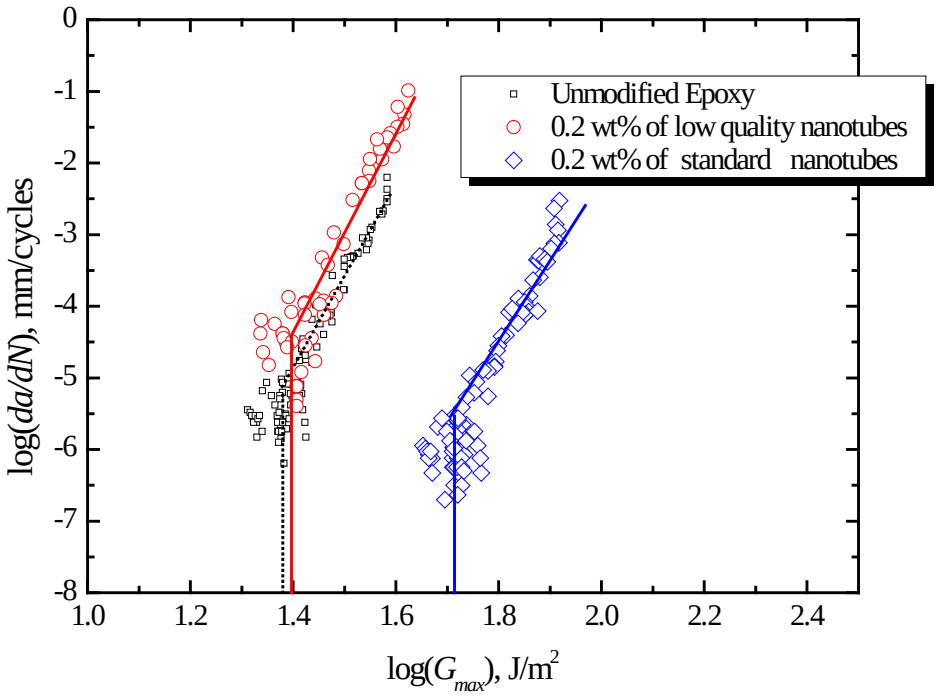


Figure 7.8.4 Rate of crack growth versus maximum applied strain energy release rate for unmodified epoxy and nanotube-modified epoxy with different types of multi-wall carbon nanotubes.

7.8.6 Fatigue Toughening Mechanisms

The fracture surfaces caused by fatigue failure were inspected by the FEG-SEM observation. Figure 7.8.5 shows the fractography of three regions after fatigue testing, and several pulled out nanotubes were found on the fracture surfaces of the low quality

carbon nanotube-modified epoxy polymer. The nanotube pull-out length had an average of 1.35 μm with a standard deviation of 0.52 μm. Not all the low quality nanotubes operated the nanotube pull-out mechanism, and a relatively low proportion of around 72% of the nanotubes pulled out from the epoxy matrix, compared with the standard nanotube-modified epoxies (100%).

The dispersion of the low quality carbon nanotubes was examined from the FEG-SEM images. At a low magnification, MWCNT agglomerates were readily found, and the size was measured to be 16 ~ 20 μm square, which is in an agreement with the observation of the fracture surfaces in the SENB tests.

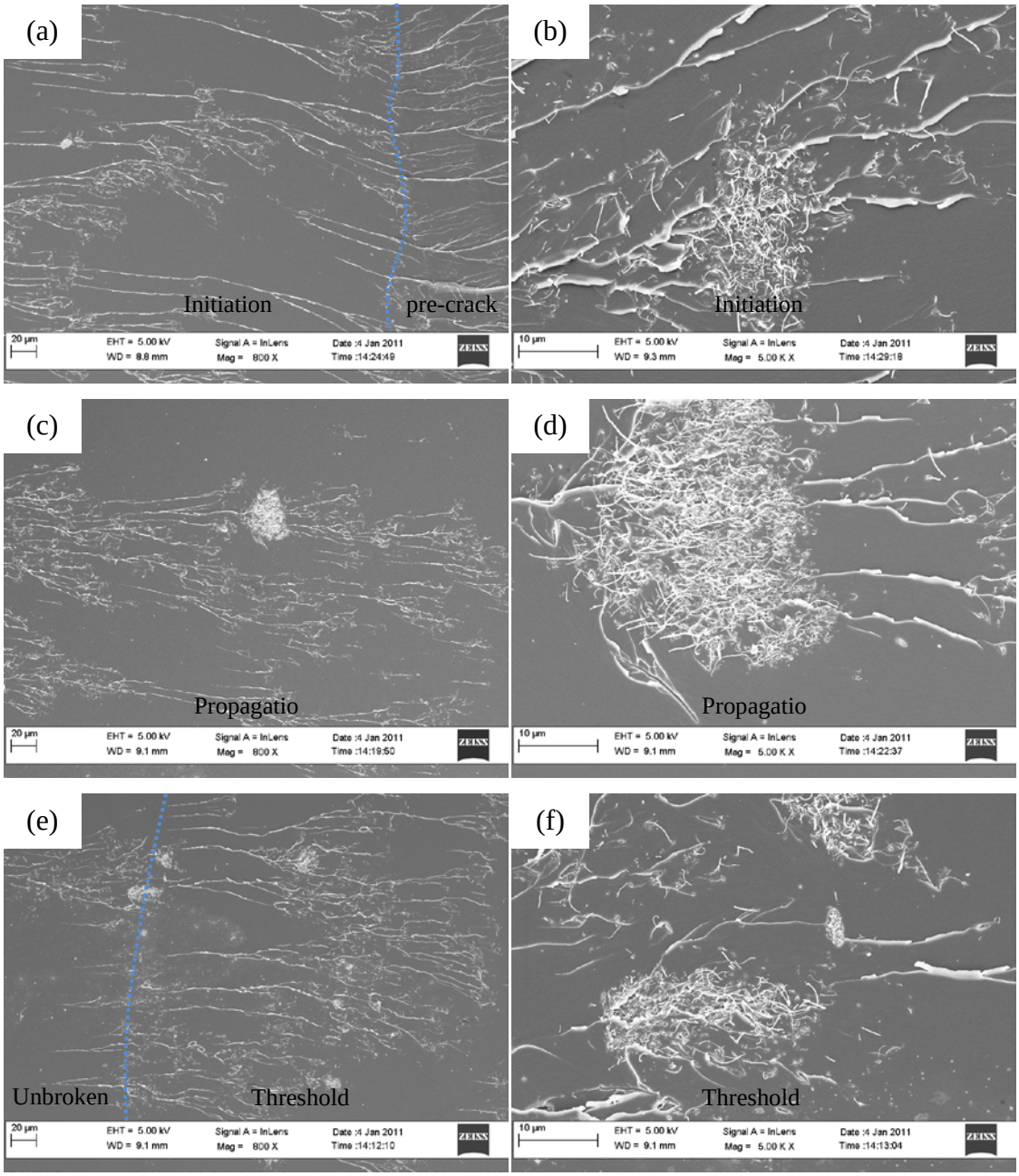


Figure 7.8.5 FEG-SEM images of the fatigue fracture surfaces of the nanocomposite containing 0.2wt% low quality MWCNTs, for the regions of (a,b) crack initiation, (c,d) propagation, (e,f) threshold. (the direction of fatigue crack growth is from right to left).

At high magnification, the void growth due to the debonding between the low quality nanotubes and the epoxy matrix can only be seen in the threshold region, as shown in Figure 7.8.6. Around 3% of the added nanotubes showed void growth, and the average diameter of the void was measured to be 198 nm, which is around 10% larger

than the original diameter of the nanotubes. Both of these are smaller than for the nanotube-modified epoxy polymer with the standard MWCNTs. For the standard nanotube-modified materials, void growth was observed in all fatigue crack growth regions, but less void growth was observed in the crack initiation and propagation regions than at the threshold.

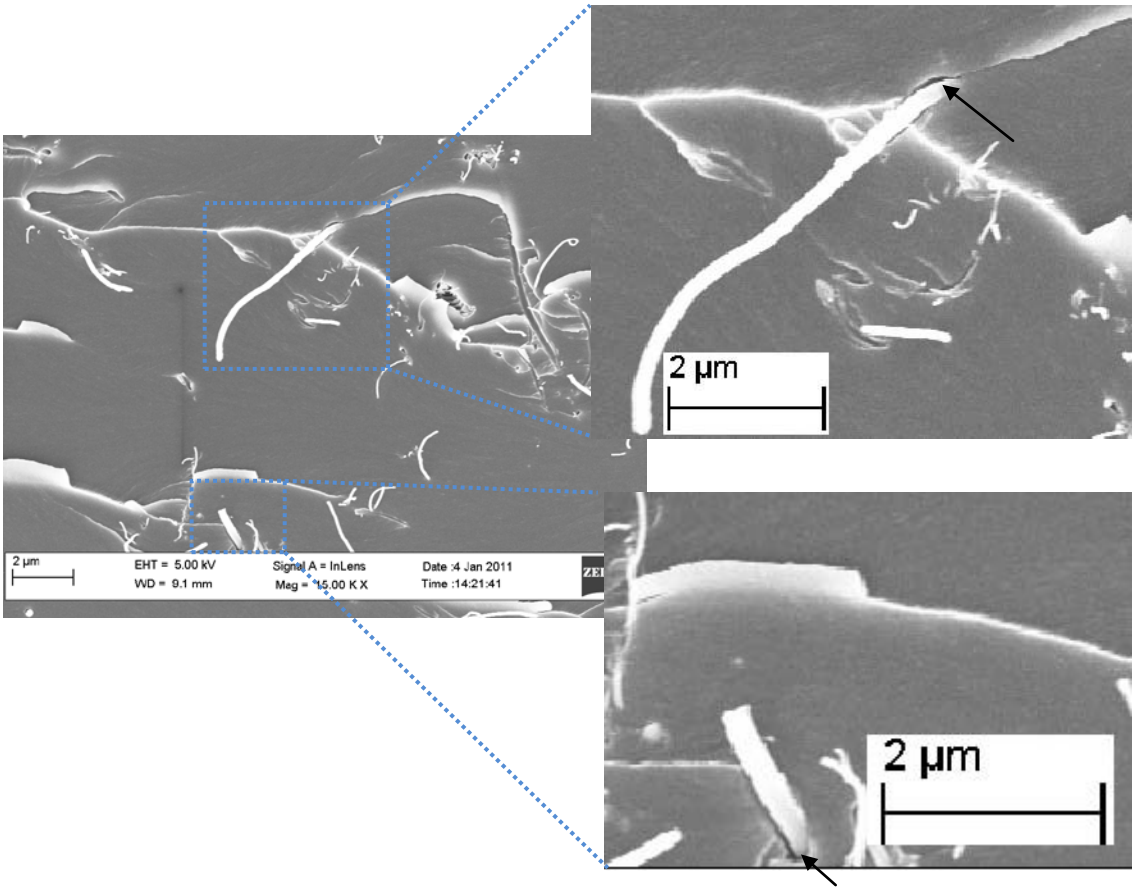


Figure 7.8.6 The FEG-SEM images of the nanotube-modified epoxy polymer by the low quality carbon nanotubes at 0.2 wt% showing the nanotube pull-out and plastic void growth (indicated with arrows).

Because of the lower wettability of the low quality nanotubes, the agglomerates cause crack deflection, as can be seen in Figure 7.8.7. Here the advancing crack is blunted and changed its direction as the crack tip came across the nanotube agglomerate.

Although all the above-mentioned toughening mechanisms benefit the fatigue performance, a short efficient nanotube pull-out length and a low amount nanotube with

void growth, as well as serious nanotube agglomerations, led to no significant improvement in the fatigue property using the low quality nanotubes.

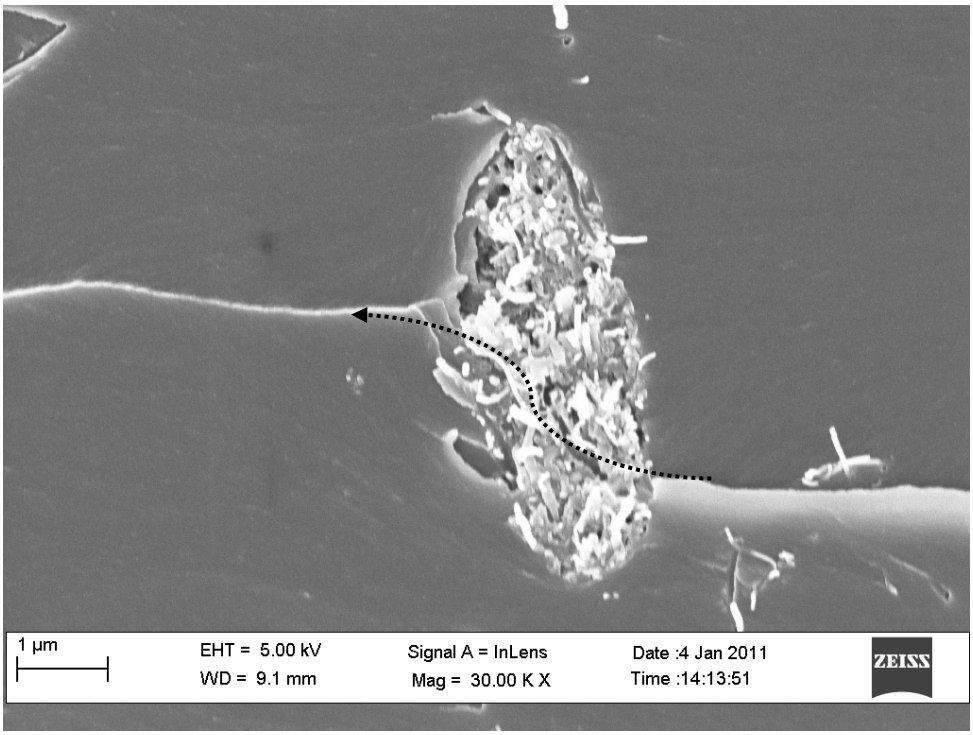


Figure 7.8.7 The FEG-SEM images of the nanotube-modified epoxy polymer with the low quality carbon nanotubes at 0.2 wt%, showing the crack deflection mechanism.

7.9 Greyscale Analysis

Greyscale analysis was used to examine the dispersion of the multi-walled carbon nanotubes. Although the nanotube dispersion has been investigated by AFM of the bulk sample and FEG-SEM of the fracture surfaces, the dispersion of the nanotubes was not graded quantitatively. In this section, the effect of the various nanotube loadings on the nanotube dispersion will be investigated, and the quantification of the nanotube dispersion will be attained using greyscale analysis.

7.9.1 Sample preparation

The samples used in the greyscale analysis were prepared from the cured polymers. A polished slice of the each formulation was bonded onto a glass microscope slide using a transparent glue, Araldite 2020 from Huntsman UK. The specimen was ground and polished to a thickness of approximately 70 μm, and then inspected using a transmission optical microscope (TOM). The TOM images, as shown in Figure 7.9.1, were imported into an image analysis program, Image J, and the greyscale histogram corresponding to each image was obtained. The mean and standard deviation of the greyscale values were also calculated.

The greyscale histogram shows the number of pixels for each shade of grey value, see Figure 7.9.1. For a sample containing well-dispersed carbon nanotubes, it would be expected that the image would be a uniform shade of grey, and the histogram would show single narrow peak on the middle, as shown in Figure 7.9.2 (mean value would be expected to be between 40-180, with a small value of the standard deviation).

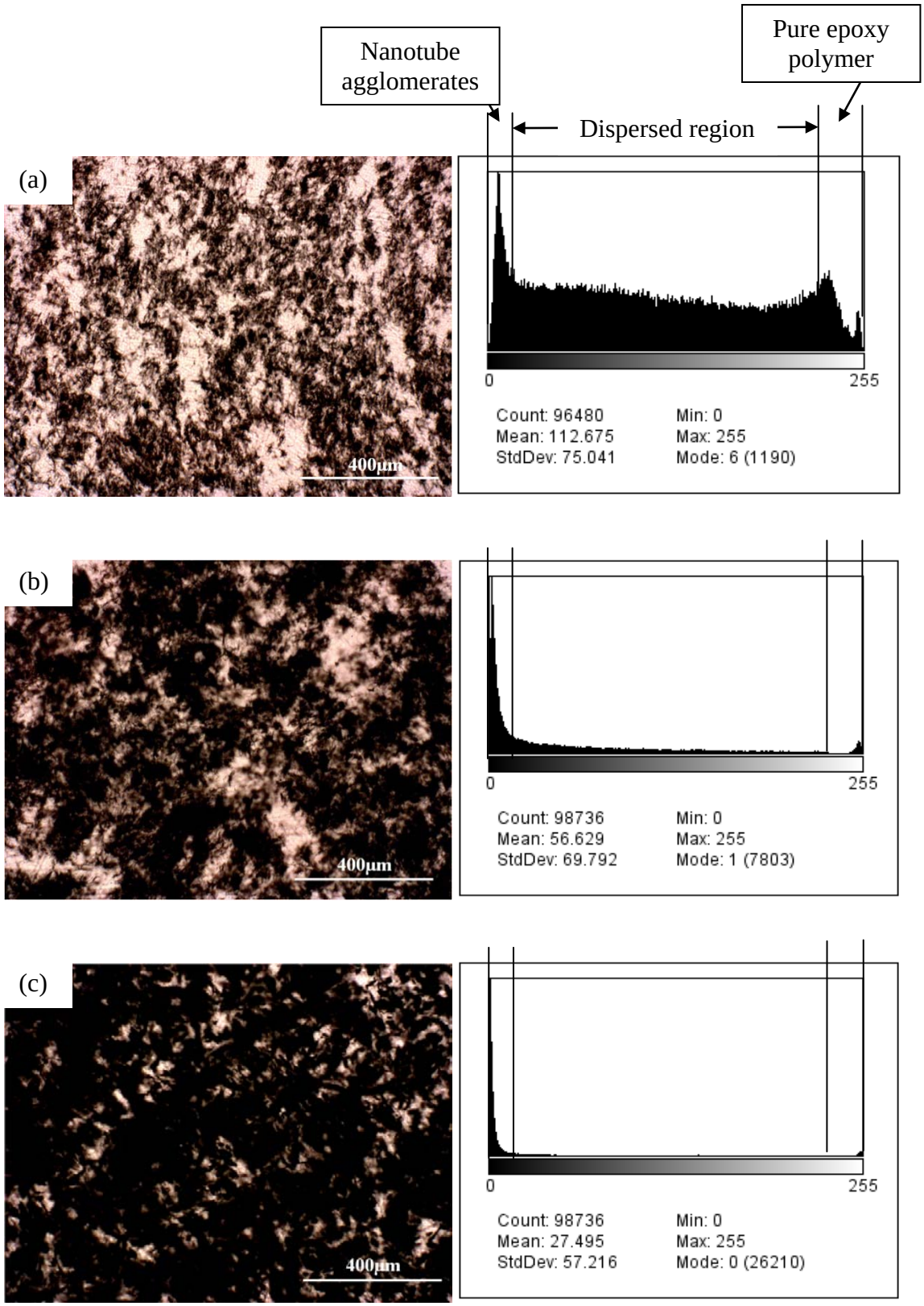


Figure 7.9.1 The TOM images and the greyscale histogram (umber of pixels versus grayscale value) of the nanotube-modified epoxy polymer with (a) 0.1wt% MWCNTs, (b) 0.2 wt% MWCNTs, (c) 0.5wt% MWCNTs.

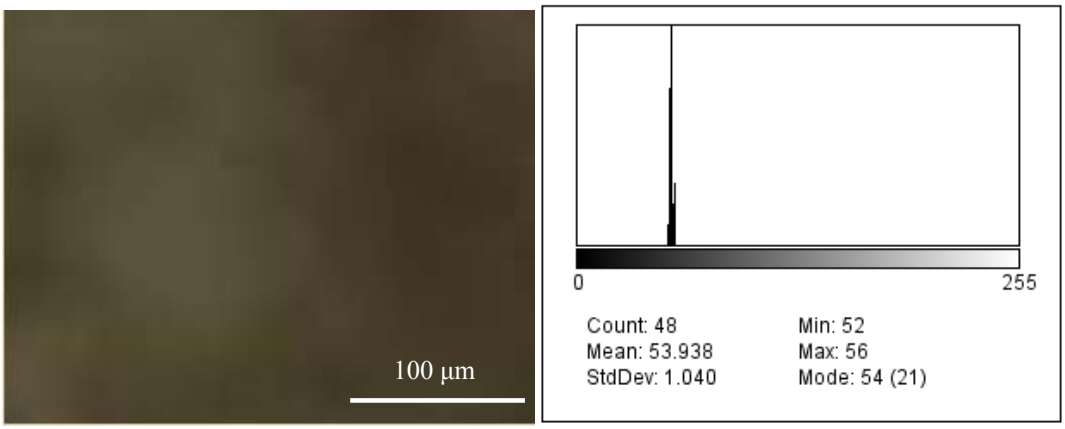


Figure 7.9.2 The TOM image and the greyscale histogram of the well-dispersed nanotube sample with 0.001 wt% (with a single and narrow peak, low value of the standard deviation and the mean lies in the centre of range).

7.9.2 Results

The greyscale analysis results are summarised in Table 7.9.1, and Figure 7.9.3 plotting the mean value of the histogram versus the nanotube loading. In Figure 7.9.1 (a), the sample of the 0.1 wt% nanotube-modified epoxy polymer shows a plateau in the histogram, which means the sample consists of a large amount of different levels of nanotube dispersion. The mean value lies in the middle range at 112, which indicates that the dispersion of the multi-walled carbon nanotubes is quite good, compared with the samples containing 0.2 wt% and 0.5 wt% nanotubes. As the nanotube loading was increased, the mean value of the histogram shifts toward lower values, which indicates serious nanotube agglomerates occurred in the cured samples, see Figure 7.9.3. Therefore, the minimum mean value of the histogram image was found for the modified polymer containing the highest nanotube loading of 0.5 wt%, indicating the multi-walled carbon nanotubes were highly agglomerated at this sample. Furthermore, in the histogram of the 0.5 wt% sample, no value lies in the dispersed region, which means there is a low level of nanotube dispersion, compared with the samples containing 0.1 wt% and 0.2 wt% nanotubes. Comparing the greyscale analysis results of the muli-walled carbon nanotube/epoxy in this study with the nanotube dispersion of nanotube-modified amine-cured epoxy [108], the modified amine-cured epoxy with 0.1 wt% and

0.5 wt% of nanotubes, as shown Figure 7.9.4, shows a plateau in the nanotube dispersion region of the histogram, indicating that both of these samples consist of a large amount of different levels of dispersion. In contrast, only the 0.1 wt% sample reveals a plateau in the histogram in this study. It can be concluded that the nanotube dispersion of the modified amine-cured epoxy polymer is better than the modified anhydride-cured epoxy polymers in this study. This is because the viscosity of the amine-cured epoxy is much higher than the anhydride-cured epoxy used in this study; high viscosity provides a high shear force in the mixture to break nanotube agglomerates during the mixing and reduces the rate of reagglomeration during curing.

Table 7.9.1 The summary of the greyscale analysis.

Weight percent of MWCNTs	Mean value of histogram image	Standard deviation of histogram image
0.1 wt%	112.7	75.0
0.2 wt%	56.2	69.8
0.5 wt%	27.5	67.2

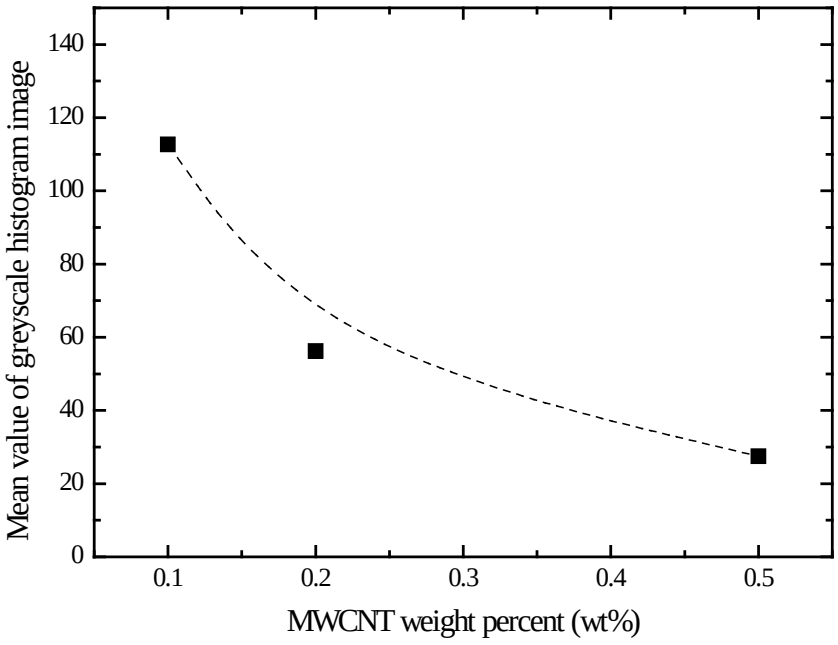
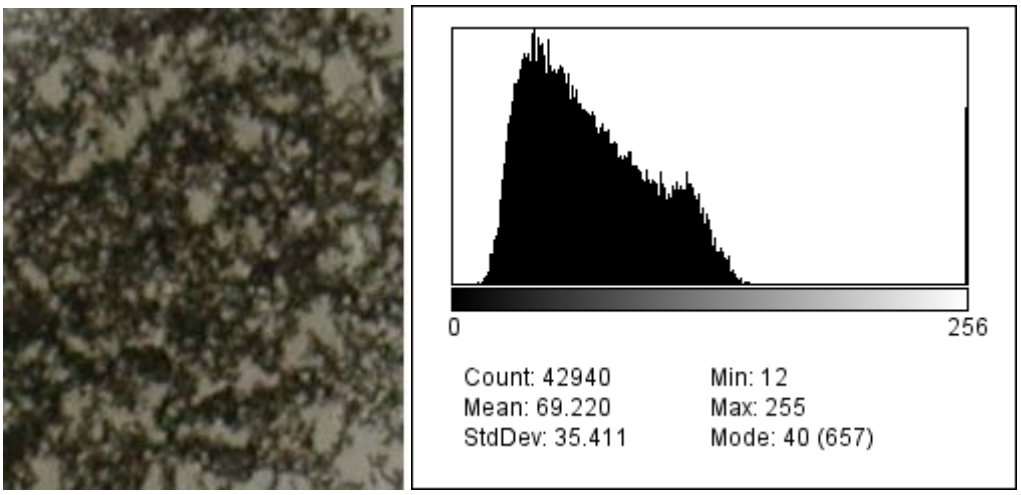
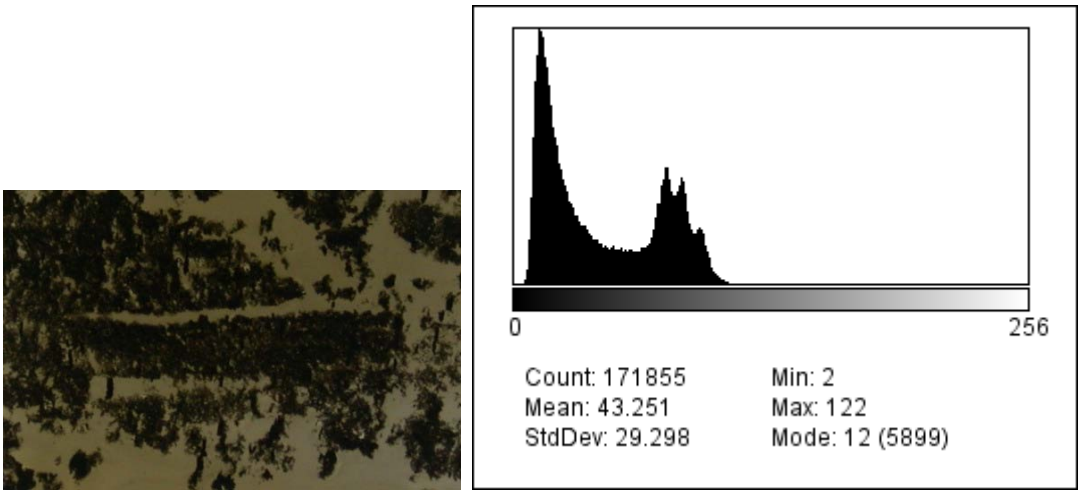


Figure 7.9.3 The greyscale analysis results showing the mean value of the histogram image versus the nanotube loading.



(a)



(b)

Figure 7.9.4 The TOM images and the greyscale histogram of the nanotube-modified amine-cured epoxy polymer with (a) 0.1wt% MWCNTs, (b) 0.2 wt% MWCNTs (the MWCNTs are from Thomas Swan & Co Ltd.) [108].

7.10 Conclusions

Both quasi-static and cyclic-fatigue tests were performed on the epoxy composites modified with the multi-walled carbon nanotubes. For the thermal and mechanical properties, it was found that using the nanotubes as a reinforcement resulted in an increase in the Young's modulus from 2.90 GPa for the pristine polymer (control) to 3.26 GPa for the modified polymer with the highest nanotube content of 0.5 wt%. However, modification with the multi-walled carbon nanotubes did not affect the glass transition temperature. The formulations showed an average T_g of 146 ±2 °C by DSC.

The fracture tests under quasi-static loading were carried out using the single-edge notched bending test. A significant improvement, compared with the unmodified material, in the toughness was demonstrated by adding the multi-walled carbon nanotubes. The fracture toughness increased significantly even at low concentrations of nanotubes, for example a value of 0.85 MPa $m^{1/2}$ was obtained by adding 0.1 wt% of the multi-walled carbon nanotubes. Although a reduction in the rate of toughness increase at a high concentration of nanotubes due to the agglomeration of the nanotubes occurred, a maximum value of the fracture toughness was found for 0.5 wt% MWCNTs. The measured fracture energy increased with the same trend, and a maximum G_{Ic} of 223 J/m^2 was measured for the nanocomposite with 0.5 wt% MWCNTs. By studying the fracture surfaces of the SENB specimens, the toughening mechanisms which contribute to the increase in toughness were clearly identified. Nanotube pull-out and debonding plus plastic void growth around the nanotubes were observed.

Turning to the fatigue tests under cyclic loading at 5 Hz, the addition of the multi-walled carbon nanotubes reveals a high resistance to crack propagation in fatigue failure. This could be demonstrated by the measured value of the maximum strain energy release rate at the threshold region, G_{th}. A maximum G_{th} of 73 J/m^2 was obtained, which was three times that of the unmodified polymer, where G_{th} = 24 J/m^2.

When using nanotubes as an reinforcement for polymer-based composites, the dispersion of the nanotubes has been a big issue because they tend to agglomerate. Agglomerations of the nanotubes could be clearly found using AFM, especially for the

nanocomposites with a high content of MWCNTs. Even though the agglomeration of the MWCNTs was also evident in FEG-SEM observation on fracture surfaces, high magnification images showed that all the nanotubes were fully wetted by the epoxy matrix. This is why all the nanocomposites with nanotubes showed a significant improvement in the toughness and fatigue property even they contained undesirable nanotube agglomerates.

Two types of multi-walled carbon nanotubes with different lengths and diameters (different aspect ratios) were used to investigate the size effect on the toughness and fatigue performance. The results showed that the MWCNTs (standard nanotubes) with a high aspect ratio (length/diameter = 1170) could allow more efficient nanotube pull-out than the low quality nanotubes with a low aspect ratio (180) in the nanotube-modified composites, and hence have a high potential for improving the mechanical properties for the epoxy polymer. Besides, the standard nanotubes were easier to disperse even they have a high aspect ratio which results in a difficulty in reaching a good dispersion. Testing results show that the addition of the 0.2 wt% low quality nanotubes led to a small improvement in the fracture energy, but no improvement in the fracture toughness, fatigue performance and modulus due to the relatively short length and low level of dispersion.

CHAPTER 8

HYBRID-MODIFIED EPOXY

8.1 Introduction

This Chapter presents the effect the combination of various modifications of carboxyl-terminated butadiene-acrylonitrile (CTBN) rubber microparticles, silica nanoparticles (as discussed in Chapter 6) and multi-walled carbon nanotubes (as discussed in Chapter 7) on the mechanical properties of thermosetting epoxy polymer-based composite. The polymer matrix used to form the hybrid-modified composites was a diglycdyl ether of bisphenol-A (DGEBA) cured by an anhydride curing agent, which is the same epoxy matrix used with the single-phase modification (silica nanoparticles in Chapter 6 and carbon nanotubes in Chapter 7). The morphology and material properties (modulus, toughness and fatigue performance) of the modified composites with the hybrid-reinforcement were investigated.

The formulations with various reinforcements of the CTBN rubber microparticles, silica nanoparticles and multi-walled carbon nanotubes discussed in this

Chapter are summarised in Table 8.1.1. As discussed in Chapter 7, the presence of the multi-walled carbon nanotubes in the polymer increased the viscosity of the mixture, which results in difficulty in sample preparation. Hence, a fixed nanotube weight fraction of 0.2 wt% was used. Previous work [5] on the modified anhydride-cured DGEBA reported an optimum loading of rubber particles and silica nanoparticles for improving the toughening performance. Fixed weight loadings of 9.0 wt% and 10 wt% were used for rubber microparticles and silica nanoparticles, respectively, in this Chapter.

The fracture and fatigue tests were performed as previously described to investigate the effect of using the hybrid-reinforcement on the material properties of the polymer-based composites. The measured properties include the Young's modulus, E, glass transition temperature, T_g, fracture toughness, K_{Ic}, fracture energy, G_{Ic} and fracture energy threshold, G_{th}, were calculated. The dispersion of reinforcements was examined using atomic force microscopy and transmission optical microscopy, and the fractography of the hybrid-modified composites was performed using field emission gun electron scanning microscopy.

Table 8.1.1 The formulations of the hybrid-modified epoxy polymers.

Formulation	**CTBN** (wt%)	**Silica Nanoparticles** (wt%)	**Carbon Nanotubes** (wt%)
Control	0.0	0.0	0.0
10N*	0.0	10.0	0.0
0.2C*	0.0	0.0	0.2
9R	9.0	0.0	0.0
9R-10N	9.0	10.0	0.0
9R-0.2C	9.0	0.0	0.2
10N-0.2C	0.0	10.0	0.2

**The nanotube-modified epoxy containing 0.2 wt% MWCNTs (labelled as 0.2C) and 10 wt% nanosiilca (labelled as 10N) were discussed in Chapter 6 and Chapter 7, respectively.*

The multi-walled carbon nanotubes used were synthesised using CVD technology in Manchester University UK. All the parameters in this CVD process were

discovered and controlled by collaborators in the Department of Materials Science, Manchester University. However, the quantity of output of the aligned multi-walled carbon nanotubes from the CVD process was low (around a few micrograms are obtained in a single run). As the quantity of these multi-walled carbon nanotubes was limited, a hybrid nano-reinforcement, called R1D1 from Nanoledge, was used to discuss the effect caused by various concentrations of nano-hybrid reinforcements on the mechanical properties. This material contains 0.36 wt% MWCNTs and 12.28 wt% silica nanoparticles in a DGEBA epoxy resin. This will be discussed in Section 8.7.

8.2 Microstructure

8.2.1 Single-phase Modified Epoxy

The morphology of the single-phase additive of CTBN rubber microparticles, silica nanoparticles or multi-walled carbon nanotubes in the epoxy polymers was observed using an atomic force microscope operated in tapping mode. Figure 6.2.3 (a) showed that the nanocomposite with 10 wt% of nanosilica (10N) had well-dispersed silica nanoparticles, and an average diameter of 20 nm was measured. The nanocomposite containing 0.2 wt% of MWCNTs (0.2C) showed some nanotube agglomerates with a size of about 0.2 ~ 0.3 μm square, see Figure 7.2.1 (a).

The AFM image of the modified polymer with the CTBN rubber particles alone, as shown in Figure 8.2.1, shows that the rubber microparticles were well-dispersed in the cured polymer. The average diameter of the rubber particles of 0.58 μm, with a standard deviation of 0.13 μm, was measured. This particle size measurement is within the range that was reported in studies of the same rubber-modified polymer [4, 5, 30].

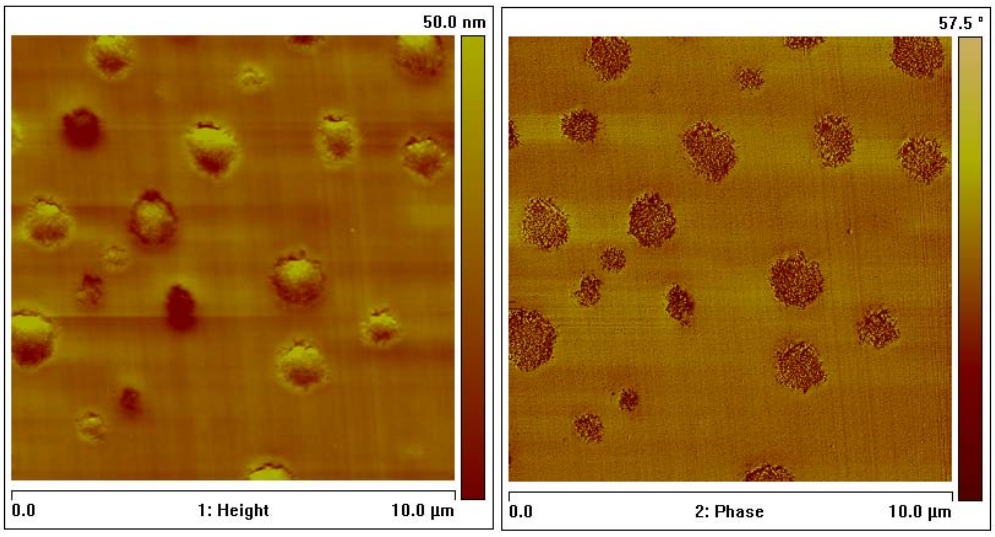


Figure 8.2.1 Atomic force microscopy (AFM) image of modified material with 9.0 wt% CTBN rubber particles.

8.2.2 Hybrid-modified Epoxy

The AFM observation of the hybrid-modified epoxy polymers, as shown in Figure 8.2.2 ~ Figure 8.2.4, shows that the CTBN rubber microparticles were well-dispersed, indicating that the dispersion of the rubber particles was not affected by the addition of the second-phase additive in the hybrid formulations, as shown in Figure 8.2.2 for the 9R-0.2C formulation and Figure 8.2.4 for the 9R-10N formulation. The diameter of the rubber particles was measured to be 0.62 ±0.14 μm for 9R-0.2C sample and 0.69 ±0.19 μm for 10N-9R sample, which is not significantly larger than for the rubber-modified epoxy polymer, see Figure 8.2.1. However, the use of the multi-walled carbon nanotubes to form the hybrid materials did not show a good dispersion of nanotubes. Figure 8.2.2 (9R-0.2C) and Figure 8.2.3 (10N-0.2C) show several nanotube agglomerates with a size of about 0.2 μm square, which is within the size range of the nanotube agglomerates measured in Chapter 7 related to the nanotube-modified alone epoxy polymers.

As discussed in Chapter 6 related to the nanosilica/epoxy nanocomposite, the silica nanoparticles were dispersed very well in the single-phase modification. Figure 8.2.3 shows the AFM image of the hybrid nanocomposites (10N-0.2C) containing 0.2 wt% nanotubes and 10 wt% silica nanoparticles; the nanosilica particles in this hybrid formulation attained a good dispersion. However, several necklace-like chains of silica agglomerates were found in the 9R-10N sample, see Figure 8.2.4. This AFM image shows a different feature from the AFM images of the 10N and 9R-10N samples; the added silica nanoparticles in the 9R-10N sample were agglomerated, and these agglomerates were up to 2 μm square, as has been reported previously [5]. According to the AFM images, it can be concluded that the use of the rubber microparticles in the hybrid materials did not affect the nanotube dispersion, but resulted in a reduction in the quality of the nanosilica dispersion. The nanotube dispersion did not change when nanosilica was used as the second-phase modifier. The morphologies for all formulations are summarised in Table 8.2.1.

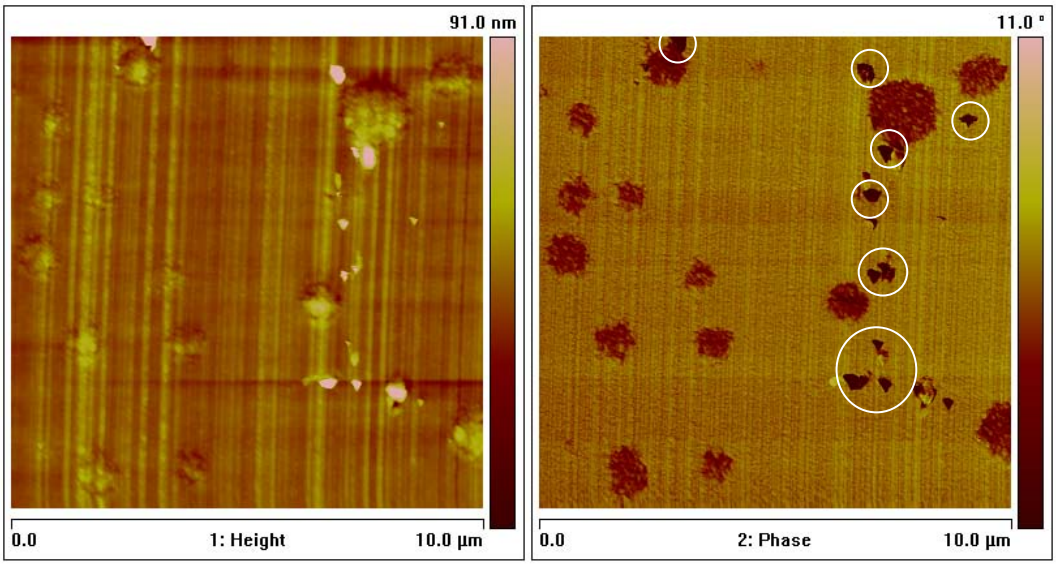


Figure 8.2.2 AFM image of the hybrid-modified epoxy polymer (9R-0.2C) containing 9.0 wt% rubber particles and 0.2 wt% carbon nanotubes, showing nanotube agglomerates as circled.

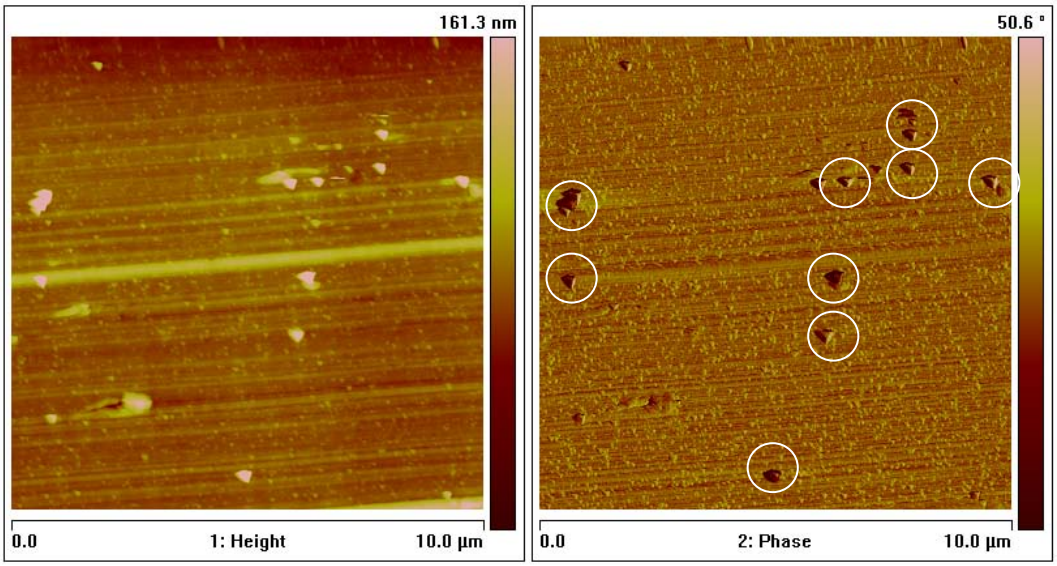
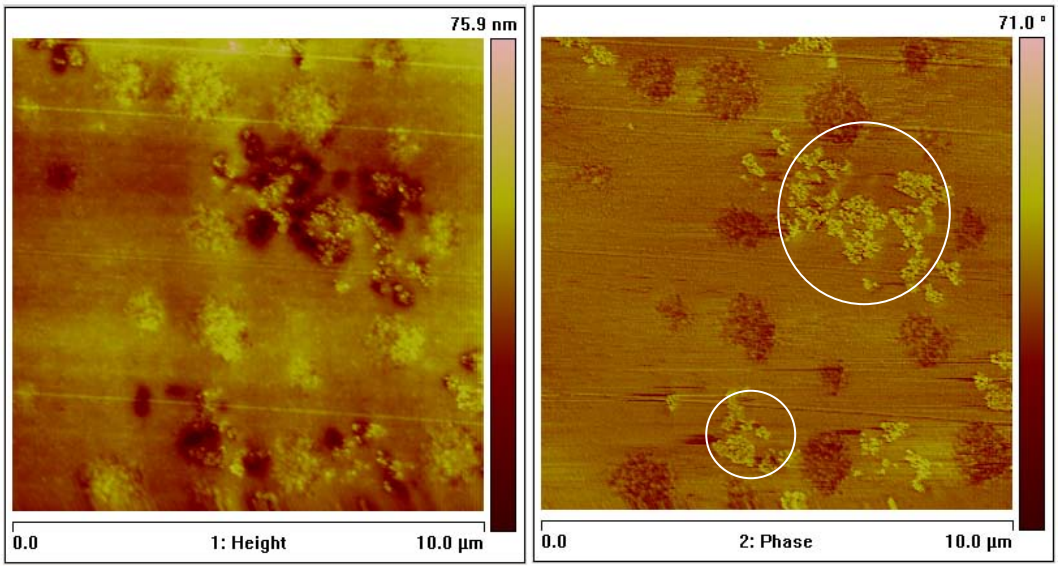
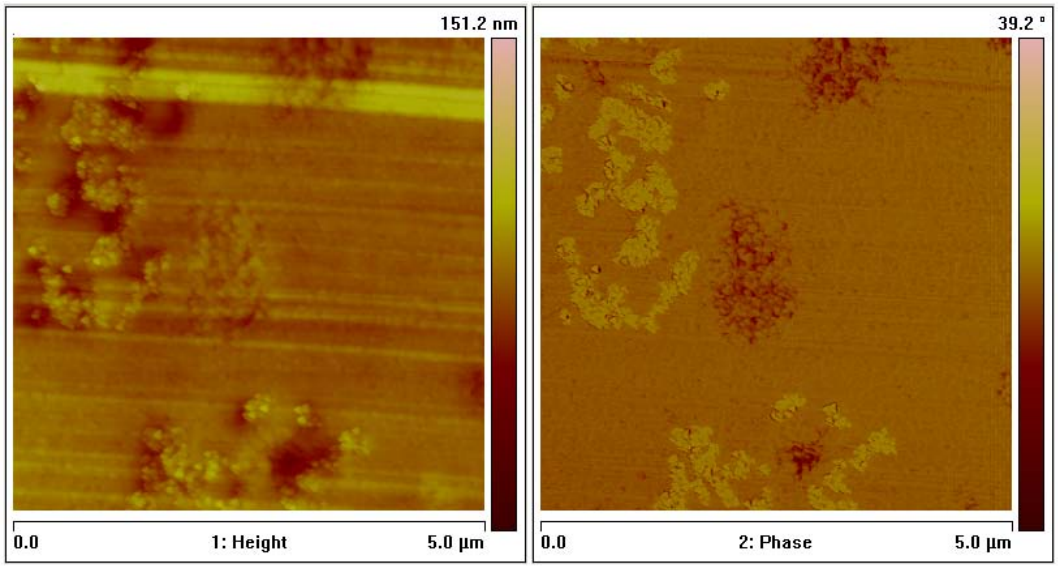


Figure 8.2.3 AFM image of the hybrid-modified epoxy polymer (10N-0.2C) containing 10 wt% nanosilica particles and 0.2 wt% carbon nanotubes, showing nanotube agglomerates as circled.



(a)



(b)

Figure 8.2.4 AFM image of the hybrid-modified epoxy polymer (9R-10N) containing 10 wt% nanosilica particles and 9 wt% rubber particles in different scanning size (a) 10 µm square and (b) 5 µm square, showing nanosilica agglomerates as circled.

Table 8.2.1 Summary of the morphology of the hybrid-modified epoxy polymers.

Formulation	CTBN (wt%)	Nanosilica (wt%)	Nanotube (wt%)	CTBN morphology	Nanosilica morphology	Nanotube morphology
control	0.0	0.0	0.0	NA	NA	NA
10N	0.0	10.0	0.0	NA	Well dispersed, Ø 18~20 nm	NA
0.2C	0.0	0.0	0.2	NA	NA	Agglomerated, 0.2 μm square
9R	9.0	0.0	0.0	Well dispersed Ø 0.5~0.7 μm	NA	NA
9R-10N	9R	10.0	0.0	Well dispersed Ø 0.6~0.8 μm	Necklace-like chains agglomerates, up to 2 μm × 2 μm	NA
9R-0.2C	9.0	0.2	0.0	Well dispersed Ø 0.6~0.8 μm	NA	Agglomerated, 0.2 μm square
10N-0.2C	0.0	10.0	0.2	NA	Well dispersed, Ø 18~20 nm	Agglomerated, 0.2 μm square

(NA: not applicable)

8.3 Mechanical and Thermal Properties

Tensile tests were conducted on the modified polymer samples to measure the Young's modulus. The tensile testing results of the unmodified, single-phase and hybrid-modified epoxy polymers are summarised in Table 8.3.1, and are shown graphically in Figure 8.3.1. A Young's modulus of 2.90 GPa was measured for the unmodified epoxy. Single-phase modification using 9.0 wt% CTBN rubber particles resulted in a decrease in the measured Young's modulus, because the rubber particles are soft and the lowest value of the modulus was recorded as 2.34 GPa for the modified polymer with 9.0 wt% rubber particles alone. By contrast to the rubber-modification, the addition of the silica nanoparticles increased significantly the Young's modulus to 3.28 GPa for the nanosilica-modified epoxy with 10.0 wt% nanosilica particles, as discussed in Chapter 6. The presence of the multi-walled carbon nanotubes in the polymer can also bring a significant improvement in the stiffness of the epoxy-based materials, even at a low content of the nanotubes, as shown in Chapter 7. Owing to the increase in the stiffness of the modified-epoxy materials by the silica nanoparticles and the carbon nanotubes, the maximum value of the Young's modulus was measured to be 3.48 GPa for the hybrid-modified epoxy (10N-0.2C) containing 10.0 wt% silica nanoparticles and 0.2 wt% multi-walled carbon nanotubes.

Regarding the single-phase rubber-modified epoxy as a baseline (Young's modulus of the 9R sample: 2.34 GPa), combining the multi-walled carbon nanotubes with the CTBN rubber particles to form the hybrid-modified epoxy (9R-0.2C) can increase significantly the stiffness, compared with that of nanosilica/CTBN/epoxy material (9R-10N). For example, the addition of the nanotubes at 0.2 wt% to the rubber-modified polymer resulted in an increase in the Young's modulus to 3.08 GPa, which is 0.34 GPa greater than that of the hybrid-modified epoxy with the nanosilica particles in the rubber-modified formulation. This means that the decrease in stiffness caused by the addition of the soft rubber microparticles can be efficiently neutralised by the addition of the silica nanoparticles or multi-walled carbon nanotubes. Furthermore, according to the experimental results, the modification of the nanotubes to stiffen the rubber-modified polymer is much more efficient than the nanosilica particles, even at a low

concentration of the multi-walled carbon nanotubes of 0.2 wt%. Note that 10 wt% of nanosilica was used.

The glass transition temperature, T_g, was measured using differential scanning calorimetry (DSC). The results are summarised in Table 8.3.1, and indicate that the glass transition temperature of each formulation is very similar, except for the materials containing the CTBN rubber particles. An average value of T_g of around 148 °C was measured for the unmodified epoxy. The addition of the silica nanoparticles or the multi-walled carbon nanotubes did not affect the T_g as discussed in Chapter 6 and Chapter 7. However, the addition of the CTBN rubber particles resulted in a reduction in T_g; an average value of about 140 °C was measured for the modified epoxy polymers containing the rubber particles (9R). This would suggest that some of the rubber remains in the solution. Even after the addition of nanosilica or nanotubes to the rubber-modified epoxy polymer, the measured T_g of the 10N-9R and 9R-0.2C samples is similar to the 9R sample, indicating that the use of these nano-reinforcements did not neutralise the decrease in T_g caused by the addition of rubber particles.

Table 8.3.1 The mechanical and thermal properties of hybrid-modified epoxy polymers.

Formulation	E (GPa)		T_g (°C)	
	Mean	SD	Mean	SD
Control	2.90	0.09	147.8	0.9
10N	3.28	0.08	148.3	1.4
0.2C	3.11	0.06	147.8	1.4
9R	2.31	0.04	140.1	2.3
9R -10N	2.74	0.05	140.3	2.1
9R-0.2C	3.08	0.06	141.3	1.9
10N-0.2C	3.48	0.06	149.5	3.0

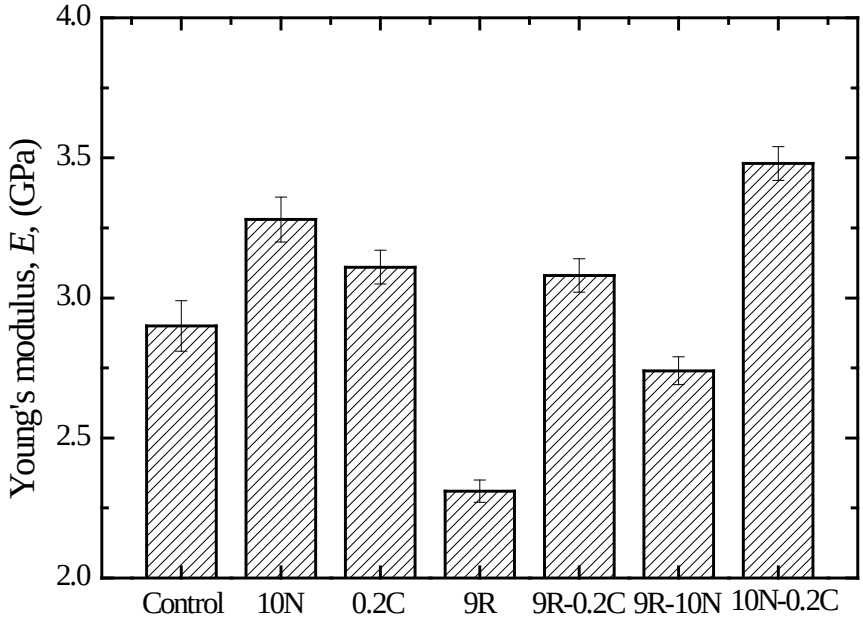


Figure 8.3.1 The Young's modulus of the hybrid-modified epoxy polymers.

8.4 Toughness

8.4.1 Fracture Toughness and Fracture Energy

Single-edge notched bend (SENB) tests were performed on the hybrid-modified epoxy samples under a three-point bend loading condition. The SENB specimen was prepared from a 6 mm-thick plate for all the formulations. The measured fracture toughness, K_{Ic}, and fracture energy, G_{Ic}, are summarised in Table 8.4.1 and shown graphically in Figure 8.4.1. For the unmodified epoxy, the measured value of the fracture toughness is 0.69 MPa.m$^{1/2}$, and the fracture energy is 133 J/m^2. The modified epoxy polymers showed a significant increase in the toughness. The use of the rubber particles led to a maximum value of the fracture toughness in both the single-phase modification and hybrid modification. A maximum value of 1.41 MPa.m$^{1/2}$ was recorded for the modified epoxy polymer (9R) with 9.0 wt% rubber particles, and 2.32 MPa.m$^{1/2}$ for the hybrid-modified polymer (9R-0.2C) with 9 wt% rubber particles and 0.2 wt% MWCNTs. The measured values of the fracture energy showed the same trend as the fracture toughness, see Figure 8.4.1.

Table 8.4.1 The fracture toughness and fracture energy of hybrid-modified epoxy polymers.

Formulation	K_{Ic} (MPa m$^{1/2}$)		G_{Ic} (J/m^2)	
	Mean	SD	Mean	SD
Control	0.69	0.03	133	8
10N	0.81	0.09	191	21
0.2C	0.88	0.02	188	7
9R	1.41	0.04	697	28
9R-10N	2.28	0.05	1059	34
9R-0.2C	2.32	0.06	1132	40
10N-0.2C	1.17	0.04	228	20

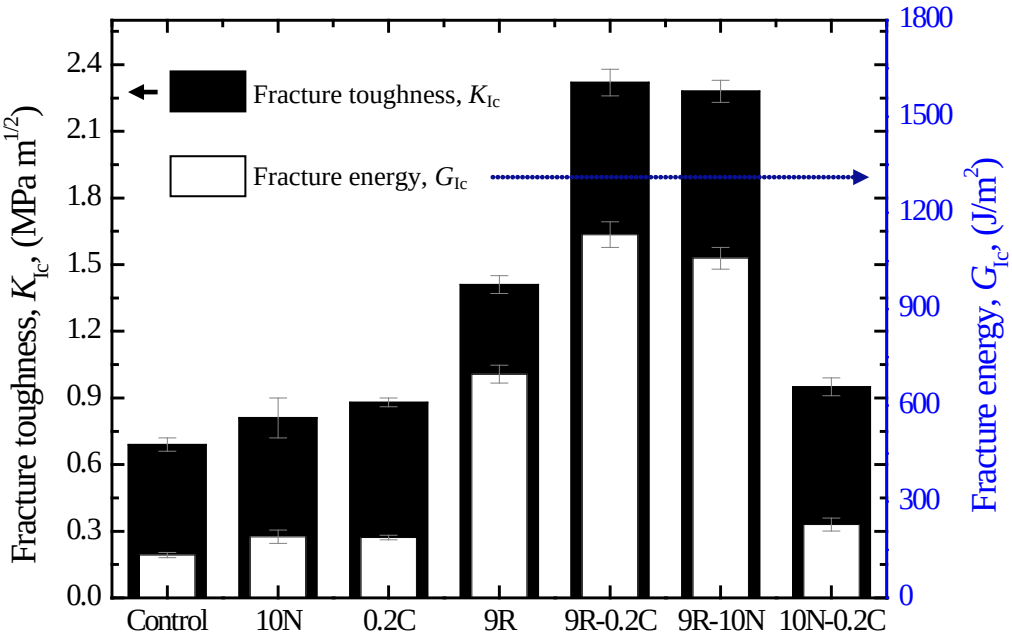


Figure 8.4.1 The fracture toughness and fracture energy of hybrid-modified epoxy polymers.

In Figure 8.4.1, the single-phase modification with the CTBN rubber particles, silica nanoparticles or multi-walled carbon nanotubes can significantly improve the toughness of the epoxy. Comparing with the unmodified polymer (133 J/m^2), a 44% increase in the fracture energy is achieved using 10 wt% silica nanoparticles. The addition of the multi-walled carbon nanotubes to the epoxy polymer also resulted in an increase in the measured fracture energy (to 188 J/m^2), even at a relatively low concentration of 0.2 wt% MWCNTs. A maximum value of the fracture energy of 697 J/m^2 was measured for the rubber-modified polymer (9R), which is around a four-fold increase in the fracture energy, compared with the unmodified polymer. Hence, the CTBN rubber particles are considered as the best toughening modification for the epoxy polymers, but the cost of a decrease in the modulus [3, 23, 144] and T_g. This suggests that the development of the hybrid-modified epoxy polymer by combining soft and stiff particles may give the best balance of properties [5].

In the literature, hybrid-modified epoxy materials result in the most significant improvement of the toughness without compromising the stiffness [5, 23]. However, these studies only used silica nanoparticles as the nano-toughener. From the experimental results shown in Table 8.4.1, a maximum value of the fracture energy was attained for the 9R-0.2C formulation, where the fracture energy was increased from 697 J/m^2 for the rubber-modified polymer (9R) to 1132 J/m^2 for the hybrid-modified epoxy polymer (9R-0.2C) with the combination of rubber particles and multi-walled carbon nanotubes. The increased fracture toughness has the same trend as the measured fracture energy. The use of the silica nanoparticles with the rubber particles to form the 9R-10N formulation also revealed a remarkable improvement of the toughening performance; the measured values of the fracture toughness and fracture energy were recorded to be 2.28 MPa $m^{1/2}$ and 1058 J/m^2, respectively. In contrast to a significant improvement in the toughness for the hybrid-modified polymer containing the rubber particles with nano-size additives, the addition of the nano-hybrid reinforcements alone, i.e. containing nanotubes and silica nanoparticles, resulted in only a small improvement in the toughening performance, with G_{Ic} = 228 J/m^2 for the 10N-0.2C sample.

For the hybrid-toughened polymers (9R-10N and 9R-0.2C), a synergy between the micron-size rubber particles and the nano-size additives of nanosilica or nanotubes was obtained, with a significant improvement in the measured values of K_{Ic} and G_{Ic}, see Table 8.4.1. Both of these increased values obviously exceed the increase in the fracture properties caused by the addition of the individual toughening. For example, the increment of the measured fracture energy for the hybrid-modified epoxy (9R-0.2C) with the rubber and nanotubes is around 1000 J/m^2, compared with the unmodified polymer. If the contribution of the hybrid modification to the toughness is considered as a superposition of the toughening improvement attributed to the constituent additives individually, the value related to the addition of the hybrid additives can be derived to be approximately 750 J/m^2 for the 9R-0.2C sample. However, the measured result (1132 J/m^2) is much higher than the value predicted by superposition, which is clear evidence of the synergistic effect, as shown schematically in Figure 8.4.2. This synergistic effect was also found in the hybrid-modified polymer (9R-10N) with rubber and nanosilica particles, as previously reported [5].

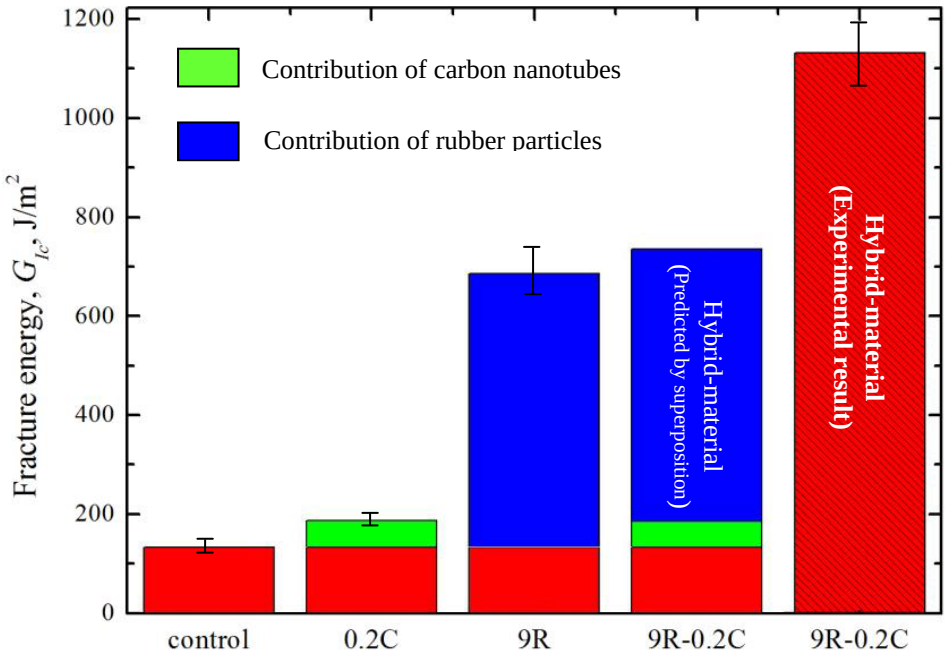


Figure 8.4.2 The schematic illustration showing the synergistic effect of the hybrid-toughener of nanotubes and rubber particles on the fracture energy.

Without the contribution of the rubber particles to the toughness, the modified epoxy polymer (10N-0.2C) with the silica nanoparticles and multi-walled carbon nanotubes revealed relatively low values of the measured fracture toughness and fracture energy. However, this modification still provides a potential for improving the toughening performance; around a 70% increment of the fracture energy was obtained for the 10N-0.2C nanocomposite, compared with the unmodified epoxy. Further, the use of nano-size additives did not significantly increase the viscosity of the mixture, which is good for sample preparation and engineering applications, such as resin infusion under flexible tooling (RIFT) for the manufacture of fibre-reinforced polymer composites [5, 145].

The synergistic effect on the toughness did not arise in the nano-hybrid modified epoxy sample (10N-0.2C). For example, the addition of the nanosilica particles alone at 10 wt% led to a 42% increase in the fracture energy, and blending 0.2 wt% nanotubes alone with the polymer brought about a 40% increase in the fracture energy, compared with the unmodified polymer. Ideally, the increased fracture energy given by the combination of both additives, corresponds to the sum of the increments of the fracture

energy in the single-phase modifications, i.e. a 82% increase in the fracture energy. A 71% increase in the fracture energy was measured, which indicates that there was no synergistic nor additive effect in this nano-hybrid modified epoxy (10N-0.2C), as shown in Figure 8.4.3.

Further investigation of the effect caused by various loadings of nano-reinforcements on the mechanical properties and dispersion will be discussed in Section 8.7, where a commercial nano-hybrid reinforcement, R1D1 from Nanoledge containing silica nanoparticles and multi-walled carbon nanotubes, will be used.

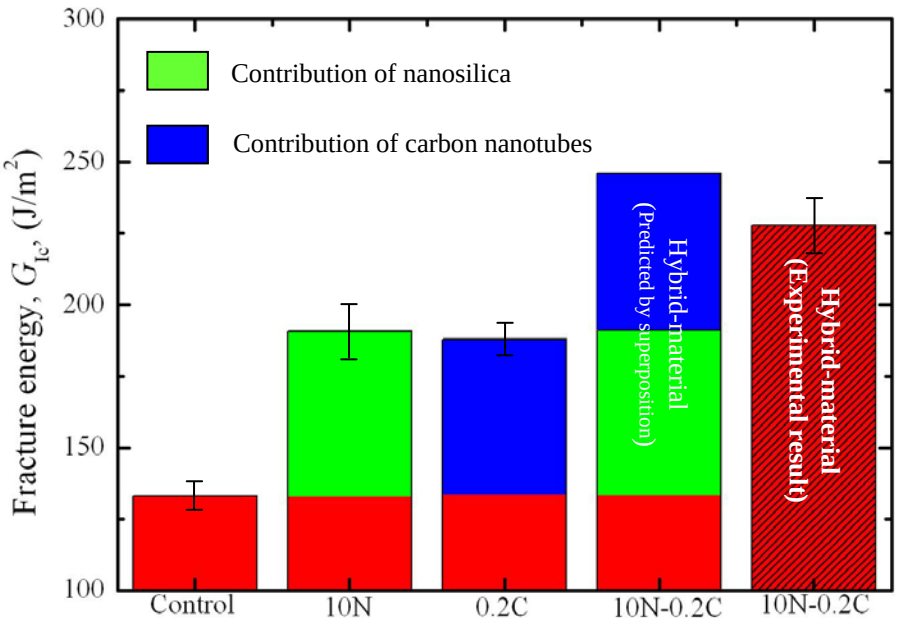


Figure 8.4.3 The schematic illustration showing no synergistic effect caused by the addition of the nano-reinforcements (nanosilica and nanotubes) on the fracture energy.

8.4.2 Fractography

The fracture surfaces of the modified epoxies were inspected using FEG-SEM. Figure 8.4.4 and Figure 8.4.5 show FEG-SEM images of the fracture surfaces for all the formulations discussed in this Chapter. Once again the direction of crack growth is from the right to the left. The FEG-SEM image of the unmodified polymer, see Figure 8.4.4 (a), shows a relatively smooth surface, which is the typical for this epoxy, as discussed previously. All the modified-epoxy samples exhibited a relatively rough surface, especially for the hybrid-modified epoxy materials, see Figure 8.4.5, due to the increase in energy dissipation. The toughening mechanisms induced by the various reinforcements will be discussed in the following Section.

These FEG-SEM images were also used to investigate the dispersion of the additives, and confirm the AFM observations. The rubber particles were well dispersed. However the multi-walled carbon nanotubes were agglomerated in the nanotube-modified polymer (0.2C), see Figure 8.4.4 (d), as discussed in Chapter 7. The introduction of the CTBN rubber particles or the silica nanoparticles with the nanotubes to form the hybrid-modified epoxy did not change the dispersion of the nanotubes. In Chapter 6, a good dispersion of the silica nanoparticles was found in the 10N formulation. However, the hybrid-modified epoxy with rubber and nanosilica particles (9R-10N) revealed nanosilica agglomerates, see Figure 8.4.5 (c).

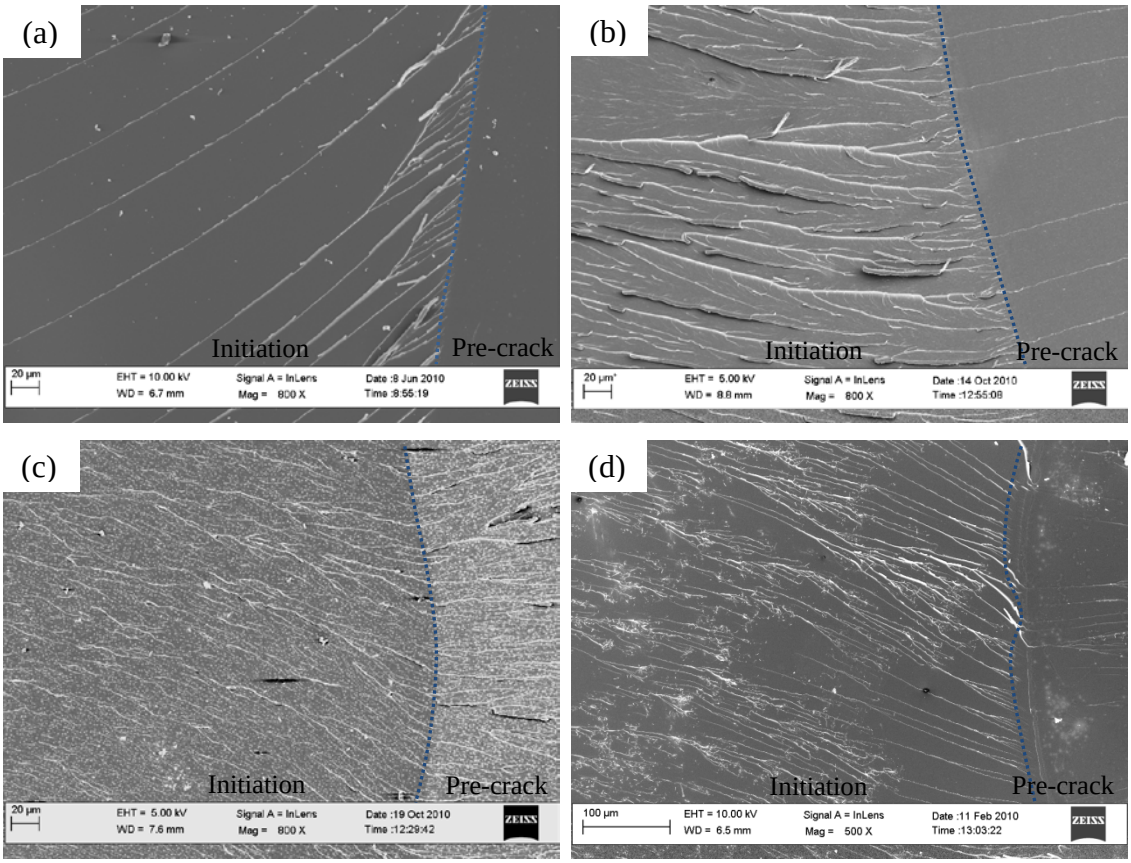


Figure 8.4.4 FEG-SEM images of the fracture surfaces of (a) unmodified polymer and single-phase modified epoxy polymers with (b)10 wt% nanosilica, (c) 9.0 wt% rubber particles, and (d) 0.2 wt% multi-walled carbon nanotubes.

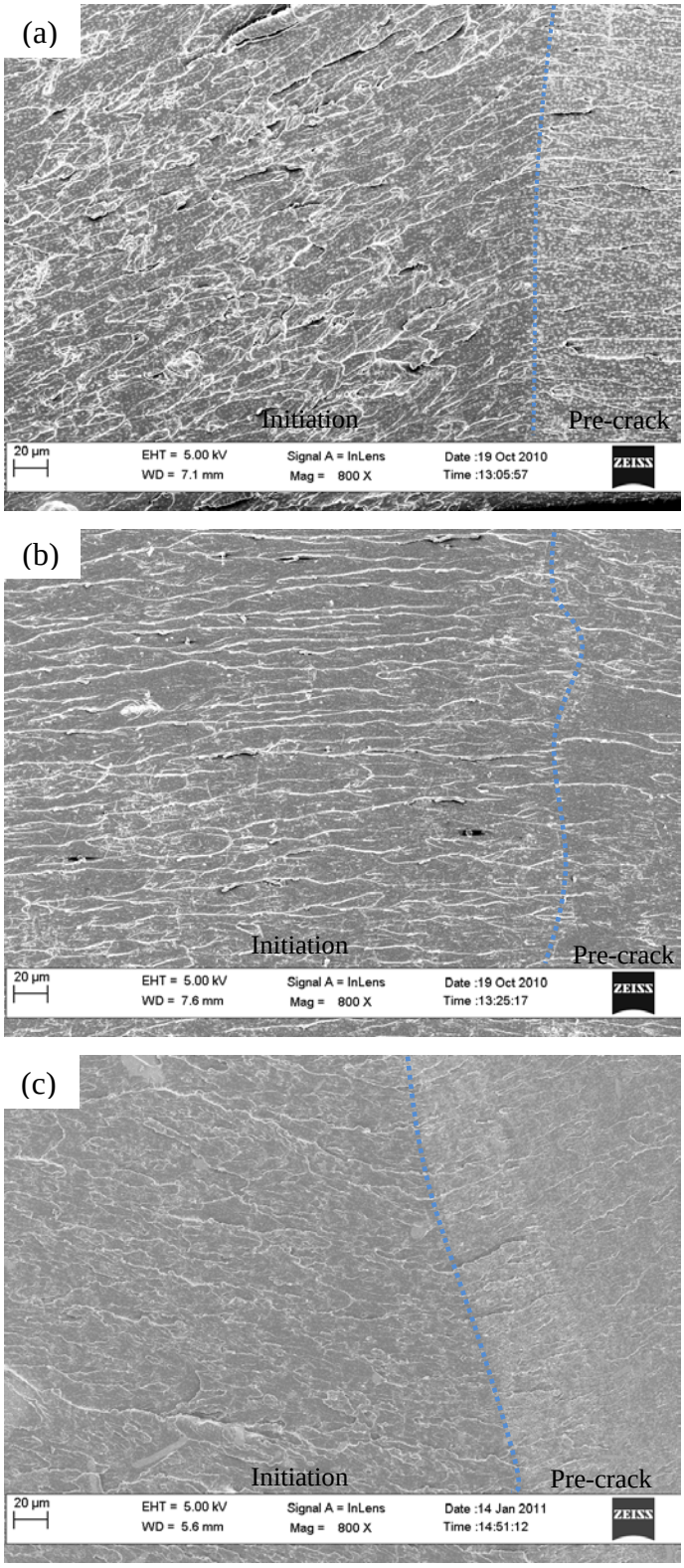


Figure 8.4.5 FEG-SEM images of the fracture surfaces for the foumulations with various hybrid reinforcements, (a) 9R-0.2C, (b) 10N-0.2C, (c) 9R-10N.

8.4.3 Toughening Mechanisms

The toughening mechanisms which contribute to the increase in the toughness were identified from high magnification images. As can be seen in Figure 8.4.6, clear evidence of rubber cavitation, and subsequent plastic void growth was found on the fracture surfaces of the CTBN rubber-modified epoxy polymer. The mean diameter of the cavities was measured to be 1.18 μm, with a range of 0.83 to 1.32μm. The size of the cavitated rubber particles is larger than the measured diameter (0.58 μm) of rubber particles in the AFM images. The main toughening mechanism from the rubber particle modification is considered to be internal cavitation of the rubber particles and subsequent void growth in the epoxy polymer [5, 23, 39]. The rubber cavitation brings about a significant improvement in the toughness via relief of constraint, which increase the plastic deformation ability of the epoxy polymer. Furthermore, several ridges (apart from the river-lines associated with the epoxy polymer fracture) started at rubber particles were found, see Figure 8.4.6. These ridges were formed by a lateral coalescence of slightly different crack plateaus when the front of the crack meets the rubber particle, this results in an increase in energy dissipation, and consequently improves the toughness, but not significantly [30, 146].

As discussed in Chapter 6 and Chapter 7, the toughening mechanisms in the nanotube-modified material are nanotube pull-out plus plastic void growth associated with the nanotube debonding and plastic deformation in the epoxy matrix, see Table 7.4.2. The plastic void growth around the silica nanoparticles, after the interfacial debonding between the silica nanoparticles and epoxy matrix, was considered to be the main toughening mechanism which contributed to the increase in the toughness for the nanosilica-modified epoxy polymers, see Table 6.4.2.

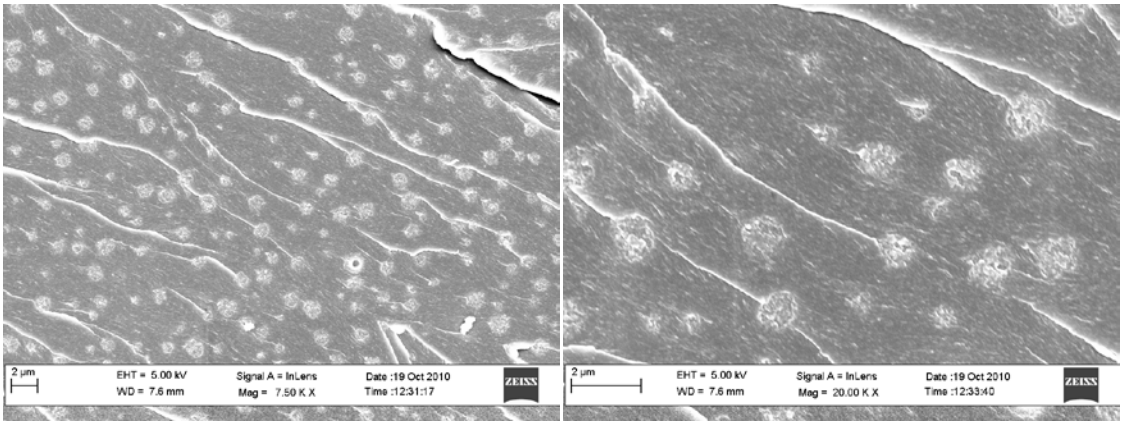


Figure 8.4.6 Field emission gun scanning electron microscopy (FEG-SEM) images of 9 wt% CTBN rubber particles (9R) sample showing rubber particle cavitation.

Moving on to the investigation of toughening mechanisms in the hybrid-modified epoxy polymers, FEG-SEM images of the 9R-0.2C formulation are shown in Figure 8.4.7. A mean diameter of the cavitated rubber particles on the fracture surface of 1.51 μm, with a standard deviation of 0.32 μm, was measured. This is larger than the original diameter of the rubber particles, and is even larger than the cavities (1.18 μm) in the single-phase rubber-modified epoxy polymer, see Figure 8.4.6. All of these confirm that the toughening mechanism of rubber cavitation followed by void growth occurred in the hybrid-modified epoxy polymer. Nanotube pull-out can be clearly identified on the fracture surface for the 9R-0.2C sample, as can be seen in Figure 8.4.7 (a)-(c). The nanotube pulled out length was measured to be 7.56 μm with a range of 4.32 to 10.28 μm, and 100 % of the carbon nanotubes present on the fracture surface were pulled out. This agrees with the measurement from the MWCNT-modified epoxy polymer, as discussed in Chapter 7. Voids due to debonding between the nanotubes and the epoxy matrix were discovered, as shown in Figure 8.4.7 (b). After the nanotube debonded from the epoxy matrix, the matrix around the nanotubes deformed plastically and void growth occurred. The size of the voids was measured to be 146 ±7 nm in diameter, and around 10% of the nanotubes showed void growth. As mentioned in Figure 8.4.3, the synergistic effect on the toughness of the hybrid-modified epoxy can be attributed to the relatively larger rubber cavities, which resulted in a higher energy contribution from the rubber cavitation for the hybrid-modified composite.

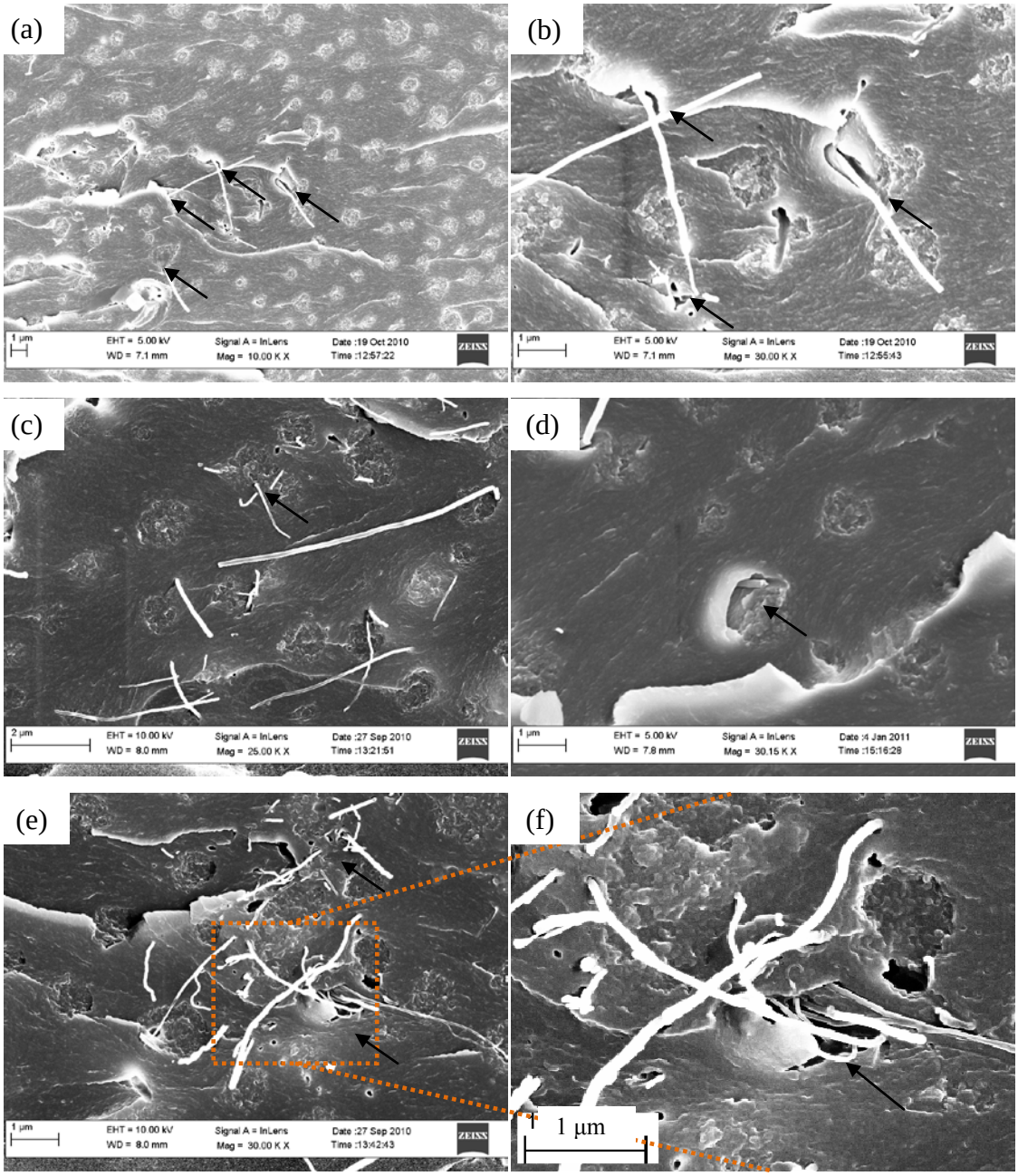


Figure 8.4.7 Field emission gun scanning electron microscopy (FEG-SEM) images captured of 9 wt% CTBN and 0.2 wt% carbon nanotubes (9R-0.2C) hybrid-modified epoxy polymer sample, showing (a) rubber cavitation and nanotube pull-out, (b) showing void growth associated with the nanotubes, (c-d) showing the nanotubes punctured into the rubber particles and void associated with rubber particle, (e-f) showing voids growth in nanotube-rich areas.

The toughening mechanisms mentioned above are similar to the toughening mechanisms identified in single-phase modification using the same reinforcements (rubber microparticles and carbon nanotubes). In addition to a higher degree of rubber cavitation in the hybrid-toughened polymer than in the single-phase rubber-toughened

polymer, further toughening mechanisms may contribute to the synergistic effect of the hybrid-toughener. The carbon nanotubes are observed to penetrate through or attach to the rubber particles, as indicated in Figure 8.4.7 (c)-(d). In case of the nanotube penetrating into the rubber particles, the process of nanotube pull-out will experience additional friction between the nanotubes and the rubber particles, and the nanotube may affect the process of rubber particle deformation and cavitation, see Figure 8.4.7 (d). This may result in an improvement in energy dissipation, consequently increasing the measured toughness. Evidence of void growth associated with the multi-walled nanotubes was also found in nanotube-rich areas. As can be seen in Figure 8.4.7(e)-(f), several voids formed in the nanotube agglomerates.

The dispersion of the multi-walled carbon nanotubes was examined from the FEG-SEM images of fracture surfaces for the hybrid-modified (9R-0.2C) epoxy polymer. The carbon nanotubes are well-dispersed, as can be readily observed in Figure 8.4.7 (a) and Figure 8.4.7 (c). Even in nanotube-rich areas, the nanotubes are distributed well and fully coated with the polymer matrix, see Figure 8.4.7 (c). Comparing this nanotube dispersion with the MWCNT-modified alone epoxy polymer at the same nanotube loading of 0.2 wt%, the nanotube dispersion in the hybrid formulation is better than that in the epoxy polymer sample containing the nanotubes alone. This is because of the relatively high shear stress in the mixture during the stirring process for the formulation containing the rubber. The use of rubber increases the viscosity of the mixture [147], as a result, the mixing shear rate increases and efficiently breaks down tangled nanotubes, as demonstrated in Figure 8.4.8, which shows viscosity versus shear rate in a polymer solution. The CTBN rubber particles reveal excellent dispersion, as can been seen in Figure 8.4.7 (a), and as demonstrated in the AFM observation in Section 8.1.

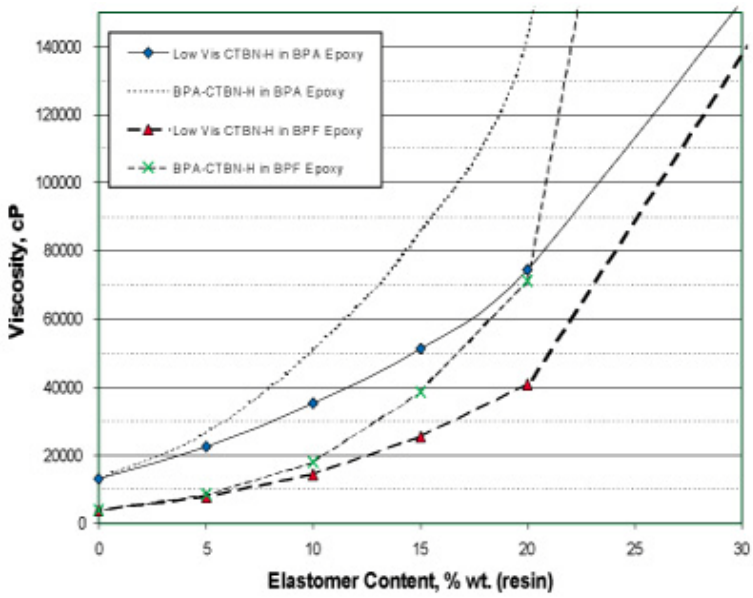


Figure 8.4.8 The viscosity versus of weight loading of CTBN rubber particles [147].

Figure 8.4.9 shows the fracture surfaces for the nanohybrid-modified (10N-0.2C) epoxy polymer. The toughening mechanism caused by the addition of the silica nanoparticles can be identified to be the plastic void growth due to debonding between the silica nanoparticles and the epoxy matrix. Only 10% of the nanoparticles have debonded with subsequent plastic void growth (with an average void diameter of 34 ±3 nm) in the nano-hybrid modified epoxy sample, compared with 15% in the nanosilica-modified epoxy sample. This indicates that the toughening capability from the addition of the nanosilica to the epoxy polymer is reduced by adding the second-phase additive to form the nano-hybrid material. The contribution of the carbon nanotubes to the toughness was found to be the nanotube pull-out, see Figure 8.4.9 (a), and plastic void growth mechanism, see Figure 8.4.9 (d)-(c). All (100%) of the added nanotubes were pulled out from the matrix, and the pull-out length was measured to be 7.98 μm with a standard deviation of 2.10 μm. The amount of voids associated with nanotube debonding and plastic deformation on the fracture surfaces was estimated to be 7 ±2%, and the average diameter of these voids was 145 ±3 nm. These values are similar to the results discussed in Chapter 7 regarding the nanotube-modified epoxy polymers.

The measured fracture energy is lower than the predicted value of fracture energy using the superposition principle for the nano-hybrid modified epoxy (10N-0.2C), see Figure 8.4.3. This may be due to the low amount of void growth associated

with the nanosilica debonding in this formulation. Hence, there was no synergistic effect on the toughness in this nano-hybrid epoxy material.

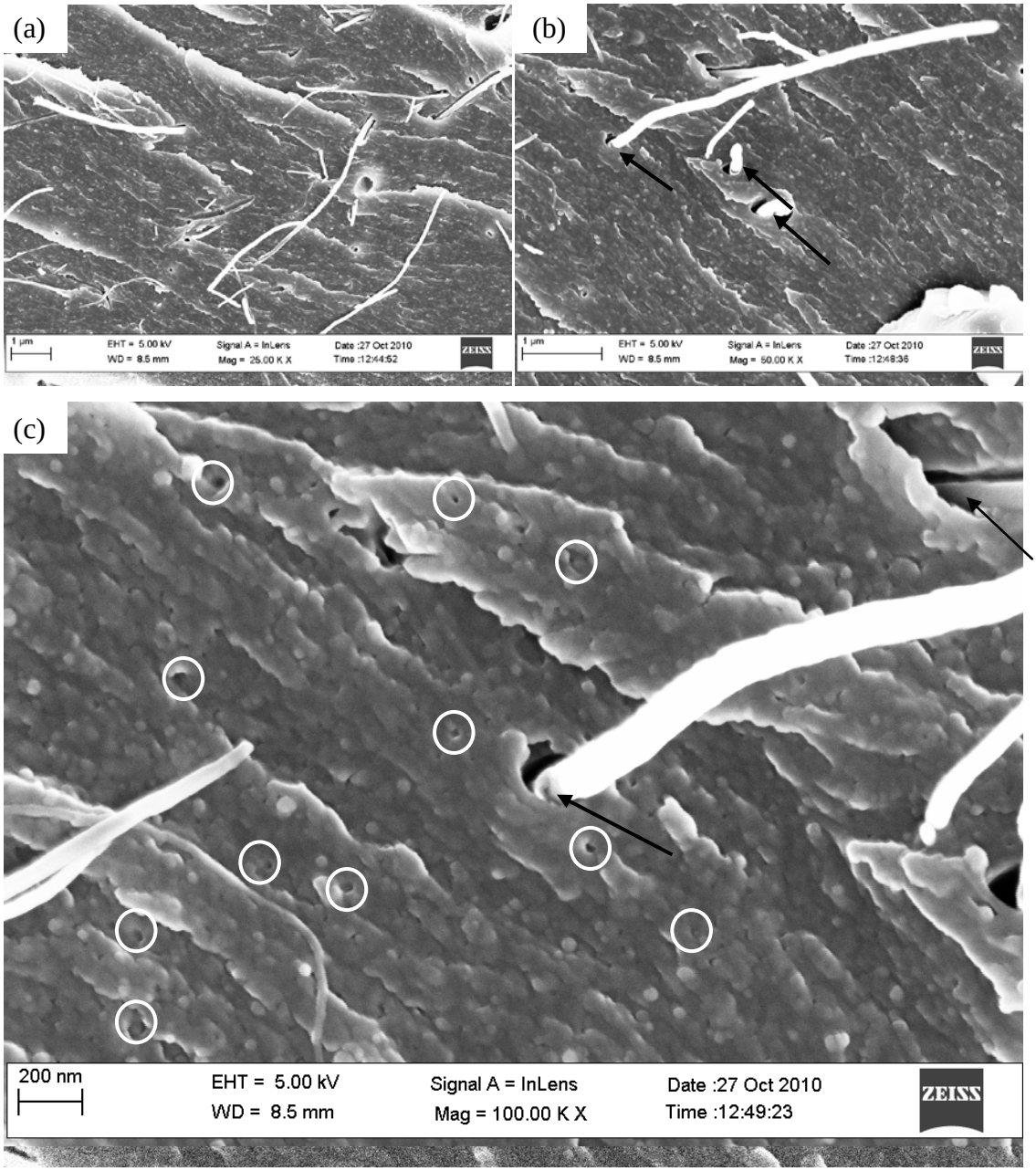


Figure 8.4.9 FEG-SEM images of the 10N-0.2C hybrid-modified epoxy polymer sample, showing (a) nanotube pull-out, (b) plastic void growth associated with nanotube debonding, (c) void growth caused by the nanotube debonding, as indicated by arrows, and nanosilica debonding as circled.

Figure 8.4.10 shows the fracture surface of the 9R-10N hybrid-modified epoxy polymer. Clear evidence of rubber particle cavitation was found, which is considered to be the main toughening mechanism for the rubber particles [5, 23]. The diameter of the cavitated rubber particles was measured to be 1.45 ±0.21 μm, which is larger than the rubber cavities in the rubber-modified alone epoxies. This can contribute to the synergistic effect on the toughness in the hybrid-modified epoxy with the rubber and nanosilica particles. FEG-SEM images showed the silica particles were present both as agglomerates, see Figure 8.4.5 (c), and individual particles, see Figure 8.4.10. Voids due to the nanosilica debonding were also found on the fracture surfaces. Around 13 ±4% of the nanosilica particles showed void growth, and the diameter of these voids was measured to be 35 ±4 nm. These values are similar to the measured results discussed in Chapter 6 regarding the nanocomposite containing the nanosilica alone.

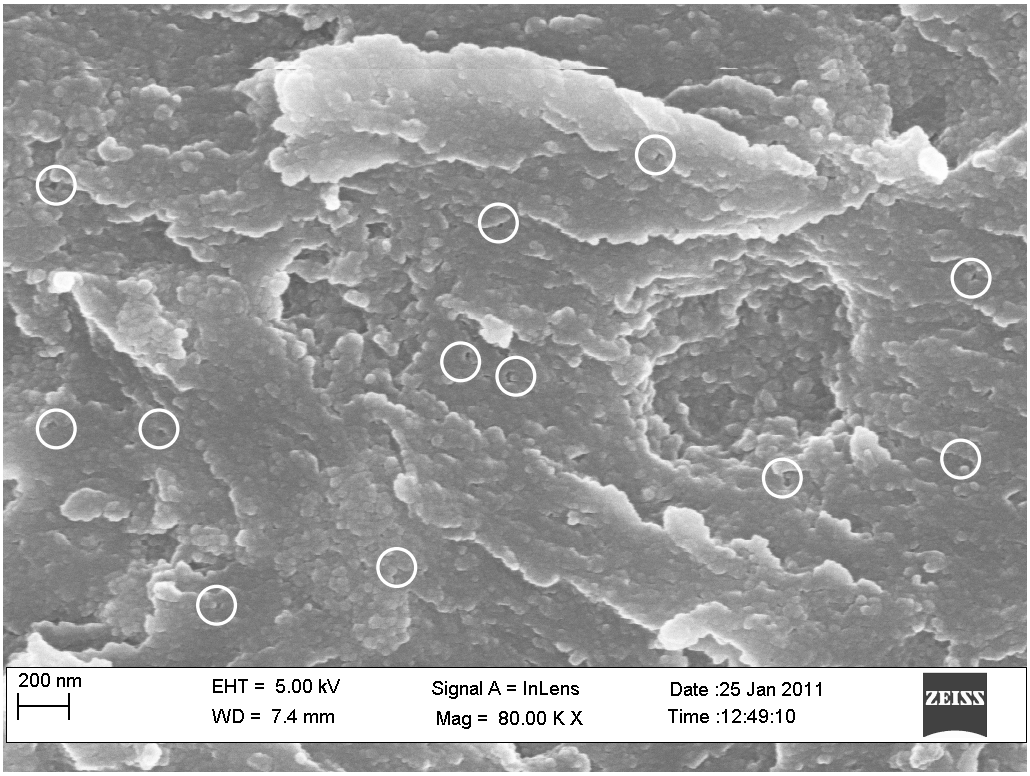


Figure 8.4.10 FEG-SEM image of the fracture surface for the 10N-9R hybrid-modified epoxy polymer sample, showing rubber cavitation and void growth caused by the nanosilica as circled.

The toughening mechanisms induced by the hybrid reinforcements are summarised in Table 8.4.2.

Table 8.4.2 Summary of the toughening mechanisms caused by the hybrid reinforcements.

Formulation	K_{Ic} (MPa $m^{1/2}$)	G_{Ic} (J/m^2)	CTBN toughening mechanism	Nanosilica toughening mechanism	Nanotube toughening mechanism
control	0.69	133	NA	NA	NA
10N	0.81	191	NA	Debonding Plastic void growth (14%, Ø 34 nm)	NA
0.2C	0.88	188	NA	NA	Pull-out (7.86 μm) Plastic void growth (8%, Ø 151 nm)
9R	1.41	697	Rubber cavitation Plastic void growth (Ø 1.18μm)	NA	NA
9R-10N	2.28	1059	Rubber cavitation Plastic void growth (Ø 1.45μm)	Debonding Plastic void growth (13%, Ø 35 nm)	NA
9R-0.2C	2.32	1132	Rubber cavitation Plastic void growth (Ø 1.51μm)	NA	Pull-out (7.56 μm) Plastic void growth (10%, Ø 146 nm)
10N-0.2C	1.17	228	NA	Debonding Plastic void growth (10%, Ø 34 nm)	Pull-out (7.98 μm) Plastic void growth (7%, Ø 145 nm)

(NA: not applicable)

8.5 Fracture Behaviour under Fatigue Loading Conditions

8.5.1 Fracture Mechanics Fatigue Data

Tests were performed to investigate the fracture behaviour under fatigue loading of the hybrid-modified epoxy polymers. Compact tension (CT) specimens with a thickness of 6 mm and a width of about 50 mm were used. After the CT specimen was mounted on a servo-hydraulic testing machine, the fatigue tests were performed using sinusoidal loading at 5 Hz with displacement-control. The tests were stopped when the advancing crack reached the threshold region where the crack effectively stops propagating (approximately 5 million cycles). In order to improve the accuracy of the testing results, at least two replicate tests were undertaken for each formulation, and the length of crack growth was recorded using a crack propagation gauge.

The experimental results obtained from the fatigue tests were analysed and presented as the crack propagation per cycle (crack propagation rate), da/dN, against the maximum applied strain energy release rate, G_{max}, as shown in Figure 8.5.1. The analysed data show a linear Paris-law region where the crack propagates, and a threshold region where the crack effectively stops growing. In the Paris-law region, linear regression was used to calculate the gradient, m. The measured results of the maximum applied strain release rate in the threshold region, G_{th}, and the gradient of the Paris-law region, m, are summarised in Table 8.5.1. This clearly shows that the modification of the epoxy with single-phase reinforcements of the CTBN rubber, nanosilica particles or multi-walled carbon nanotubes improves the fatigue performance. The combination of these reinforcements improves its resistance to fatigue crack growth even further. Generally, the addition of these additives shifts the fatigue testing curves toward higher values of the maximum applied strain energy release rate, see Figure 8.5.1. The modified epoxy composites with single-phase reinforcement showed a relatively high value of G_{th}, in a range between 53 to 61 J/m^2, compared with that of the unmodified epoxy polymer (G_{th} = 24 J/m^2).

The addition of hybrid reinforcements leads to a further increase in the fatigue performance. For example, the highest value of G_{th} was measured to be 127 J/m^2 for the

hybrid-modified polymer with 0.2 wt% nanotubes and 9 wt% CTBN (9R-0.2C). The values of G_{th} for the hybrid-modified polymers are in a wide range from 97 to 127 J/m^2, which are around double that of the single-phase modified polymers. This indicates that the synergistic effect on the fatigue performance was obtained in the hybrid-modified polymers, as demonstrated by Manjunatha et al [148]. Modifying the epoxy polymer with the CTBN rubber particles considerably reduced the gradient of the Paris-law region, *m*. For example, the modified samples containing rubber particles have an average value of 7.0 for the Paris-law gradient, which is much smaller than the unmodified epoxy (*m*=13), or the modified epoxy polymer without the micron-rubber particles (around 14). In the literature, studies focused on the CTBN modification of an anhydride-cured epoxy resin reported the same trend of the Paris-law gradient being reduced by rubbery particles; the value of *m* was decreased from 16 for the neat epoxy polymer to 6.1 for the rubber-modified polymer at 10 phr due to crack-tip shielding by rubber cavitation and plastic dilation of the matrix [146, 149].

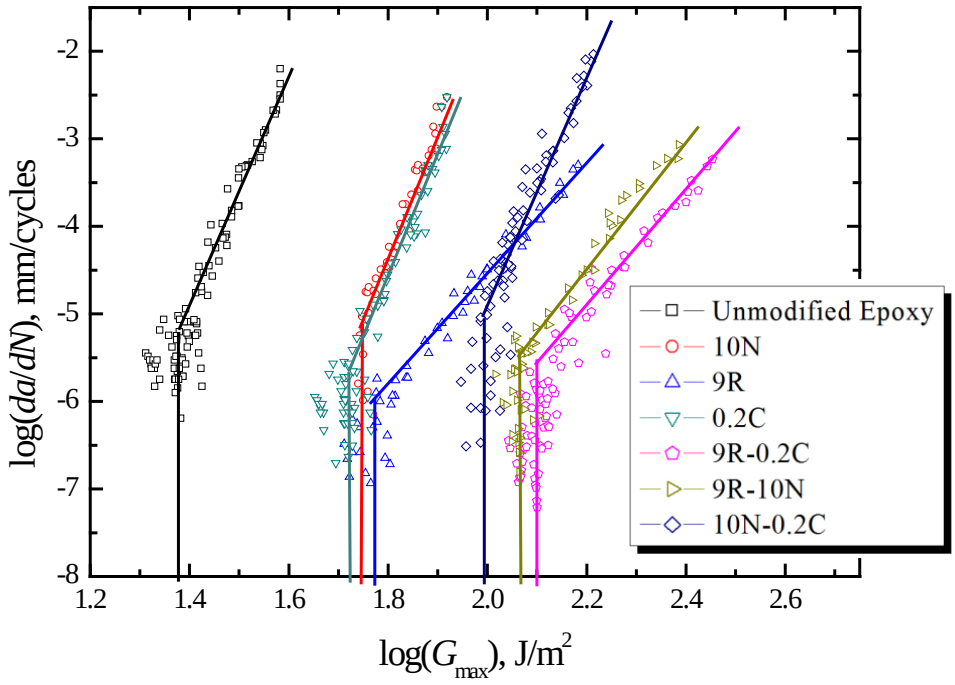


Figure 8.5.1 Rate of crack growth versus maximum applied strain energy release rate in the fatigue cycle for unmodified epoxy and modified epoxy with single-phase and hybrid reinforcements.

Table 8.5.1 Summary of the fatigue testing results of the maximum applied strain energy release rate in the threshold region and Paris-law gradient of the hybrid-modified epoxy polymers.

Formulation	G_{th} (J/m^2)		G_{th}/G_{Ic}	m	
	Mean	SD		Mean	SD
Control	24	8	0.18	13.2	0.3
10N	55	4	0.28	13.9	0.2
0.2C	53	7	0.28	14.3	0.2
9R	61	3	0.09	6.5	0.1
9R-10N	118	7	0.11	7.8	0.4
9R-0.2C	127	8	0.11	6.6	0.3
10N-0.2C	97	6	0.42	12.8	0.3

By considering the ratio of G_{th}/G_{Ic}, the effectiveness of the addition of these micron- and nano-size reinforcements on the fatigue performance was examined. A maximum value of G_{th}/G_{Ic} was recorded to be 0.42 for the hybrid-modified epoxy polymer (10N-0.2C) containing 10 wt% nanosilica particles and 0.2 wt% carbon nanotubes, indicating the introduction of this nano-hybrid reinforcement is the best way to improve the fatigue property of the polymer. This can be expected because the contribution of using the nanotubes or silica nanoparticles alone to the fatigue property is significant (G_{th}/G_{Ic}=0.28 for both 10N and 0.2C samples). However, the modified epoxy polymers containing the CTBN rubber particles showed a relatively low value of G_{th}/G_{Ic} of 0.09 for the rubber-modified alone epoxy polymer (9R) due to the large increase in G_{Ic} for the CTBN-modified epoxies, but only a small increase in G_{th}. Even adding the second-phase (nanosilica or nanotubes) with the rubber particles to form the hybrid materials, the value of G_{th}/G_{Ic} did not increase obviously, to around 0.11 for the hybrid-modified polymers with the rubber particles (9R-0.2C and 9R-10N). This indicates that the use of the CTBN rubber particles to improve the toughness of polymer-based composites is more effective than the improvement of their fatigue performance, even though the highest value of G_{th} (127 J/m^2) was attained for the hybrid-modified epoxy with the rubbery additives (9R-0.2C). This is because the rubber-modified polymer has a relatively smaller plastic zone size of around 3.5 μm at the threshold region during fatigue loading, and there are few rubber particles in the plastic zone, compared with the plastic zone size (around 35 μm) of the rubber-modified

epoxy under quasi-static loading. The investigation focused on the fatigue behaviour of the epoxy polymer showed a low effectiveness of using rubber modification on the fatigue performance of the modified polymers [102, 149]

8.5.2 Fractography

FEG-SEM observation was used to inspect the fracture surfaces of the CT specimens after fatigue failure, and the mechanisms which can contribute to the increase in the fatigue performance were investigated. The fractography of fracture surfaces were imaged along the direction of fatigue crack growth, where three different zones were seen viz: the crack initiation (where G_{max} is large), crack propagation, and threshold (where $G_{max} = G_{th}$) regions (as shown in Figure 7.6.3). The FEG-SEM images for all the formulations are shown in Figure 8.5.2 ~ Figure 8.5.6. (the fractography for the nanotube-modified epoxy polymer (0.2C) was shown in Figure 7.6.4).

All the images show river lines on the fracture surfaces for the modified polymers, the occurrence of these river lines resulted in new fracture surfaces during fatigue crack growth, consequently the resistance to crack propagation was improved. The main toughening mechanisms can also be identified from these images, as discussed below.

Again, the dispersion of the multi-walled carbon nanotubes, silica nanoparticles and CTBN rubber microparticles was examined from these FEG-SEM images. The rubber particles were well dispersed in the rubber-modified polymer (9R) and the hybrid-modified polymers (9R-0.2C and 9R-10N). However, several nanotube agglomerates and nanotube-rich areas were found on the fracture surfaces, see Figure 8.5.4 and Figure 8.5.6. Due to the low magnification of these images, it was difficult to find the individual nanosilica particles, but the agglomeration of the nanosilica was observed in the hybrid-modified polymer sample (9R-10N), as can be seen in Figure 8.5.5. This undesirable agglomeration was also identified in the AFM observation.

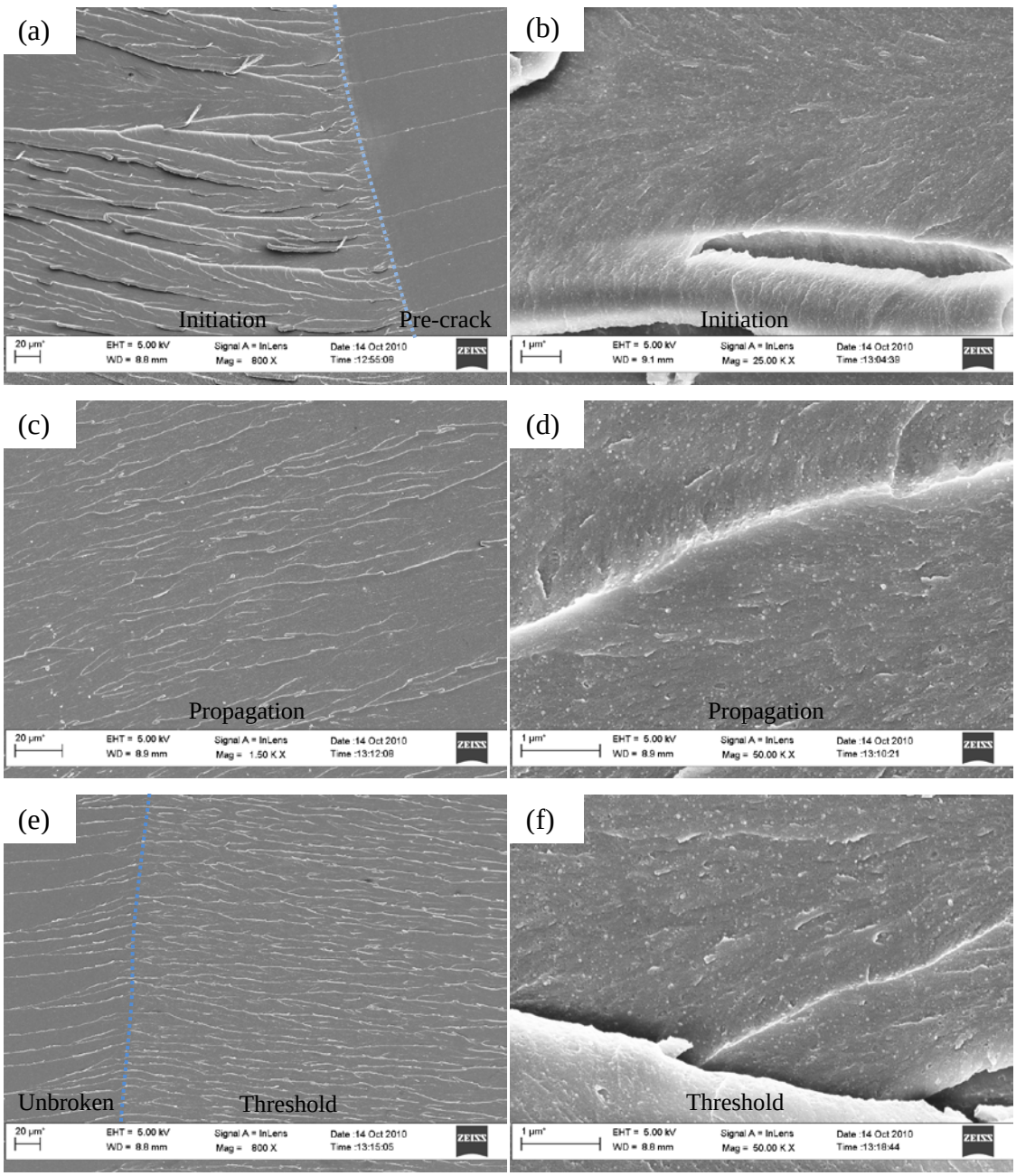


Figure 8.5.2 FEG-SEM images of the fatigue fracture surfaces of the modified polymer containing 10 wt% nanosilica particles (10N), for the regions of (a,b) crack initiation, (c,d) propagation, (e,f) threshold. (Crack growth is from right to left).

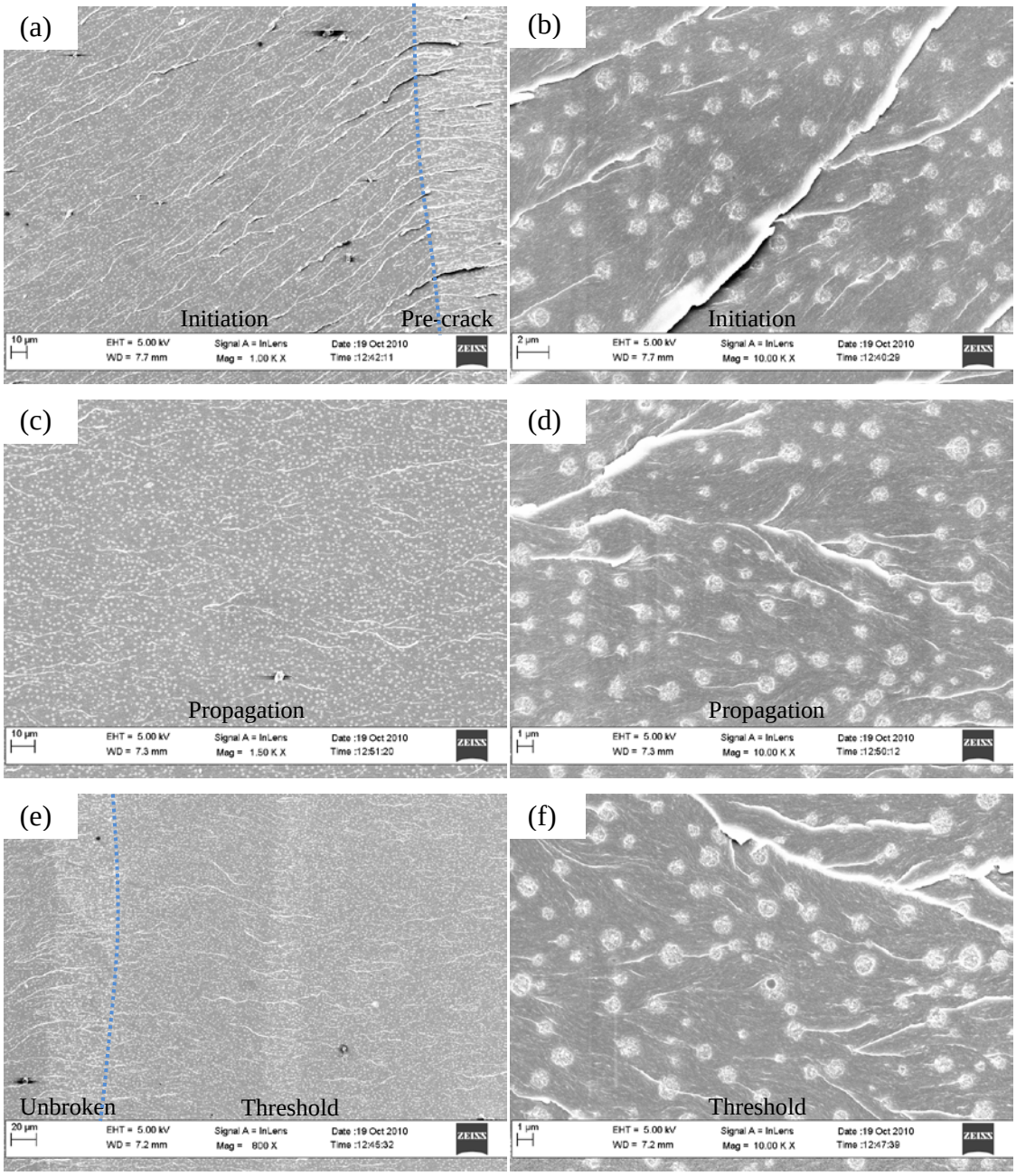


Figure 8.5.3 FEG-SEM images of the fatigue fracture surfaces of the modified polymer containing 9 wt% CTBN rubber particles (9R), for the regions of (a,b) crack initiation, (c,d) propagation, (e,f) threshold. (Crack growth is from right to left).

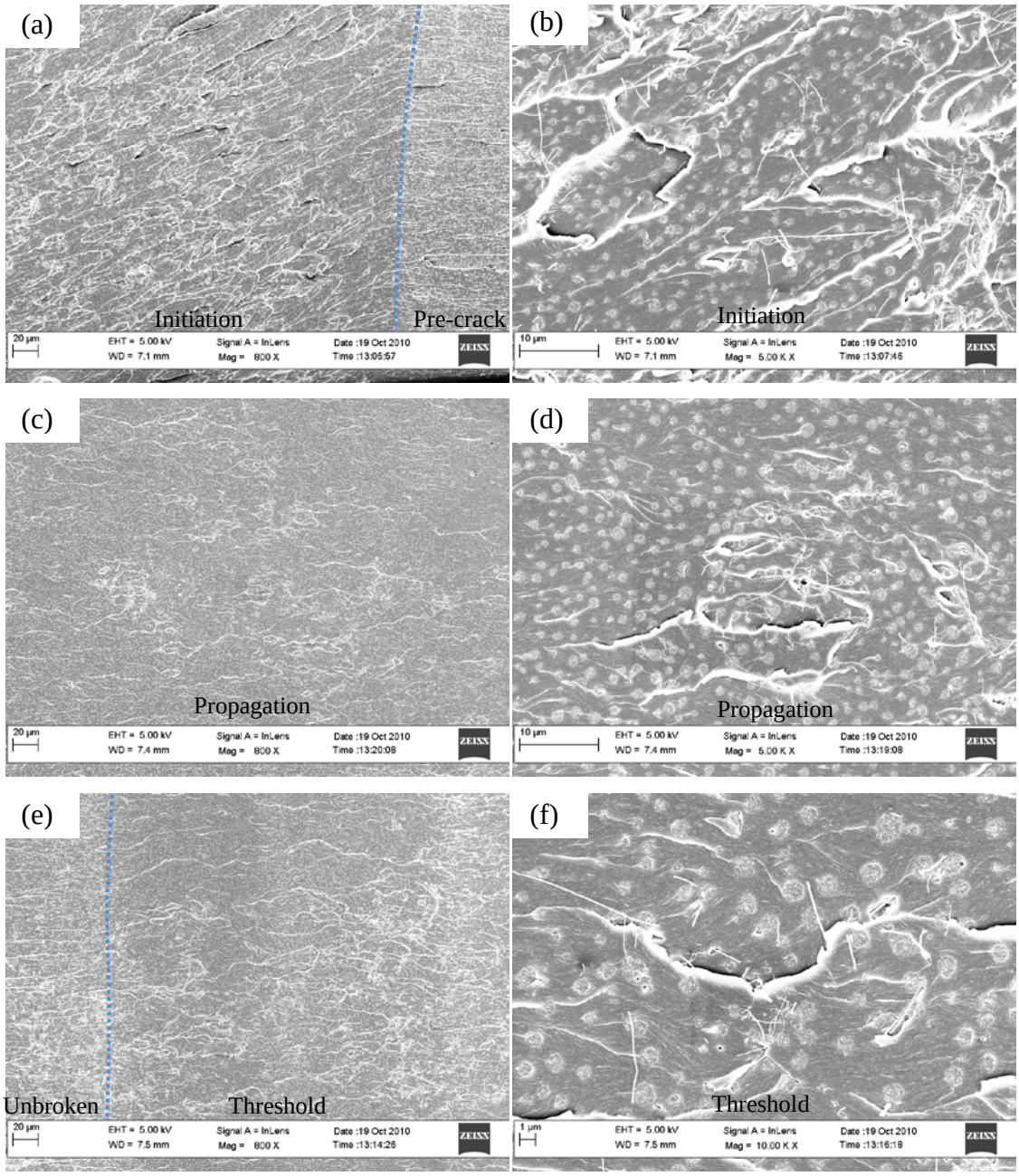


Figure 8.5.4 FEG-SEM images of the fatigue fracture surfaces of the hybrid-modified polymer containing 9 wt% CTBN rubber particles and 0.2 wt% MWCNTs (9R-0.2C), for the regions of (a,b) crack initiation, (c,d) propagation, (e,f) threshold. (Crack growth is from right to left).

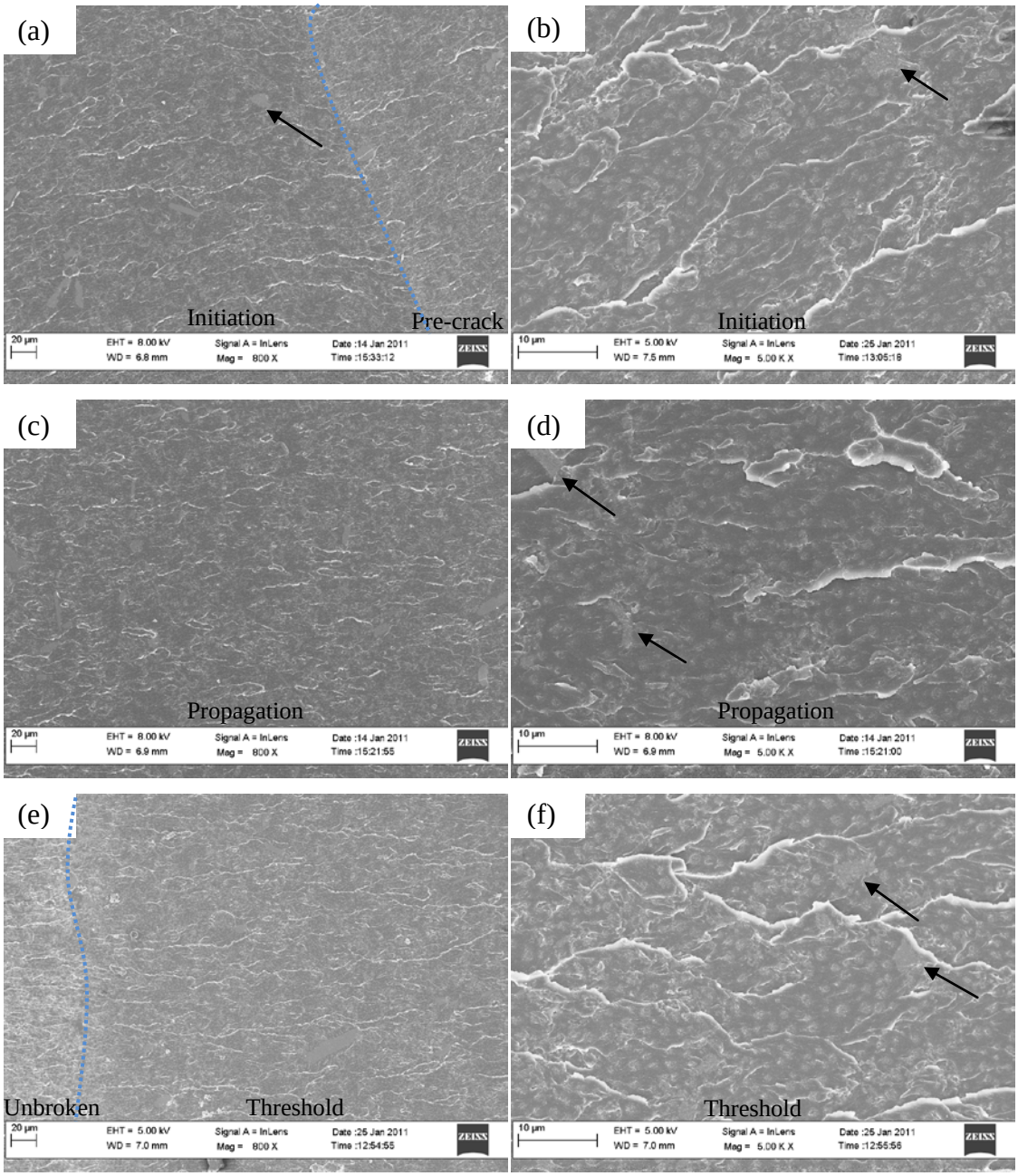


Figure 8.5.5 FEG-SEM images of the fatigue fracture surfaces of the hybrid-modified polymer containing 9 wt% CTBN rubber particles and 10 wt% nanosilica particles (9R-10N), for the regions of (a,b) crack initiation, (c,d) propagation, (e,f) threshold. The nanosilica agglomerates are indicated (Crack growth is from right to left).

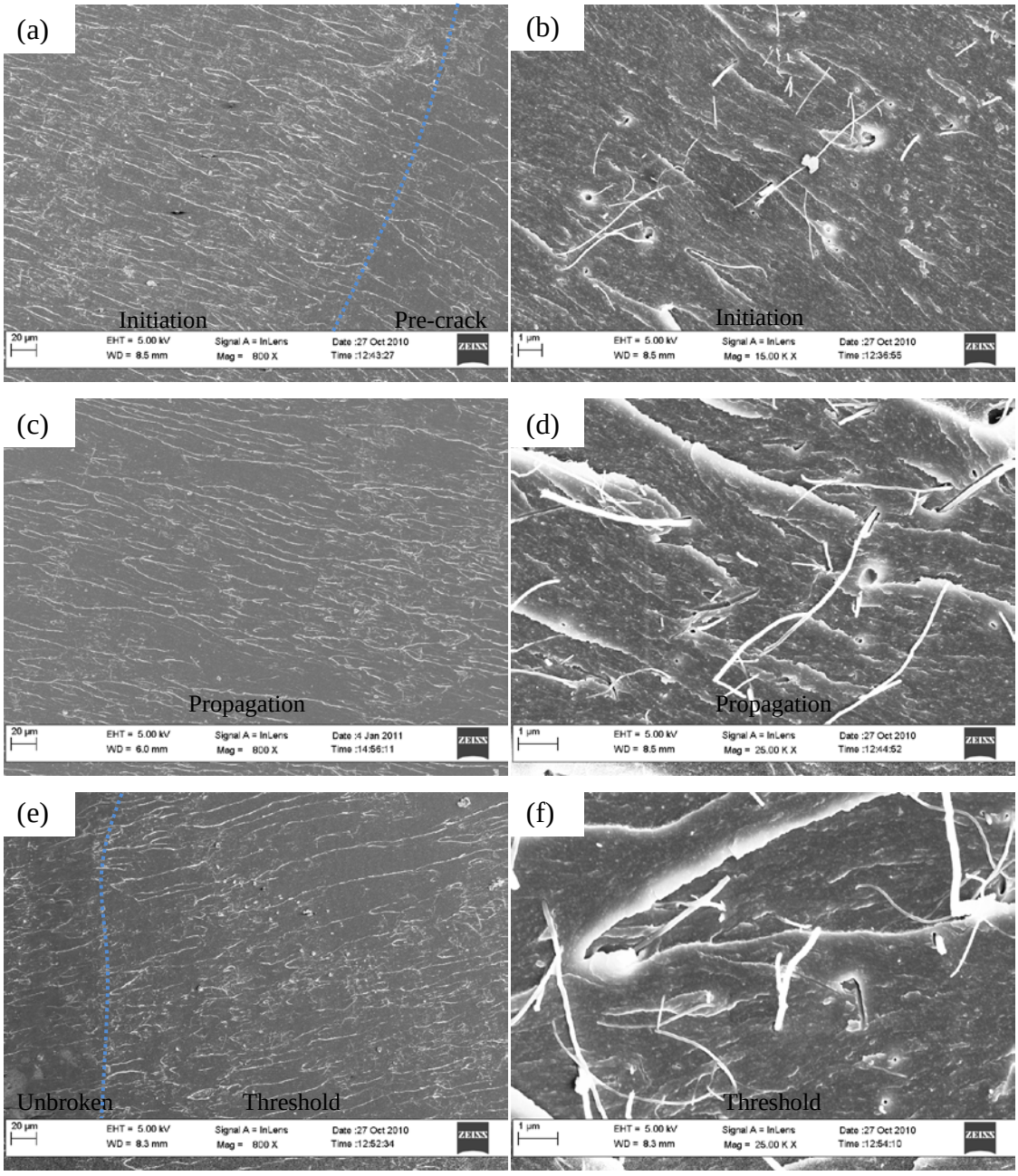


Figure 8.5.6 FEG-SEM images of the fatigue fracture surfaces of the hybrid-modified polymer containing 10 wt% nanosilica particles and 0.2 wt% MWCNTs (10N-0.2C), for the regions of (a,b) crack initiation, (c,d) propagation, (e,f) threshold. (Crack growth is from right to left).

8.5.3 Fatigue Toughening Mechanisms

From the high magnification FEG-SEM images shown in Figure 8.5.3, the fracture surfaces of the rubber-modified polymer (9R) show several ridges, all of which started at a rubber particle, as also showed clearly in a higher magnified FEG-SEM image in Figure 8.5.7. These ridges are formed by a lateral coalescence of slightly different crack plateaus as the crack tip meets the rubber particles [146, 150]. The occurrence of this ridge requires more energy, and consequently improves the crack growth resistance.

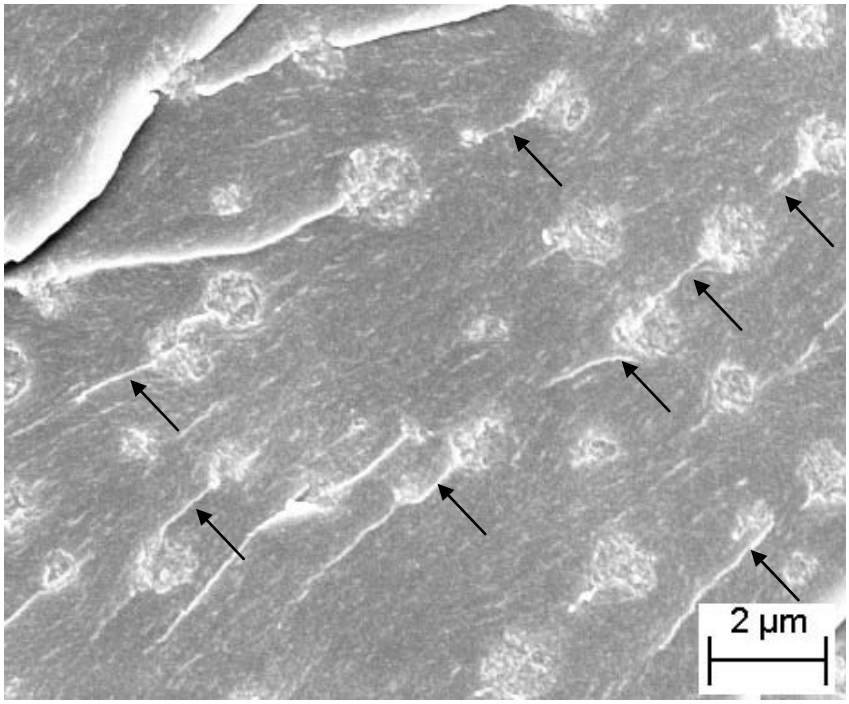


Figure 8.5.7 FEG-SEM image of the fracture surface at the threshold region of the rubber-modified polymer (9R), showing the ridges starting at rubber particles, as indicated (crack growth is from right to left).

Shown in Figure 8.5.8, the fracture surface at the threshold region of the rubber-modified sample showed clear evidence of rubber-particle cavitation. This is considered to be the main toughening mechanism for rubber modification, and has been well established, as described in [5, 102, 149]. The diameter of voids caused by the rubber cavitation was measured to be 1.25 ±0.48 µm, which is larger than the mean rubber-particle diameter of 0.58 µm measured from the AFM image shown in Figure 8.2.1. This indicates that the rubber particles cavitate internally with subsequent void growth. This process can efficiently absorb energy, hence the fatigue growth resistance of the

composites is increased. The size of the rubber cavities was also measured in both crack initiation and propagation regions of the 9R sample. A mean diameter of 1.19 ±0.51 μm and 1.20 ±0.33 μm was measured in the crack initiation region and crack propagation region, respectively. These values are similar to the size of the rubber cavities (1.18 μm) measured in the quasi-static fracture result.

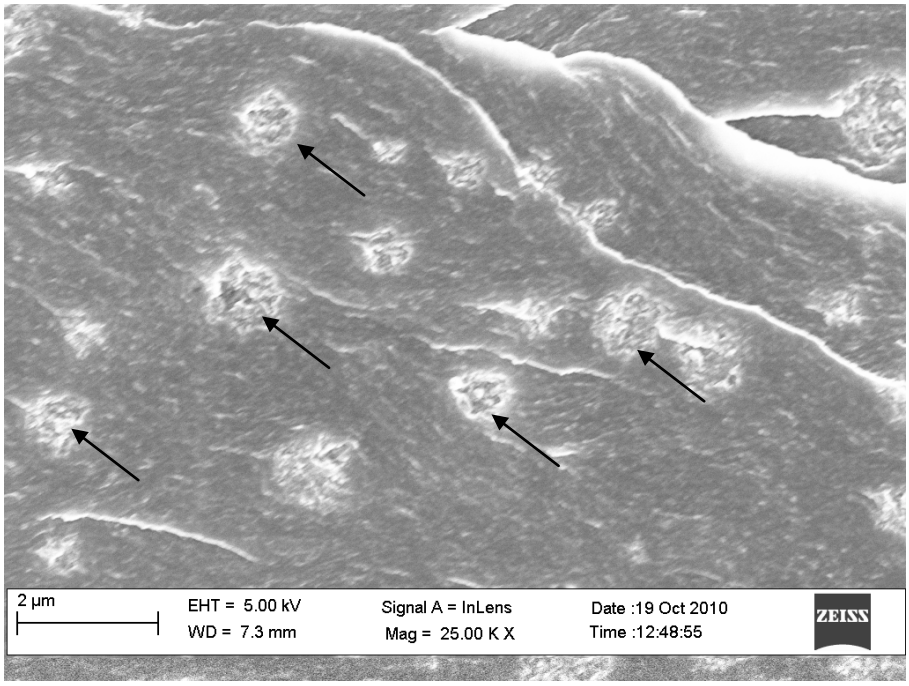


Figure 8.5.8 FEG-SEM image of the fracture surface at the threshold region of the (9R) rubber-modified polymer showing rubber-particle cavitation and subsequent void growth.

The toughening mechanism of the nanosilica particles (single-phase modification) was identified to be the plastic void growth associated with interfacial debonding between the silica nanoparticles and epoxy matrix in quasi-static tests, as discussed in Chapter 6. Figure 8.5.6 shows a high magnification FEG-SEM image of the fracture surface at threshold region, clear evidence of debonding and subsequent plastic void growth was found. Around 20 ±3% of the nanosilica particles with void growth was calculated from the fracture surface at the threshold region. This value is higher than that measured in the crack initiation and propagation regions (14 ±4%), and on the fracture surface of the tested SENB specimens (14 ±2% was calculated). This is because of a relatively slow crack propagation rate at the threshold region during the

fatigue tests. As reported by Gilat [140], low strain rate results in a high degree of plastic deformation in epoxy polymers when subjected to a tensile loading. Hence, plastic void growth associated with nanosilica debonding and the plastic deformation in the epoxy matrix was easier to form at the threshold region than in the crack initiation and propagation regions. This phenomenon also happened in the multi-walled carbon nanotube-modified epoxy polymer, as discussed in Chapter 7. The voids on the fracture surfaces at the threshold region have an average diameter of 36 ±4 nm, which is slightly larger than the voids present in the crack initiation and propagation regions. The mean diameter was measured to be 33 ±6 nm in the crack initiation region, and 34 ±3 nm in the crack propagation region.

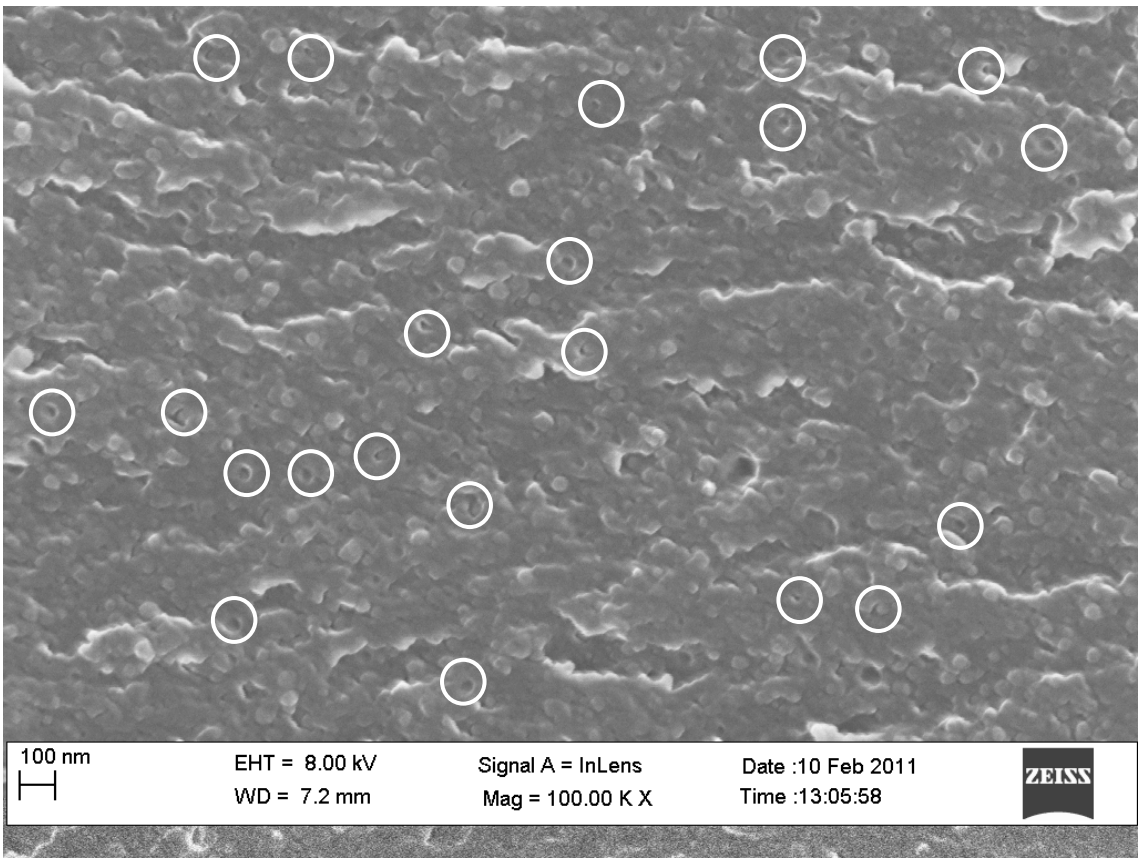


Figure 8.5.6 A high magnification FEG-SEM image of the fracture surface at threshold region of the nanosilica/epoxy material (10N), showing plastic void growth as circled.

For the other single-phase modification using the multi-walled carbon nanotubes, the fatigue toughening mechanism which contributed to the increased fatigue performance was identified to be nanotube pull-out and plastic void growth due to the debonding between the nanotubes and matrix (see Figure 8.5.7), as discussed in Chapter 7, see Table 7.6.2.

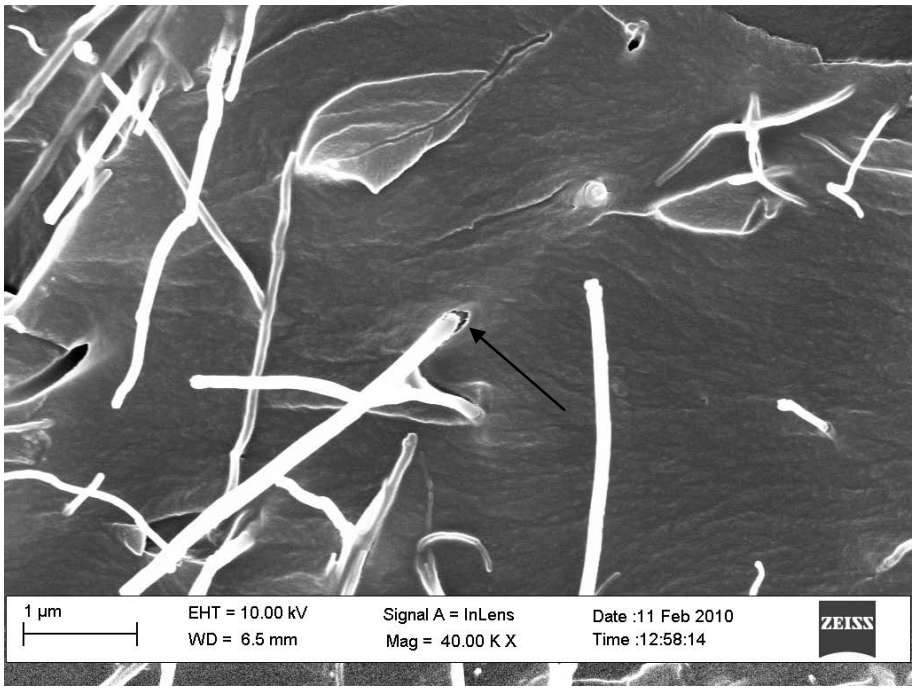


Figure 8.5.7 FEG-SEM image of the fracture surface at the threshold region for the nanotube-modified polymer at 0.2 wt% (0.2C), showing nanotube pull-out and plastic void growth as indicated.

Moving to the modified polymers with the hybrid reinforcements, Figure 8.5.8 shows the fracture surface at the threshold region of the 9R-10N composite after fatigue failure, the main toughening mechanisms caused by the addition of the rubber particles were identified to be rubber cavitation and subsequent void growth. A mean diameter of the rubber cavities was measured to be 1.49 ±0.71 μm (1.40 ±0.51 μm in the crack initiation region, and 1.41 ±0.38 μm in the crack propagation region). This measured diameter of the cavities is higher than the rubber-modified only (9R) polymer (1.25 μm at the threshold region). The contribution of using the nanosilica was identified to be the plastic void growth after silica nanoparticle debonding. Around 19 ±2% of the silica

nanoparticles showed debonding and void growth was calculated on the fracture surface at the threshold region, and the diameter of these voids was measured to be 35 ±5 nm, which is similar to the single-phase nanosilica-modified polymer (10N). The synergistic effect of the hybrid-reinforcement (rubber and nanosilica particles) on the fatigue performance can be attributed to a relatively high degree of the rubber cavitation mechanism occurred in the hybrid-modified polymer (9R-10N). Besides, a relative large plastic zone size of 7.8 μm was calculated for the hybrid-modified (9R-10N) epoxy. Hence, there are more rubber particles in the plastic zone, and more toughening contribution from the rubber cavitation was obtained in the 9R-10N sample, compared with the rubber-modified polymer 9R.

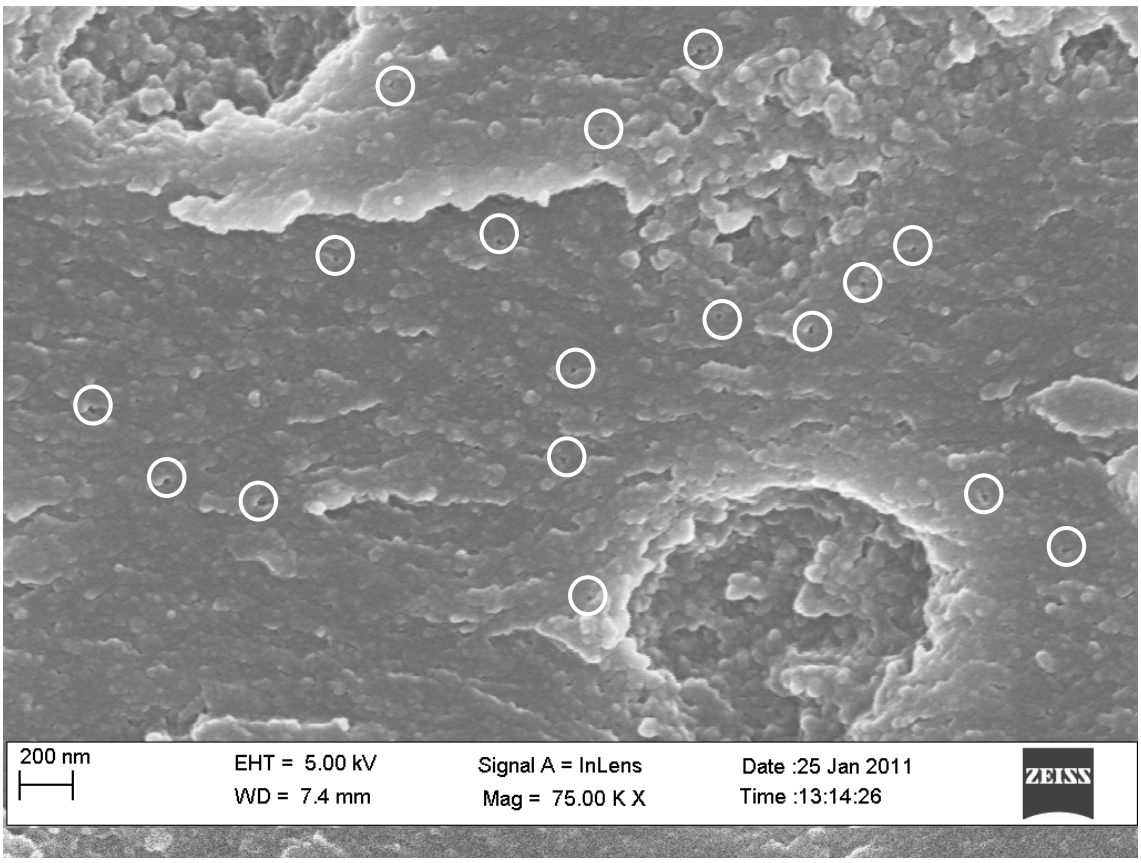


Figure 8.5.8 FEG-SEM image of the fracture surface at the threshold region of the hybrid-modified polymer containing 9 wt% rubber particles and 10 wt% silica nanoparticles (9R-10N), showing rubber cavitation and subsequent void growth, and nanosilca plastic void growth as circled.

Figure 8.5.9 shows a high magnification FEG-SEM image of the hybrid-modified sample containing 9 wt% rubber particles and 0.2 wt% multi-walled carbon nanotubes (9R-0.2C). The toughening mechanism induced by the addition of the CTBN rubber particles was clearly identified to be rubber cavitation and subsequent void growth. The mean diameter of the cavitated rubber particles was measured to be 1.56 μm with a standard deviation of 0.41 μm, which is larger than the rubber cavities in the rubber modified (9R) epoxy. Clear evidence of nanotube pull-out and void growth around the debonded nanotubes was found on the fracture surfaces. The nanotube pulled-out length at threshold region was measured to be 6.42 ±1.32 μm, which is slightly shorter than that in the crack initiation and propagation regions (7.97 ±1.82 μm), and on quasi-static loading fracture surfaces (7.56 ±3.24 μm), but is longer than the pull-out length (5.98 μm) measured in the threshold region in the nanotube-modified polymer (0.2C), as discussed in Chapter 7. The determined percentages of nanotube pull-out and plastic growth showed 100% of the nanotubes to be pulled out in all the fatigue crack growth regions. However, only 10 ±1% of the nanotubes with void growth were found in the crack initiation and propagation regions, and 16 ±3% at the threshold. The mean diameter for the void around the nanotubes in all fatigue crack growth regions was the same, and was measured to be 156 ±11 nm. All of these measured values associated with plastic void growth caused by the addition of nanotubes in the hybrid-modified polymer (9R-0.2C) are higher than for the nanotube-modified alone materials (discussed in Chapter 7). The energy contribution from these toughening mechanisms to the fatigue performance of the hybrid-modified polymer is higher than the single-phase modification. Therefore, the synergistic effect on the fatigue performance was obtained in this hybrid-modified epoxy. Indeed, the measured values of G_{th} are higher than the superposition of the increased G_{th} in single-phase modified epoxies.

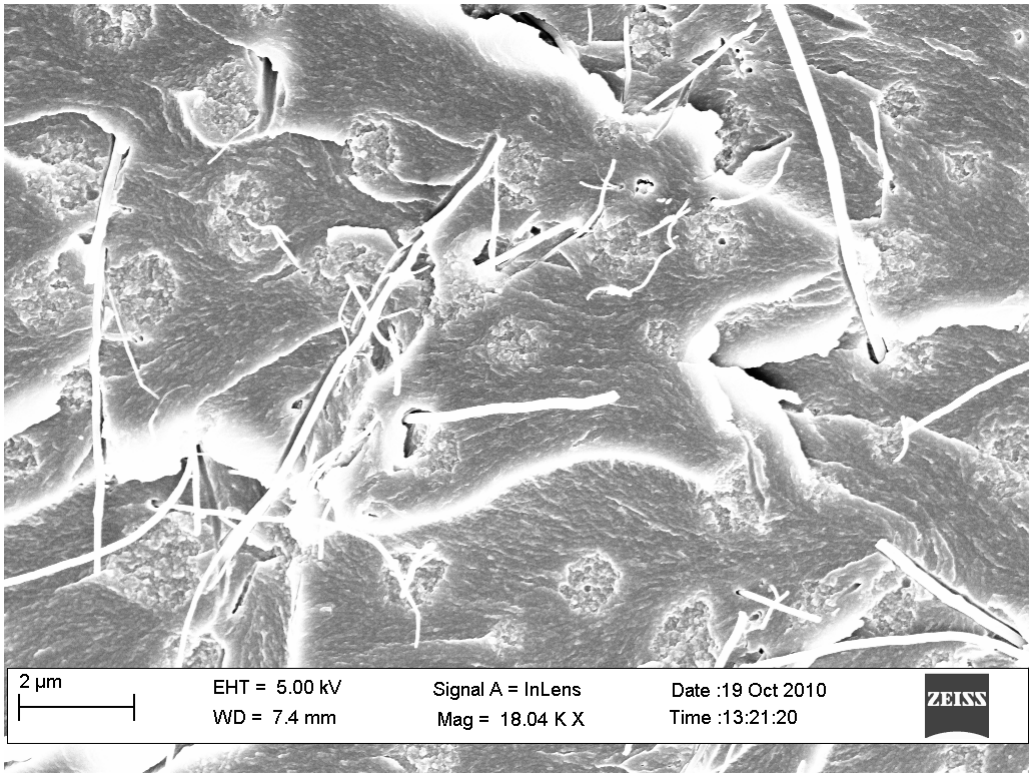


Figure 8.5.9 FEG-SEM images of the fracture surface at the threshold region for the 9R-0.2C hybrid-modified polymer, showing nanotube pull-out and plastic void growth, and rubber cavitation.

Figure 8.5.10 shows the fracture surface at the threshold region of the nano-hybrid modified epoxy polymer (10N-0.2C), where several pulled out nanotubes with void growth were clearly seen. The mean nanotube pull-out length was measured to be 5.89 μm with a standard deviation of 2.18μm, which is shorter than that observed in the crack initiation and propagation regions (7.88 ±1.81 μm), but similar to the measured pull-out length (5.98 μm) for the single-phase nanotube-modified polymer (as discussed in Chapter 7). Plastic void growth associated with the debonding between the nanotubes and matrix, and the plastic deformation in the epoxy matrix was observed. Around 14 ±2% of nanotubes showed void growth with a mean diameter of 155 ±9 nm in the threshold region, which is similar to the nanotube-modified (0.2C) polymer (14% nanotube showed void growth, 157 nm in diameter, see Table 7.6.2). No significant difference in the percentage of the nanotubes with void growth was recorded in various crack growth regions (around 12 ±2% of nanotubes with voids, with a mean diameter of 153 ±8nm, in the crack initiation and propagation regions).

Plastic void growth induced by the silica nanoparticles was also found on the fracture surfaces, see Figure 8.5.10. A relatively high percentage of 18 ±3% of nanosilica with void growth (34 ±1 nm in diameter) was recorded in the threshold region, compared with the crack initiation and propagation regions for the nano-hybrid modified polymer (10N-0.2C) and the silica-modified polymer (10N). The contribution caused by the nanosilica plastic void growth, and nanotube pull-out and void growth, in the nano-hybrid composite (9R-10N) is nearly equal to the superposition of the contribution from these toughening mechanisms in the single-phase modified polymers (10N and 0.2C) in fatigue. Hence, no obvious synergy of fatigue performance was obtained in the 10N-0.2C nanocomposite.

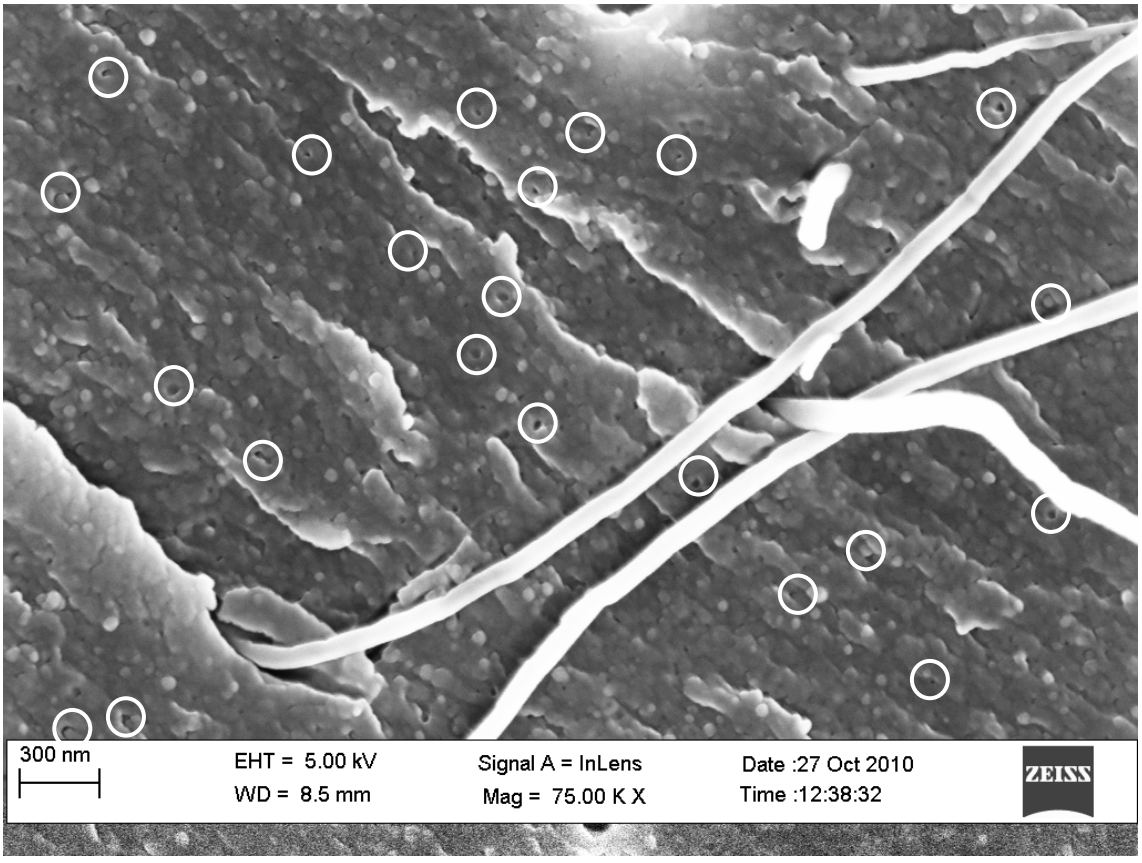


Figure 8.5.10 FEG-SEM images of fracture surface at the threshold of the nano-hybrid modified polymer containing 10 wt% nanosilica and 0.2 wt% nanotubes (10N-0.2C), showing nanotube pull-out, nanotube plastic void growth and nanosilica plastic void growth as circled.

The fatigue toughening mechanisms at threshold induced by the hybrid reinforcements were summarised in Table 8.5.2

Table 8.5.2 Summary of the fatigue toughening mechanisms caused by the hybrid reinforcements.

Formulation	G_{th} (J/m^2)	G_{th}/G_{Ic}	m	CTBN toughening mechanism	Nanosilica toughening mechanism	Nanotube toughening mechanism
control	24	0.18	13.2	NA	NA	NA
10N	55	0.28	13.9	NA	Plastic void growth (20%, Ø 36 nm)	NA
0.2C	53	0.28	14.3	NA	NA	Pull-out (5.98 μm) Plastic void growth (14%, Ø 157 nm)
9R	61	0.09	65	Rubber cavitation Plastic void growth (Ø 1.25μm)	NA	NA
9R-10N	118	0.11	7.8	Rubber cavitation Plastic void growth (Ø 1.49μm)	Plastic void growth (19%, Ø 35 nm)	NA
9R-0.2C	127	0.11	6.6	Rubber cavitation Plastic void growth (Ø 1.56μm)	NA	Pull-out (6.42 μm) Plastic void growth (16%, Ø 156 nm)
10N-0.2C	97	0.42	12.8	NA	Plastic void growth (18%, Ø 34 nm)	Pull-out (5.89 μm) Plastic void growth (14%, Ø 155 nm)

(NA: not applicable)

8.6 TOM Observation of the Nanotube Dispersion in Hybrid Modified Polymers

The dispersion of the multi-walled carbon nanotubes in the hybrid formulations (9R-0.2C and 10N-0.2C) was examined by transmission optical microscopy observation (TOM) on a 70-μm-thick slice of the cured epoxy polymers. Figure 8.6.1 shows the TOM images and the histograms for the hybrid-modified polymers with the nanotubes. The results show that the dispersion of the nanotubes in the hybrid sample (9R-10N) containing the rubber particles is much better than the hybrid material containing the silica nanoparticles and carbon nanotubes (10N-0.2C). The greyscale analysis results show that the histogram of 9R-0.2C sample consists of a wide peak which lies in the dispersed range (the mean value = 78), see Figure 8.6.1 (a). In contrast, Figure 8.6.1 (b) is the analysis result for the nano-hybrid modified polymer (10N-0.2C), and a narrow peak lies on the low value present in the histogram for the nano-hybrid sample. This indicates that a relatively low degree of nanotube dispersion was observed in this sample, but this result is similar to the dispersion for the single-phase nanotube-modified polymers.

As discussed in Section 8.4, the increased viscosity caused by the addition of rubber particles provides a high shear stress in the mixture during the mixing [147], and consequently break down the entangled nanotubes in the resin. Also, high viscosity impedes the tendency of the nanotubes to reagglomerate during the curing process. The improvement in the nanotube dispersion caused by the addition of a second-phase of fillers to the nanotube-modified materials has been demonstrated. Brooker et al. [151] investigated the nanotube dispersion in a thermoplastic-toughened epoxy polymer using greyscale analysis, and reported that increased thermoplastic content, and hence increased viscosity of the resin, resulted in a better nanotube dispersion in the mixture and in the cured sample. However, the presence of the silica nanoparticles as the second-phase modifier in the nanotube-modified mixture did not increase the viscosity of the resin. Hence, no improvement on the nanotube dispersion was obtained in the 10N-0.2C nano-hybrid sample.

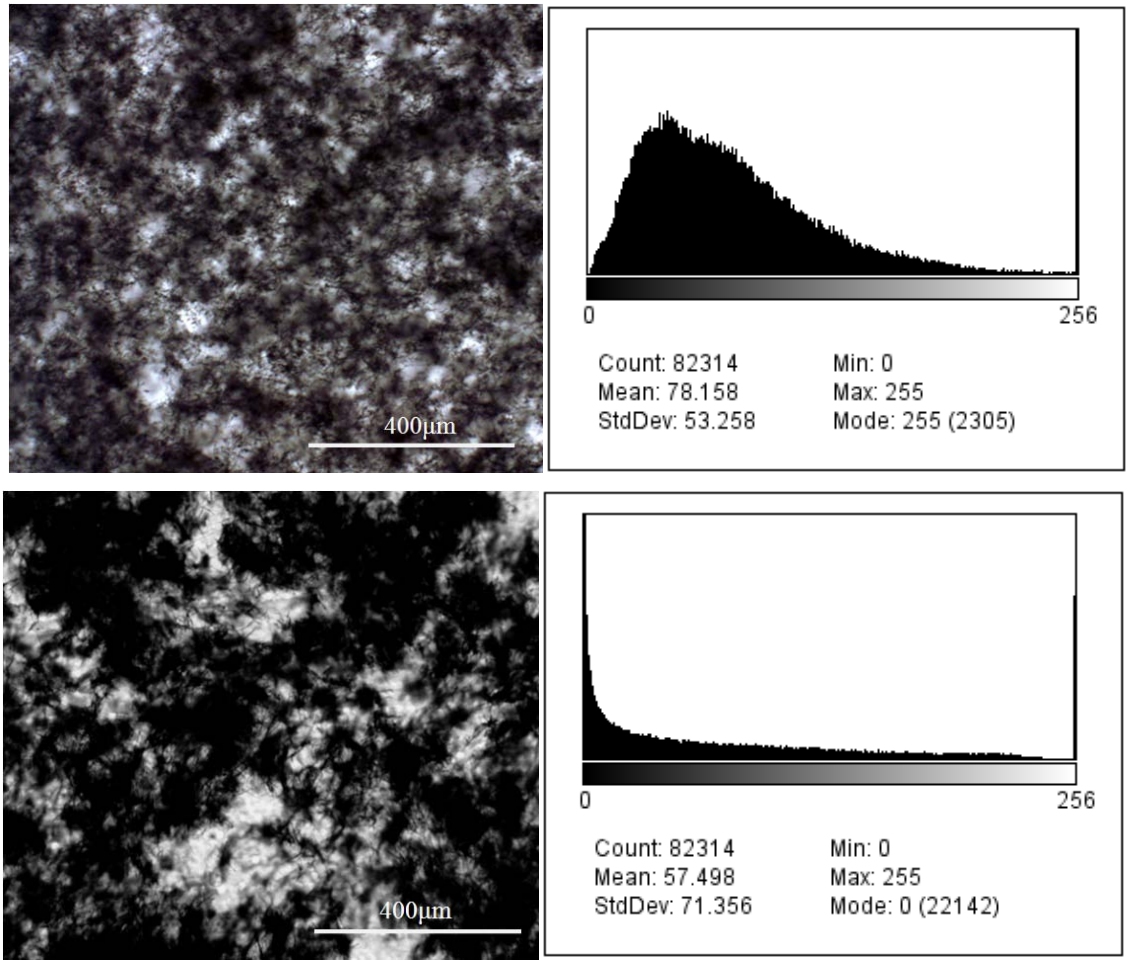


Figure 8.6.1 TOM images and the greyscale histogram of the hybrid modified epoxy polymers with nanotubes, (a) 9R-0.2C sample, (b) 10N-0.2C sample.

8.7 The Effect of the Addition of Hybrid Nano-reinforcements on the Mechanical Properties of Modified Epoxy Polymers.

The combination of the silica nanoparticles and carbon nanotubes (10N-0.2C) with the epoxy polymer to form the hybrid nanocomposites resulted in a significant improvement in the toughness and fatigue performance. However, the dispersion of nanotubes in the nanocomposites with various loadings of nanosilica particles and multi-walled carbon nanotubes was not discussed; a fixed concentration of 0.2 wt% and 10 wt% was used for the standard MWCNTs and silica nanoparticles (Nanopox F400), respectively, due to the small mass of MWCNTs available.

In this Section, a series of hybrid nanocomposites were prepared, and the effect of various concentrations of these nano-reinforcements on the stiffness and toughness was investigated. A hybrid nano-modified epoxy resin, R1D1 from Nanoledge, was used; this consists of 0.36 wt% multi-walled carbon nanotubes and 12.28 wt% silica nanoparticles premixed in a DGEBA epoxy resin. All the formulations used in this Section are shown in Table 8.7.1. The nanotubes in R1D1 have a diameter of 30-40 nm, and are several micrometers long, as measured from fracture surfaces.

Table 8.7.1 The formulations of the hybrid-modified epoxy composites with R1D1 nano-hybrid reinforcements.

Formulation	**Silica Nanoparticles** (wt%)	**Carbon Nanotubes** (wt%)
Control	0.0	0.00
2N-0C	2.0	0.00
2N-0.06C	2.0	0.06
4N-0C	4.0	0.00
4N-0.06C	4.0	0.06
4N-0.12C	4.0	0.12
6N-0.0024C	6.0	0.0024
6N-0.06C	6.0	0.06
6N-0.12C	6.0	0.12
6N-0.18C	6.0	0.18

Note that all the formulations in Table 8.7.1 were modified with both, silica nanoparticles and multi-walled carbon nanotubes, in which the multi-walled carbon nanotubes were pre-mixed with the epoxy resin by the manufacturer, and the MWCNTs in R1D1 are different to the standard nanotubes generated by the CVD process. Furthermore, silica nanoparticles dispersed in the DGEBA epoxy, i.e. Nanopox F400 from Nanoresins, were used as an additional control formulation, as no MWCNTs are present in these formulations. The F400 was blended with the R1D1 hybrid nano-modified polymer to change the concentrations of the nano-reinforcements as required.

8.7.1 Mechanical and Thermal Properties

The measured Young's modulus of the nanocomposites with the various contents of the nanosilica and nanotubes are shown in Table 8.7.2 and Figure 8.7.1. The addition of the nano-hybrid reinforcements resulted in a steady increase in the stiffness of the polymer-based nanocomposites; the maximum value of the modulus was measured to be 3.04 GPa for the nanocomposite with the highest loading of nano-reinforecments. As can be seen in Figure 8.7.1, the addition of silica nanoparticles alone to the epoxy polymer (sub-control materials) led to a steady increase in the modulus from 2.90 GPa for the unmodified epoxy polymer to 3.01 GPa for the nanocomposites containing 6.0 wt% nanosilica. However, the introduction of the MWCNTs into nanosilica-modified polymer to form the hybrid nanocomposites only increased the modulus slightly. This indicates that the use of the MWCNTs did not significantly affect the stiffness of its nanocmposites. Comparing these results to the modified polymer with the standard multi-walled carbon nanotubes discussed in Chapter 7, the MWCNTs in R1D1 have no potential for improving the stiffness of the epoxy polymer (E = 3.11 GPa for the modified polymer with 0.2 wt% standard MWCNTs). This may be because the standard MWCNTs have a relatively long length of around 120~140 nm, which is good to transfer the stress as the nanocomposites were subjected to tensile loading. However, the short MWCNTs in R1D1 are not so effective.

The glass transition temperature, T_g, of all the R1D1 nanocomposites is very similar, at around 142 °C to 147 °C, with no clear trend when adding nano-reinforcements at various concentrations. This indicates that the addition of these nano-reinforcements did not affect the glass transition temperature.

Table 8.7.2 The mechanical and thermal properties of the nanocomposites with R1D1 nano-reinforments.

Nanosilica wt%	CNT wt%	*E* (GPa)		T_g (°C)	
		Mean	SD	Mean	SD
0	0.00	2.90	0.09	147.8	0.9
2.0	0.00	2.95	0.02	145.6	1.5
	0.06	2.95	0.05	144.0	1.3
4.0	0.00	3.00	0.07	146.2	0.9
	0.06	3.00	0.05	145.0	2.2
	0.12	3.04	0.07	146.1	1.0
6.0	0.00	3.01	0.06	143.4	0.7
	0.02	3.00	0.06	145.1	1.1
	0.06	3.03	0.06	142.3	2.0
	0.12	3.04	0.04	143.2	0.9
	0.18	3.04	0.03	144.2	1.2

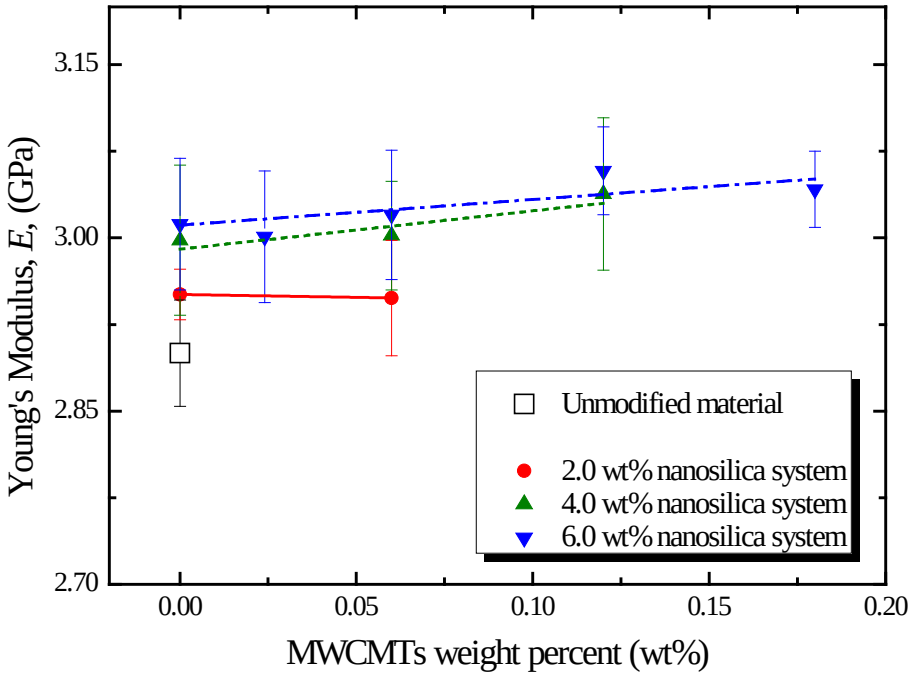


Figure 8.7.1 Young's modulus of the R1D1 nanocomposites.

8.7.2 Toughness

The measured values of the fracture toughness and the fracture energy from the SENB tests are summarised in Table 8.7.3. Figure 8.7.2 shows the values of G_{Ic} versus the different concentrations of nanosilica and nanotubes. The addition of the single-phase of nanosilica led to a increase in the fracture energy, as expected [5]. This has the same trend of increased toughness with increasing the content of the silica nanoparticles as discussed in Chapter 6. Around a 40% increment in the fracture energy (to 181 J/m^2) was obtained for the nanocomposites with 6.0 wt% nanosilica. Further enhancement of the toughness can be obtained by incorporating the multi-walled carbon nanotubes into the nanosilica-modified polymers. A maximum value of the fracture energy of 204 J/m^2 was recorded for the nanotube loading of 0.18 wt% in the 6.0 wt% nanosilica-modified system.

Table 8.7.3 Fracture toughness and fracture energy of R1D1 nanocomposites.

Nanosilica wt%	**MWCNT (wt%)**	K_{Ic} (MPa m$^{1/2}$)		G_{Ic} (J/m^2)	
		Mean	SD	Mean	SD
0	0.00	0.69	0.04	133	8
2.0	0.00	0.68	0.03	152	16
	0.06	0.75	0.02	176	17
4.0	0.00	0.72	0.08	171	23
	0.06	0.88	0.05	187	23
	0.12	0.91	0.06	192	20
6.0	0.00	0.75	0.03	181	15
	0.02	0.83	0.13	193	8
	0.06	0.96	0.12	195	17
	0.12	0.99	0.10	199	12
	0.18	1.03	0.10	204	17

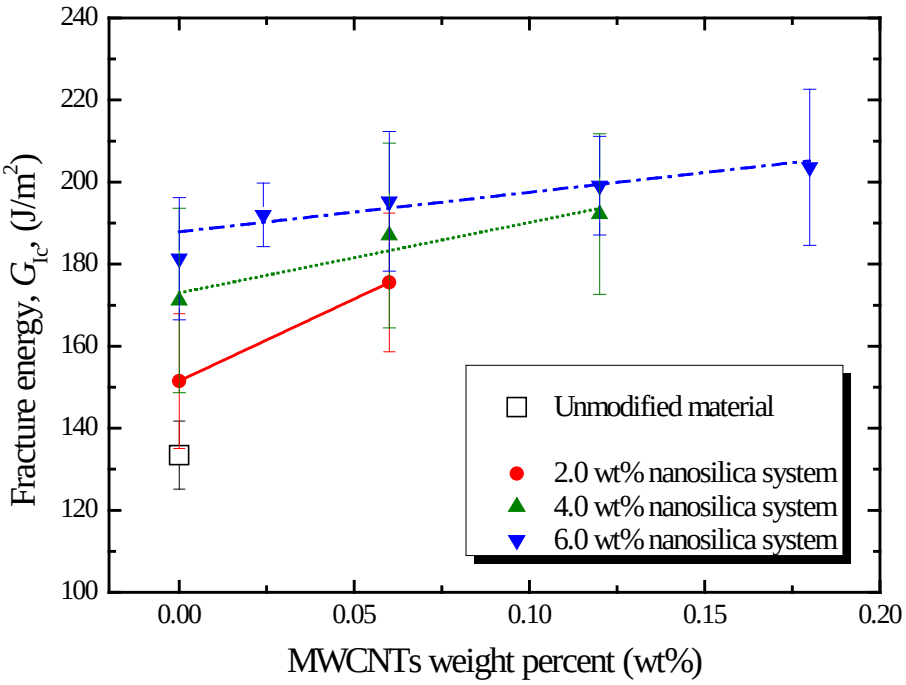


Figure 8.7.2 Fracture energy of the R1D1 nanocomposites containing nanosilica and MWCNTs.

Comparing with the single-phase modified epoxy polymer with silica nanoparticles (without nanotubes), the further addition of the MWCNTs resulted in a significant increase in the measured fracture toughness, K_{Ic}, of 22% and 28% for the 4.0 wt% nanosilica system and 6.0 wt% nanosilica system, respectively, when a relatively low concentration of 0.06 wt% nanotubes was incorporated into the hybrid nanocomposite. However, upon increasing the nanotube loading to greater than 0.06 wt%, there was no significant further increase in the value of the fracture toughness. A maximum value of the fracture toughness, K_{Ic}, was recorded to be 1.03 MPa m$^{1/2}$ for the nanocomposite with 6.0 wt% nanosilica and 0.18 wt% MWCNTs. This value is 49% higher than that of the unmodified epoxy, and is 37% higher than that of the modified material with 6.0 wt% nanosilica alone. The fracture energy, G_{Ic}, (see Figure 8.7.2) shows a maximum improvement can be attained for the sample containing the highest content the nanotubes in each system with various nanosilica loadings. The trend of the increased fracture energy caused by increasing the nanotube content is similar to the effect of addition of the standard nanotubes on the toughness, as discussed in Chapter 7.

A peak measured fracture energy of 204 J/m^2 in Figure 8.7.2 was reached for the polymer containing 6.0 wt% nanosilica and 0.18 wt% nanotubes. However, this value of the fracture energy is still lower than the 10N-0.2C nano-hybrid material (228 J/m^2), see Table 8.4.1, due to the relative higher content of nanosilica used and the longer length of the standard nanotubes.

8.7.3 Toughening Mechanisms

The toughening mechanisms which can contribute to the increase in the toughness were identified to be nanotube pull-out, see Figure 8.7.3, and plastic void growth associated with debonding between the nanotubes and epoxy matrix, see Figure 8.7.4. The mean pull-out length was measured to be 0.32 ±0.18 μm, which is much shorter than the measured effective pull-out length present on the fracture surfaces of the standard MWCNT-modified epoxy polymers (7.82 μm). All (100%) of the added nanotubes were pulled out from the matrix, as seen on the fracture surface. Voids formed around some of the nanotubes were clearly observed on the fracture surface, see Figure 8.7.4. Around 3 ±1% of the nanotubes showed void growth, and a mean diameter of 43 ±4 nm was calculated for these voids. All of these toughening mechanisms observed on the fracture surfaces show that the contribution of using the nanotubes from R1D1 to the toughness is less than the standard multi-wall carbon nanotubes, and consequently there is a relatively small improvement in the toughness in R1D1 nanocomposites, compared with the standard MWCNT-modified polymers. No clear difference in the amount of pull-out mechanism and effective pull-out length was recorded as the content of the hybrid nano-reinforcements was changed for the R1D1 nanocomposites.

Plastic void growth induced by the nanosilica debonding was clearly found on the fracture surface, as shown in Figure 8.7.5. The amount of void growth did not change as the nano-reinforcement loadings were increased (14 ±3% of nanosilica with void growth, 34 ±3 nm in diameter), which is similar to the results discussed in Chapter 6.

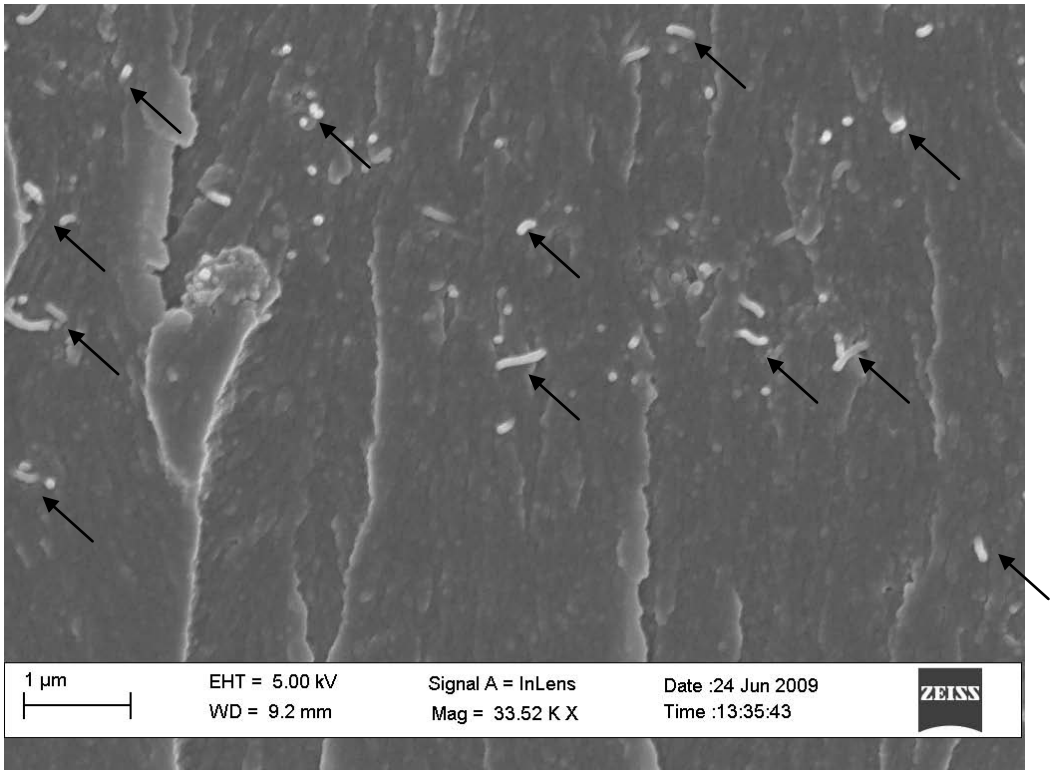


Figure 8.7.3 FEG-SEM image of the fracture surface of R1D1 nanocomposite showing nanotube pull-out as indicated (6.0 wt% silica and 0.18% nanotubes).

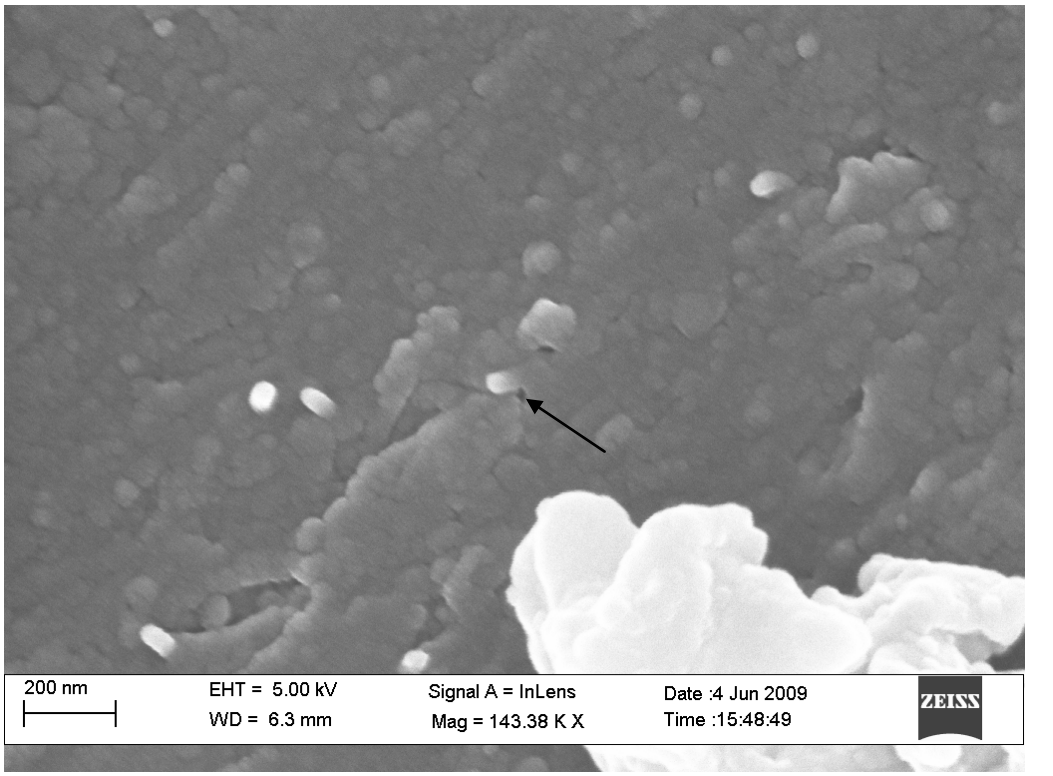


Figure 8.7.4 FEG-SEM image of the fracture surface of R1D1 nanocomposite showing void growth around the nanotube as indicated (6.0 wt% silica and 0.18% nanotubes).

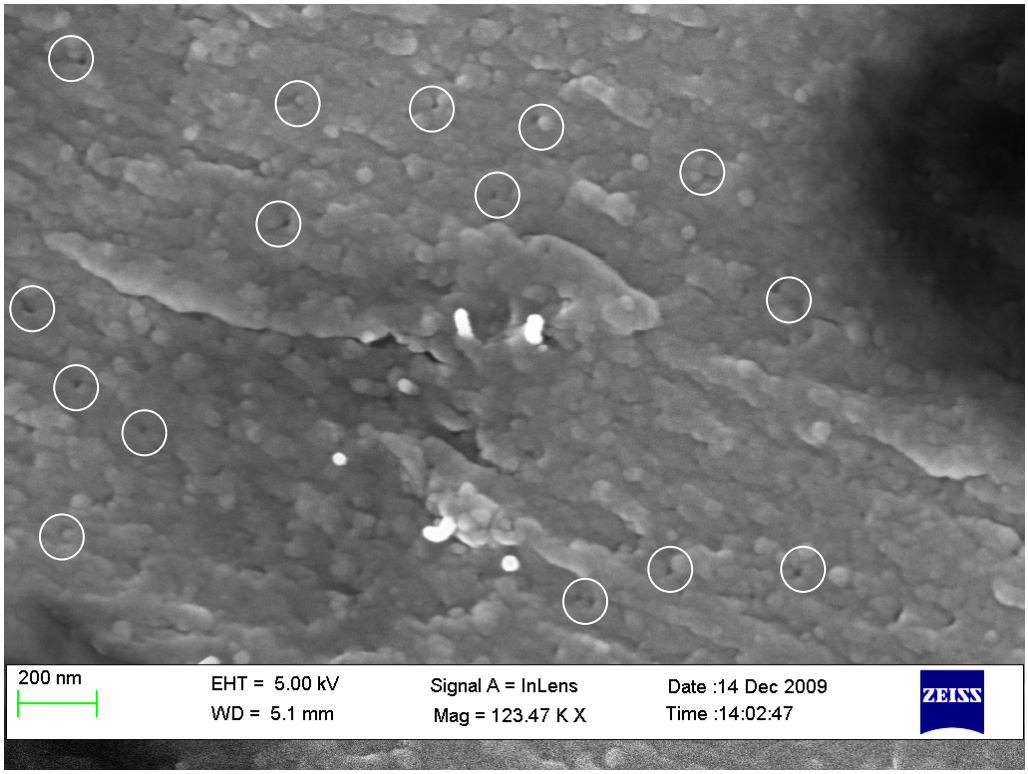


Figure 8.7.5 FEG-SEM image of the fracture surface of R1D1 nanocomposite showing void growth associated with nanosilica debonding as circled (6.0 wt% silica and 0.18% nanotubes).

8.7.4 Dispersion

Figure 8.7.6 shows the AFM image of the nanocomposite, indicating that the nanosilica particles were well dispersed, and their diameter is around 20 nm. However, the multi-walled carbon nanotubes in the cured R1D1 materials are agglomerated. The size of the nanotube agglomerates was measured to be around 0.08~0.1 μm square. A better dispersion was reached in R1D1 nanocomposites than the modified epoxy polymers with the standard nanotubes (0.2~0.4 μm^2 of nanotube agglomerate size). This is because the nanotubes in R1D1 have a relatively small aspect ratio (around 200-250), which results in better nanotube dispersion, compared with the standard nanotubes (aspect ratio = 1000).

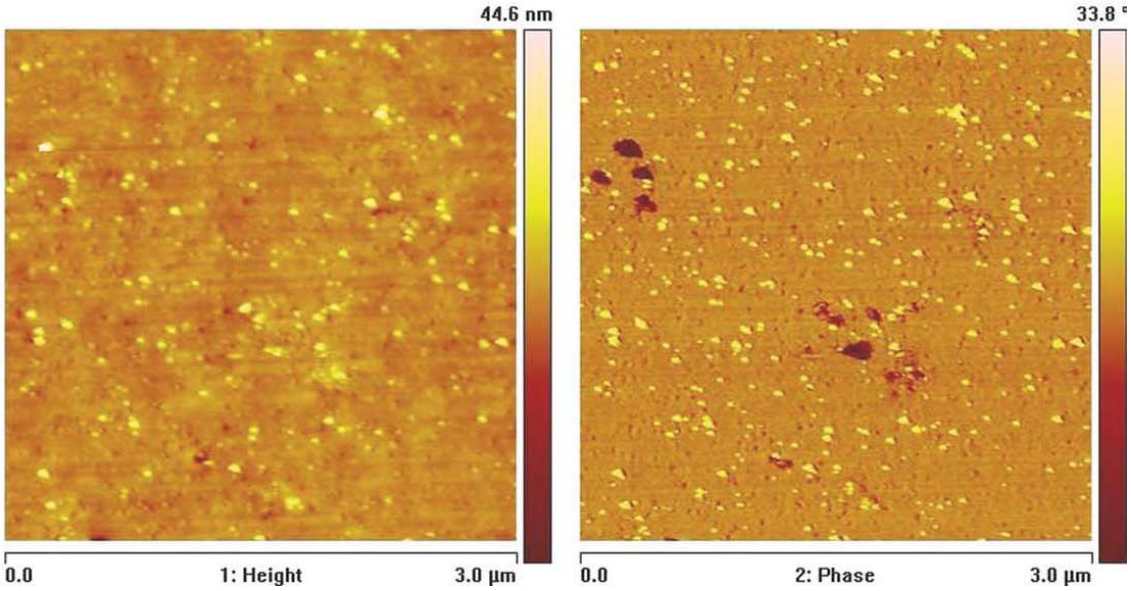


Figure 8.7.6 AFM images of the nanocompiste containing 6.0 wt% nanosilica and 0.18 wt% MWCNTs using R1D1 nano-reinforcement.

In this Section, the main purpose is to investigate the effect of different contents of nanosilica and nanotubes on the nanotube dispersion. Figure 8.7.7 shows transmission optical microscopy (TOM) images of dispersion of MWCNTs in the nanocomposites, with various concentrations of carbon nanotubes and silica nanoparticles. These images indicate that as the concentration of nanotubes is increased, the size of the nanotube agglomerates becomes larger. In contrast, increasing the nanosilica loading did not significantly affect the dispersion of the multi-walled carbon nanotubes in the cured R1D1 materials. The greyscale analysis histograms for all the formulations in the 6.0 wt% nanosilica system are shown in Figure 8.7.8. All the histograms consist of a broad peak in the dispersed region, indicating that all of these cured samples have a relatively high level of dispersion, compared with the modified polymer with the standard nanotubes, as shown in Figure 7.9.1. However, the mean value and the position of the peak in the histogram decreased as the nanotube loading was increased. This indicates that more nanotube agglomerates occur at high contents of nanotubes. The results from the TOM observation and the greyscale analysis again show that the use of R1D1 nanotubes with a low aspect ratio can reach a relatively high level of dispersion in the cured epoxy polymer.

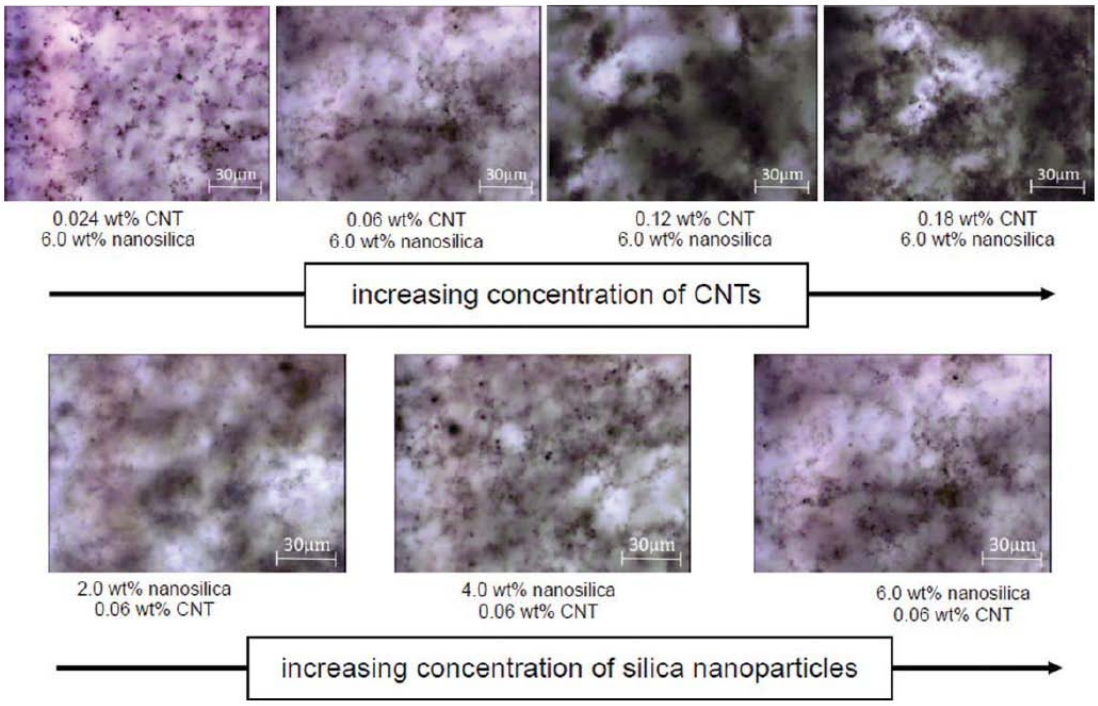


Figure 8.7.7 TOM images of R1D1 nanocomposites with various concentrations of nanosilica particles and multi-walled carbon nanotubes.

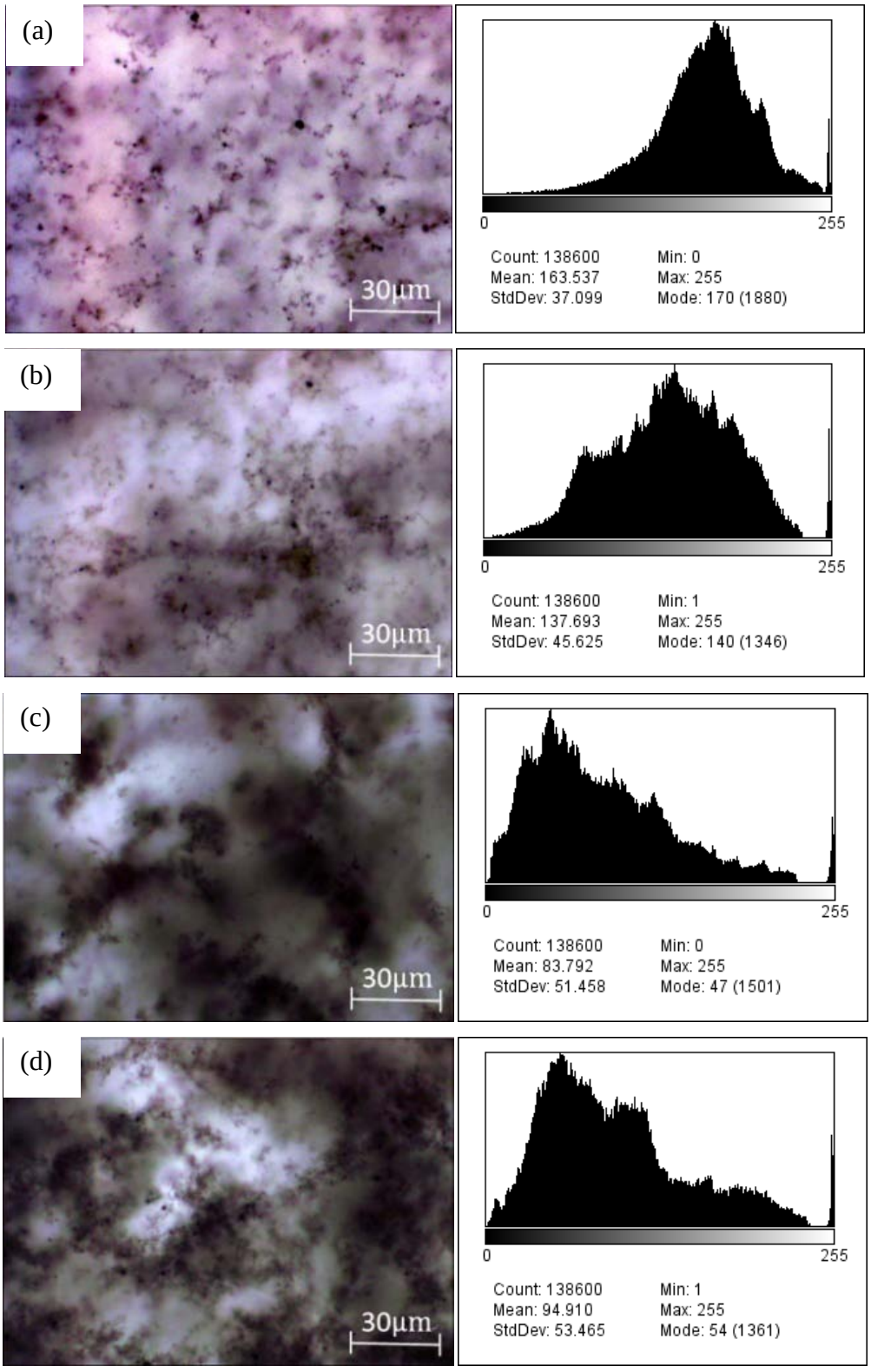


Figure 8.7.8 TOM images and greyscale histograms of the R1D1 nanocomposites of 6.0 wt% nanosilica system with various nanotube loadings at (a) 0.024 wt%, (b) 0.06 wt%, (c) 0.12 wt% and (d) 0.18 wt%.

8.8 Conclusions

The mechanical properties of an anhydride-cured epoxy polymer modified by the combination of second-phase reinforcements using rubber microparticles, silica nanoparticles and multi-walled carbon nanotubes were investigated. The morphology observed using AFM showed that the rubber particles and silica nanoparticles were well-dispersed in the epoxy. However, in the hybrid-modified material containing the rubber and nanosilica particles, some nanosilica agglomerates were observed. The multi-walled carbon nanotubes in both the single-phase and hybrid modifications were agglomerated.

The addition of the CTBN rubber particles results in a significant increase in the toughness but a decrease in the stiffness of its polymer-based composites. The introduction of the nano-size reinforcements, nanosilica and nanotubes, to the rubber-modified epoxy polymer lead to a further increase in the toughness and also improves the modulus. The fracture energy, G_{Ic}, reached a maximum of 1132 J/m^2 for the hybrid modified epoxy polymer with 9.0 wt% rubber microparticles and 0.2 wt% carbon nanotubes. Fracture testing results show that the synergistic effect of incorporating the rubber particles with nanosilica or nanotubes on the toughness can be obtained in the epoxy polymer-based composites. Hence, the hybrid modified samples containing the rubber particles show a relatively high value of the measured fracture energy, compared with the samples without the rubber additive.

Turning to the fatigue testing results, the addition of the hybrid reinforcements shifts the results towards higher values of the maximum applied strain release rate, improving the resistance to fatigue crack growth. The measured value of the maximum fracture energy at threshold, G_{th}, clearly shows the effect of the addition of the hybrid reinforcements on the fatigue performance, and the hybrid modified polymer with rubber particles and carbon nanotubes showed the highest value of G_{th} to be 127 J/m^2. Although the nano-hybrid modified polymer with nanosilica particles and nanotubes did not reveal the highest improvement in the toughness and fatigue performance, the ratio of G_{th}/G_{Ic} showed that the combination of these nano-reinforcements is the best

candidate for improving the fatigue performance of the epoxy polymer (the maximum value of G_{th}/G_{Ic} was calculated to be 0.42 for this hybrid modified polymer).

The mechanisms that cause the enhancement of the toughness and fatigue performance were identified using the FEG-SEM observation of the fracture surfaces after quasi-static fracture and fatigue failure. The rubber particles in the cured polymer cavitated with subsequent void growth. These are considered to be the main toughening mechanisms for rubber modification. The toughening mechanisms caused by the MWCNTs involve nanotube pull-out and plastic void growth associated with the nanotube debonding. The added silica nanoparticles debonded from the epoxy matrix, followed by void growth, which involves plastic deformation of the epoxy polymer. These processes form the main toughening mechanism for the silica nanoparticles.

When using nanotubes as a toughener, the distribution of nanotubes has been an issue because they have an undesirable tendency to agglomerate. A series of hybrid nanocomposites with the R1D1 (nanosilica/nanotube reinforcement) were used to investigate the effect of various nano-reinforcement loadings on the dispersion. The dispersion of the nanotubes is strongly dependent on nanotube loading, and high nanotube loadings cause serious nanotube agglomerates. The aspect ratio of the nanotubes used also affects the nanotube dispersion, the nanotubes from the R1D1 nano-reinforcement showed relatively better dispersion, compared with the standard nanotubes, due to their smaller aspect ratio. The level of the nanotube dispersion was not affected as the nanosilica loading was varied.

CHAPTER 9

ANALYTICAL MODEL OF NANOSILICA- AND NANOTUBE-MODIFIED EPOXY

9.1 Introduction

The experimental results discussed in Chapter 6 and Chapter 7, and the previous studies [23, 72, 74, 152] related to modification using nano-reinforcements in epoxy polymers have demonstrated that the addition of silica nanoparticles or carbon nanotubes results in a significant improvement in the mechanical properties. In this Chapter, the increased mechanical properties associated with the presence of the nanosilica and carbon nanotubes in the anhydride-cured DGEBA epoxy matrix will be predicted by analytical modelling.

9.2 Toughening of Nanosilica-modified Epoxy

9.2.1 Introduction

The toughening performance of nanosilica-modified epoxies was investigated (discussed in Chapter 6), and the results showed that the addition of the silica nanoparticles led to an increase in the toughness of the epoxy. Two major toughening mechanisms were identified in the nanocomposites as (i) shear band yielding between silica nanoparticles and (ii) plastic void growth associated with interfacial debonding and plastic deformation of the polymer.

Shear band yielding initiates between the rigid nanoparticles when the epoxy matrix starts to yield. This increases energy dissipation by strain energy from the epoxy polymer, improving the fracture properties of the nanosilica-modified epoxies. After the silica nanoparticles debond from the polymer, void growth formed around the debonded particles. The process of void growth brought a high level of plastic deformation of the polymer matrix, consequently an increase in the toughness of the nanocomposites was obtained.

Previous studies [33, 152] related to the modelling of rubber-toughened anhydride-cured epoxy polymers reported a generalised solution to predict the incremental increase in the fracture energy, G_{Ic}, as:

$$G_{Ic} = G_{Icu} + \psi \tag{9.1}$$

where G_{Icu} is the fracture energy of the unmodified epoxy polymer, which was measured to be 133 J/m^2, and where ψ is the increase in fracture energy, caused by the overall toughening mechanisms from the silica nanoparticles. The toughening mechanisms are: (i) shear band yielding, ΔG_s, and (ii) plastic void growth in the epoxy polymer, ΔG_{vp}. Hence, the increase in fracture energy, ψ, is given by:

$$\psi = \Delta G_s + \Delta G_{vp} \tag{9.2}$$

These two terms of the energy contribution to the toughness will be described in detail below.

9.2.2 Shear Band Yielding due to Nanosilica

The energy contribution, ΔG_s, caused by the shear band yield toughening mechanism in nanosilica-modified materials has been derived [5, 23], and is given by:

$$\Delta G_s = 0.5 v_f \sigma_{ycu} \gamma_{fu} F'(r_y) \tag{9.3}$$

where v_f is the volume fraction of the particles, σ_{ycu} and γ_{fu} are the yield stress and failure strain of the unmodified polymer, measured from plane-strain compression tests, and $F'(r_y)$ is :

$$F'(r_y) = r_y \left[\left(\frac{4\pi}{3v_f} \right)^{1/3} \left(1 - \frac{r_p}{r_y} \right)^3 - \frac{40}{35} \left(\frac{r_p}{r_y} - 1 \right)^{3/2} \left(\frac{r_p}{r_y} \right) \left(\frac{7}{5} - \frac{r_p}{r_y} \right) - 2 \left(1 - \frac{r_p}{r_y} \right)^2 + \frac{16}{35} \right] \tag{9.4}$$

where r_p is the radius of the particles (nanosilica r_p = 10 nm) and the value of r_y is defined as:

$$r_y = K_{sp}^2 \left(1 + \frac{\mu_m}{\sqrt{3}} \right) r_{pzu} \tag{9.5}$$

where K_{sp} is the maximum stress concentration around a particle. The value of K_{sp} is a function of the volume fraction of the particles, v_f, and can be calculated by [153, 154]:

$$K_{sp} = 0.59 v_f + 1.65 \tag{9.6}$$

and where μ_m is the material constant which allows for the pressure-dependency of the yield stress [29], and was taken as 0.2 [5] in this study. r_{pzu} is the plastic zone size at fracture of the unmodified epoxy polymer, and can be calculated from:

$$r_{pzu} = \frac{1}{6\pi}\frac{E_m G_{Icu}}{(1-\nu^2)\sigma_{ytu}^2} \tag{9.10}$$

where E_m, G_{Icu}, ν and σ_{yt} are the modulus, fracture energy, Poisson's ratio, and tensile yield stress of the unmodified epoxy polymer, respectively.

9.2.3 Plastic Void Growth due to Nanosilica

The energy contribution, ΔG_{vp}, from the plastic void growth mechanism in nanosilica-modified polymers was taken from [5, 23], and can be calculated by:

$$\Delta G_{vp} = \left(\frac{1-\mu_m^2}{3}\right)\left(v_{fv} - v_{fp}\right)\sigma_{ycu} r_{pzu} K_v^2 \tag{9.11}$$

where v_{fv} and v_{fp} are the volume fraction of the voids and particles which showed void growth, directly measured from the FEG-SEM images of the fracture surfaces, μ_m is the material constant allowing for the pressure-dependency of the yield stress [29], σ_{ycu} is the compressive yield stress of the unmodified polymer, r_{pzu} is the plastic zone size at the fracture of the unmodified epoxy polymer, calculated by Equation (9.10). K_v is the stress concentration factor for voids, which is dependent on the volume fraction of the reinforcement [29]. The value of K_v was allowed to vary linearly with the volume fraction, v_f, of the reinforcement, see Equation (9.12).

$$K_v = 0.918 v_f + 2.11 \tag{9.12}$$

Note that the process of plastic void growth starts with nanosilica debonding. However, the energy contribution of interfacial debonding between the particles and matrix is considered to be negligible, as the calculated debonding energy is very small at around 0.05 J/m^2 for 20 wt% nanosilica [155-157]. Hence, the energy contribution from interfacial debonding in the nanosilica-modified epoxies was not used in the analytical modelling for toughness, as previous work [5, 23].

9.2.4 Modelling of the Toughness of Nanosilica-modified Epoxy

All the parameters used in the analytical modelling to predict the fracture energy of the nanosilica-modified polymers are summarised in Table 9.2.1. The radius of the voids used to calculate the volume fraction of voids, v_{fv}, was derived from the maximum hoop strain [5], and the derived values of the void radius form as $(1+\gamma_{fu})r_p$ = 16 nm, which is similar to the measured radius (17 nm) on the fracture surfaces. Here γ_{fu} is the failure strain for the unmodified epoxy measured from the plane strain compression tests. Not all of the silica nanoparticles gave void growth. From the FEG-SEM observation, the proportion of the silica nanoparticles operating the plastic void growth mechanism is around 14% in the F400 system (v_{fp} = 0.14 v_f), see Table 6.2.2. The predictions for the nanocomposites containing the F400 silica nanoparticles (the F400 system contains the nanosilica particles with standard surface treatment for preventing agglomeration, and relatively poor nanosilica/epoxy adhesion) are summarised in Table 9.2.2 and Figure 9.2.1. The predicted values of the fracture energy agree well with the experimental results. Although the predicted results are slightly higher than the measured values, they are still within the variations of experimental data, see Figure 9.2.1. The energy contribution from shear band yielding is the predominant toughening mechanism to improve the fracture energy at lower contents of nanosilica. With increasing the nanosilica loading, the individual contributions (shear yielding and plastic void growth) to the overall toughening contribution are roughly equal, see the inset in Figure 9.2.1.

Table 9.2.1 The parameters used in the modelling for predicting the fracture energy of the nanosilica-modified polymers.

Name	**Symbol**	**Unit**	**Value**	**Source**
Radius of the nanosilica	r_p	nm	10	Present study
Fracture energy of the unmodified epoxy	G_{Icu}	J/m^2	133	Present study
Plane-strain compressive yield stress of the unmodified polymer	σ_{ycu}	MPa	123	Present study
Young's modulus of the unmodified polymer	E_m	GPa	2.90	Present study
Uniaxial tensile yield stress of the unmodified polymer	σ_{yt}	MPa	88	[5]
Failure stain of the unmodified polymer	γ_{fu}	-	0.62	Present study
Poisson's ratio of the unmodified polymer	v	-	0.35	[5]
Pressure-dependent yield stress parameter	μ_m	-	0.2	[29]
Volume fraction of the nanosilica	v_f	-	0.07-0.13	[5]
The maximum stress concentration around a particle	K_{sp}	-	1.69-1.73	[29]
The maximum stress concentration around a void	K_v	-	2.12	[29]

Table 9.2.2 The measured and predicted values of the fracture energy in the F400 system.

Nanosilica (wt%)	v_f (vol%)	v_{fv}-v_{fp} (vol%)	ΔG_s (J/m^2)	ΔG_{vp} (J/m^2)	G_{Ic} (J/m^2) predicted	G_{Ic} (J/m^2) measured
0	0	0	-	-	-	133
10	7.1	3.2	39.8	30.4	204	191
20	13.4	5.6	53.6	53.6	240	220

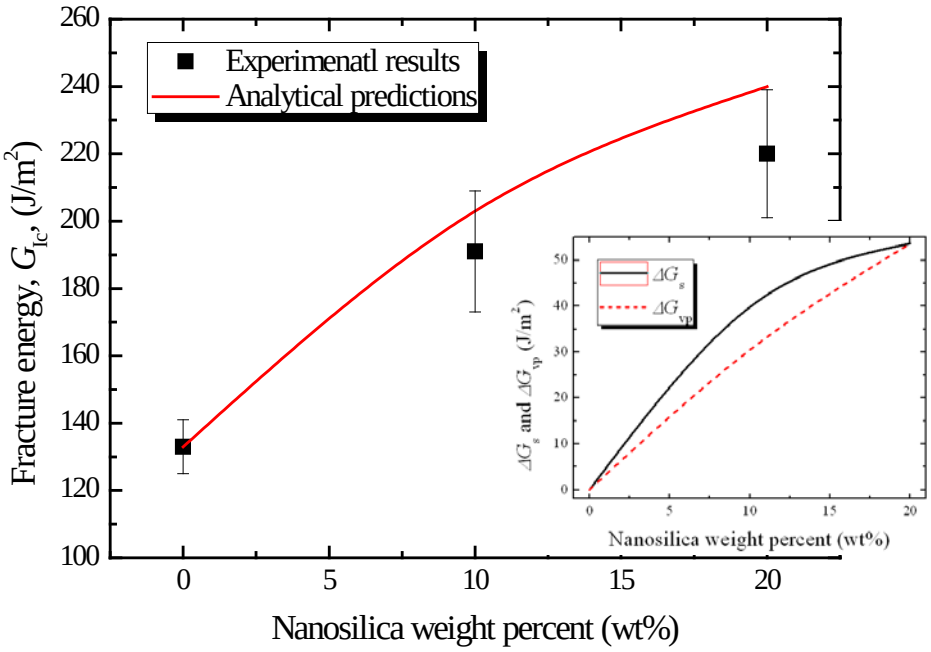


Figure 9.2.1 The experimental results of the fracture energy and the predicted values of the fracture energy in the F400 system (the individual contributions are shown inset).

For the nanocomposites (F400-S system) containing silica nanoparticles with increased adhesion by the additional silane treatment, the effect of the treatment on the toughness of the epoxy polymer was considered in the modelling. As mentioned in Section 6.2, the addition of the silane treatment (A187) to the DGEBA epoxy matrix increased the fracture energy from 133 J/m^2 for the Control sample (unmodified polymer) to 154 J/m^2 for the Control-S sample (silane/epoxy material), indicating that the toughness of the epoxy improved by the silane treatment. Hence, the value of G_{Icu} was taken as 154 J/m^2 into Equation (9.1) for the F400-S system. As the silica nanoparticles were bonded well with the epoxy matrix, a lower proportion of the silica nanoparticles showed debonding and void growth around them was measured from the FEG-SEM fracture surfaces of these systems, see Figure 6.2.14 and Figure 6.2.15 (5% for F400-S system, and 12% for the Nanopox XP system). These values were used to calculate the values of v_{fp}. The radius of the voids used to calculate the value of v_{fv} would use the radius measured from the fracture surfaces, rather than use the derived

value from the maximum hoop strain [5]. Table 6.2.3 and Table 6.2.4 show the analytical predictions for the F400-S and Nanopox XP systems.

Table 9.2.3 The measured and predicted values of the fracture energy in the F400-S system.

Nanosilica (wt%)	v_f (vol%)	v_{fv}-v_{fp} (vol%)	ΔG_s (J/m^2)	ΔG_{vp} (J/m^2)	G_{Ic} (J/m^2) predicted	G_{Ic} (J/m^2) measured
0	0	0	-	-	-	133
10	7.1	0.34	87.1	6.5	242	241
20	13.4	0.64	110.1	12.4	277	261

Table 9.2.4 The measured and predicted values of the fracture energy in the Nanopox XP system.

Nanosilica (wt%)	v_f (vol%)	v_{fv}-v_{fp} (vol%)	ΔG_s (J/m^2)	ΔG_{vp} (J/m^2)	G_{Ic} (J/m^2) predicted	G_{Ic} (J/m^2) measured
0	0	0	-	-	-	133
10	7.1	2.0	39.8	19.0	192	249
20	13.4	3.8	53.6	36.1	223	259

There is a good agreement between the predictions and the experimental results in the F400-S nanocomposites, see Figure 9.2.2. However, for the Nanopox XP system, the values of the fracture energy from the predictions are lower than the measured values, indicating that they are underestimated. This is because the additional surface treatment in the Nanopox XP may affect the material properties of the epoxy. However, the treatment of the Nanopox XP nanosilica-modified epoxy resin was done by the manufacturer, Nanoresins, as a result there was no chance to measure the fracture energy of the control sample (epoxy plus the additional surface modification only) in the Nanopox XP system. Hence, the parameters related to the control sample used in the predictions for the Nanopox XP are assumed to be the same as the F400 system. Besides, the predictions did not consider the adhesion between the silica nanoparticles and epoxy matrix, which may affect the energy contribution from interfacial debonding. All of these caused the lower values in the toughening prediction.

From the predicted results, shear band yielding is considered to be the main toughening mechanism in the nanosilica-modified polymers with good nanoparticle/epoxy adhesion, see the individual contribution in the inset in Figure 9.2.2. The plastic void growth mechanism provides a relatively small toughening contribution to the overall fracture energy. This is because a relatively smaller diameter (25~30 nm) of the voids and lower amount of nanosilica showed void growth were measured from the FEG-SEM images of the fracture surfaces, compared with the F400 system, see Table 6.2.4.

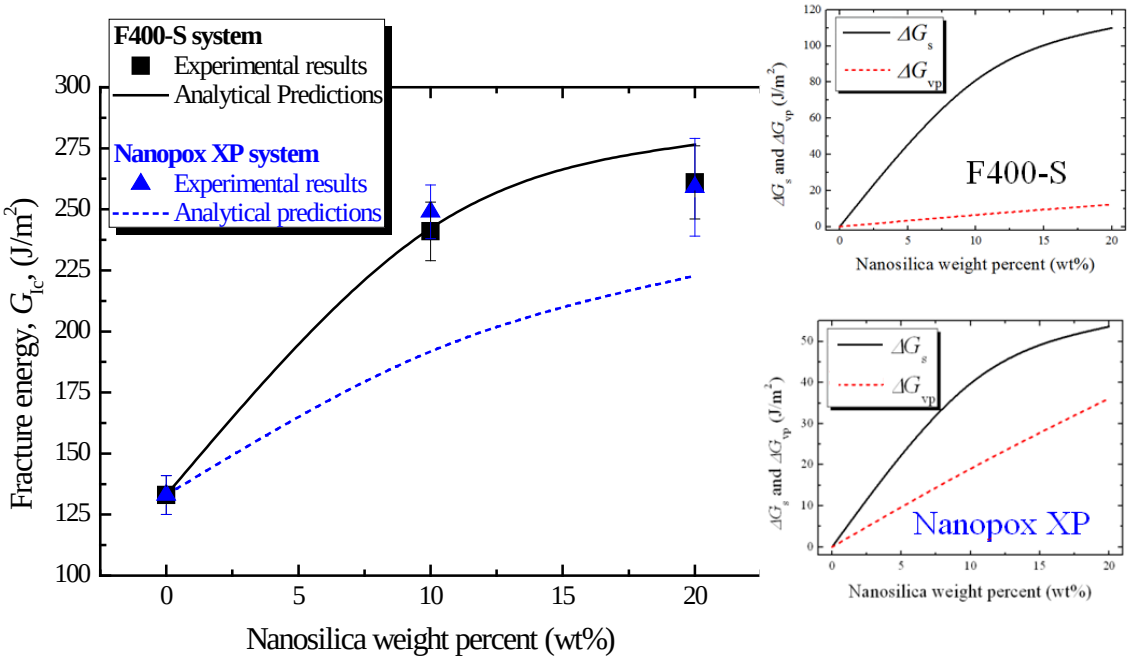


Figure 9.2.2 The experimental results of the fracture energy and the predicted values of the fracture energy of the F400-S and Nanopox XP nanocomposites (the individual contributions of ΔG_s and ΔG_{vp} are shown inset).

9.2.5 Modelling of the Toughness of Glass Microparticle-modified Epoxy

The modelling work was extended to predict the fracture energy of the polymer-based composites with small glass bead microparticles (3.5 μm in diameter). The volume fraction, v_f, of the glass beads was calculated from the fracture surfaces (5.1 vol % and 10.2 vol% were measured for the composites containing 10 wt% and 20 wt% of glass beads, respectively). Besides, the size of the voids and the proportion of the glass beads which showed void growth were directly measured from the fracture surfaces in each system with various levels of adhesion, see Section 6.3.3. Tables 9.2.5 ~ 9.2.7 show the predicted values and the volume fraction used in the modelling for the S-Control, S-Silane and S-Frekote systems.

Table 9.2.5 The measured and predicted values of the fracture energy in the S-Control system (containing untreated small glass beads).

Nanosilica (wt%)	v_f (vol%)	v_{fv}-v_{fp} (vol%)	ΔG_s (J/m^2)	ΔG_{vp} (J/m^2)	G_{Ic} (J/m^2) predicted	G_{Ic} (J/m^2) measured
0	0	0	-	-	-	133
10	5.1	0.33	11.7	3.1	148	149
20	10.2	0.67	16.2	6.3	156	158

Table 9.2.6 The measured and predicted values of the fracture energy in the S-Silane system (containing silane-treated small glass beads).

Nanosilica (wt%)	v_f (vol%)	v_{fv}-v_{fp} (vol%)	ΔG_s (J/m^2)	ΔG_{vp} (J/m^2)	G_{Ic} (J/m^2) predicted	G_{Ic} (J/m^2) measured
0	0	-	-	-	-	133
10	5.1	0.07	39.2	0.7	194	181
20	10.2	0.13	55.5	1.3	211	197

Table 9.2.7 The measured and predicted values of the fracture energy in the S-Frekote system (containing Frekote-treated small glass beads).

Nanosilica (wt%)	v_f (vol%)	v_{fv}-v_{fp} (vol%)	ΔG_s (J/m^2)	ΔG_{vp} (J/m^2)	G_{Ic} (J/m^2) predicted	G_{Ic} (J/m^2) measured
0	0	0	-	-	-	133
10	5.1	2.30	11.7	21.4	166	179
20	10.2	4.56	16.7	43.0	193	192

The predictions are in excellent agreement with the experiment results, see Figure 9.2.3. Some predicted values of the fracture energy, such as those for the Frekote-treated system at 10 wt% glass beads and the silane-treated system at 20 wt% glass beads, are in poor agreement with the measured fracture energy. This may be due to the experimental error. According to the predicted results, it can be concluded that the analytical model can efficiently work on both nano- and micron-size rigid particles. In both untreated and silane-treated systems, the shear band yielding mechanisms provides a relatively high energy contribution to the overall fracture energy, see Table 9.2.5 and 9.2.6. In contrast, plastic void growth is considered to be the main toughening mechanism in the S-Frekote system containing poorly-bonded glass beads, see Table 9.2.7. The analytical model can efficiently work on both nano- and micron-size rigid particles.

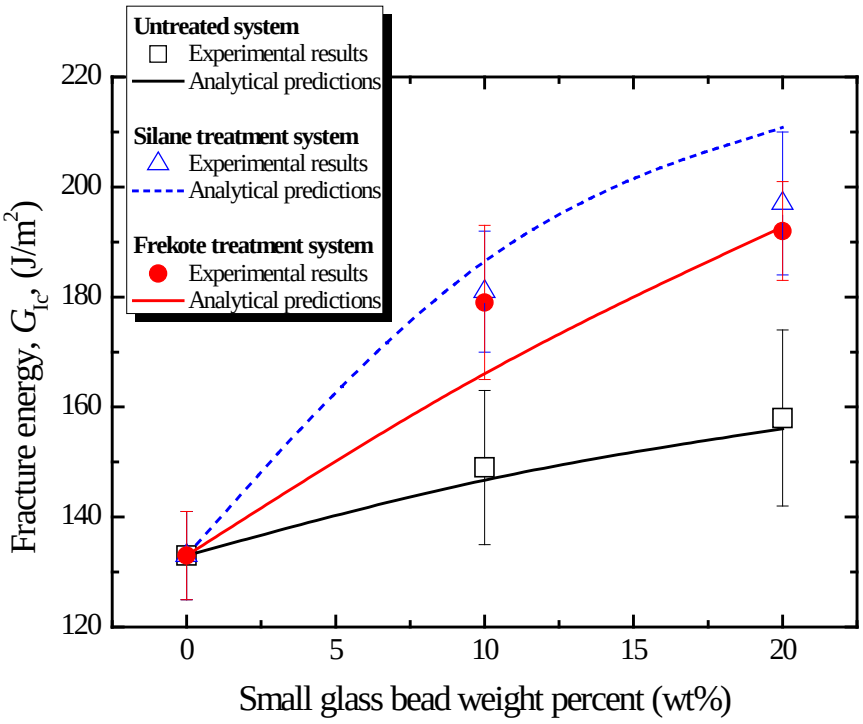


Figure 9.2.3 The experimental results of the fracture energy fitted by the predicted values of the fracture energy of the small glass bead-modified epoxies.

9.3 Toughness of Nanotube-modified Epoxy

9.3.1 Introduction

The toughening performance of the modified polymers with the multi-walled carbon nanotubes increased efficiently with increasing contents of the nanotubes, as was shown in Figure 7.4.1. The main toughening mechanisms were identified to be (i) debonding between the nanotubes and epoxy matrix, (ii) plastic void growth, associated with plastic deformation of the epoxy polymer, and (iii) nanotube pull-out. The process of the nanotube pull-out from the matrix includes interfacial debonding and friction between the nanotubes and the epoxy matrix, consequently the energy dissipation increases. The plastic void growth mechanism caused by the plastic deformation in the matrix can efficiently absorb further strain energy. Considering the toughening mechanisms in composites with fibrous reinforcements, the energy contribution from interfacial debonding between the fibres and polymer matrix should take part in improving the toughness [158]. Hence, the toughening mechanisms used in the modelling work were interfacial debonding plus nanotube pull-out and plastic void growth. Note that shear yielding is generally not considered for composites containing short fibre reinforcements, and indeed no strain softening occurred in the plane strain compression tests, see Figure 7.5.1. Strain softening is generally considered to be a requirement for shear banding to occur [133, 134]. Therefore, the contribution from shear band yielding was not considered in the prediction.

All of the above-mentioned toughening mechanisms operating in the nanotube-modified epoxies will be built into the analytical model. Hence, Equation (9.2) becomes:

$$\psi = \Delta G_{\mathrm{db}} + \Delta G_{\mathrm{p}} + \Delta G_{\mathrm{vc}} \tag{9.13}$$

where ΔG_{db} is the energy contribution from interfacial debonding between the nanotubes and polymer matrix, ΔG_{p} is the energy contribution caused by nanotube pull-out and ΔG_{vc} is the energy contribution caused by plastic void growth in the nanotube-modified polymers.

In the following Sections, these terms of the energy contribution to the toughness of the nanocomposites with nanotubes will be described.

9.3.2 Debonding due to Nanotubes

Interfacial debonding is essential because it reduces the constraint at the crack-tip, consequently allowing the nanotubes to be pulled out from the matrix, and allowing the epoxy matrix to deform plastically with subsequent void growth. Although the toughening contribution of interfacial debonding in spherical particle-modified epoxy has been considered to be negligible [155-157], the energy dissipation due to the interfacial debonding between the nanotubes and polymer matrix is considered to make a contribution to the toughness of the nanotube-modified polymers due to the high specific surface area of the nanotubes. The interfacial debonding energy, ΔG_{db}, is given by [158]:

$$\Delta G_{db} = \int_0^{l_d} \frac{N_f}{l_d} \pi 2 r_f x G_{if} dx \tag{9.14}$$

where l_d is the length of the debonded fibres, and is equal to $l_f/2$ = 60 μm as the nanoubes are assumed to be fully debonding, r_f is the radius of the nanotube, G_{if} is the interfacial fracture energy. Barber et al. [142] used the values of between 13 J/m^2 to 34 J/m^2 measured from single-fibre pull-out tests on glass fiber/vinyl ester composites (which is quite similar to the epoxy matrix used in this study) to calculate the interfacial strength between nanotubes and polymer. They found values of the interfacial fracture energy for nanotube/polyethylene-butene of a similar magnitude. Hence, 25 J/m^2 was used in this study. N_f is the number if the nanotubes per unit area, related to the nanotube volume fraction, v_f, and is:

$$N_f = \frac{v_f}{\pi r_f^2} \tag{9.15}$$

By substitution and integration, Equation 9.14 becomes:

$$\Delta G_{db} = \frac{l_f}{2r_f} v_f G_{if} \tag{9.16}$$

where v_f is the volume fraction of the nanotubes, is given by:

$$v_f = \frac{\rho_m w_f}{(\rho_f - \rho_f w_f + \rho_m w_f)} \tag{9.17}$$

where w_f is the weight fraction of the reinforcement (nanotubes), ρ_m and ρ_f are the density of the polymeric matrix and the reinforcement, respectively. In order to simplify the sample preparation for manufacturing the MWCNTs/epoxy nanocomposites, weight fraction was used to calculate the different concentrations of nanotubes. Table 9.3.1 shows the weight fraction, w_f, of the multi-walled carbon nanotubes corresponding to the volume fraction, v_f.

Table 9.3.1 The weight percent of the multi-walled carbon nanotubes corresponding to the volume fraction of nanotubes.

MWCNT weight percent (wt%)	MWCNT volume fraction (vol%)
0.0	0.0000
0.1	0.0627
0.2	0.1253
0.5	0.3134

9.3.3 Nanotube Pull-out

The fibre pull-out mechanism has been considered to be the main toughening mechanism in fibre-reinforced polymer composites [84], such as GFRP or CFRP. This toughening mechanism may significantly increase the toughness by generating friction between the reinforcing fibres and polymeric matrices. Nanotubes are analogous to nano-sized carbon fibres, and possess a high specific surface area (SSA) of typically between 1000 to 1200 m^2/g [159]. This leads to a high potential for toughening polymer-based composites via this mechanism, because the energy dissipation associated with the friction is directly proportional to the interfacial area. The experimental results showed that the addition of the multi-walled carbon nanotubes resulted in a significant improvement in the toughness, and some of this increased toughness can be attributed to the nanotube pull-out mechanism. The observation of the fracture surfaces of the nanotube-modified epoxy polymer showed that carbon nanotubes were pulled out from the epoxy matrix. The increased energy, ΔG_p, caused by the fibrous reinforcement pull-out mechanism can be given by [158]:

$$\Delta G_p = \int_0^{l_f} \frac{N_f}{l_f} \pi r_f x^2 \tau_i dx \tag{9.18}$$

where l_f is the length of the fibres (nanotube l_f = 120 μm), r_f is the radius of the fibres (nanotube r_f = 60 nm), τ_i is the interfacial shear strength and N_f is the number of the nanotubes per unit area, defined in Equation (9.15). Note that the effective length of the fibrous reinforcement for the pull-out mechanism will not be equal to the total length of the multi-walled carbon nanotubes, as only a small portion of the nanotube is pulled out from the epoxy matrix. By substitution and integration, Equation (9.18) becomes:

$$\Delta G_p = \frac{v_f l_e^2 \tau_i}{3 r_f} \tag{9.19}$$

where l_e is the effective pulled-out length, i.e. the measured length of the pulled out nanotubes on the fracture surfaces by FEG-SEM. The effective nanotube pulled-out length used in the prediction is 7.82 μm, which is the measured mean length of the pulled-out nanotubes on the fracture surface, as discussed in Chapter 7. As the nanotube

pull-out mechanism involves the nanotube rupture, with debonding and bridging, the observed nanotube bridging can be considered to be part of the pull-out process, as shown Figure 7.4.5. (Note that the definition of fibre bridging in a composite is that the reinforcement fibre acts as a ligament traversing the crack, see Figure 2.7.5 (b). During fibre bridging, the bridged fibre is deformed with the crack propagation, and consequently suppresses the crack growth and improves the toughness).

The nanotube telescopic pull-out mechanism, see Figure 2.7.6, may occur if the added nanotubes are multi-walled. For this mechanism, the outer shell of the multi-walled nanotube fractures in tension and is embedded well in the polymer, so the inner shells pull-out from the broken outer shell. However, the broken outer shells were not found on the fracture surfaces, indicating the telescopic pull-out mechanism did not occur in the MWCNTs-modified polymer in this study. Also, Blanco el al. [89] calculated that the increased energy caused by the telescopic pull-out mechanism is very small. Therefore, the telescopic pull-out mechanism was not considered in the modelling.

The interfacial shear strength, τ_i, between the nanotubes and matrix is unknown for the anhydride-cured DGEBA epoxy used in this study. Barber et al [142] reported a value of 47 MPa for nanotube-modified polyethylene-butene material. This value falls in the range of interfacial shear strength between 1 MPa to 100 MPa suggested by Blanco et al. [89]. Hence, a value of 47 MPa was used in this study [142, 160]. Note that, as discussed in Chapter 7, not all of the nanotubes (62%) were operating the pull-out mechanism in the 0.5 wt% nanotube-modified material, see Table 7.4.2.

9.3.4 Plastic Void Growth due to Nanotubes

The plastic void growth caused by the debonding between the multi-walled carbon nanotubes and the epoxy matrix is considered to be a major mechanism for improving the toughness [77]. This mechanism was demonstrated by the FEG-SEM observation on the fracture surfaces of the nanotube-modified epoxies, as voids were found around the pulled-out nanotubes. Furthermore, the studies [5, 23, 116] related to the particle-toughened epoxy polymers reported that the occurrence of plastic void growth results in a significant increase in the toughness, and derived the increased toughness caused by this mechanism, ΔG_{vc}, which can be written as:

$$\Delta G_{vc} = (\frac{1-\mu_m^2}{3})(v_{fv} - v_{fc})\sigma_{ycu} r_{pzu} K_v^2 \tag{9.20}$$

where v_{fv} and v_{fc} are the volume fraction of the voids and the volume fraction of nanotubes which showed void growth around them. μ_m is a material constant allowing for the pressure-dependency of the yield stress [29], σ_{ycu} is the compressive yield stress of the unmodified polymer, r_{pzu} is the plastic zone size at the fracture of the unmodified epoxy polymer, calculated using Equation (9.10). K_v is the stress concentration factor for a void, and was calculated using Equation (9.12).

Note that modelling for predicting the energy contribution from plastic void growth from the literature [5, 23] and Section 9.2 aimed at toughening properties of modified polymers with spherical reinforcements (silica nanoparticles). The MWCNTs used have a cylinder-like shape, therefore each void is assumed to be a conical frustum (i.e. a truncated cone), as schematically shown in Figure 9.3.1. The conical frustum has a height equal to half of the nanotube length. This means that the nanotubes are assumed to be fully debonded from the polymer matrix. The diameter of the conical frustum was calculated to be $(1+\gamma_{fu})D_f$ (γ_{fu} is the failure strain of the unmodified polymer, is measured to be 0.62, and D_f is the diameter of the MWCNTs, measured to be 120 nm). As measured from the fracture surfaces, only around 8% of the nanotubes showed void growth around them.

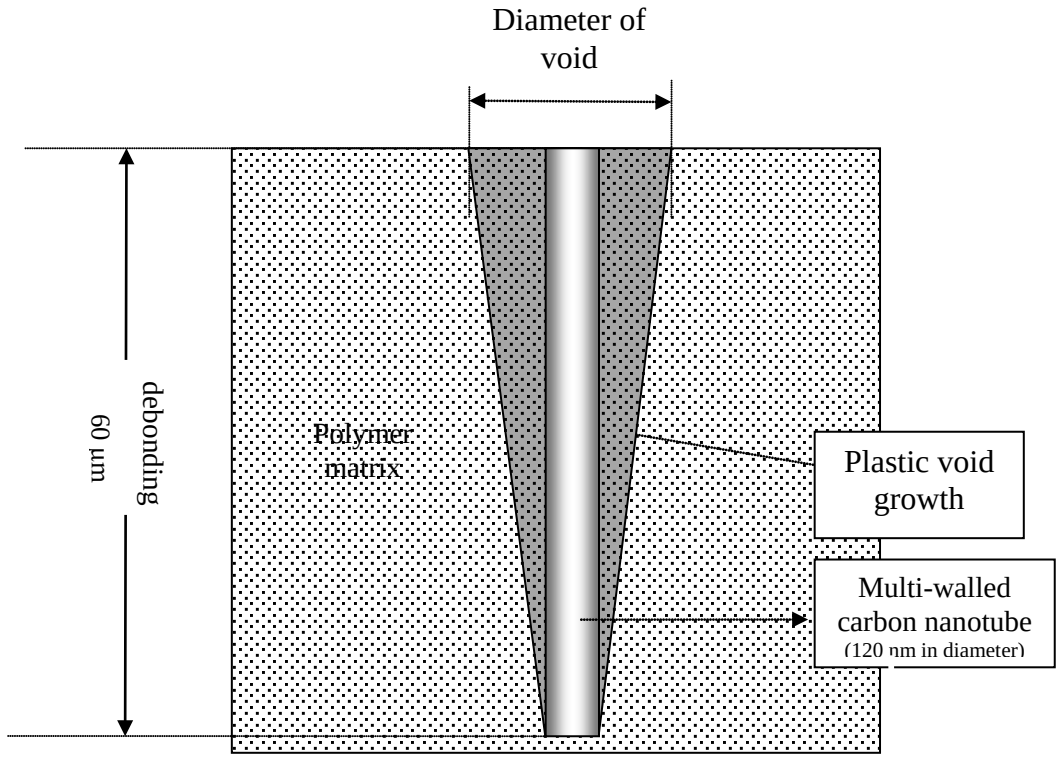


Figure 9.3.1 The illustration of the plastic void growth mechanism.

All the values used in the modelling to predict the fracture energy of the nanocomposites with the MWCNTs are shown in Table 9.3.2.

Table 9.3.2 The parameters used in the modelling studies for predicting the fracture energy of the MWCNT-modified epoxy polymers.

Name	Symbol	Unit	Value	Source
Radius of nanotube	r_f	nm	60	Present study
Length of nanotube	l_f	μm	120	Present study
Density of nanotube	ρ_f	g/ml	1.8	[71]
Density of unmodified epoxy	ρ_m	g/ml	1.2	Present study
Effective nanotube pull-out length	l_e	μm	7.82	Present study
Fracture energy of unmodified epoxy	G_{Icu}	J/m^2	133	Present study
Interfacial shear strength	τ_i	MPa	47	[142, 160]
Pressure-dependent yield stress parameter	μ_m	-	0.2	[29]
Plane-strain compressive yield stress of the unmodified polymer	σ_{ycu}	MPa	120	Present study
Interfacial debonding fracture energy	G_{if}	J/m^2	25	[142]
Stress concentration factor for a void	K_v	-	2.11	[29]

9.3.5 Modelling of the Toughness of MWCNT-modified Epoxy

The analytical results are summarised in Table 9.3.3, and in comparison with the experimental results, see Figure 9.3.2. There was a good agreement between the predicted values and experimental results. Although the analytical results showed a slightly lower fracture energy than the experiments, the predicted values are still within the experimental standard deviation of each formulation.

In Figure 9.3.2, the inset shows that the maximum energy contribution is caused by the interfacial debonding mechanism. Nanotube pull-out provides a slighter lower

energy contribution, ΔG_p, compared with the value of ΔG_{db}. Plastic void growth in the MWCNT-modified polymers did not bring an efficient contribution to the toughness. The value of ΔG_{vc} is very small (0.07~0.35 J/m^2), even though several nanotubes with voids around them were found on the fracture surfaces. Hence, it can be concluded that the efficient toughening mechanisms in the MWCNT-modified polymers are nanotube pull-out and interfacial debonding, see the inset in Figure. 9.3.2.

Table 9.3.3 The predicted and measured values of the fracture energy of the MWCNT-modified epoxy polymers.

w_f (%)	v_f (%) debonding & pull-out	v_{fv}-v_{fp} (%)	ΔG_{db} (J/m^2)	ΔG_p (J/m^2)	ΔG_{vc} (J/m^2)	G_{Ic} (J/m^2) *predicted*	G_{Ic} (J/m^2) *measured*
0.0	0	0		-	-	-	133.4
0.1	0.063	0.005	15.7	10.0	0.07	158.8	162.1
0.2	0.125	0.009	31.2	20.0	0.14	184.4	187.9
0.5	0.194	0.024	48.5	31.0	0.35	212.9	223.3

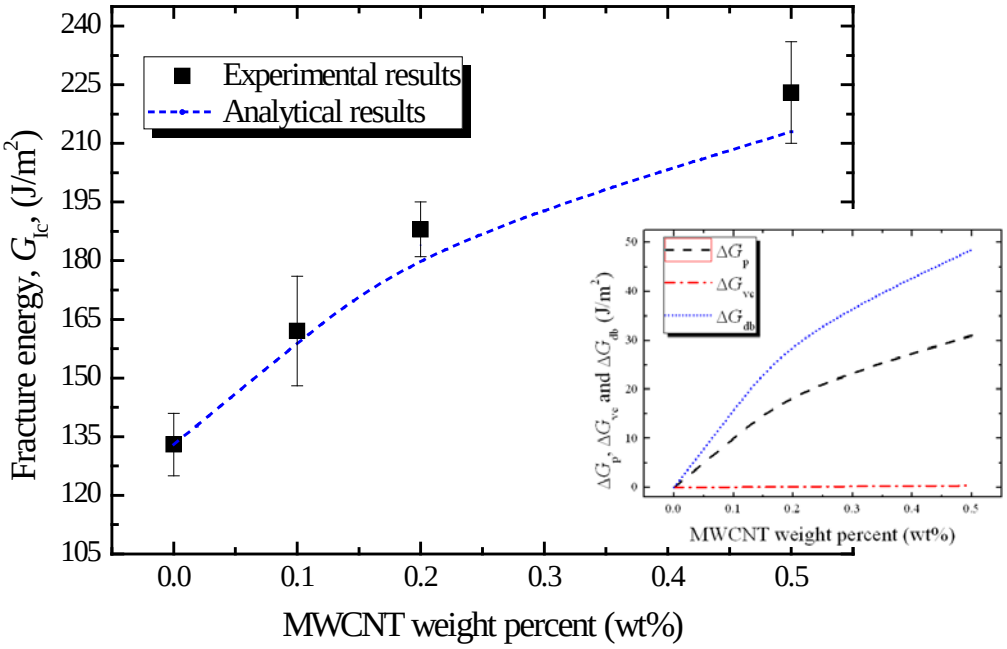


Figure 9.3.2 The experimental results of the fracture energy fitted by the predicted values of the fracture energy (the individual contributions of ΔG_p, ΔG_{vc} and ΔG_{db} are shown inset).

9.3.6 The Nanotube Size Effect on the Toughness

The size effect of the nanotube dimensions, such as nanotube length and diameter, on the toughness was investigated by experiments using different types of multi-walled carbon nanotubes, as discussed in Section 7.8. From the experimental results, the standard nanotubes with a relatively high aspect ratio, i.e. long length and small diameter, provided a significant toughening effect.

Considering the nanotube pull-out and interfacial debonding mechanisms attributed to the increased toughening performance of the nanotube-modified epoxy polymer, it is clear that the surface area of the nanotubes is a key factor for the

toughening improvement because the energy dissipation caused by the friction in the nanotube pull-out mechanism and the interfacial debonding is chiefly concerned with the interfacial area. The efficient pull-out length used in the analytical model is not equal to the nanotube length, but is in direct proportional to its real length. This was demonstrated via the investigation of the nanotube size effect in Section 7.8. The standard nanotubes with a long length of 120 μm showed a longer efficient pull-out length of 7.82 μm, compared with the low quality nanotubes (length = 32 μm and pull-out length = 1.78 μm). Hence, a proportion of 8/120 of the relationship between the pull-out length and nanotube length was used in this Section. Figure 9.3.3 shows the predicted fracture energy with various nanotube lengths from 5 μm to 200 μm (diameter = 120 nm). Generally, the predicted values of the fracture energy increase with increasing the nanotube length. The improvement in the fracture energy is negligible when the nanotube length is less than 25 μm. This indicates that a minimum nanotube length of 25 μm (aspect ratio around 200) is required to achieve the toughening improvement in the anhydride-cured epoxy polymer, see Figure 9.3.3. As the nanotube length is increased, the increases in the energy contribution from nanotube pull-out, ΔG_p, and interfacial debonding, ΔG_{db}, to fracture energy are in parity with one another. Note that the effect of nanotube dimensions on dispersion is ignored.

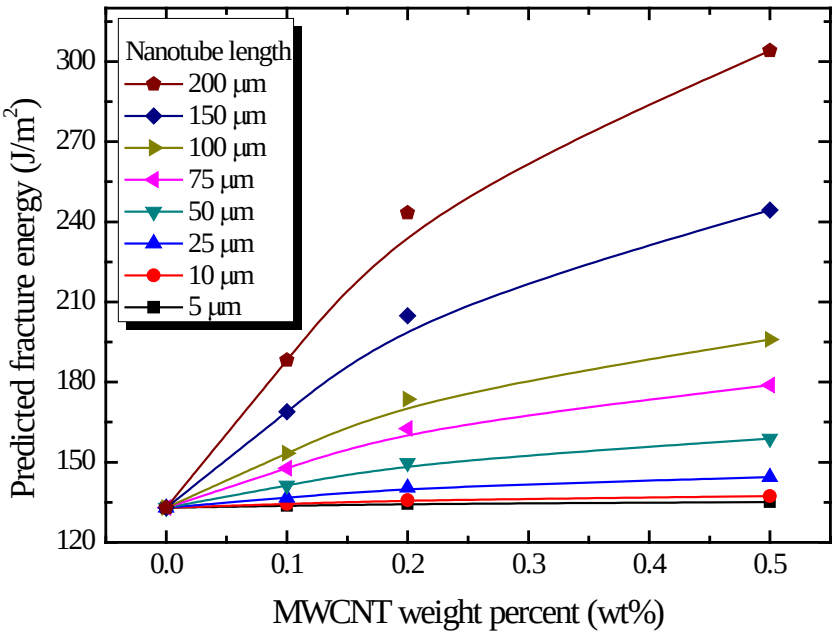


Figure 9.3.3 the effect of nanotube length on the fracture energy (nanotube diameter = 120 nm).

The effect of the nanotube diameter on the fracture energy was investigated using the modelling, see Figure 9.3.4. In contrast with the trend as to the effect of nanotube length on the toughness, see Figure 9.3.3, the decrease in the nanotube diameter provides a significant increase in the predicted values of the fracture energy. As the diameter of nanotubes is bigger than 200 nm, there is no visible toughening effect caused by the addition of the nanotubes. Again, the effect caused by changing the nanotube diameter on nanotube dispersion is ignored in this Section. Besides, the nanotube tensile strength was assumed to be the same even for a small diameter (the decrease in the nanotube diameter results in a slight decrease in its tensile strength [161]. This may reduce the efficient pull-out length). The trend of the analytical solution associated with the nanotube size effect is in good agreement with the experimental results in Section 7.8.

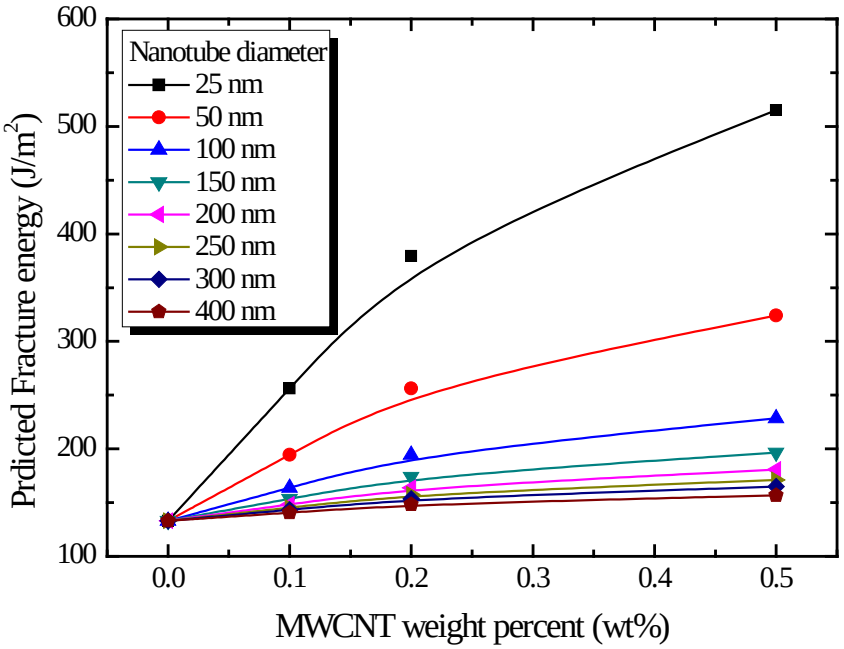


Figure 9.3.4 The effect of the nanotube diameter on the fracture energy (nanotube lenght = 120 μm).

The investigation on the size effect of the nanotube with the same aspect ratio (i.e. by changing the nanotube length and diameter simultaneously to get a constant aspect ratio) showed all the predicted values increased with increasing both nanotube length and diameter, as shown in Figure 9.3.5. This indicates that the toughening improvement caused by the increase in nanotube length is much more significant than the decrease in nanotube diameter, i.e. the nanotube toughening is much more sensitive to the length of the nanotubes. The use of nanotubes with various dimensions and the same aspect ratio will only affect the energy contribution from the nanotube pull-out mechanism, and the value of ΔG_p increased when the nanotubes used have a longer length and larger diameter. However, the energy contribution, ΔG_{db}, from debonding is independent of the nanotube dimensions, if the nanotube aspect ratio is constant. Note that the dispersion of the nanotubes with various dimensions is assumed to be the same.

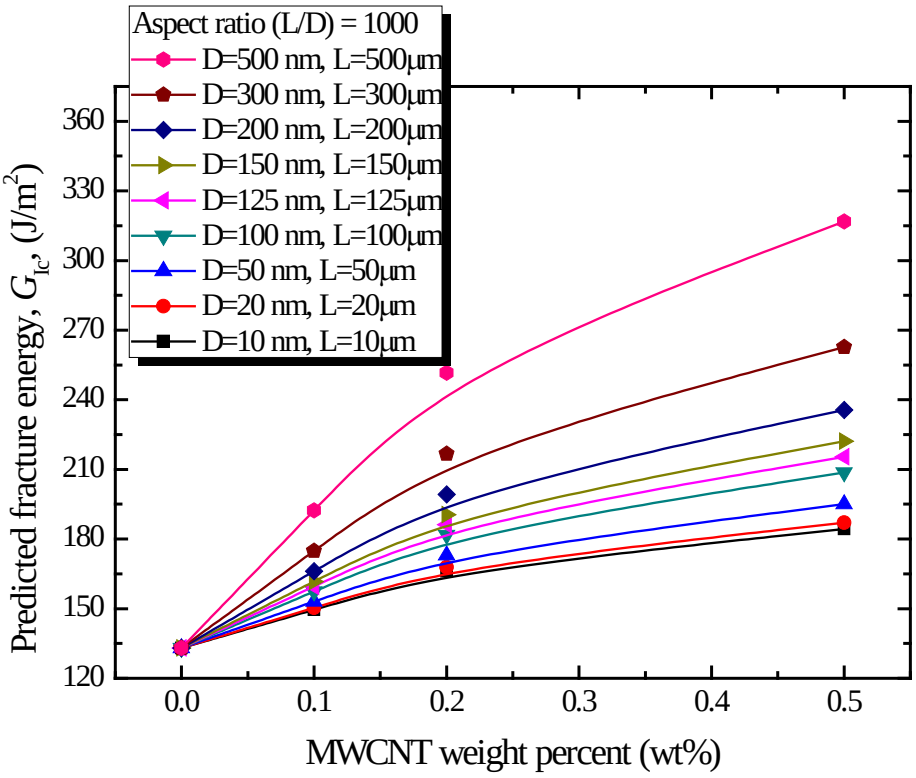


Figure 9.3.5 The effect of the nanotube diameter on the fracture energy (various nanotubes with the same aspect ratio = 1000).

9.4 The Young's Modulus of Nanotube-modified Epoxy

9.4.1 The Modified Halpin-Tsai Equation

The Young's modulus experimentally measured from the tensile tests on the multi-walled carbon nanotube-reinforced epoxy polymer (as discussed in Chapter 7) showed that the modulus was increased by the addition of the carbon nanotubes. At low nanotube contents, this is a linear increase in modulus. However, the increased modulus becomes nonlinear when the nanotube concentration is higher than 0.2 wt%. This nonlinearity (i.e. the reduced rate of stiffness increase) was ascribed to the increased agglomeration of the multi-walled carbon nanotubes at the highest concentration. In this Section, a numerical analysis based on the Halpin-Tsai equation [162-164] is fitted to the Young's modulus of the modified epoxy polymer with the multi-walled carbon nanotubes.

The Halpin-Tsai model was designed for unidirectional fibre-reinforced polymers, and the predicted modulus, E, is given by the original Halpin-Tsai equation [162]:

$$E = \frac{1+\xi\eta v_{\mathrm{f}}}{1-\eta v_{\mathrm{f}}} E_{\mathrm{m}} \tag{9.21}$$

in which E_{m} is the Young's modulus of the matrix (unmodified epoxy polymer), v_{f} is the volume fraction of the nanotubes, given by Equation (9.17), and is shown in Table 9.3.1. ξ is the shape factor (geometry factor) associated with the dimensions of the reinforcement (nanotubes), given by:

$$\xi = 2\left[\frac{l_{\mathrm{f}}}{D_{\mathrm{f}}}\right] \tag{9.22}$$

where l_{f} is the length and D_{f} is the diameter of the fibrous reinforcement (nanotubes), and η is defined as :

$$\eta = \frac{\left[\frac{E_f}{E_m}\right] - 1}{\left[\frac{E_f}{E_m}\right] + \xi} \tag{9.23}$$

where E_f is the Young's modulus of the reinforcement (nanotubes).

The Halpin-Tsai equation is well-established to predict the elastic modulus of polymer-based composites with unidirectional fibrous reinforcements. However, in this study the multi-walled carbon nanotubes reveal a random distribution in their orientation after the sample preparation, even for the CVD-generated film of aligned carbon nanotubes. In consideration of the effect of the reinforcement orientation on the stiffness of composites, Cox [165] introduced an orientation factor, α, into the Halpin-Tsai model by modifying the value of η, and Equation (9.23) becomes:

$$\eta = \frac{\left[\frac{\alpha E_f}{E_m}\right] - 1}{\left[\frac{\alpha E_f}{E_m}\right] + \xi} \tag{9.24}$$

The orientation factor, α, considers the relationship between the thickness of the specimen and the length of the fibrous reinforcement. As the length of the reinforcement is much smaller than the thickness of the specimens, α=1/6 is used. However, when the length of the reinforcement is much longer than the thickness of then testing specimens, Cox [165] recommended that α=1/3 is used. The length of the multi-walled carbon nanotubes used in this study is around 120 μm, which is much smaller than the thickness of the tensile testing specimens (of 2 mm), therefore an orientation factor of α=1/6 will be used in the analytical modelling.

In Equations (9.21), (9.22) and (9.24), the only unknown is the value of E_f; as l_f and D_f can be obtained from the micrographs (nanotube dimensions: l_f = 120 μm, D_f = 120 nm) and the value of E_m can be measured using the tensile tests on the unmodified polymer samples (E_m= 2.90 GPa). This gives the effective Young's modulus of the

multi-walled carbon nanotubes to be 1103 GPa, when the nanotube loading is 0.1 wt%. However, the effective Young's modulus decreased slightly to 1052 GPa for the nanotube loading of 0.2 wt%, and significantly decreased to 720 GPa for the highest nanotube loading of 0.5 wt%. This variation of the derived effective Young's modulus is because of the reduced rate of stiffness increase caused by the nanotube agglomeration. These values of the efficient Young's modulus of the nanotubes are in good agreement with the typical Young's modulus of carbon nanotubes; the summary of the characteristics of carbon nanotubes showed that the Young's modulus of multi-walled carbon nanotubes was quoted to be in the range from 250 to 1200 GPa [71]. Figure 9.4.1 shows the predicted values using the Halpin-Tsai equation with the orientation factor (α=1/6), in which the nanotube efficient Young's modulus used falls in a range from 300 GPa to 1200 GPa. The best fitted value of the efficient Young's modulus is 1100 GPa (as will be used in the modelling), which is deduced by fitting a linear regression to the linear portion (in a range from 0.0 wt% to 0.2 wt% of nanotubes) of the experimental results. As can be seen in Figure 9.4.1, the predicted values of the modulus using the efficient Young's modulus of 1100 GPa can fit very well when the nanotube weight loading is lower than 0.2 wt%. However, at the highest concentration of the multi-walled carbon nanotubes at 0.5 wt%, the predicted modulus is overestimated by the simple fit, indicating that serious nanotube agglomerations are occurring at the high nanotube content.

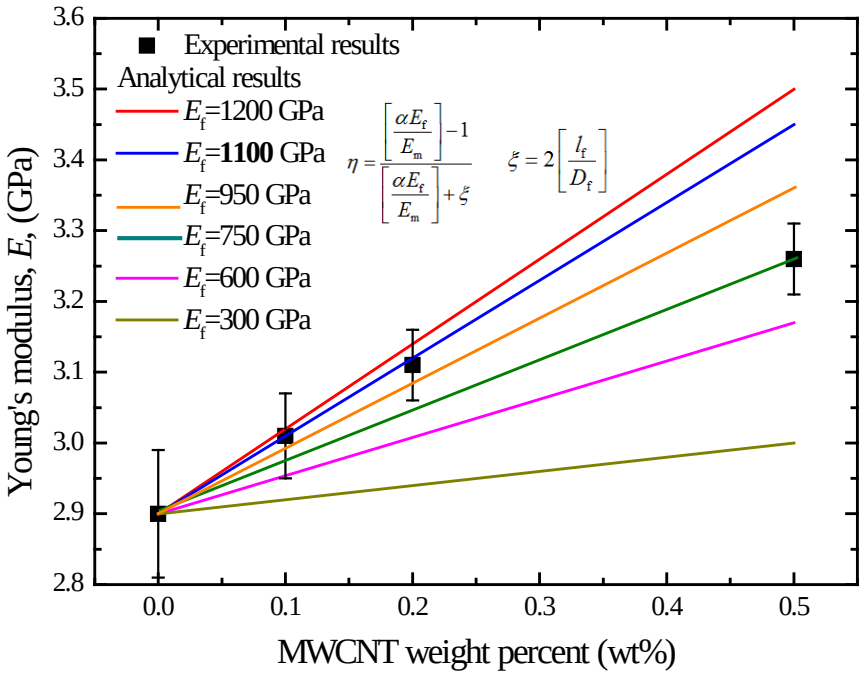


Figure 9.4.1 Experimental Young's modulus of the MWCNT-modified epoxy polymer fitted by Halpin-Tsai equation with the orientation factor by various Young's modulus of the multi-walled carbon nanotubes (the best fit is E_f =1100 GPa).

According to the tensile testing results, see Figure 7.3.1, the increased modulus caused by the addition of the multi-walled carbon nanotubes was reduced when the nanotube weight loading was higher than 0.2 wt%, so the trend for the measured Young's modulus versus MWCNT weight percent reveals nonlinearity. This is due to the agglomeration of the MWCNTs at higher contents of nanotubes, as demonstrated via the AFM, FEG-SEM and TOM observations. Yeh et al. [87, 166] have reported that the modulus of single-walled and multi-walled carbon nanotube-modified phenolic polymers did not increase proportionally to the nanotube content, and that the effectiveness of the nanotube modification on the stiffness reduced at higher concentrations of nanotubes due to the agglomeration. This is the same trend as the experimental results in this study. Yeh et al. [84, 166] modified the shape factor, ξ, via introducing an exponential factor to account for the effect of the reinforcement agglomeration on the stiffness, given by:

$$\xi = 2\left[\frac{l_f}{D_f}\right] e^{-a_C v_f - b_C} \tag{9.25}$$

in which, a_C and b_C are constants related to the CNT agglomeration. However, this expression has three unknowns, E_f, a_C and b_C. As mentioned above, the effective Young's modulus of 1100 GPa for the nanotubes used in this study was obtained using a linear regression to the linear portion of the experimental results, see Figure 9.4.1. Then further curve fitting can be used to calculate a_C, see Figure 9.4.2, and finally b_C, see Figure 9.4.3, to get the best agreement with the experiments. Finally, values of E_f = 1100 GPa, a_C = 9.15 and b_C = 0.12 were calculated. All the values used in the modified Halpin-Tsai equation are summarised in Table 9.4.1. The lower values of a_C and b_C in this study indicate less nanotube agglomeration than that observed by Yeh et al [87, 166], who calculated values of a_C = 75 and 55, and b_C = 1 and 0.5 for a modified phenolic polymer with two types of MWCNTs. The effect of the variations of the constants a_C and b_C on the modulus predication will be discussed below.

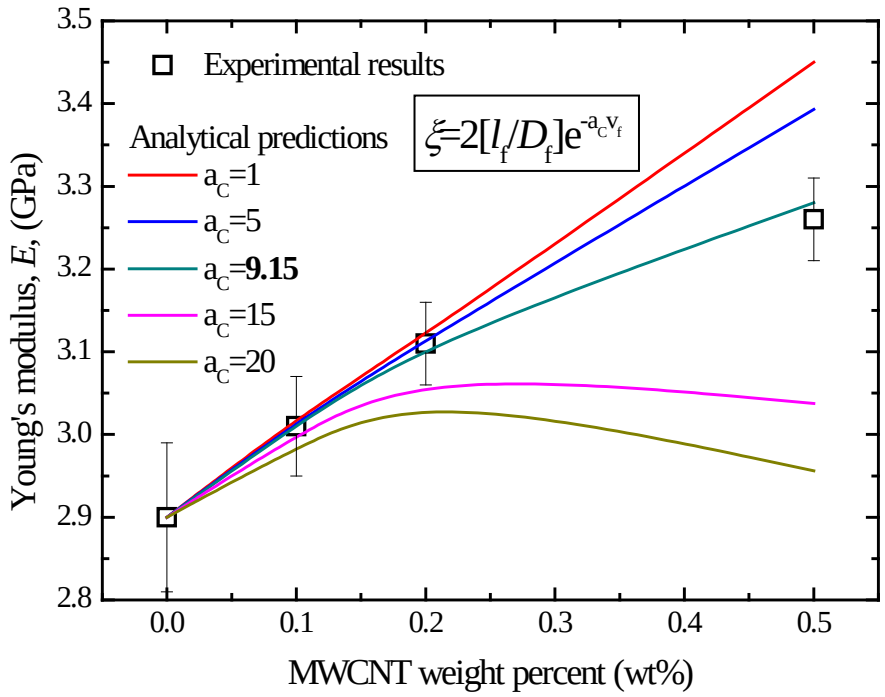


Figure 9.4.2 The effect of the agglomeration-related constant a on the Young's modulus of the MWCNT-modified epoxy polymer (the best fit is a_C=9.15).

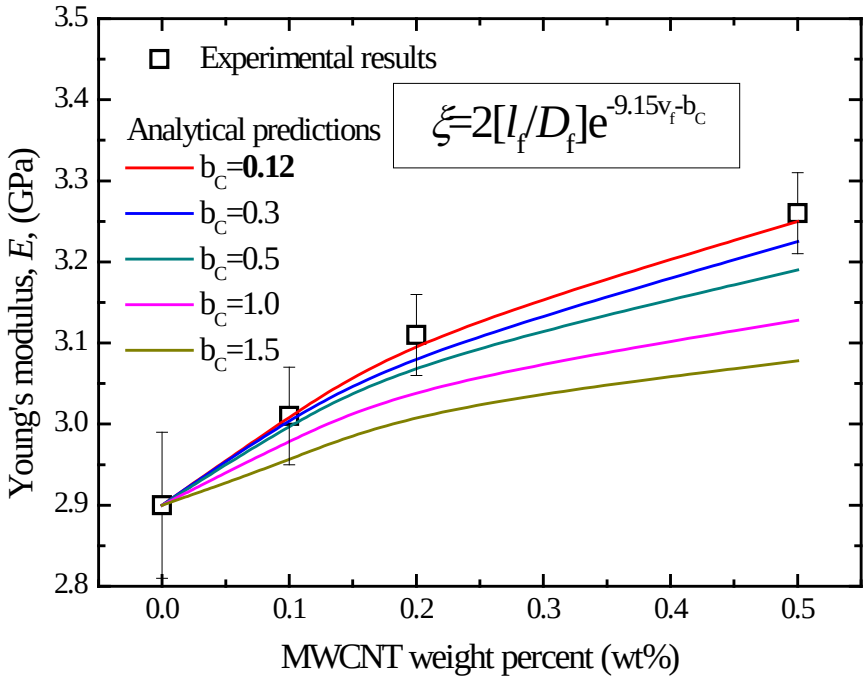


Figure 9.4.3 The effect of the agglomeration-related constant b_C on the Young's modulus of the MWCNT-modified epoxy polymer (the best fit is b_C=0.12).

Table 9.4.1 The parameters used in the modified Halpin-Tsai equation for fitting the Young's modulus of the nanotube-modified epoxy polymer.

Name	Symbol	Unit	Value	Source
Diameter of nanotube after sonication	D_f	nm	120	Present study
Length of nanotube after sonication	l_f	μm	120	Present study
Young's modulus of nanotube	E_f	GPa	1100	Calculated
Young's modulus of unmodified epoxy	E_m	GPa	2.90	Present study
Orientation-related constant	α	-	1/6	[165]
Agglomeration-related constant	a_C	-	9.15	Calculated
Agglomeration-related constant	b_C	-	0.12	Calculated

The effect of the agglomeration-related constant, a_C, on the predicted value of the Young's modulus for the MWCNT-modified epoxy polymer was investigated, see Figure 9.4.2. It is clear that the large values of a_C tend to reduce the predicted values of the Young's modulus at the high nanotube loading, indicating that more nanotube agglomerates initiated as the nanotube loading was increased. With lots of nanotube agglomerations (i.e. a_C = 20), the predicted modulus will go through a maximum predicted value at the weight loading of around 0.2 wt%, and then decrease. Besides, as the value of a_C is higher than 10, the rate of the increased modulus reduced, consequently the predicted curves diverted from linearity at higher nanotube contents.

The effect of the agglomeration-related constant, b_C, on the prediction of the Young's modulus for the modified epoxy polymer with the nanotubes is shown in Figure 9.4.3. When the value of b_C is increased, the modelling curves bend lower at higher nanotube contents. This indicates the higher values of b_C reflect lower levels of nanotube dispersion. For example, with lots of nanotube agglomeration (e.g. b_C = 1.5), the rate of the modulus increase appeared to level off at the higher nanotube loading. Both of these investigations clearly show that the introduction of the agglomeration-related constants to the Young's modulus prediction in nanotube-modified materials can efficiently consider the compromise of the stiffness due to nanotube agglomeration.

9.4.2 Modelling of the Young's Modulus of MWCNT-modified Epoxy

The analytical results of the Young's modulus of the multi-walled carbon nanotube-modified epoxy polymer are summarised in Table 9.4.2 and Figure 9.4.4. Figure 9.4.4 shows that experimental results of the multi-walled carbon nanotubes-modified epoxy polymer are fitted very well by the modified Halpin-Tsai equation with the orientation factor, α, and the (agglomeration-related) exponential shape factor, ξ. The introduction of the agglomeration-related shape factor results in a precise fitted modulus even at the higher nanotube loading. Basically, the serious agglomeration of the nanotubes initiates

at the high nanotube concentrations, above 0.2 wt%. The original Halpin-Tsai equation was derived for fibre-reinforced polymeric composites, which always possess well-dispersed reinforcement. Therefore, the predicted value using the original Halpin-Tsai equation was in good agreement with the experiment results only at low nanotube contents, but overpredicted the effect of the addition of nanotubes on improving the modulus at the high nanotube loading.

Table 9.4.2 The predicted and measured values of the Young's modulus of the MWCNT-modified epoxy polymer.

MWCNT (wt%)	*E* (GPa) modified Halpin-Tsai equation (Eq 9.21, 9.24 and 9.25)	*E* (GPa) Halpin-Tsai equation (Eq. 9.21, 9.22 and 9.23)	*E* (GPa) measured
0.0	-	-	2.90 ±0.09
0.1	**3.00**	3.00	3.01 ±0.06
0.2	**3.10**	3.12	3.11 ±0.05
0.5	**3.25**	3.45	3.26 ±0.05

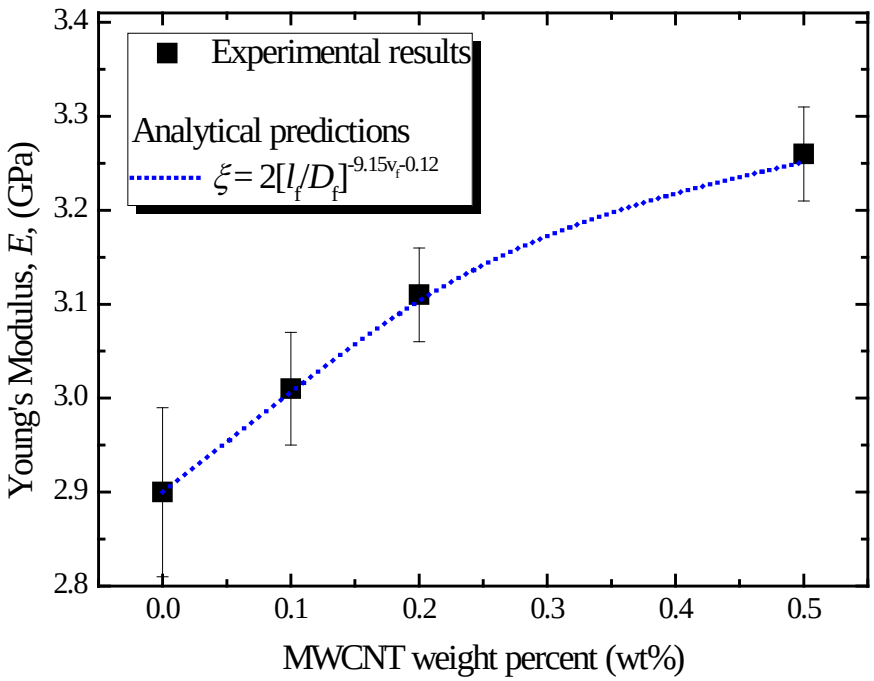


Figure 9.4.4 The experimental results of the Young's modulus fitted by the modified Halpin-Tsai equation with the orientation factor, α, and the (agglomeration-related) exponential shape factor, ξ.

9.4.3 The Nanotube Size Effect on the Young's Modulus

The nanotube size effect on the modulus was investigated using two different types of nanotubes (standard nanotubes with longer length and smaller diameter, and low quality nanotubes), as discussed in Section 7.8. The experimental results showed that the use of the nanotubes with longer length and smaller diameter (i.e. higher aspect ratio) can significantly improve the modulus of the nanocomposites with nanotubes. In this Section, the size effect of nanotube dimensions (length and diameter) will be investigated via the modelling. Note that the nanotube size effect on the dispersion was ignored in this Section.

The effect of nanotube length, l_f, on the Young's modulus was investigated using the modified Halpin-Tsai equation, as shown in Figure 9.4.5. Generally, the predicted values of the Young's modulus decrease with reducing the nanotube length. Longer nanotubes provide higher values of the Young's modulus, and the predicted values tend to bend lower when the nanotube length is shorter than 75 μm at the high nanotube loading. As the nanotube length is varied from 75 μm to 300μm, the predicted values of the modulus reveal no obvious difference when the nanotube contents are less than 0.2 wt%. However, there is a divide when the concentration of the nanotube is higher than 0.2 wt%. When the nanotubes have a relatively short length, such as 10 μm, the improved stiffness of the nanotube-modified composites increases nonlinearly, however, the decline in the increased stiffness was found once the predicted value of the Young's modulus reaches a peak for the nanotube weight loading at around 0.3 wt%. The point (wt% of nanotubes) where the decline occurring is increased with increasing the nanotube length. For example, the decline occurs at 0.25 wt% of the nanotubes with a length of 10 μm, but the point of the decline shifts to 0.35 wt% of the nanotubes with a length of 30 μm. Assumption of the same degree of dispersion was required in this investigation, as the nanotubes with a higher aspect ratio, i.e. longer length, result in a decrease in the nanotube dispersion, and consequently the contribution of the addition of nanotubes to improve the modulus reduces. According to this investigation, the length of the nanotubes is required to be longer than 75 μm in the anhydride-cured DGEBA epoxy system if the expected nanotube loading is up to 0.5 wt%.

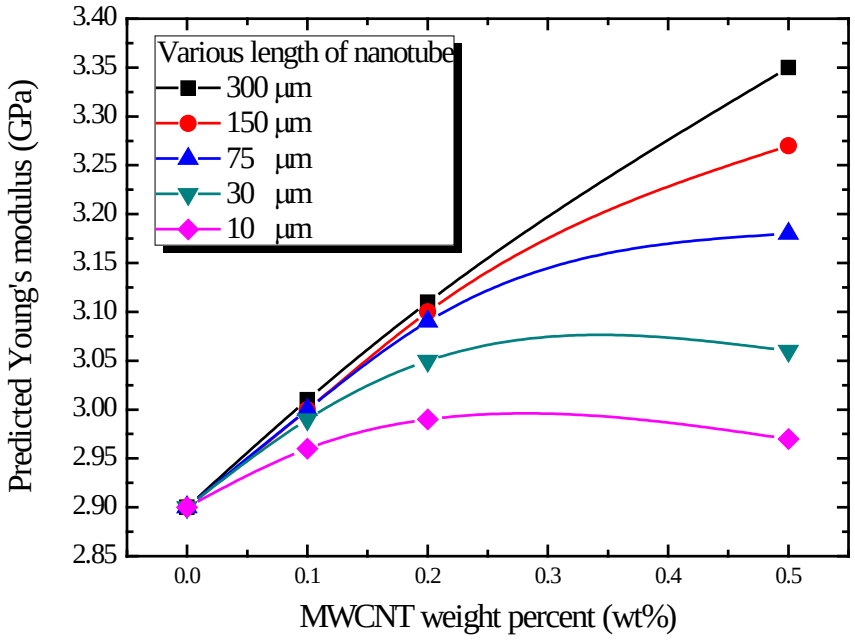


Figure 9.4.5 The effect of the nanotube length on the stiffness of nanotube-modified polymers (a fixed nanotube diameter = 120 nm).

Figure 9.4.6 shows the effect of the nanotube diameter on the modulus. The predicted values of the Young's modulus decrease with increasing the diameter (decrease in the aspect ratio) of the nanotubes. However the reduction of the stiffness caused by the increase in the nanotube diameter is less than that caused by the decrease in the nanotube length. As can been seen in Figure 9.4.6, all the predicted values are almost similar at the lower nanotube contents, less than 0.2 wt%. This indicates that the modification of nanotubes to stiffen polymer-based composites is sensitive to their length. An assumption that the level of the nanotube dispersion is independent of the nanotube dimensions is required in this investigation.

The investigation on the size effect of the nanotubes with the same aspect ratio (i.e. by changing the nanotube length and diameter simultaneously to get a constant aspect ratio) showed all the predicted values with different nanotube dimensions, but the same aspect ratio, are the same, if the degree of the nanotube agglomeration is assumed to be the same. This is because the predicted modulus is direct proportion to the nanotube aspect ratio, i.e. the predicted values are the same if the aspect ratio of

nanotubes with various dimensions is constant. In the analytical model, only the shape factor, see Equation (9.25), considers the nanotube aspect ratio, and it is directly proportional to the aspect ratio (l_f/D_f).

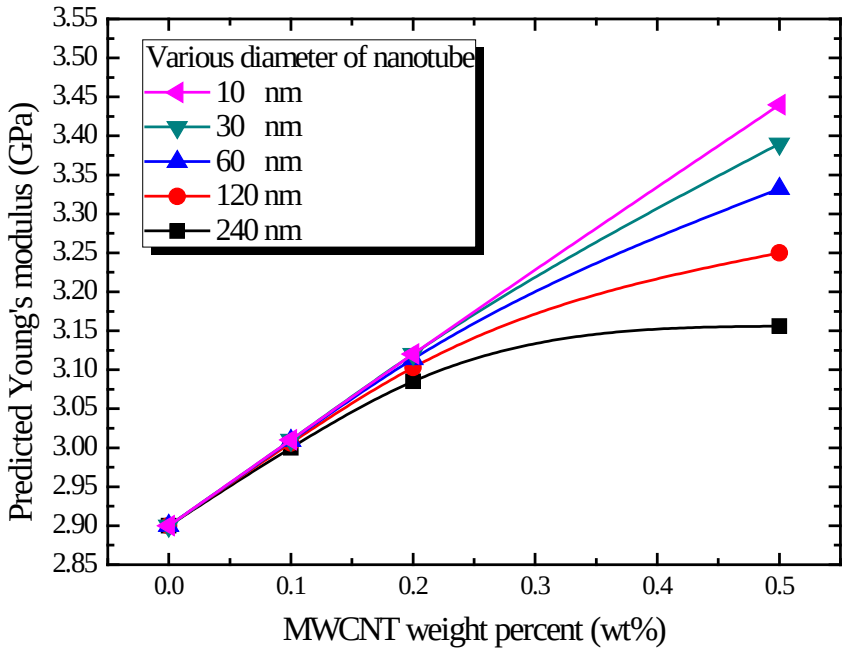


Figure 9.4.6 The effect of the nanotube diameter on the stiffness of nanotube-modified polymers (a fixed nanotube length = 120 μm).

9.5 Conclusions

An analytical study was carried out on modelling the toughening mechanisms to predict the improvement in the toughness of the nanocomposites caused by the addition of the silica nanoparticles and multi-walled carbon nanotubes. The predictions were able to provide a good agreement with the experimental values of the fracture energy of the nanosilica-modified polymers, except the Nanopox XP system. The loss of good agreement is because the effect of the surface treatment on the toughness of the epoxy is not considered in the modelling. Apart from that, the predications agree very well with the experiments.

The analytical model for nanoparticles was also used to predict the fracture energy of the glass bead microparticle-modified epoxies, and there was an excellent agreement between the predictions and experiments. This indicated that the developed model can work on the rigid particles with a wide range from nano-size to micron-size in diameter.

The fracture energy of the nanocomposites containing the multi-walled carbon nanotubes was predicted by an analytical model based on the toughening mechanisms of nanotube pull-out, nanotube debonding and plastic void growth of the epoxy matrix. The predicted values of the fracture energy are in good agreement with the measured values, and showed that the energy contribution from debonding and pull-out are significant. The contribution of void growth is almost zero. By changing the nanotube dimension, the modelling work showed that the nanotubes with high aspect ratio (i.e. long length and small diameter) have a relatively high potential for toughening the epoxy polymers, if the assumption of no effect on dispersion by nanotube dimensions is made.

The modelling study on the increased modulus of the nanotube-modified polymers showed that the modified Halpin-Tsai equation with the orientation-related shape factor and agglomeration-related constants can fit very well with the measured values of the Young’s modulus, even at higher nanotube contents which led to serious nanotube agglomeration. The investigation of the nanotube size effect on the modulus

and toughness showed that the improvement in the modulus and toughness of nanotube-modified epoxies is much more sensitive to the nanotube length, compared to the diameter.

CHAPTER 10

CONCLUDING REMARKS AND FUTURE WORK

10.1 Conclusions

The work in this thesis was carried out to investigate the effect of various reinforcements with a wide range of dimensions from nanometre to micrometre on the toughness and fatigue performance of the polymer-based composites. Four different types of reinforcements, soft rubber microparticles, rigid glass bead microparticles, silica nanoparticles and multi-walled carbon nanotubes, were used to prepare the composites in this study. The toughening mechanisms caused by these additives were identified. This Section summarises the results of this study with regard to the morphology, mechanical properties and toughening mechanisms in the modified epoxies.

10.1.1 Nanosilica-modified Epoxy

The silica nanoparticles with a mean diameter of 20 nm were supplied pre-mixed with a DGEBA epoxy resin to form a nanosilica-modified epoxy resin, Nanopox F400 from Nanoresins. In order to improve the nanosilica dispersion, a standard treatment was used in the F400 mixture. The morphology of the nanosilica in the cured polymers was investigated, and showed that they were well-dispersed even at the highest nanosilica content of 20 wt%. In the modification using the F400 nanosilica, an additional surface treatment of silane was used to improve nanoparticle/epoxy adhesion (labelled as F400-S). Nanopox XP, containing nanosilica with better adhesion in DGEBA was also used. The dispersion of the nanosilica was not affected by the addition of the surface treatments.

The Young's modulus of the nanocomposites was increased with increasing the content of the nanosilica. The presence of the F400 nanosilica in the epoxy resulted in a steady increase in the modulus from 2.90 GPa for the unmodified epoxy to 3.28 GPa for 10 wt% nanosilica, and a further increase in the modulus to 3.78 GPa as the nanosilica loading reached 20 wt%. The effect of adhesion on modulus showed that any improvement in nanosilica/epoxy adhesion did not improve the stiffness of the nanosilica-modified epoxies, but increased the yield stress of the polymer-based nanocomposites. This was demonstrated using the tensile tests under plane stress condition and plane strain compression tests. Turning to the results from the differential scanning calorimetry (DSC), these showed that the glass transition temperature, T_g, was not changed by the addition of the nanosilica, or by changing the level of adhesion.

The fracture energy, G_{Ic}, was increased from 133 J/m^2 for the unmodified epoxy to 220 J/m^2 for the epoxy with 20 wt% F400 nanosilica. For the fatigue performance, the maximum strain energy release rate at the threshold, G_{th}, was also increased with increasing the nanosilica content. The values of G_{th} for the nanocomposite containing 20 wt% F400 nanosilica was measued to be 55 J/m^2, which is more than double the value for the unmodified polymer (G_{th} = 24 J/m^2). Via examining the fracture surfaces of the nanocomposites, the toughening mechanisms which can contribute to the

increased toughness and fatigue performance were identified to be shear band yielding and plastic void growth associated with plastic deformation of the epoxy matrix.

The effect of nanosilica/epoxy adhesion on the toughness was also investigated, and showed the addition of the nanosilica with good adhesion brought an improvement in the toughness. A maximum fracture energy of 261 J/m^2 was recorded for the epoxy with 20 wt% nanosilica and silane. Both of the nanosilica-modified systems (F400-S and Nanopox XP) containing good adhesion nanosilica showed relatively high values of the fracture toughness and fracture energy, compared with the system containing F400 nanosilica.

10.1.2 Glass Bead Microparticle-modified Epoxy

Two different dimensions of glass beads, with mean diameters of 3.5 μm and 275 μm, were used to prepare the rigid microparticle-modified polymers. The coupling agent silane (caused well-bonded particles) and release agent Frekote (caused poorly-bonded particles) were used to modify the surfaces of the glass beads, to form the glass bead/epoxy composites with different levels of particle/epoxy adhesion. In the composites with 3.5 μm diameter glass beads, relatively good dispersion was obtained, even though some agglomerates composed of 5~10 glass beads were present. Serious agglomeration and sedimentation occurred in the modified epoxies with the large glass beads (275 μm in diameter).

The measured modulus of these composites showed that good adhesion can efficiently transfer the load from the polymer to the rigid particles when the composites were subjected to a tensile loading. The modified polymer with well-bonded glass beads had the highest modulus of 3.81 GPa using 20 wt% of the small glass beads with the silane treatment. The size effect of the glass beads on the modulus clearly showed that the use of the small glass beads can provide a more significant improvement in the modulus. For example, the epoxies with the large glass beads showed only a small

improvement in the modulus using 10 wt% of silane-treated large glass beads. The Frekote treatment used to give a low level of adhesion resulted in a small contribution to the modulus, compared with the untreated and silane-treated glass bead-modified epoxies. The measured values of the glass transition temperature, T_g, did not change by the addition of the glass beads. Although a slight decrease in T_g was found for the Frekote treatment systems, this decrease was not significant when the experimental variation was considered.

Results from the fracture tests showed that the addition of the small glass bead microparticles led to an improvement in the toughness. An increment of around 19% in the fracture energy was obtained for the epoxy with the glass bead loading at 20 wt%, compared with the unmodified polymer. Further increased fracture energy was given when the surface treatments were used. The introduction of both surface treatments brought a more significant improvement in the toughness, compared with the untreated glass beads. A 48% increment in the fracture energy was obtained for the composites with 20 wt% of the well-bonded (silane-treated) small glass beads, compared with the unmodified polymer. Even with the use of the Frekote-treated small glass beads, the fracture energy of the composites with 20 wt% of the poorly-bonded glass beads was increased by 44%. In contrast to the increase by the addition of the small glass beads, the presence of large glass beads led to a decrease in the toughness, even when the large beads were treated. This is because serious agglomeration and sedimentation of the large glass beads occurred in the composites. According to the fracture testing results in these glass bead-modified polymers, smaller rigid particles can provide a relatively high toughening contribution to the polymer-based composites. This can also be demonstrated by comparing the measured fracture energy of nanosilica-modified and glass bead microparticle-modified polymers. The maximum fracture energy of the nanocomposite with 20 wt% of silane-treated nanosilica reached around 260 J/m^2, but a relatively low value of 197 J/m^2 was recorded for the maximum fracture energy in the modification using the small glass bead microparticles with the silane treatment.

Toughening mechanisms such as crack deflection and debonding with subsequent void growth were identified on the fracture surfaces of the glass bead-modified epoxies. The glass beads present on the fracture surfaces were coated well with the epoxy matrix in the silane treatment systems. Hence, a low amount of glass

beads showed debonding and void growth in the composites with the silane-treated glass beads, compared with the Frekote-treated glass bead/epoxy composites.

10.1.3 Nanotube-modified Epoxy

Aligned multi-walled carbon nanotubes (MWCNTs) were synthesised using a chemical vapour deposition (CVD) technique. The as-produced MWCNTs are straight and unentangled, with an average length of 140 μm and an average diameter of 120 nm. In order to attain good nanotube dispersion in the epoxy, various dispersion methods were examined. The dispersion method of using an ultrasonic probe for 30 minutes was chosen for sample preparation of the nanotube-modified epoxies.

Atomic force microscopy (AFM) of the polymers with various weight loadings of the multi-walled carbon nanotubes showed that the nanotubes agglomerated, and the level of the nanotube dispersion was reduced with increasing the nanotube loading. Although the nanotubes were sonicated to improve the dispersion, the well-dispersed nanotubes reagglomerated during the cure schedule, as demonstrated by the hot stage investigation. Serious agglomeration of the nanotubes was found in the nanocomposites containing the highest concentration of 0.5 wt%, the size of the nanotube agglomerates was measured to be around 0.6 μm square in this nanocomposite.

Carbon nanotubes possess high stiffness and strength, and are analogous to nano-scale carbon fibres, therefore, an increase in the modulus of the nanotube-modified polymers is expected. The experimental results showed that the addition of the MWCNTs resulted in a significant increase in the Young's modulus from 2.90 GPa for the unmodified polymer to 3.26 GPa for the nanocomposite containing 0.5 wt% nanotubes. The rate of the increased modulus was reduced for the sample with the highest content of nanotubes, due to nanotube agglomeration. This was demonstrated by the morphology observation, in which a relatively large size of the nanotube agglomerates was observed in the modified polymer with 0.5 wt% nanotubes. The glass

transition temperature of the epoxy did not change by the addition of the nanotubes. All the measured values of T_g are around 146 °C.

A significant improvement in the toughness was attained by the addition of the MWCNTs to the epoxy. The fracture toughness of the nanocomposites was increased from 0.69 MPa $m^{1/2}$ for the unmodified epoxy to a maximum value of 0.98 MPa $m^{1/2}$ for the 0.5 wt% sample. Even at lower nanotube contents, the epoxy modified with 0.1 wt% nanotubes showed a 23% increment in the fracture toughness, compared with the unmodified epoxy. The measured fracture energy of the nanotube-modified epoxies was increased with increasing the nanotube content, and showed the same trend as the increased fracture toughness. A maximum fracture energy of 223 J/m^2 was recorded for the nanocomposite containing 0.5 wt% nanotubes This is around an 75% increment in the fracture energy, compared with the unmodified epoxy.

The effect of using the carbon nanotubes on the fatigue performance of the nanocomposites was investigated. The results showed that resistance to crack propagation under fatigue loading was significantly improved when the nanotubes were used. This could be demonstrated by the increased G_{th}. The value of G_{th} was increased from 24 J/m^2 for the unmodified epoxy to 53 J/m^2 for 0.2 wt% nanotubes, and reached the maximum value of 73 J/m^2 for the epoxy with 0.5 wt% nanotubes.

Nanotube pull-out was identified from the field emission gun scanning electron microscopy images of the fracture surfaces of the specimens after the quasi-static and fatigue fracture tests. Nanotube pull-out was considered to be the main toughening mechanism in the nanotube-modified epoxies. This mechanism starts with interfacial debonding then nanotube rupture, and resulted in a significant increase in energy dissipation by friction between the nanotubes and epoxy matrix. Void growth of the epoxy matrix surrounding the carbon nanotubes was identified on the fracture surfaces, which led to an increase in toughness by plastic deformation of the epoxy matrix. The contribution of debonding to the increased toughness was also significant. Shear band yielding is generally not considered for short-fibre composites. This was demonstrated using the plane strain compression tests, in which no strain softening occurred. The occurrence of strain softening is generally considered to be a requirement for shear band yielding to occur. Hence, the main toughening mechanisms operating in the nanotube-

modified epoxies are nanotube pull-out plus interfacial debonding and plastic void growth.

Two different types of MWCNTs with different dimensions were used to investigate the nanotube size effect on the mechanical properties. The standard nanotubes with longer length and smaller diameter, i.e. high aspect ratio, have a relatively high potential to improve the toughness and fatigue resistance. The measured values of G_{Ic} and G_{th} for the composites containing the standard nanotubes are higher than those for the modified polymer with low quality nanotubes (short length and large diameter). This relatively higher toughening contribution from the standard nanotubes is because the standard nanotube showed a longer pull-out length on the fracture surfaces, and a relatively high amount of nanotubes operating the pull-out mechanism.

10.1.4 Rubber-modified Epoxy

A common rubber modification was used to improve the fracture properties of the epoxy polymer. The addition of phase separating carboxyl-terminated butadiene-acrylonitrile (CTBN) to the epoxy polymer led to the formation of micron-size well-dispersed rubber particles in the cured epoxies, and provided a significant improvement in the toughness and fatigue performance. However, blending the rubber particles with the epoxy resulted in a decrease in the modulus of the modified epoxies, because the rubber is soft. The tensile testing results showed that the addition of 9.0 wt% CTBN decreased the Young's modulus from 2.90 GPa for the unmodified to 2.34 GPa for the rubber-modified polymer. The measured values of T_g showed the same trend, as the addition of the rubber particles resulted in a decrease in the T_g, by about 8 °C. This is because some of the rubber remained in solution.

In contrast to the undesirable decrease in the modulus and T_g by the rubber modification, the rubber-modified polymer showed the highest toughness for the epoxies with single-phase modifications. The fracture toughness and the fracture energy of the 9.0 wt% rubber modified epoxy were measured to be 1.14 MPa.m$^{1/2}$ and 697 J/m^2,

respectively. This increased fracture energy is around two and half-times the fracture energy of the nanosilica/epoxy or nanotube/epoxy materials. The fracture behaviour of the epoxies under fatigue loading was improved significantly with the addition of the rubber particles, compared with the neat polymer. The maximum strain energy release rate at the threshold, G_{th}, was measured to be 61 J/m^2. However, the increased fatigue performance by blending the rubber is only slightly higher than that in the modified polymers with the nano-reinforcements. This indicates that the rubber modification to improve the toughness of the polymer-based composites is more efficient than the improvement in the fatigue performance.

Rubber cavitation is considered to be the main toughening mechanism in the rubber-modified polymers. Rubber cavities were clearly found on the fracture surfaces of the modified epoxy, and the diameters of these cavities were larger than those of the un-deformed rubber particles, indicating that the rubber particles were cavitated. The rubber cavitation mechanism results in a significant improvement in the fracture properties of the epoxies via relief of constraint, allowing the epoxy to deform plastically.

10.1.5 Hybrid-modified Epoxy

Combinations of various toughening particles were used to prepare the hybrid-modified polymers. The different formulations of rubber/nanosilica (9R-10N), rubber/nanotube (9R-0.2C) and nanosilica/nanotube (10N-0.2C) modified epoxies were made, and their mechanical properties were measured. The morphology of these hybrid-modified polymers showed that the rubber particles were well dispersed in the hybrids. However, agglomeration of the silica nanoparticles and carbon nanotubes were found in the hybrid-modified epoxies. Nanotube agglomerates formed in the hybrid-modified epoxies, but the nanotube dispersion in the 9R-0.2C sample is better than the nanotube-modified alone (0.2C) sample. The high viscosity caused by the addition of the rubber particles can provide higher shear force during the mixing to efficiently break entangled nanotubes, and reduce the rate of nanotube reagglomeration during the cure cycle. The

level of the nanotube dispersion did not improve in the nanocomposite containing nanosilica and nanotubes. The silica nanoparticles showed good dispersion in the single-phase modified polymer and nano-hybrid (nanosilica/nanotubes) modified polymer, but they agglomerated in the rubber/nanosilica modified epoxy.

As discussed for the rubber-modified alone epoxy polymer, the addition of the rubber particles led to a significant increase of the toughness, but at cost of the decrease in the modulus. This decrease in modulus can be neutralized by the addition of rigid particles of nanosilica or carbon nanotubes to the rubber-modified polymers. Although the Young's modulus of 2.74 GPa for the 9R-10N (rubber/nanosilica) composite is slightly lower than the unmodified epoxy, the measured value of the Young's modulus was increased to 3.08 GPa when the carbon nanotubes were used to stiffen the rubber-modified polymer. The maximum Young's modulus was recorded to be 3.48 GPa for the nano-hybrid modified polymer containing 10 wt% of nanosilica and 0.2 wt% of nanotubes. The decrease in T_g caused by the addition of the rubber particles was not neutralised by the addition of the silica nanotubes and carbon nanotubes. The hybrid-modified epoxies with the rubber particles had an average T_g of 140 °C.

All the hybrid-modified epoxies showed a significant improvement in the toughness and fatigue performance. As the synergy between the soft microparticles (rubber) and the rigid nanoparticles was obtained, the maximum values of K_{Ic}, G_{Ic} and G_{th} were attained in the hybrid-modified polymer containing 9 wt% of rubber particles and 0.2 wt% of nanotubes. The measured fracture energy was increased from 133 J/m^2 for unmodified to 1132 J/m^2 for the rubber/nanotube-modified epoxy (9R-0.2C). The fatigue performance was also increased significantly from 24 J/m^2 for the unmodified polymer to 127 J/m^2 for the hybrid-modified polymer. Even for the hybrid-modified (9R-10N) epoxy with nanosilica showed significant increase in the toughness and fatigue performance, the G_{Ic} of 1059 J/m^2 and G_{th} of 118 J/m^2 are similar to the values for the 9R-0.2C sample. Although no synergistic effect of the combination of nanosilica and nanotubes on the toughness and fatigue performance was obtained, the measured values of G_{Ic} (228 J/m^2) and G_{th} (97 J/m^2) are still much higher than the unmodified polymer and the nanocomposites with the single-phase modification of nanosilica or nanotubes.

The mechanisms that contribute to the improvement of the toughness and fatigue performance were identified via FEG-SEM of fracture surfaces. The rubber particles cavitated followed by void growth. Debonding, pull-out and plastic void growth associated with the nanotubes were found on the fracture surfaces. The added nanosilica debonded from the epoxy, subsequently voids formed around the debonded nanoparticles. This involves plastic deformation of the epoxy polymer, consequently increasing the energy dissipation and toughness.

10.1.6 Analytical Modelling

Modelling work was performed to predict the toughness of the nanosilica- and nanotube- modified epoxies. In the prediction for the nanosilica, the model considered the toughening mechanisms of shear band yielding and plastic void growth. The predictions of the nanocomposites containing F400 or silane-treated F400 nanosilica provided a good agreement with the experimental results. However, in the Nanopox XP system, which contains relatively high adhesion nanosilica, the predicted values of the fracture energy are lower than the measured values. This suggested that not considering the energy contribution from interfacial debonding may underestimate the fracture energy of the nanosilica-modified epoxies with good adhesion. Besides, the loss of excellent agreement between the predictions and experiments in the Nanopox XP system can be attributed to the inability to consider the effect of the surface treatment on the material properties of the epoxy. Indeed, the toughness of the epoxy polymer was improved by the addition of the additional surface treatment of silane, which was taken into account in the modelling. Hence, in the F400-S system with good nanosilica/epoxy adhesion, a good agreement between the predictions and experimental results was obtained.

The developed model was used to predict the fracture energy in the glass bead microparticle-modified epoxies. The results showed that the predicted values agree well with the measured values.

An analytical model based on the toughening mechanisms of nanotube pull-out, nanotube debonding and plastic void growth of the epoxy matrix was built. It can efficiently predict the increase in the toughness caused by the addition of nanotubes. The predicted values of the fracture energy are in good agreement with the measured values. The energy contribution from interfacial debonding and pull-out are significant. However, plastic void growth of the epoxy only provides a very small energy contribution to the overall fracture energy.

The Halpin-Tsai equation was modified by introducing the orientation-related shape factor and agglomeration-related constants, and was used to fit the modulus of the nanocomposites containing nanotubes. The predicted values of the Young's modulus can fit very well with the measured values, even at the highest nanotube content which led to serious agglomeration. By changing the nanotube dimensions to investigate the size effect via analytical modelling, the results showed that the nanotubes with longer length and smaller diameter have a relatively high potential for improving the toughness and modulus, which has been confirmed by the experiments using two different types of multi-walled carbon nanotubes.

10.2 Recommendations for Future Work

Although the present work had investigated systematically the fracture behaviour of the epoxy polymer modified with various reinforcements, some possible further work has surfaced. The recommendations are outlined below.

1. **Adhesion** – The effect of particle/epoxy adhesion on the toughness has been investigated, and showed the use of glass beads or nanosilica with good adhesion provided a relatively high potential to improve the toughness. The different microstructures of the fracture surfaces caused by the different levels of adhesion were identified. However, the chemical bonding between the silica and epoxy initiated by the introduction of silane coupling agent to improve the adhesion is still not clear. Nuclear magnetic resonance (NMR) spectroscopy has been widely used to investigate the interfacial interaction between silane-modified silica and epoxy [167]. This can examine whether the expected chemical bonding for improving adhesion occurs. Besides, ^{1}H-^{1}H spin-spin relaxation experiments can be used to realise whether the surface of the nanoparticles enhances the mobility of the chains between the network of the epoxy polymer [168].

2. **Dispersion of nanotubes** – Improvement in the mechanical properties, modulus, toughness and fatigue performance, caused by the addition of the multi-walled carbon nanotubes has been demonstrated. However the relationship between the nanotube dispersion and the material properties of the epoxies with nanotubes were not investigated. It is still an open question of whether there is still room to improve the nanotube dispersion using surface treatments, and the effect of different levels of dispersion on the mechanical properties.

3. **Orientation of nanotubes** – The addition of the nanotubes resulted in a significant improvement in the toughness and fatigue performance. However, the orientation of the nanotubes was not controlled, and was shown to be random in the cured polymer, even for the aligned MWCNTs synthesised by CVD. In the CVD process, the aligned MWCNTs can be grown on titanium

substrates [92]. These substrates with aligned nanotubes can be bonded together using the epoxy polymer to prepare specimens for double-cantilever beam fracture tests. In these DCB specimens, the core material is epoxy/nanotubes, and the orientation of the nanotubes is perpendicular to the direction of crack propagation.

4. **Application of nanotube-modified polymer** – Epoxy polymer has been widely used as the matrix in fibre-reinforced polymer (FRP) composites. Previous work [5, 23] reported that the use of modified epoxies with nanosilica, rubber and hybrid modifiers to prepare FRP composites resulted in a significant improvement in the delamination resistance and strength of these FRP composites. The nanotube-modified epoxies can be used to prepare FRP composites. The improvement in the material properties of the FRP with the nanotube-modified epoxy matrix would be expected, even though a high viscosity of nanotube/epoxy resin will result in difficulty in FRP sample preparation.

5. **Consideration of nanosilica debonding in modelling** – The predicted values from the analytical model agree well with the experiments. However, the energy contribution of well-bonded nanosilica is underestimated. The lost excellent agreement can be retrieved by a developed model considering the effect of adhesion on the toughness of nanosilica-modified epoxies.

REFERENCES

1. A. J. Kinloch, *Adhesion and Adhesives: Science and Technology*, Chapman and Hall, London, 1987.
2. A. J. Kinloch, M. L. Yuen and S. D. Jenkins, "Thermoplastic-toughened Epoxy Polymers", *Journal of Materials Science*, Vol. 29, pp. 3781-2790, 1994.
3. A. C. Moloney, H. H. Kausch, T. Kaiser and H. R. Beer, "Review: Parameters Determining the Strength and Toughness of Particulate Filled Epoxide Resins", *Journal of Materials Science*, Vol. 22, pp. 381-393, 1987.
4. A. F. Yee and R. A. Pearson, "Toughening Mechanisms in Elastomer-modified Epoxies. Part 1 Mechanical Studies", *Journal of Materials Science*, Vol. 21, pp. 2462-2474, 1986.
5. T. H. Hsieh, A. J. Kinloch, K. Masania, J. Sohn-Lee, A. C. Taylor and S. Sprenger, "The Toughness of Epoxy Polymers and Fibre Composites Modified with Rubber Microparticles and Silica Nanoparticles", *Journal of Materials Science*, Vol. 45, pp. 1193-1210, 2010.
6. A. J. Kinloch, J. H, Lee, A. C. Taylor, S. Sprenger, C. Eger and D. Egan, "Toughening Structural Adhesives Via Nano- and Micro-phase Inclusions, *Journal of Adhesion*, Vol. 79, pp. 867-873, 2003.
7. B. B. Johnsen, A. J. Kinloch, R. D. Mohammed, A. C. Taylor and S. Sprenger, "Toughening Mechanisms of Nanoparticle-modified Epoxy Polymers, *Polymer*, Vol. 48, pp. 530-541, 2007.
8. Y. L. Liang and R. A. Pearson, "Toughening Mechanisms in Epoxy – Silica Nanocomposites (ESNs)", *Polymer*, Vol. 50, pp. 4895-4905, 2009.
9. J. H. Lee, *The Fracture Behaviour of Nano-particle Toughened Epoxy Adhesives*, PhD Thesis in Mechanical Engineering, imperial College London, 2006.
10. R. D. Mohammed, *Material Properties and Fracture Mechanisms of Epoxy Nanocomposites*, PhD Thesis in Mechanical Engineering, Imperial College London, 2007.
11. Y. Ganesan, C. Peng, Y. Lu, P. E. Loya, P. Moloney, E. Barrera, B. I. Yakobson, J. M. Tour, R. Ballarini and J. Lou, "Interface Toughness of Carbon Nanotube Reinforced Epoxy Composites", *ASC Applied Materials and Interfaces*, Vol. 3, pp. 129-134, 2011.
12. R. Hollertz, S. Chatterjee, H. Gutmann, T. Geiger, F. A. Nuesch and B. T. T. Chu, "Improvement of Toughness and Electrical Properties of Epoxy Composites with Carbon Nanotubes prepared by Industrially Relevant Processes", *Nanotechnology*, Vol. 22, pp. 125702 1-9, 2011.
13. A. A. Griffith, "The Phenomena of Rupture and Flow in Solids", *Philisophical Transactions of the Royal Society of London*, Vol. 221, pp. 163-198, 1920.

14. G. C. Irwin, "Structural Aspects of Brittle Fracture", *Applied Materials Research*, Vol. 3, pp. 65-81, 1964.

15. W. D. Callister, *Materials Science and Engineering – An Introduction*, John Wiley and Sons, New York, 2000.

16. P. C. Paris, M. R. Gomez and W. E. Anderson, "A Rational Analytic Theory of Fatigue", *The Trend Engineering*, Vol. 13, pp. 9-14, 1961.

17. Adhesives Toolkit, *Fracture Toughness Test Mode I*, Accessed (10/04/11), Available from: http://www.adhesivestoolkit.com/Docs/test/MECHANICAL%20TEST%20METHOD%201%20.

18. N. G. McCrum, C. P. Buckley and C. B. Bucknall, *Principles of Polymer Engineering*, Oxford University Press, 1997.

19. N. J. Mills, *Plastic:Microstructure, Properties and Applications*, Edward Arnold, London, 1986.

20. S. Sprenger, A. J. Kinloch and A. C. Taylor, "Silica Nanoparticles and Rubber Toughening – a Synergy in Adhesives and Composites Applications", *Presented at a meeting of the Thermoset Resin Formulators Association*, Chicago, 2008.

21. S. S. Ray and M. Bousmina, *Polymer Nanocomposites and their Applications*, American Scientific Publishers, 2006.

22. A. Ram, *Fundamentals of Polymer Engineering*, Plenum Press, New York, 1997.

23. K. Masania, *Toughening Mechanisms of Silica Nanoparticle-modified Epoxy Polymers*, PhD Thesis in Mechanical Engineering, Imperial College London, 2010.

24. H. Miyagawa, M. Misra, L. T. Drzal and A. K. Mohanty, "Fracture Toughness and Impact Strength of Anhydride-cured Biobased Epoxy", *Polymer Engineering and Science*, Vol. 45, pp. 487-495, 2005.

25. M. P. Stevens, *Polymer Chemistry: an Introduction*, Oxford University Press, 1999.

26. A. J. Kinloch, *Structural Adhesives: Developments in Resins and Primers*, Elsevier Applied Science Publishers Ltd., London, 1986.

27. J. A. Brydson, *Plastics Materiasl*, Butterworth - Heinemann, Oxford, 1999.

28. C. B. Bucknall, *Toughened Plastics*, Applied Science Publishers Ltd., London, 1977.

29. J. N. Sultan and F. J. McGarry, "Effect of Rubber Particle Size on Deformation Mechanisms in Glassy Epoxy", *Polymer Engineering and Science*, Vol. 13, pp. 29-34, 1973.

30. A. J. Kinloch, S. J. Shaw D. A. Tod and D. L. Hunston, "Deformation and Fracture Behaviour of a Rubber-toughened Epoxy: 1. Microstructure and Fracture Studies", *Polymer*, Vol. 24, pp. 1341-1354, 1983.

31. S. C. Kunz-Douglass, P. W. R. Beaumont and M. F. Ashby, "A Model for the Toughness of Epoxy-rubber Particulate Composites", *Journal of Materials Science*, Vol. 15, pp. 1109-1123, 1980.

32. A. J. Kinloch, C. A. Finch and S. Hashemi, "Effect of Segmental Molecular Mass between Cross-links of the Matrix Phase on the Toughness of Rubber-modified Epoxies", *Polymer Communications*, Vol. 28, pp. 322-325, 1987.

33. Y. Huang and A. J. Kinloch, "Modelling of the Toughening Mechanisms in Rubber-modified Epoxy Polymers. Part II: A Quantitative Description of the Microstructure-fracture Property Relationships", *Journal of Materials Science*, Vol. 27, pp. 2763-2769, 1992.

34. S. M. Zebarjad, R. Bagheri, A. Lazzeri and S. Serajzadeh, "Dilatational Shear Bands in Rubber-modified Isotactic Polypropylene", *Materials and Design*, Vol. 25, pp. 247-250, 2004.

35. R. C. Batra and Z. G. Wei, "Instability Strain and Shear Band Spacing in Simple Tensile/compressive Deformations of Thermoviscoplastic Materials, *International Journal of Impact Engineering*, Vol. 34, pp. 448-463, 2007.

36. C. Liu, Y. Huang and M. G. Stout, "Enhanced Mode -II Fracture Toughness of an Epoxy Resin due to Shear Banding", *Acta Materialia*, Vol. 46, pp. 5647-5661, 1998.

37. L. T. Manzione and J. K. Gillham, "Rubber-modified Epoxies. II. Morphology and Mechanical Properties", *Journal of Applied Polymer Science*, Vol. 26, pp. 907-919, 1981.

38. Y. Huang, *Microstructure-property Relationships in Toughened Polymers*, PhD Thesis in Imperial College London, University of London, London, 1991.

39. Y. Huang and A. J. Kinloch, "The Sequence of Initiation of the Toughening Micromechanisms in Rubber-modified Epoxy Polymers", *Polymer*, Vol. 33, pp. 5338-5340, 1992.

40. D. Dompas and G. Groeninckx, "Toughening Behaviour of Rubber-modified Thermoplastic Polymers Involving Very Small Rubber Particles: 1. A Criterion for Internal Rubber Cavitation", *Polymer*, Vol. 35, pp. 4743-4749, 1994.

41. E. Crawford and A. J. Lesser, "Mechanics of Rubber Particle Cavitation in Toughened Polyvinylchloride (PVC)", *Polymer*, Vol. 41, pp. 5865-5870, 2000.

42. Y. Huang and A. J. Kinloch, "The Role of Plastic Void Growth in the Fracture of Rubbr-toughened Epoxy Polymers", *Journal of Materials Science Letter*, Vol. 11, pp. 484-487, 1992.

43. A. F. Yee, D. Li and X. Li, "The Importance of Constrain Relief Caused by Rubber Cavitation in the Toughening of Epoxy", *Journal of Materials Science*, Vol. 28, pp. 6392-6398, 1993.

44. X. Wang, F. J. Guild, A. J. Kinloch, A. C. Taylor and H. Hadavinia, "Modelling of Rubber Toughened Adhesives: the Effect of Particle Cavitation", *Proceedings of the 28th annual meeting of the Adhesion Society*, USA, 2005.

45. J. Spanoudakis and R. J. Young, "Crack Propagation in a Glass Particle-filled Epoxy Resin: Part 1 Effect of Particle Volume Fraction and Size", *Journal of Materials Science*, Vol. 19, pp. 473-486, 1984.

46. J. Spanoudakis and R. J. Young, "Crack Propagation in a Glass Particle-filled Epoxy Resin: Part 2 Effect of Particle-matrix Adhesion", *Journal of Materials Science*, Vol. 19, pp. 487-496, 1984.

47. N. Amdouni, H. Sautereau and J. F. Gerard, "Epoxy Composites Based on Glass Beads. II. Mechanical Properties", *Journal of Applied Polymer Science*, Vol. 46, pp. 1723-1735, 1992.

48. S. Debnath, S. L. Wunder, J. I McCool and G. R. Baran, "Silane Treatment Effects on Glass/resin Interfacial Shear Strength", *Dental Materials*, Vol. 19, pp. 441-448, 2003.

49. P. K. Mallick and L. J. Broutman, "Mechanical and Fracture Behaviour of Glass Bead Filled Epoxy Composites", *Materials Science and Engineering*, Vol. 18, pp. 63-73, 1975.

50. F. F. Lange, "The Interaction of a Crack Front with a Second-phase Dispersion", *Philosophical Magazine*, Vol. 22, pp. 983-992, 1970.

51. A. G. Evans, "The Strength of Brittle Materials Containing Second Phase Dispersions", *Philosophical Magazine*, Vol. 26. Pp. 1327-1344, 1972.

52. D. J. Green, P. S. Nicholson and J. D. Embery, "Fracture of a Brittle Particlate Composite. Part 2 – Theoretical Aspects, *Journal of Materials Science*, Vol. 14, pp. 1657-1661, 1979.

53. A. J. Kinloch, D. A. Maxwell and R. J. Young, "Micromechanisms of Crack Propagation in Hybrid-particulate Composites", *Journal of Materials Science Letters*, Vol. 4, pp. 1276-1279, 1985.

54. D. A. Norman and R. E. Robertson, "Rigid-particle Toughening of Glassy Polymers", *Polymer*, Vol. 44, pp. 2351-2362, 2003.

55. N. Amdouni, H. Sautereau, J. F. Gerard, F. Fernagut, G. Coulon and J. M. Lefebvre, "Coated Glass Beads Epoxy Composites - Influence of the Interlayer Thickness on Pre-yielding and Fracture Properties, *Journal of Materials Science*, Vol. 25, pp. 1435-1443, 1990.

56. G. Xu, M. Gong and W. Shi, "Effects of Hyperbranched Poly(ester-silane) as a Coupling Agent on the Mechanical Behavior of Glass Bead Filled Epoxy Resin", *Polymers for Advanced Technologies*, Vol. 16, pp. 473-479, 2005.

57. J. Lee and A. F. Yee, "Fracture of Glass Bead/epoxy Composites: on Micro-mechanical Deformations", *Polymer*, Vol. 41, pp. 8363-8373, 2000.

58. T. Kawaguchi and R. A. Pearson, "The Effect of Particle-matrix Adhesion on the Mechanical Behavior of Glass Filled Epoxies: Part 1. A Study on Yield Behavior and Cohesive Strength", *Polymer*, Vol. 44, pp. 4229-4238, 2003.

59. A. J. Kinloch and A. C. Taylor, "The Toughening of Cyanate-ester Polymers. Part I Physical Modification using Particles, Fibres and Woven-mats", *Journal of Materials Science*, Vol. 37, pp. 433-460, 2002.

60. A. S. Argon and R. E. Cohen, "Toughenability of Polymers", *Polymer*, Vol. 44, pp. 6013-6032, 2003.

61. S. Sprenger, A. J. Kinloch, A. C. Taylor and R. D. Mohammed, "Rubber-toughened GFRCs Optimised by Nanoparticles", *JEC-Composites*, pp. 66-69, 2005.

62. A. J. Kinloch, R. D. Mohammed, A. C. Taylor, C. Eger, S. Sprenger and D. Egan, "The Effect of Silica Nano Particles and Rubber Particles on the Toughness of Multiphase Thermosetting Epoxy Polymers", *Journal of Materials Science*, Vol. 40, pp. 5083-5086, 2005.

63. H. Zhang, Z. Zhang, K. Friedrich and C. Eger, "Property Improvements of in situ Epoxy Nanocomposites with Reduced Interparticle Distance at High Nanosilica Content", *Acta Materialia*, Vol. 54, pp.1833–1842, 2006.

64. R. P. Singh, M. Zhang and D. Chan, "Toughening of a Brittle Thermosetting Polymer: Effects of Reinforcement Particle Size and Volume Fraction", *Journal of Materials Science*, Vol. 37, pp. 781-788, 2002.

65. D. J. Green, P. S. Nicholson and J. D. Embury, "Fracture of Brittle Particulate Composite. Part 2 Theoretical Aspects", *Journal of Materials Science*, Vol. 14, pp. 1657-1661, 1979.

66. S. Iijima, "Helical Microtubles of Graphitic Carbon" *Nature*, Vol. 354, pp. 56-58, 1991.

67. M. M. J. Treacy, T. W. Ebbesen and J. M. Gibson, "Exceptionally High Young's Modulus Observed for Individual Carbon Nanotubes", *Nature*, Vol. 381, pp. 678-680. 1996.

68. S. Xie, W. Li, Z. Pan, B. Chang and L. Sun, "Mechanical and Physical Properties of Carbon Nanotubes", *Journal of Physics and Chemistry of Solids*, Vol. 61, pp. 1153-1158, 2000.

69. M. R. Falvo, G. J. Clary, R. M. Taylor, V. Chi, F.P. Brooks, S. Washburn and R. Superfine, "Bending and Bucking of Carbon Nanotubes under Large Strain", *Nature*, Vol. 389, pp. 582-584, 1997.

70. M. F. Yu, O. Lourie, M. J. Dyer, K. Moloni, T. F Kelly and R. S. Ruoff, "Strength and Breaking Mechanism of Multiwalled Carbon Nanotubes under Tensile Load", *Science*, Vol. 287, pp. 637-640, 2000.

71. X. L. Xie, Y. W. Mai and X. P. Zhou, "Dispersion and Alignment of Carbon Nanotubes in Polymer Matrix: A Review", *Materials Science and Engineering: R: Reports*, Vol. 49, pp. 89-112, 2005.

72. M. K. Yeh, T. H. Hsieh and N. H. Tai, "Fabrication and Mechanical Properties of Multi-walled Carbon Nanotubes/epoxy Nanocomposites", *Materials Science and Engineering: A*, Vol. 483-484, pp. 289-292, 2008.

73. N. H. Tai, M. K. Yeh and J. H. Liu, "Enhancement of the Mechanical Properties of Carbon Nanotube/phenolic Composites Using a Carbon Nanotube Network as the Reinforcement", *Carbon*, Vol. 42, pp. 2774-2777, 2004.

74. F. H. Gojny, M. H. G. Wichmann, U. Kopke, B. Fiedler and K. Schulte, "Carbon Nanotube-reinforced Epoxy-composites: Enhanced Stiffness and Fracture Toughness at Low Nanotube Content", *Composites Science and Technology*, Vol. 64, pp. 2363-2371, 2004.

75. K. L. Kepple, G. P. Sanborn, P. A. Lacasse, K. M. Gruenberg and W. J. Ready, "Improved Fracture Toughness of Carbon Fiber Composite Functionalized with Multi Walled Carbon Nanotubes", *Carbon*, Vol. 46, pp. 2026-2033, 2008.

76. Y. L Chen, B. Liu, Y. Huang and K. C. Hwang, "Fracture Toughness of Carbon Nanotube-reinforced Metal- and Ceramic-Matrix Composites", *Journal of Nanomaterials*, Vol. 2011, pp. 1-9, 2011.

77. T. H. Hsieh, A. J. Kinloch, A. C. Taylor and S. Sprenger, "The Effect of Silica Nanoparticles and Carbon Nanotubes on the Toughness of a Thermosetting Epoxy Polymer, *Journal of Applied Polymer Science*, Vol. 119, pp. 2135-2142, 2011.

78. W. Zhang, R. C. Picu and N. Koratkar, "Suppression of Fatigue Crack Growth in Carbon Nanotube Composites", *Applied Physics Letters*, Vol. 91, pp. 193109 1-3, 2007.

79. B. Marrs, R. Andrews and D. Pienkowski, "Multiwall Carbon Nanotubes Enhance the Fatigue Performance of Physiologically Maintained Methyl Methacrylate-styrene Copolymer", *Carbon*, Vol. 45, pp. 2098-2104, 2007.

80. W. Zhang, R. C. Picu and N. Korakar, "The Effect of Carbon Nanotube Dimensions and Dispersion on the Fatigue Behavior of Epoxy Nanocomposites", *Nanotechnology*, Vol. 19, pp. 285709 1-5, 2008.

81. F. H. Gojny, J. Nastalczyk, Z. Roslaniec and K. Schulte, "Surface Modified Multi-walled Carbon Nanotubes in CNT/epoxy-composites", *Chemical Physics Letter*, Vol. 370, pp. 820-824, 2003.

82. H. Chen, O. Jacobs, W. Wu, G. Rudiger and B. Schadel, "Effect of Dispersion Method on Tribological Properties of Carbon Nanotube Reinforced Epoxy Resin Composites", *Polymer Testing*, Vol. 26, pp. 351-360, 2007.

83. H. F. Wei, G. H. Hsiue and C. Y. Liu, "Surface Modification of Multi-walled Carbon Nanotubes by a Sol-gel Reaction to Increase Their Compatibility with PMMA resin", *Composites Science and Technology*, Vol. 67, pp. 1018-1026, 2007.

84. R. M. Bagwell and R. C. Wetherhold, "Fiber Pullout Behavior and Impact Toughness of Short Shaped Copper Fibres in Thermoset Matrices", *Composite: Part A*, Vol. 36, pp. 683-690, 2004.

85. F. H. Gojny, M. H. G. Wichmann, B. Fiedler and K. Schulte, "Influence of Different Carbon Nanotubes on the Mechanical Properties of Epoxy Matrix

Composites – a Comparative Study", *Composites Science and Technology*, Vol. 65, pp. 2300-2313, 2005.

86. M. H. G. Wichmann, K. Schulte and H. D. Wagner, "On Nanocomposite Toughness", *Composites Science and Technology*, Vol. 68, pp. 329-331, 2008.

87. M. K. Yeh, N. H. Tai and J. H. Liu, "Mechanical Behavior of Phenolic-based Composites Reinforced with Multi-walled Carbon Nanotubes", *Carbon*, Vol. 44, pp. 1-9, 2006.

88. D. Qian, E. C. Dickey, R. Andrews and T. Rantell, "Load Transfer and Deformation Mechanisms in Carbon Nanotube-polystyrene Composites", *Applied Physics Letters*, Vol. 76, pp. 2868-2870, 2000.

89. J. Blanco, E. J. Garcia, R. G. D. Villoria and B. L. Wardle, "Limiting Mechanisms of Mode I Interlaminar Toughening of Composites Reinforced with Aligned Carbon Nanotubes", *Journal of Composite Materials*, Vol. 43, pp. 825-841, 2009.

90. Azom, *Particle Size – US Sieve Series and Tyler Mesh Size Equivalents*. Accessed (02/03/11), Available from: http://www.azom.com/article.aspx?ArticleID=1417.

91. Nanoresins, *Modifying epoxy resins with nanocomposites*, Accessed (12/1/06), 2005. Available from: http://www.nanoresins.ag/content/view/52/55/lang,en/.

92. J. Garcia-Cespedes, S. Thomasson, K. B. K. Teo, I. A. Kinloch and W. I. Milne, E. Pascual and E. Bertran, "Efficient Diffusion Barrier Layers for the Catalytic Growth of Carbon Nanotubes on Copper Substrates", *Carbon*, Vol. 47, pp. 613-621, 2009.

93. C. Singh, M. S. P. Shaffer and A. H. Windle, "Production of Controlled Architectures of Aligned Carbon Nanotubes by an Injection Chemical Vapour Deposition Method", *Carbon*, Vo. 41, pp. 359-368, 2003.

94. B. Olalde, J. M. Aizpurua, A. Garcia, I. Bustero, I. Obieta and M. J. Jurado, "Single-walled Carbon Nanotubes and Multi-walled Carbon Nanotubes Functionalized with Poly(L-lactic acid): a Comparative Study", *Journal of Physical Chemistry C*, Vol. 112, pp. 10663-10667, 2008.

95. ASTM D 638, *Standard Test Method of Tensile Properties of Plastics*, American Society for Testing and Materials, 2001.

96. ISO-527-1, *Plastics - Determination of Tensile Properties - Part 1: General Principles*, International Standards Organisation, 1993.

97. ASTM D 5045, *Standard Test Methods for Plane-Strain Fracture Toughness and Strain Energy Release Rate of Plastic Materiasl*, American Society for Testing and Materials, 1999.

98. BS 7448-4, *Fracture Mechanics Toughness Tests - Part 4: Method for Determination of Fracture Resistance Curves and Initiation Values for Stable Crack Extension in Metallic Materials*, British Standards Institute,1997.

99. J. G. Williams and H. Ford, "*Stress-strain Relationships for Some Unreinforced Plastics*", *Journal of Mechanical Engineering Science*, Vol. 6, pp. 405-417, 1964.

100. ASTM E 647, *Standard Test Methods for Measurement of Fatigue Crack Growth Rates*, American Society for Testing and Materials, 2008.

101. ISO 15850, *Plastics-determination of Tension-tension Fatigue Crack Propagation - Linear Elastic Fracture Mechanics (LEFM) Approach*, International Organization for Standardization, 2002.

102. J. Sohn-Lee, *The Fatigue Behaviour of Nano-modified Epoxy Adhesives*, PhD Thesis in Mechanical Engineering, Imperial College London, 2009.

103. Wikipedia, *Differential Scanning Culorimery*, Accessed (04/05/10), available from: http://en.wikipedia.org/wiki/Differential_scanning_calorimetry.

104. ISO 11357-2, *Plastics-Differential Scanning Calorimetry (DSC)*, International Organization for Standardization, 1999.

105. Y. H. Liao, O. Marietta-Tondin, Z. Liang, C. Zhang and B. Wang, "Investigation of the Dispersion Process of SWNTs/SC-15 Epoxy Resin Nanocompsoites", *Materials Science and Engineering: A*, Vol. 385, pp. 175-181, 2004.

106. E. A. Zaragoza-Gontreras, E. D. Lozano-Rodriguez, M. Roman-Aguirre, W. Antunez-Flores, C. A. Hernandez-Escobar, S. G. Flores-Gallardo and A. Aguilar-Elguezabal, "Evidence of Multi-walled Carbon Nanotube Fragmentation Induced by Sonication During Nanotube Encapsulation via Bulk-suspension Polymerization", *Micron*, Vol. 40, pp. 621-627, 2009.

107. S. Y. Park, P. G. Kim, I. B. Jeong, D. W. Shin, J. B. Yoo and S. H. Hyun, "Fabrication of Flexible Transparent Conductive Film (TCF) Using Single Walled Carbon Nanotubes", *Journal of Nanoscience and Nanotechnology*, Vol. 9, pp. 7491-7495, 2009.

108. R. D. Brooker, *The Morphology and Toughness of Thermoplastic-modified Epoxy Polymer with Carbon Nanotubes or Silica Nanoparticles*, PhD Thesis in Mechanical Engineering, Imperial College London, 2008.

109. J. L. Capelo, C. Maduro and C. Vilhena, "Discussion of Parameters Associated with the Ultrasonic Solid-liquid Extraction for Elemental Analysis (Total Content) by Electrothermal Atomic Absorption Spectrometry. An Overview", *Ultrasonics Sonochemistry*, Vol. 12, pp. 225-232, 2005.

110. G. C. Papanicolaou, A. G. Xepapadaki and G. A. Aggelakopoulos, "Mechanical Characterization and Modeling of Aluminum-epoxy Particulate Composites with and without Notches", *IVth International Conference Times of Polymers and Composites*, Vol. 1042, pp. 126-128, 2008.

111. E. H. Andrews, *Fracture in Polymers*, Oliver and Boyd, London, 1986.

112. M. Jarnthong, Z. Peng and C. Nakason, "Surface Modification of Silica Nanoparticles for Reinforcement of Epoxidized Natural Rubber", *Advanced Materials Research*, Vol. 93-94, pp. 370-376, 2010.

113. Technical Data Sheet for Silane Glass Treatment "AP115", 3M Industrial Adhesives and Tapes Division, St. Paul (USA), 2008.

114. United Chemical Technologies Ltd, *Silane Coupling Agent Guide*, Accessed 05/05/2010, Available from: www.nnitedchem.com.

115. D. Broek, *Elementary Engineering Fracture Mechanics*, Noordhoff International Publishing, 1974.

116. T. H. Hsieh, A. J. Kinloch, K. Masania, A. C. Taylor and S. Sprenger, "The Mechanisms and Mechanics of the Toughening of Epoxy Polymers Modified with Silica Nanoparticles", *Polymer*, Vol. 51, pp. 6284-6294, 2010.

117. T. P. Selvin, J. Kuruvilla and T. Sabu, "Mechanical Properties of Titanium Dioxide-filled Polystyrene Microcomposites", *Materials Letters*, Vol. 58, pp. 281-289, 2004.

118. L. F. Cai, Y. L. Mai, M. Z. Rong, W. H. Ruan and M. Q. Zhang, "Interfacial Effect in Nano-silica/polypropylene Composites Fabricated by in-situ Chemical Blowing", *Express Polymer Letters*, Vol. 1, pp. 2-7, 2007.

119. A. J. Kinloch, C. F. Korenberg, K. T. Tan and J. F. Watts, "Crack Growth in Structural Adhesive Joints in Aqueous Environments", *Journal of Materials Science*, Vol. 42, pp. 6353-6370, 2007.

120. J. Chrusciel and L. Slusarski, "Synthesis of Nanosilica by the Sol-gel method and its Activity toward Polymers", *Materials Science*, Vol. 21, pp. 461-469, 2003.

121. T. B. Lewis and L. E. Nielsen, "Dynamic Mechanical Properties of Particulate-Filled Composites", *Journal of Applied Polymer Science*, Vol. 14, pp. 1449-1471, 1970.

122. M. Imanaka, Y. Takeuchi, Y. Nakamura, A. Nishimura and T. Iida, "Fracture Toughness of Spherical Silica-filled Epoxy Adhesives", *International Journal of Adhesion and Adhesives*, Vol. 21, pp. 389-396. 2001.

123. J. Lee and A. F. Yee, "Inorganic Particle Toughening I: Micro-mechanical Deformations in the Fracture of Glass Bead Filled Epoxies", *Polymer*, Vol. 42, pp. 577-588, 2001.

124. S. K. Brown, "Mechanisms of Fracture in Filled Thermosetting Resins", *The British Polymer Journal*, pp. 24-30, March 1980.

125. Wikipedia, Carbon nanotube, Accessed (05/03/09), Available from: *http://en.wikipedia.org/wiki/Carbon_nanotube*

126. I. M. Low and C. Shi, "Vickers Indentation Responses of Epoxy Polymers", *Journal of Materials Science Letters*, Vol. 17, pp. 1181-1183, 1998.

127. M. K. Yeh and T. H. Hsieh, "Dynamic Properties of Sandwich Beams with MWNT/polymer Nanocomposites as Core Materials", *Composites Science Technology*, Vol. 63, pp. 2930-2936, 2008.

128. F. H. Gojny and K Schulte, "Functionalisation Effect on the Thermo-mechanical Behaviour of Multi-wall Carbon Nanotube/epoxy-composites", *Composites Science and Technology*, Vol. 64, pp. 2303-2308, 2004.

129. P. C. Ma, J. K. Kim and B. Z. Tang, "Effect of Silane Functionalization on the Properties of Carbon Nanotube/epoxy Nanocomposites*", Composites Science and Technology*, Vol. 67, pp. 2965-2972, 2007.

130. Y. Zhou, F. Pervin, L. Lewis and S. Jeelani, "Fabrication and Characterization of Carbon/epoxy Composites Mixed with Multi-walled Carbon Nanotubes", *Materials Science and Engineering A*, Vol. 475, pp. 157-165, 2008.

131. J. Sumfleth, K. Prehn, M. H. G. Wichmann, S. Wedekind and Karl Schulte, "A Comparative Study of the Electrical and Mechanical Properties of Epoxy Nanocomposites Reinforced by CVD- and Arc-grown Multi-wall Carbon Nanotubes", *Composites Science and Technology*, Vol. 70, pp. 173-180, 2010.

132. N. Yu, Z. H. Zhang and S. Y. He, "Fracture Toughness and Fatigue Life of MWCNT/epoxy Composites, *Materials Science and Engineering: A*, Vol. 494, pp. 380-384, 2008.

133. P. B. Bowden, "A Criterion for Inhomogeneous Plastic Deformation", *Philosophical Magazine A, Physics of Condensed Matter, Defects and Mechanical Properties*, Vol. 22, pp.455-462, 1970.

134. P. B. Bowden and J.A. Jukes, "The Plastic Flow of Isotropic Polymers", *Journal of Materials Science*, Vol. 7, pp. 52-63, 1972.

135. W. Zhang, I. Srivastava, Y.F. Zhu, R. C. Picu and N. A. Koratkar, "Heterogeneity in Epoxy Nanocomposites Initiates Crazing: Significant Improvements in Fatigue Resistance and Toughening", *Small*, Vol. 5, pp. 1403-1407, 2009.

136. M. A. Rafiee, J. Rafiee, Z. Wang, H. Song, Z. Z. Yu and N. Koratkar, "Enhanced Mechanical Properties of Nanocompsoites at Low Graphene Content, *ACS Nano*, Vol. 3, pp. 3884-3898, 2009.

137. M. Fernando, W. W. Harjoprayitno and A. J. Kinloch, "A Fracture Mechanics Study of the Influence of Moisture on the Fatigue Behaviour of Adhesively Bonded Aluminium-alloy Joints", *International Journal of Adhesion and Adhesives*, Vol. 16, pp. 113-119, 1996.

138. S. Azari, M. Papini, J. A. Schroeder and J. K. Spelt, "The Effect of Mode Ratio and Bond Interface on the Fatigue Behavior of a Highly-toughened Epoxy", *Engineering Fracture Mechanics*, Vol. 77, pp. 395-414, 2010.

139. M. L. Abel, A. N. N. Adams, A. J. Kinloch, S. J. Shaw and J. F. Watts, "The Effects of Surface Pretreatment on the Cyclic-fatigue Characteristics of Bonded Aluminium-alloy Joints", *International Journal of Adhesion and Adhesives*, Vol. 26, pp. 50-61, 2006.

140. A. Gilat, R. K. Goldberg and G. D. Roberts, "Strain Rate Sensitivity of Epoxy Resin in Tensile and Shear Loading", *NASA/TM*, 213595, 2005.

141. T. Belytschko, S. P. Xiao and R. Ruoff, "Effects of Defects on the Strength of Nanotubes: Experimental-Computational Comparisons", *Los Alamos National Laboratory, Preprint Archive, Physics*, pp. 1-6, 2002.

142. A. H. Barber, S. R. Cohen and H. D. Wagner, "Measurement of Carbon Nanotube-polymer Interfacial Strength", *Applied Physics Letters*, Vol. 82, pp. 4140-4142, 2003.

143. A. Hernandez-Perez, F. Aviles, A. May-Pat, A. Valadez-Gonzalez, P. J. Herrera-Franco and P. Bartolo-Perez, "Effective Properties of Multiwalled Carbon Nanotubes/epoxy Composites Using Two Different Tubes", *Composites Science and Technology*, Vol. 68, pp. 1422-1431, 2008.

144. P. J. Pearce, C. E. M. Morris and B. C. Ennis, "Rubber Toughening of Practical Tetraglycidyl Methylenedianiline-Piperidine Adduct Systems", *Polymer*, Vol. 37, pp. 1137-1150, 1996.

145. A. J. Kinloch, K. Masania, A. C. Taylor, S. Sprenger and D. Egan, "The Fracture of Glass-fibre-reinforced Epoxy Composites Using Nanoparticle-modified Matrices", *Journal of Materials Science*, Vol. 43, pp. 1151-1154, 2008.

146. J. Karger-Kocsis and K. Friendrich, "Fatigue Crack Propagation and Related Failure in Modified, Anhydride-cured Epoxy Resins", *Colloid & Polymer Science*, Vol. 270, pp. 549-562, 1992.

147. Adhesives & Sealants Industry, New Epoxy Tougheners Widen the Adhesive-formulating Window, Accessed (25/05/2011). Available from: *http://www.adhesivesmag.com/Articles/Cover_Story/2e5170fc67ac8010VgnVCM100000f932a8c0*

148. C. M. Manjunatha, A. C. Taylor, A. J. Kinloch and S. Sprenger, "The Cyclic-fatigue Behaviour of an Epoxy Polymer Modified with Micron-rubber and Nano-silica Particles", *Journal of Materials Science*, Vol. 44, pp. 4487-4490, 2009.

149. J. Karger-Kocsis and K. Friedrich, "Microstructure-related Fracture Toughness and Fatigue Crack Growth Behaviour in Toughened, Anhydride-cured Epoxy Resins", *Composites Science and Technology*, Vol. 48, pp. 263-272, 1993.

150. D. Purslow, "Matrix Fractography of Fibre-reinforced Epoxy Composites", *Composites*, Vol. 17, pp. 289-303, 1986.

151. R. D. Brooker, F. J. Guild and A. C. Taylor, "Quantifying the Dispersion of Carbon Nanotubes in Thermoplastic-toughened Epoxy Polymers", *Journal of Materials Science*, Vol. 46, pp. 3108-3118, 2011.

152. Y. Huang and A. J. Kinloch, "Modelling of the Toughening Mechanisms in Rubber-modified Epoxy Polymers: Part I: Finite Element Analysis Studies", *Journal of Materials Science*, Vol. 27, pp. 2753-2762, 1992.

153. F. J. Guild and R. J. Young, "A Predictive Model for Particulate-filled Composite Materials. Part 1 Hard Particles", *Journal of Materials Science*, Vol. 24, pp. 298-306, 1989.

154. F. J. Guild and R. J. Young, "A Predictive Model for Particulate Filled Composite Materials. Part 2 Soft Particles", *Journal of Materials Science*, Vol. 24, pp. 2454-2460, 1989.

155. C. I. Vallo, L. Hu, P. M. Frontini and R. J. J. Williams, "Toughened-hybrid Epoxies - Influence of the Rubber-phase Morphology on Mechanical-properties", *Journal of Materials Science*, Vol. 29, pp. 2481-2486, 1994.

156. J. Baller, N. Becker, M. Ziehmer, M. Thomassey, B. Zielinski, U. Muller and R. Sanctuary, "Interactions Between Silica Nanoparticles and an Epoxy Resin Before and During Network Formation", *Polymer*, Vol. 50, pp. 3211-3219, 2009.

157. J. Chen, Z. Huang and J. Zhu, "Size Effect of Particles on the Damage Dissipation in Nanocomposites", *Composites Science and Technology*, Vol. 67, pp. 2990-2996, 2007.

158. D. Hull and T. W. Clyne, *An Introduction to Composite Materials*. Cambridge University Press, 1996.

159. A. Peigney, C. Laurent, E. Flahaut, R. R. Bacsa and A. Rousset, "Specific Surface Area of Carbon Nanotubes and Bundles of Carbon Nanotubes", *Carbon*, Vol. 39, pp. 507-514, 2001.

160. B. Fiedler , F. H. Gojny, M. H. G. Wichmann, M. C. M. Nolte and K. Schulte, "Fundamental Aspects of Nano-reinforced Composites", *Composites Science and Technology*, Vol. 66, pp. 3115-3125, 2006.

161. X. Sun and W. Zhao, "Prediction of Stiffness and Strength of Single-walled Carbon Nanotubes by Molecular-mechanics based Finite Element Approach", *Materials Science and Engineering A*, Vol. 390, pp. 366-371, 2005.

162. J. C. Halpin and N. J. Pagano, "The Laminate Approximation for Randomly Oriented Fibrous Composites", *Journal of Composite Materials*, Vol. 3, pp. 720, 1969.

163. J. C. Halpin, "Stiffness and Expansion Estimates for Oriented Short Fiber Composites", *Journal of Composite Materials*, Vol. 3, pp.732-734, 1969.

164. J. C. Halpin and S. W. Tsai, *Air Force Material Laboratory Technical Report*, AFML-TR-67-423, 1969.

165. H. L. Cox, "The Elasticity and Strength of Paper and other Fibrous Materials", *British Journal of Applied Physics*, Vol. 3, pp. 72-79, 1951.

166. M. K. Yeh, N. H. Tai and T. H. Peng, "Experimental Study and Theoretical Analysis on the Mechanical Properties of SWNTs/phenolic Composite", *Composite: Part B*, Vol. 39, pp. 926-932, 2008.

167. E. Bugnicourt, *Development of Sub-micro Structured Composites based on an Epoxy Matrix and Pyrogenic Silica*, PhD Thesis in Engineer in Materials of the National Institute of Applied Science of Lyon, 2005.

168. J. Spevacek, "Structures and Interactions in Polymer System Characterized by NMR Methods", *The Open Macromolecules Journal*, Vol. 4, pp. 22-25, 2010.